

**A critical evaluation of the "Tilt-Depth" method of  
magnetic data interpretation: Application to  
aeromagnetic data from NorthEastern  
(NE) Nigeria.**

**by**

**Esuene Mkpongonyong Akpekanim Samson**

**Submitted in accordance with the requirements  
for the degree of Doctor of Philosophy.**



**The University of Leeds  
School of Earth and Environment**

**December, 2012**

# Declarations

**The candidate confirms that the work submitted is his own and that appropriate credit has been given where reference has been made to the work of others.**

**This copy has been supplied on the understanding that it is copyright material and that no quotation from the thesis may be published without proper acknowledgement.**

©2012 The University of Leeds and Esuene M. A. Samson

## Acknowledgements

I am grateful to Professor J. D. Fairhead for his painstaking supervision of this study and for providing proprietary GETECH Group Plc. UK's software (GETgrid), the "Tilt-Depth" method menu in Geosoft Plc.'s Oasis montaj, as well as much of the Nigerian aeromagnetic data grid used for this study. Periodic criticisms from Professor G. W. Stuart and Dr. Ahmed Salem, and initial support with Matlab programming by Dr. Simon Williams are highly appreciated. Professor Greg Houseman and Dr. Jon Mound were very generous with advice, often on short notice.

Special thanks to Dr. Sally Baritt (ITC, Netherlands) for providing complementary digital dataset for parts of Northern Nigeria, and to Professor Chiedu. S. Okereke (University of Calabar, Nigeria), who provided aeromagnetic survey map sheets of NorthEastern Nigeria and invaluable moral support during this study. Professor Richard J. Blakely (U.S. Geological Survey) and Dr. Alan Reid (Reid Geophysics, UK) are gratefully acknowledged, for their insightful help with complex concepts in magnetic data interpretation. Dr. Simon Campbell, Dr. Matthew and Mrs. Melanie Stewart, Neil Woburn, Mrs. Kaxia Lee, Paul East, Dr. Chris Green and Mrs. Sarah Wilkinson, all of GETECH Plc., UK, as well as Professor Aniekan E. Edet and Dr. Therese N. Nganje (both of University of Calabar, Nigeria), are appreciated for their support.

I am eternally indebted to my dearly beloved wife, Dawn, who has endured immense loneliness and made the best job of managing our daughter, Idara Gwyneth, as well as my fatigue while I bridged my huge knowledge gap and conducted this study. My profound gratitude goes to my hero and father who taught me to persevere and surmount challenges; to my mother for her tireless labour of love; and to my siblings for always keeping me on the straight and narrow. The unflinching moral support of my parents-in-law, Terry and Daphne Gedney, is well appreciated.

I am also grateful to my colleagues: Stephen G. Amuda, for his enduring friendship and being an excellent landlord during the waning days of this study; Lucky C. Moffat, for his invaluable challenges on DSP and Linux programming; Ben Dando for his invaluable support with Shell and Matlab scripting; and Sheona Masterton, for geomagnetism banter. Isaac C. S Okereke, Oghenechavwe Akoroda, Christian Akpan and Lanre Akinrogunde are well appreciated for the comic relief they provided.

Thanks also to Professor Kathryn A. Whaler (University of Edinburgh, UK) and Dr. Jon Mound for their constructive criticism of the finished thesis during my viva. Above all else, I thank Jehovah God for making all good things possible and beautiful in His TIME.

# Abstract

To simplify the complex total magnetic field intensity anomalies ( $\Delta T$ ) on datasets obtained from locations close to the geomagnetic Equator (inclinations  $|\alpha| \leq 20^\circ$ ) such datasets are routinely reduced-to-equator (RTE), since they cannot be stably reduced-to-pole (RTP). RTE anomalies tend to have small amplitudes and exhibit azimuth-based anisotropy, unlike RTP anomalies. Anisotropy describes the dependence of the amplitude and shape of an RTE anomaly on the strike direction of its source. For example, an East-West striking contact/fault will generate a strong RTE anomaly response whereas a North-South striking equivalent will not. Where adjacent sources occur, anisotropy causes interference between anomalies, displacing anomalies relative to their sources. This makes using magnetic data to map structures in regions that are close to the geomagnetic equator difficult or potentially of limited value. This thesis develops a strategy to interpret RTE datasets and applies it to determine the basement structure in NE Nigeria where  $|\alpha| \leq 8^\circ$ . This area has  $>50\%$  of the basement concealed beneath Cretaceous and Quaternary sediments of the Benue Trough and Chad basin, respectively. The aim of the study is to structurally map the basement underlying the Benue and Chad rifted basins in NE Nigeria, by tracing and determining the depths of basement faults and associated structures.

The first-order derivative-based "Tilt-Depth" method has been evaluated to determine its effectiveness when applied to RTE datasets to determine the location and depth of structures. The method was tested first using RTE and RTP equivalents of synthetic  $\Delta T$  datasets obtained from profiles across East-West striking, 2D contacts at various depths, inclinations of effective magnetisation ( $\phi$ ), and dips ( $d$ ). RTP datasets were used throughout as reference models. Errors in "Tilt-Depth" method estimates were invariant to changes in depth, but sensitive to changes in  $\phi$  and  $d$  of sources. At error limits of 0-20%, the method effectively estimates locations and depths of 2D contacts when dip is within the  $75 \leq d^\circ \leq 105$  range, inclination of remanent magnetisation relative to induced magnetisation is within the  $155 \leq \beta^\circ \leq 205$  range (magnetisations are collinear), and Koenigsberger ratio ( $Q$ ) of remanent to induced magnetisation amplitudes  $\leq 1$ . Relationships between  $Q$ ,  $\alpha$ ,  $\beta$  and  $\phi$  suggests that the simplification of remanence-laden anomalies due to magnetisations being collinear results from deviations of  $\phi$  from  $\alpha$  of  $\leq 12^\circ$  when  $Q \leq 1$ . Similar deviations occur between  $\phi$  and  $\alpha$ , for all  $\beta$  values, when  $Q \leq 0.2$ . Hence, remanent magnetisation is negligible for RTP or RTE datasets when *a priori* information suggests  $Q \leq 0.2$ .

The "Tilt-Depth" method was further tested for anisotropy-induced anomaly interference effects using RTP or RTE of the Complex "Bishop" Model (CBM) and Tanzania grids. The CBM grid contains 2D contacts of various strikes and three-dimensional (3D) sources with non-2D contacts at various depths (all precisely known), and satisfy the  $d$ ,  $\phi$  and  $Q$  requirements above. The Tanzania grid presented a real dataset from a Karoo rift basin, where more randomly striking 2D contacts occur at unknown depths. For comparison, the second vertical derivative, analytic signal amplitude, local wavenumber, and the horizontal gradient magnitudes of  $\theta$  ( $HGM_{(\theta)}$ ) and  $\Delta T$  ( $HGM_{(\Delta T)}$ ) methods were also tested using these grids. Locations estimated from all these methods show that: **(1)** Sources of all shapes and strikes are correctly imaged on RTP grids; **(2)** North-

South striking 2D contacts are not imaged at all on RTE datasets, but can be inferred from linear alignments of stacked short wavelength East-West striking anomalies; **(3)** 2D contacts with strikes ranging from N045 to N135° are correctly imaged on RTE datasets; **(4)** Anomalies from poorly isolated 2D contacts with  $N\pm 020^\circ$  strikes interfere to further complicate RTE datasets, making it difficult to correctly image these sources; and **(5)** RTE anomalies from 3D sources tend to smear in an East-West direction, extending such anomalies well past edges of their sources along this direction. These North-South striking non-2D edges are not imaged at all, whilst their East-West striking non-2D (Northern and Southern) edges are correctly imaged.

Depths estimated for 2D and non-2D contacts with strikes ranging from N045 to N135°, from RTP and RTE of the CBM grids, using the local wavenumber, analytic signal amplitude and  $|\theta| = 27^\circ$ -based "Tilt-Depth" methods show that: **(1)** "Tilt-Depth" and local wavenumber methods underestimate the actual depth of sources, while the analytic signal amplitude method provided both severely underestimated and overestimated depths. Thus, "Tilt-Depth" and local wavenumber estimates were easier to utilise and interpret; **(2)** "Tilt-Depth" and local wavenumber methods underestimate 2D contacts from RTP and RTE grids by up to 25 and 35% of their actual depths, respectively; **(3)** "Tilt-Depth" and local wavenumber methods, respectively, underestimate depths of East-West striking non-2D edges of 3D sources by about 35 and 30% from the RTP grid; and **(4)** "Tilt-Depth" method consistently underestimates non-2D contacts from RTE grids by up to 40%.

Using knowledge gained from the above tests, all the methods were applied to a NE Nigeria  $\Delta T$  (RTE) dataset, to delineate basement structures in the area. The dataset was a 1 km upward-continued grid with 1 km  $\times$  1 km cell size, and extended well beyond NE Nigeria into Niger, Chad and Cameroon Republics. While basement depths were estimated from the dataset using the "Tilt-Depth" and local wavenumber methods only, these methods and the second vertical derivative, analytic signal amplitude, local wavenumber, as well as the horizontal gradient magnitudes of  $\theta$  ( $HGM_{(\theta)}$ ) and  $\Delta T$  ( $HGM_{(\Delta T)}$ ) methods, were used to map source edge locations.

A basement structure map of NE Nigeria was obtained using the above methods and found not to be dominated by North-South striking faults. Instead the basement is dissected mainly by near-vertical, NE-SW trending faults against which NW-SE or E-W trending faults terminate. The relationship between these inferred faults, basement horsts, volcanic plugs, and basement depressions, and outcrop information suggests that rifting was episodic as the mainly NorthEast directed rift propagation direction was occasionally deflected by transcurrent faults to relieve differential stresses built up from wall rock and/or crustal resistance. Apparent stress relief features include the Yola basin, flood basalts, Lamurde Anticline and Kaltungo Inlier. A number of isolated depocenters, mainly half grabens, with sediment thickness exceeding 11 km seem to occur in NE Nigeria. Outside these depocenters, basement occur at depths generally shallower than 0.5 km, except where intra-basinal horsts occur, at depths shallower than 2.5 km. These depths agree well with well information and seismic data interpretation, and show the SW Chad basin depocenter to be isolated from adjoining basins in Cameroon, Chad and Niger Republics.

# **Dedication**

To

**Janet Akpe'kanim Samson (nee Janet Ude),**

and to the everlasting memories of

**Akpe'kanim (Mkpongonyong) Samson Inoh Akpe'kanim**

and

**Esuene (Samson) Inoh Akpe'kanim.**

# Contents

0.1	Glossary of terms and keywords . . . . .	xix
<b>1</b>	<b>Introduction</b>	<b>1</b>
1.1	Background . . . . .	1
1.2	The research problem and motivation . . . . .	2
1.3	Aims and objectives . . . . .	3
1.4	Structure of thesis . . . . .	4
<b>2</b>	<b>Introducing geomagnetic field concepts, research problems and methodology adopted for interpreting TMI anomaly datasets</b>	<b>5</b>
2.1	The geomagnetic field and its sources . . . . .	5
2.1.1	The core-derived or main field ( $\mathbf{B}_{core}$ ) and its dipolar constituent ( $\mathbf{B}_{dipole}$ )	7
2.1.2	The crustal or lithospheric geomagnetic field ( $\mathbf{B}_{crust}$ ) . . . . .	8
2.1.3	The external geomagnetic field ( $\mathbf{B}_{external}$ ) . . . . .	9
2.2	Magnetisation ( $\mathbf{J}_v$ ), Total magnetic field intensity (TMI), magnetic susceptibility ( $k$ )	10
2.2.1	Volume magnetisation ( $\mathbf{J}_v$ ) . . . . .	10
2.2.2	Magnetic field strength or intensity ( <b>TMI</b> ) . . . . .	11
2.2.3	Induced and remanent magnetisations ( $\mathbf{J}_i$ and $\mathbf{J}_r$ ), magnetic susceptibility ( $k$ ) and Koenigsberger ratio ( $Q$ ) . . . . .	12
2.2.4	Initial conclusions . . . . .	13
2.3	Problems with TMI anomaly ( $\Delta T$ ) datasets obtained at or close to the geomagnetic equator . . . . .	14
2.3.1	Effects of inclination ( $\alpha$ ) on spectral contents of $\Delta T$ datasets . . . . .	14
2.3.2	Retaining the spectral content and simplifying shapes of $\Delta T$ . . . . .	18
2.3.3	Problems with RTE-transformed $\Delta T$ . . . . .	19
2.4	Methodology adopted: Choice of $\Delta T$ model source . . . . .	20
2.4.1	The two-dimensional (2D) magnetic contact model . . . . .	20
2.4.2	Problems due to RTE of $\Delta T$ responses from 2D magnetic contacts . . . . .	21
2.5	Semi-automatic methods and $\Delta T$ data interpretation . . . . .	25
2.5.1	Spatial Cartesian derivatives of $\Delta T$ from 2D magnetic sources . . . . .	25
2.5.2	The horizontal gradient magnitude of $\Delta T$ (HGM <sub>(<math>\Delta T</math>)</sub> ) method . . . . .	29
2.5.3	The analytic signal amplitude (ASA) method . . . . .	30
2.5.4	The local wavenumber, LW or SPI <sup>TM</sup> method . . . . .	31
2.5.5	Estimating magnetic susceptibility contrast ( $\delta k$ ) and dip ( $d$ ) of 2D sources	31
2.6	Tilt angles ( $\theta$ ) of $\Delta T$ and the “Tilt-Depth” method . . . . .	32
2.6.1	Tilt angles ( $\theta$ ) of $\Delta T$ . . . . .	32
2.6.2	The “Tilt-Depth” method . . . . .	34

<b>3</b>	<b>The “Tilt-Depth” method: Tested using profile <math>\Delta T</math> datasets from 2D magnetic contacts</b>	<b>35</b>
3.1	The “Tilt-Depth” method . . . . .	35
3.2	Methodology adopted for testing the “Tilt-Depth” method . . . . .	37
3.2.1	Obtaining profile $\Delta T$ , its derivatives and $\theta$ datasets from contacts . . . . .	37
3.2.2	Defining errors in estimates of location and depth of magnetic geological features . . . . .	38
3.3	Testing the method using vertical, East-West striking contacts . . . . .	40
3.3.1	Effect of varying inclination of induced magnetisation ( $\alpha$ ) . . . . .	40
3.3.2	Reducing the effects of magnetic anomaly interference on errors in "Tilt-Depth" method estimates . . . . .	44
3.3.3	Estimates based either on the horizontal distance $+h$ or $-h$ . . . . .	46
3.3.4	Effect of varying remanent magnetisation on estimates from RTP or RTE datasets . . . . .	48
3.4	Testing the “Tilt-Depth" method using dipping, East-West striking contacts . . . . .	54
3.4.1	Estimates of locations . . . . .	55
3.4.2	Estimates of depths . . . . .	55
3.5	Testing the “Tilt-Depth" method using vertical contacts with various strike directions . . . . .	56
3.5.1	TMI anomaly ( $\Delta T$ ) shapes from contacts at RTP and RTE compared . . . . .	57
3.5.2	Location estimates . . . . .	58
3.5.3	Estimates of depths . . . . .	60
<b>4</b>	<b>Application of “Tilt-Depth” method to gridded “Bishop” model <math>\Delta T</math> datasets</b>	<b>62</b>
4.1	Introduction . . . . .	62
4.2	“Bishop” model (BM) datasets . . . . .	64
4.2.1	Simple “Bishop” model (SBM) $\Delta T$ grid . . . . .	65
4.2.2	Complex “Bishop” model (CBM) $\Delta T$ grid . . . . .	65
4.3	RTP and RTE-transformed SBM and CBM grids compared . . . . .	68
4.3.1	TMI anomaly ( $\Delta T$ ) grids . . . . .	68
4.3.2	Tilt angle ( $\theta$ ) grids . . . . .	72
4.4	Prerequisites for analysing location and depth estimates . . . . .	75
4.5	Location estimates from RTP and RTE-transformed SBM and CBM grids . . . . .	77
4.6	Depth estimates from RTP and RTE of SBM and CBM grids . . . . .	80
4.6.1	Methods used for analysing depth estimates . . . . .	81
4.6.2	Comparisons between distributions of actual and estimated depths . . . . .	82
4.6.3	Relationship between estimated and actual depths of “Bishop” model sources . . . . .	87
<b>5</b>	<b>Application of other methods to complex “Bishop” model (CBM) datasets.</b>	<b>99</b>
5.1	Introduction. . . . .	99
5.2	Comparisons between RTP and RTE grids obtained from each method. . . . .	100
5.2.1	Amplitude-based methods. . . . .	101
5.2.2	Phase-based methods. . . . .	105

5.2.3	Comparisons using profiles across RTP and RTE grids. . . . .	107
5.3	Location estimates. . . . .	109
5.3.1	Comparison between estimates from RTP and RTE grids. . . . .	110
5.3.2	Strategies for estimating location of source edges from RTE datasets. . . . .	113
5.3.3	Structure maps derived from CBM (RTP and RTE) grids. . . . .	115
5.4	Depths estimated from all source locations using ASA and LW methods. . . . .	117
5.4.1	Distributions of ASA and LW estimates compared with actual basement depths. . . . .	119
5.4.2	ASA and LW estimates from all source locations on RTP or RTE grid. . . . .	123
5.5	Depths estimated from equivalent RTP and RTE locations using the ASA, LW and $\theta = \pm 27^\circ$ -based “Tilt-Depth” methods. . . . .	129
5.6	Summary of edge location and depth estimation from RTE grids . . . . .	134
<b>6</b>	<b>Interpretation of northeastern (NE) Nigeria aeromagnetic dataset.</b>	<b>136</b>
6.1	The study area (NE Nigeria). . . . .	136
6.1.1	Location . . . . .	136
6.1.2	Geology . . . . .	138
6.1.3	Tectonic framework. . . . .	140
6.2	NE Nigeria TMI anomaly ( $\Delta T$ ) dataset and its quality. . . . .	142
6.2.1	The dataset. . . . .	142
6.2.2	Dataset quality. . . . .	145
6.2.3	Reduced-to-equator (RTE) of dataset. . . . .	147
6.3	Qualitative structural interpretation . . . . .	149
6.3.1	Amplitudes, shapes and wavelengths of anomalies ( $\Delta T$ ) from NE Nigeria. . . . .	150
6.3.2	Location and trends of basement-involved faults, and other structures in NE Nigeria. . . . .	155
6.3.3	Attitude of basement faults in NE Nigeria. . . . .	161
6.4	Depth estimates from semi-automatic inversion methods. . . . .	163
6.5	Distribution of magnetic susceptibilities in NE Nigeria. . . . .	169
<b>7</b>	<b>Discussion and conclusions</b>	<b>171</b>
7.1	Discussion . . . . .	171
7.1.1	General observations from comparing RTE and RTP of profile and gridded model $\Delta T$ datasets . . . . .	171
7.1.2	Mapping NE Nigeria basement . . . . .	173
7.1.3	Propositions and synopsis of tectonic evolution . . . . .	175
7.1.4	Significance to petroleum exploration . . . . .	182
7.1.5	Significance to seismic hazard preparedness . . . . .	183
7.2	Conclusions . . . . .	184
7.2.1	Locating structural edges from RTE grids . . . . .	184
7.2.2	Depths of structural edges from RTE grids . . . . .	186
7.2.3	Structural features of the basement . . . . .	187

<b>References</b>	<b>188</b>
<b>Appendices</b>	<b>203</b>
<b>A Attitude and amplitudes of the main or dipolar geomagnetic field.</b>	<b>204</b>
<b>B “Tilt-Depth” method estimates from two-dimensional (2D) magnetic contacts.</b>	<b>207</b>
<b>C “Tilt-Depth” method applied to “Bishop” model <math>\Delta T</math> grids.</b>	<b>211</b>
<b>D Estimates from “Bishop” model TMI anomaly (<math>\Delta T</math>) grids using other methods.</b>	<b>217</b>
<b>E Comparisons between interpretations from RTP and RTE of a Southern Tanzania TMI anomaly (<math>\Delta T</math>) grid.</b>	<b>224</b>
<b>F NE Nigeria dataset.</b>	<b>231</b>
<b>G Correspondences requesting more NE Nigeria datasets for constraint.</b>	<b>246</b>
<b>H Magnified, and/or more annotated, versions of some NE Nigeria-wide figures presented in chapter 6.</b>	<b>248</b>

## List of Figures

2.1	A sketch of the radial average power ( $R_n$ ) of models of the geomagnetic field obtained from the low-Earth orbiting satellite. . . . .	6
2.2	Grids showing variations in the size and shape of $\Delta T$ of dipolar (spherical) anomalous magnetic sources with changes in inclinations of induced magnetisation, $\alpha$ (Sources at constant depth = 0.5 km, and with dipole moment magnitude, $m = 10$ Wb m). . . . .	15
2.3	Comparisons between South-North (S-N) profiles across grids shown in figure 2.2 and equivalent grids with twice as much dipole moment (Mom = $m$ ) magnitudes. . . . .	16
2.4	A comparison between South-North, S-N (Green-coloured) and East-West, E-W (Pink-coloured) profiles across $\Delta T$ grids from model dipolar sources. . . . .	18
2.5	A magnetic body in different 2D-type contacts with non-magnetic rocks. . . . .	21
2.6	Schematic showing changes in the distribution of surface magnetostatic charges with changes in the inclination of the inducing geomagnetic field vector. . . . .	22
2.7	Schematic showing North-South, N-S (Red-coloured) and East-West, E-W (Blue-coloured) profiles across North-South (N-S) cross sections of $\Delta T$ resulting from the magnetostatic charge distributions shown in figure 2.6. . . . .	23
2.8	An illustration to show the generation of linear dipolar $\Delta T$ (string of pearls) from magnetostatic charges along East-West (E-W) corners of locally discontinuous or en-echelon North-South (N-S) striking 2D magnetic contacts. . . . .	24
2.9	Sketch showing the spatial relationship between the magnetic contact/step model and the variables used to derive its $\Delta T$ and spatial Cartesian amplitude derivatives. . . . .	26
2.10	Strike (Spatial horizontal orientation) of 2D magnetic contacts relative to the geomagnetic North (N) pole. . . . .	27
3.1	$\theta$ curves from RTP and RTE of $\Delta T$ datasets. . . . .	36
3.2	Effects of inclination of induced magnetisation on spatial Cartesian derivatives of $\Delta T$ of vertical, E-W contacts. . . . .	41
3.3	Effects of inclination of induced magnetisation on $\theta$ of $\Delta T$ from vertical, E-W contacts. . . . .	41
3.4	Effects of depth and inclination of induced magnetisation ( $\alpha$ ) on horizontal locations estimates of vertical, East-West striking contacts. . . . .	42
3.5	Effects of depth and inclination of induced magnetisation ( $\alpha$ ) on "Tilt-Depth" method estimates of depths of East-West striking, vertical contacts. . . . .	43
3.6	Length of arc (Ranges) of $\theta$ used in testing the "Tilt depth" method. . . . .	44
3.7	Percentage error in depth estimates ( $Err_{(\%)}{}_z$ ) using "Tilt-Depth" method from $ \theta =45, 30, 26.6, 15, 10$ and $5$ : Effects of induced magnetisation and magnetic anomaly interference. . . . .	46

3.8	Percentage error ( $Err_{(\%)}$ ) in depth estimates from $\Delta T$ data from either $+\theta$ ( $-h$ or $-h_s$ ) or $-\theta$ ( $+h$ or $+h_s$ ) values. . . . .	47
3.9	Spatial relationship between induced, remanent and effective (net) magnetisation ( $\mathbf{J}_i$ , $\mathbf{J}_r$ and $\mathbf{J}_v$ ). . . . .	49
3.10	Relationship between magnitudes and inclinations of effective magnetisation and selected Koenigsberger ratio (Q) values. Induced magnetisation is either at RTP or RTE and various magnitudes. . . . .	51
3.11	Angular difference between the inclinations of the inducing magnetisation ( $\alpha$ ) and that of the effective inclination ( $\phi$ ) for selected Koenigsberger ratios (Q). Deviation is with respect to the direction of the inducing field. $\alpha$ is either at RTP or RTE and various magnitudes. . . . .	52
3.12	$\theta$ -transformed $\Delta T$ curves obtained from vertical, West-East striking contacts when at RTP or RTE, and characterised by remanent magnetisations of various Q and inclinations ( $\beta=0, 30, 90$ and $180^\circ$ ). . . . .	53
3.13	The 0-20% error distribution of "Tilt-Depth" method estimates of locations and depths of remanence-laden East-West striking contacts at RTP and RTE. . . . .	54
3.14	Effect of dips ( $d$ ) of East-West striking contacts on their location estimates. . . . .	56
3.15	"Tilt-depth" method estimates of depths of dipping, East-West striking magnetic contacts at RTP or RTE, using $\theta = \pm 27$ , or 45 range. . . . .	56
3.16	Effect of strike azimuth of vertical contacts on amplitude and shape of $\Delta T$ , when effective and induced magnetisations are vertical (RTP). . . . .	57
3.17	Effect of strike azimuth of vertical contacts on amplitude and shape of $\Delta T$ , when effective and induced magnetisations are horizontal (RTE). . . . .	58
3.18	Effects of the strike azimuth ( $A$ ) of vertical contacts on $\theta$ of their $\Delta T$ (RTP or RTE). . . . .	59
3.19	Effect of strike direction on amplitudes of Cartesian derivatives and $\theta$ of $\Delta T$ at locations of vertical contacts, at RTP or RTE. . . . .	60
3.20	Effect of azimuthally varying strike of vertical contacts on "Tilt-Depth" estimates of depth, when contact is either at RTP or RTE. . . . .	61
4.1	Work-flow adopted for evaluating estimates obtained from "Bishop" model (BM) and real Southern Tanzania $\Delta T$ datasets. . . . .	63
4.2	The input "Bishop" model basement grids. . . . .	65
4.3	"Bishop" model $\Delta T$ grids generated by magnetic basement at depths shown in figure 4.2a, for inducing magnetisation with inclination, $\alpha = 25^\circ$ , declination= $0^\circ$ and strength= $50,000$ nT. . . . .	66
4.4	RTP and RTE transformed equivalents of the SBM grid. . . . .	68
4.5	RTP and RTE transformed equivalents of the CBM grid. . . . .	70
4.6	$\theta$ equivalents of the SBM grid. . . . .	73
4.7	$\theta$ equivalents of the CBM grid. . . . .	74
4.8	Locations of edges of $\Delta T$ sources on the input BM basement grids. . . . .	76
4.9	Actual depth of edges of all anomalous sources on the simple and complex BM grids. . . . .	76

4.10	“Tilt-Depth” method estimates of location of model anomaly sources on SBM and CBM grids. . . . .	77
4.11	“Tilt-Depth” estimation of depth of fault scarp (FS) edges from SBM (RTP and RTE) grids, using $0 \leq  \theta  \leq 45$ range. . . . .	81
4.12	“Tilt-Depth” estimation of depth of geological structures; fault scarp (FS) and magnetic contact edges, on CBM (RTP and RTE) grids, using $0 \leq  \theta  \leq 45$ range. . . . .	82
4.13	Histograms showing the distribution of “Tilt-Depth” method estimates of model source depths from SBM (RTP and RTE) grids. . . . .	83
4.14	Histograms showing the distribution of “Tilt-Depth” method estimates of model source depths from CBM (RTP and RTE) grids. . . . .	85
4.15	“Tilt-Depth” method estimates of SBM (RTP and RTE) source depths, using the $ \theta  = 0$ to 45, 27 or 10 distance. . . . .	88
4.16	Error in “Tilt-Depth” method estimates of SBM (RTP and RTE) source depths. The method was implemented in three modes, using $ \theta  = 0$ to 45, 27 or 10 distance. . . . .	89
4.17	Relationship between SBM (RTP) and SBM (RTE) source depths estimated using $ \theta  = 0$ to 45, 27 or 10 distance. . . . .	91
4.18	“Tilt-Depth” method estimates of source depths from CBM (RTP and RTE) grids, using $ \theta  = 0$ to 45, 27 or 10 distance. . . . .	93
4.19	Error in “Tilt-Depth” method estimates of CBM (RTP and RTE) source depths, using $ \theta  = 0$ to 45. . . . .	94
4.20	Relationship between depths estimated using $ \theta  = 0$ to 45, 27 or 10 distance at corresponding CBM (RTP) and CBM (RTE) grid locations. . . . .	97
5.1	Horizontal gradient magnitude ( $HGM_{(\Delta T)}$ ) and analytic signal amplitude (ASA) of CBM (RTP and RTE) $\Delta T$ grids. . . . .	102
5.2	Second vertical derivative (SVD) of CBM (RTP and RTE) of $\Delta T$ grids. . . . .	104
5.3	Local wavenumber (LW) and $HGM_{(\theta)}$ of CBM (RTP and RTE) of $\Delta T$ grids. . . . .	106
5.4	Location and orientation of profiles used to compare method-specific functions in figures 5.2, 5.1 and 5.3. . . . .	108
5.5	NW-SE oriented profiles of method-specific special functions of CBM (RTP and RTE) grids. . . . .	109
5.6	NE-SW and E-W oriented profiles of method-specific special functions of CBM (RTP and RTE) grids. . . . .	110
5.7	Comparisons between location estimates derived from various derivatives of the CBM (RTP and RTE) grids. . . . .	111
5.8	Comparisons between all estimates of edge locations from CBM (RTP or RTE) $\Delta T$ grids. . . . .	114
5.9	Structure maps derived from CBM (RTP and/or RTE) grids. . . . .	116
5.10	Unedited and edited ASA estimates from CBM (RTP and RTE) grid sources. . . . .	118
5.11	LW estimates from CBM (RTP and RTE) grid sources. . . . .	118
5.12	Histograms for ASA, LW and $-27 \leq \theta \leq 27$ estimates of source depths from RTP and RTE grids. . . . .	120

5.13	Histograms for edited ASA estimates of depths of source edges on CBM (RTP and RTE) grids. . . . .	121
5.14	Histograms for LW estimates of depths of source edges on CBM (RTP and RTE) grids. . . . .	122
5.15	Comparisons between actual depth and depths estimated from RTP and RTE grids, using ASA and LW methods. . . . .	124
5.16	Comparisons between errors in depths estimated from RTP and RTE grids, using ASA method. . . . .	127
5.17	Comparisons between errors in depths estimated from RTP and RTE grids, using LW method. . . . .	128
5.18	Depths estimated at equivalent locations on the CBM (RTP and RTE) grids, using the ASA, LW and $\theta = \pm 27$ -based “Tilt-Depth” methods. . . . .	131
5.19	Error in depths estimated at equivalent locations on the CBM (RTP and RTE) grids, using the ASA, LW and $\theta = \pm 27$ -based “Tilt-Depth” methods. . . . .	133
6.1	Maps showing the location, extent and elevation of the study area. . . . .	137
6.2	Simplified geological and tectonic map of NE Nigeria. . . . .	139
6.3	Lithostratigraphic chart for NE Nigeria. . . . .	139
6.4	The NE Nigeria TMI anomaly ( $\Delta T$ ) dataset. . . . .	143
6.5	Inclination and declination of the regional DGRF (1945-1985), NE Nigeria. . . .	147
6.6	RTE of NE Nigeria $\Delta T$ grid (Figure 6.4). . . . .	148
6.7	3 <sup>rd</sup> -order Butterworth-filtered versions of the RTE of NE Nigeria $\Delta T$ grid. . . . .	149
6.8	Bouguer gravity anomaly (BA) grid of NE Nigeria. . . . .	151
6.9	SVD and $\theta$ maps of NE Nigeria. . . . .	157
6.10	ASA and $HGM_{(\Delta T)}$ maps of NE Nigeria. . . . .	157
6.11	LW and $HGM_{(\theta)}$ maps of NE Nigeria. . . . .	158
6.12	Gross magnetic basement structure map of NE Nigeria. . . . .	159
6.13	A comparison between $\theta = 0$ contour lines for upward-continued versions of the CBM (RTP) grid and an extract from NE Nigeria RTE grid. . . . .	162
6.14	Maps showing the spread of $\theta = 0$ contours of variously upward-continued NE Nigeria $\Delta T$ (RTE) dataset away from structural edges/faults. . . . .	163
6.15	Attitude of prominent faults and volcanic features in NE Nigeria basement, inferred using $\theta = 0$ contours of variously upward-continued NE Nigeria (RTE) grids. . . . .	164
6.16	Local wavenumber (LW) method depth estimates. . . . .	165
6.17	“Tilt-Depth” method depth estimates, from $\theta = \pm 45$ and $\theta = \pm 27$ ranges. . . . .	166
6.18	North-South (NS) and East-West (WE) profiles showing the variations in depths estimated using local wavenumber (LW) and $\theta = \pm 45$ and $\theta = \pm 27$ -based “Tilt-Depth” methods from SouthWestern Chad basin, NE Nigeria. . . . .	167
6.19	Depth-structure map of sedimentary basin area of NE Nigeria showing the major depositional centres and horst structures. . . . .	168
6.20	Relative magnetic susceptibility contrasts estimated for NE Nigeria from using “Tilt-Depth”-analytic signal amplitude method. . . . .	169

6.21	Relative magnetic susceptibility distribution map for NE Nigeria basement. . . . .	170
7.1	Inferred directions of propagation of the Benue rift, Mesozoic tectonism, and sedimentary features of NE Nigeria. . . . .	177
A.1	Global map of the inclination of the main geomagnetic field, i.e., 11 <sup>th</sup> generation IGRF for 1900-2015 (Finlay et al., 2010), showing the location of NorthEastern Nigeria across the geomagnetic equator. . . . .	205
A.2	Global map of the magnitude of the main geomagnetic field, i.e., 11 <sup>th</sup> generation IGRF for 1900-2015 Finlay et al. (2010). Map also shows the location of North-Eastern Nigeria. . . . .	206
B.1	Testing computer codes using the independence of $\theta$ from vertical, E-W magnetic 2D contacts at RTP on susceptibility contrasts ( $\delta k$ ). . . . .	207
B.2	Effect of inclination of induced magnetisation on derivatives of the $\Delta T$ from vertical, E-W, 2D contacts in the Southern geomagnetic hemisphere. . . . .	207
B.3	Effects of induced magnetisation and depth of vertical, East-West striking 2D magnetic contacts. . . . .	208
B.4	Absolute error in depths of dipping East-West striking, 2D contacts at RTP or RTE, estimated using the $\theta = \pm 27$ or 45 range. . . . .	208
B.5	Effects of the strike azimuth of vertical, 2D contacts on first-order Cartesian derivatives (total horizontal derivatives, THDR and vertical derivatives) of their $\Delta T$ (RTP). 209	
B.6	Effects of the strike azimuth of vertical, 2D contacts on first-order Cartesian derivatives (total horizontal derivatives, THDR and vertical derivatives) of their $\Delta T$ (RTE). 210	
C.1	Enhanced (GETgrid <sup>TM</sup> ) visualization of the input grids for “Bishop” models. . . . .	211
C.2	Enhanced (GETgrid <sup>TM</sup> ) visualization of the “Bishop” model $\Delta T$ grids for inclination of induced magnetisation of 25°. . . . .	211
C.3	Enhanced (GETgrid <sup>TM</sup> ) visualization of the simple “Bishop” $\Delta T$ model (SBM) grids. . . . .	212
C.4	Enhanced (GETgrid <sup>TM</sup> ) visualization of the complex “Bishop” model (CBM) grids. 212	
C.5	$\theta$ equivalents of RTE-transformed simple and complex “Bishop” model (SBM and CBM) grids. . . . .	213
C.6	Examples showing how locations of edges on the input basement grids in figures 4.2a and 4.2b were extracted. . . . .	214
C.7	An attempt to extract the actual locations of structural edges on the model “Bishop” basement grid, using analytic signal amplitude. . . . .	215
C.8	$\theta = \pm 27$ estimates from CBM (RTP and RTE) grid sources. . . . .	216
D.1	Comparisons between estimates of edge locations on CBM (RTP or RTE) TMI anomaly grids. . . . .	217
D.2	Demonstrating the additional clarity gained by editing estimated locations obtained from CBM (RTP) grid, using $\mathbf{HGM}_{(\Delta T)}$ method. . . . .	218

D.3	Equivalent locations obtained from $\theta$ of CBM (RTP and RTE) grids (In red), compared with $\theta$ of CBM (RTP and RTE) grid locations (In green and black, respectively). . . . .	219
D.4	Equivalent locations obtained from $\mathbf{HGM}_{(\Delta T)}$ of CBM (RTP and RTE) grids (In red), compared with $\mathbf{HGM}_{(\Delta T)}$ of CBM (RTP and RTE) grid locations (In green and black, respectively). . . . .	220
D.5	Equivalent locations obtained from $\mathbf{HGM}_{(\theta)}$ of CBM (RTP and RTE) grids (In red), compared with $\mathbf{HGM}_{(\theta)}$ of CBM (RTP and RTE) grid locations (In green and black, respectively). . . . .	221
D.6	Equivalent locations obtained from $\mathbf{LW}$ of CBM (RTP and RTE) grids (In red), compared with $\mathbf{LW}$ of CBM (RTP and RTE) grid locations (In green and black, respectively). . . . .	222
D.7	Equivalent locations obtained from $\mathbf{ASA}$ of CBM (RTP and RTE) grids (In red), compared with $\mathbf{ASA}$ of CBM (RTP and RTE) grid locations (In green and black, respectively). . . . .	222
D.8	Windowed versions of the $\mathbf{LW}$ of CBM (RTP and RTE) grids. . . . .	223
F.1	Available TMI datasets from NE Nigeria. . . . .	232
F.2	Spatial relationship between inclination and TMI amplitude of the regional DGRF in NE Nigeria. . . . .	234
F.3	Power spectra for NE Nigeria $\Delta T$ grid and its RTE equivalent. . . . .	236
F.4	Low-pass (LP)-filtered TMI (RTE) anomaly data from NE Nigeria upward-continued to: (a) 5 km and (b) 8 km. . . . .	237
F.5	Locations estimated from SVD and $\theta$ maps of NE Nigeria. . . . .	238
F.6	Locations estimated from $\mathbf{ASA}$ and $\mathbf{HGM}_{(\Delta T)}$ maps of NE Nigeria. . . . .	239
F.7	Locations estimated from $\mathbf{LW}$ and $\mathbf{HGM}_{(\theta)}$ maps of NE Nigeria. . . . .	240
F.8	Additive inverse ( $\times -1$ ) of $\theta \geq 0$ map of NE Nigeria. . . . .	241
F.9	Additive inverse ( $\times -1$ ) of $\theta$ -transformed 5 km (a) and 8 km (b) upward-continued NE Nigeria $\Delta T$ (RTE) grid. . . . .	242
F.10	North-South (NS) and East-West (WE) profiles showing the variations in depths estimated using local wavenumber ( $\mathbf{LW}$ ) and $\theta = \pm 45$ and $\theta = \pm 27$ -based “Tilt-Depth” methods from SouthWestern Chad basin, NE Nigeria. . . . .	243
F.11	North-South (NS) profiles showing variations in depths estimated using $\mathbf{LW}$ and $\theta = \pm 45$ and $\theta = \pm 27$ -based “Tilt-Depth” methods from Upper Benue Trough, NE Nigeria. . . . .	244
F.12	East-West (E-W) profiles showing variations in depths estimated using $\mathbf{LW}$ and $\theta = \pm 45$ and $\theta = \pm 27$ -based “Tilt-Depth” methods from Upper Benue Trough, NE Nigeria. . . . .	245
G.1	Letter to a Nigerian government official requesting his assistance with the new aeromagnetic dataset from Nigeria (Chandler, 2010). . . . .	246

G.2 Letter to a Chevron Inc, USA official requesting his assistance with additional geological and geophysical dataset from NE Nigeria and neighbouring regions. Similar letters were also sent to Total and Shell. . . . . 247

## List of Tables

2.1	Variation of the geometrical factors of $\Delta T$ (Equations (2.1.3c) and (2.2.4)) with latitudes and inclination of the inducing geomagnetic field ( $\alpha$ , Equation (2.1.4)).	14
3.1	Depth conversion factors, $zF$ for distances between the location of $\theta = 0$ and different magnitudes of $\theta$ ( $ \theta $ ) used to implement “Tilt depth” method.	45
3.2	Magnitudes of induced and remanent magnetisation used for examining the effects of remanence at RTP and RTE.	49
4.1	Retention of depth estimates from FS on the SBM (RTP or RTE) grid, relative to the total number of actual depth locations in figure 4.9a.	84
4.2	Comparing $CoV$ statistics of depth estimates from CBM (RTP and RTE) grids (Figure 4.14) with actual source depths (Figure 4.9).	86
4.3	Retention of depth estimates from CBM (RTP and RTE) sources, relative to the number of actual depth locations in figures 4.8b and 4.9a.	87
4.4	Statistical parameters for least-squares functions to each cross-plot in figures 4.15 and 4.16.	89
4.5	Comparing equations and statistics of least-squares functions to cross-plots shown in figures 4.18 and 4.19.	92
4.6	Summary of average percentage depth error for estimates from magnetic (2D and non-2D) contacts on CBM (RTP and RTE) grids. The magnitude of maximum difference in range of error are shown in brackets. Data were extracted from figure 4.19.	96
4.7	Comparing statistical parameters for least-squares fits to cross-plots in figure 4.20.	98
5.1	Correlation statistics for location estimates from CBM (RTP or RTE) grids.	112
5.2	Summary of ASA, LW and $\theta = \pm 27$ estimates.	120
5.3	Distributions of ASA and LW estimates, at source edges.	122
5.4	Comparing equations and statistics of least-squares functions to cross-plots shown in figure 5.15.	125
5.5	Correspondence between grid locations of estimated and actual depths of CBM sources, and correlation between the depth values.	126
5.6	Equations and statistics of least-squares functions to cross-plots shown in figure 5.16.	127
5.7	Summary of average depth error for ASA, LW and $-27 \leq \theta \leq 27$ estimates for magnetic (2D and non-2D) contacts on RTP or RTE grid. The magnitude of maximum difference in range of error are shown in brackets. Data for ASA and LW estimates were extracted, respectively, from figures 5.16 and 5.17. Data for $-27 \leq \theta \leq 27$ estimates were previously presented in table 4.19.	129
5.8	Equations and statistics of least-squares functions to cross-plots shown in figure 5.18.	132
5.9	Equations and statistics of least-squares functions to cross-plots shown in figure 5.19.	134

5.10	Summary of average error in depths estimated at corresponding 2D and non-2D contacts locations on CBM (RTP and RTE) grids, using the ASA, LW and $\theta = \pm 27$ -based “Tilt-Depth” methods. The magnitude of maximum difference in range of error are shown in brackets. . . . .	134
E.1	Geomagnetic field elements for $\Delta T$ subgrids extracted from Southern Tanzania grid (Figures E.3a, E.3b and E.3c). . . . .	228

## 0.1 Glossary of terms and keywords

$\Delta T$  refers to anomaly in total magnetic field intensity, TMI ( $T$ ).

**Additive inverse** of a function (e.g., Tilt angles or  $\theta$ ) refers to the function obtained when the original function is multiplied by -1 (e.g.,  $-\theta$ ). It is used mainly to align functions of RTE anomalies with their RTP equivalents.

**Anomaly or geophysical anomaly** refers to "the difference between the observed (measured) geophysical field or survey value and the value that would be observed at the same location if the Earth were more uniform than it is (Lyatsky, 2004). Anomalies in gravity and magnetic field measurements used in this study are the *Bouguer anomaly (BA)* and **total magnetic field intensity (TMI) anomaly ( $\Delta T$ )**, respectively.

**Azimuth** refers to angular measurements, relative to the North direction, of the orientation of an oblong object (structure) on the  $x, y$  (horizontal) plane. The North direction may refer to the Earth's geographic or magnetic field coordinate system. Most references to azimuth connotes the latter usage in this study .

**Anisotropy** refers to variations in the shape and amplitude (spectral characteristics) of  $\Delta T$  as a consequence of the azimuth of a magnetic structure.

**Basement or magnetic basement** rocks refers to basic and mafic crystalline igneous and/or metamorphic rocks that are rich in naturally-occurring magnetic minerals (Section 2.2.4).

**CBM and SBM** refers to complex "Bishop model"  $\Delta T$  grid (Section 4.2.2) and simple "Bishop model"  $\Delta T$  grid (Section 4.2.1), respectively.

**Cutoff wavelength ( $\lambda$ ) or Cutoff wavenumber ( $k$ )** refers to a user-specified wavelength or spatial frequency (wavenumber) value, which marks the boundary between wavelengths or wavenumbers that any chosen filter must allow to pass or stop.  $\lambda$  and  $k$  are related by the expression:  $k = \frac{2\pi}{\lambda}$ . According to Smith (2003), cutoff  $\lambda$  are usually defined to be at points where the amplitude of the signal is reduced to 70.7% (for analog filters), and anywhere between the range 50-99% for digital filters. The cutoff  $\lambda$  for GETgrid<sup>TM</sup> is at 50% of the amplitude response.

**Depth** refers to the vertical location (0, 0,  $z$ ) of edges of 2D and/or 3D structures.

**Error** quantifies the difference between the estimated and actual value of either the location or depth of a magnetic edge (Section 3.2.2).

**Absolute error ( $Err_{(abs)}$ )** refers to the absolute difference between the actual and estimated

quantity. It is  $Err_{(abs)_{x_0}}$  in terms of the horizontal location ( $x_0$ ) of magnetic edges, and  $Err_{(abs)_z}$  in terms of the depth ( $z$ ) of magnetic edges.

**Relative error**  $Err_{(rel)}$  refers to the ratio of the absolute error ( $Err_{(abs)}$ ) to the actual (model) depth.  $Err_{(rel)_{x_0}}$  in reference to the location of magnetic edges, but  $Err_{(rel)_z}$  in reference to the depth of magnetic edges.

**Percentage error** ( $Err_{(\%)}$ ) expresses relative error ( $Err_{(rel)_{x_0}}$ ) in percent.

**Faults** refer to “elongated zones of concentrated shearing, parallel to which adjacent rocks have been offset” (Mandl, 2000, p. 101). Faults typically have lengths that are many orders of magnitude larger than their widths. The closest approximation to a fault is the *two-dimensional (2D) magnetic contact/step* model (Grant & West, 1965).

**GETECH** refers to GETECH Group Plc., UK.

**GETgrid<sup>TM</sup>** is GETECH’s fully licensed Gravity and Magnetics software.

**Grid or gridded** describe data presented in three-dimensional ( $x, y, z$ ) format.

**Location** refers to the horizontal location ( $x, y, 0$ ) of edges of magnetic structures.

**International Geomagnetic Reference Field (IGRF)** is a global spherical harmonic model which describes the smooth, but time-varying, main Earth’s core-sourced component of the dipolar geomagnetic field and its annual rate of change or secular variation (Section 2.1.1).

**Koenigsberger ratio,  $Q$**  is the ratio between the magnitudes of remanent and induced components of magnetisation. It reflects the relative importance of each component for any magnetic rock volume (Section 2.2.3).

**Magnetisation,  $\mathbf{J}$**  refers to magnetic moments  $\mathbf{m}$  per unit volume of magnetic material, in the direction of the axis of an inducing source (Section 2.2.3).

**Pole or magnetic pole** refers interchangeably to the North or South magnetic poles of the Earth, points at which the TMI ( $T$ ) is perpendicular to the Earth’s surface. These poles are different from *geomagnetic poles*, i.e., locations at which the axis of the dipolar geomagnetic field intersects the Earth’s surface.

**Profile** or the *principal profile* (Sheriff, 2002) refers to a geophysical traverse defined such that it is perpendicular to the regional strike of an oblong or linear structure.

**Profile direction ( $A^\circ$ )** refers to the orientation of a survey profile relative to the magnetic North pole. It ranges from  $0^\circ$ , for North-South profiles, to  $\pm 90^\circ$ , for West-East profiles (Fig-

ure 2.10).

**RTE (Reduction-to-equator)** refers to transformation of  $\Delta T$  datasets to their equivalents at the magnetic equator.

**RTP (Reduction-to-pole)** refers to transformation of  $\Delta T$  datasets to their equivalents at the magnetic pole.

**Semi-automatic methods** are inverse techniques for determining parameters like the location, depth, dip and/or susceptibility contrast of magnetic source edges. Such methods include the “Tilt-Depth”, second vertical derivative (SVD), analytic signal amplitude (ASA), local wavenumber (LW), and horizontal gradient magnitude (HGM) of  $\theta$  ( $HGM_{(\theta)}$ ) and  $\Delta T$  ( $HGM_{(\Delta T)}$ ) methods.

**SLAR** refers to **S**ide **L**ooking **A**irborne **R**adar.

**SRTM** refers to **S**huttle **R**adar **T**opography **M**ission.

**Strike, strike direction or azimuth ( $\eta$ )** of edges of oblong magnetic sources describes their angular orientation on the horizontal plane ( $x, y$ ) relative to the magnetic North (N) direction (Section 2.5.1).  $\eta$  was kept perpendicular to profile azimuth or orientation,  $A$  (Figure 2.10), and ranges from 0 to  $360^\circ$ , with subsets described as follows throughout this study:

- (i)  $\eta=N000, N360$  or  $N180^\circ$  (North-South, N-S);
- (ii)  $\eta=N\pm 20^\circ$  (Near-North-South, Near-N-S);
- (iii)  $\eta=N021$  to  $N044^\circ$  (NorthNorthEast-SouthSouthWest, NNE-SSW);
- (iv)  $\eta=N045$  to  $N089^\circ$  (NorthEast-SouthWest, NE-SW);
- (v)  $\eta=N090$  or  $N270^\circ$  (West-East, W-E);
- (vi)  $\eta=N091$  to  $N135^\circ$  (NorthWest-SouthEast, NW-SE); and
- (vii)  $\eta=N136$  to  $N159^\circ$  (NorthNorthWest-SouthSouthEast, NNW-SSE).

# Chapter 1

## Introduction

---

### 1.1 Background

A magnetic survey reflects lateral variations in magnetic field strength or intensity of the rocks underlying its area of coverage. Since the 1940s, it has been routine to use scalar magnetometers which measure the total magnetic field intensities (TMI or  $T$ ) for these surveys (Vacquier et al., 1951, Reford & Sumner, 1964).<sup>1</sup> Magnetic surveys may be acquired on land, from the air (using aircraft, e.g., fixed-wing planes, or spacecraft like satellites) or on ships. Irrespective of the mode of acquisition, responses from sedimentary rocks are extremely low in amplitude compared with those from basement rocks. This is because  $T$  also reflects the magnetisation of naturally-occurring magnetic minerals, which are ubiquitous in basic and mafic crystalline igneous or metamorphosed rocks (Grauch et al., 2001, 2004).<sup>2</sup> Sedimentary rocks are effectively considered to be non-magnetic, where magnetic basement rocks occur, so that magnetic responses are attributed to the magnetic basement (Nettleton, 1971, Grant, 1985).<sup>3</sup>  $T$  datasets are thus, effective in mapping lineaments (discontinuities) or contrasts in the magnetic basement, for example.

Major advantages of aeromagnetic survey data over other geophysical data include its lower cost, rapid speed of acquisition and aerial coverage, as well as easy access to otherwise inaccessible geographic terrains (Dobrin & Savit, 1988; Blakely, 1996 and Reynolds, 1997). Such data are routinely used to: (1) map locations and depths of faults in the basement (Cordell & Grauch, 1985; Phillips, 1997; Phillips, 2000; Grauch et al., 2004; Airo & Wennerström, 2010); (2) aid seismic resolution of basement depth, where salt tectonism and/or intra-basinal basalts diffract seismic energy (Reynisson et al., 2008, 2009); (3) map cultural magnetic sources (Wilson et al., 1997); as well as (4) detect unexploded ordnances, UXO (Butler, 2003). Grauch & Hudson (2007) and Hudson et al. (2008) have also used high-resolution aeromagnetic datasets to map the distribution of intra-sedimentary magnetic faults.

---

<sup>1</sup> $T$  is the vectorial sum of both the local magnetic field perturbations due to magnetite-bearing rocks and the main geomagnetic field intensity (Blakely, 1996).

<sup>2</sup>A detailed discussion of these concepts is presented in chapter 2.

<sup>3</sup>Unless otherwise indicated, basement will be used where the magnetic basement is implied.

The assumption in obtaining these  $T$  measurements is that both the directions of rock magnetisation and the inducing main field are vertical (Blakely & Simpson, 1986). Departures from this fundamental assumption introduces phase shifts to the measured anomalies ( $\Delta T$ ).<sup>4</sup> Consequently, such anomalies are laterally displaced relative to the location of their sources, and have shapes that are different to anomalies for which magnetisation directions are vertical (MacLeod et al., 1993, Nabighian et al., 2005 and Li, 2008).

## 1.2 The research problem and motivation

To simplify and center anomalies over their sources, magnetic survey data from locations where the Earth's geomagnetic field inclination is outside the  $\pm 20^\circ$  range are usually reduced-to-pole, i.e., RTP (Baranov, 1957; MacLeod et al., 1993). On the other hand, data obtained from localities with inclination within this range are usually reduced-to-equator, RTE (Leu, 1981). RTP and RTE anomalies are therefore symmetric and centred above their sources. However, unlike RTP anomalies which have constant shapes irrespective of orientation (strike) of their sources, the shape of RTE anomalies change with orientation. Hence, RTE anomalies exhibit anisotropy and generally show no simple correlation with their sources (Nabighian et al., 2005; Arkani-Hamed, 2007 and Li, 2008). Locations from which  $\Delta T$  data are potentially affected by RTE-induced anisotropy include: (1) the Northern part ( $\geq 50\%$ ) of Southern America; (2) all of Western Africa and most of Central and Eastern Africa ( $\geq 50\%$ ) of continental Africa; (3) most of the Arabian Sea; (4) all of SouthEast Asia; as well as (5) the large swathes of ocean bordering these lands (Appendix A, figure A.1). This belt includes some of the world's major fossil fuel provinces (BP, 2012).

Forecasts of our world's unsustainable energy consumption (IEA, 2011; BP, 2012) show that this primarily tropical belt is increasingly a prime target for increased location of renewable energy projects and for fossil fuels prospecting. Therefore, the need for studies aimed at facilitating a better understanding of the gross geology, shape, and configuration of the basement underlying this belt cannot be over-emphasized. For this reason, much effort has been, and continues to be, expended to develop algorithms for minimising anisotropy of simplified (RTE)  $\Delta T$  datasets from regions with geomagnetic field inclinations within the  $\pm 20^\circ$  range. Such algorithms include those by Silva (1986), Hansen & Pawlowski (1989), MacLeod et al. (1993), Keating & Zerbo (1996), Li & Oldenburg (2001), Luo & Xue (2009) and Luo et al. (2010). Li (2008) evaluated some of these algorithms, showing them to be incapable of minimising anisotropy effects and strongly advised against their use in quantitative interpretation of data from locations with low geomagnetic field inclination.

Nigeria, with geomagnetic field inclination in the range  $\pm 10^\circ$ , lies within this belt (Appendix A, figure A.1). The Nigerian Government has acquired country-wide aeromagnetic datasets since

---

<sup>4</sup>Magnetic anomalies ( $\Delta T$ ) are local departures from the Earth's main (regional) magnetic field values or the projection of local magnetic field intensities induced in source bodies along the direction of the regional magnetic field (Blakely & Simpson, 1986). More on this concept is presented in chapter 2.

1964 (McCurry, 1989), most of which have been integrated into the African Magnetic Mapping Project (AMMP) compilation (ULIS, 1993), extending the dataset well beyond Nigeria into the adjoining basement and sedimentary outcrops of northern Cameroon and southern Niger Republics. However, perhaps owing to low geomagnetic field inclination-related complexities and the lack of simple correlations between the dataset and outcrop and/or subcrop geology, only a handful of studies exist that have used slivers of the Nigerian aeromagnetic dataset. They include: (i) qualitative studies (Ajakaiye et al., 1986; Ofoegbu, 1985); (ii) quantitative profile data interpretations (Abubakar et al., 2010; Ofoegbu, 1988) using spectral analysis method (Spector & Grant, 1970); and (iii) the only regional qualitative and quantitative interpretation, integrated with Side-looking airborne radar (SLAR) images and seismic data (Benkhelil et al., 1989). Benkhelil et al. (1989)'s depths were determined using Peters (1949)'s half-slope method.

Neither Ofoegbu (1988) and Abubakar et al. (2010) nor Benkhelil et al. (1989) transformed their data to their RTE equivalents prior to the application of the spectral or half-slope methods, respectively. This is a significant flaw, since these methods extract depth information from anomaly shapes (Vacquier et al., 1951), which are severely altered by the low inclination in Nigeria. The methods also require the removal of the regional field, which is poorly defined on a profile-by-profile basis. In fact, Benkhelil et al. (1989) assumed a horizontal regional field. New approaches for removing the regional field from gridded datasets exist (e.g., Ravat et al. (2003)). Also, these Nigerian studies disregarded the near-vertical ( $\geq 60^\circ$ ) to vertical ( $90^\circ$ ) magnetic field inclinations required for these methods to work. Consequently, the subsurface basement geology of Nigeria is unknown (Obaje et al., 2004).

This study was conceived to develop an interpretation strategy for  $\Delta T$  datasets from regions with low geomagnetic field inclinations ( $\pm 20^\circ$ ), using grid-based semi-automatic methods of magnetic data interpretation.<sup>5</sup> This strategy will then be applied to map the generally unknown configuration of, and structures in, the northeastern (NE) Nigeria basement, where apart from structural trends mapped from outcrops of basement rocks, the basement is concealed beneath Cretaceous and Quaternary sediments.

### 1.3 Aims and objectives

A key objective of this research is to determine how much structural information is irretrievably lost to anisotropy on RTE anomaly datasets relative to their RTP equivalents. This objective will be achieved by comparing: (1) RTE with RTP of model profile and gridded, as well as real  $\Delta T$  datasets; (2) derivatives (enhanced equivalents or functions) of these datasets; and (3) location and depths estimated from these  $\Delta T$  datasets, using the "Tilt-Depth" (Salem et al., 2007) and other semi-automatic magnetic interpretation methods, which have been applied mainly to RTP datasets

---

<sup>5</sup>Grid-based methods afford the interpreter the two-dimensional spectral attributes of the dataset, compared with the one-dimensional access provided along profiles.

from around the globe. Results from these comparisons will be integrated to develop a robust strategy for interpreting RTE datasets.

The resulting strategy will be applied to an aeromagnetic grid from NE Nigeria, to determine the: (1) location, trend and depth of basement structures (Faults, horsts, grabens and/or volcanic plugs); (2) gross composition; and (3) shape/configuration, of the basement underlying the area. These constitute essential information for mapping subcrop basement geology and structure of NE Nigeria, basic ingredients for fossil fuel and mineral exploration and exploitation planning, seismic hazard forecasting, and palaeogeographic history reconstruction.

Determining the basement structure, its tectonic imprints and their relationships with the sedimentary-fill of the area constitute the main objectives of this study. The significance of these structural and compositional inferences will be discussed, with limited speculations on post-depositional deformation of basin-fill (e.g., basin inversion).

## 1.4 Structure of thesis

This section describes how subsequent contents of this thesis are organised. The concepts, theories, research problems, choice of geometric model and methodology adopted for this study are discussed in chapter 2. This chapter also introduces the semi-automatic methods used in this study. Chapter 3 presents a detailed discussion of the “Tilt-Depth” method, introduces the algorithmic generation of profiles of  $\Delta T$  datasets from variously delimited versions of the geometric model chosen in chapter 2, and presents the contextual meaning of the term ‘error’, its ramifications and how they are applied throughout this thesis. Chapter 3 also presents tests of the “Tilt-Depth” method, using RTP and RTE equivalents of the profile  $\Delta T$  datasets, as well as the results obtained from these tests.

Chapter 4 introduces gridded model  $\Delta T$  datasets, and presents the methods used to test the “Tilt-Depth” method with RTP and RTE equivalents of these datasets, as well as the results obtained from these tests. Chapter 5 presents tests of other semi-automatic methods with RTP and RTE equivalents of gridded model  $\Delta T$  datasets introduced in chapter 4, and also reports the results obtained from these tests. Results obtained from testing the “Tilt-Depth” and other methods in chapters 3 to 5 are applied to RTE of NE Nigeria  $\Delta T$  dataset in chapter 6. Finally, the main results obtained from this study, and a synopsis of the inferred sequence of tectonic events in NE Nigeria, are discussed in chapter 7. The main conclusions drawn from this study are also presented in this chapter.

## Chapter 2

# Introducing geomagnetic field concepts, research problems and methodology adopted for interpreting TMI anomaly datasets

---

### 2.1 The geomagnetic field and its sources

The geomagnetic field can be described as the space through which the influence of an Earth-centred magnet is exerted (Sheriff, 2002). Also called *geomagnetic field induction* ( $\mathbf{B}$ ), it is the magnetic flux density per unit area (Blakely, 1996; Campbell, 2003) and has a scalar potential,  $\psi$  (Equation (2.1.1)).

$$\mathbf{B} = -\nabla\psi \quad (2.1.1)$$

where  $\nabla$  is the grad operator, and  $\psi$  is the scalar magnetic potential of a source region  $R$ , at a distance  $\mathbf{r}$ .

Only geomagnetic field data acquired by Low Earth Orbiting (LEO) satellites contain the spectral information required to fully describe long wavelength constituents (sources) of geomagnetic field measurements on Earth. LEO satellites like POGO (1965-1971), Magsat (1979-1980), POGS (1990-1993), Oersted (1999-), SAC-C (2000-) and CHAMP (2000-) have acquired high resolution (vector and scalar) geomagnetic datasets with global coverage (McLean et al., 2004; Macmillan, 2007; Maus et al., 2007; Hulot et al., 2010; Maus et al., 2010b; Olsen et al., 2010; Thébaud et al., 2010). The high-accuracy instrumentation and long life at low orbital altitudes (350-450 km) of the CHAMP satellite enables the generation of accurate maps of large-scale crustal magnetic anomalies (Maus et al., 2007) and ionospheric fields (Hulot et al., 2010).

Satellite-acquired geomagnetic field measurements obtained over the Earth are best represented by an infinite sum of *spherical surface harmonic functions*, i.e., weighted orthogonal sinusoidal functions and associated Legendre polynomials with fundamental period  $2\pi$  (Cain et al., 1989; Lowes, 1974). The surface integral of the square of coefficients of normalized spherical harmonic functions of vector magnetic fields reflects the *relative power or contribution* of each term in the har-

monic function.<sup>1</sup> The *Lowes-Mauersberger radial average power spectrum* (Figure 2.1) displays the average power ( $R_n$ ), i.e., the mean-square magnitude of each term in surface harmonic functions of the magnetic field over a sphere produced by harmonics of degree  $n$  of the field (Brodie, 2002; Campbell, 2003; McLean et al., 2004; Merrill et al., 1996; Thébaud et al., 2010).

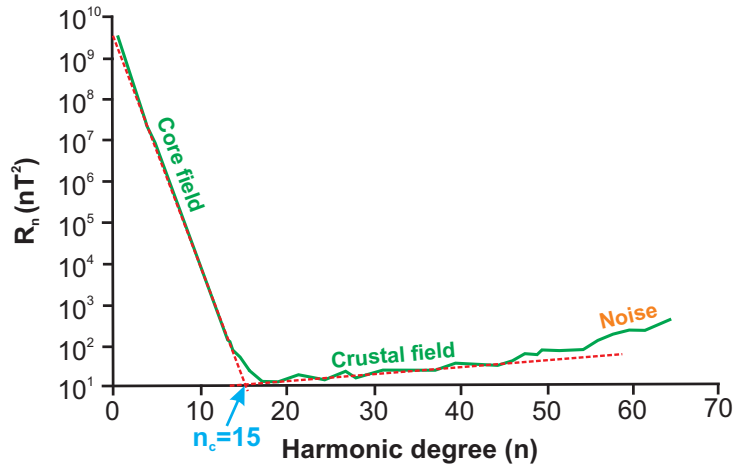


**Figure 2.1:** A sketch of the radial average power ( $R_n$ ) of models of the geomagnetic field obtained from the low-Earth orbiting (LEO) satellite: MAGSAT, as a function of spherical harmonic ( $n$ ). The red dashed lines indicate linear fits to  $2 \leq n \leq 15$  and  $n > 15$ , believed to indicate the two main sources of the Earth’s magnetic field. Modified from (Cain et al., 1989; Sabaka et al., 2004 and Gubbins, 2010).

Since power ( $R_n$ ) decreases with increasing harmonic degree, and can be approximated by the two red dashed lines with distinct straight slopes in figure 2.1, this figure is often employed to discriminate between the various sources of the geomagnetic field. The steeply-sloping segment ( $2 \leq n \leq \approx 15$ ) of figure 2.1 is dominated by long wavelength core-derived sources, while the flat segment ( $n > 15$ ) is dominated by crustal and/or lithospheric sources (typically of shorter wavelengths). Consequently, the point of intersection between the two sloping lines ( $n_c, R_{n_c}$ ) is believed to represent the cross-over from one source to the other.  $n_c$  has increased historically from  $\approx 8$  (Lowes, 1974) to  $\approx 15$  (Cain et al., 1989; Olsen et al., 2010) as data acquisition and processing techniques have improved (Olsen et al., 2010). The geomagnetic field comprises three major sources (Equation (2.1.2), Figure 2.1), each of which is introduced below.

$$\mathbf{B}_{obs} = \mathbf{B}_{core} + \mathbf{B}_{crust} + \mathbf{B}_{external} \quad (2.1.2)$$

where  $\mathbf{B}_{obs}$  is measured/observed  $\mathbf{B}$ -field;  $\mathbf{B}_{core}$  represents core-derived field;  $\mathbf{B}_{crust}$  represents local perturbations of  $\mathbf{B}$  due to the presence of anomalous crustal and/or lithospheric magnetic sources, and  $\mathbf{B}_{external}$  represents atmospheric, ionospheric and magnetospheric contributions (Considered to be *noise* in studies of the crust or core). The SI unit of  $\mathbf{B}$  is the Tesla, i.e., Weber per metre squared ( $\text{Wb m}^{-2}$ ). Geomagnetic field measurements are usually on the order of tens of thousands of nanoTeslas, nT (Figure A.2, where  $1 \text{ nT} \equiv 1 \gamma$  in CGS unit).

<sup>1</sup>Normalisation is achieved using *Schmidt’s functions* (Blakely, 1996), a process referred to as *Schmidt’s quasi-normalisation* (Winch et al., 2005).

### 2.1.1 The core-derived or main field ( $\mathbf{B}_{core}$ ) and its dipolar constituent ( $\mathbf{B}_{dipole}$ )

The steeply-sloping line fit to harmonic degrees  $2 \leq n \leq 15$  of the geomagnetic power spectrum (Figure 2.1) and the  $n = 1$  harmonic that lies above this line, correspond to geomagnetic field sources with the longest wavelengths, and with origins in the Earth's core (Gubbins, 2010; Thébault et al., 2010). The  $n = 1$  describes an essentially geocentric *dipole (main) field*, which accounts for well over 90% of core-derived sources, while the remaining  $2 \leq n \leq 15$  describe *non-dipolar* components of the core-field (Blakely, 1996). The dipole field accounts for over 95% (95%, Maus et al., 2010b; 98%, Thébault et al., 2010; or 99%, Friis-Christensen et al., 2009) of the geomagnetic field observed at the Earth's surface. Therefore, the Earth's geomagnetic field is essentially dipolar.

Temperatures in the Earth's core ( $\geq 4000^\circ\text{C}$ ) and mantle ( $\geq 1400^\circ\text{C}$ ) far exceed the Curie temperatures of magnetic minerals.<sup>2</sup> So, magnetism in the core can only be attributed to loops of electric currents, believed to be sustained by a self-exciting dynamo which results from non-uniform motion of conductive Fe-Ni fluids at yet unknown depths below the core-mantle boundary, CMB (Gubbins, 2010), i.e., within the outer core of the Earth (Olsen et al., 2010; Thébault et al., 2010).

Modelling of satellite-derived datasets show the dipolar geomagnetic field ( $\mathbf{B}_{dipole}$ ) to be best approximated by a dipole with its centre displaced 400 km North of the center of the Earth, and with its axis inclined  $11^\circ$  from the Earth's axis of rotation (Blakely, 1996, p.169).<sup>3</sup> The dipolar field, which represents the longest wavelength component of magnetic field data acquired by Low Earth Orbiting (LEO) satellites, can thus be expressed in terms of its scalar magnetic potential (Equations (2.1.1) and (2.1.3) of Blakely, 1996).

$$\psi = \frac{\mu_o}{4\pi} \int_R \frac{\mathbf{m} \cdot \mathbf{r}}{|\mathbf{r}|^3} \delta v \quad (2.1.3a)$$

$$\mathbf{B}_{dipole} = \frac{\mu_o \mathbf{m}}{4\pi r^3} (3 \cos \theta_B \hat{\mathbf{r}} - \hat{\mathbf{m}}) \quad (2.1.3b)$$

$$\therefore B_{dipole} = \frac{\mu_o m}{4\pi r^3} (3 \cos^2 \theta_B + 1)^{0.5} \quad (2.1.3c)$$

where:  $\psi$  is the scalar magnetic potential of a geocentric dipole (Equation (2.1.1));  $\mathbf{r}$  is the vector directed from the centre of the source to the observation point;  $\mu_o$  is the permeability of vacuum ( $\approx 1.257 \times 10^{-6} \text{ Hm}^{-1}$ ); *dipole moment*,  $\mathbf{m} = (pr)\hat{\mathbf{r}}$  (Wb m);  $p$  is the strength of a unit magnetic charge or monopole (in Wb);  $m$  is dipole moment magnitude;  $\hat{\mathbf{r}}$  and  $\hat{\mathbf{m}}$  are unit vectors in the directions of  $\mathbf{r}$  and  $\mathbf{m}$ , respectively;  $\theta_B$  (*magnetic colatitude*) is the angle between  $\hat{\mathbf{r}}$  and  $\hat{\mathbf{m}}$ ; *Geomagnetic latitude* =  $90 - \theta_B$ ;  $\delta v$  refers to an infinitesimal volume of the magnetic material; and  $B_{dipole}$  is the magnitude of  $\mathbf{B}_{dipole}$ .

<sup>2</sup>The Curie temperature is the temperature at which ferromagnetic minerals like magnetite lose their ability to retain magnetism.

<sup>3</sup>The dipole field is thus also called, the *eccentric dipole field*.

The elements of this major component of the inducing main magnetic field ( $\mathbf{B}_{dipole}$ ) that are significant to this study are: its (1) magnitude,  $B_{dipole}$  (Equation (2.1.3c)), which varies only along magnetic meridians  $\theta_{\mathbf{B}}$  (Equation (2.1.3b)); and (2) its inclination ( $\alpha$ ), which can be expressed in terms of  $\theta_{\mathbf{B}}$  (Equation 2.1.4, Garland, 1971).<sup>4</sup> These elements relate geomagnetic field measurements with both the longitude and colatitude of the observation point.

$$\alpha = \arctan(2 \cot \theta_{\mathbf{B}}) \quad (2.1.4)$$

The 11<sup>th</sup> Generation International Geomagnetic Reference Field, IGRF (Finlay et al., 2010) and the World Magnetic Model (WMM) 2010 (Maus et al., 2010b) are the standard mathematical models used to describe the Earth's core field for the period 2010-2015. Spherical harmonics  $1 \leq n \leq 13$  (wavelengths,  $\lambda \geq 3000$  km) were used for the IGRF, whilst  $1 \leq n \leq 12$  ( $\lambda \geq 3200$  km) were used for the WMM. The comprehensive models, CM3 and CM4 (Sabaka et al., 2004) use slightly wider range of harmonics;  $1 \leq n \leq 16$  ( $\lambda \geq 2500$  km).

While magnitudes of the 11<sup>th</sup> Generation IGRF (Finlay et al., 2010) ranges from  $\approx 25,000$  nanoTesla (nT) at the equator to  $\approx 65,000$  nT at the poles (Figure A.2), its inclination ranges from  $0^\circ$  at its equator to  $\approx 90^\circ$  at its poles (Figure A.1). Its North geomagnetic pole is located at latitude  $80.08^\circ$  and longitude  $-72.22^\circ$ , while the South geomagnetic pole is located at latitude  $-80.08^\circ$  and longitude  $107.78^\circ$  (BGS, 2011). The IGRF has wavelengths up to 3083 km (IAGA Working Group V-8, 1996), and is successively revised every five years to define the Definitive Geomagnetic Reference Field (DGRF) for that five-year period (Barraclough, 1987; Finlay et al., 2010). The valid IGRF for the 1900-2015 period is its 11<sup>th</sup> generation, which is the valid DGRF for the 1945-2005 period (Finlay et al., 2010).

Slow temporal, but regular yearly changes of between 40 and 100 nT/yr occur in the main field (IGRF or WMM). These changes termed *secular variation* (Blakely, 1996; Campbell, 2003), arise from the westward drift of outer core fluids at an average velocity of  $\approx 0.18^\circ/\text{year}$  across low latitudes. This drift correlate well with changes in the angular momentum of the Earth's mantle (Gubbins, 2010; Roberts & Glatzmaier, 2000). Secular variation is taken into account by Definitive Geomagnetic Reference Fields (DGRF), e.g., the 1945 to 2015 DGRF (Finlay et al., 2010).

### 2.1.2 The crustal or lithospheric geomagnetic field ( $\mathbf{B}_{crust}$ )

Thébault et al. (2010) used *crustal fields* to describe the non-core, Earth-sourced magnetic field data acquired on the ground, by aeroplanes or ships, but referred to crust-related fields gleaned from satellite measurements as *lithospheric fields*. These fields ( $\mathbf{B}_{crust}$ ) correspond to the nearly flat segment ( $n \geq 15$ ) of the Lowes-Mauersberger power spectrum (Figure 2.1). They are contri-

<sup>4</sup> $\alpha$  will represent the inclination of the inducing field.

butions, at or below satellite altitudes, from spontaneous magnetisation in ferromagnetic mineral (magnetite, titanomagnetite and/or pyrrhotite)-bearing crustal rocks that are at temperatures below the Curie point of these minerals (Telford et al., 1990; Blakely, 1996). Crustal magnetic fields may also be sourced below crustal depths in subduction zones, where they result from the serpentinisation (hydration) of the uppermost mantle (Blakely et al., 2005; Purucker & Clark, 2011).

Ferromagnetic minerals are more characteristic of crustal parts of the lithosphere (Thébault et al., 2010). For example, Curie temperatures for titanomagnetite and titanohematite (580 and 670°C, respectively) may be reached at depths  $\leq 30$  km beneath cratons and shields (stable continental masses), or at depths of 6 to 7 km beneath oceanic regions (Thébault et al., 2010). These Curie temperatures are significantly higher than the  $\approx 550^\circ\text{C}$  for most rock-forming minerals (Reeves, 2005; Sheriff, 2002). Temperature controlled (spontaneous) magnetisation in ferromagnetic mineral-bearing rocks is locked in as rocks crystallise through these Curie temperatures (remanent or permanent magnetisation). Additional magnetisation may also be induced by an external magnetic field in similar, but susceptible, rocks (i.e., induced magnetisation). For clarity, these magnetisations are briefly discussed in section 2.2.3.

Although wavelength contributions from  $\mathbf{B}_{crust}$  to the observed field may only be 0.1% of the full signal at satellite altitudes (Thébault et al., 2010), global models of the crustal geomagnetic field are produced by removing the core field from satellite datasets (Blakely, 1996; and Maus, 2010). Examples of such models include the: (1) Comprehensive model (CM4), which used harmonic numbers  $16 \leq n^\circ \leq 90$  ( $2500 \geq \lambda(\text{km}) \geq 400$ ) with regularisation for all  $n > 60^\circ$  (Sabaka et al., 2004); (2) NGDC-720 model (Maus, 2010), which uses spherical harmonic degrees  $16 \leq n^\circ \leq 720$  ( $2500 \geq \lambda(\text{km}) \geq 56$ ); and (3) MF7 model, which uses  $16 \leq n^\circ \leq 133$ , extending the waveband of the MF6 model (Maus et al., 2008) to  $2500 \geq \lambda(\text{km}) \geq 300$  (Maus et al., 2010a). Maps of clearly defined long wavelength crustal/lithospheric fields aid our understanding of crustal structure, composition and dynamics.

### 2.1.3 The external geomagnetic field ( $\mathbf{B}_{external}$ )

Contributions to the geomagnetic field, which are external to the Earth ( $\mathbf{B}_{external}$ ), arise from the Earth's ionosphere and magnetosphere (altitudes ranging from about 110 to  $\approx 1000$  km). Externally-sourced magnetic fields result from the complex interaction and coupling between the ionised plasma-laden solar wind, rotating Earth, tidal forces and thermal effects (Blakely, 1996; Merrill et al., 1996).  $\mathbf{B}_{external}$  varies with time in two significant ways: (i) Regular changes on time-scales of one day and on the order of  $\approx 20$  to 30 nT per day (*diurnal variation*); and (ii) Irregular and transient changes due to magnetic storms, which results from enhanced sunspot activity. Such activity can produce anomalies up to 1000 nT in amplitude (Blakely, 1996). External fields ( $\mathbf{B}_{external}$ ) contribute short wavelength noise to marine and aeromagnetic datasets (Maus et al., 2007). Since, crustal and external field sources have similar amplitudes (Figure 1 of Thébault et al., 2010), these disturbances cannot be removed only on the basis of amplitudes. But, magnetic data

acquisition platforms (on land, aircraft or ships) move relatively slowly when compared with rapid changes that characterize strong external field. Hence, [Maus et al. \(2007\)](#) used an along-track derivative threshold value to filter off all data with higher rates of change.

Although the two segments in figure 2.1 indicate the dominance of core and lithospheric or crustal geomagnetic field sources over sources external to the Earth (Shown as “Noise” in figure 2.1), core and lithospheric (crustal) geomagnetic fields interfere ([Cain et al., 1989](#); [Hulot et al., 2009](#)). Hence, short wavelengths from core sources are masked by long wavelength lithospheric (crustal) geomagnetic fields. Similarly, long wavelengths from lithospheric (crustal) sources are masked by short wavelength core-sourced geomagnetic fields. These wavelength contributions can usually be separated using the wavenumber  $n_c$  (Figure 2.1). However, where wavelengths of crustal and main field contributions overlap, it is difficult to separate crustal and core fields using only differences in wavelength ([Gubbins, 2010](#)). Such overlapping wavelengths may only be separated using differences between forward models of the total magnetisation of the Earth’s core and crust ([Gubbins, 2010](#)). Also, due to geometric attenuation, long-wavelength crustal magnetic anomalies are not reliably presented in regional airborne and/or marine magnetic datasets. These long wavelengths can be extracted from crustal field models. For instance, if crustal fields from CM4 are to be used: (1) all wavelengths exceeding 400 km (the minimum wavelength of the CM4) will be removed from a dataset; and then (2) wavelengths  $>400$  km from the CM4 are added to the aeromagnetic or marine dataset.

Combined models define all the long wavelength (core) fields, as well as external fields that must be subtracted from magnetic field observations, to obtain crustal magnetic anomalies. The CM4 version of the comprehensive model ([Sabaka et al., 2004](#)) provides the best representation of the core and external geomagnetic fields ([Maus et al., 2009](#)). A global long wavelength Earth Magnetic Anomaly Grid, EMAG2 grid has been compiled from satellite, ship, and airborne magnetic measurements ([Maus et al., 2009](#)).

## 2.2 Magnetisation ( $\mathbf{J}_v$ ), Total magnetic field intensity (TMI), magnetic susceptibility ( $k$ )

### 2.2.1 Volume magnetisation ( $\mathbf{J}_v$ )

Magnetisation ( $\mathbf{J}_v$ , Equation (2.2.1)) is a vector defined as the dipole moment ( $\mathbf{m}$ ) per unit volume ( $V$ ) of magnetic rock ([Blakely, 1996](#); [Kaufman et al., 2009](#)).

$$\mathbf{J}_v = \frac{\mathbf{m}}{V} \quad (2.2.1)$$

Equation (2.2.1) describes *volume magnetisation*, which is commonly explained in terms either of the distribution of: (i) magnetic moments; (ii) atomic electric currents associated with each

magnetic moment; or (iii) volume and surface magnetostatic charges (Blakely, 1996). Assuming that net volume magnetostatic charge is zero, the distribution of surface magnetostatic charges will be more frequently used to explain magnetic responses of structures throughout this study. Components of  $\mathbf{J}_v$  are described in section 2.2.3.

## 2.2.2 Magnetic field strength or intensity (TMI)

Magnetic field intensity or strength (**TMI or T**) represents local magnetic field perturbations superimposed on  $\mathbf{B}_{obs}$  where magnetite-bearing crustal media occur (Equation (2.2.2b)). Blakely (1996) relates  $\mathbf{B}_{obs}$  (Equation (2.1.2)) to the scalar magnitude of  $T$  using equation (2.2.2a).

$$\mathbf{B}_{obs} = \mu_0(\mathbf{T} + \mathbf{J}_v) \quad (2.2.2a)$$

$$\therefore \mathbf{T} = \frac{\mathbf{B}_{obs}}{\mu_0} - \mathbf{J}_v \quad (2.2.2b)$$

where  $\mathbf{B}_{obs}$  is measured/observed **B**-field;  $\mu_0$  is the permeability of vacuum (Equation (2.1.3)); and  $\mathbf{J}_v$  is volume magnetisation. Like  $\mathbf{B}_{obs}$  the SI unit of **T** is nanoTeslas (nT).

Whereas  $\mathbf{B}_{obs}$  represents the cumulative magnetic response of all magnetisation (microscopic or volume, and macroscopic or surface) currents, **T** represents magnetic fields produced only in response to macroscopic magnetisation currents on the surface of anomalous magnetic media in the subsurface (Blakely, 1996). Consequently, using equation (2.2.2b), scalar magnetometers obtain scalar magnitudes of *total magnetic field intensity* (TMI or  $T$ ) from the scalar magnitude of  $\mathbf{B}_{obs}$  ( $B_{obs}$ ) without regard to its vector components (Grant & West, 1965; Blakely, 1996). Equation (2.2.3) presents the TMI ( $T$ ) equivalent of equation (2.1.2), provided that all vector fields are parallel.

$$T_{obs} = T_{core} + T_{crust} + T_{external} \quad (2.2.3)$$

where  $T_{obs}$  is the measured  $T$ ,  $T_{core}$  represents the core-derived field,  $T_{crust}$  represents local perturbations of  $T$  due to the presence of anomalous crustal magnetic sources, and  $T_{external}$  represents atmospheric contributions (Noise).

**Total magnetic field intensity (TMI) anomaly**,  $\Delta T$  (Equation (2.2.4)) describes the difference between the observed and theoretical TMI values for each location (Lyatsky, 2004), assuming that external contributions have been removed (Blakely, 1996)

$$\Delta T \equiv T_{crust} = T_{obs} - (T_{core} + T_{external}) \quad (2.2.4)$$

where the variables are as declared for equation (2.2.3) and are all parallel, and  $\Delta T$  is the contribution of magnetic crustal rocks in the direction of the main dipolar field ( $T_{core}$ ) since  $T_{core}$  is more than two orders of magnitude greater than  $T_{crust}$  (Pedersen et al., 1990; Reeves, 2005).

### 2.2.3 Induced and remanent magnetisations ( $\mathbf{J}_i$ and $\mathbf{J}_r$ ), magnetic susceptibility ( $k$ ) and Koenigsberger ratio ( $Q$ )

Volume magnetisation,  $\mathbf{J}_v$  (Section 2.2.1) consists of two parts; (i) induced magnetisation, and (ii) remanent or permanent magnetisation.

#### (A) Induced and remanent magnetisations ( $\mathbf{J}_i$ and $\mathbf{J}_r$ ), magnetic susceptibility ( $k$ ) and effective magnetisation ( $\mathbf{J}_v$ )

The main geomagnetic field ( $\mathbf{T}_{core}$ ) induces secondary magnetic fields ( $\mathbf{T}$ ) in crustal magnetic minerals via its magnetisation. This component of volume magnetisation ( $\mathbf{J}_v$ ) called *induced magnetisation*,  $\mathbf{J}_i$  (Equation (2.2.5)), is observed in rocks that contain ferrimagnetic minerals like magnetite, pyrrhotite and/or maghemite (Section 2.2.4) in the presence of inducing (ambient) magnetic fields.

$$\mathbf{J}_i = k\mathbf{T} \quad (2.2.5)$$

where  $k$  is a dimensionless constant called *magnetic susceptibility*, which is positive when the induced magnetisation ( $\mathbf{J}_i$ ) is in the same direction as the inducing magnetic field ( $\mathbf{T}_{core}$ , Equation (2.2.3)).

The other component of  $\mathbf{J}_v$ , called *remanent magnetisation*, ( $\mathbf{J}_r$ ) also observed in ferrimagnetic materials occurs when there is no inducing magnetic field ( $\mathbf{T}_{core}$ ). Remanent magnetisation is the permanent record of magnetisations acquired by a rock over its history (Moskowitz, 1991). Although  $\mathbf{J}_r$  may not always be present, when present, it may be neither co-axial nor equal in magnitude with  $\mathbf{J}_i$  (Lanza & Meloni, 2006; Lelievre & Oldenburg, 2009). Hence, equation (2.2.1) may also be written as (Bath, 1968; Blakely, 1996; Lanza & Meloni, 2006; Lelievre & Oldenburg, 2009; Parasnis, 1997):

$$\mathbf{J}_v = \mathbf{J}_i \pm \mathbf{J}_r \quad (2.2.6)$$

where  $\mathbf{J}_i$  and  $\mathbf{J}_r$  represent, respectively, the induced and remanent magnetisations.  $\mathbf{J}_v$  is *effective (net) magnetisation*.

I will use  $\alpha$  to represent inclination of induced magnetisation ( $\mathbf{J}_i$ ),  $\beta$  to represent inclination of remanent magnetisation ( $\mathbf{J}_r$ ), and  $\phi$  to represent inclination of effective magnetisation ( $\mathbf{J}_v$ ). When remanent magnetisation is absent, therefore,  $\alpha = \phi$ .

#### (B) Koenigsberger ratio ( $Q$ ).

The *Koenigsberger ratio*,  $Q$  (Equation (2.2.7)) is the ratio of the magnitude of remanent magnetisation ( $J_r$ ) to that of induced magnetisation ( $J_i$ ). Therefore,  $Q$  expresses the relative dominance of

remanent magnetisation in a rock sample (Parasnis, 1997; Lanza & Meloni, 2006).

$$Q = \frac{|\mathbf{J}_r|}{|\mathbf{J}_i|} \quad (2.2.7)$$

Maus & Haak (2002) show from satellites-derived TMI anomaly ( $\Delta T$ ) datasets (at  $\approx 400$  km altitude) that the continents are dominated by induced magnetisation ( $\mathbf{J}_i$ ). McEnroe et al. (2009) considers terrains in which  $Q < 0.5$  to be dominated by induced magnetisation, while Thébault et al. (2010) indicate that  $Q \ll 1$  for continental regions. However, Finn & Morgan (2002) show that some continental terrains are dominated by remanent magnetisation, with  $Q$  exceeding 20.

## 2.2.4 Initial conclusions

### (A) Dependence of TMI magnitude ( $T$ ) on latitude and magnetisation.

The following conclusions were derived from equations (2.1.3b), (2.1.3c), (2.2.2a) and (2.2.2b).

- (1) TMI magnitude ( $T$ ) depends on: (i) the distance from the centre of the source ( $\mathbf{r}$ ). The inverse-cubed dependence of  $T$  on  $r$  means that it decreases rapidly with increasing distance from the centre of the source ( $r$ ); (ii) latitude, where  $latitude^\circ = 90 - \theta_B$  and  $\theta_B$  is magnetic colatitude. The  $\cos \theta_B$  relationship guarantees that  $T$  increases from its minimum value when  $\theta_B = 90^\circ$  (i.e., at the magnetic equator) to its maximum value when  $\theta_B = 0$  or  $180^\circ$  (i.e., at the magnetic North or South pole).
- (2)  $T$  increases with increasing  $J_v$  (the magnitude of effective magnetisation,  $\mathbf{J}_v$ ).
- (3) The induced magnetisation-only assumption for  $Q < 0.5$  (McEnroe et al., 2009) may not be valid where large volcanoes occur in continental regions (Thébault et al., 2010).

### (B) The role of magnetite in crustal rock magnetism.

Equation (2.2.5) shows: (1) that the strength and direction of  $\mathbf{J}_i$  depends principally on that of the main (core) field ( $T_{core}$ ), and (2) that magnetic susceptibility ( $k$ , Equation (2.2.5)) is the main bulk magnetic property of rocks sought in magnetic prospecting. Magnetic susceptibility ( $k$ ) reflects the magnetic mineralogy, as well as the textural and thermal properties of rocks. Ferrimagnetic minerals include magnetite ( $Fe_3O_4$ ), pyrrhotite ( $Fe_7S_8$ ), maghemite ( $\gamma Fe_2O_3$ ) or hematite ( $\alpha Fe_2O_3$ ). However, the comparatively large and wide range of magnetic susceptibilities of magnetite, its large spontaneous magnetisation and wide occurrence, imply that *bulk rock magnetism primarily reflects magnetite content* (Belley et al., 2009; Grant, 1985; Paterson & Reeves, 1985).<sup>5</sup> The mag-

<sup>5</sup>The spontaneous magnetisation (in  $Am^2kg^{-1}$ ) of: magnetite is 90-92; maghemite is  $\approx 80$ ; pyrrhotite is 20; and hematite is 0.4 (Moskowitz, 1991).

netite content of rocks and its Curie temperature exert the most dominant control on rock magnetisation and susceptibility (Clark & Emerson, 1999). Consequently, Paterson & Reeves (1985) recommends caution when inferring bulk basement rock composition from  $\Delta T$  datasets.

### 2.3 Problems with TMI anomaly ( $\Delta T$ ) datasets obtained at or close to the geomagnetic equator

This section demonstrates and discusses the problems posed by low or horizontal inclinations of the geomagnetic field ( $|\alpha| \leq 20^\circ$ ) using  $\Delta T$  datasets from simple models of dipolar (spherical) magnetic sources at a depth of 0.5 km, using GETgrid<sup>TM</sup> software.<sup>6</sup> The software utilizes equations (2.1.1) and (2.2.4) to generate  $\Delta T$  responses from buried dipolar sources at specific depth and  $\alpha$ . Examples of the  $\Delta T$  grids generated are presented in figure 2.2. Table 2.1 presents the  $\alpha$ , as well as the  $\cos \theta_{\mathbf{B}}$ -related geometrical factors used to generate the grids in figure 2.2.<sup>7</sup> North-South (N-S) and/or East-West (E-W) profiles across the generated grids will now be used to highlight some of the problems that characterise  $\Delta T$  datasets from regions located at, or close to, the geomagnetic equator (Section 2.3.1).

#### 2.3.1 Effects of inclination ( $\alpha$ ) on spectral contents of $\Delta T$ datasets

Key parameters controlling the amplitude (size) and phase (shape) of  $\Delta T$  from magnetic sources (geophysical structures) include: (1) the magnitude and inclination ( $\alpha$ , Equation (2.1.4)) of the ambient geomagnetic field; as well as (2) the depth, relative orientation and magnetic susceptibility  $k$  of the source (Dobrin & Savit, 1988; Telford et al., 1990).  $\Delta T$  wavelengths are depth-controlled (Vacquier et al., 1951). Hence, the magnetic dipoles used to discuss changes in  $\Delta T$  spectral contents below were buried at the same depth (e.g., dipoles in figure 2.2).

**Table 2.1:** Variation of the geometrical factors of  $\Delta T$  (Equations (2.1.3c) and (2.2.4)) with latitudes and inclination of the inducing geomagnetic field ( $\alpha$ , Equation (2.1.4)).

Latitude	90	47	26.6	0
Colatitude ( $\theta_{\mathbf{B}}$ )	0	43	63.4	90
Inclination ( $\alpha$ )	90	65	45	0
$\cos \theta_{\mathbf{B}}$ -based geometrical factors of $\Delta T$	2	1.6	1.3	1
$m$ used for $\Delta T$ grids in figure 2.2	10	8	6.5	5

<sup>6</sup>GETgrid<sup>TM</sup> is GETECH Group Plc., UK's proprietary software.

<sup>7</sup> $\cos \theta_{\mathbf{B}}$ -related geometrical factors on table 2.1 were determined from equations (2.1.3c), (2.1.4) and (2.2.4).

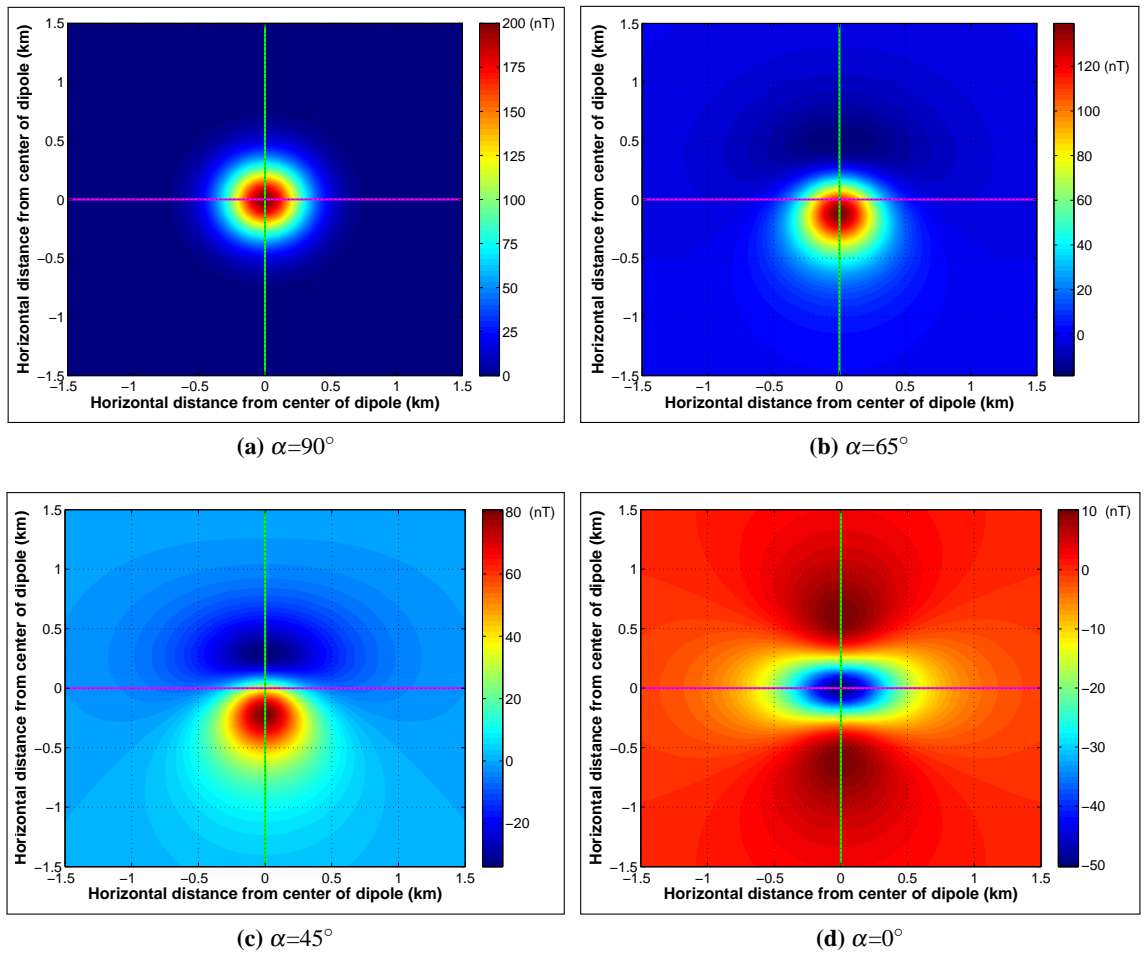


**Figure 2.2:** Grids showing variations in the size and shape of  $\Delta T$  of dipolar (spherical) anomalous magnetic sources with changes in inclinations of induced magnetisation,  $\alpha$  (Sources at constant depth = 0.5 km). Dipole moment magnitude,  $m = 10 \text{ Wb m}$ . However,  $\Delta T$  varies with inclination by a geometrical factor which is twice its value when  $\alpha = 90^\circ$  compared with when  $\alpha = 0^\circ$  (Table 2.1). At the pole (Figure 2.2a)  $\Delta T$  is positive, symmetric and centred directly above its source. At the geomagnetic equator (Figure 2.2d)  $\Delta T$  is symmetric but largely negative, with small positive side-lobes North and South of the centre of the dipolar magnetic anomaly source. Between the magnetic poles and equator, the symmetric and centred positive anomaly is redistributed as shown in figures 2.2b and 2.2c. South-North (S-N) and East-West (E-W) profiles are shown, respectively as solid green and pink lines.

### (A) Size of $\Delta T$

When examined together, equations (2.1.3c) and (2.1.4) show the simple relationship that amplitudes and inclinations of the main geomagnetic field have with latitude (Appendix A). Also, equation (2.2.5) shows that large total field strengths,  $T$  (implying large magnetic dipole moments) result in large magnetisations. Hence, each grid in figure 2.2 varied from the other three in terms of the inclination of the inducing field ( $\alpha$ ) and the  $\cos \theta_B$ -related geometrical factor of the dipole moment magnitude ( $m$ ) used to generate it (Table 2.1). Changing  $\alpha$  and geometrical factors also imply changes in magnetisation,  $\mathbf{J}_v$  (Equation (2.2.1)), in this case, the induced magnetisation ( $\mathbf{J}_i$ ).

To examine the effect of changing  $\mathbf{J}_i$  on  $\Delta T$  amplitudes, I compare South-North (S-N) profiles extracted from  $\Delta T$  grids generated from dipoles with equivalent inclination ( $\alpha^\circ$ ), but different

dipole moments ( $m$ ) in figure 2.3.<sup>8</sup> Profiles show that  $\Delta T$  is at its maximum when inclination is vertical ( $|\alpha| = 90^\circ$ , at the poles), and at its weakest when inclination is horizontal ( $\alpha = 0^\circ$ , at the equator). This is because  $\cos\theta_{\mathbf{B}}$ -related geometrical factors of the dipole moment reduced from the magnetic poles to half their value at the equator (Table 2.1). Consequently, induced magnetisation ( $J_i$ ) decreased from its maximum strength at the poles ( $\alpha = 90^\circ$ ), to half its value at the equator,  $\alpha = 0^\circ$  (Table 2.1). Therefore, amplitudes of  $\Delta T$  decrease with decreasing inclination, from a maximum at the geomagnetic North or South pole to a minimum at the geomagnetic equator.

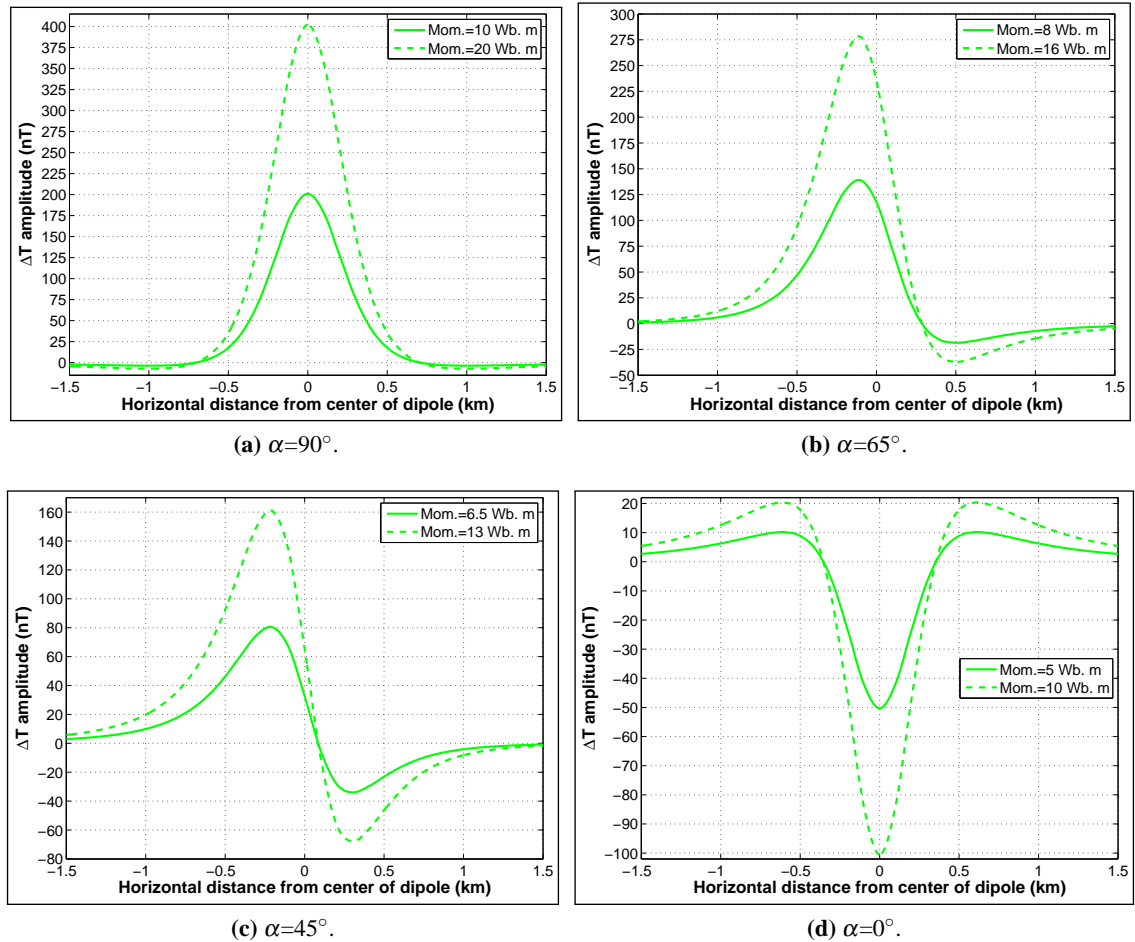


**Figure 2.3:** Comparisons between South-North (S-N) profiles across grids shown in figure 2.2 and equivalent grids with twice as much dipole moment ( $m$ ) magnitudes.  $\alpha$  is inclination of induced magnetisation. Dashed green profiles are from grids with dipole moment magnitude ( $m$ ) twice those of grids from which the solid green profiles were extracted. South is left, while North is right of the figure.

<sup>8</sup>South-North (S-N) profiles were preferred because the  $\cos\theta_{\mathbf{B}}$  variable in equations (2.1.3c) and (2.1.4) predicts maximum  $\Delta T$  amplitudes to occur only along this direction.

**(B) Phase (shape) changes in  $\Delta T$** 

$\Delta T$  shapes depend on the relative orientation of the effective magnetisation (Equation (2.2.6)).<sup>9</sup> Consequently, the shapes of the  $\Delta T$  responses of the dipolar sources also changed with  $\alpha$  (Figure 2.3). At the magnetic pole where  $\alpha$  is vertical ( $90^\circ$ ), the anomaly is positive, symmetric and centred directly above the source (Figure 2.3a). When  $\alpha$  is horizontal ( $0^\circ$ ) the anomaly is still symmetric but largely negative, with small positive side-lobes North and South of the centre of the dipolar source (Figure 2.3d). However, when  $\alpha$  is neither vertical nor horizontal ( $0 < \alpha^\circ < 90$ ), the symmetric and centred positive anomaly is redistributed into two lobes across the centre of the dipolar source. While a negative anomalous lobe appears to the North of the source, a positive lobe appears to its South (Figure 2.3b and 2.3c). For example, when  $\alpha = 45^\circ$  (Figure 2.3c), the negative and positive lobes of the anomaly are of unequal amplitudes and located, respectively, North and South of the body. Hence, the relative amplitudes and locations of the anomalous lobes reflect the net distribution of magnetic flux induced by  $\alpha$ .

The shape (phase) of  $\Delta T$  generated by some of the dipolar models also changed with the direction of profiles across the grid, e.g., in figure 2.2d.<sup>10</sup> The term *azimuthal anisotropy* is used to describe  $\Delta T$  shape changes that result from changes in profile azimuth or direction (e.g., North-South, East-West, etc.). To examine the phenomenon of anisotropy, South-North (S-N) and East-West (E-W) profiles have been extracted from  $\Delta T$  grids that have twice the dipole moment magnitudes of grids in figure 2.2 (Green and Pink curves, respectively, in figure 2.4). The location of these S-N and E-W profiles (Figures 2.4a, b, c and d) are similar to those shown on corresponding  $\Delta T$  grids in figure 2.2. Comparisons between the profiles (Figure 2.4) show that: (1) irrespective of profile orientation, anisotropy does not occur, when  $\alpha$  is vertical,  $90^\circ$  (Figure 2.4a); and (2) once  $\alpha$  is not vertical, i.e.,  $< 90^\circ$  (Figures 2.4b, c and d), S-N and E-W profiles and, indeed, profiles in other directions across the same  $\Delta T$  grid exhibit anisotropy.

**(C) Implications of changes in spectral contents of  $\Delta T$** 

The magnetisation effects discussed in section 2.3.1 assumes the presence only of induced magnetisation ( $\mathbf{J}_i$ ). To ease the interpretation of  $\Delta T$  datasets, common assumptions are made (Blakely, 1996; Grant & West, 1965). These include the absence of significant remanent magnetisation ( $\mathbf{J}_r$ ). Experimental and laboratory analyses of ferromagnetic rock samples largely validate this assumption (Blakely, 1996; Lanza & Meloni, 2006). Magnetisation is usually also assumed to be uniform and isotropic throughout magnetised volumes of magnetic rocks.

A magnetic body is said to be uniformly magnetised when its net magnetisation (Equation (2.2.6))

<sup>9</sup>Since remanent magnetisation is absent for dipoles used in this section, the inclination of induced magnetisation ( $\alpha$ ) is essentially the same as inclination of effective magnetisation,  $\phi$  (Section 2.2.3).

<sup>10</sup>Profile directions are usually chosen so that they are perpendicular to the strike of oblong structures. Hence, changes in profile directions imply changes in strike direction.

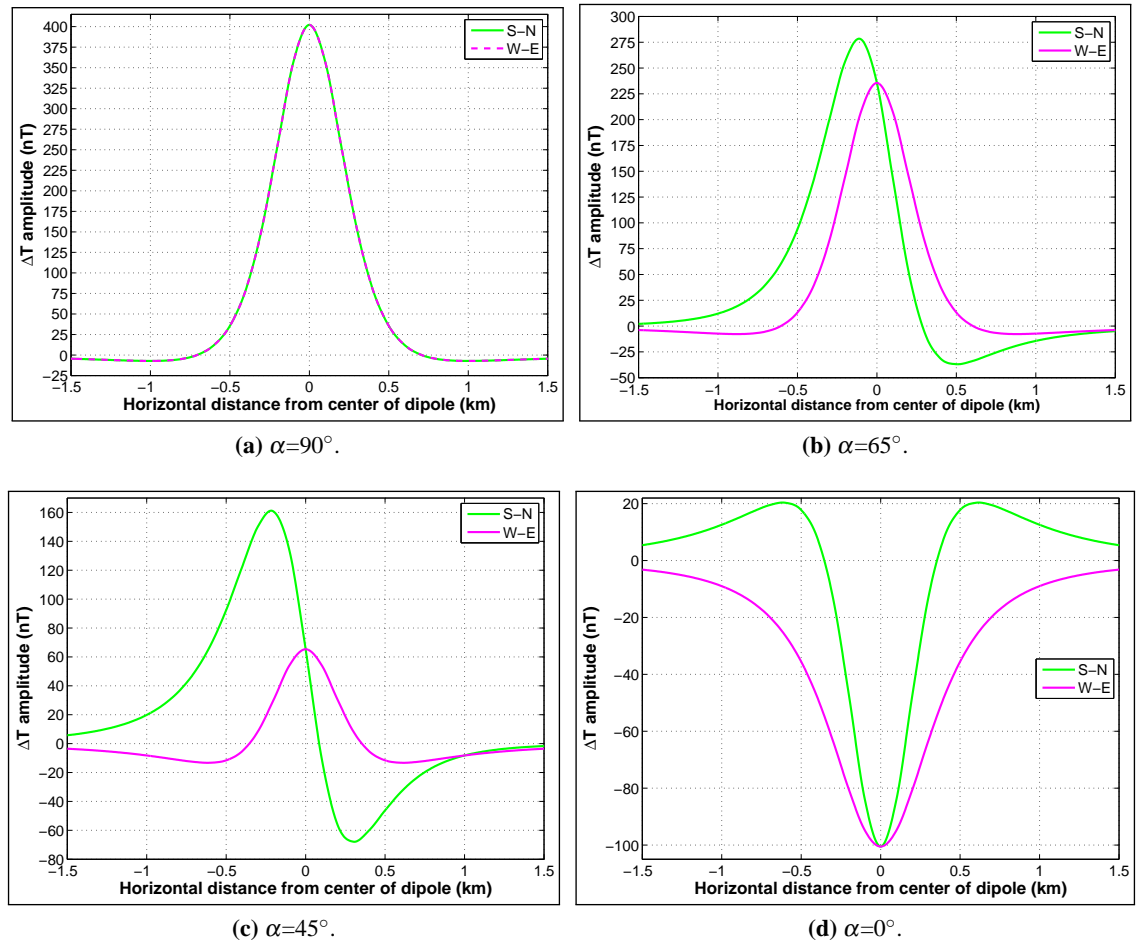


**Figure 2.4:** A comparison between South-North, S-N (Green-coloured) and East-West, E-W (Pink-coloured) profiles across  $\Delta T$  grids from model dipolar sources.  $\Delta T$  profiles show the response of a dipole model at a depth of 0.5 km and  $\mathbf{m}=20$  Wb m when  $\alpha = 90, 65, 45$  and  $0^\circ$ . Except when inclination is vertical ( $\alpha = 90^\circ$ , Figure 2.4a),  $\Delta T$  shapes and sizes vary with the direction of the profile, a phenomenon termed *anisotropy*. South and West are to the left, while North and East are to the right of the figure.

is constant, in magnitude and direction, at all points throughout the body. However, the distribution of magnetisation in the subsurface may be more complex, and if present, remanent magnetisation ( $\mathbf{J}_r$ ) may be directed differently from  $\mathbf{J}_i$ . Even in the absence of  $\mathbf{J}_r$ , anisotropy in  $\Delta T$  due to non-vertical inclination of  $\mathbf{J}_i$  ( $\alpha \leq 90^\circ$ ) results in two main difficulties: (1) the task of imaging anomalous magnetic structures is complex; (2) interpretation of poorly imaged magnetic features is even more complex and difficult. There is, therefore, a demand for technique(s) or their amalgams with potential(s) for simplifying/minimizing these complexities.

### 2.3.2 Retaining the spectral content and simplifying shapes of $\Delta T$

Spectral contents of  $\Delta T$  are least complex and most directly related to the location of the causative or anomalous body when  $\alpha$  is vertical (Figures 2.2a and 2.4a), since the shape and size of these anomalies were stable and independent of profile direction. This is the situation in which  $\Delta T$  are *reduced-to-pole*, RTP (Baranov, 1957). Other than the RTP situation,  $\Delta T$  only appear simplified

when  $\alpha$  is horizontal (Figures 2.2c and 2.4c). This is the *reduced-to-equator, RTE* (Leu, 1981) case.<sup>11</sup> However, although a measure of simplification is achieved by the RTE, as these figures show,  $\Delta T$  exhibit anisotropy as their amplitudes and shapes depend on profile directions.

Transforming  $\Delta T$  data to their RTP or RTE equivalent simplifies anomaly shapes. Consequently,  $\Delta T$  datasets are customarily transformed to their: (1) RTP equivalents when  $\alpha > 20^\circ$  (Baranov & Naudy, 1964; Reford, 1964; MacLeod et al., 1993); or (2) RTE equivalents when  $\alpha \leq 20^\circ$  (Gerovska & Stavrev, 2006; Li, 2008). This is because the RTP transformation is not stable, when applied to  $\Delta T$  datasets derived from locations with such low  $\alpha$  (Gerovska & Stavrev, 2006).

### 2.3.3 Problems with RTE-transformed $\Delta T$

Although the RTE process simplifies anomaly shapes when  $\alpha \leq 20^\circ$  (MacLeod et al., 1993), unfortunately, the process also presents key problems to interpretation. Such problems include:

- (1) Reduction in amplitudes of  $\Delta T$  and magnetisation ( $\mathbf{J}_i$ ), since the strength of the magnetic field is at its weakest at the magnetic equator ( $\alpha = 0^\circ$ , Section 2.3.1);
- (2) Positive  $\Delta T$  on RTP datasets become mainly negative  $\Delta T$  on their RTE equivalents. These negative RTE  $\Delta T$  can be associated, depending on direction, with low amplitude, positive  $\Delta T$  side-lobes (Compare figure 2.4d with 2.4a). Changes in sign, from positive  $\Delta T$  on RTP datasets to negative  $\Delta T$  on RTE datasets, will be subsequently referred to as *polarity reversals or changes*; and
- (3) Anisotropy reflected by: (i) the direction (azimuth)-dependence of the additional positive side-lobes of the mainly negative RTE anomalies (Figures 2.2d and 2.4d); and (ii) the preferential East-West (E-W) extension of RTE anomalies relative to other directions (Figure 2.2d).

Consequently, significant effort has been expended to develop modified versions of the simpler RTP filter, for application to  $\Delta T$  datasets from regions of low or horizontal geomagnetic field inclinations. These algorithms produce smooth anomalies, but include terms that correct  $\Delta T$  amplitudes erroneously (Gerovska & Araúzo-Bravo, 2006) and magnifies noise content and remanent magnetisation effects (MacLeod et al., 1993). Li (2008) analysed the four existing algorithms used for transforming  $\Delta T$  datasets from regions of low magnetic latitudes to their reduce-to-pole (RTP) equivalents. He concluded that the methods stretch  $\Delta T$  in the direction perpendicular to the declination.

---

<sup>11</sup>Hereafter, most references to the terms “reduced-to-pole” and “reduced-to-equator” will be abbreviated to RTP and RTE, respectively.

## 2.4 Methodology adopted: Choice of $\Delta T$ model source

Determining the locations, depths and geometry of magnetic anomaly sources (Section 1.3) from  $\Delta T$  dataset is a non-linear inverse problem, since the anomaly is not a linear function of these parameters. Linearising this dependence requires the designation of a context (geology and tectonic framework)-sensitive  $\Delta T$  source model (Blakely, 1996). A simplifying geometric model that readily approximates geological sources in rifted tectonic zones, where faults dominate, is the two-dimensional (2D) magnetic contact (Nabighian, 1972; Dobrin & Savit, 1988; Blakely, 1996).

### 2.4.1 The two-dimensional (2D) magnetic contact model

The dominant tectonic regime in NorthEastern (NE) Nigeria is crustal extension (Cratchley et al., 1984; Fairhead & Okereke, 1990), as part of the West African rift System, WAS (Fairhead, 1988a; Fairhead & Green, 1989). Rosendahl (1987) and Ingersoll (1988) report that such extensional tectonic settings are characterised by structural blocks, i.e., horsts and grabens, which may be rotated or tilted. McKenzie (1978), Wernicke & Burchfiel (1982) and Leeder & Gawthorpe (1987) observed that these high-angle crustal or basement blocks are bound by listric and planar normal faults of large extent. Fault-bounded blocks (Leeder & Gawthorpe, 1987) are typically 10 km wide and have length-to-width ratios of up to 10 (Rosendahl, 1987). Faults associated with domino-type blocks are shallow (McKenzie, 1978), while boundaries of major tilted crustal blocks or basement are characterised by planar or normal faults which may extend down to between 10 and 15 km (Kusznir & Ziegler, 1992).

The geometric model that best approximates these basement faults is the **two-dimensional (2D) magnetic contact or step model**. Magnetic geologic bodies are bound by two-dimensional contacts if, according to Cook (1950), Baranov (1957), Hall (1959), Grant & West (1965) and Nabighian et al. (2005), they: (1) have infinite length along their strike directions; (2) are uniformly magnetized; (3) are bound by planar surfaces, which may be vertical or inclined, i.e., dip  $d \leq 90^\circ$ ; and (4) their depth greatly exceeds (is not less than half) their width, essentially depth is infinite. Assuming infinite depth of magnetic anomaly source implies negligible contribution from the bottom face of the source. However, boundaries between rocks of different magnetisations are frequently gradational, rather than abrupt/sharp (Affleck, 1957).

The 2D contact model (Figure 2.5) is a valid geometric approximation for many magnetic geological bodies bound by planar edges, e.g., basement-involved faults, thrust structures, thin dikes and slab-like bodies provided the individual faces can be resolved (Smellie, 1956; Reford, 1964; Stanley, 1977; Grant & West, 1965; Dobrin & Savit, 1988; Sheriff, 2002). Such boundaries are characterised by significant magnetic susceptibility contrasts ( $\delta k$ ), hence generate  $\Delta T$ . Although for ease of computation, these bounding faults are considered to be of constant two-dimensional (2D) geometry, fault planes in the Earth's crystalline basement display various attitudes in terms of

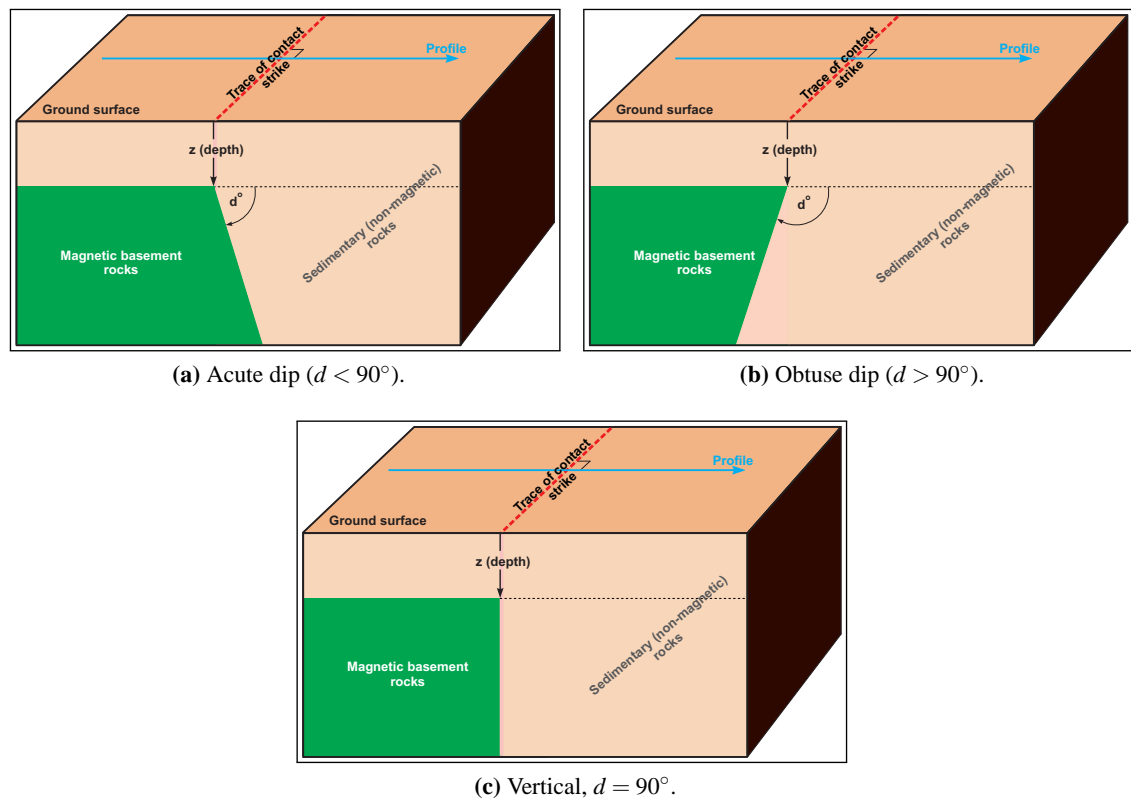


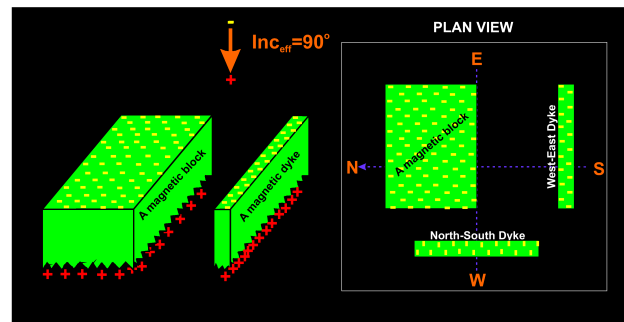
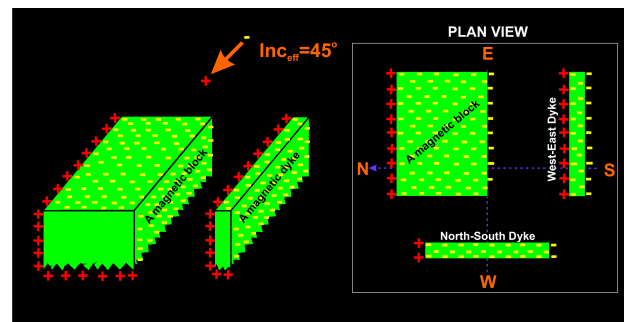
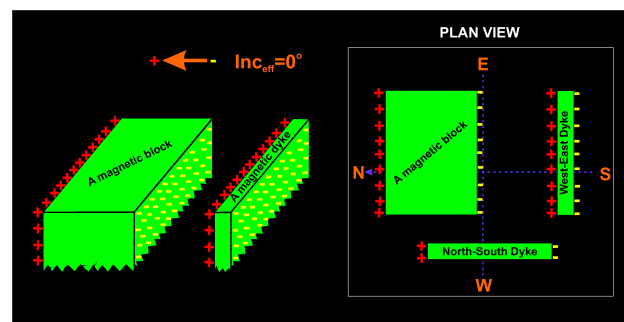
**Figure 2.5:** A magnetic body (Green-coloured) in different 2D-type contacts with non-magnetic rocks (Brown-coloured). Note that the angle between the contact strike (Dashed red line) and profile direction (Blue line) is usually kept constant at  $90^\circ$ : (a) Contact is acutely dipped (inclined), typical of normal faults; (b) Contact is obtusely dipped, as for reverse faults; and (c) Contact is vertical, typical of strike-slip faults. Note that profiles are directed from magnetic to non-magnetic rocks, as indicated by arrowheads.

their strikes and dips, respectively, within and relative to the horizontal plane (Wernicke & Burchfiel, 1982). Figure 2.5 depicts the different configurations possible for vertical and dipping faults or magnetic two-dimensional (2D) contacts within the crystalline basement. The vertical magnetic contact is depicted in figure 2.5c.

#### 2.4.2 Problems due to RTE of $\Delta T$ responses from 2D magnetic contacts

Approximation by 2D magnetic contact model (Figure 2.5) presents an additional challenge, which results from interactions between the geometry of the model and the distribution of induced magnetisation around edges of the model, under the influence of the North-oriented inducing (main) geomagnetic field. Here, I use schematic magnetic block and dyke models that are essentially bound by 2D contacts to discuss this additional problem (Figure 2.6). Figure 2.6 presents the distribution of surface magnetostatic charges around these models (assuming that models are uniformly magnetised, so that net volume magnetostatic charge=0; Blakely, 1996). The figure shows magnetic blocks, represented by green rectangular cuboids of infinite depth extent and polygons (in plan view), when the inclination of the inducing geomagnetic field ( $\alpha$ ) is: (a)  $90^\circ$  (vertical or RTP, Figure 2.6a); (b)  $45^\circ$  (Figure 2.6b); and (c)  $0^\circ$  (horizontal or RTE, Figure 2.6c). As portrayed

in figure 2.6, magnetic anomalies only occur at boundaries at which magnetostatic charges are generated as a result of intersections between magnetic flux lines induced by the magnetisation vector, and such boundaries. Thus, the top (horizontal) and/or vertical boundaries between the anomalous polygonal magnetic bodies (Green-coloured) and their non-magnetic host rocks (Transparent) in figure 2.6 generate  $\Delta T$ . Positive (+) surface magnetostatic charges and their negative (-) equivalents are directed parallel to the direction of induced magnetisation ( $\mathbf{J}_i$ ) as shown. Consequently, only 2D magnetic boundaries along which this condition is satisfied can be imaged on  $\Delta T$  maps. Schematics showing the magnetic field lines (flux) for the respective  $\alpha$  values used are also shown in the lower panels in figure 2.7.

(a)  $\alpha=90^\circ$  (RTP).(b)  $\alpha=45^\circ$ .(c)  $\alpha=0^\circ$  (RTE).

**Figure 2.6:** Schematic showing changes in the distribution of surface magnetostatic charges with changes in the inclination of the inducing geomagnetic field ( $\alpha^\circ$ , orange-coloured arrow). Magnetic bodies (green-coloured) are bound by polygonal 2D edges. Examples are for magnetic block model, North-South and East-West trending dykes at inclinations of: (a)  $90^\circ$ ; (b)  $45^\circ$ ; and  $0^\circ$ . Red positive symbols (+) depict positive magnetostatic charges, while yellow negative symbols (-) depict negative magnetostatic charges. Sketches of North-South (N-S) and East-West (E-W) profiles across the resulting  $\Delta T$  are presented in Figure 2.7.

When the inclination of the inducing geomagnetic field is vertical ( $\alpha = 90^\circ$  at the poles or RTP, Figures 2.6a and 2.7a) the induced flux intersects only the top and/or bottom boundaries (contacts) of the anomalous body. Such boundaries produce  $\Delta T$ , and are, therefore, imaged on  $\Delta T$  maps. The amplitude and shape of such anomalies are equal irrespective of the strike of the boundary, i.e., anomalies do not exhibit anisotropy. This is shown in figure 2.7a for East-West (E-W) and North-South (N-S) profiles across the source in figure 2.6a. When inducing magnetisation is oblique, say  $\alpha=45^\circ$  (e.g., figures 2.6b and 2.7b), the induced magnetic flux always intersects both the top and vertical contacts (edges) of the anomalous source. Consequently, irrespective of their azimuthal orientation (strike), the 2D edges of such sources produce  $\Delta T$  and can be imaged. However, the amplitude and shape of resulting anomalies vary with the strike of the contact, i.e., anomalies exhibit anisotropy. Thus,  $\Delta T$  profiles from East-West (E-W) and North-South (N-S) striking contacts are not the same (Figure 2.7b).

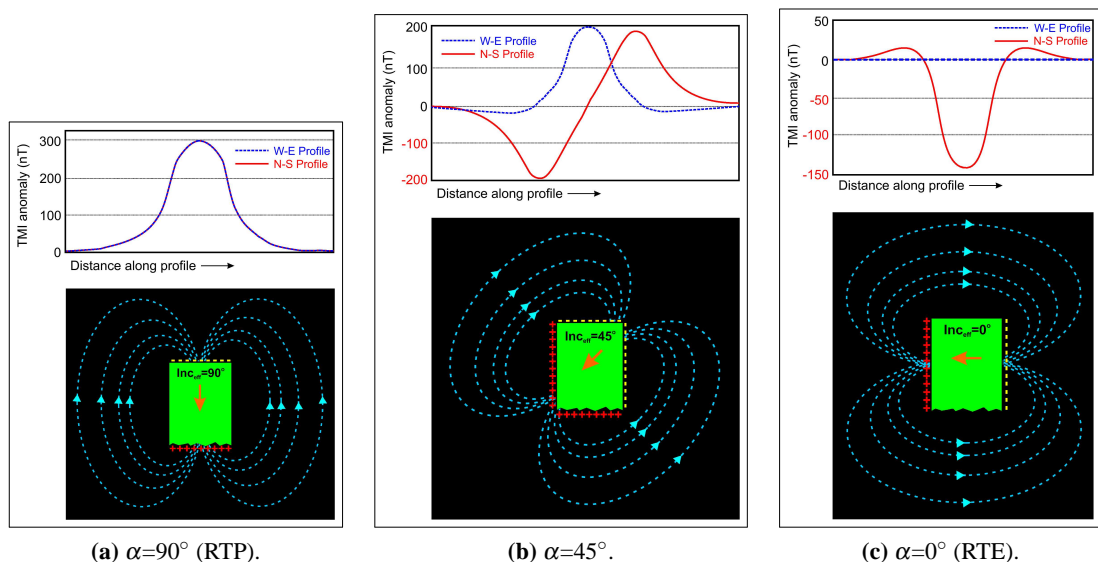


**Figure 2.7:** Schematic showing North-South, N-S (Red-coloured) and East-West, E-W (Blue-coloured) profiles across North-South (N-S) cross sections of  $\Delta T$  resulting from the magnetostatic charge distributions shown in figure 2.6. The green-coloured structure and its magnetic 2D contacts strike perpendicularly into the page.

Once the inducing geomagnetic field (and magnetisation) is horizontal (reduced-to-equator or RTE), magnetic flux lines are parallel to North-South (N-S) striking 2D edges (contacts) and cannot intersect both the top and N-S striking edges of the anomalous source (Figure 2.6c). Only East-West (E-W) and other non-N-S trending edges/contacts can be intersected by the flux. Therefore, N-S striking 2D contacts do not produce any anomalies and cannot, therefore, be imaged on RTE  $\Delta T$  maps. On the other hand, anomalies from E-W and other non-N-S trending contacts exhibit anisotropy at RTE. This is illustrated by the E-W and N-S profiles in figure 2.7c. However, Beard (2000) demonstrated that N-S striking 2D magnetic dikes at the equator generate detectable  $\Delta T$  when folded and/or strike-slip faulted. E-W directed en-echelon strike-slip faulting of N-S striking magnetic structures are discontinuities at which an otherwise parallel induced flux intersects the East-West discontinuities. Since these strike-slip faults are locally discontinuous, the intersec-

tions result in discrete, pearl-like (dipolar)  $\Delta T$  that are localised at such sites (Figure 2.8b). These anomalies result from positive and negative magnetic poles, which reside, respectively, on opposing (North and South) edges of each faulted piece of the N-S magnetic structure (Figure 2.8a). Hence, these dipolar anomalies increase in size with increasing offsets along faults (Beard, 2000), and the distinctive linear *string of pearly dipoles* (Figure 2.8) may be the only indicator of locally discontinuous North-South (N-S) striking regional basement faults on RTE  $\Delta T$  maps. Beard (2000) also showed that significant along-strike variations in the magnetic susceptibility of North-South structures produce alternating bands of magnetic anomaly lows (for zones of high susceptibili-

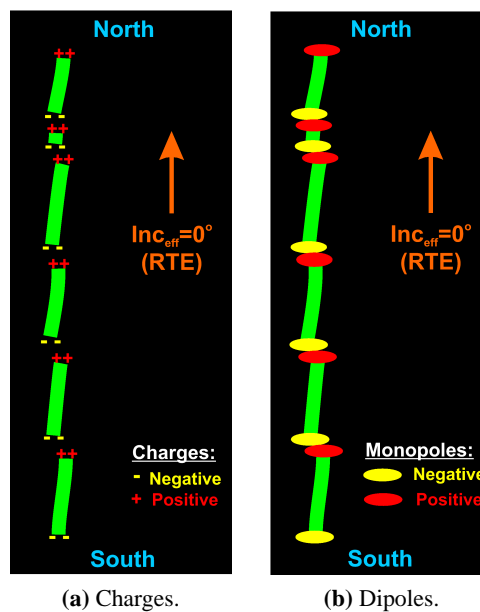


**Figure 2.8:** An illustration to show the generation of linear dipolar  $\Delta T$  (string of pearls) from magnetostatic charges along East-West (E-W) corners of locally discontinuous or en-echelon North-South (N-S) striking 2D magnetic contacts. The 2D magnetic contacts in this figure are the North-South (N-S) edges of the green-coloured structure (See also figure 2.6c).

ties) and highs (for zones of low susceptibilities). A valid interpretation of the reduced-to-equator version of the NE Nigeria  $\Delta T$  dataset must, therefore, account for the effects of: (1) anomaly amplitude reduction due to the minimal magnetisation at the geomagnetic equator (Section 2.3.1); (2) phase changes or anisotropic anomalies (Sections 2.3.1 and 2.3.2); (3) anomaly interference due to its preferential East-West (E-W) elongation; and (4) any processing noise in the data. Such an interpretation must also recover the subtle anomalies that are attenuated in the dynamic range of anomalies present (Section 2.3.3), as well as attempt to account for any North-South striking 2D contacts that may be present on the  $\Delta T$  grid. The semi-automatic methods and the approach adopted to achieve these objectives are discussed below.

## 2.5 Semi-automatic methods and $\Delta T$ data interpretation

Semi-automatic methods are rapid non-linear inverse methods employed in the initial stages of magnetic data interpretation to estimate the location, depth, dip, as well as susceptibility contrasts of edges of magnetic anomaly sources directly from either TMI ( $T$ ) or  $\Delta T$  datasets (Blakely, 1996). These methods require the *a priori* stipulation of a geometric model, e.g., the 2D contact, and are based on functions of Cartesian derivatives of  $\Delta T$  datasets or ratios between these derivatives. A couple of such methods will be evaluated for application to NE Nigeria  $\Delta T$  dataset. This section discusses the basis of, and justification for, these methods.

### 2.5.1 Spatial Cartesian derivatives of $\Delta T$ from 2D magnetic sources

Potential fields, e.g., TMI ( $T$ ) and its anomalies, are spherical solid harmonic functions since they satisfy both Euler's and Laplace's equations (Blakely, 1996). Harmonic functions and their spatial derivatives satisfy Laplace's equation outside the region containing their sources, so that  $\nabla^2 T = 0$ . This condition is only satisfied at the inflection point(s) of any function.<sup>12</sup> The second vertical derivative is, therefore, an ultimate measure of the rate of change of slope of a function (Blakely, 1996; Chapra, 2012). Inflection points of harmonic functions occur directly over the edges of vertical magnetic anomaly sources (Vacquier et al., 1951; Wickerham, 1954). Also, first vertical derivatives ( $\frac{\partial T}{\partial z}$ )=0, while first horizontal derivatives ( $\frac{\partial T}{\partial x}$ ) are at their maxima, at inflection points. Consequently, inflection points are employed for locating edges of anomalous magnetic bodies (Vacquier et al., 1951, Wickerham, 1954, Smith, 1959, Cordell & Grauch, 1982, Hood & Teskey, 1989, Miller & Singh, 1994). To determine inflection points (or locate edges) across a  $\Delta T$  dataset, spatial derivatives of the dataset ( $\frac{\partial \Delta T}{\partial z}$ ,  $\frac{\partial \Delta T}{\partial x}$  and/or  $\frac{\partial \Delta T}{\partial y}$ ) must first be obtained.

$\Delta T$  measurements are usually obtained at discrete (sampling) intervals along profiles, the general direction (orientation) of which is chosen such that they are perpendicular to the general direction of strike (Figure 2.5) of major geological features in the survey area (Reeves, 2005). Figure 2.9 presents a cross-section of a 2D magnetic contact with infinite strike in the  $y$  direction. Observe that the profile is kept perpendicular to the strike of the contact as earlier shown in figure 2.5.

The  $\Delta T$  response of a 2D magnetic contact with the attitude and extent shown in figure 2.9 can be determined from its scalar magnetic potential,  $V$ . Using equation (2.1.1) Jia & Meng (2009)

<sup>12</sup>The inflection points of any function are locations at which its curvature is zero.

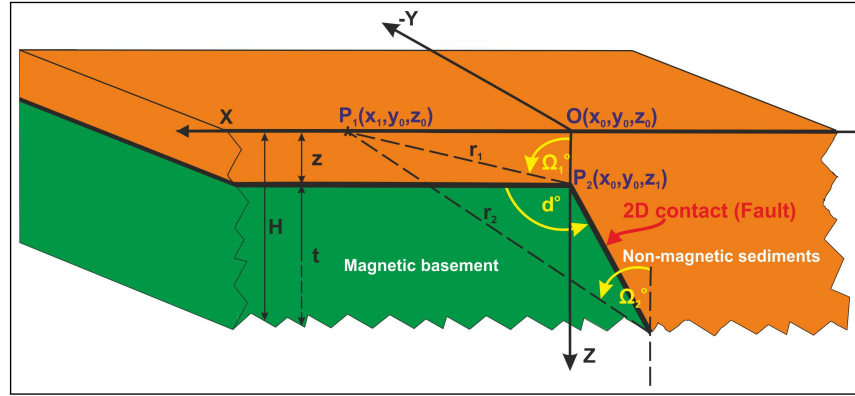


**Figure 2.9:** Sketch showing the spatial relationship between the magnetic contact/step model and the variables used to derive its  $\Delta T$  and spatial Cartesian derivatives. Note that the profile is along the  $x$ -axis, the contact strike is along the  $y$ -axis, and depth is positive downward along the  $z$ -axis. The figure is modified from Nabighian (1972).

expressed the scalar magnetic potential of a 2D magnetic contact as follows (Equation (2.5.1)):

$$V_{(x,z)} = \frac{\mu_o}{2\pi} \iint_S \frac{\mathbf{m} \cdot \mathbf{r}}{|\mathbf{r}|^2} \delta x \delta z \quad (2.5.1a)$$

$$V_{(x,z)} = \frac{\mu_o}{2\pi} \iint_S \frac{\mathbf{m}_x(x_1 - x_0) + \mathbf{m}_z(z_0 - z_1)}{(x_1 - x_0)^2 + (z_0 - z_1)^2} \delta x \delta z \quad (2.5.1b)$$

where  $\mu_o$  is permeability of vacuum;  $S$  is the cross section of the 2D source in  $x$ - $z$  plane (Figure 2.9);  $\mathbf{m}$  is the magnetic dipole moment, with components  $m_x$  and  $m_z$ , respectively, in the  $x$  and  $z$  directions;  $\mathbf{r}$  is the vector directed from the source to the observation point, with magnitude  $|\mathbf{r}| = \sqrt{\{(x_1 - x_0)^2 + (z_0 - z_1)^2\}}$ ; and  $(x_1, z_0)$  represents location of observation, while  $(x_0, z_1)$  is the location of the 2D contact.

Where an edge of a geological body can be approximated by a 2D magnetic contact of infinite depth extent (Figure 2.9), Nabighian (1972) related its  $\Delta T$  response to its physical properties and geometry (Equation (2.5.1)) using equation (2.5.2):

$$\Delta T_x = \tau \left\{ (\Omega_1 - \Omega_2) \cos \omega + \sin \omega \ln \frac{r_1}{r_2} \right\} \quad (2.5.2)$$

where all trigonometric quantities are in degrees;  $\Delta T_x$  is the scalar magnitude of the  $\Delta T$  along the profile direction ( $x$ -axis);  $\tau = 2\delta k F c \sin d$ ;  $F$  is the magnitude of the inducing magnetic field;  $c = 1 - \cos^2(\phi) \sin^2 A$ ;  $\delta k$  is the magnetic susceptibility contrast;  $d$  is the dip (measured from the positive  $x$ -axis, Figure 2.9);  $\phi$  is the effective inclination of the magnetisation vectors derived from  $\alpha$  and/or  $\beta$  (See equation (2.2.6));  $\omega = 2I - d - 90$ ;  $I$  is the component of the inducing field in the plane at right angles to the strike of the contact. This plane contains the profile direction;  $A$  is the angle between the positive  $x$ -axis (of the profile) and the magnetic north direction (Figure 2.10). Thus,  $A$  is related to the strike ( $\eta$ ) of the contact (Figure 2.10). When  $A = 0^\circ$  the contact strike is  $\eta = \pm 90^\circ$  from the geomagnetic North direction, i.e., contact strikes East-West (E-W). Consequently, varying the profile direction by  $\zeta$  so that  $A = A + \zeta$  has the effect of automatically changing the strike of the magnetic contact to  $A + \zeta \pm 90^\circ$ ; and  $z$  is the depth of the contact model;

$\tan I = \frac{\tan(\phi)}{\cos A}$ ;  $\Omega_1, \Omega_2$  and other variables are as shown in figure 2.9.

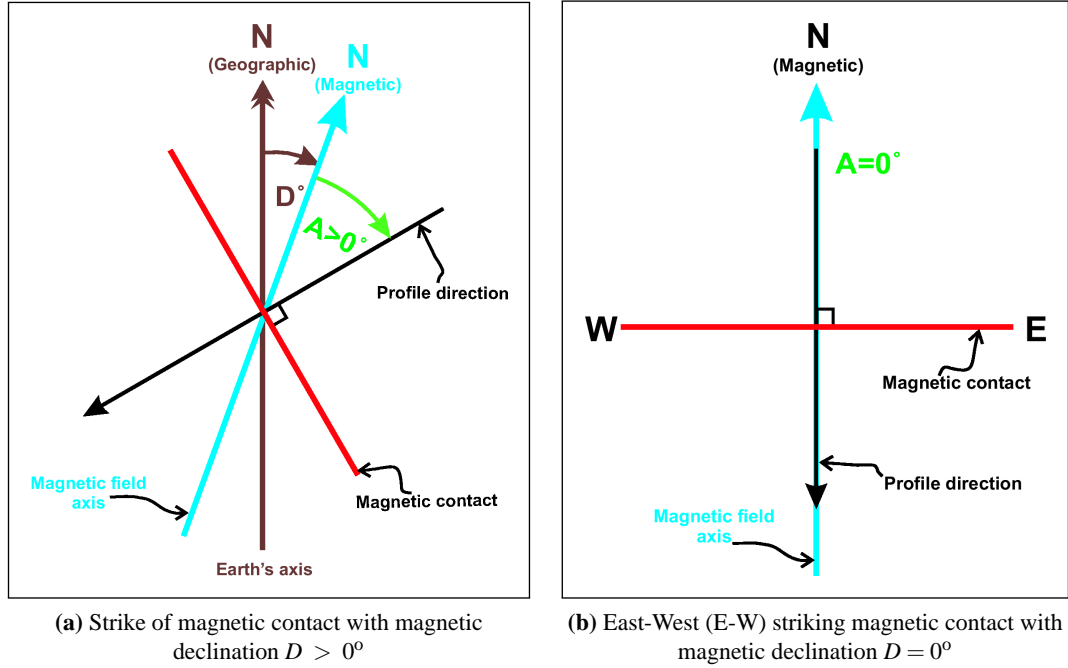


**Figure 2.10:** Strike (Spatial horizontal orientation) of 2D magnetic contacts relative to the geomagnetic north (N) pole. NB: For all variations of the contact, the profile direction is always perpendicular to the strike of the 2D contact.

**Horizontal derivatives** of the  $\Delta T$  in equation (2.5.2) along the Cartesian  $x$  or  $y$  direction of figure 2.9 is defined as follows (Nabighian, 1972):

$$\frac{\partial \Delta T_x}{\partial x} = \tau \left\{ \frac{z \cos \omega + x \sin \omega}{z^2 + x^2} \right\} \quad (2.5.3a)$$

$$\frac{\partial \Delta T_x}{\partial y} = \tau \left\{ \frac{z \cos \omega + y \sin \omega}{z^2 + y^2} \right\} \quad (2.5.3b)$$

where  $x = x_1 - x_0$ ,  $y = y_0$  and  $z = z_1 - z_0$  (Figure 2.9). All other variables and quantities are as defined for equation (2.5.2). Because 2D magnetic contacts are assumed to be of infinite strike along the  $y$ -axis  $\Delta T$  varies only along the  $x$  and  $z$ -axes so that  $\frac{\partial \Delta T_x}{\partial y} = 0$ , and  $\left| \frac{\partial \Delta T_x}{\partial x} \right| \geq 0$ .

Also, Nabighian (1972) defined the **vertical derivative** (Equation (2.5.4)) of the  $\Delta T$  in equation (2.5.2) along the Cartesian  $z$  direction of figure 2.9 as the Hilbert transform pair of its horizontal derivative in either the  $x$  or  $y$  direction (Equation (2.5.3)).

$$\frac{\partial \Delta T_x}{\partial z} = \tau \left\{ \frac{x \cos \omega - z \sin \omega}{z^2 + x^2} \right\} \quad (2.5.4)$$

where  $x = x_1 - x_0$ ,  $y = y_0$  and  $z = z_1 - z_0$  (Figure 2.9). All other variables and quantities are as

defined in equation (2.5.2).

The central difference scheme of Cordell & Grauch (1985), which uses the operator  $(\frac{-1}{2\Delta x}, 0, \frac{1}{2\Delta x})$  where  $\Delta x$  is the sampling interval or grid spacing is a stable means of obtaining horizontal derivatives from gridded  $\Delta T$  datasets (Reeves, 2005). Nabighian (1972) showed the vertical and horizontal derivatives of a  $\Delta T$  profile ( $\frac{\partial \Delta T_x}{\partial z}$  and  $\frac{\partial \Delta T_x}{\partial x}$ ) to be Hilbert transform pairs. Therefore, for profile data, vertical derivatives can be computed from their horizontal derivatives. Using this approach ensures that these derivative pairs are smoothed equally (Phillips, 2000; Pilkington & Keating, 2004). However, for gridded  $\Delta T$  datasets, the vertical derivative can only be computed in the wavenumber (spatial frequency) domain using Fast Fourier transforms (Phillips, 2000). Equations (2.5.3) and (2.5.4) will be used to obtain derivatives for profile  $\Delta T$  datasets using MATLAB<sup>TM</sup> in chapter 3.<sup>13</sup> The same equations will be implemented in GETgrid<sup>TM</sup> and Oasis montaj<sup>TM</sup> software to obtain equivalent derivatives for gridded data in chapters 4 and beyond. Pedersen et al. (1990) show that first and higher-order horizontal derivatives of gridded  $\Delta T$  data along any Cartesian coordinate axis enhance anomalous features (structures) with strikes perpendicular to the chosen axis.

In summary, semi-automatic methods of magnetic data interpretation depend on the curvature (derivatives) of  $\Delta T$  (Equations (2.5.3) and (2.5.4)). Each method assume the presence of only 2D magnetic contacts, and depends on a “special function” (Phillips, 2000) whose magnitude is either zero (inflection point) or a maximum directly above locations of anomalous magnetic sources, e.g., above the point  $O(x_0, y_0, z_0)$  in figure 2.9. The same function can then be manipulated, either by direct substitution or in combination with other special functions to estimate depths and/or magnetic susceptibility contrasts at that location,  $O(x_0, y_0, z_0)$ . Several of these methods have and continue to be proposed (e.g., Phillips, 2000; Salem et al., 2007; Pilkington, 2007).

Excellent reviews of the selected semi-automatic methods, are presented in Li (2003); Phillips (2000); Phillips et al. (2007); Pilkington (2007); Pilkington & Keating (2004). I am not aware of any application of these methods to RTE  $\Delta T$  datasets, particularly, in terms of depth estimation. Therefore, elaborate tests have been designed to examine the effectiveness of selected semi-automatic methods (Chapters 3 to 5). Observations from these tests will be applied to NE Nigeria  $\Delta T$  dataset in chapter 6.

Since considerable complexities are expected from the inevitable RTE of datasets when  $|\alpha| \leq 20^\circ$ , and derivatives amplify the noise content of datasets, when present (Section 2.3.3), semi-automatic methods to be applied to the Nigerian dataset are carefully selected here. Methods that are based on first-order derivatives or are independent of  $\alpha$  and/or magnetic susceptibility are preferred to those that depend on second and/or higher-order derivatives. This is because first-order derivatives do not significantly amplify noise or processing artefacts in datasets. Based on these, the methods I have selected for comparison with the “Tilt-Depth” method include the horizontal gradient magnitude

---

<sup>13</sup>MATLAB<sup>TM</sup> is The MathWorks Inc., USA's high-level computing language and interactive software environment.

of  $\Delta T$  ( $\text{HGM}_{(\Delta T)}$ ), analytic signal amplitude (ASA), local wavenumber ( $\text{SPI}^{TM}$ ), second vertical derivative (SVD) and horizontal gradient magnitude of  $\theta$  ( $\text{HGM}_{(\theta)}$ ). These methods are introduced below.

### 2.5.2 The horizontal gradient magnitude of $\Delta T$ ( $\text{HGM}_{(\Delta T)}$ ) method

The horizontal gradient magnitude or the absolute value of the horizontal derivatives of  $\Delta T$ ,  $\text{HGM}_{(\Delta T)}$  (Finn & Morgan, 2002) is expressed in equation (2.5.5).

$$\frac{\partial \Delta T}{\partial H} = \sqrt{\left(\frac{\partial \Delta T_x}{\partial x}\right)^2 + \left(\frac{\partial \Delta T_y}{\partial y}\right)^2} \quad (\text{For grid data on the } x, y \text{ plane}) \quad (2.5.5a)$$

$$\frac{\partial \Delta T_x}{\partial H} = \sqrt{\left(\frac{\partial \Delta T}{\partial x}\right)^2} \quad (\text{For profile data along the } x \text{ axis}) \quad (2.5.5b)$$

where  $x = x_1 - x_0$ ,  $y = y_0$  and  $z = z_1 - z_0$  (Figure 2.9). All other variables and quantities are as defined for equation (2.5.2). Because 2D magnetic contacts are assumed to be of infinite strike along the  $y$  axis  $\Delta T$  varies only along the  $x$  and  $z$  axes so that  $\frac{\partial \Delta T}{\partial y} = 0$ .

Peaks (maxima) of the  $\text{HGM}_{(\Delta T)}$  occur directly over edges of magnetic anomaly sources, but can be displaced slightly when the contact is not vertical. According to Pilkington & Keating (2004), the limit of effectiveness of the  $\text{HGM}_{(\Delta T)}$  method in locating edges of anomalous sources is prescribed by the anomaly interference and noise content of data. However, the  $\text{HGM}_{(\Delta T)}$  is inclination dependent (Phillips, 2000). Hence, the method is not suitable for depth estimation from RTE datasets.

$\text{HGM}_{(\Delta T)}$  maxima on gridded datasets can be efficiently located and traced using the curve-fitting maxima detection technique of Blakely & Simpson (1986). Throughout this study, this technique will be employed to trace maxima from other methods, whenever they are required. The method searches for maxima or peaks in gridded data, by comparing each grid point, except those on grid margins, with its eight nearest neighbours in four directions (along the row, column and diagonals, containing the grid point). Hence, the algorithm for this method uses a  $3 \times 3$  moving window within which it solves for inequalities between each grid point and its eight neighbouring points.

The Blakely & Simpson (1986) method solves for four inequalities, one for each of the four directions containing the current grid point, and assigns a counter for each inequality satisfied. This counter ranges from 0 (when none of the four inequalities is satisfied) to 4 (when all four inequalities are satisfied) and indicates the quality of the maximum at the centre of the window. In order to minimise uncertainties and reduce excessive clusters of located maxima, only location traces obtained from the minimum counter required to represent observable trends in the dataset are retained.

### 2.5.3 The analytic signal amplitude (ASA) method

The analytic signal amplitude (ASA or  $|A|$ ) refers to the amplitude of the complex analytic function ( $A$ ), defined as follows (Nabighian, 1972):

$$A(x, z) = \frac{\partial \Delta T_x}{\partial x} - i \frac{\partial \Delta T_x}{\partial z} \quad (\text{Complex analytic function along the } x \text{ axis}) \quad (2.5.6a)$$

$$\equiv |A(x, z)| e^{i\Theta} \quad (\text{Thurston \& Smith, 1997}) \quad (2.5.6b)$$

$$|A(x, z)| = \sqrt{\left(\frac{\partial \Delta T_x}{\partial x}\right)^2 + \left(\frac{\partial \Delta T_x}{\partial z}\right)^2} \quad (\text{For profile data along the } x \text{ axis}) \quad (2.5.6c)$$

$$|A(x, y, z)| = \sqrt{\left(\frac{\partial \Delta T_x}{\partial x}\right)^2 + \left(\frac{\partial \Delta T_y}{\partial y}\right)^2 + \left(\frac{\partial \Delta T}{\partial z}\right)^2} \quad (\text{For grid data, in the } x, y \text{ plane}) \quad (2.5.6d)$$

where  $\frac{\partial \Delta T_x}{\partial x}$ ,  $\frac{\partial \Delta T_y}{\partial y}$  and  $\frac{\partial \Delta T}{\partial z}$  are amplitude derivatives of  $\Delta T$ , respectively, along the  $x$  and  $y$  Cartesian directions,  $i = \sqrt{-1}$  is the imaginary number, and  $\Theta$  is the local phase (Thurston & Smith, 1997).

In the 2D case ( $\frac{\partial \Delta T_y}{\partial y} = 0$ ),  $|A_{(x,z)}| = |A_{(x,y,z)}|$ , and  $|A_{(x,z)}|$  is the envelope over all possible values of  $\alpha$  and source types, of both the vertical and horizontal derivatives of  $\Delta T$ .  $|A_{(x,z)}|$  is thus a signal that is independent of the direction of magnetisation (Haney et al., 2003).

In the non-2D case ( $\frac{\partial \Delta T_y}{\partial y} \neq 0$ ). Hence,  $|A_{(x,y,z)}| \neq |A_{(x,z)}|$ , the ASA is not the envelope of the total gradient of gridded datasets (Lin-ping & Zhi-ning, 1998), especially, when  $\Delta T$  is not at RTP (Haney et al., 2003). Comparisons between the 3D analytic signal amplitude versions of RTE and RTP of  $\Delta T$  datasets show that the method is also independent of magnetisation when data is RTE (Haney et al., 2003). Hence, the analytic signal amplitude provides an effective means of delineating locally discontinuous North-South (N-S)-striking magnetic contacts from RTE-transformed  $\Delta T$  datasets, on which they appear as linear "string of pearls" (Section 2.4.2).

Like the horizontal gradient magnitude of transformed  $\Delta T$  ( $\text{HGM}_{(\Delta T)}$ ) method, the ASA method is also at its peaks or maxima when it is directly over the edges of 2D magnetic contacts (Nabighian, 1972). The analytic signal amplitude method is very useful when dealing with  $\Delta T$  datasets from regions of low or horizontal geomagnetic field inclinations (MacLeod et al., 1993), and when remanent magnetisation is present (Beard, 2000).

Since ASA is a symmetric function with its peak directly located above source edges, irrespective of magnetisation direction and dip, Nabighian (1972) showed that the depths ( $z_{(ASA)}$ ) may be determined using equation (2.5.7).

$$z_{(ASA)} = \frac{1}{\left\{ \frac{\partial}{\partial x} \left( -\frac{|A_1|}{|A_0|} \right) \right\}} \quad (2.5.7)$$

where  $|A_0|$  refers to the 2D analytic signal amplitude at  $x = 0$  (local maximum of  $|A|$ ), and  $|A_1|$  is the first-order horizontal derivative of  $|A_0|$ .

#### 2.5.4 The local wavenumber, LW or SPI<sup>TM</sup> method

The local wavenumber (LW) method (Thurston & Smith, 1997 and Smith et al., 1998) is based on spatial horizontal derivatives of the local phase ( $\Theta$ ) of the complex analytic function (Equation (2.5.6b)). The  $x$  and  $y$  components of the local wavenumber ( $\kappa$ ) are denoted as  $\kappa_{(x,z)}$  and  $\kappa_{(y,z)}$ , respectively. Thurston & Smith (1997) defined  $\kappa_{(x,z)}$  as follows (Equation (2.5.8)).

$$\kappa_{(x,z)} = \frac{\partial \Theta_x}{\partial x} \quad (\text{For profile along } x \text{ axis), where;} \quad (2.5.8a)$$

$$\Theta_x = \tan^{-1} \left\{ \frac{\partial \Delta T_x}{\partial z} / \frac{\partial \Delta T_x}{\partial x} \right\} \quad (2.5.8b)$$

$$\therefore \kappa_{(x,z)} = \frac{1}{|A_{(x,z)}|} \left\{ \frac{\partial^2 \Delta T}{\partial x \partial z} \frac{\partial \Delta T}{\partial x} - \frac{\partial^2 \Delta T}{\partial x^2} \frac{\partial \Delta T}{\partial z} \right\}, \text{ and} \quad (2.5.8c)$$

$$z_{(LW)} = \frac{1}{\text{Local maximum of } \kappa_{(x,z)}} \quad (2.5.8d)$$

where  $|A_{(x,z)}|$  is the analytic signal amplitude. Equivalent equations for gridded  $(x,y)$   $\Delta T$  data exist (Phillips, 2000; Pilkington & Keating, 2004).

The local wavenumber is independent of magnetisation direction and dip effects (Pilkington, 2007, Li et al., 2010), and peaks directly above edges of magnetic sources irrespective of their geometry (Thurston et al., 2002). Depths for 2D sources are estimated using reciprocals of local wavenumber maxima at those locations (Equation (2.5.8d)). A major drawback of this method is that it requires second-order derivatives (Equation (2.5.8c)) which almost always leads to noise amplification (Phillips, 2000, Li, 2003, Salem et al., 2008). Salem et al. (2008) recommends upward continuation of noise-laden  $\Delta T$  datasets, prior to inversion.

#### 2.5.5 Estimating magnetic susceptibility contrast ( $\delta k$ ) and dip ( $d$ ) of 2D sources

Using equation (2.5.9a), Nabighian (1972) and MacLeod et al. (1993) related peak amplitudes of ASA of 2D sources ( $|A(x,z)|_{max}$ ), their horizontal location ( $x_o$ ) and depth ( $z$ ) to susceptibil-

ity contrast ( $\delta k$ ) at that location. Hence, depths estimated from ASA method (Equation (2.5.7)), LW method (Equation (2.5.8d)) and/or any other method are routinely substituted into equation (2.5.9a), to determine  $\delta k$ .

$$|A(x, z)|_{max} = \frac{\tau}{\sqrt{(x_o)^2 + (z)^2}} \quad (2.5.9a)$$

$$|A(x, z)|_{max}^2 = \frac{(\tau)^2}{z^2}, \text{ since } x_o = 0. \quad (2.5.9b)$$

$$\therefore \delta k = \frac{\sqrt{|A(x, z)|_{max}^2 \cdot z^2}}{2Fc \sin d} \quad (2.5.9c)$$

where  $x_o$  and  $z$  refer, respectively, to location and depth of contact; and  $\tau = 2\delta k Fc \sin d$  is the amplitude factor. Other variables were introduced in section 2.5.1 on page 25 and/or shown in figure 2.9.

Once  $z$  and  $\delta k$  are obtained, Nabighian (1972) showed that apparent dip ( $d$ ) can be determined from the horizontal derivative of  $\Delta T$  ( $\frac{\partial \Delta T_x}{\partial x}$ ) at locations corresponding to  $|A(x, z)|_{max}$  ( $x = 0$ ), using equation (2.5.10).

$$\frac{\partial \Delta T_x}{\partial x}_{(x=0)} = \frac{\tau \cdot \cos(\omega)}{z} \quad (2.5.10)$$

where  $\frac{\partial \Delta T_x}{\partial x}_{(x=0)}$  refers to the value of equation (2.5.3) at  $x = 0$ ,  $\tau = 2\delta k Fc \sin d$  and  $\omega = 2I - d - 90$  (Equation (2.5.2)). Other variables were introduced in section 2.5.1 on page 25 and/or shown in figure 2.9. Observe that the required quantity  $\frac{\tau}{z}$  (Equation (2.5.10)) is easily obtained from equation (2.5.9b).

## 2.6 Tilt angles ( $\theta$ ) of $\Delta T$ and the “Tilt-Depth” method

### 2.6.1 Tilt angles ( $\theta$ ) of $\Delta T$

Miller & Singh (1994) defined the tangent of  $\theta$  (Equation (2.6.1)) as the ratio of the spatial first-order vertical derivative to the total horizontal derivative of the  $\Delta T$ .

$$\theta = \tan^{-1} \left\{ \frac{\partial \Delta T_x / \partial z}{\partial \Delta T_x / \partial H} \right\} \quad (\text{For profile data along } x \text{ direction}) \quad (2.6.1a)$$

$$= \tan^{-1} \left\{ \frac{\partial \Delta T / \partial z}{\partial \Delta T / \partial H} \right\} \quad (\text{For grid data in } x, y \text{ plane}) \quad (2.6.1b)$$

where  $\frac{\partial \Delta T_x}{\partial z}$  and  $\frac{\partial \Delta T}{\partial z}$  are first-order vertical derivatives of  $T_x$  and  $T$ , respectively.  $\frac{\partial \Delta T_x}{\partial H}$  and  $\frac{\partial \Delta T}{\partial H}$  refer to the total horizontal derivatives of  $T_x$  and  $T$  (Equation (2.5.5)).

The many merits of transforming RTP  $\Delta T$  data to their  $\theta$  equivalent include:

1.  $\theta$  of  $\Delta T$  (RTP) datasets is positive over vertical magnetic anomaly sources with positive magnetic susceptibilities, but is zero at, or near, the edge of the source (Verduzco et al., 2004, Cooper & Cowan, 2006, Fairhead & Williams, 2006, Salem et al., 2007);
2. First-order Cartesian derivatives are less prone to noise amplification compared to second and higher-order derivatives; and
3. Amplitudes of first vertical and total horizontal derivatives depend directly on the amplitude of the input  $\Delta T$ . However, as a ratio which is also constrained by the arctan function,  $\theta$  is able to normalise the amplitudes present in the input  $\Delta T$  dataset, to range from  $\frac{-\pi}{2}$  to  $\frac{\pi}{2}$  (i.e.,  $-90^\circ$  to  $90^\circ$ ). Therefore,  $\theta$  acts as an unbiased automatic-gain-control (AGC) filter, equalizing and preserving long and short wavelength anomalies (Miller & Singh, 1994, Verduzco et al., 2004, Cooper & Cowan, 2006).

Since,  $\Delta T$  datasets contain anomalies from both shallow (high frequency/short wavelength) and deep (low frequency/long wavelength) sources and when obtained from regions characterised by horizontal and/or low inclinations of the geomagnetic field vector contain a large dynamic range of  $\Delta T$  (MacLeod et al., 1993; Miller & Singh, 1994; Verduzco et al., 2004) due to anisotropy and interference (Section 2.4.2), the automatic-gain-control (AGC) filter provided by  $\theta$  is better suited to evenly resolve both shallow and deep magnetic anomaly sources from such datasets (Miller & Singh, 1994). Transforming  $\Delta T$  maps to their  $\theta$  equivalent enhances important attributes of magnetic anomaly observations, facilitating the interpretation of the data as the  $\theta$  maps are simpler to interpret than other  $\Delta T$  derivative maps (Pilkington & Keating, 2004, Verduzco et al., 2004, Cooper & Cowan, 2006).

Also, because  $\theta$  are ratios of the derivatives of  $\Delta T$  they are independent of the magnetic susceptibility contrast ( $\delta k$ ) across the edge of the magnetic anomaly source. This is true irrespective of the approximating magnetic model under consideration.  $\theta$  is, therefore, a more direct response to the depths of anomalous magnetic sources (Miller & Singh, 1994) than the other derivatives (filters), which are  $\delta k$ -dependent. This independence of  $\theta$  from  $\delta k$  is a very well sought after

property in magnetic anomaly data interpretation since  $\Delta T$  datasets and their spatial derivatives depend directly on the  $\delta k$  between a magnetic anomaly source and its host rocks.  $\Delta T$  datasets and their derivatives cannot be directly inverted for magnetic anomaly source depth, without recourse to second and higher-order derivatives of the dataset which accentuate the noise content of data. The "Tilt-Depth" method (Salem et al., 2007) is an easy-to-implement special function designed to take advantage of the independence of  $\theta$  from  $\delta k$ . Since the method relies on  $\theta$  derived from first-order derivatives of  $\Delta T$ , it may be the most useful for interpreting low-resolution  $\Delta T$  data like those from NE Nigeria.

The total horizontal derivative of  $\theta$  or  $\text{HGM}_{(\theta)}$  method (Equation (2.6.2); Verduzco et al., 2004) can be used to further image subtle sources in  $\Delta T$  datasets.

$$\text{HGM}_{(\theta)} = \sqrt{\left(\frac{\delta\theta}{\delta x}\right)^2 + \left(\frac{\delta\theta}{\delta y}\right)^2} \quad (\text{For grid data}) \quad (2.6.2)$$

where  $\theta$  is Tilt angle,  $x$  and  $y$  refer to horizontal Cartesian axes.

The total horizontal derivative of  $\theta$  ( $\text{HGM}_{(\theta)}$ ) is equivalent to the absolute value of the local wavenumber (Verduzco et al., 2004).

### 2.6.2 The "Tilt-Depth" method

The "Tilt-Depth" method was proposed for application to RTP equivalents of total magnetic field intensity (TMI) anomaly obtained from East-West striking, vertical 2D magnetic contact models (Salem et al., 2007). Since this method is the main subject of investigation of this thesis, chapter 3 presents a more detailed introduction of the method prior to its application to profile  $\Delta T$  datasets.

Semi-automatic methods discussed in this section have been extensively evaluated using RTP  $\Delta T$  datasets (Phillips, 2000, Li, 2003, Pilkington & Keating, 2004, Pilkington, 2007). I am not aware of any comparisons of these methods using either profile or gridded RTE  $\Delta T$  datasets. Therefore, I will be evaluating the fidelity between structural edges outlined and the depths estimated for them by these methods from RTP and RTE equivalents of model  $\Delta T$  datasets. The "Tilt-Depth" method will now be tested using model  $\Delta T$  profile datasets (Chapter 3), and gridded datasets (Chapter 4). Depth estimates from gridded datasets will be statistically compared to establish the relative effectiveness of each method when applied to  $\Delta T$  (RTE) datasets.

## Chapter 3

# The “Tilt-Depth” method: Tested using profile $\Delta T$ datasets from 2D magnetic contacts

---

### 3.1 The “Tilt-Depth” method

Salem et al. (2007) obtained a simple relationship between the location and depth of vertical two-dimensional (2D) magnetic contacts (e.g., Figure 2.5c) and Tilt angles ( $\theta$ ) calculated from reduced-to-pole (RTP)  $\Delta T$  responses of such contacts.<sup>12</sup> This method, called “Tilt-Depth” assumes that contacts are only magnetised by induction in a vertical sense, RTP (i.e., remanent magnetisation is absent or negligible) with constant magnetic susceptibility contrast ( $\delta k$ ) throughout the entire length of the contact. The method relies on  $\theta$ , obtained from first-order horizontal and vertical derivatives of  $\Delta T$  (RTP) datasets using equation (2.6.1a) (For profile datasets) or (2.6.1b) (For gridded datasets).  $\theta$  of RTP datasets present many advantages (Section 2.6.1). Hence, a major objective of this study is to determine if these advantages can be extended to  $\Delta T$  (RTE) datasets. By relying on  $\theta$  from first-order derivatives of  $\Delta T$  datasets, known to be less prone to noise amplification compared with second and higher-order derivatives, the “Tilt-Depth” method also seems to offer a stable means of interpreting old archive magnetic datasets, which are typically of low to medium resolutions and, therefore, potentially noisy.

Two  $\theta$  curves obtained using  $\Delta T$  datasets from profiles across a vertical, East-West striking contact, when remanent magnetisation is zero and the induced magnetisation ( $\alpha$ ) is either vertical (RTP, i.e., red-coloured  $\theta$  curve) or horizontal (RTE, i.e., blue-coloured  $\theta$  curve) are shown in figure 3.1. The contact in this example is the vertical boundary between the embedded magnetic rocks (green-coloured) and the orange-coloured non-magnetic host rocks (Compare figures 2.5c and 3.1).<sup>3</sup> The red-coloured  $\theta$  curve (Figure 3.1) replicates the curve in Salem et al. (2007, Figure 1). Salem et al. (2007) showed that the location of the contact is traced by  $\theta = 0$  (the dashed-green line in figure 3.1). They also showed that the depth of the contact ( $z_{(est)}$ ) can be estimated using

---

<sup>1</sup>The word *contact* will hereafter refer to *two-dimensional (2D) magnetic contact*, unless otherwise qualified.

<sup>2</sup>Tilt angles will henceforth be replaced by the symbol  $\theta$ , with unit in degrees ( $^\circ$ ).

<sup>3</sup>The same contact was used to generate both  $\theta$  curves using equation (2.6.1a).

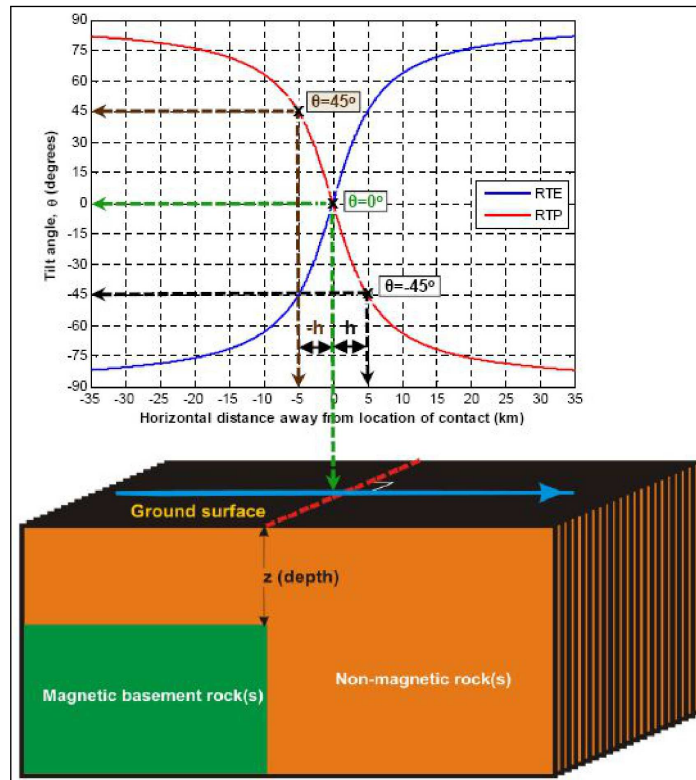


**Figure 3.1:**  $\theta$  curves from RTP and RTE of  $\Delta T$  datasets, obtained from profiles across a laterally extensive magnetic rock (basement, shown in green) in contact with non-magnetic rocks (orange-coloured) at its top and vertical edges. The solid, red curve is for the RTP dataset (Salem et al., 2007), while the blue curve is for the RTE equivalent. The dashed, red line traces the strike of the vertical contact. The light-blue line represents the profile, with arrowhead pointing to the North (N). The direction of the profile is always kept perpendicular to the strike of the contact (See figure 2.5). Note that the blue-coloured (RTE)  $\theta$  curve is the additive inverse ( $\times -1$  equivalent) of the red-coloured (RTP)  $\theta$  curve.

equation (3.1.1) as follows:

$$z_{(est)} = \frac{(|h| + |-h|)}{2} \quad (3.1.1)$$

where  $h$  and  $-h$  are determined, from the horizontal distances between locations corresponding to  $\theta = 0$  and, respectively,  $\theta = -45$  and  $\theta = 45$  on the profile, as shown by the dashed brown, green and black lines in figure 3.1.

Fairhead et al. (2008) show that strike directions of contacts, as well as throw directions across these contacts can also be estimated from  $\Delta T$  (RTP) datasets, using the “Tilt-Depth” method. Apparent susceptibility contrasts ( $\delta k$ ) at contact locations can also be derived when, as suggested in section 2.5.5, “Tilt-Depth” method estimates are combined, for example, with those from the analytic signal amplitude method (Section 2.5.3). This extended version of the “Tilt-Depth” method is the “Tilt-Depth-Dip- $\delta k$ ” method. The simplicity, elegance and utility of the “Tilt-Depth” method are demonstrated, for example, by Fairhead et al. (2011).

The blue-coloured (RTE)  $\theta$  curve (Figure 3.1) is the *additive-inverse* ( $\times -1$  equivalent) of the red-coloured (RTP)  $\theta$  curve, and shows that a similarly simple relationship also exists between  $\theta$

calculated from  $\Delta T$  (RTE) datasets and the location and depth of vertical contacts.<sup>4</sup> This is a very important and desirable observation in terms of the suitability of the “Tilt-Depth” method to the interpretation of  $\Delta T$  datasets, wherever datasets require RTE transformation. However, the shape and amplitude of  $\Delta T$  are strongly azimuth-dependent at the magnetic equator, RTE (Section 2.4.2, Figure 2.7c). Therefore, whether this relationship is also true for contacts with strike in directions other than East-West (E-W), or not, will be examined using profiles that are perpendicular to contact strike. The effect of contact azimuth on  $\theta$  and “Tilt-Depth” method estimates will be examined in section 3.5.

Magnetic contacts are not always vertical (Figures 2.5a and 2.5b) or orientated East-West (E-W) relative to the direction of the magnetic field. Consequently, prior to the application of the method to RTE datasets, this chapter investigates “Tilt-Depth” method estimates of the locations and depths of contacts in terms of the following effects: the inclination of induced magnetisation,  $\alpha$  (assuming remanent magnetisation is zero) or effective magnetisation,  $\phi$  (if remanent magnetisation is present); and the dip and strike direction of contacts. The main objective of chapters 3 and 4, therefore, will be to determine how deviations from “Tilt-Depth” method’s assumptions may affect the effectiveness of the method, using profile and gridded  $\Delta T$  datasets, respectively. The following sections deal with testing the method using  $\Delta T$  profile datasets obtained from profiles across contacts.

## 3.2 Methodology adopted for testing the “Tilt-Depth” method

### 3.2.1 Obtaining profile $\Delta T$ , its derivatives and $\theta$ datasets from contacts

The main objective of this section is to establish the robustness/effectiveness of the method in recovering the horizontal locations and depths of contacts of various depths, attitudes and magnetic properties. To achieve this objective the  $\Delta T$  response, as well as its first-order horizontal and vertical derivatives were generated, respectively, using Nabighian (1972)’s equations (2.5.2), (2.5.3a) and (2.5.4) from contacts, each of which was defined by a unique set of simple physical properties: its strike (Figure 2.10), dip and depth (Figures 2.5 and 2.9), magnetic susceptibility contrast ( $\delta k$ , Equation (2.2.5)) and magnetisation (Section 2.2.1).  $\theta$  representing each magnetic contact was then obtained using these derivatives (Equation (2.6.1a)).

Contacts were kept fixed in space, at 0 km (i.e.,  $O_{(x_o, y_o, z_o)}$  shown in figure 2.9 is at 0 km along all profiles) as shown in figure 3.1. Also, profiles were kept perpendicular to the strikes of contacts (Figure 2.10), directed from magnetic to non-magnetic (i.e., higher to lower susceptibility) rocks, were centred directly above the contact (at 0 km), and either 60 or 100 km long.  $\Delta T$ , its horizontal and vertical derivatives, and  $\theta$  were computed at 0.01 km intervals. The process I adopted to test

---

<sup>4</sup>*Additive-inverse* is used to distinguish this operation from ordinary inverse, which generally suggests a reciprocal.

the “Tilt-Depth” method using these profile datasets consist of the following steps:

- (a) Obtain spatial Cartesian derivatives of the  $\Delta T$  using equations (2.5.3a) and (2.5.4);
- (b) Convert derivatives to  $\theta$  using equation (2.6.1a);
- (c) Along each profile extract the location(s) corresponding to the desired  $\theta$  values. Where such  $\theta$  values occur at more than one location along a given profile, preferentially extract the occurrence closest to the known location of the contact for further analysis;
- (d) Determine the horizontal distance between  $\theta = 0$  and the location(s) corresponding to the desired  $\pm\theta$  values;
- (e) Compute depth estimates (Equation (3.1.1)) from the distance(s) between  $\theta = 0$  and the above-specified  $\pm\theta$  values; and
- (f) Determine the *error* in estimated location and depth of each contact. Section 3.2.2 explains the term error in the context of this study.

### 3.2.2 Defining errors in estimates of location and depth of magnetic geological features

Testing the method involved comparing estimates of locations ( $x_{o(est)}$ ) and depths ( $z_{(est)}$ ) of magnetic contacts obtained from the method with their precisely known (actual) equivalents,  $x_{o(mod)}$  and  $z_{(mod)}$ , respectively. Since these estimates may differ from the actual locations and depths of the contacts, I will use the term *error* to report the degree of accuracy (effectiveness) of the method. The accuracy of magnetic source parameter estimates using the method is reported in this study as absolute, relative and/or percentage errors.

#### (A) Absolute error ( $Err_{(abs)}$ ) in estimates of location and depth.

This refers to the difference between the estimated location or depth of two-dimensional (2D) magnetic contacts and the actual location or depth of the same contact. The ***absolute error in estimated location*** of contact edges ( $Err_{(abs)_{x_o}}$ ) is expressed mathematically as;

$$Err_{(abs)_{x_o}} = x_{o(est)} - x_{o(mod)} \quad (3.2.1)$$

where  $x_{o(est)}$  and  $x_{o(mod)}$  refer, respectively, to the estimated and actual location of the contact. The ***absolute error in estimated depth*** of edges of contacts ( $Err_{(abs)_{z}}$ ) is expressed as follows:

$$Err_{(abs)_{z}} = z_{(est)} - z_{(mod)} \quad (3.2.2)$$

where  $z_{(est)}$  and  $z_{(mod)}$  refer, respectively, to the estimated depth (Equation (3.1.1)) and actual depth of the contact.

**(B) Percentage error ( $Err_{(rel)}$  or  $Err_{(\%)}$ ) in estimates of location and depth.**

Percentage error in location and depth estimates refer to relative errors expressed in percent. So, **percentage error in location estimates** ( $Err_{(\%)_{x_o}}$ ) =  $Err_{(rel)_{x_o}} \times 100$ , while **percentage error in depth estimates** ( $Err_{(\%)_z}$ ) =  $Err_{(rel)_z} \times 100$ . Results from this study are mainly reported and discussed as percentage errors. This should enable easier comparison between results from this study and similar studies.

$Err_{(rel)_{x_o}}$  (relative error in location estimate) is the ratio of the absolute error in location (Equation (3.2.1)) to the actual depth of the contact. That is,  $Err_{(rel)_{x_o}} = \frac{Err_{(abs)_{x_o}}}{z_{(mod)}}$ ; where  $z_{(mod)}$  is the actual depth of the contact. It is negative when  $Err_{(abs)_{x_o}}$  is negative and vice versa. Similarly,  $Err_{(rel)_z}$  (relative error in depth estimate) is the ratio of the absolute error in depth (Equation (3.2.2)) to the actual depth of the contact. That is,  $Err_{(rel)_z} = \frac{Err_{(abs)_z}}{z_{(mod)}}$ ; where  $z_{(mod)}$  is the actual depth of the contact.

**(C) Significance of errors in estimates.**

The definitions of “error” above show that the *magnitude of error* reflects the degree to which the estimates approach the actual location or depth of model. Smaller magnitudes are closer to the actual than larger magnitudes. The *sign of the error* indicates the following: (i) For location estimates. Location error is zero when the estimated and actual locations are the same ( $x_{o(est)} = x_{o(mod)}$ ), i.e., location is accurately estimated. Otherwise, the estimated location is shifted away from the actual location of the magnetic body; (ii) For depth estimates. Depth error is zero when the estimated and actual depths are equal ( $z_{(est)} = z_{(mod)}$ ), i.e., *accurate depth estimate*. Error is positive only when estimated depth exceeds the actual depth of the contact ( $z_{(est)} > z_{(mod)}$ ), i.e., *overestimated depth*. It is negative when depth estimate is less than the actual depth of the model ( $z_{(est)} < z_{(mod)}$ ), i.e., *underestimated depth*.

Williams (2004), Reeves (2005) and Whitehead (2010) report accuracy limits of  $\pm 20\%$  of model depths for depths estimated from reduced-to-pole (RTP)-transformed  $\Delta T$  datasets, using other semi-automatic methods (e.g., local wavenumber and Euler deconvolution). Consequently, throughout this study, *depth estimates within  $\pm 20\%$  of model depth will be considered effective*. This limit will also apply to location estimates since none has been published.

Because Salem et al. (2007) showed the "Tilt-Depth" method to be effective for vertical, E-W striking contacts when vertically magnetised (RTP), I will start by examining location and depth estimates from these contacts, when at various depths and inclinations of induced and/or remanent magnetisation (Section 3.3). I begin by testing the method with vertical, E-W striking contacts at

various depths and inclinations of induced magnetisation ( $\alpha$ ) only in sections 3.3.1 to 3.3.3, and for effects of the Koenigsberger ratio (Q) and inclination of effective magnetisation,  $\phi$  (when remanent magnetisation is introduced) in section 3.3.4. The method will also be tested using dipping, E-W striking contacts in section 3.4. Finally, the method will be tested for the effect of changing strikes of vertical contacts relative to the magnetic North direction (Figure 2.10) in section 3.5. To ensure that my MATLAB<sup>TM</sup> scripts and functions worked well, they were first tested to see that the  $\theta$  profiles produced were independent of magnetic susceptibility contrasts,  $\delta k$  (See appendix B, figure B.1).

### 3.3 Testing the method using vertical, East-West striking contacts

#### 3.3.1 Effect of varying inclination of induced magnetisation ( $\alpha$ )

I used 111  $\Delta T$  profile datasets and their derivatives from vertical, East-West striking contacts, to test the method in this section. Profiles were obtained using Nabighian (1972)'s equations (Section 3.2.1), by varying only the depth and inclination of induced magnetisation ( $\alpha$ ), while assuming the following constants for each magnetic contacts: (1) Magnetic susceptibility contrast ( $\delta k$ )=0.002 SI units throughout its length and depth; (2) Dip,  $d = 90^\circ$  (i.e., Vertical); (3) Strike is kept constant throughout its infinite length (East-West,  $A = 0^\circ$ , Figure 2.10); (4) Magnetisation is only by induction ( $\mathbf{J}_i$ ) with ambient field strength,  $J_i = 65000$  nT at the magnetic poles (NGDC, 2010); and (5) Remanent magnetisation is absent.<sup>5</sup> Contacts were buried at depths of 3, 4 and 10 km. Spatial orientation of contacts has been discussed (Section 3.2.1). With these simple assumptions, Nabighian (1972)'s equations correspond to the ‘‘Tilt-Depth’’ method assumptions of Salem et al. (2007), when  $\alpha = 90^\circ$  (reduced-to-pole, RTP). The  $\Delta T$  response of the contacts was sampled at 0.01 km intervals along each profile computed. This sampling interval will apply to all profiles used in this chapter.

Figures 3.2a and 3.2b present examples, respectively of vertical and total horizontal Cartesian derivatives ( $\frac{\partial \Delta T}{\partial z}$  and  $\frac{\partial \Delta T}{\partial H}$ ) obtained from equations (2.5.3a) and (2.5.4) for various inclinations of induced magnetisation ( $\alpha$ ) when contacts are at a depth of 4 km.  $\theta$  obtained from these derivatives using equation (2.6.1a) are presented in figure 3.3. These figures demonstrate the effect that changing a variable ( $\alpha$  in this case) in these equations can have on the shapes and amplitudes of  $\Delta T$  and their  $\theta$  equivalents. For instance, when induced magnetisation is vertically or horizontally inclined ( $\alpha = 90^\circ$ , RTP or  $\alpha = 0^\circ$ , RTE), the zero value of the vertical derivative (Figure 3.2a), the maximum value of the total horizontal derivative (Figure 3.2b), as well as the zero value of their  $\theta$  (Figure 3.3), occur directly above the location of the vertical contact. However, such a simple correlation does not exist between the location of the contacts and the same derivatives once induced magnetisation is not vertically or horizontally inclined ( $\alpha \neq 90^\circ$  or  $\alpha \neq 0^\circ$ ). Consequently,

<sup>5</sup> $\alpha = \phi$  when remanent magnetisation is absent (Section 2.2.3).

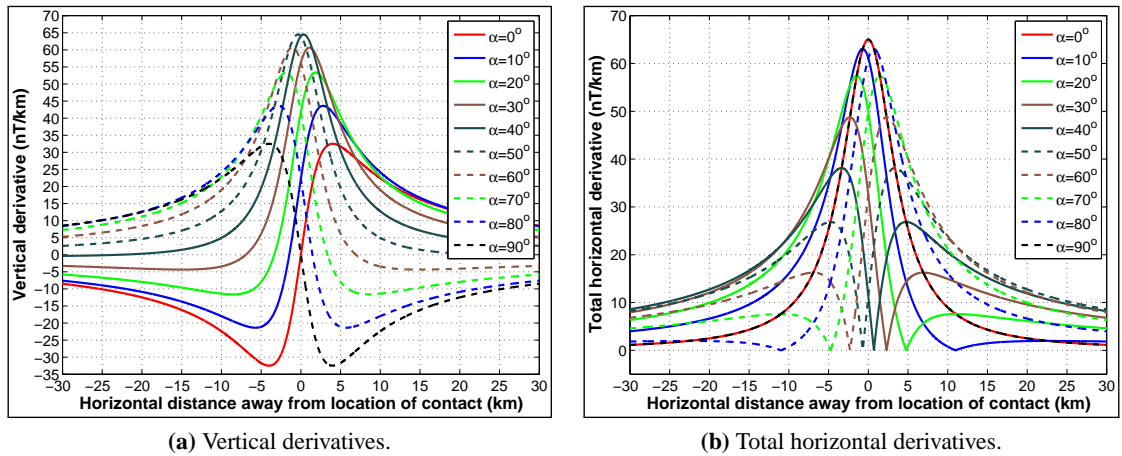


**Figure 3.2:** Effects of inclination of induced magnetisation ( $\alpha$ ) on the shape and amplitude of spatial Cartesian derivatives: (a) Vertical derivatives ( $\frac{\partial \Delta T}{\partial z}$ ); and (b) Total horizontal derivatives ( $\frac{\partial \Delta T}{\partial H}$ ), of  $\Delta T$  from vertical, E-W striking 2D magnetic contacts (depth=4 km) in the northern geomagnetic hemisphere.

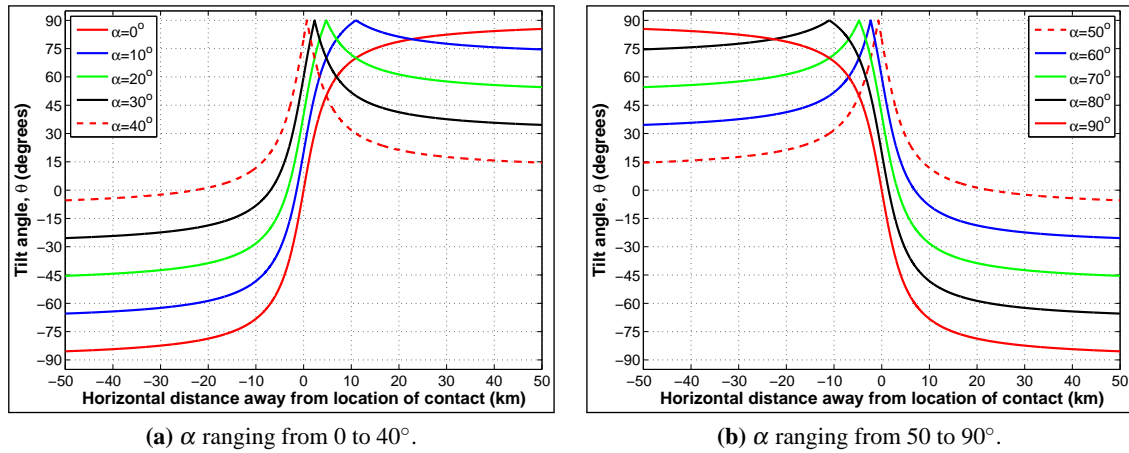


**Figure 3.3:** Effects of inclination of the induced magnetisation ( $\alpha$ ) on the shape and amplitude of  $\theta$  of  $\Delta T$  from vertical, E-W striking contacts (depth=4 km) in the northern geomagnetic hemisphere. Note that  $\theta = 0$  is centred directly above the contact only when  $\alpha = 0$  or  $90^\circ$ . Also, note certain  $\theta$  values do not exist on  $\theta$  curves for some  $\alpha$  values. For example, there are no  $\theta \leq -10$  when  $\alpha = 40$  or  $50^\circ$ .

estimates of the locations and depths of contacts using the "Tilt-Depth" method are also expected to vary with changing inclinations of induced or effective magnetisation. These variations will be examined further below.

The "Tilt-Depth" method requires  $\theta = 0$  and  $\pm 45$  to determine the location and depth of contacts, respectively. So, I begin by examining the specific effect that amplitudes of vertical and total horizontal derivatives ( $\frac{\partial \Delta T}{\partial z}$  and  $\frac{\partial \Delta T}{\partial H}$ ) have on these and other  $\theta$  values, using equation (2.6.1a) (Section 2.6.1). Equation (2.6.1a) predicts that: (1)  $\theta = 0$  only when vertical derivative is zero; (2)  $\theta = \pm 90$  only if total horizontal derivative is zero; and (3)  $|\theta| = 45$  only occurs where there is a 1:1 equivalence between non-zero ( $\neq 0$ ) magnitudes of both vertical and total horizontal derivatives. However, as figure 3.3 shows, the range of  $\theta$  predicted by equation (2.6.1a) are only always present when  $\alpha = 0$  or  $90^\circ$  (RTE or RTP). More importantly, the figure also shows that the  $\theta = 45$  and  $\theta = -45$  values required for estimating contact depths from the "Tilt-Depth" method only occur

when  $\alpha \geq 70^\circ$ . For instance,  $\theta = 0$  occurs once while  $\theta = 45$  occurs twice along profiles for  $\alpha = 40$  and  $50^\circ$ , but  $\theta = -45$  does not exist for these curves because  $\theta > -10$  (Figure 3.3). Therefore,  $\Delta T$  datasets need to be RTP or RTE-transformed before computing their  $\theta$  equivalents, to ensure that the  $\theta$  values required for depth estimation exist for the dataset.

These observations influenced the Matlab<sup>TM</sup> programs that I wrote for the extraction of estimated locations and depths of contacts from each  $\Delta T$  profile used. For example, where  $\theta = 45$ ,  $\theta = -45$  or other required  $\theta$  values occur more than once along a profile, my programs were designed to extract only the occurrence closest to  $\theta = 0$  for depth analyses. This special consideration will not be necessary once  $\Delta T$  datasets are RTP or RTE-transformed.

In summary, the range of  $\theta$  required for un-biased implementations of the ‘‘Tilt-Depth’’ method are only present in RTP or RTE-transformed  $\Delta T$  datasets. The effect of various inclinations of induced magnetisation and the absence of some of these  $\theta$  values on estimates of the locations and depths of vertical, East-West striking contacts is examined below.

#### (A) Error in location estimates

Here I use  $\theta$  curves for vertical, East-West striking contacts presented in figure 3.3 and their equivalents at depths of 3 and 10 km to examine the effectiveness of the method in estimating their locations. The absolute and percentage errors in  $\theta = 0$  estimates of locations of vertical, E-W striking magnetic contacts buried at depths ( $z_{mod}$ )=3, 4 and 10 km below the profiles are presented, respectively, in figures 3.4a and 3.4b. These figures show that ‘‘Tilt-Depth’’ method estimates of

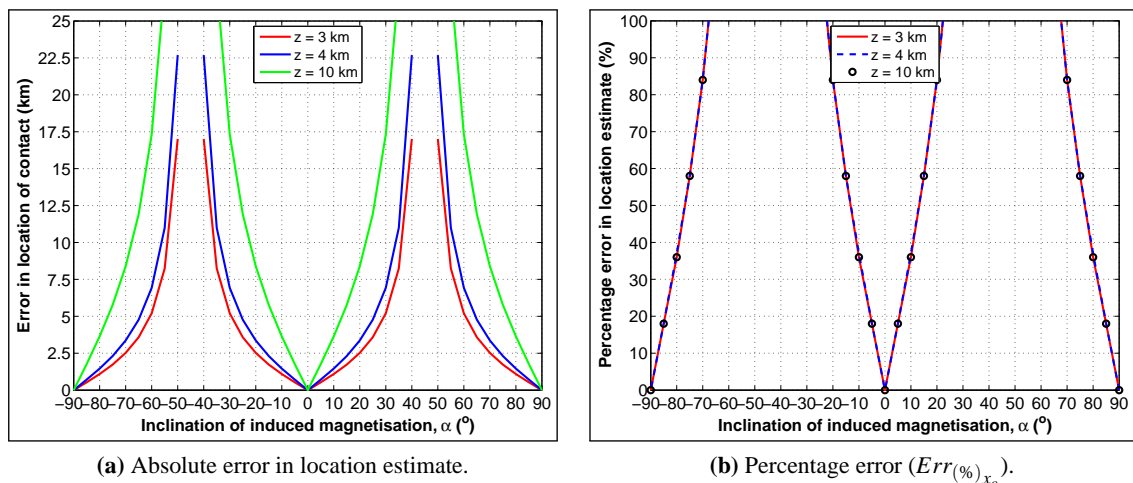


**Figure 3.4:** Effects of depth and inclination of induced magnetisation ( $\alpha$ ) on ‘‘Tilt-Depth’’ method estimates of the location of edges of vertical, East-West striking, 2D contacts. Only error ranging from 0 to 100% is shown. Remanent magnetisation is absent. Note that errors in location estimates are invariant with depth (Figure 3.4b).

location are only accurate (0% error) when  $\Delta T$  data from vertical, E-W striking magnetic contacts are correctly reduced-to-pole (RTP) or reduced-to-equator (RTE), i.e., when the inducing magneti-

sation is vertical or horizontal, respectively. Error in location estimates exceed 0%, but are  $\leq 20\%$  when the inclination of induced magnetisation is within  $7^\circ$  of the vertical (RTP) or horizontal (RTE). Errors exceed 20% when inclination of induced magnetisation exceeds  $7^\circ$  of the vertical or horizontal. Also, "Tilt-Depth" method estimates of the location of edges of vertical, E-W striking contacts are invariant/constant with changing depths (Figure 3.4b).

### (B) Error in depth estimates

Depths of vertical, East-West striking contacts were estimated using equation (3.1.1). These as well as percentage errors in the estimates are presented in figure 3.5. The absolute errors in these estimates are presented in figure B.3. Figure 3.5b shows that the method accurately estimates the depths for contacts when the inclination ( $\alpha$ ) is either horizontal ( $0^\circ$ , i.e., correctly reduced-to-the-equator, RTE) or vertical ( $90^\circ$  or  $-90^\circ$ , i.e., correctly reduced-to-the-pole, RTP). However, when inclination ( $\alpha$ ) is neither vertical nor horizontal the method consistently overestimates the depths of contacts.

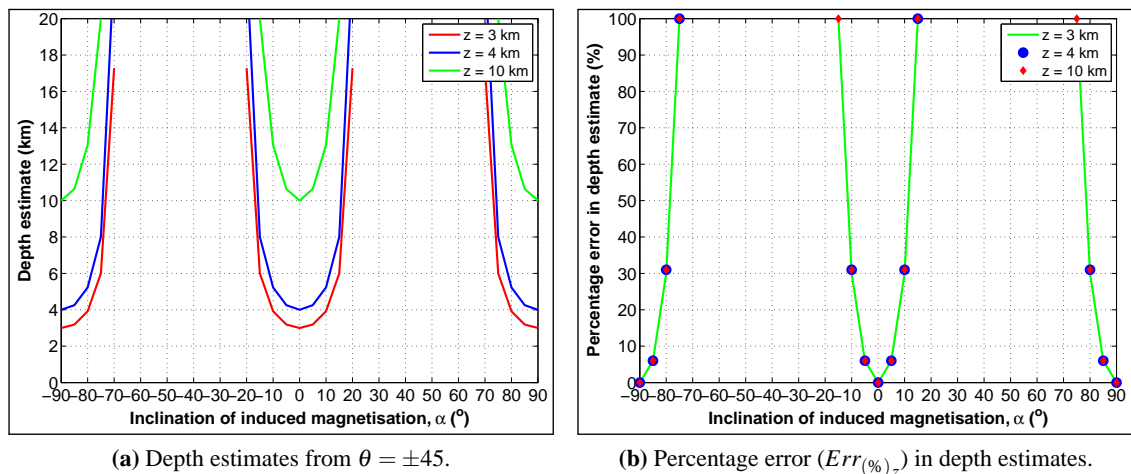


**Figure 3.5:** Effects of depth and inclination of induced magnetisation ( $\alpha$ ) on "Tilt-Depth" method estimates of depths of East-West striking, vertical, 2D contacts. Only percentage error ranging from 0 to 100% is shown. Note that errors in depth estimates are invariant with depth (Figure 3.5b).

For inclinations of induced magnetisation ( $\alpha$ ) within  $7^\circ$  of the vertical (RTP) or horizontal (RTE), the method overestimated the depths of contacts by up to 20% (Figure 3.5b). Errors in depth estimates were  $>20\%$  once the inclination exceeded  $7^\circ$  from the vertical or horizontal. These errors appear to be imposed by those for location estimates (Figure 3.4). Errors in depth estimates are invariant with changing depths of burial of the contacts (Figure 3.5b). Similar depth-invariance was observed for location estimates (Figures 3.4b). These results seem to indicate that estimates of depth of vertical, E-W contacts using "Tilt-Depth" method are more influenced by changing inclinations of induced magnetisation compared with the depths of sources. This implies that the method is effective for determining the location and depth of edges of both shallow and deep anomalous magnetic two-dimensional (2D) sources.

In summary, the range of  $\theta$  required to implement the "Tilt-Depth" method may only be present in RTP or RTE-transformed datasets. The constancy (invariance) of the percentage errors in "Tilt-Depth" method estimates of location and depth with changing depth of contacts appears to show the dominant influence of changing inclination of induced magnetisation relative to depths of contacts. "Tilt-Depth" method estimates of the locations and depths of vertical, E-W contacts are accurate (0% error) when induced magnetisation is either RTP or RTE. But, errors are only  $> 0$  but  $\leq 20\%$  when the inclination of induced magnetisation is within  $7^\circ$  of the vertical or horizontal.

### 3.3.2 Reducing the effects of magnetic anomaly interference on errors in "Tilt-Depth" method estimates

Magnetic anomalies do not occur in isolation since their geological sources are finite and interconnected in space. Magnetic anomalies from adjacent sources are known to interfere with each other, thereby, masking and/or distorting the shape and slope of observed anomalies. The length of arc (range) of  $\theta$  used by Salem et al. (2007) and in section 3.3.1 to implement the "Tilt-Depth" method is presented in figure 3.6a (See also figure 3.1). It appears that implementing the "Tilt-Depth" method using shorter arcs of  $\theta$ , i.e.,  $|\theta| \leq 45$  (Figure 3.6b) might offer a means for reducing the effect of interference between adjacent and/or interfering anomalies. Consequently, in this section I tested the "Tilt-Depth" method for its errors in depth estimates using various ranges of  $\theta$  values. (Figure 3.6b). These  $\theta$  values are designated  $\theta_s$ . I used 37  $\Delta T$  profile datasets obtained from vertical, E-W striking magnetic contacts with varying inclinations of induced magnetisation ( $\alpha$ , at  $5^\circ$  intervals) at a constant depth of 4 km, to test this approach. I assumed that remanent magnetisation was absent.

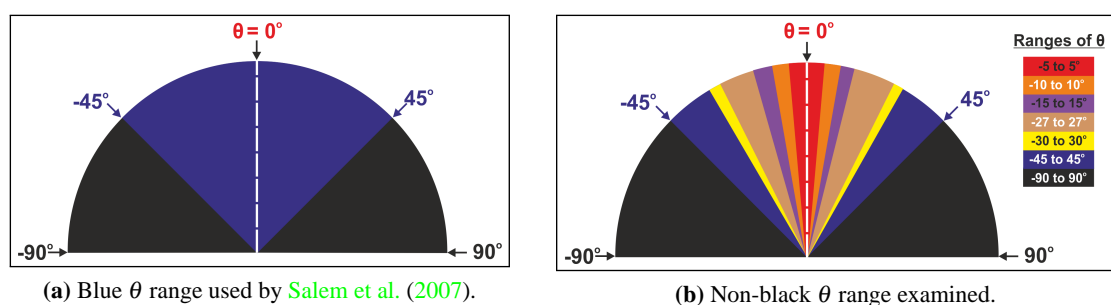


**Figure 3.6:** Length of arc (Ranges) of  $\theta$  ( $\theta_s$ ) used in testing the "Tilt depth" method. Black-coloured sectors on the  $\theta$  range-defined semicircle were not tested.

Half the total horizontal distance between  $\theta = 0$  and the respective  $-\theta_s$  and  $+\theta_s$  values shown in figure 3.6b will be shorter than the equivalent distance between  $\theta = -45$  and  $\theta = 45$  (Figures 3.6a and 3.1). Therefore, before applying the method using this approach, initial depth estimates from the range of  $\theta$  in figure 3.6b required a correction, to convert them to true depth estimates ( $z_{est}$ ). For this purpose, I used depth scale (*conversion*) factors,  $zF$  (Equation (3.3.1b)) which I derived

from equation (2.6.1) using equation (3.3.1a). Depth conversion factors for  $\theta$  used in this study are presented in table 3.1. The fraction ( $hF$ ) of the physical distance between  $\theta = -45$  and 45, which was used for computing the depth estimates when using the shorter ranges of  $\theta$  are also presented on table 3.1.

$$z_{est} = \frac{|h_s|}{\tan\left(\frac{\theta_s \times \pi}{180}\right)} \quad (3.3.1a)$$

$$zF = \frac{z_{est}}{|h_s|} \quad (3.3.1b)$$

where  $|h_s| = \frac{(|+h_s|) + (|-h_s|)}{2}$ ,  $|h_s|$  and  $|-h_s|$  are determined from the horizontal distances between  $\theta = 0$  and, respectively,  $+\theta_s$  and  $-\theta_s$ . The subscript  $s$  indicates short  $|h|$ , as opposed to full  $|h|$  that is determined from the horizontal distance between  $\theta = 0$  and  $|\theta| = 45$  (Equation (3.1.1) and figure 3.1).

**Table 3.1:** Depth conversion factors,  $zF$  for distances between the location of  $\theta = 0$  and different magnitudes of  $\theta$  ( $|\theta|$ ) used to implement ‘‘Tilt depth’’ method.

$-\theta$	$+\theta$	$ \theta $	$zF$	Factor of $ h $ , $hF =  h_s  /  h $
-45	45	45	1	1
-30	30	30	1.7	0.6
-26.6	26.6	27	2	0.5
-15	15	15	3.7	0.3
-10	10	10	5.7	0.2
-5	5	5	11.4	0.1

Since the location of  $\theta = 0$  remains unchanged, location estimates remain as shown in figure 3.4. Results obtained from implementing ‘‘Tilt-Depth’’ method with various  $|\theta| \leq 45$  are presented in figure 3.7a. The difference between errors in depths estimated using  $|\theta| = 45$  and those from  $|\theta| < 30$  appear to be significant, especially, since interest is in keeping depth error within the  $\leq 20\%$  range. Implementing the ‘‘Tilt-Depth’’ method using  $|\theta| = 45$  provided depth estimates below 20% error of  $z_{mod}$  when RTP or RTE transformations are in error of  $\approx 7^\circ$  of the inclination of induced magnetisation ( $\alpha$ ), while implementations using  $|\theta| \leq 30$  provided depth estimates (at the imposed 0-20% error limit) when RTP or RTE transformations are in error of up to  $\approx \pm 10^\circ$  of  $\alpha$  (Figure 3.7a).

No significant difference existed between implementations of the ‘‘Tilt-Depth’’ method using  $|\theta| \leq 27$  and  $|\theta| \leq 30$  (Figure 3.7b). Interestingly,  $|\theta| = 26.6$  ( $\approx 27$ ) happens to correspond to *half the physical distance between  $\theta = 0$  and  $|\theta| = 45$*  (See  $hF$  for  $|\theta| = 27$  in table 3.1). Implementing ‘‘Tilt-Depth’’ method in two or more modes for comparison, e.g., using  $|\theta| = 10$ ,  $|\theta| = 27$  and  $|\theta| = 45$ , might help identify locations on a  $\Delta T$  grid at which interference effects are significant. This approach will be tested further on noise and anomaly interference-bearing gridded  $\Delta T$  datasets in chapter 4.

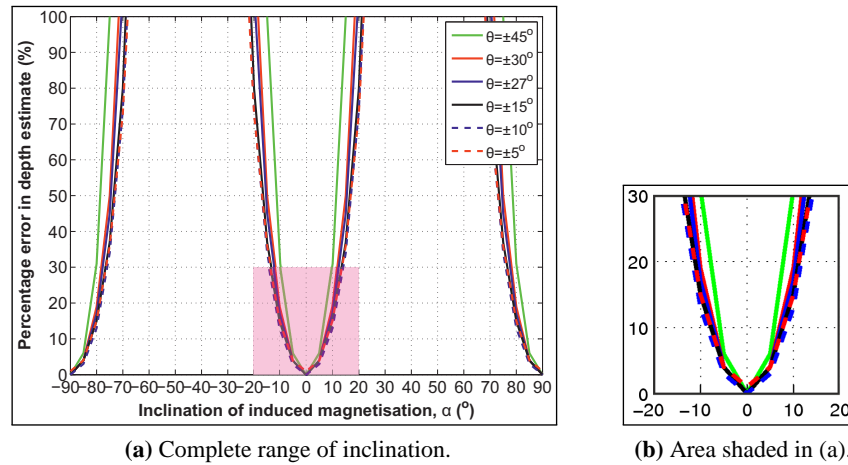


**Figure 3.7:** Percentage error ( $Err_{(z)}(\%)$ ) in depth estimates using "Tilt-Depth" method from  $|\theta| = 45, 30, 26.6, 15, 10$  and  $5$ : Effects of induced magnetisation and magnetic anomaly interference on vertical, East-West contacts. Note that error exceeds 20% for  $\theta = \pm 45$  and  $\theta = \pm 27$  at  $7$  and  $10^\circ$ , respectively, from the vertical or horizontal direction of magnetisation.

In summary,  $\Delta T$  datasets need to be transformed to their RTP or RTE equivalents prior to the application of the "Tilt-Depth" method. Errors in depth estimates from the method were less when implemented using  $|\theta| \leq 30$  than when the method was implemented using  $|\theta| = 45$ . Depth errors exceed the 20% error limit when inclination exceeds  $7$  and  $10^\circ$  of the vertical or horizontal magnetisation (i.e., RTP or RTE) when the method is implemented, respectively, using  $|\theta| = 45$  and  $|\theta| \leq 30$  range. Implementations of the method using  $|\theta| < 27$  ranges only seem to provide marginal benefits (Figure 3.7b). Hence, the  $|\theta| = 27$  range, which uses only *half the physical distance between  $\theta = 0$  and  $|\theta| = 45$*  appears to be a  $\theta$  range for examining  $\Delta T$  grids for interference effects. Therefore, standard applications of the "Tilt-Depth" method to gridded datasets should compare results from two modes (using  $|\theta| = 27$  and  $45$ ) or more, for the identification of locations on a  $\Delta T$  grid at which interference effects are significant.

### 3.3.3 Estimates based either on the horizontal distance $+h$ or $-h$

The shapes of  $\theta$  curves on figure 3.3 indicate that the distances  $+h$  and  $-h$  vary with the inclination of induced magnetisation ( $\alpha$ , since remanence is absent).<sup>6</sup> Figure 3.3, for instance, shows that when  $\alpha = 40$  or  $50^\circ$ , there are no intercepts for estimating  $h$  from  $\theta = -45$ , since  $\theta \geq -10$ . Hence, the distances  $h$  and  $-h$  are not always equal. Since these variations in  $h$  and  $-h$  depend on changes in inclination of induced magnetisation ( $\alpha$ ), the objective of this section is to examine the extent to which these variations of  $h$  and  $-h$  affect estimates of depths of vertical, E-W striking, magnetic contacts. Attention will be paid to when the inclination of effective magnetisation assumed for RTP or RTE transformation of  $\Delta T$  data differs from the actual value. Here,  $+h \equiv +h_s$  refers to the horizontal distance between  $\theta = 0$  and specific  $-\theta$  values, while  $-h \equiv -h_s$  refers to the horizontal distance between  $\theta = 0$  and equivalent  $+\theta$  values (Table 3.1).

<sup>6</sup>Examples of  $-h$  and  $+h$ , respectively, for  $\theta = 45$  and  $\theta = -45$  were shown in figure 3.1.  $-h = -h_s$  and  $+h = +h_s$  for distances less than  $+h$  and  $-h$  (Section 3.3.2).

Equation 3.1.1 requires the distances  $+h$  and  $-h$  (or  $-h_s$  and  $+h_s$ ) to compute depth estimates from the “Tilt-Depth” method. To independently evaluate errors in depths estimated from  $+h$  or  $-h$  (or  $-h_s$  and  $+h_s$ ), I decomposed depth estimates obtained from 37 of the 111 profile  $\Delta T$  datasets in figure 3.5 (For depth = 4 km) into its  $h$  and  $-h$  (or  $-h_s$  and  $+h_s$ ) constituents. Results are presented in figure 3.8a. Figure 3.8a presents percentage errors in depth estimates using various  $+\theta$  values, while figure 3.8b presents percentage errors in depth estimates using equivalent  $-\theta$  values.

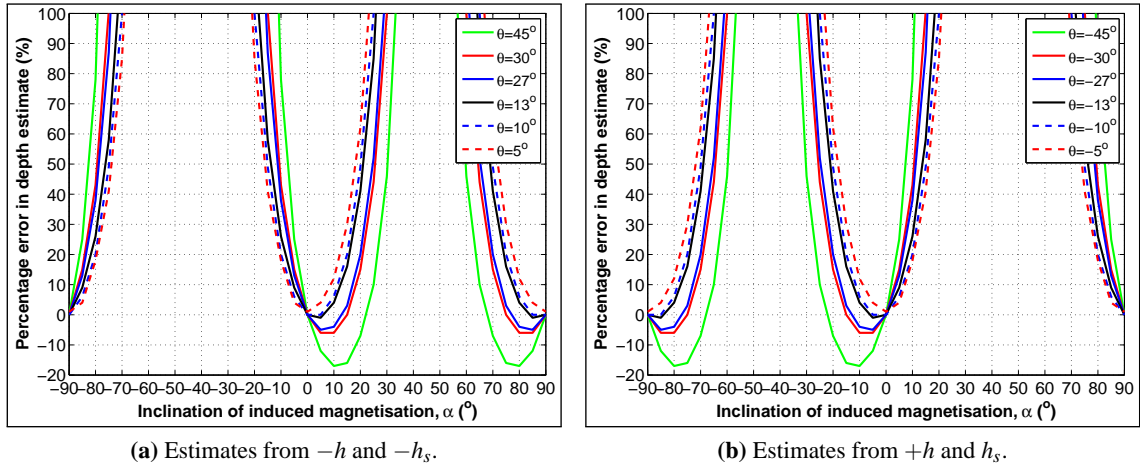


**Figure 3.8:** Percentage error ( $Err_{(\%)}$ ) in depth estimates from  $\Delta T$  data from either  $+\theta$  ( $-h$  or  $-h_s$ ) or  $-\theta$  ( $+h$  or  $+h_s$ ) values for vertical, E-W contacts.  $+h$  or  $+h_s$  is distance between  $\theta = 0$  and  $-\theta$  values, while  $-h$  or  $-h_s$  is distance between  $\theta = 0$  and  $+\theta$  values.

Depths estimated using the distance  $-h$  or  $-h_s$  (Figure 3.8a) are mirrored by those obtained from  $h$  or  $+h_s$  (Figure 3.8b). These figures show that when inclination of induced magnetisation  $\alpha=90^\circ$  (RTP) or  $\alpha=0^\circ$  (RTE), this approach accurately estimated the depth of the contact ( $Err_{(\%)} = 0$ ). However, when  $\alpha$  is neither vertical (RTP) nor horizontal (RTE), it provided both overestimated and underestimated depths<sup>7</sup>, for specific ranges of  $\alpha$ .  $-h$  provided only overestimated depths in the southern geomagnetic hemisphere, but provided both overestimated and underestimated depths in the northern geomagnetic hemisphere (Figure 3.8a). On the other hand,  $+h$  provided only overestimated depths in the northern geomagnetic hemisphere, but both overestimated and underestimated depths in the southern geomagnetic hemisphere (Figure 3.8b). The figures show that  $-h$  and  $+h$  are unstable both in the northern and southern geomagnetic hemispheres, respectively. On the contrary,  $-h$  and  $+h$  are most stable both in the northern and southern geomagnetic hemispheres, when estimated using  $\theta = 5$  and  $\theta = -5$ , respectively. Using  $\theta = \pm 5$  provides depth estimates with  $\leq 20\%$  errors when RTP or RTE transformations are in error of  $\leq 10^\circ$ . However, this  $\leq 10^\circ$  inclination error from RTP or RTE was also achieved by using  $|\theta| \leq 30$  (Figure 3.7a). Hence, the stability of  $|\theta| = 5$  both in the northern and southern geomagnetic hemispheres affords no additional advantage, unless where anomalies interfere. However,  $|\theta| = 5$  involves only  $0.1|h|$ , i.e., 10% of the  $\theta$  anomaly hence, its use may lead to the loss of 90% of the anomaly. Consequently,

<sup>7</sup>Positive errors ( $+Err_{(\%)}$ ) represent overestimates, while negative errors ( $-Err_{(\%)}$ ) represent underestimates.

more reliable and stable depth estimates should be obtained from RTP or RTE of  $\Delta T$  data using, for example, the  $\theta = \pm 27$  range-based “Tilt-Depth” method. Therefore, when applied to gridded  $\Delta T$  data, in which noise is usually present, it is beneficial to implement the “Tilt-Depth” method in two modes, e.g., using both  $|\theta| = 27$  and  $|\theta| = 45$ . The more accurate depth estimates will be those obtained using  $|\theta| = 27$ , but any differences between these estimates and those obtained from  $|\theta| = 45$  will be indicative of interference from adjacent anomalies.

In summary, results show that  $\Delta T$  datasets should be transformed to RTP or RTE equivalents before applying the “Tilt-Depth” method. The most stable  $|\theta|$  value both in the northern and southern geomagnetic hemispheres was  $|\theta| = 5$ . It provided depth estimates at  $\leq 20\%$  when inclination of magnetisation is  $\leq 10^\circ$  from RTP or RTE.  $|\theta| \leq 27$  provided similar results, and is preferred since  $|\theta| = 5$  involves only  $0.1|h|$ , i.e., 10% of each  $\theta$  anomaly. Standard implementation of the “Tilt-Depth” method gridded  $\Delta T$  data should use both  $|\theta| = 27$  and  $|\theta| = 45$ . Depth estimates from  $|\theta| = 27$  are more accurate than those from  $|\theta| = 45$ , but differences are due to anomaly interference.

### 3.3.4 Effect of varying remanent magnetisation on estimates from RTP or RTE datasets

In this section I examine the effect that changing magnitudes and inclinations of induced and remanent magnetisations ( $\mathbf{J}_i$  and  $\mathbf{J}_r$ ) have on “Tilt-Depth” method estimates of the location and depth of vertical, East-West contacts when the inclination of induced magnetisation ( $\alpha$ ) is either vertical (RTP) or horizontal (RTE).<sup>8</sup>

The simplifications provided by the RTP or RTE process (Sections 2.3.2, and 2.3.3) applied only when remanent magnetisation is absent,  $\mathbf{J}_r=0$  (Sections 3.3.1 to 3.3.3). Neither the RTP nor RTE process is able to simplify the complexity in  $\Delta T$  datasets that result from the presence of  $\mathbf{J}_r$ . Hence, anomalies on RTP or RTE of such datasets have little or no spatial correlation with their sources (Finn & Morgan, 2002; Lelievre et al., 2006). Since the objective of this section is to examine the effect of such remanence-sourced complexities on “Tilt-Depth” method estimates, in this section I use RTP or RTE to refer, respectively, to vertically or horizontally inclined induced magnetisation ( $\alpha = 90$  or  $0^\circ$ ) in the presence of remanent magnetisation ( $\mathbf{J}_r$ ) of various inclinations ( $\beta$ ) and magnitudes. Figure 3.9 presents the directions of induced and remanent magnetisation at RTP and RTE. The figure also shows how I vary  $\beta$  from 0 to  $360^\circ$ , in an anticlockwise sense relative to  $\alpha$ .  $\mathbf{J}_i$  and  $\mathbf{J}_r$  were assigned various magnitudes at RTP and RTE, with magnitudes of  $\mathbf{J}_i$  at RTP twice their equivalents at RTE (Table 3.2) in consonance with equation (2.1.3c) and section 2.3.1. The inclination of remanent magnetisation ( $\beta$ ) was varied from 0 to  $360^\circ$  at intervals of  $5^\circ$ . Constants used for computing these  $\Delta T$  datasets include depth ( $z_{mod} = 4$  km),  $\delta k = 0.002$  SI Units and  $A = 0^\circ$ . 1752 profile datasets were obtained, using methods described in

<sup>8</sup> $\mathbf{J}_r$  and  $\mathbf{J}_i$  were introduced in section 2.2.1.

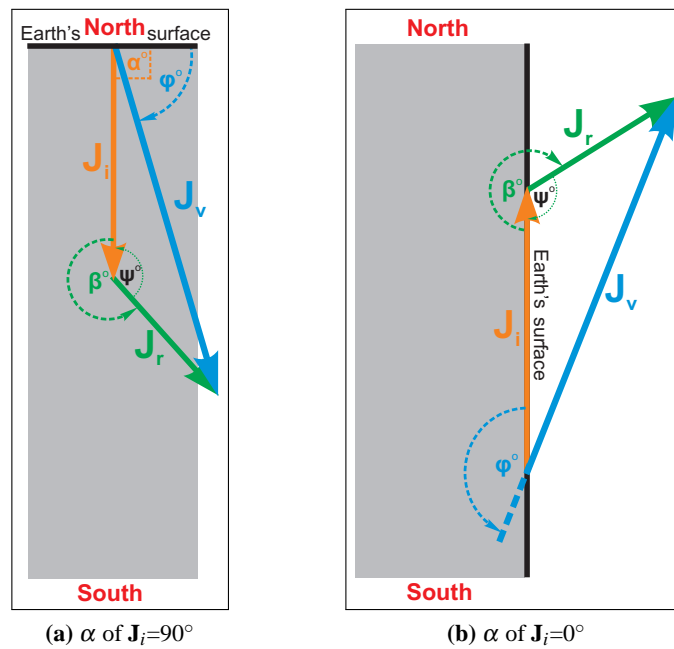


**Figure 3.9:** Spatial relationship between induced, remanent and effective (net) magnetisations ( $J_i$ ,  $J_r$  and  $J_v$ ) at the: (a) North pole (RTP); or (b) equator (RTE). The relative magnitude (length) of  $J_r$  and  $J_i$  is expressed by the Koenigsberger ratio ( $Q$ ). Magnetisation vectors are shown in cross-section through an appropriately oriented, section of a magnetic rock unit (grey-coloured) at the Earth's surface.

**Table 3.2:** Magnitudes of induced and remanent magnetisation used for examining the effects of remanence at RTP and RTE.

Magnitudes ( $\times 10^3$ nT) of magnetisations (RTP)		Magnitudes ( $\times 10^3$ nT) of magnetisations (RTE)		Koenigsberger ratio ( $Q$ )
Induced	Remanent	Induced	Remanent	
50	5	25	2.5	0.1
50	10	25	5	0.2
50	15	25	7.5	0.3
50	20	25	10	0.4
50	25	25	12.5	0.5
50	30	25	15	0.6
50	35	25	17.5	0.7
50	40	25	20	0.8
50	45	25	22.5	0.9
50	50	25	25	1
40	50	20	25	1.25
5	50	2.5	25	10

section 3.2.1. Of these, 876 profiles were for contacts at RTP, while the remaining profiles were for contacts at RTE.

The Koenigsberger ratio ( $Q$ ) imposed by the magnitudes of  $J_i$  and  $J_r$  used for these computations ranged from 0.1 to 10 (Table 3.2), thus covering the range of  $Q$  values encountered in induced magnetisation-dominated geological terrains, i.e.,  $Q \leq 0.5$  (McEnroe et al., 2009; Thébault et al., 2010), as well as remanence-dominated terrains, i.e.,  $Q > 0.5$  (Finn & Morgan, 2002). These values of  $Q$  were used to compute the effective (net) magnetisation ( $J_v$ ) when the contacts are either at

RTP or RTE.<sup>9</sup>  $\mathbf{J}_v$  is fully described by its inclination,  $\phi$  (Figures 3.10c and 3.10d) and magnitude (Figures 3.10a and 3.10b).<sup>10</sup> Figure 3.11 presents variations in the angle between the inclination of inducing magnetisation ( $\alpha$ ) and inclination of effective magnetisation ( $\phi$ ), with respect to the direction of the inducing field (See figure 3.9 for the angles referred to).

### (A) Relationships between effective and remanent magnetisations at RTP or RTE

The inclinations of induced and effective magnetisations ( $\alpha$  and  $\phi$ ) can be exactly determined if  $\beta$  is known (Lelievre & Oldenburg, 2009). For most magnetic surveys, however,  $\beta$  is usually not known. Consequently,  $\phi$  is also not usually known, hence, remanent magnetisation is usually assumed to absent, for simplicity (e.g., Baranov, 1957; Li et al., 2004). For this reason, I aim to extract generic information, which may be useful for further simplifying magnetic data interpretation when  $\alpha = 90^\circ$  (RTP) or  $\alpha = 0^\circ$  (RTE), by examining the relationship between  $\beta$ ,  $\alpha$ , Koenigsberger ratio (Q) and  $\phi$ . Consequently, analyses and discussions in this section will be based on changes in  $\beta$  rather than  $\alpha$ , which is always known. This way, any *a priori* information on  $\beta$  can be easily integrated into the RTP or RTE and interpretation processes. Figures 3.10c and 3.10d present the inclination of effective magnetisation ( $\phi$ ) when Q,  $\alpha$  and  $\beta$  are all known. Angular relations between  $\alpha$  and  $\beta$  for various values of Q are presented in figures 3.11a and 3.11b. For clarity, plots for some Q values have been omitted from these figures.

The magnitudes of effective magnetisation, for all values of Q and at RTP or RTE, increased from their minima when the inclination of remanent magnetisation is anti-parallel ( $\beta = 0$  or  $360^\circ$ ) to induced magnetisation (Figures 3.10a and 3.10b). Maximum and minimum magnitudes of effective magnetisation occurred when remanence was directed parallel ( $\beta = 180^\circ$ ) and anti-parallel ( $\beta = 0$  or  $360^\circ$ ) to induced magnetisation, respectively (Figures 3.10a and 3.10b). These figures confirm that effective magnetisation,  $J_v \approx |J_i| \pm |J_r|$  when  $\beta$  is within  $\pm 25^\circ$  of  $\alpha$  (Bath, 1968; Lelievre & Oldenburg, 2009).

For all Q values at RTP or RTE, figures 3.10c and 3.10d show, that the inclination of effective magnetisation ( $\phi$ ):

- (1) is the same as  $\alpha$  whenever  $\alpha$  is coaxial with  $\beta$ , so that  $\mathbf{J}_r$  is directed parallel or anti-parallel ( $\beta = 0$  or  $180^\circ$ ) from  $\mathbf{J}_i$ ;
- (2) is greater than  $\alpha$ , when  $\beta < 180^\circ$ ;
- (3) is less than  $\alpha$  when  $\beta > 180^\circ$ ; and

<sup>9</sup> $\mathbf{J}_v$  and Q were introduced in section (2.2.3)

<sup>10</sup> $\alpha \neq \phi$  when both induced and remanent magnetisation are present (Figure 3.9 and section 2.2.1). Magnitudes of  $\mathbf{J}_v$  were obtained using the *cosine rule* for angle  $\psi$ , while inclinations of  $\mathbf{J}_v$  were obtained using the *sine rule* for angle  $\psi$  (Figure 3.9).

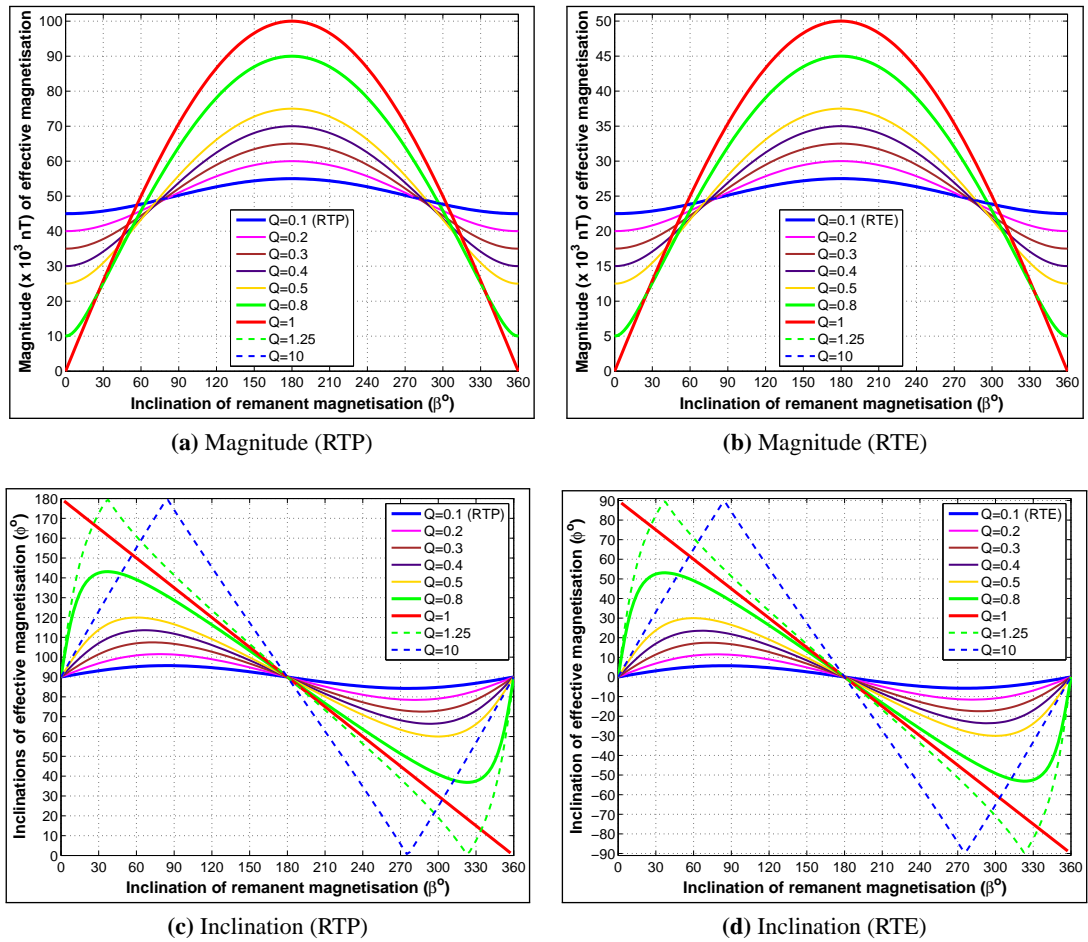


**Figure 3.10:** Relationship between magnitudes and inclinations of effective magnetisation and selected Koenigsberger ratio (Q) values. Induced magnetisation is either at RTP or RTE and various magnitudes. Only plots for selected Q values are shown, for clarity. Magnitudes of remanent magnetisation were at half their RTP equivalents and varied, while their inclinations ranged from 0 to  $360^\circ$ , at intervals of  $2.5^\circ$ . For both RTP and RTE, when inclination of remanent magnetisation is parallel or anti-parallel ( $\beta = 0$  or  $180^\circ$ ) to that of induced magnetisation, the inclinations of effective and induced magnetisations are equal. The magnitude of effective magnetisation is the sum of the magnitudes of both the induced and remanent magnetisations. This relationship changes when induced and remanent magnetisations are not coaxial, i.e.,  $\beta \neq 0$  or  $180^\circ$ .

(4) increased rapidly, for  $Q > 0.5$  when  $\beta = 10$  to  $120$  or  $240$  to  $350^\circ$ ; and

(5) is zero, when  $Q = 1$  and  $\beta = 0$  or  $360^\circ$ .  $\phi$  is undefined, since it involves equal and opposing magnetisations (division by zero). Figures 3.10a and 3.10b show that the magnitude of effective magnetisation is zero for this case.

Along with figures 3.10c and 3.10d, these figures highlight the undesirable consequences and complexities introduced by the presence of remanent magnetisation. For example, figure 3.10c shows that  $\phi$  for RTP datasets can approach the horizontal ( $0$  or  $180^\circ$ ) when  $Q > 0.5$  and  $\beta$  ranges from  $10$  to  $120$  or  $240$  to  $350^\circ$ . Consequently,  $\Delta T$  and  $\theta$  anomalies on such datasets become different and more complex from their simple and symmetric equivalents which were located directly above their sources when remanence was absent. With  $\phi$  approaching the horizontal, these RTP anomalies are translated to look more like those encountered near the equator (or at RTE)

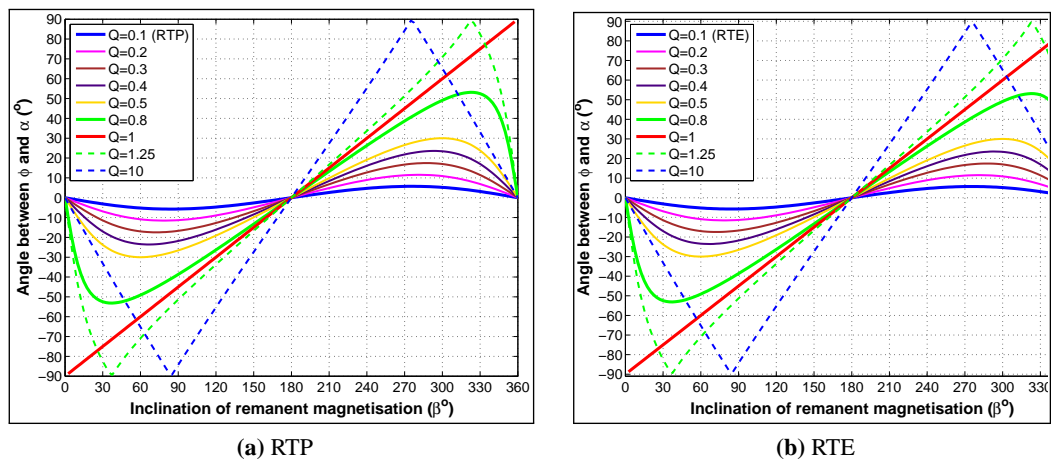


**Figure 3.11:** Angular difference between the inclination of the inducing magnetisation ( $\alpha$ ) and that of the effective inclination ( $\phi$ ) for selected Koenigsberger ratios ( $Q$ ). Deviation is with respect to the direction of the inducing field.  $\alpha$  is either at RTP or RTE and various magnitudes. Only plots for selected  $Q$  values are shown, for clarity. Magnitudes of remanent magnetisation were at half their RTP equivalents and varied, while their inclinations ranged from 0 to 360°. The inclinations and magnitudes of the effective magnetisation obtained from these configurations of remanent and induced magnetisations were presented in figure 3.10.

when remanent magnetisation is absent.

The complex nature of  $\theta$  anomalies (and, by extension,  $\Delta T$ ) resulting from deviations of  $\beta$  from  $\alpha$  (RTP or RTE) are demonstrated for vertical, East-West contacts in figure 3.12. Remanent magnetisations with various  $Q$  values (0.1, 0.2, 0.3, 0.4, 0.5, 0.8, 1, 1.25 and 10) were directed 0, 30, 90 and 180° from the inducing RTP or RTE field (Figure 3.9).

The directions (inclinations) of remanent and induced magnetisations ( $\beta$  and  $\alpha$ ) are considered collinear when they are within 25° of each other (Bath, 1968, p. 140). This collinearity condition (negligible remanent magnetisation direction) is assumed, usually for RTP datasets, by all semi-automatic methods of magnetic data interpretation. This assumption is generally correct for RTP or RTE datasets, when  $Q \leq 1$  and remanent magnetisation is parallel or near-parallel ( $\beta$  ranging from 155 to 205°) to the induced magnetisation direction (Figure 3.11). This represents a deviation of about  $\pm 12^\circ$  between  $\alpha$  and  $\phi$ . However, when  $\alpha$  is RTP or RTE, and neither parallel nor near-parallel to  $\beta$ , wider deviations occur between effective and induced magnetisations ( $|\phi - \alpha| > 12^\circ$ ), especially, when  $Q > 0.2$  (Figure 3.11). Hence, the simplification of remanence-laden anomalies due to collinear induced and remanent magnetisations results from this  $\leq 12^\circ$  deviation of  $\phi$  from  $\alpha$ .

The range of deviation between  $\alpha$  and  $\phi$  decreased from  $\pm 12^\circ$  as  $Q$  decreased from 1 (Figure 3.11). Consequently, the range of  $\beta$  for which  $|\phi - \alpha| \leq 12^\circ$  increased as  $Q$  decreased. Ultimately, when  $Q \leq 0.2$  the deviation between  $\alpha$  and  $\phi$  is  $\leq 12^\circ$ , for all possible values of  $\beta$  (Figure 3.11). Consequently, the effect of remanent magnetisation on RTP or RTE of datasets for which *a priori* information suggests  $Q < 0.2$  can be treated as negligible, though not collinear. These  $Q$ ,  $\alpha$ ,  $\beta$  and  $\phi$  relationships show that the collinearity condition of Bath (1968) only applies when  $Q \leq 1$ .

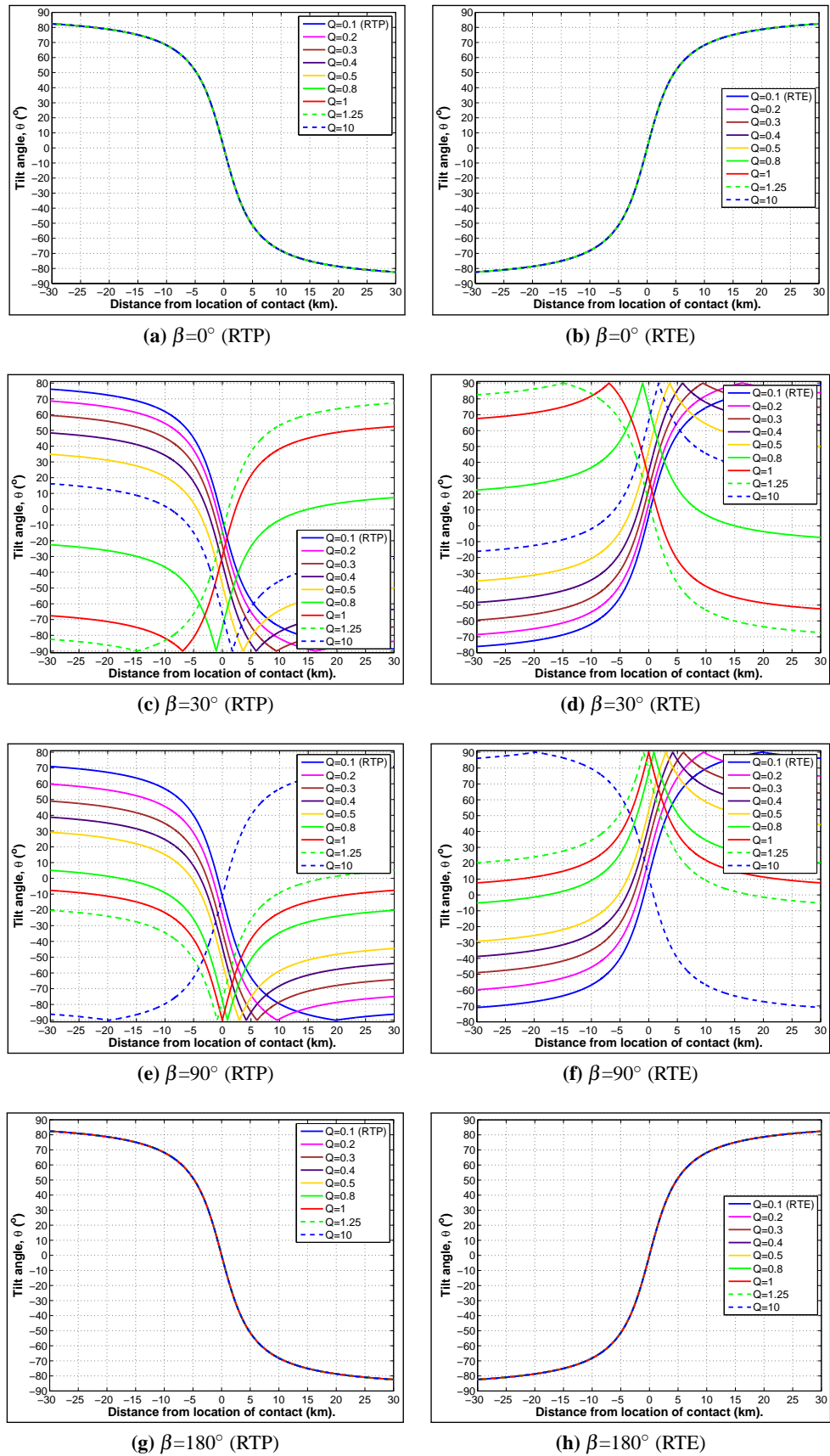


**Figure 3.12:**  $\theta$ -transformed  $\Delta T$  curves obtained from vertical, West-East striking contacts when at RTP or RTE, and characterised by remanent magnetisations of various  $Q$  and inclinations ( $\beta=0, 30, 90$  and  $180^\circ$ ). Note that anomalies are only simplified when  $\beta=0, 90$  or  $180^\circ$ .

### (B) Location and depth estimates

The distribution of remanent magnetisation ( $\mathbf{J}_r$ ) directions ( $\beta$ ) at which percentage errors in estimates of the location and depth of remanence-laden, but vertically or horizontally induced (RTP or RTE), East-West striking contacts are within the 0-20% error limit are shown in figure 3.13. The figure shows, for each Q value, that location and depth estimates were only within the 0-20% error limit for ranges of  $\beta$  for which the deviation between  $\alpha$  and  $\phi$  is  $\leq 12^\circ$  (Figure 3.11). When  $0.1 < Q < 0.2$  estimates are within the 0-20% error limit for all  $\beta$  values. However, as Q increases from about 0.15 to 1, this error limit is only achieved for narrow ranges of  $\beta$ . This range of  $\beta$  increased as Q decreased from 1 towards 0.1 (Figure 3.13).

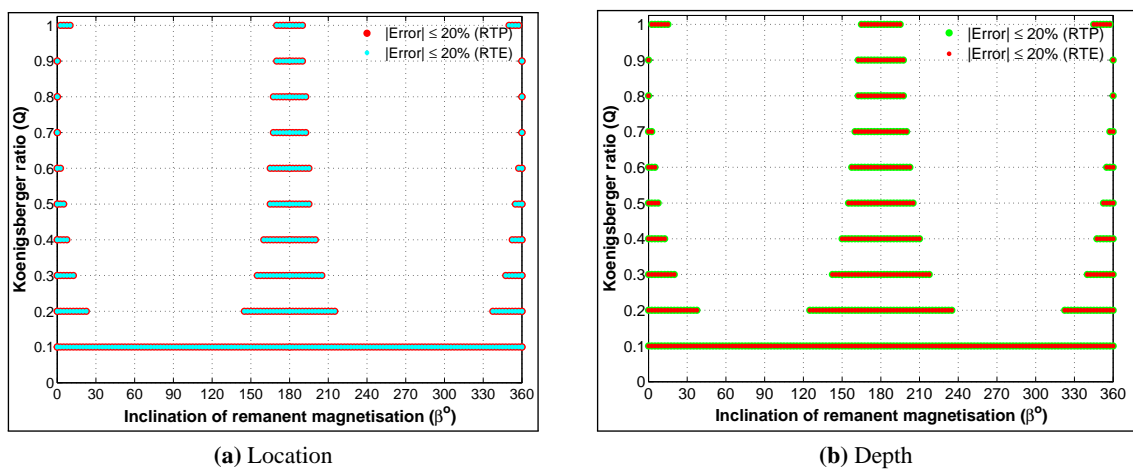


**Figure 3.13:** The 0-20% error distribution of “Tilt-Depth” method estimates of locations and depths of remanence-laden East-West striking contacts at RTP and RTE. Contacts are characterised by variously-sized induced and remanent magnetisations ( $\mathbf{J}_i$  and  $\mathbf{J}_r$ ) and Koenigsberger ratios, Q. Note that estimates were only within the error limit when  $\mathbf{J}_r$  is either parallel, near-parallel or anti-parallel to  $\mathbf{J}_i$ , and that the corresponding ranges of  $\beta$  increased as Q decreased from 1 towards 0.1. Table 3.2 and figure 3.9, respectively, presented the full range of magnetisation magnitudes and their spatial relationships.

## 3.4 Testing the “Tilt-Depth” method using dipping, East-West striking contacts

This section examines the dependence of location and depth estimates from “Tilt-Depth” method on the dip of E-W striking, magnetic contacts (Figure 2.5) when they are either vertically magnetised (at RTP) or horizontally magnetised (at RTE). Contacts at RTP or RTE will be used because the method has been shown (Section 3.3) to provide accurate (0% error) estimates for these directions of effective magnetisation.

The occurrence and orientation of fault planes, in isotropic rocks, are mainly controlled by the spatial distribution of the principal normal stresses (Mandl, 2000). Continental rifted terranes like

NorthEastern (NE) Nigeria result from *axial extension* (Twiss & Moores, 1992) or *triaxial extension* (Zoback, 2007), where the fracture angle is typically  $\approx 30^\circ$  (Twiss & Moores, 1992; Zoback, 2007).<sup>11</sup> In such stress regimes, faults and/or fracture planes are usually orientated  $\approx 60^\circ$  away from  $\sigma_1$  (Twiss & Moores, 1992, p. 166). However, Wilson et al. (1992) and Mandl (2000, p. 45) show that fracture angles can occur within  $\pm 45^\circ$  of  $\sigma_1$  in basement terrains where surface-reaching faults require  $\sigma_1$  to be contained in the vertical plane. These geometries correspond to faults/fractures with dips of 30 and 45°. Also, Ramsey & Chester (2004) showed that fracture angles: (i) remained constant for faults/fractures resulting from extensional stresses; but (ii) increased monotonically with confining pressure for hybrid and shear fractures.<sup>12</sup> Consequently, the dips of contacts used in this section were allowed to vary from 0 to 180° at intervals of 5°. Thus contacts represent: (1) *vertical faults*, when dip is vertical ( $d = 90^\circ$ ); (2) *normal faults*, when dip is acute ( $d < 90^\circ$ ); and (3) *reverse faults*, when dip is obtuse ( $d > 90^\circ$ ). Assuming that remanent magnetisation was absent, constants included the depth ( $z_{mod} = 4 \text{ km}$ ),  $\delta k = 0.002$  SI Units,  $A = 0^\circ$ ,  $J_i = 65000$  nT for RTP profiles, and  $J_i = 25000$  nT for RTE profiles. In all, 74  $\Delta T$  profile datasets obtained from dipping, E-W striking contacts were used to test the "Tilt-Depth" method. While 37 of these profiles were at RTP, the other 37 were at RTE.

### 3.4.1 Estimates of locations

The absolute and percentage errors in "Tilt-Depth" method location estimates obtained from RTP or RTE equivalents of the  $\Delta T$  datasets derived from profiles across dipping, E-W striking contacts are, respectively, presented in figures 3.14a and 3.14b. The method accurately located these contacts when RTP or RTE transformation is accurate and contacts are vertical (Figure 3.14). However, error in location estimates were within the 0-20% limit when contact dips range from about 75 to 105°, (Figure 3.14b).

### 3.4.2 Estimates of depths

"Tilt-Depth" method estimates of depths were obtained from RTP or RTE of  $\Delta T$  datasets derived from profiles across dipping, E-W striking contacts in two modes. The method was implemented using the distances between  $\theta = \pm 27$  and 45 values, for comparison. The estimated depths, as well as the percentage and absolute errors associated with these estimates are presented, respectively, in figures 3.15a and 3.15b, and appendix B.4.

Error in "Tilt-Depth" method estimates of contact depths from RTP and RTE datasets using the  $\theta = \pm 45$  range are within the 0-20% error limit when contact dip is within the range 75 to 105°

---

<sup>11</sup>Fracture angle is the angle between the normal to the resulting fracture plane and the direction of the principal axis of stress,  $\sigma_1$ .

<sup>12</sup>Confining pressure refers to the pressure of fluids in the vicinity of a geological structure, and includes pore fluids pressure.

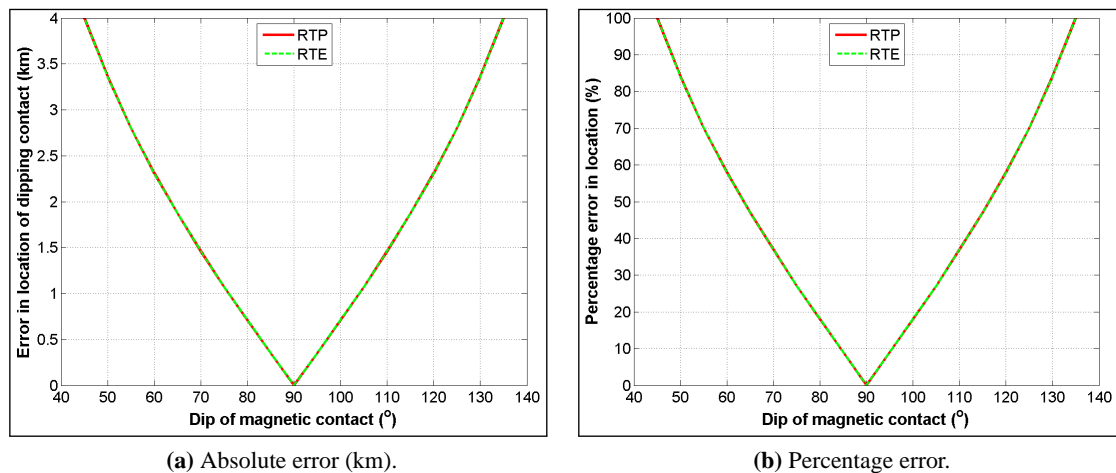


**Figure 3.14:** Effect of dips ( $d$ ) of East-West striking contacts on their location estimates. Only error ranging from 0 to 100% is shown.

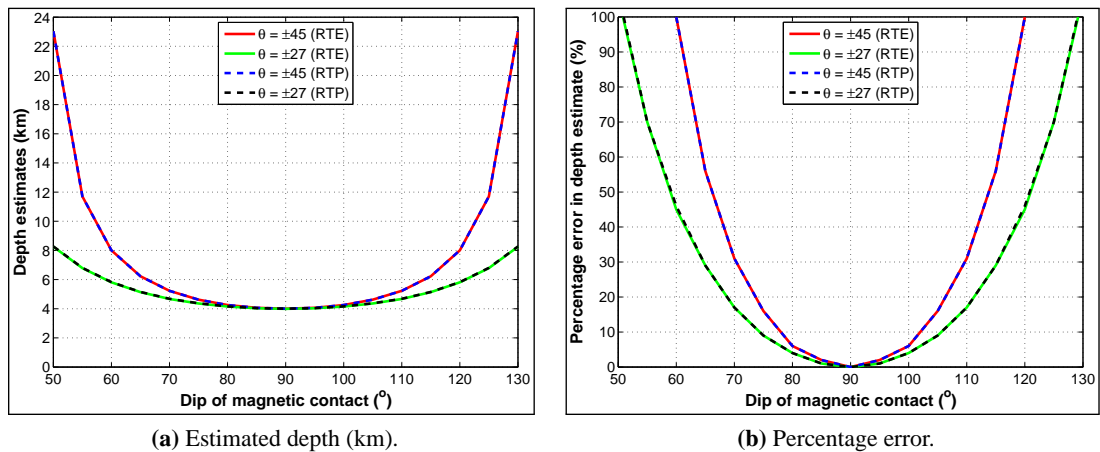


**Figure 3.15:** “Tilt-depth” method estimates of depths of dipping, East-West striking magnetic contacts at RTP and RTE, using  $\theta = \pm 27$ , or 45 range. Only error ranging from 0 to 100% is shown in figure 3.15b. Absolute error is presented in figure B.4.

(Solid red and dashed-blue curves in figure 3.15b). Estimates from RTP and RTE datasets using the  $\theta = \pm 27$  range are within the error limit when contact dip is within the range 70 to 110° (Solid red and dashed-blue curves in figure 3.15b). High angle dips such as these range of dips of fault planes are typical of basin/block-bounding faults.

Thus far, discussions have centred on East-West striking contacts. Next, I examine the effectiveness of the “Tilt-Depth” method when strike directions of magnetic contacts vary.

### 3.5 Testing the “Tilt-Depth” method using vertical contacts with various strike directions

Here, the “Tilt-Depth” method is tested using RTP and RTE datasets from vertical contacts that strike in various directions. The objective here is to examine the effect of azimuth-induced anisotropy

(variations in  $\Delta T$  shapes, i.e., amplitudes and phases, due to changes in contact strike azimuth) on the effectiveness of the method in estimating the location and depth of variously orientated contacts. Using equations (2.5.2), (2.5.5b) and (2.5.4), 114  $\Delta T$  profile datasets were obtained from vertical contacts with various strikes and depths. Profile direction was varied from North-South, N-S ( $A = 0^\circ$ ) to East-West, E-W ( $A = 90^\circ$ ), at intervals of  $5^\circ$ .<sup>13</sup> Since profiles are kept perpendicular to these contacts (Figure 2.10) contact strike directions correspondingly varied from E-W to N-S at intervals of  $10^\circ$ . Hence contact strike direction ranged from  $90$  to  $180^\circ$ . The contacts were at depths ( $z_{mod}$ ) of 3, 4 and 10 km, while remanent magnetisation was assumed absent. Also,  $\delta k = 0.002$  SI Units while  $J_i = 65000$  or  $25000$  nT, respectively, for RTP or RTE profiles. In all, 57 RTP and 57 RTE  $\Delta T$  profile datasets were used for testing the method. Examples of the  $\Delta T$  (RTP) dataset for contacts at a depth of 3 km are presented in figure 3.16. Equivalent datasets for the RTE case are presented in figure 3.17.

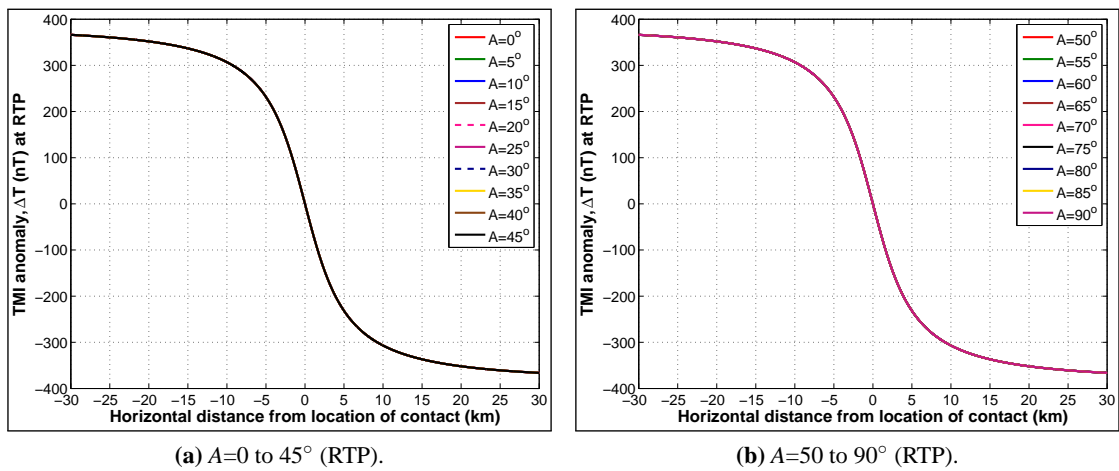


**Figure 3.16:** Effect of strike azimuth of vertical contacts on amplitude and shape of  $\Delta T$ , when effective and induced magnetisations are vertical (RTP). Amplitudes and shapes of  $\Delta T$  for the various strike directions ( $A$ ) are the same, so these plots stack on top of each other irrespective of the strike of contact.

### 3.5.1 TMI anomaly ( $\Delta T$ ) shapes from contacts at RTP and RTE compared

Comparisons between  $\Delta T$  (RTP and RTE) datasets (Figures 3.16 and 3.17) show that RTP anomalies retained their amplitudes and shapes irrespective of contact strike direction (Figure 3.16), whilst RTE anomalies exhibit anisotropy, whereby their amplitudes and shapes varied with contact strike direction (Figure 3.17). RTE anomalies were only at their maximum amplitudes ( $1/2$  of RTP anomaly amplitudes) when the contact strike direction was East-West, i.e.,  $A = 0^\circ$  (Figure 3.17). RTE anomaly amplitudes decayed systematically as contact strike changed from East-West to North-South ( $A = 90^\circ$ ). Anisotropy and the problems it presents to interpretation of RTE datasets were introduced in section 2.3.3 (Figures 2.4 and 2.7). The main objective of this section is to examine the effect of these variations (anisotropy) on locations and depths estimated for these

<sup>13</sup>All directions are relative to the magnetic North (Figure 2.10).

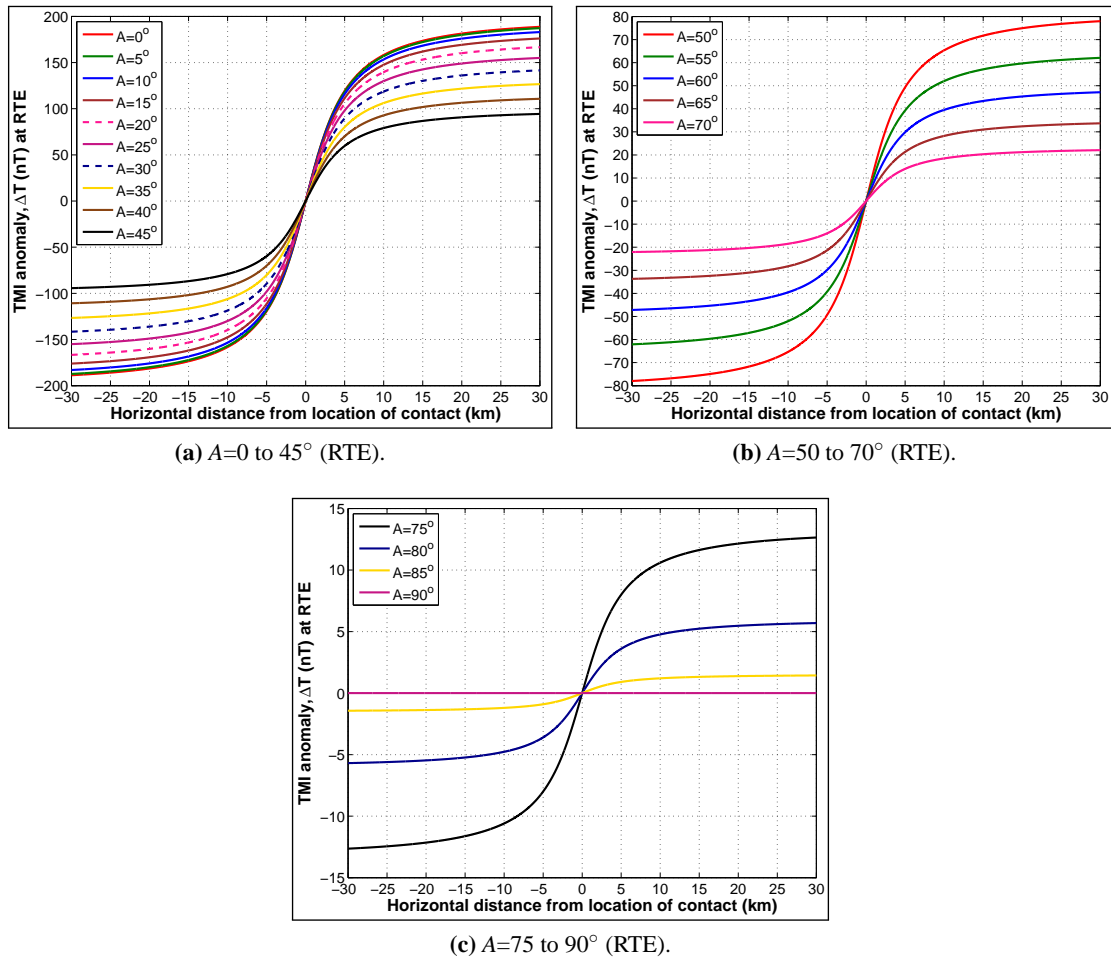


**Figure 3.17:** Effect of strike azimuth of vertical contacts on amplitude and shape of  $\Delta T$ , when effective and induced magnetisations are horizontal (RTE). Unlike the case in figure 3.16, amplitudes of  $\Delta T$  vary systematically from a maximum when the contact strikes East-West ( $A = 0^\circ$ ) to 0 when the contact strikes North-South ( $A = 90^\circ$ ). Also, the maximum amplitude when the contact strike is East-West is half its equivalent at RTP.

contacts, using the “Tilt-Depth” method.

### 3.5.2 Location estimates

$\theta$  curves for vertical contacts with varying strike directions ( $A + 90^\circ$ ) at RTP or RTE are shown in figure 3.18. Curves for the  $\Delta T$ , as well as the first-order Cartesian derivatives (total horizontal- and vertical derivatives, i.e.,  $\frac{\partial \Delta T}{\partial H}$  and  $\frac{\partial \Delta T}{\partial z}$ , respectively) from which these  $\theta$  curves were obtained are presented in figures 3.16 and 3.17 and appendix B.5.  $\Delta T$  and its horizontal and vertical derivatives were zero for North-South striking contacts ( $A = 90^\circ$ ). Consequently, equation (2.6.1a) predicts  $\theta$  to be undefined (Not a number or NaN) when  $\Delta T$  and its derivatives are zero. Hence,  $\theta$  does not exist for North-South striking contacts ( $A = 90^\circ$  in figure 3.18e), and North-South structures cannot be imaged on  $\theta$ -transformed  $\Delta T$  (RTE) datasets.

$\theta$  does not vary with contact strike direction irrespective of whether the contacts is at RTP or

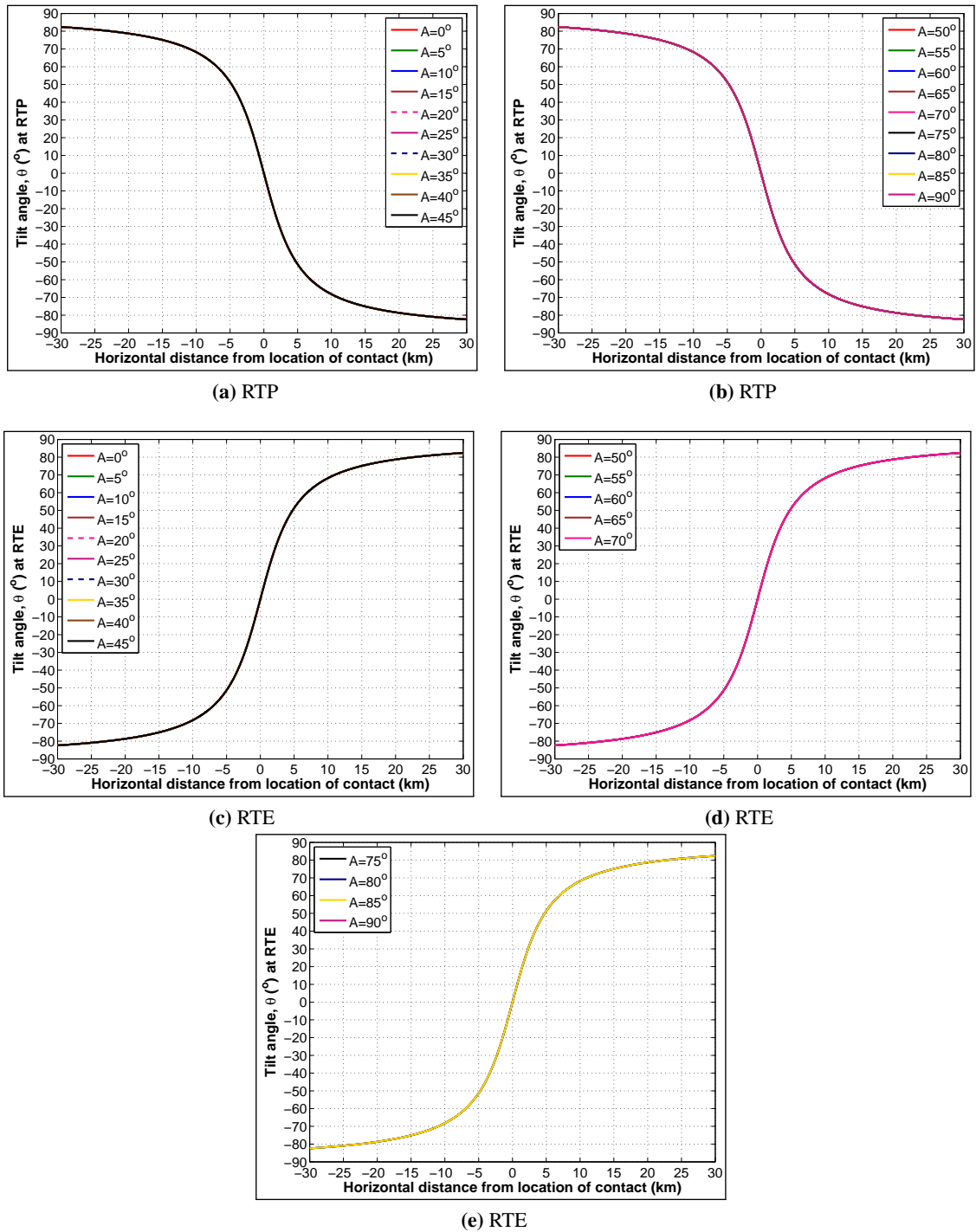


**Figure 3.18:** Effects of the strike azimuth ( $A$ ) of vertical contacts on  $\theta$  of their  $\Delta T$  (RTP or RTE).  $\theta$  curves have the same shape for contacts at RTP or RTE, the RTE curves remaining mirror images or additive inverses of their RTP equivalents, as in figure 3.1. Note that  $\theta$  profiles for all non-North-South ( $A < 90^\circ$ ) striking contacts at RTE are of the same shape. Hence these RTE profiles stack on each other so that only the last in the legend is visible. Note also that there is no  $\theta$  response for North-South ( $A = 90^\circ$ ) striking contacts, when at RTE.

RTE (Figure 3.18). This is easily appreciated for the RTP case in which  $\Delta T$  and its Cartesian derivatives are independent of contact strike direction (Figures 3.16 and 3.17 and appendix B.5). However, when contacts are at RTE, the amplitude and shape of  $\Delta T$  and these derivatives vary with contact strike direction. Being a ratio of these Cartesian derivatives (Equation (2.6.1a)), they are transformed by  $\theta$  to the additive inverses, i.e.,  $\theta$  (RTP) equivalents.

Amplitudes of Cartesian derivatives (total horizontal- and vertical derivatives, i.e.,  $\frac{\partial \Delta T}{\partial H}$  and  $\frac{\partial \Delta T}{\partial z}$ , respectively) and  $\theta$  at locations of azimuthally varying contact strikes, when at RTP or RTE, are presented in figure 3.19. For contacts at RTP, amplitudes of total horizontal derivatives at contact locations are at their maximum, while vertical derivatives and  $\theta$  are zero. These derivatives maintain these constant values, irrespective of contact strike direction (Figure 3.19a). When contacts are at RTE, amplitudes of total horizontal derivatives at contact locations decreased monotonically from its maximum value when contact strikes East-West, to zero when the contact strikes North-South. Vertical derivatives are zero, while  $\theta$  is zero until it becomes undefined when contact strikes North-South (Figure 3.19b).

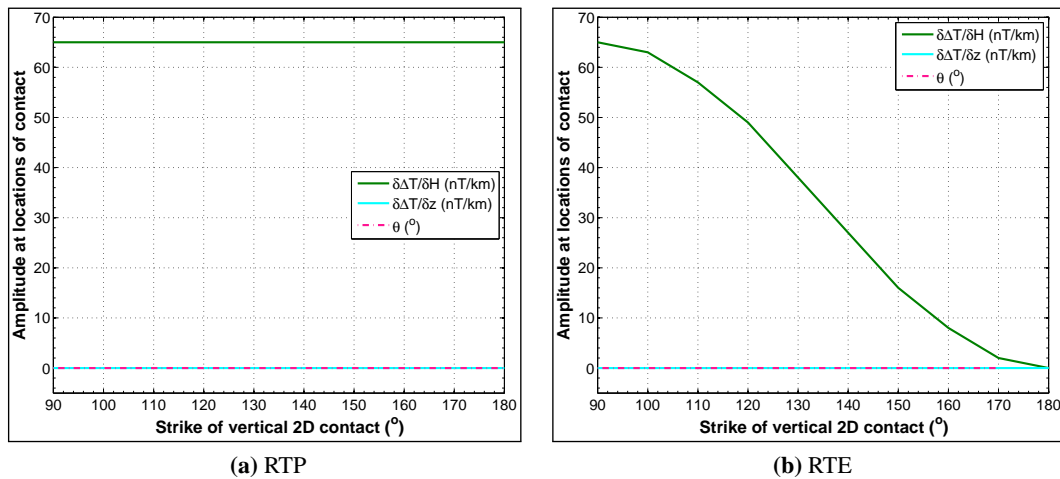


**Figure 3.19:** Effect of strike direction on amplitudes of Cartesian derivatives and  $\theta$  of  $\Delta T$  at locations of vertical contacts, at RTP or RTE. Cartesian derivatives shown are: total horizontal derivatives (Green line); vertical derivatives (Cyan line); and  $\theta$  (Pink dashed line). Note that  $\theta$  does not exist when other derivatives are essentially zero.

### 3.5.3 Estimates of depths

The “Tilt-Depth” method was implemented in two modes, i.e., the  $\theta = \pm 27$  or  $45$  range, to estimate contact depths. Estimates from  $\Delta T$  (RTP) datasets are presented in figure 3.20a for comparison with estimates from RTE equivalents of these datasets (Figure 3.20b). Any differences between these figures are attributable to the effects of anisotropy. The “Tilt-Depth” method effectively and accurately estimated the depth of these well isolated and noise-free models, when at RTP (Figure 3.20a). In practice, however, because of anisotropy effects when the contact is at RTE, the method cannot estimate the depth of contacts with strike directions within  $\approx \pm 10^\circ$  of the magnetic

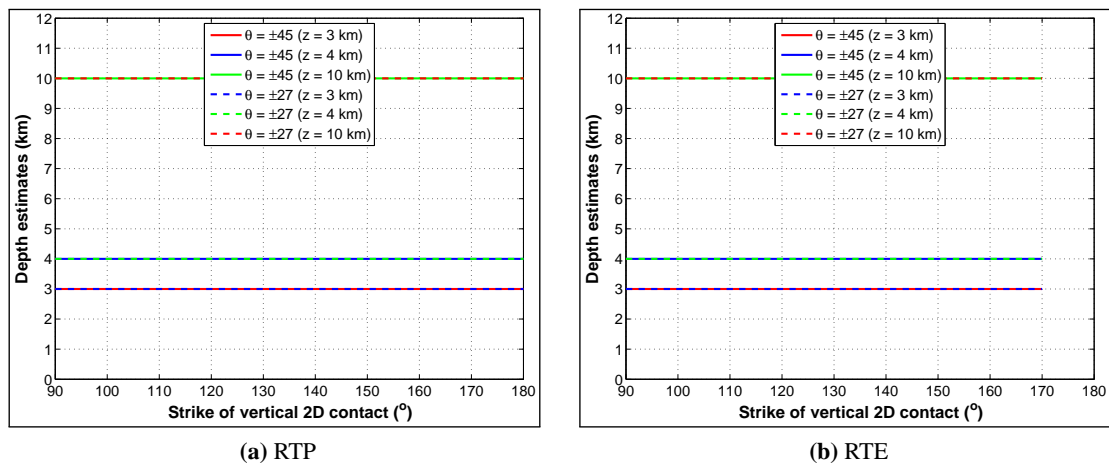


**Figure 3.20:** Effect of azimuthally varying strike of vertical contacts on “Tilt-Depth” estimates of depth, when contact is either at RTP or RTE. The method works well on contacts of all strike directions when RTP, but only for contacts with non-North-South strike directions (90 to 170°), when at RTE. See Figure 3.19 and text for explanation.

North direction, including North-South striking contacts which produce no magnetic anomalies. Because  $\theta$  curves were the same for all non-North-South strike directions (Figure 3.18), when contacts are at RTE, the method also effectively and accurately estimated the depths of these well isolated, noise-free models.

Contact models used in this chapter are single and well isolated. Consequently, their  $\Delta T$  profiles are without interference and/or noise. The additional effects that anomaly interference and noise may have on “Tilt-Depth” method estimates will be examined using more complex, gridded  $\Delta T$  datasets in chapter 4. Profile and gridded  $\Delta T$  datasets are, respectively, two-dimensional (2D) and three-dimensional (3D) magnetic responses of the subsurface.

## Chapter 4

# Application of “Tilt-Depth” method to gridded “Bishop” model $\Delta T$ datasets

---

### 4.1 Introduction

The “Tilt-Depth” method works well on both reduced-to-pole (RTP) and reduced-to-equator (RTE) TMI anomaly ( $\Delta T$ ) profile datasets, when obtained from isolated vertical and near-vertical 2D magnetic contacts (Chapter 3).<sup>1</sup> However,  $\Delta T$  datasets are now rapidly acquired across large areas and, thus, commonly presented in grid rather than profile format. While profile  $\Delta T$  datasets have 2D cross-sections, gridded datasets have three dimensional (3D) cross-sections. Gridded  $\Delta T$  datasets are, therefore, more likely to contain anomaly sources from unisolated structures of various geometries, strikes and depths. The main problems that affect interpretation of such datasets include: masking of subtle anomalies when anomalies of very high amplitudes are present; mapping continuous sources when edges are characterised by changing depths and magnetic susceptibilities; and determining the nature of effective magnetisation responsible for the observed anomalies (Verduzco et al., 2004).

Depending on the inclination of the inducing geomagnetic field over a survey area magnetic data grids must either be transformed to their equivalents at the geomagnetic North pole (RTP) or equator (RTE). In general, high resolution magnetic data from regions close to the geomagnetic equator, i.e., inclinations in the range  $-15$  to  $15^\circ$  (or  $-30$  to  $30^\circ$  for low resolution datasets) cannot be transformed to their true RTP equivalents (Baranov & Naudy, 1964; Reford, 1964; Silva, 1986; MacLeod et al., 1993). Only RTE transformation is stable at this range of geomagnetic field inclinations. Unlike the RTP process which produces simple, radially symmetric magnetic anomalies that are centred directly above their sources, the RTE process produces anomalies that are characterised by azimuthally varying amplitudes and shapes, i.e., *anisotropy* (Section 2.3.3). RTE anomalies from adjacent sources with various strikes are likely to interfere, due to anisotropy. Consequently, RTE-transformed  $\Delta T$  datasets are more complex, and thus prone to interpretation problems (Section 2.3.3). Work in this chapter, as well as chapter 5, will be dedicated to comparisons between estimates of anomalous source edge locations and depths obtained from RTP and

---

<sup>1</sup>RTP or RTE will hereafter be used in place of reduced-to-pole or reduced-to-equator, respectively.

RTE equivalents of gridded datasets.

The “Tilt-Depth” method depends on Tilt angles ( $\theta$ ) of  $\Delta T$  datasets.<sup>2</sup> The many advantages gained from  $\theta$  equivalents of RTP-transformed  $\Delta T$  profiles and grids were outlined in section 2.6.1. Figure 3.1 show that these advantages can also apply to RTE-transformed datasets. Hence, the anomaly interference and other azimuth-related problems that characterize RTE-transformed grids may be minimised when transformed to their  $\theta$  equivalents. Evaluating the gains or otherwise of transforming RTE grids to their  $\theta$  equivalents, and from the application of “Tilt-Depth” method to these grids is the focus of this chapter. “Bishop” model (BM)  $\Delta T$  grids (Section 4.2) will be used for these evaluations. The effectiveness of the “Tilt-Depth” method will be examined by comparing its estimates of source locations and depths from RTP and RTE equivalents of BM grids. The first (left) column of the flowchart shown in figure 4.1 presents the work-flow adopted for this chapter.

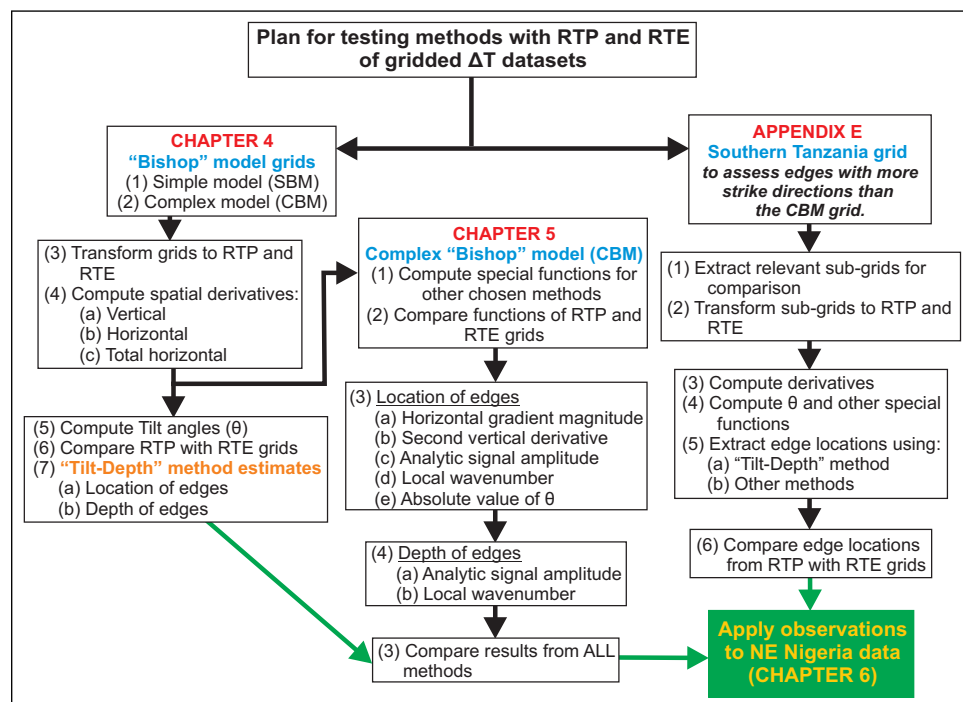


**Figure 4.1:** Work-flow adopted for evaluating estimates obtained from “Bishop” model (BM) and real Southern Tanzania  $\Delta T$  datasets, using the “Tilt-Depth” and other methods.

Source locations and depths estimated from RTP and RTE equivalents of BM grids using other semi-automatic interpretation methods are examined and compared with “Tilt-Depth” estimates in chapter 5, using the work-flow outlined in the second (middle) column of figure 4.1. Ultimately, estimates from these methods will also be examined using RTP and RTE equivalents of a real  $\Delta T$  grid from Southern Tanzania (Appendix E). The work-flow adopted for evaluating methods using Southern Tanzania  $\Delta T$  dataset is shown in the third (right) column of figure 4.1. By examining the effects of RTE transformation on source edge location and depth estimates from BM and Tanzania

<sup>2</sup>Tilt angles will hereinafter be replaced by the symbol  $\theta$ .

$\Delta T$  datasets this study aims to provide a well constrained strategy for mapping the locations and depths of two-dimensional (2D) and/or non-2D magnetic source edges in NE Nigeria.

## 4.2 “Bishop” model (BM) datasets

BM  $\Delta T$  grids are three-dimensional (3D) datasets sourced from model geological structures with known locations, shapes, depth and magnetic susceptibilities. They were introduced by Williams et al. (2002) and Fairhead et al. (2004), but the physical model was developed by Guy Flanagan (ConocoPhillips, Houston, USA) using Fugro-LCT’s 3MOD<sup>TM</sup> software. Anomalies on these realistic grids result from a known topographic surface, which was treated to serve as standard approximations for real, three-dimensional (3D) geological distributions of magnetic basement features. The grids (Williams et al., 2002; Fairhead et al., 2004) were created by assigning magnetic susceptibility values to a 30 m UTM digital elevation model (DEM) of the topography of an area of the Volcanic Tablelands, North of Bishop, California, USA. The original DEM grid covers an area 10.5 km × 10.8 km. In order to produce a grid on the scale of a typical geological basin the DEM grid was expanded by a factor of 30 in all three dimensions assuming that faulting patterns are fractal (Williams et al., 2002). Hence, the areal coverage of the BM is now approximately 315 km × 324 km. With grid cell size of 0.5 km × 0.5 km, the grid is a matrix of 649 × 631 data points.<sup>3</sup> The expanded DEM is shown in figure 4.2a.

The dominant features of this expanded DEM grid (Figure 4.2a) are two major faults: one strikes approximately North-South (N-S); the other strikes approximately East-West (E-W). Other structural features of the DEM include smaller en echelon faults which generally strike N-S and NW-SE (NorthWest-SouthEast), transfer zones and an unfaulted deep basin area in the SouthEastern (SE) corner of the grid (Williams et al., 2002). The DEM is assumed to represent the top of the magnetic basement, and has been covered with non-magnetic sediments which range in thickness from about 430 m in the NorthWestern (NW) corner to just over 9160 m in the SouthEastern corner of the grid. The depth to basement increased generally from NW to SE (Figure 4.2a).

By assigning user-defined parameters such as inclination and declination of magnetisation vector, strength of inducing magnetic field, and magnetic susceptibility ( $k$ ) to the expanded DEM grid (Figure 4.2a) unique  $\Delta T$  grids are generated for unique sets of magnetic parameters. Figure 4.2b is an example grid of complex distribution of magnetic susceptibilities, of the same size as the DEM grid, which can be used to generate  $\Delta T$  grids from sources with variable magnetic susceptibilities. Consequently,  $\Delta T$  resulting from “Bishop” basement models are sourced from a mixture of major two-dimensional (2D) anomalous magnetic contacts and minor en-echelon faults, which strike in a variety of directions, at depths ranging from  $\approx 0.4$  to 9 km. Unlike  $\Delta T$  from the well isolated two-dimensional (2D) magnetic contact sources in chapter 3, these anomalies are not isolated. The resulting anomaly interference is one unique feature of "Bishop" model grids. The roughness

---

<sup>3</sup>These statistics apply to all BM grids used in this study.

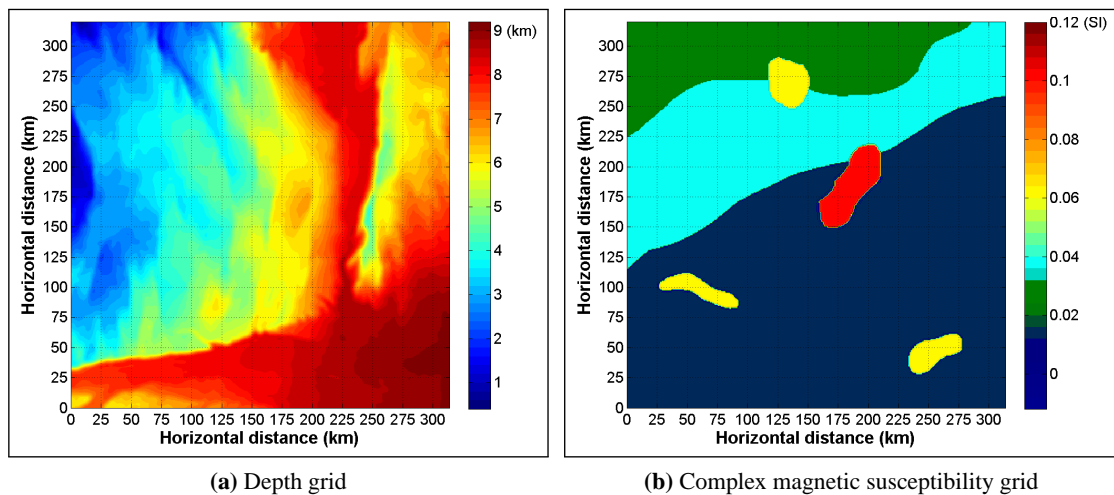


**Figure 4.2:** The input "Bishop" model basement grids: (a) Magnetic basement depth; and (b) Complex magnetic susceptibility distribution. (See clearer GETgrid<sup>TM</sup> version of grids in appendix C (Figure C.1).)

of the basement surface, a good proxy for geologically-sourced noise, is another important feature of these models. Two types of model  $\Delta T$  grids (Figure 4.3) generated from the model "Bishop" basement depth grid (Figure 4.2a) will be used to test the "Tilt-Depth" method in this chapter. They are: (1) the homogeneous or simple "Bishop" model (SBM), grid (Williams et al., 2002), and (2) the heterogeneous or complex "Bishop" model (CBM) grid (Fairhead et al., 2004).

#### 4.2.1 Simple "Bishop" model (SBM) $\Delta T$ grid

The SBM  $\Delta T$  grid (Figure 4.3a, Williams et al., 2002) was generated by assigning a constant magnetic susceptibility,  $k = 1.26 \times 10^{-2}$  (SI units), as well as induced magnetisation with inclination of  $25^\circ$ , declination of  $0^\circ$  and strength of 50,000 nT to the modified magnetic DEM grid in figure 4.2a.<sup>4</sup> The SBM grid is, therefore, a grid of  $\Delta T$  sourced from a homogeneous magnetic basement. The main geological features of this basement grid are basement-involved fault scarps. These faults scarps, designated "FS" in subsequent figures, represent sudden and localized linear changes in the depth of the modified magnetic basement surface (Figure 4.2a). Although the grid in figure 4.3a was generated from these features of figure 4.2a, features clearly identifiable in figure 4.2a cannot be easily identified in figure 4.3a.

#### 4.2.2 Complex "Bishop" model (CBM) $\Delta T$ grid

The CBM  $\Delta T$  grid (Figure 4.3b, Fairhead et al., 2004) was generated from a heterogeneous magnetic basement model grid for induced magnetisation with inclination of  $25^\circ$ , declination of  $0^\circ$  and

<sup>4</sup>A sharper GETgrid<sup>TM</sup> version of this grid (without graticule and range of values) is presented in appendix C (Figure C.2a).

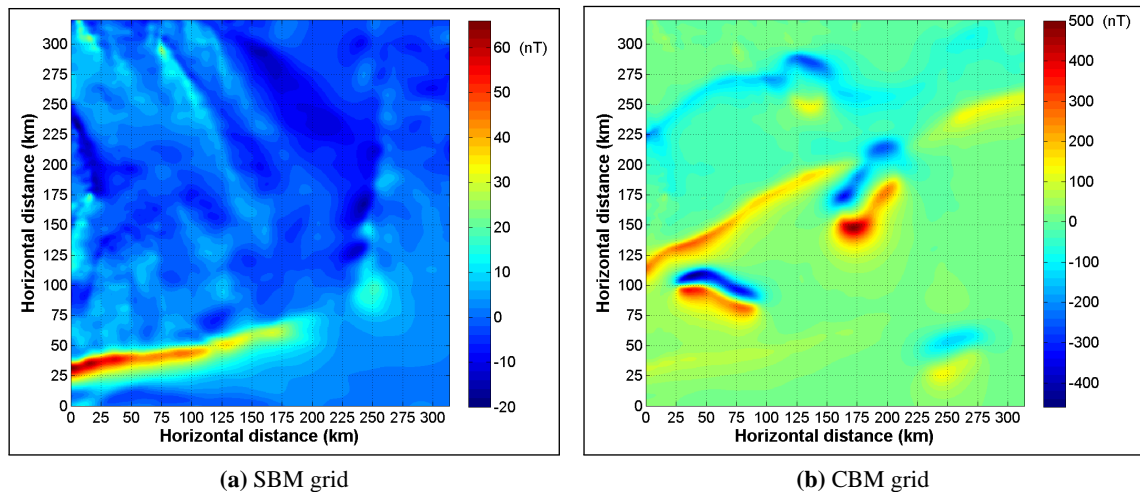


**Figure 4.3:** "Bishop" model  $\Delta T$  grids generated by magnetic basement at depths shown in figure 4.2a, for inducing magnetisation with inclination,  $\alpha = 25^\circ$ , declination= $0^\circ$  and strength= $50,000$  nT: (a) The simple "Bishop" model (SBM) grid of Williams et al. (2002) assumes constant magnetic susceptibility,  $k$  (Section 4.2.1); and (b) The complex "Bishop" model (CBM) grid of Fairhead et al. (2004) assumes variable  $k$  as shown in figure 4.2b (Section 4.2.2). Note that it is not possible to correlate structures on grids in figures 4.3a and 4.2a. For the same reason, structures on the grid in figure 4.3b do not correlate with their respective sources in figures 4.2a and 4.2b. Hence, grids require RTP or RTE.

strength of  $50,000$  nT.<sup>5</sup> The model basement was at depths defined by the DEM grid (Figure 4.2a), but consisted of vertical prisms, each of which were assigned a distinct magnetic susceptibility,  $k$  (Figures 4.2b), to simulate various basement terrains and intrusive bodies with different magnetic susceptibilities. The CBM, thus, presents a contiguous set of magnetic geological basement terranes separated by 2D contact-like boundaries, as well as a series of isolated intrusive magnetic bodies. The surface of the magnetic basement and depths are identical to that of the SBM grid, with non-magnetic sediments superimposed. Unlike the SBM which was dissected by fault scarps (FS) only (Section 4.2.1),  $\Delta T$ -generating geological sources on the CBM can be broadly grouped into two (2) categories;

(1) **Fault scarps, "FS"** - linear or curvilinear features which occur due, only, to abrupt local changes in the depth of the magnetic basement surface, and

(2) **Magnetic contacts** - linear (2D) or curved features (non-2D and 3D) which are due to abrupt local changes in the susceptibility contrast ( $\delta k$ ) between either the magnetic basement and the overlying non-magnetic sediments or between the intrusive bodies and their surrounding basement host rocks. In this study these magnetic contacts have been further subdivided into; (i) **two-dimensional (2D) magnetic contacts**, where contact is between two contiguous basement terranes (e.g., between the dark blue and light sky-blue terrains in Figure 4.2b), and (ii) **non-2D magnetic contacts**, where contact is between intrusive bodies (e.g., yellow and red elongated bodies in figure 4.2b) and their host basement rocks. The yellow spherical intrusion is in 3D contact with adjacent rocks. These boundaries are not 2D contacts since they have finite strike lengths.

<sup>5</sup>A sharper GETgrid<sup>TM</sup> version of this grid (without graticule and range of values) is presented in appendix C (Figure C.2b).

The three dominant strikes of basement fault scarps (FS) on the SBM grid are NW-SE, NNW-SSE and ENE-WSW. The CBM grid, additionally, presents two dominant NE-SW trending magnetic contacts, as well as non-2D contacts. Therefore, on the CBM grid,  $\Delta T$  responses from these additional features are superimposed on the topographic basement trends, FS (Figure 4.2a) of the SBM grid (Figure 4.3a). It is difficult to visually correlate anomalies on the SBM grid (Figure 4.3a) with FS on the basement depth grid (Figure 4.2a). Similarly,  $\Delta T$  on the CBM grid (Figure 4.3b) are dominated by those from magnetic sources (Figure 4.2b), while those from topographic basement trends are obscure. FS sources, are therefore, difficult to visually correlate with their respective sources.

The range of  $\Delta T$  values on the CBM grid (Figure 4.3b) is one order of magnitude higher than that of the SBM grid (Figure 4.3a). This is because of the significant contrasts in magnetic susceptibility ( $\delta k$ ) between the uniform susceptibility SBM grid, and the varying susceptibility basement terranes of the CBM grid (Figure 4.2b). Consequently, only the strongest anomalies on the SBM grid are visible, as subtle anomalies, on the CBM grid. Weaker SBM grid anomalies are over-printed by the stronger anomalies present on the CBM grid. Hence these grids present characteristic problems faced during interpretation of gridded magnetic data (Verduzco et al., 2004). “Bishop” models were designed invariably to help bridge the methods-testing gap by serving as intermediate models between models of 2D idealized structures and sources of real field-acquired  $\Delta T$  data. Until the introduction of “Bishop” models, magnetic interpretation methods were tested using simple 2D models, after which the methods were directly applied to complex, real field data.

Since the shapes, locations, depths and composition of source edges, as well as the inclination of induced magnetisation of BM grids are all precisely known, these grids are ideal for testing the effectiveness of semi-automatic methods and techniques of magnetic data interpretation before applying the method/technique to real field data. Also, since induced magnetisation is inclined at  $25^\circ$  and remanence is zero, these model grids, are easily transformed to their RTP and RTE equivalents. Interpretations from these grids can be compared to evaluate the effects of anisotropy in RTE datasets, for example. Hence, these BM grids can be used to evaluate how well magnetic data interpretation methods work when applied to the RTP or RTE equivalent of real field-acquired  $\Delta T$  datasets. BM grids have been used to test the local wavenumber method (Fairhead et al., 2004), Euler deconvolution (Reid et al., 2005; Williams et al., 2005), and phase or normalised derivatives (Fairhead & Williams, 2006).

The main objective of this chapter is to initially evaluate the effectiveness of the “Tilt-Depth” method when applied to gridded  $\Delta T$  datasets obtained from regions like NorthEastern Nigeria, where inclination of induced magnetisation is low. Strategies adopted in this chapter were, therefore, designed to help determine, using BM  $\Delta T$  grids, the maximum possible loss in information due to RTE-transformation as the strike azimuths of two-dimensional (2D) magnetic contacts change from East-West (E-W) to North-South (N-S). The principal approach adopted involves qualitative and/or quantitative comparisons between “Tilt-Depth” method estimates of the locations and depths of edges of model structures from RTE and RTP equivalents of the SBM and

CBM grids. Since remanent magnetisation is absent, any differences between “Tilt-Depth” method estimates from the RTP and RTE BM grids must be consequences of anisotropy due to RTE-transformation of grids. These analyses assume that structures on the grids are mainly vertical, two-dimensional (2D) structures.

### 4.3 RTP and RTE-transformed SBM and CBM grids compared

#### 4.3.1 TMI anomaly ( $\Delta T$ ) grids

The SBM and CBM  $\Delta T$  grids (Figures 4.3a and 4.3b) derive from various sources, of different compositions, shapes and strike azimuths. It is not possible to correlate locations of edges on both the basement depth grid (Figure 4.2a) and the heterogeneous magnetic susceptibility grid (Figure 4.2b), with  $\Delta T$  on either the SBM grid (Figure 4.3a) or CBM grid (Figure 4.3b). Hence, with induced magnetisation ( $\alpha$ ) inclined at  $25^\circ$ , RTP and RTE versions of these grids were obtained in order to compare the grids.

The SBM and CBM grids were each transformed to their RTP and RTE equivalents using magnetisation vector with inclination of  $25^\circ$ , declination of  $0^\circ$  and strength of 50,000 nT. The RTP and RTE-transformed equivalents for the SBM grid are shown, respectively, in figures 4.4a and 4.4b.<sup>6</sup> The RTP and RTE-transformed equivalents for the CBM grid are shown, respectively, in figures 4.5a and 4.5b.<sup>7</sup>

<sup>6</sup>See less annotated, but sharper images of these grids in appendix C (Figure C.3).

<sup>7</sup>Less annotated, but sharper versions of CBM grids are shown in appendix C (Figure C.4).

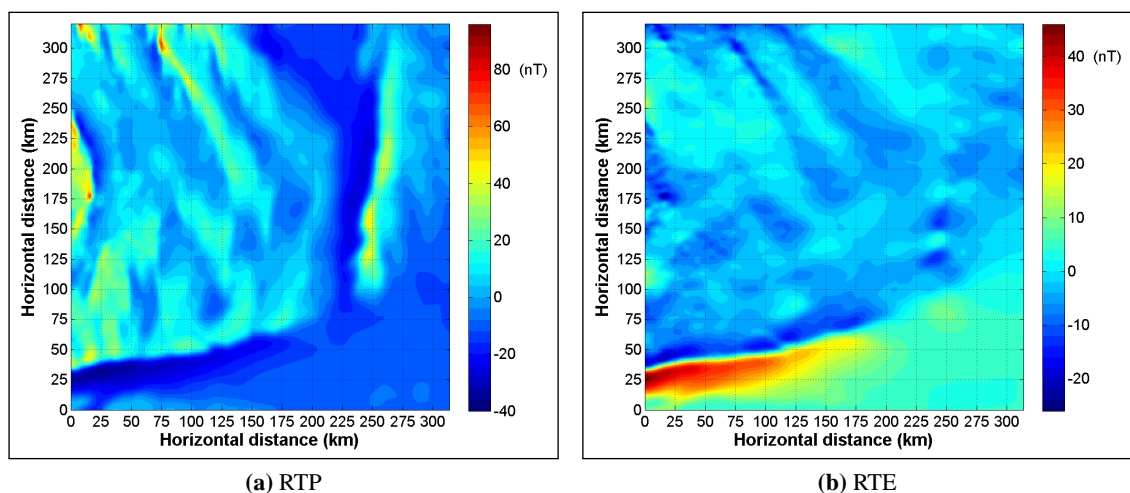


**Figure 4.4:** RTP and RTE transformed equivalents of the SBM grid (Figure 4.3a). All fault scarps (FS) in figure 4.2a are visible on SBM (RTP) grid (Figure 4.4a) irrespective of strike directions. Of the three major FS strike directions (N-S, E-W and NW-SE) in figure 4.2a, the E-W striking FS is well imaged, NW-SE striking FS are poorly imaged, while N-S trending FS are not imaged at all on the SBM (RTE) grid (Figure 4.4b).

(A) **SBM grids** I begin by visually comparing the apparent locations of structures on both the RTP and RTE equivalents (Figures 4.4b and 4.4a, respectively) of the SBM grid (Figure 4.3a) with locations of sources on the homogeneous basement grid (Figure 4.2a). These transformed grids derive from a grid of only morphologically changing, but compositionally uniform basement that is offset by vertically sided fault scarps, FS (Figure 4.2a).

Most structures on the basement depth grid (Figure 4.2a) produce anomalies that are imaged on the **SBM (RTP) grid** (Figure 4.4a) at their correct locations, irrespective of their strike. Of particular significance, in the context of this study is the fact that the laterally extensive and approximately NNE-SSW striking FS centred at grid locations (205,160) and (262,212) in the Eastern part of figure 4.2a also generate persistent and continuous magnetic anomalies throughout their entire lengths, and are completely obvious on the SBM (RTP) grid (Figure 4.4a).<sup>8</sup> The most prominent  $\Delta T$  on the SBM (RTP) grid (Figure 4.4a) are associated with shallow (< 4,500 m) two-dimensional (extensive, linear) features on the SBM basement grid (Figure 4.2a).

The range of anomaly amplitudes on the **SBM (RTE) grid** (Figure 4.4b) is 72 nT, representing a significant (50%) reduction from 136 nT on the SBM (RTP) grid (Figure 4.4a). The only prominent feature of the RTE grid is the ENE-WSW striking FS, with a positive anomaly, which extends from the SouthWest corner of the grid. The occurrence of anisotropy-induced interference between adjacent anomalies and the anomaly amplitude difference makes it difficult to impossible to correlate any FS on the input basement depth grid (Figure 4.2a) with anomalies on the SBM (RTE) grid (Figure 4.4b). This is mainly because North-South (N-S) structures are invisible (not imaged) on RTE grids (See figures 2.6c and 2.6a, also figures 2.7c and 2.7a). Also NorthNorthEast-SouthSouthWest (NNE-SSW) and NorthNorthWest-SouthSouthEast (NNW-SSE), i.e., FS striking with the range;  $N \pm 20^\circ$ , are only imaged on RTE grids when isolated, invariant in cross-section and continuous throughout their entire lengths. These criteria are not met in nature, as the input basement depth grid (Figure 4.2a) shows. Consequently, such sources generate discrete (discontinuous) E-W dipolar anomalies that mimic their extents on RTE grids.

Dipole-like anomalies result from the leakage of magnetic flux induced in such (locally discontinuous) structures along the en-echelon E-W striking plane of displacement (See figure 2.8). These dipolar anomalies are further enhanced by local changes in the strike of such structures. Where such structures occur in close proximity to sources which strike in other directions, their RTE anomalies interfere to produce artefacts that are not related to any real sources. Examples of such RTE artefacts for NNW-SSE sources occur at grid nodes (10,200), (75,300), (108,250) and (189,237) on the SBM (RTE) grid (Figure 4.4b) compared with its RTP equivalent (Figure 4.4a). Similar examples for NNE-SSE sources on these grids occur at grid nodes (250,162) and (262,262).<sup>9</sup> The frequent occurrence of NNW-SSE and NNE-SSW sources and the closeness of sources on the basement depth grid (Figure 4.2a) appears to be a major reason for the inability to recognise and correlate anomalies from similar sources on the RTP and RTE of SBM grids. It

<sup>8</sup>Grid location or node refers to a specific grid point with coordinates (x,y).

<sup>9</sup>These artefacts are more obvious on equivalent figures in appendix C (Figure C.3).

was not possible to distinguish anomaly interference due to nearness of sources from those caused by the RTE-induced azimuthal anisotropy. Consequently, any future reference(s) to anomaly interference on RTE grids will imply both origins.

Anomalies due to the well isolated NorthWest-SouthEast (NW-SE) fault scarp along grid nodes (92,281) and (125,225) are preserved on the SBM (RTE) grid (Figure 4.4b). This applies also to the NorthWest-SouthEast (NE-SW) structure containing grid nodes (50,50) and (175,75). Unfortunately, the basement depth grid (Figure 4.2a) does not contain as many structures with these strike directions.

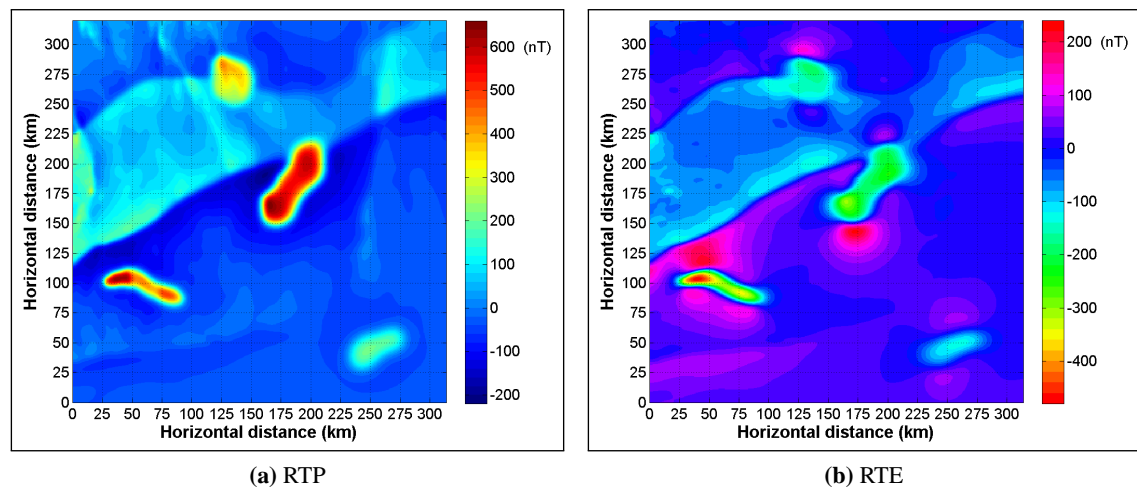


**Figure 4.5:** RTP and RTE transformed equivalents of the CBM grid (Figure 4.3b). All magnetic sources (with 2D or non-2D contacts) in figure 4.2b are visible on CBM (RTP) grid (Figure 4.5a) irrespective of shape and orientation. Fault scarps (FS) are only visible as subtle anomalies in figure 4.5a. Subtle FS and topographic anomalies are invisible on CBM (RTE) grid (Figure 4.5b) as they are swamped by the relatively higher amplitude anomalies of basement origin. Unlike the SBM (RTE) grid, edges of magnetic sources are visible on CBM (RTE) grid. Negative anomalies occur directly above source bodies with mainly positive anomalies occurring to the North and South of the edges of these sources.

**(B) CBM grids** TMI anomalies ( $\Delta T$ ) on the CBM grid (Figure 4.3b) result from varying magnetic composition (Figure 4.2b), as well as depths (Figure 4.2a) of basement (Section 4.2.2). CBM grid anomalies are significantly higher in amplitude (by a factor of 2 or more) than those on SBM grids, in direct response to the higher lateral magnetic susceptibilities ( $k$ ) of CBM anomaly sources (Figure 4.2b).

The range of anomalies on the **CBM (RTP) grid** (Figure 4.5a) is 840 nT compared with the 136 nT range of the SBM (RTP) grid, a range factor  $> 6$ . Except where FS were significantly shallow and located within lithologic terrains of high enough susceptibilities ( $k$ ), these weaker (subtle) anomalies are swamped (dominated) by the higher amplitudes rendering these sources semi-visible, if not invisible, on the CBM (RTP) grid. Unlike the SBM (RTP) grid (Figure 4.4a) in which the most prominent  $\Delta T$  were mainly associated with shallower model sources, the most prominent anomalies ( $>250$  nT) on the CBM (RTP) grid are generally associated with intrusive model sources with magnetic susceptibility contrasts ( $\delta k$ ) exceeding 0.04 SI (Figure 4.2b) and at depths shallower

than 7 km. Note that anomalies from the equally strongly magnetised intrusive source located at grid node (253,46) near the SouthWest (SW) corner of the grid, at depths exceeding 7 km are significantly attenuated to intermediate range anomalies (50-250 nT). The NorthEast-SouthWest (NE-SW) trending basement terrain (slab) with  $k=0.038$  SI, which dominates the northern half of the grid in figure 4.2a is outlined by intermediate anomalies, which vary with depth on the CBM (RTP) grid (Figure 4.5a). The varying width of this structure seems to affect how it is imaged on this CBM grid. For example, this intermediate  $k$  slab is at its thinnest around grid location (232,250), but at depths exceeding 8 km. Consequently, it is not as well imaged as it is when shallower, West and East of grid location (232,250). Therefore, sources with small widths need to either be at shallow depths or possess considerably higher magnetic susceptibility, to be fully imaged. The dramatic impact that the combined effects of variable source depth and composition ( $k$ ), as well as interference from adjacent sources can have on anomalies is demonstrated by the rapid gradation of anomaly amplitudes across the intrusive source at grid node (130,272) in the North-Central part of the CBM (RTP) grid (Figure 4.5a). This grid (Figure 4.5a) shows that anomaly amplitudes increased generally with increasing magnetic susceptibility contrast ( $\delta k$ ) and reducing basement depth, with susceptibility changes having more significant effects on magnetic anomaly magnitudes than the depth changes.

The **CBM (RTE) grid** (Figure 4.5b) presents similar symptoms to those observed on the SBM (RTE) grid (Figure 4.4b). For instance, the range of anomalies (575 nT) on the CBM (RTE) grid is considerably weaker than that on the CBM (RTP) grid (Figure 4.5a) by a factor of 1.5, reflecting the weaker induced field intensity at the geomagnetic equator (See section 2.3.1 for more details). High susceptibility ( $> 0.013$  SI) sources (Figure 4.2b) that were imaged in figure 4.5a as positive anomalies are imaged as negative anomalies on the CBM (RTE) grid (Figure 4.5b), with positive side-lobes to the North and South of each major negative anomaly. These side-lobes can interfere to dominate anomalies from relatively weaker sources to the North and South of such anomalies. Such interference will further complicate matters, especially where a number of adjacent E-W striking non-2D sources also occur. Fortunately, this is not the case on the CBM grids. In general, negative  $\Delta T$  on the CBM (RTE) grid (Figure 4.5b) correspond to positive anomalies on the CBM (RTP) grid (Figure 4.5a). This seems to confirm the existence of the additive inverse relationship suggested in figure 3.1 for profile datasets. Such an inverse relationship cannot exist for the entire grid, since North-South (N-S) structures are not imaged at RTE. Also, NorthNorthEast-SouthSouthWest (NNE-SSW) and NorthNorthWest-SouthSouthEast (NNW-SSE) structures are only imaged on RTE grids when invariant in cross-section and continuous throughout their entire lengths. These criteria are not met in nature. Hence, NNE-SSW and NNW-SSE structures generate discrete (discontinuous) E-W striking anomalies on RTE grids that interfere to produce additional artefacts that are not related to any real sources.<sup>10</sup> Therefore, although RTE grids of real, unisolated anomalies may contain inverses of their RTP equivalents from sources that are not orientated N-S, NNE-SSW or NNW-SSE, such grids also contain anomalies that result from complex in-

<sup>10</sup>See examples of these artefacts for NNW-SSE sources at grid nodes (10,200), (75,300) and (108,250) on the CBM (RTP) and CBM (RTE) grids (Figures 4.5a and 4.5b, respectively). Similar examples for NNE-SSE sources on these grids occur at grid nodes (250,137) and (262,262).

teractions between anomalies generated by genuine sources and artefacts resulting from the RTE process.

In summary, RTP of “Bishop”  $\Delta T$  grids show that strong positive  $\Delta T$  are sourced from magnetic basement sources with susceptibilities greater than the surrounding lower susceptibility ( $k$ ) basement. Boundaries between such sources are contacts (locations of significant magnetic susceptibility contrasts,  $\delta k$ ). Moderate, positive to negative  $\Delta T$  are sourced from higher reliefs on the basement surface, but these are significantly more attenuated with increasing depth. All sources, irrespective of their spatial orientation (strike), were imaged at the correct locations on RTP grids. Comparisons between SBM (RTP) and CBM (RTP) grids (Figures 4.4a and 4.5a) and their RTE equivalents (Figures 4.4b and 4.5b, respectively) show that negative  $\Delta T$  on RTE grids correspond to positive anomalies on the RTP grids, suggesting an additive inverse ( $\times -1$ ) relationship. N-S striking sources are not imaged at RTE. NW-SE or NE-SW structures appear to be well imaged, while NNE-SSW or NNW-SSE striking sources are imaged as linear arrangements of discrete, E-W striking dipolar anomalies on RTE grids (See figure 2.8). Hence, RTE anomalies represent inverses of their RTP equivalents for isolated sources striking in directions other than N-S, NNE-SSW or NNW-SSE. Also, artefacts (not associated with any basement sources) generated by RTE transformation and interference of anomalies from NNE-SSW and NNW-SSE structures confirm that grids of RTE anomalies are not exactly additive inverses of their RTP equivalents. Interfering anomalies caused by the RTE process could not be distinguished from those due to anisotropy.

Magnetic basement sources were generally associated with positive or moderately negative anomalies (local crests/peaks) bound by relatively lower anomalies (local saddles/troughs) on the RTP grids. The reverse is true for the RTE grids, barring the effects of anomaly interference due to NNE-SSW or NNW-SSE striking structures. An example is centred close to grid node (62,50) on both the CBM (RTP) and CBM (RTE) grids (Figures 4.5a and 4.5b, respectively).

### 4.3.2 Tilt angle ( $\theta$ ) grids

$\theta$  grids consist of amplitude-gain-controlled and equalized equivalents of  $\Delta T$  (Section 2.6.1). Unlike grids generated from other derivatives that depend directly on  $\Delta T$  amplitudes, with grid values decreasing with decreasing  $\Delta T$  amplitudes,  $\theta$  equalizes prominent and subtle anomalies on both RTP and RTE grids, by amplifying the ratio between Cartesian derivatives (Equation (2.6.1)), making it possible to map both shallow and deeper sources of all compositions.<sup>11</sup> Importantly,  $\theta$  is independent of susceptibility contrast ( $\delta k$ ) distribution on the grid. Hence, anomalies on the SBM (RTP) and SBM (RTE) grids (Figures 4.4a and 4.4b), as well as the CBM (RTP) and CBM (RTE) grids (Figures 4.5a and 4.5b) were further simplified by transforming each grid to their  $\theta$  equivalents. However, positive  $\theta$  of RTP anomalies correspond, in general, to negative  $\theta$  of RTE anomalies, and vice versa (Figure 3.1). Consequently, *only the additive inverse* ( $\times -1$ )

<sup>11</sup>Subtle SBM and CBM  $\Delta T$  were sourced by lower susceptibility or deeper sources on RTP grids, while anisotropy also contributed subtle anomalies to RTE grids.

of  $\theta$ -transformed RTE- $\Delta T$  grids will be compared, qualitatively and/or quantitatively, with their RTP equivalents in this study. Hence, the  $\theta$  of the SBM (RTP) grid in figure 4.4a is presented in figure 4.6a, while the additive inverse of  $\theta$  of the SBM (RTE) grid in figure 4.4b is shown in figure 4.6b.<sup>12</sup> Equivalent grids for RTP and RTE equivalents of the CBM grid (Figure 4.3b) are shown in figure 4.7.<sup>13</sup>

Major sources of  $\Delta T$  on the initial CBM grid (Figure 4.3b), including those that were not apparent even on the CBM (RTP) grid (Figure 4.5a), are imaged on the  $\theta$  of CBM (RTP) grid (Figure 4.7a), irrespective of their strike direction (azimuth). However, not all fault scarp locations on the SBM grid are imaged in figure 4.7a. This is because the weak  $\Delta T$  from these structures have been lost, mainly to interference between  $\Delta T$  originating from basement morphology and lithology (magnetic susceptibility,  $\delta k$ ). The higher  $\Delta T$  amplitude contrasts at intersections between the higher susceptibility intrusives and NE-SW striking 2D magnetic contacts on the CBM (RTP) grid appear to displace its  $\theta = 0$  contours from locating these intersections. These intersections are better defined by  $\theta = 0$  contours of the CBM (RTE) grid. See grid nodes (180,205) and (212,212) for examples.

Angular measurements of the strike directions of two-dimensional (2D) and non-2D contacts, as well as, FS on the  $\theta$  of CBM (RTP) grid (Figure 4.7a) present four strike directions: (i) NW-SE striking two-dimensional (2D) contacts; (ii) NNW-SSE striking FS; (iii) NNE-SSW striking FS; and (iv) NE-SW striking 2D contacts. While two of the intrusive (3D and Non-2D) magnetic bodies mainly have NE-SW trends, the other two strike NW-SE. The dominant orientations (strikes) of structures on the complex "Bishop" model (CBM) is NE-SW (Sharper images of these grids are presented in figure C.4).

<sup>12</sup>Figure 4.6b was derived from  $\theta$  of SBM (RTE) grid in appendix C (Figure C.5a).

<sup>13</sup>Figure 4.7b was derived from the  $\theta$  of CBM (RTE) grid shown in appendix C (Figure C.5b).

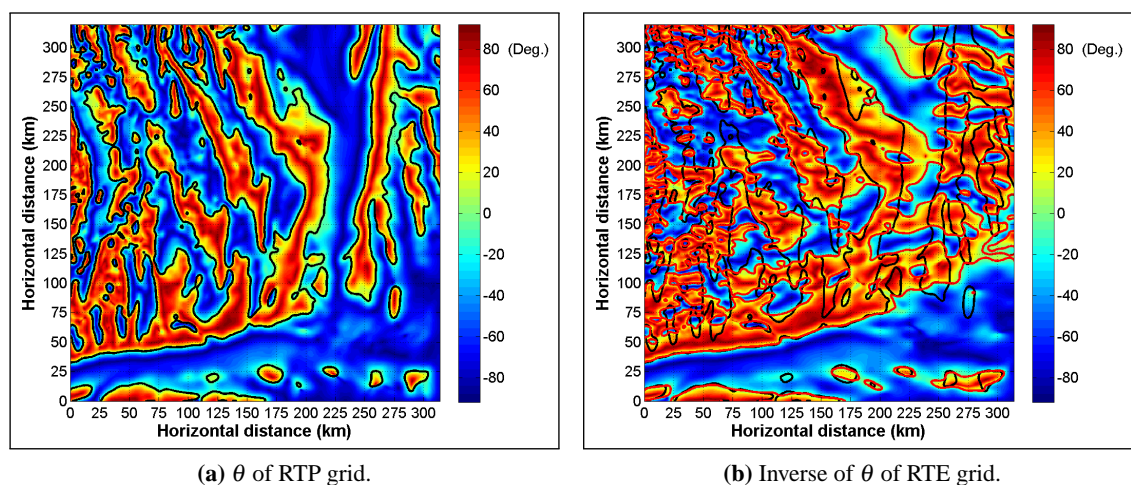


**Figure 4.6:**  $\theta$  equivalents of the SBM grid (Figure 4.3a). Black contour lines in figures 4.6a and 4.6b trace  $\theta = 0$ , but also marks the edges of *all* FS on the basement depth grid (Figure 4.2a). Red contour in figure 4.6b trace  $\theta = 0$  on the RTE  $\theta$  grid. Note that the black contour line in figure 4.6b is same as that in figure 4.6a.

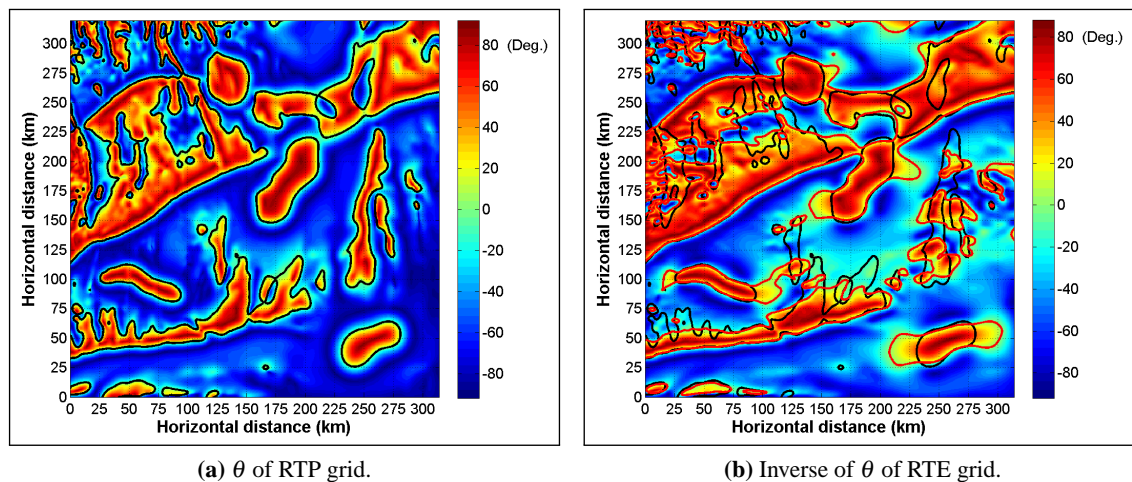


**Figure 4.7:**  $\theta$  equivalents of the CBM grid (Figure 4.3b). Black contour lines in figures 4.7a and 4.7b trace  $\theta = 0$  on figure 4.7a, but also marks the edges of all magnetic contacts on the magnetic susceptibility grid (Figure 4.2b) and *some FS* on the basement depth grid (Figure 4.2a). Red contour in figure 4.7b traces  $\theta = 0$  on the RTE  $\theta$  grid. Note that the black contour line in figure 4.7b is same as that in figure 4.7a.

The general loss of spatial relations between actual locations of sources and their anomalies occasioned by the RTE process are more obvious on their equivalent  $\theta$  grids. These displacements of locations of anomalies on RTE grids relative to their actual locations were not undone by transforming RTE grids to their  $\theta$  equivalents. For instance, although the 3 discrete three-dimensional sources located at grid nodes (222,25), (263,20) and (292,20) on the SBM (RTP) grid (Figure 4.6a) are more obvious than they were on the equivalent  $\Delta T$  grid (Figure 4.4a), these sources were fused to form a spurious elongate E-W structure centred at (238,25) on the SBM (RTE) grid (Figure 4.6b). Including the now more obvious continuous NNE-SSW or NNW-SSE ( $N000 \pm 20^\circ$ ) striking  $\theta$  anomalies on the SBM (RTP) and CBM (RTP) grids (Figures 4.6a and 4.7a), these structures cannot be identified with any certainty on the equivalent  $\theta$  of SBM (RTE) and CBM (RTE) grids (Figures 4.6b and 4.7b). Also, interfering E-W striking anomalies from adjacent sources have produced altogether new anomalies on RTE grids that are not related to any structures on the input basement grids (Figure 4.2).

$\Delta T$  side-lobes developed due to RTE transformation are welded onto anomalies from the Western and Eastern curved (non-2D) edges of intrusive bodies, resulting in Westward and Eastward extension of these edges by about 100% of the radius of curvature of the actual edge. An example of such spurious extensions imaged on  $\theta$  of CBM (RTE) grid (Figure 4.7b) is located at grid node (250,50). Side-lobes such as these may have led to further interference between adjacent  $\Delta T$ . The extent of anomaly interference, and its effect on the apparent location of source edges on RTE- $\Delta T$  grids are certainly more obvious on their  $\theta$  equivalents. It is from these  $\theta$  RTP and RTE versions of SBM and CBM grids that estimates of the locations and depths of edges will be obtained, using the “Tilt-Depth” method. Estimates of locations from SBM and CBM grids in figures 4.6 and 4.7, respectively, will be compared in section 4.5, while depths estimated for those locations will be compared in section 4.6.

## 4.4 Prerequisites for analysing location and depth estimates

Critical variables required for assessing location and depth estimates from the “Tilt Depth” method are the exact locations and depths of structural edges on the input SBM and CBM basement grids (Figures 4.2a and 4.2b, respectively). These were not provided for this study. So, to enable me to extract these critical pieces of information from BM grids for evaluating the “Tilt-Depth” method, I tried different approaches. For example, I initially isolated the actual locations of FS on the input basement depth grid (Figures 4.2a) using the method of ridge maxima detection of Blakely & Simpson (1986) (Section 2.5.2). The method correctly traced most linear features on the grid (Appendix C, Figure C.7). Unfortunately, the locations traced by this method could not be used for this study.<sup>14</sup> I expect edges of structures to be located at the inflection points (not at peaks) of other input grids.

Since structural edges on the input basement grids (Figures 4.2a and 4.2b) must be characterized by significant depth and/or magnetic susceptibility contrasts ( $\delta k$ ), applying a combination of spatial derivatives (Section 2.5.1) to the grids could preferentially accentuate the locations of the edges. The attributes corresponding to these edge locations can then be mapped. Different derivative-based methods (Section 2.5) or their combinations, including second vertical derivatives (SVD), Tilt angles ( $\theta$ ), total horizontal derivatives (HGM), analytic signal amplitude (ASA) were applied to the input basement depth and complex magnetic susceptibility grids (Figures 4.2a and 4.2b, respectively). Some intermediate location grids extracted from BM input grids (Figures 4.2a and 4.2b) are presented in appendix C (Figure C.6).

The  $\theta = 0$  contour of the SBM (RTP) grid correlated well (Figure C.6c) with edges of the major features of the input basement grid (Figure 4.2a). Hence, I extracted locations within the  $\theta \leq 45$  range, so as to include a significant strip of fault scarp edges from figure 4.2a. These actual locations (extracted from figure 4.2a) are presented in figure 4.8a. Locations of edges on the input complex basement (Figure 4.2b) could only be obtained through the application of several filters to the grid (Figure C.6d). These actual magnetic contact locations (extracted from figure 4.2b) were further distinguished on the basis of edge-shape in plan view. Thus, these locations, as well as those for FS (Figure 4.8a) are denoted by different colours (Blue and red-coloured sources) in figure 4.8b.<sup>15</sup> Hence, only the locations shown in figure 4.8a for FS edges will be used to evaluate estimates obtained from all SBM grids. Similar evaluations for CBM grids will use only the locations shown in figure 4.8b. This grid of combined locations (Figure 4.8b) was used to extract a grid for the actual depth of edges of all  $\Delta T$  sources on the CBM (RTP) and CBM (RTE) grids at these locations (Figure 4.9a). It is to these extracted BM source-edge location and depth grids (Figures 4.8 and 4.9) that “Tilt-Depth” method location and depth estimates derived from RTP and RTE versions of the SBM and CBM grids will be quantitatively compared in sections 4.5 and 4.6.

<sup>14</sup>Since there are no peaks on the variable susceptibility grid (Figure 4.2b), this method was not tested on it.

<sup>15</sup>These colours will be used to distinguish results obtained for each set of structures in most plots of depth estimates later in this chapter.

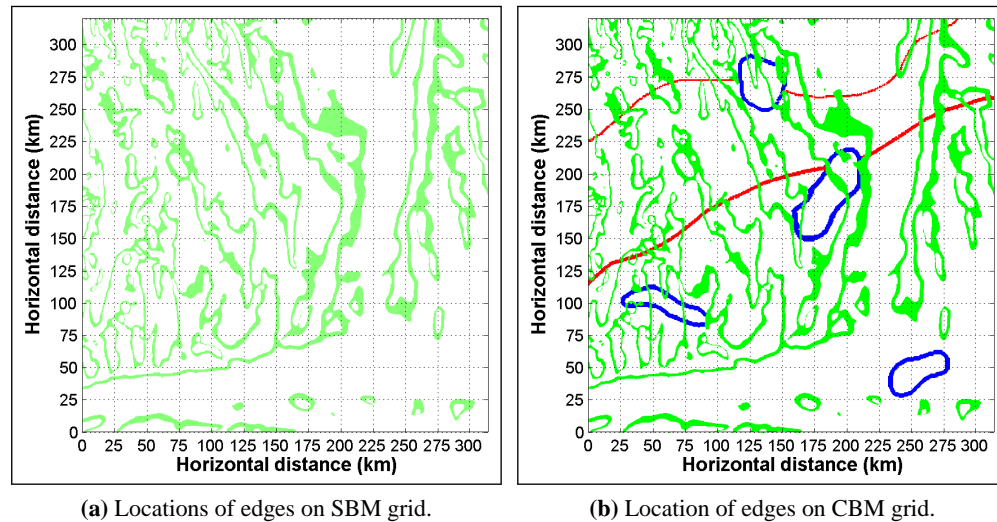


**Figure 4.8:** Locations of edges of  $\Delta T$  sources on the input BM basement grids. Edges of SBM and CBM anomaly sources are colour-coded for clarity: FS (Green), 2D magnetic contacts (Red) and non-2D (3D) magnetic contacts (Blue).

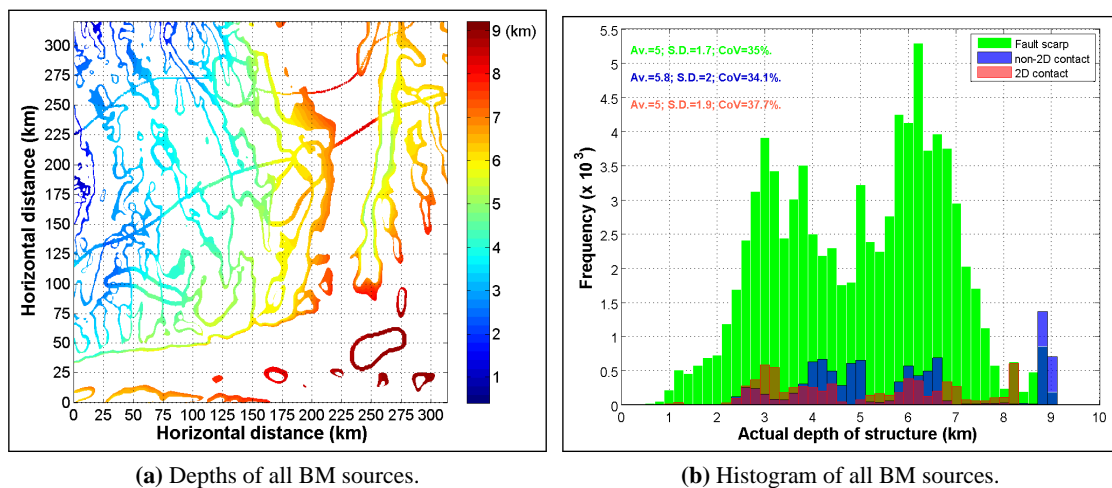


**Figure 4.9:** Actual depth of edges of all anomalous sources on the simple and complex BM grids. Depths were extracted using the combined locations grid (Figure 4.8b). Unlike figure 4.8b, colours in figure 4.9a represent depths of basement, and not the type/shape of edges. Figure 4.9b shows distribution statistics; mean depth ( $Av.$ ), standard deviation ( $S.D.$ ) and coefficient of variation ( $CoV$ ).

The bands of extracted locations and depths shown in figures 4.8 and 4.9 represent significant and varied distances across the edges. However, these width variations pose no problems to the evaluations intended since only “Tilt-Depth” method location or depth estimates at corresponding grid locations on RTP and RTE grids will be used for the evaluations.

A composite histogram of the distribution of actual depths of edges of all BM sources, with class size of 200 m (43 bins), is shown in figure 4.9b. Depths are colour-coded to reflect source-types in figure 4.8b. I will use statistical parameters like mean depth ( $Av.$ ), standard deviation ( $S.D.$ ) and coefficient of variation ( $CoV$ ) to describe the variability of the actual depth of BM source edges.<sup>16</sup>

<sup>16</sup> $S.D.$  increases as depth values spread out from the mean depth ( $Av.$ ). Hence, smaller  $S.D.$  values characterize depth distributions with data tightly grouped around the sample mean. The  $CoV$  of a distribution is the ratio of its  $S.D.$  to its mean ( $Av.$ ), reported as a percentage (Chapra, 2012, p.327).

However, BM source depth distributions differ in their shapes and symmetries (Figure 4.9b). They are not Gaussian. Also, the depth distribution for each source type displays a number of local peaks, reflecting the fact that each source type occurred more than once, at different locations and depths, across the BM depth grid (Figure 4.8b). Consequently, the statistical parameters obtained for these generally multi-modal depth distributions (Figure 4.9b) were compromise values (Press et al., 1992, p.615). It is these compromise parameters that will be used to qualitatively compare each histogram in figure 4.9b with those obtained from depths estimated for similar sources, from RTP and RTE versions of SBM and CBM grids in section 4.6.2.

## 4.5 Location estimates from RTP and RTE-transformed SBM and CBM grids

In order to examine the accuracy of location estimates from the “Tilt-Depth” method,  $0^\circ$  contours from  $\theta$  of RTP and RTE versions of both SBM and CBM grids were extracted and are presented in figure 4.10 and compared below. Contours obtained from SBM grids (Figure 4.6) are shown in figure 4.10a, while contours from the CBM grids (Figure 4.7) are shown in figure 4.10b. The black and red contour lines represent estimated locations of edges, respectively, from RTP

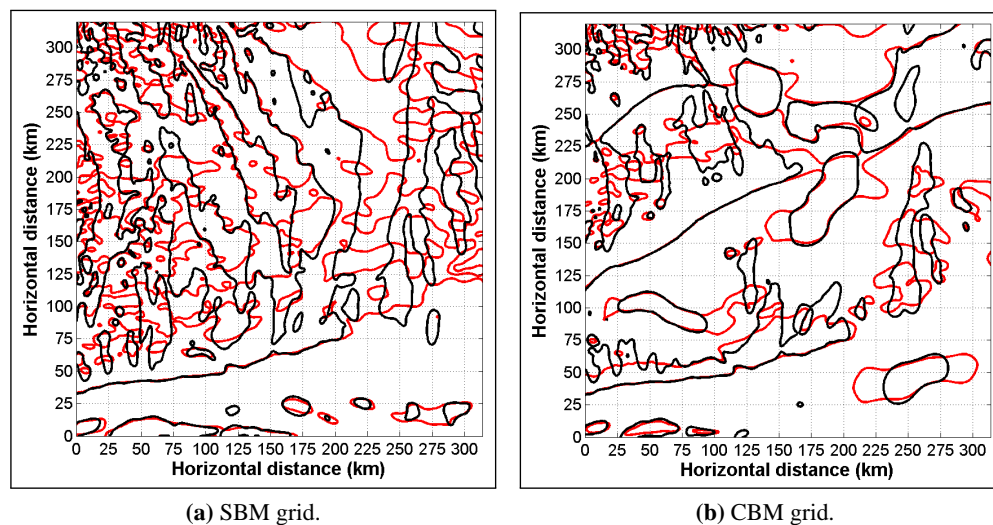


**Figure 4.10:** “Tilt-Depth” method estimates of location of model anomaly sources on SBM and CBM grids. Contour lines were extracted from  $\theta$  of RTP and RTE versions of: (a) SBM grids in figures 4.6a and 4.6b; and (b) CBM grids in figures 4.7a and 4.7b. Black contours trace  $\theta = 0$  from  $\theta$  of RTP grids, while red contours trace  $\theta = 0$  from Tilt angle of RTE grids, respectively. While contours estimate edges of FS on the SBM grid, they estimate edges of both faults scarps and magnetic contacts on the CBM grid.

and RTE grids. Anomalies from intersecting edges of sources interfere. Consequently, edges at such locations could not be accurately imaged on RTP grids. Examples occur around grid nodes (115,270) and (212,212). However, edges at such locations were better traced on the RTE grid, probably because the discrete, dipolar E-W RTE  $\theta$  anomalies which characterise such locations aligned to make such edges continuous.  $\theta = 0$  contours of RTP grids are located directly above

well isolated edges, but slightly displaced away from source edges where considerable anomaly contrast and interference occur.  $\theta = 0$  contours of RTE grids tend to be shifted inwards from their RTP equivalents at such locations.

Where possible, estimated locations (and subsequently, depths) were compared quantitatively, using the non-parametric Spearman's rank-order correlation coefficient,  $r_s$  (Equation (4.5.1)) and its coefficient of determination ( $r_s^2$ ).<sup>17</sup> Unlike  $r_s$  which ranges from  $-1$  to  $1$ ,  $r_s^2$  ranges from  $0$  to  $1$  (or  $0$  to  $100\%$ ), allowing correlation coefficients from similar sample populations to be compared (Press et al., 1992; Hogg & Craig, 1995; Everitt, 2006).<sup>18</sup>

$$r_s = \frac{\sum_{j=1}^m \sum_{k=1}^n (C_{j,k} - \bar{C}) (D_{j,k} - \bar{D})}{\sqrt{\sum_{j=1}^m \sum_{k=1}^n \{(C_{j,k} - \bar{C})^2\}} \sqrt{\sum_{j=1}^m \sum_{k=1}^n \{(D_{j,k} - \bar{D})^2\}}} \quad (4.5.1)$$

where:  $C$  and  $D$  are  $m \times n$  matrices containing the ranks of any pair of  $m \times n$  matrices  $A$  and  $B$ , respectively;  $\bar{C}$  and  $\bar{D}$  are the mean of the values in  $C$  and  $D$ , respectively; Subscripts  $j, k$  locate elements in the corresponding  $j$ th row and  $k$ th column of  $C$  and  $D$ , so that correlation is between ranks at equivalent locations in  $A$  and  $B$ .  $m = 649$  while  $n = 631$  for BM grids, a maximum degree of freedom ( $N$ ) of 409519.

The statistical significance ( $\rho$ ) for all  $r_s$  and  $r^2$  discussed in this study is the conventional value  $0.05$  ( $5\%$ ) used in scientific studies, assuming that  $A$  and  $B$  have equal means (Press et al., 1992, p.616).<sup>19</sup> This  $\rho$  value corresponds to a confidence interval of  $95\%$ . Equation (4.5.1) will be used to highlight any relationship(s) that may exist between actual locations of BM anomaly sources and their estimated locations derived from RTP and RTE grids. Different approaches used for comparison of location estimates are discussed below.

**(1) Comparisons between actual and  $\theta = 0$  estimated locations of edges on RTP and RTE versions of the SBM and CBM grids.** For this analysis, locations corresponding to the  $\theta = 0$  contours obtained from SBM (RTP) and SBM (RTE) grids (Figure 4.10a) and CBM (RTP) and CBM (RTE) grids (Figure 4.10b) were extracted from the grid of actual location of SBM and CBM edges (Figure 4.8a and 4.8b, respectively). Unfortunately, these locations covered only  $\approx 0.3$  to  $0.5\%$  of the grids. The number of locations obtained from the SBM (RTP) and SBM (RTE) grids were  $2000$  and  $2215$ , respectively, while it was  $1406$  and  $1950$  for the CBM (RTP) and CBM (RTE) grids, respectively.  $\approx 11$ - $40\%$  more locations were obtained from RTE grids than RTP grids.

Since  $\theta = 0$  contour of the SBM (RTP) grid traced the edges of FS on the input basement grid (Figure 4.2a), its locations were used for correlating location estimates from both the SBM (RTP

<sup>17</sup>This technique highlights the existence or otherwise of a linear relationship between the ranks of any two paired datasets, thus outperforming its parametric equivalent; the Pearson's product-moment correlation coefficient,  $r_p$  (Press et al., 1992, p.640).

<sup>18</sup> $r_s^2$  will be hereafter shortened to  $r^2$ .

<sup>19</sup> $\rho$  defines the probability of obtaining the observed  $r_s$  value by random chance, i.e., when the true  $r_s = 0$ .

and RTE) grids. For SBM (RTP) grid  $r^2 = 100\%$  with degrees of freedom ( $N$ )=2000 and  $\rho = 0$ . For the SBM (RTE) grid  $r^2 \approx 6\%$  with  $N = 22$  and  $\rho = 0.29$  (far below the confidence limit set for this study). Hence,  $r_s$  and  $r^2$  for SBM (RTE) grid are unreliable for any inference(s). Similarly, locations of  $\theta = 0$  contours on the CBM (RTP) grid were extracted from grid in figure 4.8b for correlation between location estimates obtained from CBM (RTP and RTE) grids.  $r^2 = 100\%$  with  $N = 1406$  and  $\rho = 0$  for the CBM (RTP) grid, while  $r^2 \approx 27\%$  with  $N = 16$  and  $\rho = 0.04$  for the CBM (RTE) grid indicates a moderate positive correlation. Although 27% correlation for the CBM (RTE) grid is significant at 95% confidence level,  $N = 16$  represents only 0.8% or 1.1% of the total number of locations obtained from the CBM (RTE or RTP) grid, respectively. These results show that RTE location estimates were generally unrelatable to their RTP equivalents. I effectively assume that there is little or no correlation between estimated and actual locations of sources on the BM (RTE) grid.

(2) **Comparisons between whole RTP and RTE grids** in figures 4.6 and 4.7 ( $N = 409519$ ). Since  $\theta$  grids present equalized anomalies, any correlation or otherwise between RTP and additive inverse of RTE grids should reflect the fidelity between these grids. For  $\theta$  of SBM (RTP and RTE) grids (Figure 4.6)  $r_s = 0.67$ ,  $r^2 = 45\%$  and  $\rho = 0$  indicating a weak, but positive correlation between  $\theta$  anomalies on both grids. Only about 45% of anomalies on the SBM (RTE) grid were correlatable with those on the SBM (RTP) grid. Consequently, 55% of  $\theta$  anomalies on the SBM (RTE) were spurious, originating mainly from en-echelon NNE-SSW and NNW-SSE striking sources on the basement depth grid (Figure 4.2a).

For  $\theta$  of CBM (RTP) and CBM (RTE) grids (Figure 4.7)  $r_s = 0.79$ ,  $r^2 = 62\%$  and  $\rho = 0$ , indicating moderately strong, positive correlation between  $\theta$  anomalies on both grids. About two-thirds ( $\approx 62\%$ ) of anomalies on the CBM (RTE) grid were correlatable with those on the CBM (RTP) grid, while the remaining 38% of CBM (RTE) anomalies were of spurious origins. The significantly improved correlation, compared with that obtained for the SBM grids, appears to result from attenuation of anomalies from NNW-SSE and NNE-SSW striking sources. Anomalies from NNW-SSE and NNE-SSW striking sources on the CBM grids were lost to those from the broad and extensive NE-SW striking, high susceptibility terrane on the CBM input grid (Figure 4.2b). The strong correlation between CBM (RTE and RTP) grids as opposed to less strong correlation between SBM (RTE and RTP) grids reflects the dependence of RTE-induced anisotropy and anomaly interference on the shape, strike and persistence of anomaly sources.

In conclusion, correlation coefficients obtained from comparisons between  $\theta$  of RTP and RTE versions of BM grids increased with absence of NNW-SSE and NNE-SSW striking sources. In general,  $\theta = 0$  contours of RTP anomalies accurately located source edges. However it has problems and provides less accurate location estimates where source edges intersect each other. The dominance of spurious anomalies which could not be correlated with actual BM sources on RTE grids render  $\theta = 0$  contours from RTE anomaly grids ineffective for locating anomaly source edges. The occurrence and dominance of these spurious  $\theta$  of RTE anomalies depend on the susceptibility, shape, strike and persistence of anomaly sources. These results show that source locations

estimated from  $\Delta T$  (RTE) grids, using only the “Tilt-Depth” method are unreliable. Hence, the effectiveness of other semi-automatic methods of locating 2D source edges from  $\Delta T$  (RTE) grids will also be evaluated in chapter 5.

## 4.6 Depth estimates from RTP and RTE of SBM and CBM grids

“Tilt-Depth” method estimates of depth from profile  $\Delta T$  datasets showed least errors when implemented using the distance between  $0 \leq |\theta| \leq 30$  compared with  $0 \leq |\theta| \leq 45$  (Sections 3.3.2 and 3.3.3). Hence, depths of source edges on RTP and RTE versions of the SBM and CBM grids were estimated in three modes, using the distances between  $0 \leq |\theta| \leq 45$ ,  $0 \leq |\theta| \leq 27$  and  $0 \leq |\theta| \leq 10$ . The  $-27 \leq \theta \leq 27$  and  $-10 \leq \theta \leq 10$  range, respectively, represent 0.5 and 0.2 of the physical distance ( $|h|$ ) covered by  $-45 \leq \theta \leq 45$  range (Table 3.1 on page 45). The effectiveness of the method will be evaluated in terms of the differences (errors) between the actual source depths (Figure 4.9) and depths estimated for these sources from  $\theta$  of SBM and CBM grids (Figures 4.6 and 4.7). Depth estimates obtained from SBM grids (Figures 4.11b and 4.11d) and the corresponding grids of  $0 \leq |\theta| \leq 45$  range used for these estimations (Figures 4.11a and 4.11c), are presented in figure 4.11. Similar grids for estimates from the CBM grids are presented in figure 4.12.<sup>20</sup>

Discrepancies were observed when I compared grids of depths estimated from both the SBM and CBM grids by the GETECH Plc’s Geosoft EXecutable (GX) used in this study with grids of the respective  $\theta$  ranges ( $0 \leq |\theta| \leq 10$ ,  $0 \leq |\theta| \leq 27$  or  $0 \leq |\theta| \leq 45$ ) from which these estimates were meant to be derived (Figures 4.11 and 4.12). Comparisons show that depths were estimated for some locations outside those within the specified  $\theta$  range. These discrepancies were computational artefacts introduced to the depth estimates grid by a bug that I discovered in the GETECH Plc’s Geosoft EXecutable (GX) used in this study. For instance, comparisons between depths estimated from the  $0 \leq |\theta| \leq 45$  range show that these artefacts occur around grid nodes (205,30), (238,40), and (305,50) on the SBM (RTP) grid (Figure 4.11b), as well as grid nodes (175,250), (200,315), and (315,38) on the SBM (RTE) grid (Figure 4.11d). Artefacts also occur at grid nodes (150,25), (175,315), and (305,38) on the RTP and RTE versions of the CBM grid (Figures 4.12b and 4.12d). The SouthEastern part of these CBM grids is dominated by a major artefact. To minimise this problem, only depth estimates from locations at which  $\theta$  values were within the ranges required for depth computation ( $0 \leq |\theta| \leq 10$ ,  $0 \leq |\theta| \leq 27$  and  $0 \leq |\theta| \leq 45$ ) were retained for further analysis.

<sup>20</sup> $0 \leq |\theta| \leq 10$  and  $0 \leq |\theta| \leq 27$  ranges are subsets of  $0 \leq |\theta| \leq 45$  range (Figure 3.6). Hence, all  $\theta$  ranges used for depth estimation from SBM grids are presented in figures 4.11a and 4.11c, while equivalents for CBM grids are presented in figures 4.12a and 4.12c.

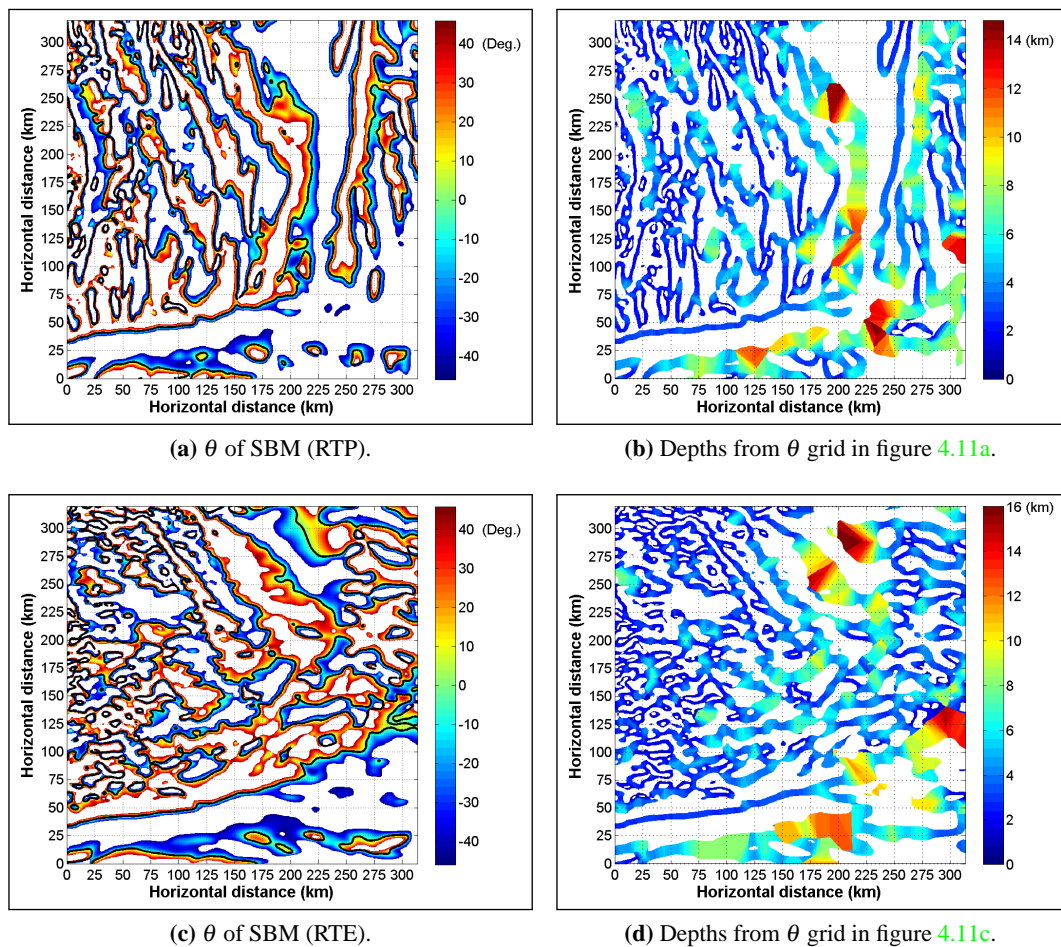


**Figure 4.11:** “Tilt-Depth” estimation of depth of fault scarp (FS) edges from SBM (RTP and RTE) grids, using  $0 \leq |\theta| \leq 45$  range. Black contour lines in figures 4.11a and 4.11c trace  $\theta = 0$ . Note that estimated depths are for locations traced by the  $\theta = 0$  contours. Erroneous locations (discussed in text) are introduced in RTE grids, and depths for such locations are spatially misplaced.

#### 4.6.1 Methods used for analysing depth estimates

Analyses of depth estimates initially involved comparisons between histograms of the actual depths of BM grid sources (FS and magnetic 2D and non-2D contacts) in figure 4.9b with those of depths estimated for these sources from both the SBM and CBM grids (Section 4.6.2). Depths estimated from RTP and RTE of BM grids or the errors associated with these estimates were also compared with actual source depths using depth cross-plots.<sup>21</sup> Cross-plots of depth estimates obtained at BM source locations are discussed in section 4.6.3.

<sup>21</sup>Cross-plots present paired datasets:  $(x_1, y_1), (x_2, y_2), (x_3, y_3), \dots, (x_n, y_n)$ , where  $x$  and  $y$ , respectively, refer to data at equivalent locations on the actual basement depth grid and/or BM estimated depth grids (See figures 4.15 and 4.18).

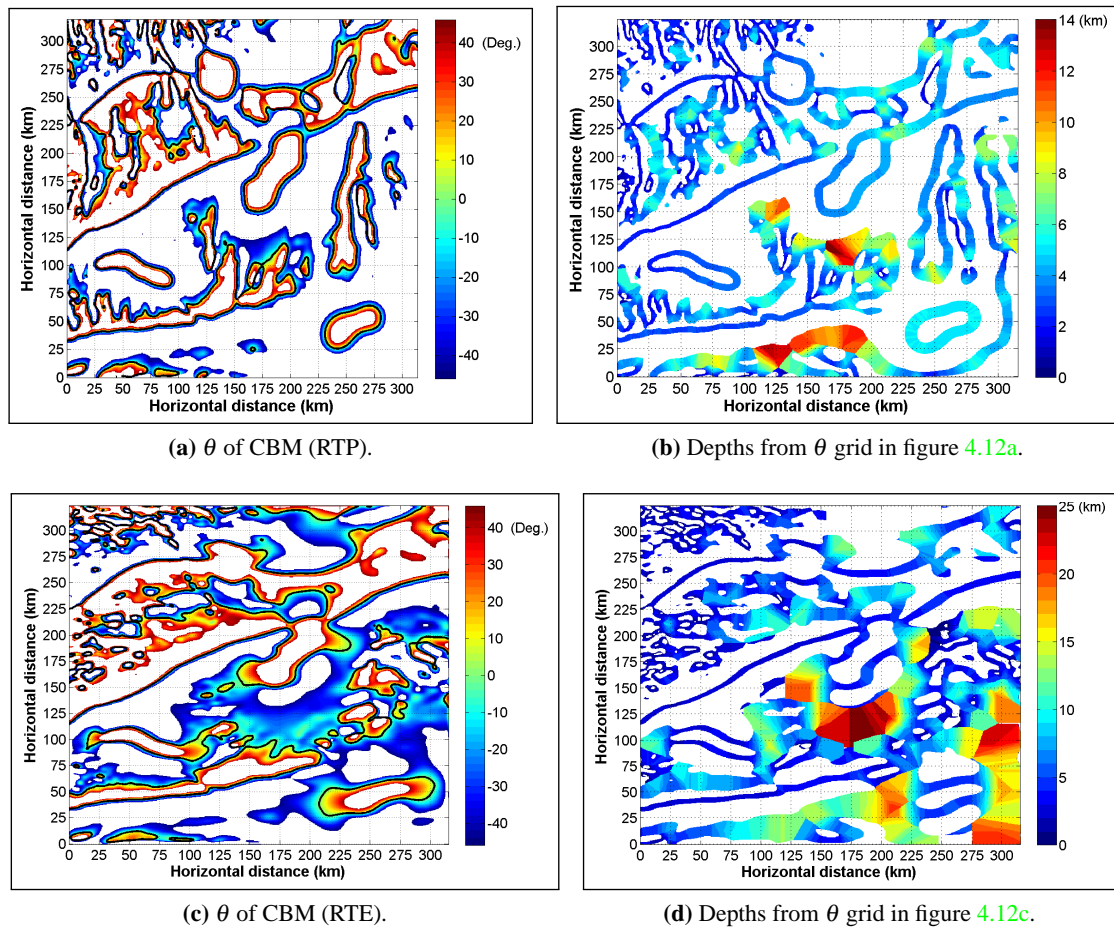


**Figure 4.12:** “Tilt-Depth” estimation of depth of geological structures; fault scarp (FS) and magnetic contact edges, on CBM (RTP and RTE) grids, using  $0 \leq |\theta| \leq 45$  range. Black contour lines in figures 4.12a and 4.12c trace  $\theta = 0$ . Note that estimated depths are for locations traced by the  $\theta = 0$  contours. Erroneous locations (discussed in text) are introduced in RTE grids, and depths for such locations are spatially misplaced.

## 4.6.2 Comparisons between distributions of actual and estimated depths

Here, I compared the shapes and spreads of actual and estimated depths of all sources on BM grids using histograms and statistical parameters like the mean ( $Av.$ ), standard deviation ( $S.D.$ ), and coefficient of variation ( $CoV$ ).<sup>22</sup> Histograms of actual depths of FS, as well as 2D and non-2D contacts are shown in figure 4.9b. These distributions are briefly discussed below.

**(A) Actual depths of sources on BM grids** The actual depths of FS (Green-coloured histogram in figure 4.9b) ranged from 0.43 to 9.1 km (Figure 4.9a). This distribution is bimodal but symmetric about its mean ( $Av.$ ) of 5 km, with most sources at depths of 2.3 to 4.7, and 4.7 to 8.3 km.  $S.D.$  and  $CoV$  for actual depths of FS were 1.7 km and 35%, respectively. FS represent  $\approx 83\%$  (degrees of freedom,  $N=85197$ ) of all BM grid sources. **2D contacts** (Pale-red-coloured histogram in figure 4.9b) were at depths ranging from 1 to 8.5 km (Figures 4.9a), with  $Av.$ ,  $S.D.$  and  $CoV$  of 5 km, 1.9 km and 38%, respectively. 2D contacts represent only  $\approx 7\%$  ( $N=6999$ ) of all BM grid

<sup>22</sup>Introduced in section 4.4.

sources. **Non-2D contacts** (Blue-coloured histogram in figure 4.9b) were at depths ranging from 2.4 to 9 km (Figures 4.9a), with  $Av.$ ,  $S.D.$  and  $CoV$  of 5.8 km, 2 km and 34%, respectively. This distribution represents  $\approx 10\%$  ( $N = 9813$ ) of all BM grid sources.

**(B) Depth estimates from SBM (RTP and RTE) grids** The distributions of depths estimated for FS obtained from SBM (RTP and RTE) grids using the distance between  $0 \leq |\theta| \leq 45$ ,  $0 \leq |\theta| \leq 27$  and  $0 \leq |\theta| \leq 10$  contours are shown in figure 4.13. Histograms (Figure 4.13) show all SBM

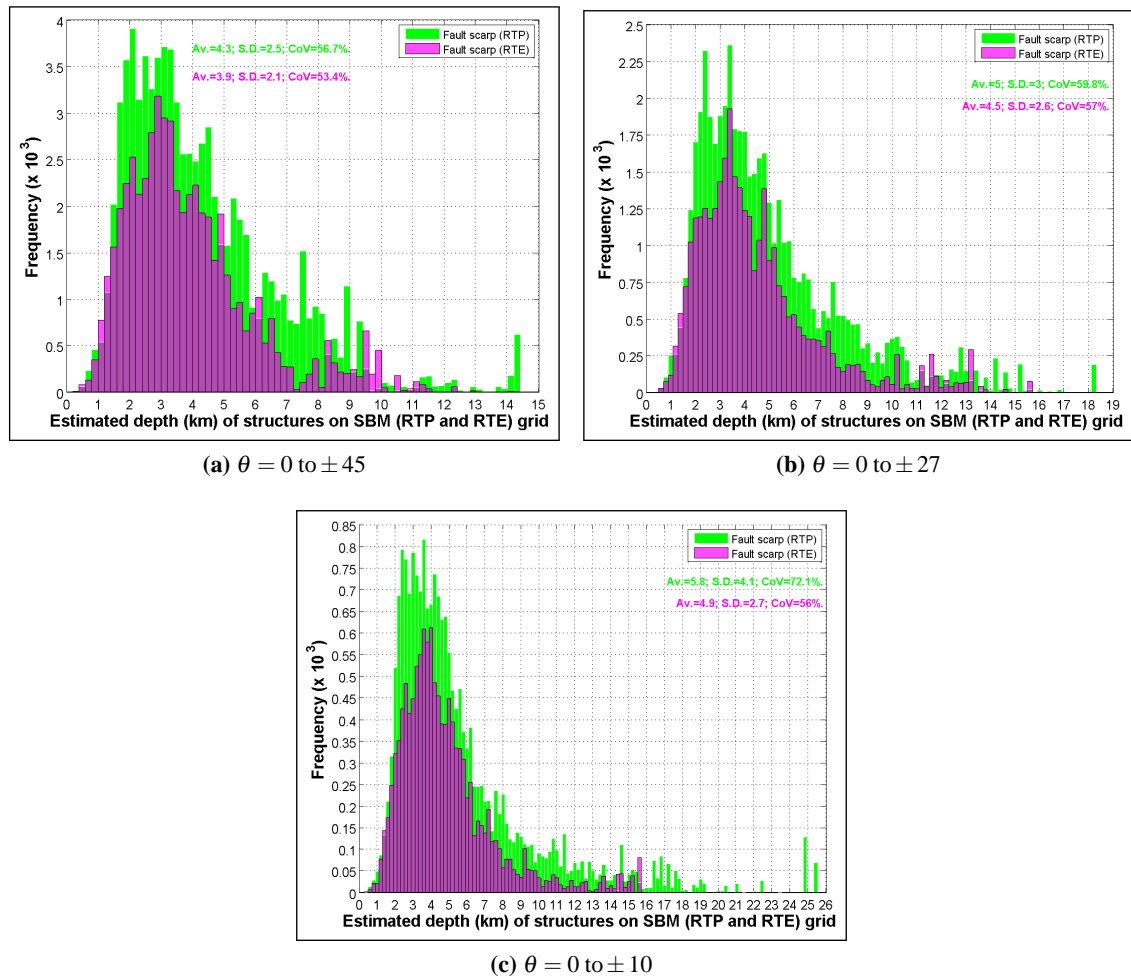


**Figure 4.13:** Histograms showing the distribution of “Tilt-Depth” method estimates of model source depths from SBM (RTP and RTE) grids. The method was implemented in three modes;  $\theta = \pm 45$ ,  $\pm 27$  and  $\pm 10$ .

depth estimates to be skewed to the right, compared with the mainly bimodal, but symmetrically distributed actual depths shown in figure 4.9b. According to Press et al. (1992), the mean of values drawn from a probability distribution with broad tails may converge poorly or not at all. I expect any poor convergence of the mean depth value ( $Av.$ ) of each distribution to be reflected in its  $S.D.$  and  $CoV$ .<sup>23</sup> Hence, comparisons of dispersion between these multi-modal and/or skewed distributions of actual and estimated depths for each BM sources, relies mainly on the  $CoV$  of each distribution.

<sup>23</sup>For the relationship between these parameters, see section 4.4.

The number of estimates from SBM grids decreased, while the maximum depth estimated generally increased as the magnitude of  $\theta$  decreased from 45 to 10. The  $CoV$  captures these variabilities. For instance, for SBM (RTE) estimates, it increased from  $\approx 57\%$  for  $\theta = \pm 45$  (Figure 4.13a) through  $\approx 60\%$  for  $\theta = \pm 27$  (Figure 4.13b) to  $\approx 72\%$  for  $\theta = \pm 10$  (Figure 4.13c). Compared with actual depth of FS (Figure 4.9b) depths estimated from the SBM (RTP or RTE) grids were only about 20% more spread out, except for estimates from the SBM (RTE) grid using  $\theta = \pm 10$  with a spread of about 35% more.

Next, I compared the percentage of source edge locations retained, for depths estimated from each range of  $\theta$ , on the SBM (RTP or RTE) grid. Percentages represent the ratio of the number of depths estimated from each  $\theta$  range (Figure 4.13) to the total number of actual depth for FS (Green-coloured histogram of figure 4.9b). These percentages of retained estimates are presented in table 4.1. The ratio of the occurrence (frequency) of estimates obtained from SBM (RTP) or SBM (RTE) grid to the total occurrence on both histograms from the SBM (RTP and RTE) grids (Figure 4.13) are also presented in table 4.1. Estimates from the SBM (RTP) grid using  $0 \leq \theta \leq 45$

**Table 4.1:** Retention of depth estimates from FS on the SBM (RTP or RTE) grid, relative to the total number of actual depth locations in figure 4.9a.

Fault scarps, SBM grids	Ratio of estimates retained on grid, for $\theta = 0$ to:			Ratio of occurrence of estimates in histogram, for $\theta = 0$ to:		
	$\pm 45^\circ$ (%)	$\pm 27^\circ$ (%)	$\pm 10^\circ$ (%)	$\pm 45^\circ$ (%)	$\pm 27^\circ$ (%)	$\pm 10^\circ$ (%)
(1) RTP	95	59	23	59	60	62
(2) RTE	65	39	15	41	40	38

distance cover 95% of FS locations on the input basement grid (Figure 4.8b) compared with those from the SBM (RTE) grid, which represent 65% of FS locations. These statistics varied from 59% (SBM, RTP) and 39% (SBM, RTE) for estimates from  $0 \leq \theta \leq 27$  distance, to 23% (SBM, RTP) and 15% (SBM, RTE) for estimates from  $0 \leq \theta \leq 10$  distance. There was an approximately 60%:40% constant ratio between SBM (RTP) and SBM (RTE) estimates on each set of histograms in figure 4.13, irrespective of the  $\theta$  range used (Table 4.1). These relationships will be further examined using estimates from the CBM grid.

**(C) Depth estimates from CBM (RTP and RTE) grids** Distributions of estimated depths for FS, and 2D and non-2D contacts obtained from CBM (RTP and RTE) grids, using the distances between  $0 \leq |\theta| \leq 45$ ,  $0 \leq |\theta| \leq 27$  and  $0 \leq |\theta| \leq 10$  contours are shown in figure 4.14. These histograms (Figure 4.14), colour-coded to reflect source-types in figure 4.8b, showed all CBM depth estimates to be skewed to the right, compared with the symmetrically distributed actual depths of sources (Figure 4.9b). Histograms for FS and non-2D contacts were more right-skewed. Depth estimates obtained from CBM grids were dominated by those from FS sources, irrespective of the  $\theta$  value used for the estimation. Estimates from 2D sources were generally within the range of their actual depths. The dominant trailing tails of histograms of FS and non-2D contacts, well beyond the range of actual source depths identify these sources as major contributors to errors in CBM depth estimates. Other than for FS, there were no significant differences between mean

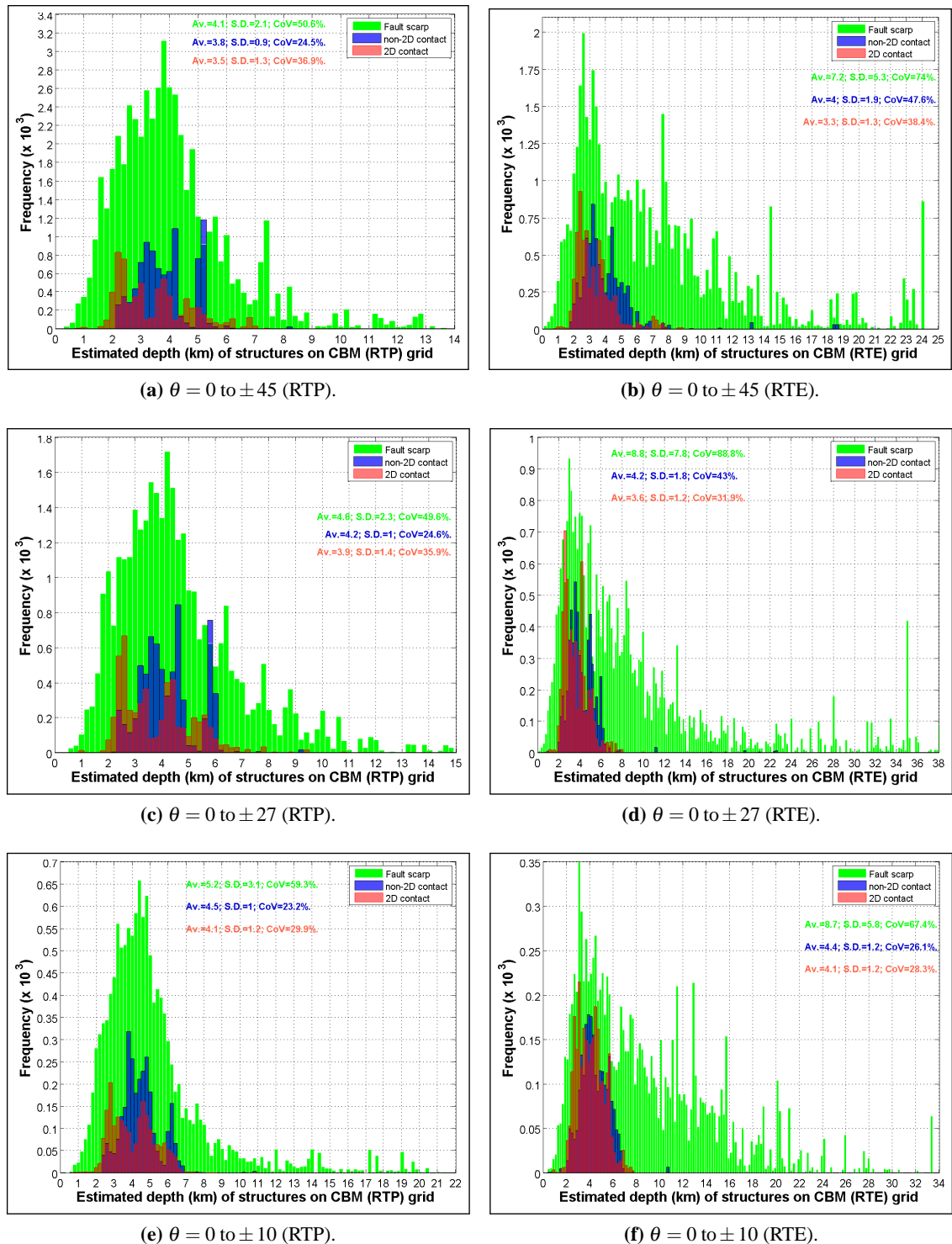


**Figure 4.14:** Histograms showing the distribution of “Tilt-Depth” method estimates of CBM model source depths. The method was implemented in three modes, using the distances between;  $\theta = 0$  and  $\pm 45$ ,  $\pm 27$  or  $\pm 10$ . Histograms are mainly skewed to the right. The most skewed histograms were those for fault scarps (FS), while the least skewed were those for 2D contacts. The dominance of FS depth estimates well beyond the actual source depths can be a good reason for minimising certain wavelengths in  $\Delta T$  datasets, based on *a priori* basement depth information.

depth estimates ( $Av.$ ) for 2D and non-2D contacts on CBM (RTP and RTE) grids (Figure 4.14). However, the  $S.D.$  varied significantly, allowing mainly for the use of the  $CoV$  for comparisons between the spread of distributions of estimated and actual depth of CBM sources (Table 4.2). The

**Table 4.2:** Comparing  $CoV$  statistics of depth estimates from CBM (RTP and RTE) grids (Figure 4.14) with actual source depths (Figure 4.9).

All source types, CBM grids	$CoV$ , for estimates from $\theta = 0$ to:			$CoV$ (%), actual depths	Mean ratio of $CoV$
	$\pm 45^\circ$ (%)	$\pm 27^\circ$ (%)	$\pm 10^\circ$ (%)		
<b>(1) RTP</b>					
(i) Fault scarps (FS)	51	50	59	35	1.5
(ii) non-2D contacts	25	25	23	34	0.7
(iii) 2D contacts	37	36	30	38	0.9
<b>(2) RTE</b>					
(i) Fault scarps (FS)	74	89	67	35	2.2
(ii) non-2D contacts	48	43	26	34	1.1
(iii) 2D contacts	38	32	28	38	0.9

average dispersion (Mean ratio of  $CoV$ ) in depths estimated for CBM sources from the various  $\theta$  ranges (Table 4.2) were compared. Results showed that FS depth estimates from CBM (RTE and RTP) grids were, respectively, 2.2 and 1.5 times more dispersed than their actual depths. Estimates for non-2D contacts on these grids were dispersed, respectively, by 1.1 and 0.7 times their actual depths. However, estimates for 2D contacts from the same grids showed constant dispersion of 0.9 times their actual depths.

I also compared the percentage of depth estimates retained for each range of  $\theta$ , when applied to the CBM (RTP and RTE) grid. These percentages were determined from the ratio of the number of depths estimated from each  $\theta$  range (Figure 4.14) to the total number of actual depth locations, for each CBM source (Figure 4.9a). For all sources on the CBM (RTP or RTE) grids, the percentage of depth estimates decreased with decreasing range of  $\theta$  values used. For example, percentage depths of 2D contacts retained reduced from 95 to 76% for CBM (RTP) and from 98 to 38% as maximum  $\theta$  used reduced from  $\pm 45$  to  $\pm 10$  (Table 4.3). For all  $\theta$  ranges used, percentage depth estimates retained increased from its minimum values for FS, through intermediate values for non-2D contacts to its largest values for 2D contacts (Table 4.3). This observation may have resulted from the attenuation of weaker anomalies sourced from basement topography.

Relative contributions of depths estimated from each source on CBM (RTP and RTE) grids were also examined. These were reported as ratios of depth estimates in histogram and are presented in table 4.3. Irrespective of the range of  $\theta$  values used for depth estimation, the ratios were highest ( $> 70\%$ ) for FS, and low ( $\approx 12$  and  $14\%$ ) for 2D and non-2D contacts (Table 4.3). The dominance of estimates from FS, especially at significantly greater depths than on actual basement, may indicate a need to filter off certain short and/or long wavelength  $\Delta T$  from given datasets prior to the application of the "Tilt-Depth" method.

**Table 4.3:** Retention of depth estimates from CBM (RTP and RTE) sources, relative to the number of actual depth locations in figures 4.8b and 4.9a.

All source types, CBM grids	Ratio of estimates retained on grid, for $\theta = 0$ to:			Ratio of estimates in histogram, for $\theta = 0$ to:		
	$\pm 45^\circ$ (%)	$\pm 27^\circ$ (%)	$\pm 10^\circ$ (%)	$\pm 45^\circ$ (%)	$\pm 27^\circ$ (%)	$\pm 10^\circ$ (%)
<b>(1) RTP</b>						
(i) Fault scarps (FS)	61	38	15	77	73	73
(ii) non-2D contacts	93	70	28	13	15	15
(iii) 2D contacts	95	76	30	10	12	12
<b>(2) RTE</b>						
(i) Fault scarps (FS)	59	34	13	77	72	70
(ii) non-2D contacts	81	57	23	12	14	14
(iii) 2D contacts	98	83	38	10	14	16

In conclusion, assuming that contact-like magnetic sources were infinite in depth extent did not significantly simplify depth estimates from the "Tilt-Depth" method, in the presence of a rugose, weakly magnetic basement. Comparisons between actual depths of BM sources and their percentage of "Tilt-Depth" method estimates retained, as well as average dispersions showed FS sources were responsible for the significant errors in depth estimates. Consequently, to obtain less erratic depth estimates from the "Tilt-Depth" method, any non-magnetic contributions from basement topography to the  $\Delta T$  datasets must be minimised. Such contributions may be estimated from a-priori basement depth information from boreholes, seismic section, etc.

### 4.6.3 Relationship between estimated and actual depths of "Bishop" model sources

Here, I compared estimates of source depths obtained using half the physical distances between three ranges of  $\theta$ ;  $\theta = 0$  to  $\pm 45$ ,  $0$  to  $\pm 27$  and  $0$  to  $\pm 10$  for the three BM anomaly sources in figure 4.8b with their actual depths (Figure 4.9a) using composite cross-plots. That is, although estimates from each magnetic geological source-type (Figure 4.8b) were obtained separately, results for each source-type on each BM grid will be presented along with results from other sources on the same grid on the same figure. Three types of composite cross-plots were used in this section, including; cross-plots between actual and estimated depths of sources, cross-plots between actual and percentage errors in estimated depths of sources, and cross-plots between depths estimated from RTP of BM grid and its RTE equivalent. Where involved, the actual depths of source(s) were plotted on the abscissae while estimated depths or percentage errors for these sources at equivalent locations were plotted on the ordinates of the cross-plots. Cross-plots which compared RTP with RTE estimates had RTP estimates on the abscissae and RTE estimates on the ordinate.

#### (A) Estimated and actual depths of SBM sources

The only anomaly source on SBM grids are fault scarps, FS. Hence, actual depths will refer only to depths extracted from figure 4.9a at locations shown in figure 4.8a. Cross-plots between these actual FS depths and their estimates from SBM (RTP and RTE) grids (Figures 4.11b and 4.11d) are presented in (Figure 4.15). Errors in these estimated SBM depths are presented as percentage

errors in figure 4.16. All analyses of depth estimates and error will include every estimated location from the RTP or RTE grid, without consideration for whether or not the estimated locations were accurate.<sup>24</sup>

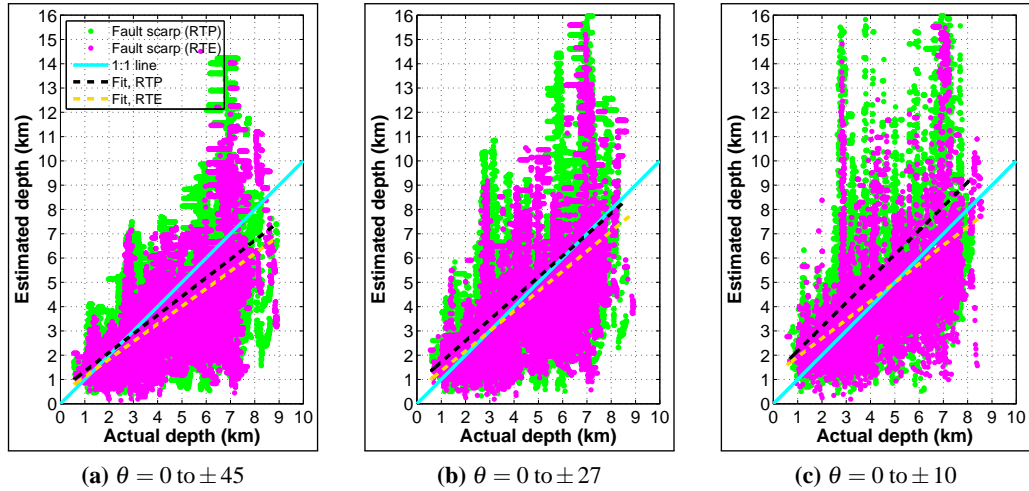


**Figure 4.15:** “Tilt-Depth” method estimates of SBM (RTP and RTE) source depths, using the  $|\theta| = 0$  to 45, 27 or 10 distance. The solid light-blue line is where a 1:1 correlation between the actual and estimated depths should plot. The legend to figure 4.15a applies also to figures 4.15b and 4.15c. Note the wide spreads in data. Each dashed line represents the best-fitting least-squares function for each cross-plot of paired datasets. For clarity, the equation and related statistical parameters for these least-squares functions are presented in table 4.4.

Cross-plots of estimated depths (Figure 4.15) and those of their errors (Figure 4.16) displayed very wide spreads. These spreads were attributed to the non-magnetic composition of FS structures, since these structures do not meet the strict assumption of contrasting magnetic susceptibility inherent in the “Tilt-Depth” method software used for estimating depths.<sup>25</sup> Consequently, only estimates from strictly 2D and non-2D features of the CBM grid may be relied upon. However, to extract any meaningful information from these SBM cross-plots for quantitative comparisons, the best-fitting least-squares functions/models for these paired datasets were computed, to describe relationships in each cross-plot. Relationships between actual and estimated FS depths were best described by linear least-square lines. I relied on the coefficient of determination,  $r^2$  (Equation (4.5.1)) and standard error,  $SE$  (Equation (4.6.1)) for regressions on these cross-plots to compare them.<sup>26</sup> The equations of the best-fitting function and the values of  $SE$  and/or  $r^2$  are presented on tables introduced in the caption to related sets of cross-plots. For example, see the captions to figures 4.15 and 4.16.

$$SE = \sqrt{\frac{SS_r}{N-2}} \quad (4.6.1)$$

where  $SE$  refers to the error in average estimates,  $SS_r$  and  $N$  refer to the sum of squares of residuals

<sup>24</sup>This is to simulate what obtains in practice.

<sup>25</sup>This software belonged to Getech PLC, UK.

<sup>26</sup> $r^2$  and  $SE$  quantified the “goodness-of-fit” and spread of data around regression lines, respectively (Chapra, 2012, 341). The statistical significance ( $\rho$ ) for all  $r_s$  and  $r^2$  presented is 0.05 (5%), corresponding to a confidence interval of 95%.

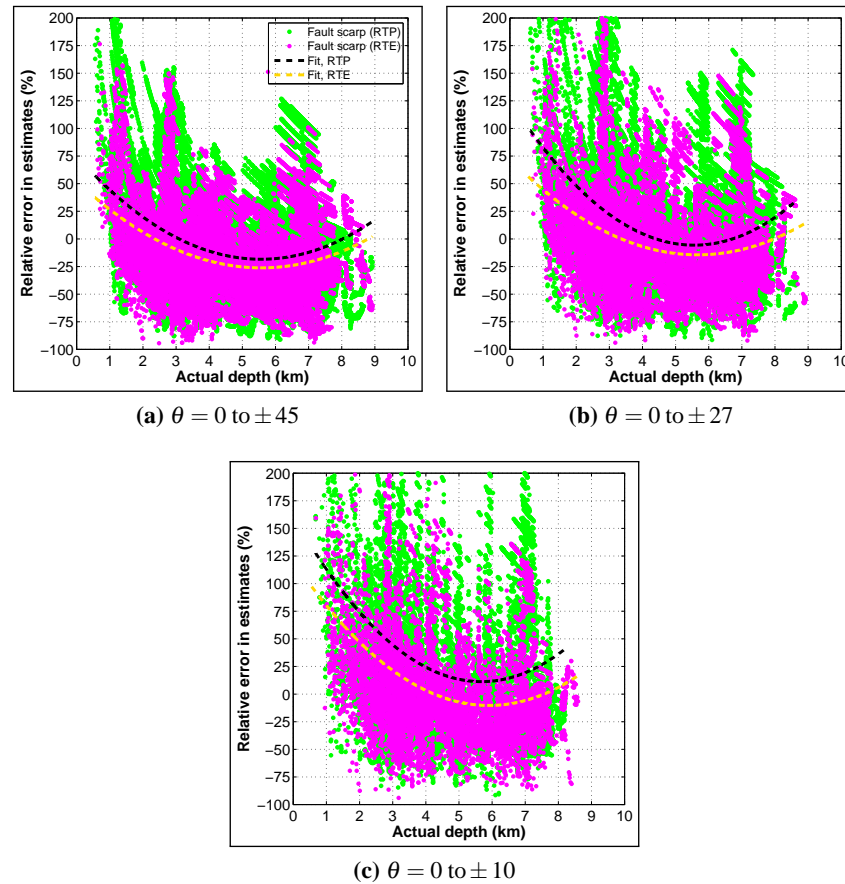


**Figure 4.16:** Error in “Tilt-Depth” method estimates of SBM (RTP and RTE) source depths. The method was implemented in three modes, using  $|\theta| = 0$  to 45, 27 or 10 distance. The legend to figure 4.16a applies also to figures 4.16b and 4.16c. Note the wide spreads in data. Each dashed line represents the best-fitting least-squares function for each cross-plot of paired datasets. For clarity, equations for these least-squares functions and related statistical parameters were presented in table 4.4.

and degrees of freedom, respectively.

**Table 4.4:** Statistical parameters for least-squares functions to each cross-plot in figures 4.15 and 4.16.

Figure	RTP (Black, dashed line)	RTE (Brown, dashed line)
4.15a	$y = 0.8x + 0.6$ ; $SE = 2.3$ ; $r^2 = 27.6\%$	$y = 0.7x + 0.4$ ; $SE = 2.1$ ; $r^2 = 36.6\%$
4.15b	$y = 0.9x + 0.8$ ; $SE = 2.8$ ; $r^2 = 24.6\%$	$y = 0.8x + 0.5$ ; $SE = 2.5$ ; $r^2 = 32.2\%$
4.15c	$y = x + 1.2$ ; $SE = 3.9$ ; $r^2 = 17\%$	$y = 0.8x + 1.2$ ; $SE = 2.7$ ; $r^2 = 25.4\%$
4.16a	$y = 3x^2 - 33.6x + 74.9$ ; $SE = 42.9$	$y = 2.5x^2 - 28.2x + 52.3$ ; $SE = 33.6$
4.16b	$y = 4.2x^2 - 47.2x + 125.7$ ; $SE = 56.4$	$y = 2.7x^2 - 30.7x + 72.6$ ; $SE = 42.6$
4.16c	$y = 4.6x^2 - 52.8x + 161.2$ ; $SE = 85.1$	$y = 0.8x + 1.2$ ; $SE = 52.2$

$r_s$  were computed using  $m \times n$  matrices  $A$  and  $B$  which, respectively, contained the actual and estimated depths at corresponding locations in the model basement depth grid (Figure 4.2a) and the grid of depth estimates obtained from the RTP or RTE version of the BM grid being compared. These pair of matrices  $A$  and  $B$  were converted to column vectors, which contained data from corresponding locations with significant depth figures.  $C$  and  $D$  were column vectors containing the ranks of depth data in  $A$  and  $B$ , respectively. In this case,  $m = N$  and  $n = 1$ . The size of  $N$  varied with type of structure being considered and whether estimates were from RTP or RTE of BM grid.

The minimum  $N$  for cross-plots of SBM depths was 12469.

Irrespective of the  $\theta$  range used, estimated FS depths were not accurate (as they did not plot on or very close to the 1:1 lines) in figure 4.15. Depth estimates may be higher than, equal to or lower than the actual depths of FS. This dispersion in the cross-plot increased with increasing depths of FS. Linear best-fits (treated as averages) to these cross-plots (Figure 4.15) and the  $r^2$  and  $SE$  values associated with them (Table 4.4) will be used to compare these dispersions. Best-fit lines show that depths estimated from SBM (RTP) and SBM (RTE) grids were generally closer when  $-45 \leq \theta \leq 45$  range was used (Figure 4.15a). However, these estimates were, on average, less than the actual depths of FS. Estimates using  $-27 \leq \theta \leq 27$  range (Figure 4.15b) were the most accurate, since they were closest to the 1:1 line. Average estimates obtained from SBM (RTE) grid were closer to the 1:1 line (more accurate) than those from its RTP equivalent.  $r^2$  were lower for RTP estimates compared with RTE estimates.  $r^2$  generally reduced as  $SE$  increased, with reducing range of  $\theta$  used.

The equation for mean depths estimated ( $\bar{y}$ ) from the SBM (RTP) grid in terms of actual depths ( $x$ ) of FS was  $\bar{y} = 0.9(x + 1)$ . The equivalent for SBM (RTE) grid was  $\bar{y} = 0.8x + 0.7$ . *These equations overestimate the actual FS depth, at errors of 20% or less when the ratio  $\frac{y}{x} \leq 1.2$ .* Percentage depth errors obtained from SBM grids were shown in figure 4.16.<sup>27</sup> Neither quadratic, cubic and quartic least-square functions could satisfactorily relate cross-plots between percentage errors and actual depths of FS sources. For example, the best-fitting quadratic function for the cross-plots are shown (Figure 4.16). For this function,  $SE$  increased from 43 (RTP) and 34 (RTE) when using  $-45 \leq \theta \leq 45$  (Figure 4.16a) through 56 (RTP) and 43 (RTE) when using  $-27 \leq \theta \leq 27$  (Figure 4.16b), to 85 (RTP) and 52 (RTE) when using  $-10 \leq \theta \leq 10$  (Figure 4.16c). The increasing  $SE$  values associated with decreasing  $\theta$  range used indicated that quadratic least-squares fits could not adequately explain the relationship between actual depths of FS on SBM (RTP and RTE) grids and errors in their "Tilt-Depth" method estimates.

Next, I examine the relationship between depths estimated for FS from SBM (RTP and RTE) grids, by directly comparing RTP and RTE estimates (Figure 4.17). The equations of the best-fitting lines to cross-plots in figure 4.17 show RTE estimates were generally smaller than RTP estimates, irrespective of the  $\theta$  range used (Table in figure 4.17d).

The equation for mean depths estimated from the SBM (RTE) grid ( $y$ ) in terms of mean depths estimated from the SBM (RTP) grid ( $x$ ) was  $\bar{y} = 0.5x + 1.6$ . *This equation overestimates the RTP depth, at errors of 20% or less when the ratio  $0.8 \leq \frac{y}{x} \leq 1.2$ , or 35% or less when the ratio  $0.7 \leq \frac{y}{x} \leq 1.3$ .* Hence, using these equations *a priori* depth information may be used to correct depths estimated for those locations from  $\Delta T$  datasets from uniformly magnetised terranes. The corrections may then be applied to the entire dataset. However, the extremely wide dispersions in cross-plots of FS depth estimates and their errors indicate that conclusions drawn from analyses

<sup>27</sup>Outliers in percentage depth errors for FS sources occasionally exceeded 200%, but were not removed.

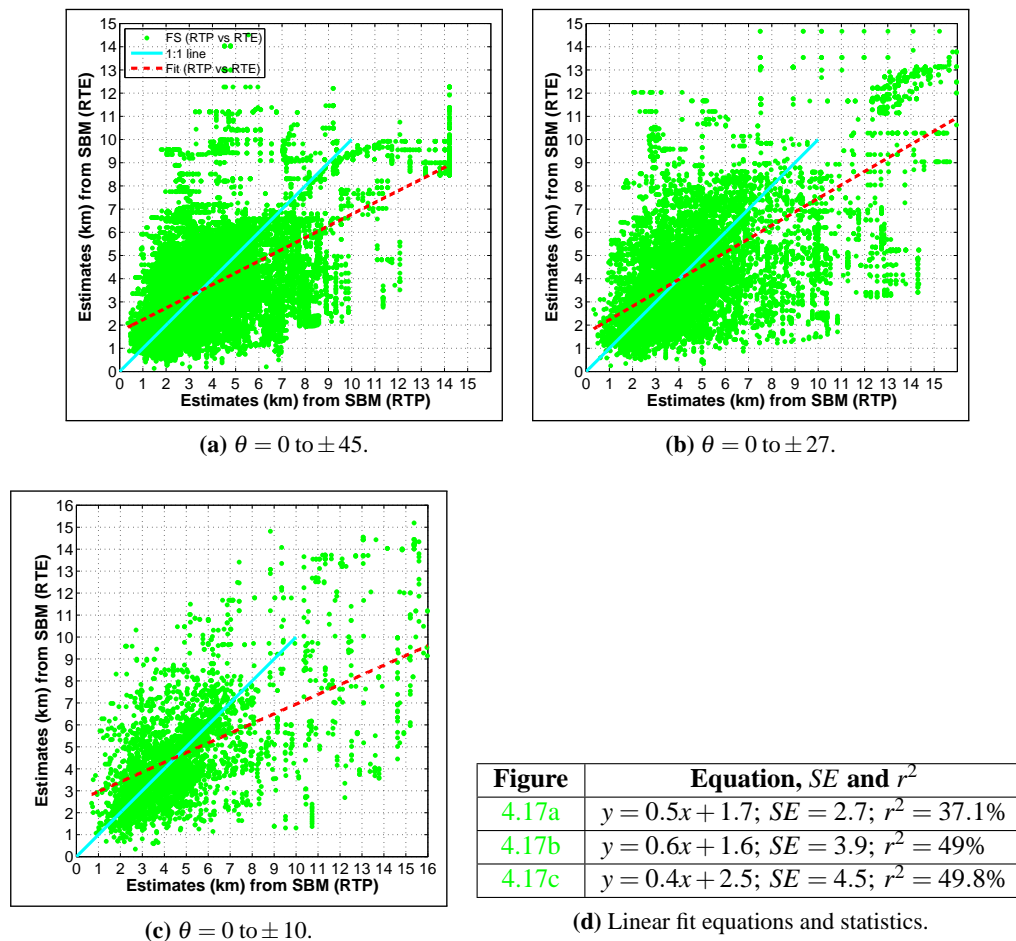


**Figure 4.17:** Relationship between SBM (RTP) and SBM (RTE) source depths estimated using  $|\theta| = 0$  to 45, 27 or 10 distance. The best relationship was obtained when  $|\theta| = 0$  to 27 range was used. The legend to figure 4.17b applies also to all other figures here. The solid light-blue line is where a 1:1 (100%) correlation between depths estimated from SBM (RTP) and SBM (RTE) grids should plot, while the dashed, magenta-coloured line represents the best-fitting least-squares function for each cross-plot of paired datasets. For clarity, equations of these least-squares lines and related statistical parameters are presented in the table in figure 4.17d.

above may be far-fetched. These wide dispersions were expected, since these sources (FS) do not conform to the strict assumption of vertical infinite contact specified by the method.

### (B) Estimated and actual depths of CBM sources

$\Delta T$  sources on CBM grids included fault scarps (FS), as well as 2D and non-2D magnetic contacts (Figure 4.2b). “Tilt-Depth” estimates of the depths of these sources from the CBM (RTP) grid were shown in figure 4.12b, while figure 4.12d presented estimates from the CBM (RTE) grid. The actual and estimated depth of sources have been extracted from these respective grids, and are presented as cross-plots in figure 4.18.<sup>28</sup> Cross-plots were colour-coded to reflect source-types (Figure 4.8b). Cross-plots for RTP estimates are shown in figures 4.18a, 4.18b and 4.18c, while similar plots for RTE estimates are shown in figures 4.18d, 4.18e and 4.18f. Percentage errors in these CBM estimates are presented in figure 4.19.

<sup>28</sup>The actual locations and depths of these sources were shown in figures 4.8b and 4.9a, respectively.

**Table 4.5:** Comparing equations and statistics of least-squares functions to cross-plots shown in figures 4.18 and 4.19.

Figure	2D estimate (km)	Non-2D estimate (km)	FS estimate (km)
4.18a (RTP)	$y = 0.6x + 0.5$ ; $SE = 1$ ; $r^2 = 80.2\%$	$y = 0.4x + 1.3$ ; $SE = 0.4$ ; $r^2 = 83.7\%$	$y = 0.5x + 1.4$ ; $SE = 2$ ; $r^2 = 21.6\%$
4.18d (RTE)	$y = 0.5x + 0.7$ ; $SE = 1$ ; $r^2 = 58.6\%$	$y = 0.5x + 1.3$ ; $SE = 1.6$ ; $r^2 = 23.5\%$	$y = 1.3x + 0.5$ ; $SE = 5.1$ ; $r^2 = 18.2\%$
4.18b (RTP)	$y = 0.7x + 0.5$ ; $SE = 1.1$ ; $r^2 = 81.1\%$	$y = 0.5x + 1.2$ ; $SE = 0.4$ ; $r^2 = 88.6\%$	$y = 0.6x + 1.3$ ; $SE = 2.2$ ; $r^2 = 25.7\%$
4.18e (RTE)	$y = 0.5x + 0.9$ ; $SE = 0.8$ ; $r^2 = 74.8\%$	$y = 0.5x + 1.2$ ; $SE = 1.5$ ; $r^2 = 31.7\%$	$y = 1.5x + 1$ ; $SE = 7.6$ ; $r^2 = 10.9\%$
4.18c (RTP)	$y = 0.6x + 0.9$ ; $SE = 0.9$ ; $r^2 = 86.5\%$	$y = 0.6x + 1.4$ ; $SE = 0.6$ ; $r^2 = 83.7\%$	$y = 0.8x + 1.1$ ; $SE = 3$ ; $r^2 = 21\%$
4.18f (RTE)	$y = 0.5x + 1.2$ ; $SE = 0.9$ ; $r^2 = 82.5\%$	$y = 0.5x + 1.7$ ; $SE = 0.8$ ; $r^2 = 60.6\%$	$y = 1.2x + 2.1$ ; $SE = 5.7$ ; $r^2 = 13.1\%$
Figure	2D error (%)	Non-2D error (%)	FS error (%)
4.19a (RTP)	$y = 0.2x^2 - 4.5x - 12.7$ ; $SE = 9.5$	$y = 0.6x^2 - 11.8x + 14.4$ ; $SE = 7.7$	$y = x^2 - 17.1x + 45.9$ ; $SE = 38.6$
4.19b (RTE)	$y = 0.5x^2 - 8.2x - 3.8$ ; $SE = 12.7$	$y = 0.2x^2 - 5.9x + 0.3$ ; $SE = 25.9$	$y = -2.3x^2 - 23.1x + 11.7$ ; $SE = 88.2$
4.19c (RTP)	$y = 0.4x^2 - 6.3x - 0.7$ ; $SE = 9.8$	$y = 0.5x^2 - 10x + 15.8$ ; $SE = 6.1$	$y = 2x^2 - 27.7x + 78.7$ ; $SE = 41.6$
4.19d (RTE)	$y = 0.5x^2 - 9.8x + 8$ ; $SE = 8.9$	$y = 0.4x^2 - 9x + 11.1$ ; $SE = 20.4$	$y = -5.7x^2 + 58x - 63.3$ ; $SE = 129.6.2$
4.19e (RTP)	$y = 0.6x^2 - 10.8x + 21.2$ ; $SE = 9.8$	$y = 0.7x^2 - 12.9x + 31.5$ ; $SE = 7.9$	$y = 4.4x^2 - 51.4x + 140.5$ ; $SE = 53.5$
4.19f (RTE)	$y = 0.9x^2 - 14.4x - 28.5$ ; $SE = 9$	$y = 0.2x^2 - 8.1x + 16.6$ ; $SE = 12.9$	$y = -5.1x^2 + 46.5x - 23.6$ ; $SE = 99.8$

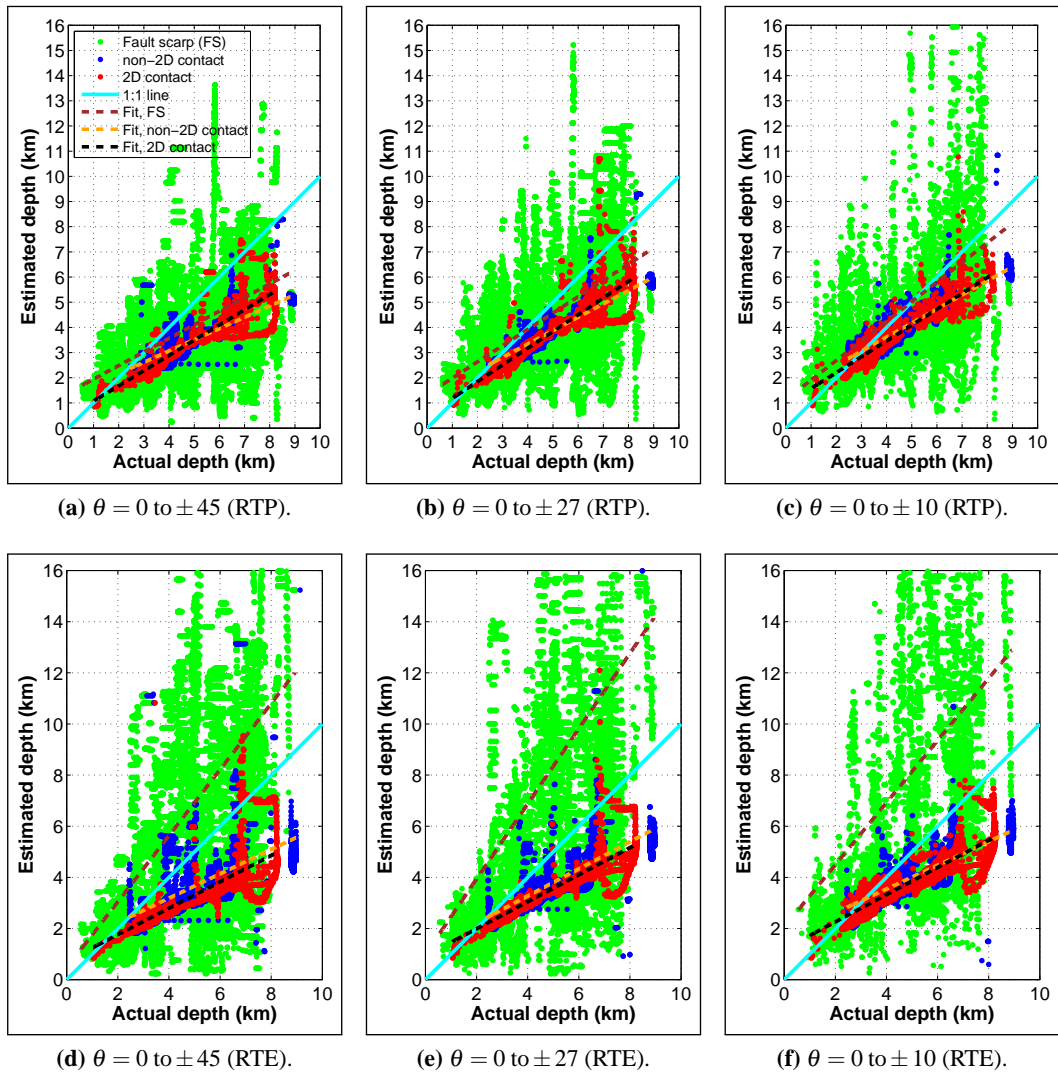


**Figure 4.18:** “Tilt-Depth” method estimates of source depths from CBM (RTP and RTE) grids, using  $|\theta| = 0$  to 45, 27 or 10 distance. Estimates were truncated at 16 km for clarity of figures. The solid light-blue line is where a 1:1 (100%) correlation between the actual and estimated depths should plot. The legend to figure 4.18a applies also to all other figures here. Note the wider spreads in FS data compared with those for 2D and non-2D contacts. Each dashed line represents the best-fitting least-squares function for each cross-plot of paired datasets. Errors in these estimates are presented in figure 4.19. For clarity, equations describing these least-squares functions, as well as related statistical parameters are presented in table 4.5.

To simulate what obtains in practice, all analyses of depth estimates and error included every estimated location from the RTP or RTE grid, without consideration for whether or not the estimated locations were accurate. Hence, data on each cross-plot were extracted only from corresponding locations in the actual depth grid and depth estimates or percentage depth error grid. The number of such corresponding locations for each BM source defined the degree of freedom ( $N$ ) for such cross-plots.

Locations of depths estimated for 2D contacts from the CBM (RTP) grid corresponded well with locations of their actual depths (Section 4.4). However, only about 80% of locations of estimates of non-2D contacts and FS sources from the CBM (RTE) grid correspond with locations of their actual depths.  $N$  generally reduced as the  $\theta$  range used for depth estimation reduced. For example,

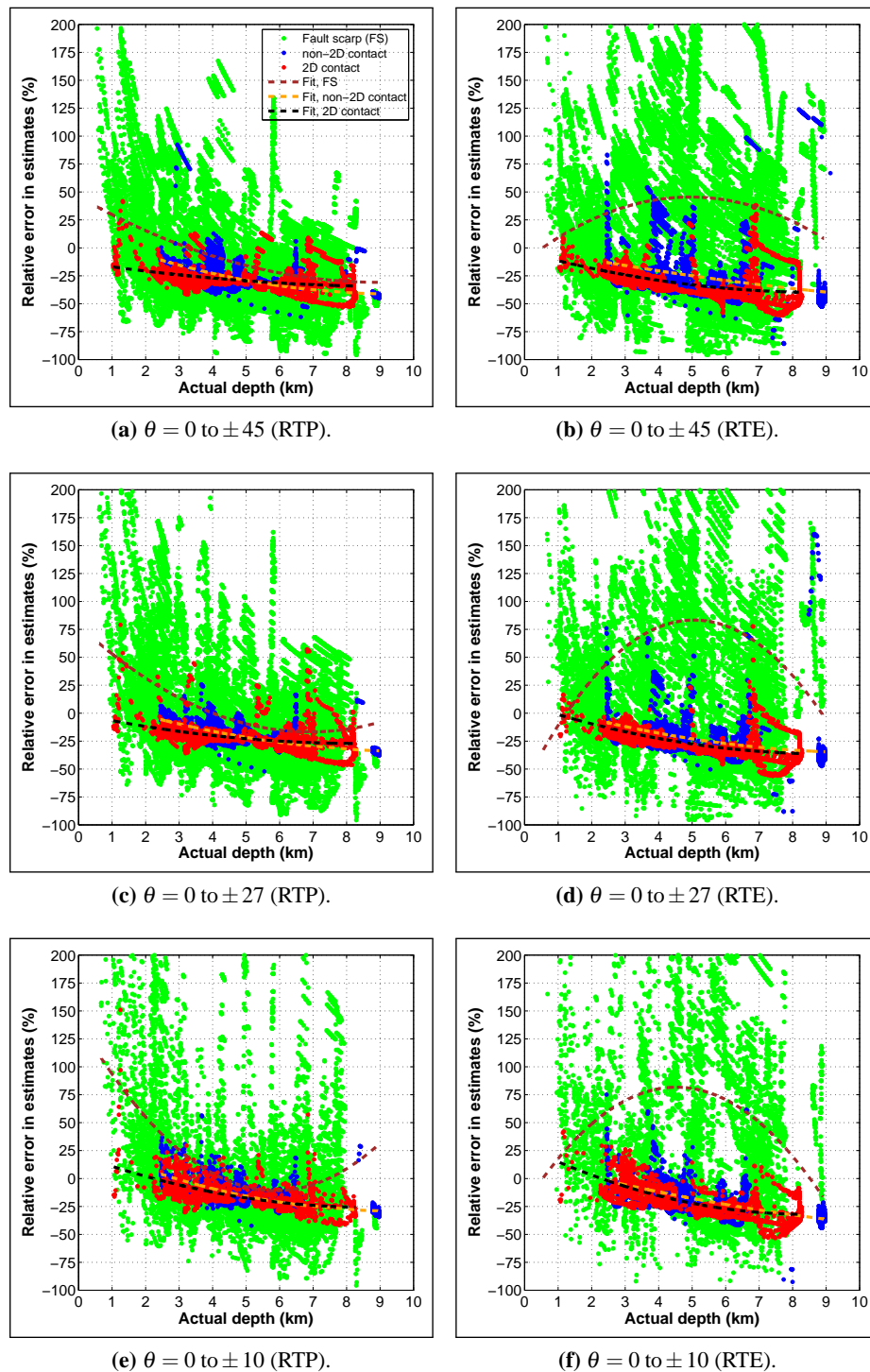


**Figure 4.19:** Error in “Tilt-Depth” method estimates of CBM (RTP and RTE) source depths, using  $|\theta| = 0$  to 45. The legend to figure 4.19a applies also to all other figures here. Note the wider spreads in FS data compared with those for 2D and non-2D contacts. Each dashed line represents the best-fitting least-squares function for each cross-plot of paired datasets. For clarity, equations describing these least-squares functions, as well as related statistical parameters are presented in table 4.5.

only  $\approx 22\%$  of FS locations and  $\approx 30\%$  of 2D and non-2D locations correspond when  $-10 \leq \theta \leq 10$  range was used. The minimum  $N$  (from  $-10 \leq \theta \leq 10$ ) for cross-plots of depths of CBM (RTP) were 2066 (for 2D contacts), 2748 (for 3D contacts) and 12941 (for FS). Equivalent for cross-plots of depths of CBM (RTE) were 2632 (for 2D contacts), 2253 (for 3D contacts) and 11110 (for FS). Consequently, irrespective of the  $\theta$  value used, depths obtained for magnetic (2D and non-2D) contacts were more tightly clustered than those obtained for FS on CBM (RTP and RTE) grids showed. Also, the regression equations and goodness-of-fit statistics ( $r^2$  and  $SE$ ), show that these estimates improved generally as the range of  $\theta$  used reduced from  $-45 \leq \theta \leq 45$ , through  $-27 \leq \theta \leq 27$  to  $-10 \leq \theta \leq 10$  (Figure 4.18).

Despite the occurrence of significant anomaly interference on the CBM (RTP and RTE) grids, depth estimates from these grids were dominated by estimates from FS (Figure 4.18). Cross-plots of estimated depths for CBM sources (Figure 4.18) and those of their errors (Figure 4.19) displayed wide spreads. In order to quantitatively compare these cross-plots, I obtained best-fitting least-squares functions for the relationships between the paired datasets in each cross-plot. I also computed  $SE$  (Equation (4.6.1)) and/or  $r^2$  (Equation (4.5.1)) for the best-fitting function of the cross-plot, using  $N$ . Relationships between actual and estimated depths were well described by linear functions. Best fitting functions on cross-plots of actual depth and percentage errors in estimated depths for CBM sources were more complicated. For instance, while quadratic and cubic functions satisfactorily described relationships on cross-plots of percentage depth errors and actual depths of magnetic (2D or non-2D) contacts, these and even quartic functions could not satisfactorily describe relationships on similar cross-plots for FS sources. Consequently, I adopted linear least-squares functions of actual source depths to compare cross-plots of actual and estimated depths (Figure 4.18). Quadratic least-squares functions of actual source depths were adopted for comparing cross-plots of actual depths and percentage errors in depth estimates (Figure 4.19). Equations describing these least-squares functions, as well as the relevant values of  $SE$  and/or  $r^2$  are presented in table 4.5.

The very wide dispersions in cross-plots of FS depth estimates and their errors for CBM (RTP and RTE) grids, and inability to provide a convincing best-fit for FS depth errors for CBM (RTE) grid, made it impossible to consider any further analyses of estimates from these sources. Hence, attention focussed on the analyses of depths estimated for magnetic (2D and non-2D) contacts from CBM (RTP and RTE) grids, and the errors associated with these estimates. Depths of 2D and non-2D contacts obtained from CBM (RTP and RTE) grids, using  $-45 \leq \theta \leq 45$  and  $-27 \leq \theta \leq 27$  were generally lower than their actual depths, while depths using  $-10 \leq \theta \leq 10$  appear to be overestimated at shallow depths  $< 2.5$  km, but underestimated at depths  $\geq 2.5$  km. Implementing "Tilt-Depth" method using  $-10 \leq \theta \leq 10$  range offered no significant improvement on estimated depths of magnetic (2D and non-2D) contacts. The equations for mean depth estimates of 2D and non-2D contacts from the CBM (RTP) grid were,  $\bar{y} = 0.6(x + 1)$  and  $\bar{y} = 0.5x + 1.1$ , respectively. Similar equations for estimates from the CBM (RTE) grids, were  $\bar{y} = 0.5x + 0.9$  and  $\bar{y} = 0.5x + 1.4$ , respectively.

Whereas estimated depths of 2D and non-2D contacts obtained from the CBM (RTP) grid using  $-45 \leq \theta \leq 45$  range were in error of -20 to -35% and -12 to -40%, respectively, estimates from the CBM (RTE) grid were in error of -12 to -40% (Figures 4.19a and 4.19b). Depth errors for 2D and non-2D contacts were -8 to -25% and -5 to -35% on CBM (RTP) grid, respectively, when  $-27 \leq \theta \leq 27$  range was used (Figure 4.19c). Depth error for estimates from the CBM (RTE) grid using this range of  $\theta$  were 0 to -35% and -8 to -38%, respectively (Figures 4.19d). Estimated depths of 2D and non-2D contacts obtained from the CBM (RTP) grid using  $-10 \leq \theta \leq 10$  range were in error of 10 to -25% and 8 to -30%, respectively, while these estimates from the CBM (RTE) grid were in error of 12 to -30% and 0 to -38%, respectively (Figures 4.19a and 4.19b). These depth errors are summarised in table 4.6. Error in depth estimates generally increased with the actual

**Table 4.6:** Summary of average percentage depth error for estimates from magnetic (2D and non-2D) contacts on CBM (RTP and RTE) grids. The magnitude of maximum difference in range of error are shown in brackets. Data were extracted from figure 4.19.

CBM grid/ source types	Percentage error for depths estimated using $\theta = 0$ to:		
	$\pm 45^\circ$ (%)	$\pm 27^\circ$ (%)	$\pm 10^\circ$ (%)
<b>(1) RTP</b>			
(i) 2D contacts	-20 to -35 (15)	-8 to -25 (17)	10 to -25 (35)
(ii) non-2D contacts	-12 to -40 (28)	-5 to -35 (30)	8 to -35 (43)
<b>(2) RTE</b>			
(i) 2D contacts	-12 to -40 (28)	0 to -35 (35)	12 to -30 (42)
(ii) non-2D contacts	-12 to -40 (28)	-8 to -38 (30)	0 to -38 (38)

depth of magnetic (2D and non-2D) contacts, irrespective of the range of  $\theta$  used (Figure 4.19). Curves representing best-fitting functions to depth errors for these sources tend to be slightly steeper for estimates from the CBM (RTE) grid than the CBM (RTP) grid. Hence, the magnitude of maximum difference in range of depth error (Numbers in brackets in table 4.6) were generally larger for estimates from the CBM (RTE) grid than CBM (RTP) grid. However, the method works almost as well for non-2D contacts as it does for 2D contacts when the grid is RTE, irrespective of the range of  $\theta$  used (Table 4.6).

Implementing "Tilt-Depth" method using the  $-27 \leq \theta \leq 27$  range seemed more advantageous since its errors for both 2D and non-2D contacts on CBM (RTP and RTE) grids were much less than estimates using  $-45 \leq \theta \leq 45$  range (Tables 4.5 and 4.6). These implementations only underestimated the actual depths of these sources, hence were easier and faster to interpret, as opposed to implementations using the  $-10 \leq \theta \leq 10$  range which underestimated as well as overestimated depths of contacts. The fact that the magnitude of maximum difference in range of depth errors for estimates using  $-27 \leq \theta \leq 27$  were lower than those for  $-10 \leq \theta \leq 10$  appears to indicate the  $-27 \leq \theta \leq 27$  range as a limiting distance for estimating depth from the "Tilt-Depth" method (Table 4.6). Grids of depths estimated from CBM (RTP and RTE) grids, using the  $-27 \leq \theta \leq 27$  range are presented for comparison in appendix C (Figure C.8).

Comparisons between depths of 2D and non-2D contacts estimated at corresponding locations

on the CBM (RTP and RTE) grids (Figure 4.20) showed that estimates from the RTE grid were generally less than their equivalents from the RTP grid. However, RTE estimates approached RTP estimates as the  $\theta$  range used reduced from  $-45 \leq \theta \leq 45$  to  $-10 \leq \theta \leq 10$  (Table 4.7). Depths

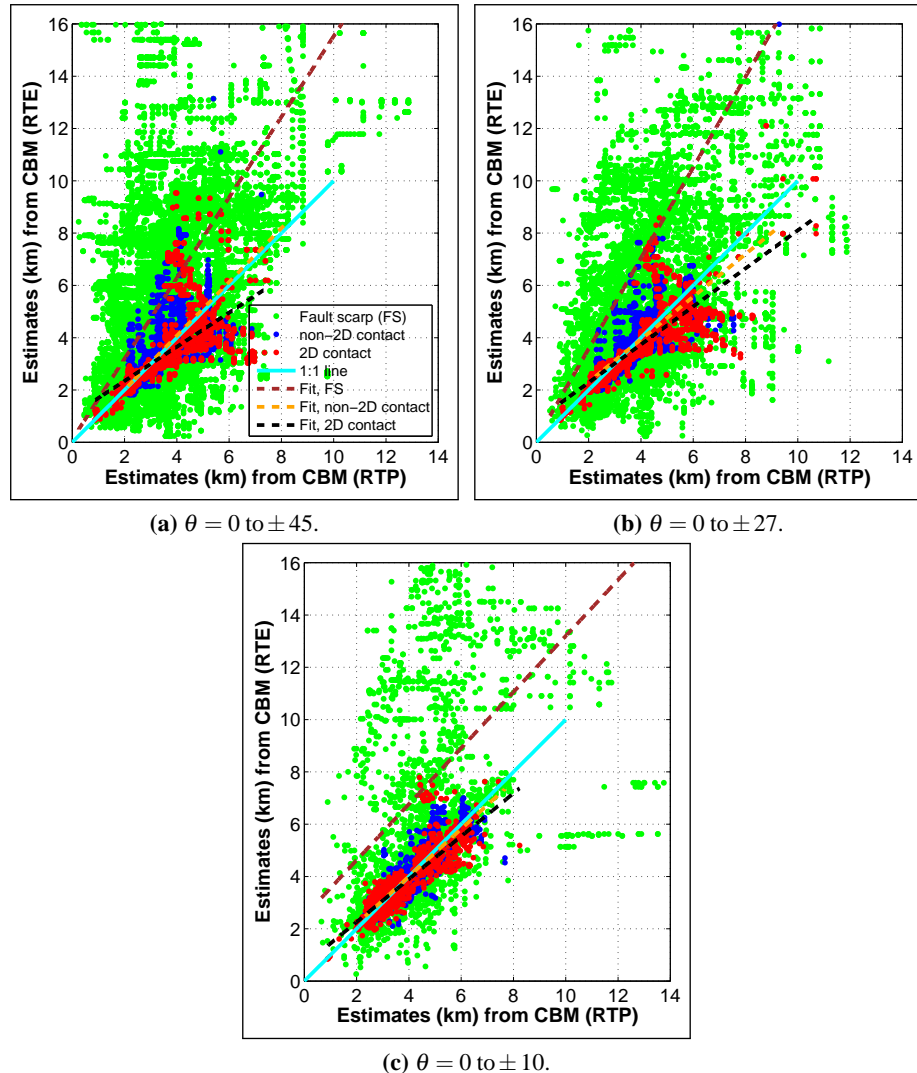


**Figure 4.20:** Relationship between depths estimated using  $|\theta| = 0$  to 45, 27 or 10 distance at corresponding CBM (RTP) and CBM (RTE) grid locations. Note that relationships improved with decreasing range of  $\theta$  used. The solid light-blue line is where a 1:1 correlation between the actual and estimated depths should plot. Each dashed line represents the best-fitting least-squares function for each cross-plot of paired datasets. Figure 4.20a (or 4.18a) presents the legend to all figures here. For clarity, equations describing least-squares functions to these cross-plots, as well as related statistical parameters are presented in table 4.7.

estimated for 2D contacts from the CBM (RTE) grid represented  $\approx 70\%$  of their RTP equivalents when obtained using either  $-45 \leq \theta \leq 45$  or  $-27 \leq \theta \leq 27$ . They represented  $\approx 80\%$  of their RTP value when obtained using  $-10 \leq \theta \leq 10$ . For 3D contacts, depths estimated from the CBM (RTE) grid represented  $\approx 100\%$ ,  $\approx 80\%$  and  $\approx 90\%$  of their RTP equivalents when obtained using  $-45 \leq \theta \leq 45$ ,  $-27 \leq \theta \leq 27$  and  $-10 \leq \theta \leq 10$  range, respectively. These relationships were only for corresponding CBM (RTP and RTE) grid locations.

In summary, cross-plots of depths estimated (and their errors) for 2D and non-2D contacts show

**Table 4.7:** Comparing statistical parameters for least-squares fits to cross-plots in figure 4.20.

Figure	2D estimate (km)	Non-2D estimate (km)
4.20a	$y = 0.7x + 1; SE = 1.1; r^2 = 43\%$	$y = 1.03x; SE = 2.1; r^2 = 43.4\%$
4.20b	$y = 0.7x + 0.8; SE = 2; r^2 = 68.6\%$	$y = 0.8x + 0.7; SE = 1.7; r^2 = 60.1\%$
4.20c	$y = 0.8x + 0.6; SE = 1.3; r^2 = 76.6\%$	$y = 0.9x + 0.4; SE = 1; r^2 = 75.8\%$
Figure	FS estimate (km)	
4.20a	$y = 1.5x + 0.1; SE = 7.6; r^2 = 40.6\%$	
4.20b	$y = 1.7x + 0.1; SE = 10.5; r^2 = 26.2\%$	
4.20c	$y = 1.1x + 2.5; SE = 9.5; r^2 = 20\%$	

the “Tilt-Depth” method to under-estimate the actual depths of these sources. Estimates using  $-27 \leq \theta \leq 27$  range were more advantageous, with errors much less than estimates using either the  $-45 \leq \theta \leq 45$  or  $-10 \leq \theta \leq 10$  range. For estimates from the RTP grid, cross-plots for 2D sources (in red) were tightly well and linearly clustered, with depth error linear to depth. Depth estimates and associated errors for non-2D (3D) contacts (in blue) were slightly more dispersed than those for 2D contacts, mainly because these sources do not conform to the assumption of vertical infinite contact on which the “Tilt-Depth” method is based. However, the “Tilt-Depth” method works about as well for non-2D contacts as it does for 2D contacts when the grid is RTE, irrespective of the range of  $\theta$  used. This seems to be due to azimuthal anisotropy effects on the RTE grid, which preferentially accentuates and images the northern and southern W-E, NE-SW or NW-SE edges of 3D bodies at the expense of their western and eastern near-North-South edges.

Estimates using  $-27 \leq \theta \leq 27$  range were in error of 25% or less, for 2D contacts on the RTP grid. Similar estimates were in error of 25% or less, for non-2D contacts on the RTP grid, as well as all (2D and non-2D) contacts on the RTE grid.

In this chapter, analyses of depths estimated from RTP or RTE of SBM and CBM grids using “Tilt-Depth” method included all estimated locations, without consideration for whether or not the estimated locations were accurate. Similar evaluations will be conducted, in chapter 5, for locations and depths of CBM sources obtained from other semi-automatic methods of magnetic data interpretation, for comparison with those obtained from the  $-27 \leq \theta \leq 27$ -based “Tilt-Depth” method. Ultimately, location and depth estimates at only accurately estimated locations from the CBM (RTP or RTE) grid will be compared (Chapter 5).

## Chapter 5

# Application of other methods to complex “Bishop” model (CBM) datasets.

---

### 5.1 Introduction.

Previously (Chapter 4), I tested the "Tilt-Depth" method on RTP and RTE versions of the SBM and CBM grids. While conclusive results were obtained from tests using the CBM (RTP and RTE) grids, results from the SBM (RTP and RTE) were inconclusive since the underlying assumptions of significant magnetic susceptibility contrasts ( $\delta k$ ) were not met. Hence, only CBM (RTP and RTE) grids will be used to compare results obtained from other derivatives-based semi-automatic methods in this chapter.<sup>1</sup> The objective here is to develop an interpretation strategy for RTE datasets, by evaluating the relative effectiveness of these other method(s) on CBM (RTP and RTE) grids. While RTP datasets are simpler to interpret, RTE datasets are characterised by anisotropy-related problems (Section 2.3.3).

Based on published reviews of the effectiveness of semi-automatic methods on RTP profile and/or gridded datasets (Li, 2003; Phillips, 2000; Pilkington & Keating, 2004 and Phillips et al., 2007), I selected five semi-automatic methods for the estimation of source edge locations on the CBM (RTP and RTE) grids.<sup>2</sup> These methods include: the analytic signal amplitude (ASA: Nabighian, 1972); second vertical derivative (SVD: Hood & Teskey, 1989; Miller & Singh, 1994); horizontal gradient magnitude of (RTP or RTE) dataset ( $HGM_{(\Delta T)}$ : Finn & Morgan, 2002); local wavenumber (LW or  $SPI^{TM}$ : Thurston & Smith, 1997; Smith et al., 1998); as well as total horizontal gradient of  $\theta$  ( $HGM_{(\theta)}$ : Verduzco et al., 2004). I will further examine the ASA and LW methods in terms of effectiveness in estimating depths of source edges from these grids. These methods were introduced in section 2.5.<sup>3</sup> They are briefly discussed below.

The  $HGM_{(\Delta T)}$  is the least sensitive to the noise content of the dataset, since it depends entirely on first-order horizontal Cartesian derivatives (Phillips, 2000). Although the  $HGM_{(\Delta T)}$  yields co-

---

<sup>1</sup>CBM (RTP and/or RTE) grid(s) or CBM grid imply CBM (RTP and/or RTE)  $\Delta T$  grid(s). Also, references to CBM (RTP) grid and CBM (RTE) grid will imply CBM (RTP)  $\Delta T$  grid and CBM (RTE)  $\Delta T$  grid, respectively.

<sup>2</sup>Dataset refers to  $\Delta T$  dataset.

<sup>3</sup>Future reference(s) to  $HGM_{(\Delta T)}$ , SVD, ASA, LW and/or  $HGM_{(\theta)}$  will imply the method.

herent contact locations for vertical contacts and is very resilient when applied to noisy RTP datasets, its accuracy degrades when magnetisation direction and/or contact dips are not vertical (Pilkington, 2007). On the contrary, the ASA, SVD, LW and  $HGM_{(\theta)}$  additionally require vertical and/or second-order horizontal derivatives of the dataset. Using these derivatives makes the ASA, LW and  $HGM_{(\theta)}$  independent of magnetisation directions and dips of two-dimensional (2D) magnetic sources (Pilkington, 2007). These are very desirable attributes for interpreting any  $\Delta T$  dataset. However, these methods require second-order derivatives. While these derivatives are capable of delineating source locations from high-to-medium-resolution (low noise) datasets, they can degrade (mask) source locations as they enhance the noise content of low-resolution (noisy) datasets (Phillips, 2000 and Li, 2003). These magnetisation direction-independent methods are, therefore, sensitive to data quality.

Anomalous magnetic sources should be poorly resolved when these methods are applied to low-quality datasets resulting from under-sampled anomalies or flight-line effects due to poor survey design and data-processing strategies. Since RTE anomalies exhibit anisotropy, these methods may be even less effective when applied to the typically low resolution RTE datasets, like the NE Nigeria dataset to be interpreted in this study. These methods, all of which assume that anomaly sources are mainly 2D contacts (Sections 2.5.2 to 2.5.5), have been extensively evaluated using reduced-to-pole (RTP) datasets (e.g., Phillips, 2000, Li, 2003, Pilkington & Keating, 2004, Fairhead et al., 2004, Phillips et al., 2007 and Pilkington, 2007). I am, however, not aware of any evaluation(s) of these methods using either profile or gridded reduced-to-equator (RTE)  $\Delta T$  data. By simultaneously evaluating location estimates from  $HGM_{(\Delta T)}$ , ASA, SVD, LW and  $HGM_{(\theta)}$ , I aim to gain insights to how these methods can be used to obtain optimum (best) location and depth estimates from RTE datasets.

## 5.2 Comparisons between RTP and RTE grids obtained from each method.

CBM (RTP and RTE) grids were transformed to their SVD,  $HGM_{(\Delta T)}$ , ASA, LW and  $HGM_{(\theta)}$  equivalents by applying functions of the vertical and horizontal derivatives specified for each method (Section 2.5) to the the grids. Amplitudes on these transformed CBM grids were quite small ( $\leq 0.1 \times 10^{-2}$ ), and poorly rendered for visualisation in Matlab<sup>TM</sup>. Hence, GETgrid<sup>TM</sup> versions of the derived RTP and RTE grid pairs are presented (Figures 5.1, 5.2 and 5.3). For clarity, graticules are not shown on these maps.<sup>4</sup> Colour ranges on these GETgrid<sup>TM</sup> maps range from cyan to deep-blue at function minima, through greenish-blue and/or yellow at intermediate amplitudes, to orange, gold or saddle-brown colour at function maxima. These transformed grids form the basis for all subsequent discussions in this chapter.

<sup>4</sup>The difference between coordinates on these GETgrid<sup>TM</sup> figures  $(x_0, y_0)$  and those on Matlab<sup>TM</sup> figures  $(x_1, y_1)$ , e.g., figures 4.5a and 4.5b, is that  $x_1 = \frac{x_0 - 25000}{1000}$  (km) and  $y_1 = \frac{y_0 - 200000}{1000}$  (km).

In this section, each transformed RTP and RTE grid pair is compared, visually, for any differences that they might exhibit in terms of anomaly trends. Comparisons will be with reference to transformed RTP grids, assuming that, like  $\theta$  of CBM (RTP) grid, anomaly trends on transformed RTP grids are correctly located above their sources. For easy comparison, 2D contacts are labelled A1-A1 and A2-A2, while intrusive bodies with non-2D contacts are labelled B1, B2, B3 and B4. Major fault scarps (FS) are labelled C1-C1 and C2-C2, while minor FS are labelled aa, bb, cc, dd, ee, ff, gg and hh. Locations estimated from these derived RTP and RTE grids (Figures 5.1, 5.2 and 5.3) are discussed in section 5.3. Subsequently, each grid pair will be compared with those derived from the other methods.

### 5.2.1 Amplitude-based methods.

The  $HGM_{(\Delta T)}$ , SVD and ASA are amplitude-based methods, because they depend directly on the amplitude of  $\Delta T$ , directly reflecting magnetic susceptibility contrasts ( $\delta k$ ).

**(A)  $HGM_{(\Delta T)}$  grids:**  $HGM_{(\Delta T)}$  (Equation (2.5.5a)) of CBM (RTP and RTE) grids are shown in figures 5.1a and 5.1b.  $HGM_{(\Delta T)}$  maxima of CBM (RTP) grid correspond well with locations of contacts and fault scarps, FS (Figure 5.1a). All 2D and non-2D contacts are clearly imaged, and traceable across intersections between anomalies on this grid. Also, most FS are imaged at their correct locations. Subtle FS on the CBM (RTP) grid that were imaged using  $HGM_{(\Delta T)}$  are labelled aa, bb, cc, dd, ee, ff, gg and hh (In black). However, false (secondary)  $HGM_{(\Delta T)}$  maxima occur parallel and to the North and South of the primary maxima that trace 2D contacts A1-A1 and A2-A2. Similar examples labelled 2b and 3b (In white) occur around non-2D contacts. These locations including those labelled 1a, 1b, 2a and 3b will be compared with equivalent locations on the RTE grid (Figure 5.1b). Pilkington (2007) attribute these false maxima to additional inflections in anomalies sourced from bottom surfaces of dipolar sources. These maxima migrate towards the source, while their magnitudes increase relative to the accompanying primary maxima, either as the width of the dipolar anomaly decreases or its depth reduces Pilkington & Keating (2004). Hence, primary maxima on B1 and B4 sources were not accompanied by false maxima.

On the  $HGM_{(\Delta T)}$  of CBM (RTE) grid (Figure 5.1b) all contacts (A1-A1, A2-A2, B1, B2, B3 and B4) were well imaged, except where they were intersected by FS. FS were poorly imaged except where they strike E-W, NW-SE or NE-SW (Only FS labelled dd was correctly imaged, for example). N-S striking FS (C1-C1, aa, bb and cc) were not imaged. Anomalies from these sources are imaged as discrete E-W striking sources, where they do not interfere (See sources labelled aa, bb and cc). More prominent false (secondary)  $HGM_{(\Delta T)}$  maxima occur parallel to 2D and non-2D contacts as a result of interfering RTE-induced anomalies. Unlike on the RTP grid (Figure 5.1a) where false maxima were not limited to specific directions, maxima on CBM (RTE) grid occur close to the Northern and Southern edges of the primary maxima. Examples of these false maxima occur at locations labelled 1a and 1b, 2a and 2b, and 3a and 3b (Figure 5.1a). These magnitudes appear to increase as the primary maxima increases or as depth reduces.

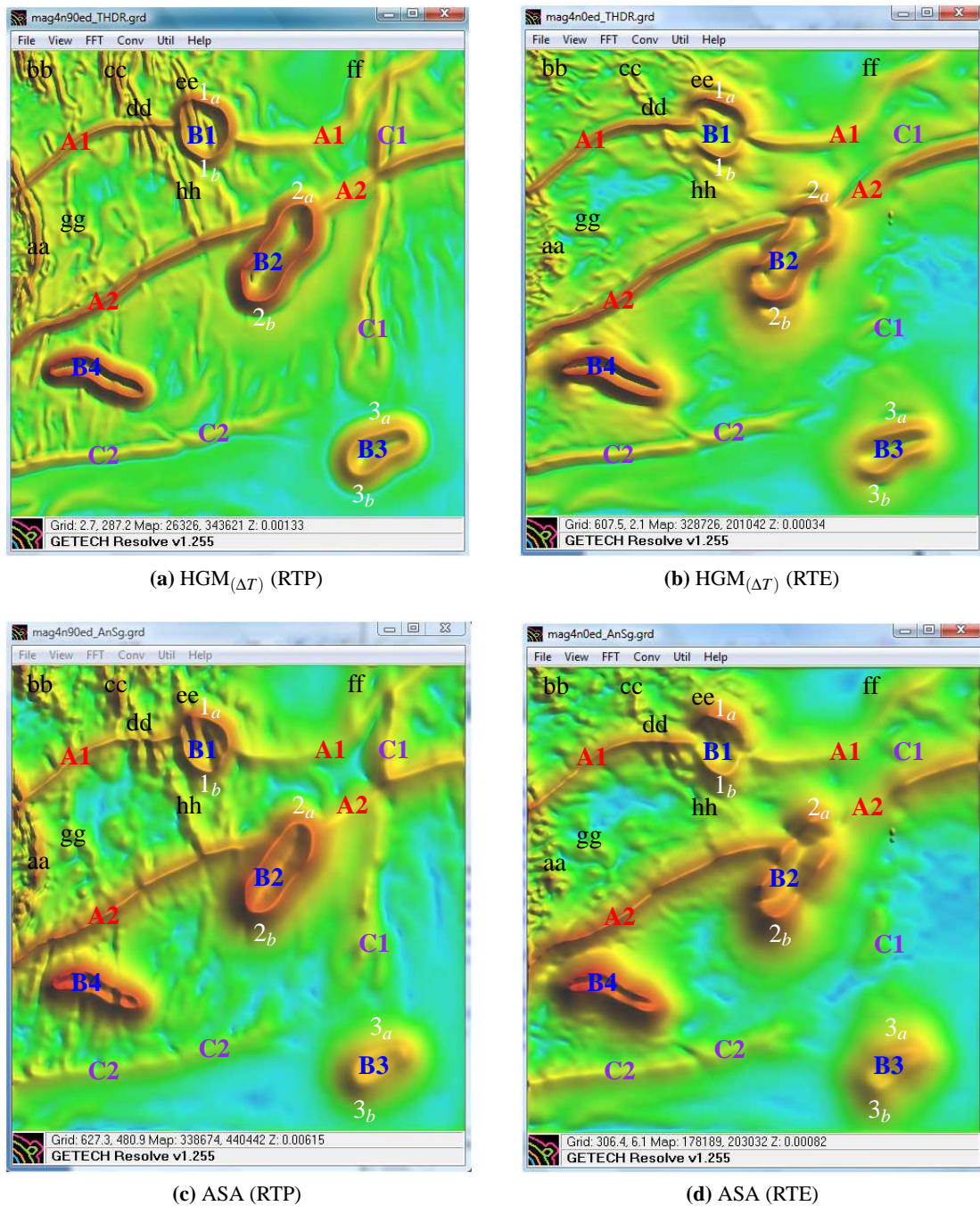


**Figure 5.1:** Horizontal gradient magnitude ( $HGM_{(\Delta T)}$ ) and analytic signal amplitude (ASA) of CBM (RTP and RTE)  $\Delta T$  grids. 2D contacts (A1, A2) are labelled, in red; intrusive magnetic bodies (B1, B2, B3 and B4 labelled in blue) with non-2D contacts; and fault scarps, FS (C1 and C2) are labelled in blueish-violet. Other locations where differences occur between RTP and RTE grids are labelled in black lower case alphabets or white alpha-numeric codes. Colour ranges on maps reflect function amplitudes: minima are cyan to deep-blue, intermediate amplitudes are greenish-blue to yellow; while maxima are orange, gold or saddle-brown in colour. Locations of 2D and non-2D contacts from CBM (RTP and RTE) grids correlate well, but those for fault scarps correlate less. More details in text.

In summary,  $HGM_{(\Delta T)}$  maxima correspond well with locations of all contacts and FS on RTP grid, irrespective of their depths. All contacts on RTE grid and the E-W trending FS were imaged at their correct locations. Correspondence between  $HGM_{(\Delta T)}$  maxima and source locations was azimuth-dependent, so that N-S and near-N-S sources were not imaged. Discretised anomalies from near-N-S sources interfered with adjacent anomalies, making them invisible. Source depths did not hinder their imaging on the RTE grid. This may be a consequence of the dependence of the  $HGM_{(\Delta T)}$  on only horizontal derivatives. Edges of dipolar (non-2D contacts) were clearly imaged on both RTP and RTE grids irrespective of the geometric shape of the source. True  $HGM_{(\Delta T)}$  maxima may be associated with false (secondary) maxima.

**(B) ASA:** The ASA (Equation (2.5.6c)) depends directly on both susceptibility contrast ( $\delta k$ ) and depth distributions of the input grid (Equation 2.5.6d). Because of its reliance on the vertical derivative, otherwise distinct ASA maxima coalesce as source depths increase and/or source width decrease (Pilkington & Keating, 2004). Hence, the ASA images more 2D and non-2D contacts than the non-magnetic FS, as depth increased across the grid. For example, the non-2D edges of the deeper B3 were not as well resolved as those of other magnetic sources on the ASA of CBM (RTP) grid (Figure 5.1c). By incorporating the third component of magnetisation direction via the vertical derivative, the ASA offered source-related 3D images of the subsurface, which appear simpler than those afforded by the  $HGM_{(\Delta T)}$ . Maxima of ASA of CBM (RTP) grid (Figure 5.1c) correspond well with locations of all contacts (2D and non-2D), as well as FS. However, lateral discontinuities or locations where these sources intersect each other were marked by discrete monopolar anomalies which interfered with adjacent anomalies, along-strike, to re-enforce the dominant trends of contact edges on the grid (See intersections between A1-A1 and FS marked cc, dd, ff, as well as intersections between A2-A2 and FS marked gg, hh, ff, and C1-C1 in figure 5.1c, for examples).

ASA maxima from the CBM (RTE) grid correspond well with locations of all contacts; A1-A1, A2-A2, B1, B2, B3 and B4 (Figure 5.1d). Unlike the  $HGM_{(\Delta T)}$  of CBM (RTE) grid, the dominant N-S trending en-echelon FS (C1-C1) was imaged on the ASA (RTE) grid, at low ASA amplitudes, as monopolar E-W anomalies originating at the discontinuities between fault segments aligned to form a N-S string of pearl-shaped dipoles (See figure 2.8 and related section for details). However, the segments of C1-C1, North of 2D contact labelled A2-A2 were not imaged, perhaps because anomalies from these sources were swamped by the comparatively higher amplitudes associated with 2D contacts (A1-A1 and A2-A2). Severe interference between monopolar ASA anomalies from adjacent en-echelon (locally discontinuous) FS sources resulted in the re-enforcement of mainly dominant E-W trending FS sources e.g., C2-C2, at the expense of the unisolated NE-SW, NW-SE, N-S and near-N-S striking FS (Compare FS labelled aa, bb, cc, dd, ee, ff, gg, and hh on figures 5.1c and 5.1d). Where correctly imaged, ASA anomalies were wider than their RTP equivalents.

In summary, ASA maxima correspond well with locations of susceptibility contrast ( $\delta k$ ) and prominent FS on RTP grid, irrespective of source orientation. However, shallower sources were

more obvious than deeper sources. On the RTE grid, correspondence between maxima and source locations was azimuth-dependent, so that near-N-S sources were not directly imaged. However, discrete dipolar anomalies from prominent N-S and near-N-S sources aligned to indicate the presence of N-S sources. Shallower sources were more obvious than deeper sources on ASA of RTE grids.

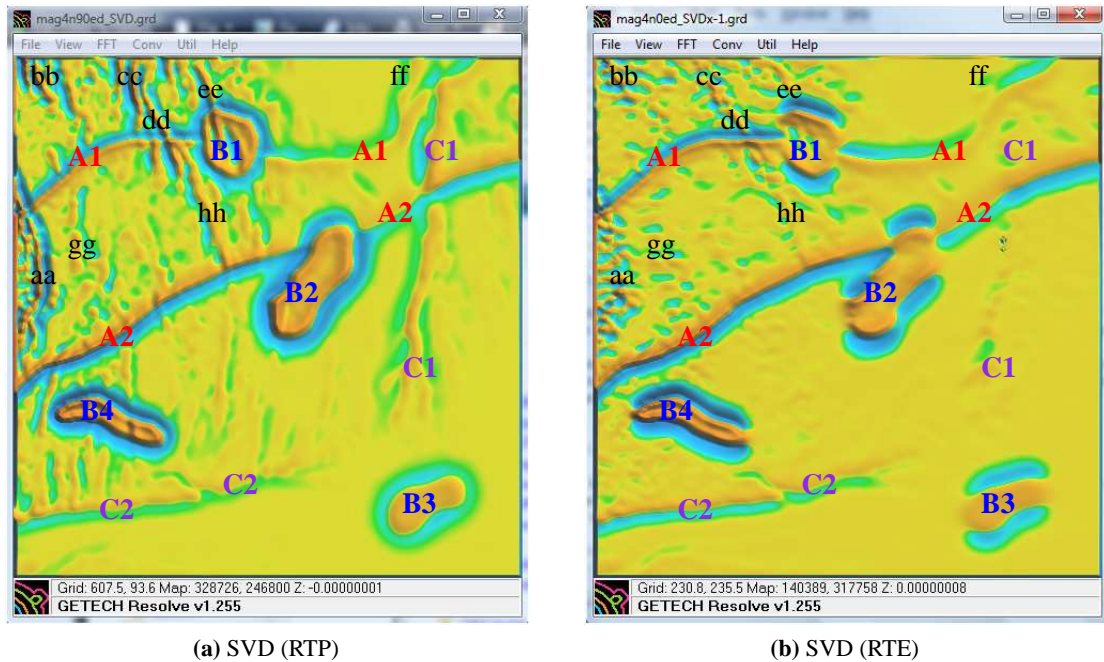


**Figure 5.2:** Second vertical derivative (SVD) of CBM (RTP and RTE) of  $\Delta T$  grids. Traces of: (1) 2D contacts (A1, A2) are labelled in red; (2) intrusive magnetic bodies (B1, B2, B3 and B4) with non-2D contacts are labelled in blue; and (3) fault scarps (C1 and C2) are labelled in blueish-violet. Locations of sources are marked by SVD frequency changes across grids. Colour ranges on maps reflect function amplitudes: minima are cyan to deep-blue, intermediate amplitudes are greenish-blue to yellow; while maxima are orange, gold or saddle-brown in colour. Locations of 2D and non-2D contacts from CBM (RTP and RTE) grids correlate well (See text). Other locations where differences occur between RTP and RTE grids are labelled in black lower case alphabets.

**(C) SVD:** SVD (Vertical derivative of equation (2.5.4)) of CBM (RTP and RTE) grids are presented in figure 5.2. All source edges on CBM grid were imaged on the SVD of CBM (RTP) grid (Figure 5.2a). 2D and non-2D contacts (A1-A1, A2-A2, B1, B2, B3 and B4), major FS (C1-C1 and C2-C2) and minor FS at shallow depths were imaged as persistent low-amplitude SVD anomalies. Minor FS sources at greater depths were imaged indirectly as strings of discontinuous alternating anomalies, the trends and lateral extents of which correspond with sources on the input basement grids (Figures 4.2a and 4.2b). The frequency of occurrence of these aligned anomalies, as well as rate of change of these frequencies appear to be a useful tool for discriminating between highly dissected (faulted) and unfaulted terrains on the grid.

Only contacts (2D and non-2D) and the major E-W striking FS (C2-C2) were imaged directly on the the additive inverse ( $\times -1$ ) of SVD of CBM (RTE) grid (Figure 5.2b).<sup>5</sup> Also, only well isolated

<sup>5</sup> Additive inverse of SVD used to keep its features in phase with those on SVD of CBM (RTP) grid (Figure 5.2a).

E-W, NW-SE striking FS were indirectly imaged (by strings of discontinuous alternating anomalies, e.g., C1-C1, bb, cc, dd and hh) on the RTE grid. The combined effects of source depths and anomaly interference rendered subtle sources around B4 and below B2 invisible. Higher frequencies at locations labelled aa and bb indicate terrain characterised by shallower sources. The boundaries of these terrains correspond with transitions from fast to low rates of frequency changes.

The common benefits and/or problems of  $HGM_{(\Delta T)}$ , ASA and SVD-enhanced RTP and RTE versions of the CBM  $\Delta T$  grid can be summarised as follows:

- (1) On the CBM (RTP) grid, all major FS and contact (2D and non-2D) edges were well imaged at their correct locations. Weaker E-W and N-S striking FS were also reasonably imaged. The degree of resolution of minor FS edges reduced as depth of the FS increased. Edges of contacts persisted and were well resolved at great depths.
- (2) N-S striking FS and non-2D contact edges were not imaged at all on the CBM (RTE) grid. However, E-W and well isolated NW-SE trending FS and contact edges were well imaged. Also well imaged were the Northern and Southern E-W trending edges of non-2D contacts. Anisotropy-induced anomaly interference makes it difficult, if not impossible, to image subtle FS edges in their correct locations. Thus, FS location estimates in the NW quadrant and Western parts of the grid were totally unreliable. E-W, NW-SE and NE-SW edges of contacts persisted and were well resolved, even at great depths.

### 5.2.2 Phase-based methods.

The local wavenumber, LW (Equation (2.5.8)) and the horizontal magnitude of tilt angles,  $HGM_{(\theta)}$  (Equation (2.6.2)) are compared next. LW and  $HGM_{(\theta)}$  of CBM (RTP and RTE) grids are shown in figure 5.3. These methods are based on the local wavenumber (Verduzco et al., 2004), hence, are not discussed independently.

All 2D and non-2D contacts were correctly imaged on the both the LW and  $HGM_{(\theta)}$  of CBM (RTP) grid (Figures 5.3a and 5.3c, respectively). Like Tilt angles ( $\theta$ ), these methods depend on ratios between Cartesian derivatives, hence, are independent of susceptibility contrast,  $\delta k$  (and amplitudes of  $\Delta T$ ). Consequently, LW and  $HGM_{(\theta)}$  provided more detailed images of subtle FS on the CBM grid than previous methods (Section 5.2.1). The  $HGM_{(\theta)}$  of CBM (RTP) grid (Figure 5.3c) provided more detail of sources imaged on its LW equivalent (Figure 5.3a). However, some sources that were visible on the LW grid were invisible on the  $HGM_{(\theta)}$  grid. Examples include the outer edge of the unfaulted basin (labelled F1, SE of B3) as well as other FS sources (labelled F2 and F3, SW of B3) which were only visible on the LW grid (Figure 5.3a). This difference between LW and  $HGM_{(\theta)}$  resolution might be a consequence of interference between adjacent  $HGM_{(\theta)}$  anomalies (Pilkington, 2007).

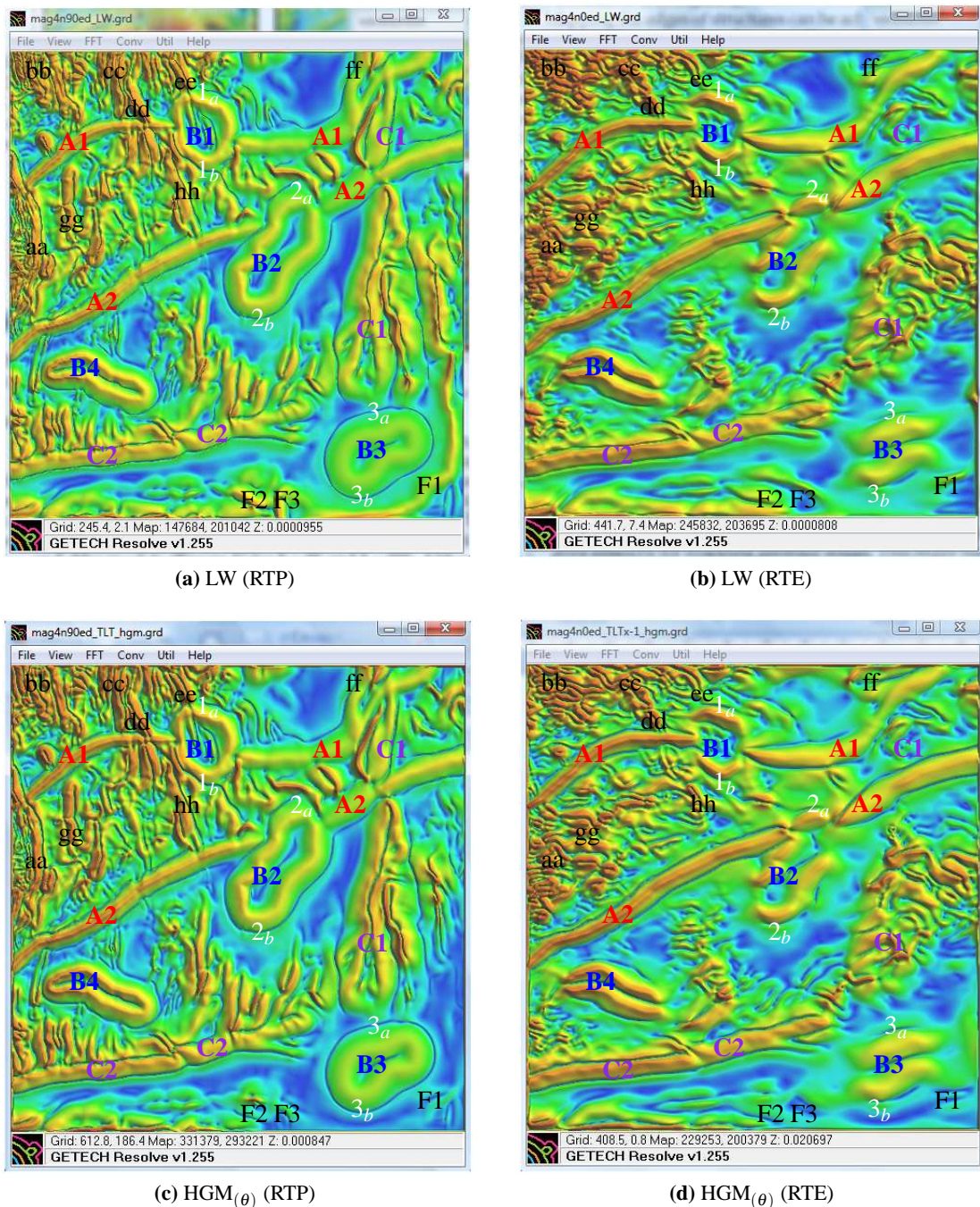


**Figure 5.3:** Local wavenumber (LW) and  $HGM_{(\theta)}$  of CBM (RTP and RTE) of  $\Delta T$  grids. Colour ranges on maps reflect function amplitudes: minima are cyan to deep-blue, intermediate amplitudes are greenish-blue to yellow; while maxima are orange, gold or saddle-brown in colour. 2D magnetic contacts (A1, A2) are labelled in red; intrusive magnetic bodies (B1, B2, B3 and B4) with non-2D contacts are labelled in blue; and fault scarps (C1 and C2) are labelled in blueish-violet. Other locations where differences occur between RTP and RTE grids are labelled in black lower case alphabets or white alpha-numeric codes. Locations of 2D and non-2D contacts from CBM (RTP and RTE) grids correlate well, but those for fault scarps correlate less. Observe also that sources marked F1, F2 and F3 in figures 5.3a and 5.3b were not imaged in figures 5.3c and 5.3d.

Although LW and  $HGM_{(\theta)}$  are independent of magnetisation and dip effects, for sources at RTP (Thurston & Smith, 1997, Verduzco et al., 2004, and Pilkington, 2007), interference effects due to RTE-induced anisotropy on the LW and  $HGM_{(\theta)}$  of CBM (RTE) grids (Figures 5.3b and 5.3d) show the methods to be affected by the horizontal magnetisation direction (For examples, compare locations labelled aa to hh, in black, on the RTP of these methods with their RTE equivalents). All 2D and non-2D contacts were correctly imaged on the both the LW and  $HGM_{(\theta)}$  of CBM (RTE) grids (Figures 5.3b and 5.3d, respectively). Similarly, well isolated NW-SE and NE-SW sources were well imaged (e.g., compare locations labelled dd and hh on RTP and RTE pair of maps). The N-S striking FS (C1-C1) was not directly imaged on both LW and  $HGM_{(\theta)}$  of CBM (RTE) grids. However, the presence of this and other N-S sources (e.g., labelled aa and gg) could be imprecisely inferred from linear N-S alignments of discrete E-W trending LW and  $HGM_{(\theta)}$  anomalies.

Primary maxima of LW and  $HGM_{(\theta)}$  of CBM (RTP and RTE) grids were also accompanied by secondary maxima, especially around non-2D contacts. These false maxima were not visible where anomalies between adjacent sources interfered. Examples occurred at locations labelled (in white) 1b, 2b and 3b on LW and  $HGM_{(\theta)}$  of CBM (RTP) grids. More of these maxima occurred on CBM (RTE) grids at locations labelled 1a, 1b, 2a, 2b, 3a and 3b.

### 5.2.3 Comparisons using profiles across RTP and RTE grids.

Additional comparisons between  $HGM_{(\Delta T)}$ , SVD, ASA, LW and  $HGM_{(\theta)}$  of CBM (RTP and RTE) grids were carried out using eight profiles with identifiers and orientations as shown in figure 5.4a. Profiles were overlaid on figure 4.8b to illustrate relationships between profiles and source types on the CBM grid. The distribution and general orientation of the profiles (reflected by the different profile colours in figure 5.4a) were: NW-SE (4 profiles); NE-SW (2 profiles); and E-W (2 profiles). Profiles were so orientated to intersect major CBM sources. I begin by comparing the amplitudes of the method-specific functions when applied to the CBM grids (Figure 5.4b). Because  $HGM_{(\Delta T)}$  and ASA of CBM (RTP and RTE) grids depend directly on  $\Delta T$  amplitudes and their first derivatives, profiles extracted from these grids show amplitudes that are several orders of magnitude larger than those from SVD, LW and  $HGM_{(\theta)}$  of CBM (RTP and RTE) grids (Figure 5.4b). Consequently, SVD amplitudes were multiplied by 1000, while LW and  $HGM_{(\theta)}$  amplitudes were multiplied by 100 to make them visible for comparison. The resulting profiles are presented in figures 5.5 and 5.6. Consequently, it is mainly the shapes and the widths of these functions that are compared.

Profiles show that all major sources, irrespective of strike, were imaged as peaks of functions of the RTP grid (Figures 5.5 and 5.6). However, only non-N-S, NE-SW, NW-SE and E-W striking sources were imaged on RTE grid. Examples include absence of peaks of functions for N-S striking FS located between 50 to 75 km along RTE profiles, relative to their RTP equivalents in figure 5.5a. Where only single ASA peaks occur over adjacent sources,  $HGM_{(\Delta T)}$ , LW and  $HGM_{(\theta)}$  peaks revealed the finer structural details at such locations. Clear examples occur be-

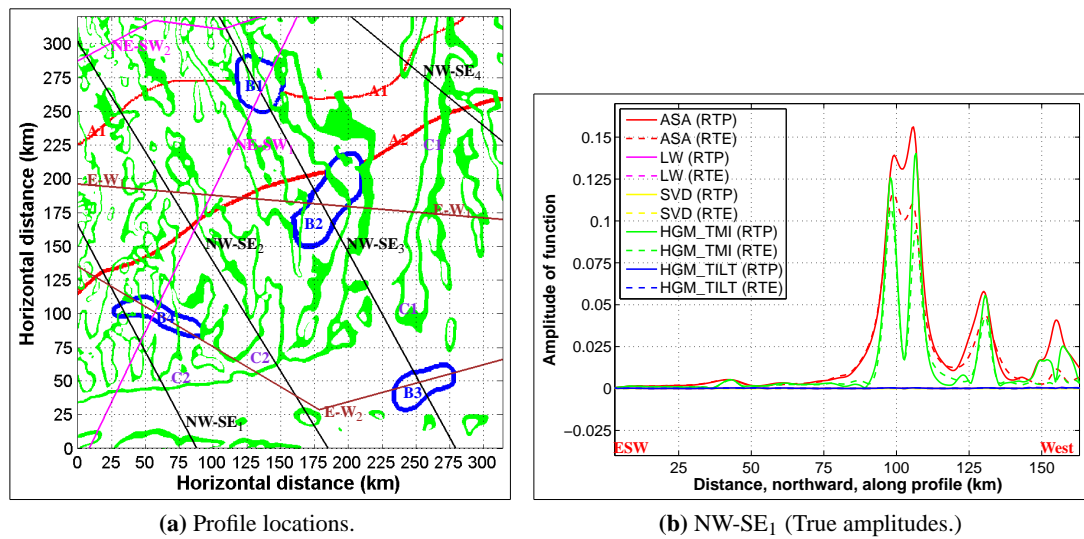


**Figure 5.4:** Location and orientation of profiles used to compare method-specific functions in figures 5.2, 5.1 and 5.3. Profiles are overlaid on the actual location of edges of CBM (RTP and RTE) grid anomaly sources (Figure 4.8b): fault scarps, FS (Green); 2D contacts (Red lines for A1 and A2); and non-2D contacts (Blue for intrusives B1, B2, B3 and B4). Profiles were colour-coded to reflect their orientation. SVD, LW and  $HGM_{(\theta)}$  amplitudes were very small compared with those of ASA and  $HGM_{(\Delta T)}$ , e.g., compare true amplitudes along profile NW-SE<sub>1</sub> (Figure 5.4b). Hence, SVD, LW and  $HGM_{(\theta)}$  amplitudes were enhanced by several factors: SVD $\times 1000$ ; LW $\times 100$ ; and  $HGM_{(\theta)}\times 100$ , for easy comparison in figures 5.5 and 5.6.

tween 120 to 175 km (Figure 5.5a), 75 to 100 km (Figure 5.5c), and in figure 5.5d. However, some of the finer details provided by these methods were false maxima, where sources were significantly isolated. For example 2D contacts (Labelled A1 and/or A2) were flanked by smaller maxima (Figures 5.5a, 5.5b, 5.6a, and 5.6d).

Because of their small amplitudes, false LW and  $HGM_{(\theta)}$  maxima were not obvious where high susceptibility sources were juxtaposed with FS. An example occurs between 135 and 155 km (Figure 5.6c). However, very high amplitude false maxima resulting from interference between adjacent false maxima dominated locations where FS were closely spaced. Examples includes locations labelled gg (Figure 5.5a), ff (Figure 5.5d), hh (Figure 5.6a) as well as bb, cc, ee (Figure 5.6b).

Where profiles cut across 2D and non-2D contacts, they were dominated by  $HGM_{(\Delta T)}$  and ASA amplitudes. Since  $HGM_{(\Delta T)}$  and  $HGM_{(\theta)}$  peaks were associated with locations of these isolated edges on grids (See location labelled B4 and A2 in figure 5.5a), the minimum width of contact-like edges may be determined from inflection points of these functions.<sup>6</sup> Maximum widths of such edges may similarly be obtained from inflection points of the ASA. Slopes of  $HGM_{(\Delta T)}$ , ASA and  $HGM_{(\theta)}$  were generally steeper for RTP grid than RTE grid (Figures 5.5a and 5.5c). Consequently, widths (or lengths) obtained from RTP grids are expected to be narrower (or shorter) than RTE equivalents.

<sup>6</sup>or length, depending on profile direction, relative to source strike.

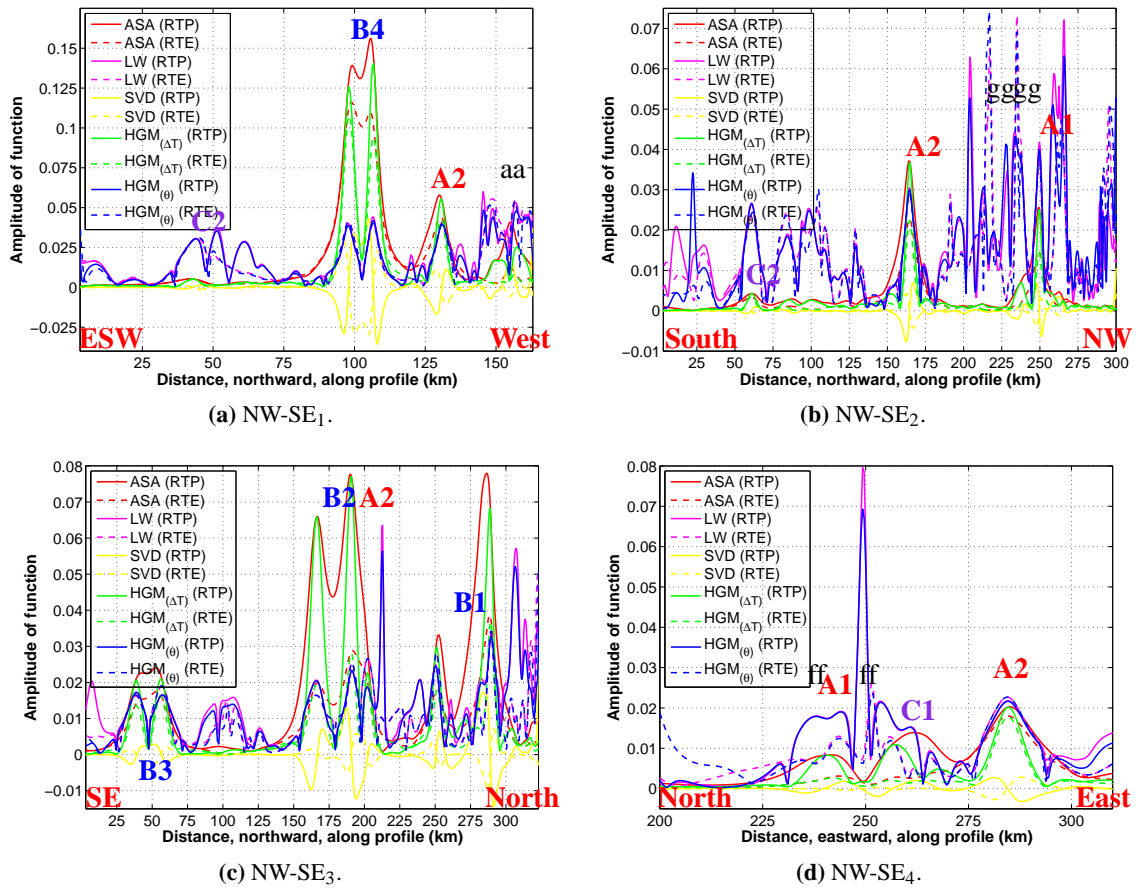


**Figure 5.5:** NW-SE oriented profiles of method-specific special functions of CBM (RTP and RTE) grids. NW, SE and ESW, respectively, represent NorthWest, SouthEast and East of SouthWest, of the variously transformed CBM (RTP and RTE) grids. Profiles are shown in figure 5.4a. Actual cardinal direction of profile on the grids are shown at the bottom right and left corner of each figure.

### 5.3 Location estimates.

The  $HGM_{(\Delta T)}$ , ASA, LW and  $HGM_{(\theta)}$  are usually at their maximum (peak) directly above or very close to locations of well isolated, vertical 2D edges, when obtained from RTP datasets (Phillips, 2000; Pilkington, 2007; Pilkington & Keating, 2004). It is the inflection points of the SVD, on the other hand, that trace these edge locations on RTP datasets (Wickerham, 1954, Miller & Singh, 1994). Since, Tilt angles ( $\theta$ ) of RTE (Section 4.3.2) and SVD of RTE (Section 5.2.1) are mainly additive inverses of their RTP equivalents, the RTP maxima or inflection point principle was extended to the applicable special function(s) of the CBM (RTE) grids. Hence, estimates of source edge locations on CBM (RTP and RTE) grid have been extracted from the SVD,  $HGM_{(\Delta T)}$ , ASA, LW, and  $HGM_{(\theta)}$  grids in figures 5.1 to 5.3. These edge location grids are shown in figure 5.7. For easy comparison of RTP and RTE estimates from each method, each grid shown in figure 5.7 presents locations obtained from RTP grid (in red) and RTE grid (in blue) using the specified method.

SVD location estimates were extracted using the SVD=0 contour (Figure 5.7a), while maxima

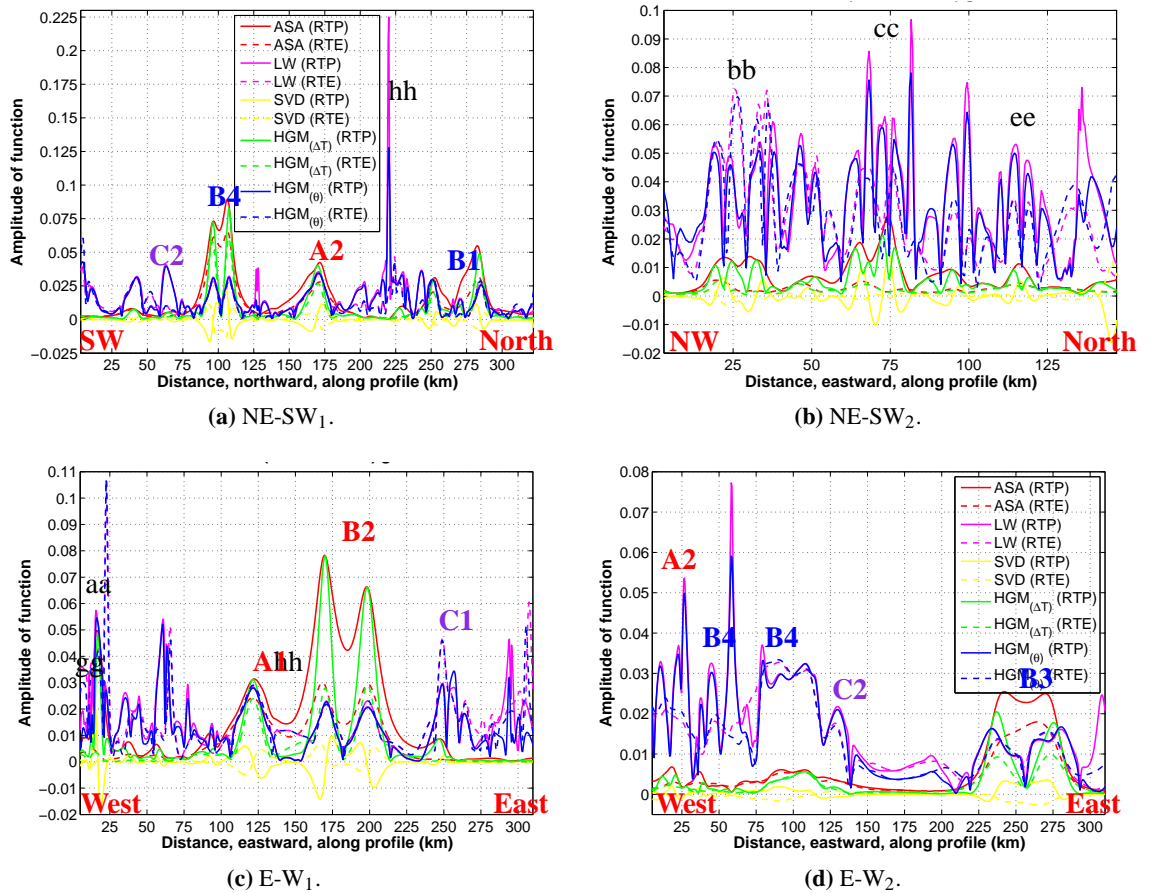


**Figure 5.6:** NE-SW and E-W oriented profiles of method-specific special functions of CBM (RTP and RTE) grids. W, E, NW, NE and SW, respectively, represent West, East, NorthWest, NorthEast and SouthWest, of the variously transformed CBM (RTP and RTE) grids. Profiles are shown in figure 5.4a. Actual cardinal direction of profile on the grids are shown at the bottom right and left corner of each figure. Legend is the same for all figures.

locations were effectively traced from  $HGM_{(\Delta T)}$ , ASA, LW, and  $HGM_{(\theta)}$  of CBM (RTP and RTE) grids using Blakely & Simpson (1986)'s method of local maxima detection (Section 2.5.2). To minimise uncertainties and declutter traces, only locations at which two or more of Blakely & Simpson (1986) inequalities were satisfied, were retained from these grids (Figures 5.7b, 5.7c, 5.7d and 5.7e).

### 5.3.1 Comparison between estimates from RTP and RTE grids.

Location estimates extracted from CBM (RTP and RTE) grids (Figure 5.7) will now be quantitatively compared, using Spearman's rank-order correlation coefficient,  $r_s$  (Equation (4.5.1); Press et al., 1992) and coefficient of determination ( $CoD = r^2$  in %).<sup>7</sup> The main objective here was to highlight any differences between estimates from RTP and RTE grids, in terms of anomaly trends and correlation statistics (correlation coefficient,  $r$  and coefficient of determination,  $CoD = r^2\%$ ). For each method, the total number of edges estimated from the CBM (RTP) grid ( $N_1$ ), the CBM (RTE) grid

<sup>7</sup>Statistical significance,  $\rho=0.05$ , i.e., confidence interval of 95%. The inherent assumption is that the RTP and RTE datasets being compared have equal means (Press et al., 1992, p.616).

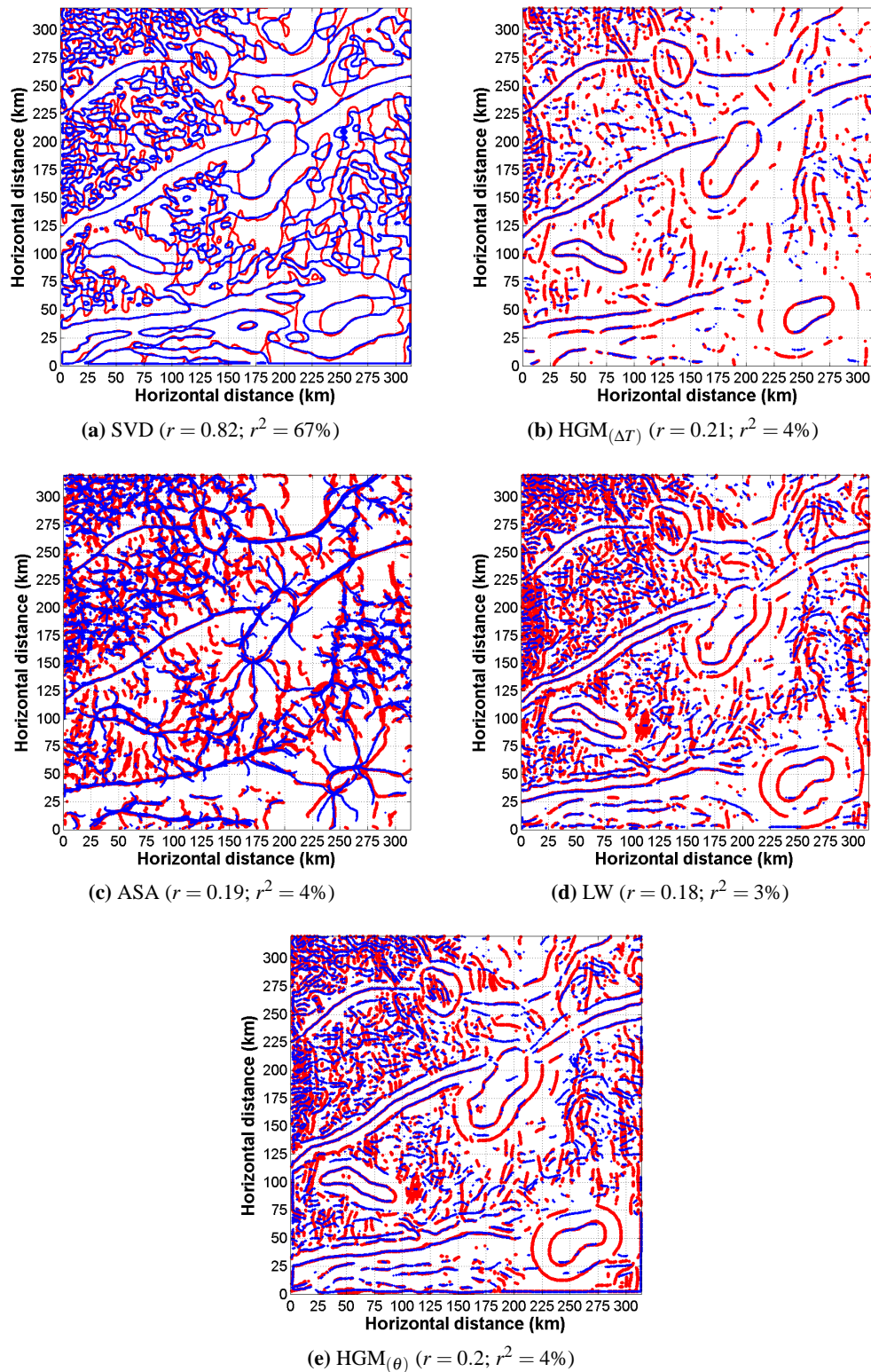


**Figure 5.7:** Comparisons between location estimates derived from various derivatives of the CBM (RTP and RTE) grids:  $\text{HGM}_{(\Delta T)}$  and  $\text{HGM}_{(\theta)}$ , respectively, represent the absolute value or magnitude of the horizontal gradient of the  $\Delta T$  and local wavenumber (LW); SVD and ASA represent the second vertical derivative and analytic signal amplitude. Locations from the CBM (RTP) grid are in red, while those from the CBM (RTE) grid are shown in blue. More locations were obtained from RTE than RTP grid (Table 5.1). However, many RTE locations correspond well with RTP locations, although not reflected in the correlation statistics  $r$  and  $r^2$  quoted for each figure.

( $N_2$ ), the number of corresponding (equivalent) RTP and RTE edge locations (Degree of freedom,  $N$ ) used in each correlation, and results obtained are presented in table 5.1.

**Table 5.1:** Correlation statistics for location estimates from CBM (RTP or RTE) grids.

Method	Estimated locations for:		Equivalent locations ( $N$ )	$\frac{N_2}{N_1}$ (%)	$\frac{N}{N_1}$ (%)	$\frac{N}{N_2}$ (%)	$r^2$	CoD (%)
	RTP ( $N_1$ )	RTE ( $N_2$ )						
SVD	407937	408341	407652	100.09	99.93	99.83	0.82 <sup>a</sup>	67
HGM <sub>(<math>\Delta T</math>)</sub>	9253	5818	1879	62.88	20.31	32.3	0.21 <sup>a</sup>	4
	406963	388750	388750	95.52	95.52	100	- <sup>b</sup>	-
ASA	31036	26968	6541	86.89	21.08	24.25	0.19	4
	406963	406963	406963	100	100	100	-	-
LW	18478	13483	2362	72.97	12.78	17.52	0.18	3
	406963	406334	406334	99.85	99.85	100	-	-
HGM <sub>(<math>\theta</math>)</sub>	17936	15763	2829	87.88	15.77	17.95	0.2	4
	406963	406334	406334	99.85	99.85	100	-	-

<sup>a</sup> Approach 1: Raw data from Blakely & Simpson (1986)'s maxima score varied from 1 to 4, hence a mean and its residuals exist for RTP and RTE estimates. Therefore,  $r$  and  $r^2$  could be computed. Approach 1 yields minimum  $N_1$ ,  $N_2$  and  $N$ .

<sup>b</sup> Approach 2: Assigned a constant value, 4, to all estimates from Approach 1, irrespective of actual score. Means exist for both RTP and RTE estimates, but residuals do not. Hence,  $r$  and  $r^2$  do not exist when approach 2 is used. Approach 2 yields accurate  $N_1$ ,  $N_2$  and  $N$ .

Visual inspection of the SVD estimates (Figure 5.7a) suggested generally poor correlation. However, an  $r^2 = 0.82$  and  $CoD = 67\%$  indicates strong, positive correlation between RTP and RTE estimates (Table 5.1). SVD estimates of the Western and Eastern curved (non-2D) edges of intrusive bodies were extended further Westward and Eastward by about 50% of the radius of curvature of the actual edge, compared with extensions of 100% in  $\theta$  estimates. The resulting lower rate of anomaly interference on SVD of RTE compared with  $\theta$  of RTE explains the significantly higher correlation for SVD (CoD of 67% between  $N=407652$  equivalent) RTP and RTE location estimates (Table 5.1). On the other hand, the quality of peaks detected from HGM<sub>( $\Delta T$ )</sub>, ASA, LW and HGM<sub>( $\theta$ )</sub> of CBM (RTP and RTE) grids varied randomly (from 1 to 4; Blakely & Simpson, 1986). Hence, the medium-good visual correlations exhibited by RTP and RTE estimates from these maxima-based methods (Figures 5.7b, 5.7c, 5.7d and 5.7e) were not confirmed by the generally low correlation coefficients,  $r \leq 0.25$  and  $r^2 \leq 4\%$  computed for these RTP and RTE estimates. These statistics were difficult to explain since these RTP and RTE estimates seemed to be well correlated visually. The SVD, thus appeared to outperform the other methods in terms of locating edges of RTP and RTE estimates.

To verify discrepancies in qualitative and quantitative correlations between RTP and RTE estimates derived from maxima-based methods, I assigned a constant score to all location estimates from the CBM (RTP and RTE) grids. I referred to this approach as **Approach 2**, while the previous comparisons between RTP and RTE estimates derived from Blakely & Simpson (1986) was referred to as **Approach 1**. The main difference between these approaches were as follows:

- (i) Data used in approach 1 were Blakely & Simpson (1986) maxima scores, which varied from 1 to 4. Since the resulting RTP and RTE datasets varied, each dataset had a mean and set of residuals. Therefore,  $r$  and  $r^2$  could be computed. This approach yielded minimum  $N_1$ ,  $N_2$

and  $N$ .

- (ii) Since approach 2 assigned a constant value of 4, irrespective of the actual [Blakely & Simpson \(1986\)](#) maxima score, to RTP and RTE location estimates, each dataset had a mean, but no residuals (since datasets did not vary). Consequently,  $r$  and  $r^2$  did not exist for this approach. However, approach 2 yielded more accurate  $N_1$ ,  $N_2$  and  $N$  than approach 1. Higher  $N$  from approach 2 confirm the existence of good to excellent correlations between RTP and RTE estimates.

Results obtained from approaches 1 and 2 for RTP and RTE estimates from the  $HGM_{(\Delta T)}$ , ASA, LW and  $HGM_{(\theta)}$  of CBM grids are also presented in table [5.1](#). While results from approach 1 were presented on top, those from approach 2 were presented below. More estimates were obtained from RTP than RTE grid from approach 1. Approach 2 showed that even where good visual correlation between RTP and RTE estimates existed, RTP estimates were denser than their RTE equivalents (Table [5.1](#)).

In conclusion, results showed medium to strong positive correlations between RTP and RTE location estimates from SVD,  $HGM_{(\Delta T)}$ , ASA, LW and  $HGM_{(\theta)}$  methods. Like correlations between estimates from  $\theta$  of CBM (RTP and RTE) grids, correlations between estimates obtained from these grids, using these methods increased as the density of NNW-SSE and NNE-SSW (or near-N-S) striking sources reduced.

### 5.3.2 Strategies for estimating location of source edges from RTE datasets.

Edges estimated from the CBM (RTP or RTE) grid are co-presented in figure [5.8](#) for initial comparison. Estimates from the CBM (RTP) grid are compared in figure [5.8a](#), while estimates from the CBM (RTE) grid are presented in figure [5.8b](#). Estimates were colour-coded for easy identification of the method used, and plotted in the following order: ASA (Black); LW (Red);  $HGM_{(\theta)}$  (Green);  $HGM_{(\Delta T)}$  (Yellow); SVD (Pink); and  $\theta$  (Brown, dashed line). ASA and other maxima-based estimates were plotted first because these also included traces from rugose, sloping surfaces of anomalies, which were unrelated to and directed at various angles away from actual source edges. SVD and  $\theta$  estimates were not so affected (Figure [5.7](#)). Cleaner equivalents of figure [5.8](#) that exclude ASA estimates are presented in appendix [D](#) (Figure [D.1](#)).

Anomalies on the CBM grid were mainly sourced from NE-SW and NW-SE striking 2D contacts (labelled A1-A1 and A2-A2), variously shaped and oriented intrusives or 3D sources (labelled B1, B2, B3 and B4) with non-2D contact-like edges, as well as two major en-echelon fault scarps (FS); one striking N-S (labelled C1-C1), and the other striking E-W (labelled C2-C2). FS were locally discontinuous, in general.

Except where anomalies from these sources interfered, estimated locations of contacts and well

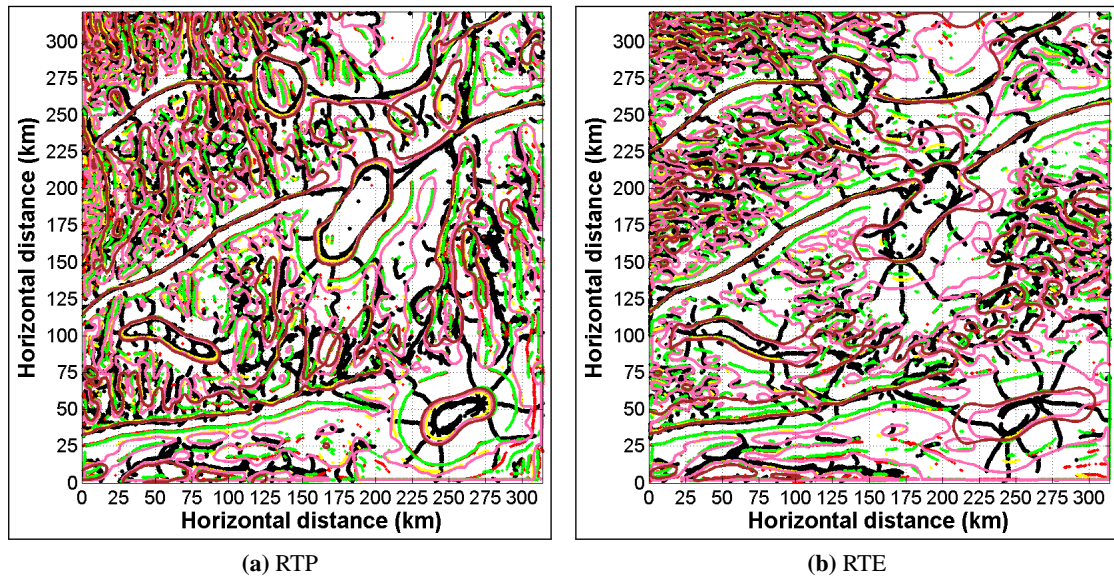


**Figure 5.8:** Comparisons between all estimates of edge locations from CBM (RTP) grid (BMgridALLloxRTP) or CBM (RTE) grid (BMgridALLloxRTE). Estimated location plots are colour-coded for easy identification of the method used:  $HGM_{(\Delta T)}$  (Yellow); SVD (Pink); ASA (Black); LW (Red);  $\theta$  (Brown, dashed line); and  $HGM_{(\theta)}$  (Green). Because of the wider spread of ASA estimates, they were plotted first, followed by estimates from LW,  $HGM_{(\theta)}$ ,  $HGM_{(\Delta T)}$  and SVD. Estimates from  $\theta$  were included for comparison. Figure D.1 is equivalent to this figure, but it excludes ASA estimates.

isolated NE-SW and NW-SE striking minor FS, as well as E-W striking FS from both CBM (RTP and RTE) grids exhibited excellent visual correlation, irrespective of the method used (Figure 5.8). Consequently, these, as well as the isometric 3D and rectangular intrusives with 3D edges can be confidently interpreted as tracing actual source edge locations on RTE grids. The LW and  $HGM_{(\theta)}$  mainly traced the Northern and Southern edges of 3D sources on the RTE grid. Like  $\theta$ , both  $HGM_{(\Delta T)}$ , ASA and SVD traced all edges of 3D sources. However, ASA edges were reliable only where 3D sources had constant or near-constant planar cross-section. Otherwise ASA traces represented only a fraction of edges of 3D sources. Correspondences between zero contours of SVD and  $\theta$  of RTE datasets confirmed the presence of sources at their correct orientations. For 3D sources (non-2D edges), any N-S dimensions between SVD and  $\theta$ -located edges were accurate. These may be used to estimate the actual planar dimensions of 3D sources. 3D edges of isolated rectangular intrusives were located inward of the SVD estimate by a distance equal to its radius of curvature. These edges were located inward of the  $\theta$  estimate by a distance approximately equal to twice its radius of curvature.

Intersecting edges were better imaged on the RTE than the RTP grid, using these methods. Examples occur around grid nodes (115,272) and (212,212) in figure 5.8. Such differences in source edge continuity were attributed to local alignment of RTE-induced discrete, E-W striking dipolar anomalies on RTE grids.

Few or no correlations were observed between RTP and RTE locations where near-N-S trending FS (C1-C1) or minor FS occurred (Figure 5.7). Linear stacks of short wavelength E-W trending maxima of  $HGM_{(\Delta T)}$ , ASA and  $HGM_{(\theta)}$  indicated the presence of these near-N-S striking edges

on RTE grids. They were also inferable from isolated linear frequency changes across SVD of RTE grids. Similarly located trends on both the LW and  $HGM_{(\theta)}$  will be used to confirm these sources and map more sources with near-N-S and/or other trends that were not obvious on the  $HGM_{(\Delta T)}$ , SVD and ASA of RTE grids. Minimising uncertainties by removing peak locations with certain [Blakely & Simpson \(1986\)](#)'s score while tracing maxima locations appear to bias location estimates in favour of wavelengths that are generally longer than those that characterise locations of N-S sources. For example, few of the high frequency E-W peaks associated with the N-S striking FS (C1-C1) were retained in RTE estimates shown in figures [5.7b](#), [5.7d](#) and [5.7e](#), for which a score of 2 or more satisfied inequalities was used. To effectively map locations of near-N-S sources by inference, from RTE grids, estimates need to include all location traces (score 1 to 4 of [Blakely & Simpson, 1986](#)).

Not all minor FS were resolvable, since the subtle anomalies associated with these sources were suppressed within the dynamic range of signals on the grid. Amplitude-based methods ( $HGM_{(\Delta T)}$  and ASA) were ineffective in resolving subtle anomalies from the CBM (RTP and RTE) grids, while phase-based methods like LW and  $HGM_{(\theta)}$  were effective in tracing subtle anomalies. However, these methods are sensitive to noise and interference effects, especially since estimates from these methods also include secondary (false) maxima locations (Figures [5.7](#) and [5.8](#)).  $HGM_{(\Delta T)}$  estimates were similarly characterised by false maxima. Hence, only  $HGM_{(\Delta T)}$ ,  $HGM_{(\theta)}$ , ASA and LW estimates that are coincident or closest to  $\theta$  and/or SVD estimates should be treated as certain and retained. RTE estimates that do not meet this criterion should be treated as false edges (Figure [5.8](#)), and not be included in the final interpretation.

Since curvilinear FS edges in the Western part of CBM grid were better imaged by  $HGM_{(\Delta T)}$  and ASA of CBM (RTE) grid than their LW and  $HGM_{(\theta)}$  equivalents, comparisons between transformed RTP and RTE of  $\Delta T$  grids or location estimates from these grids should commence with ASA and  $HGM_{(\Delta T)}$ , then SVD and  $\theta$ , and finally LW and  $HGM_{(\theta)}$ . Each set of estimated locations should first be overlain on its source grid, to establish relationships between trends, taking notes of any near-N-S trends, where present.

### 5.3.3 Structure maps derived from CBM (RTP and RTE) grids.

Maps have been generated for structures which could be mapped with certainty from the CBM (RTP and RTE) grids (Figure [5.9](#)), using strategies outlined in section [5.3.2](#). While structures mapped from the CBM (RTP) grid are shown in black, corresponding structures from the CBM (RTE) grid are shown in red (Figure [5.9a](#)). For clarity, RTE structures are also presented separately in figure [5.9b](#). Each structure map is underlain by an image of figure [4.9a](#), which shows the actual locations and depths at or close to CBM source edges.

Mapped structures in figure [5.9](#), represent locations of magnetic susceptibility contrasts ( $\delta k$ ), while arrows (Green or orange-coloured) point across structures in directions of decreasing  $k$  (from

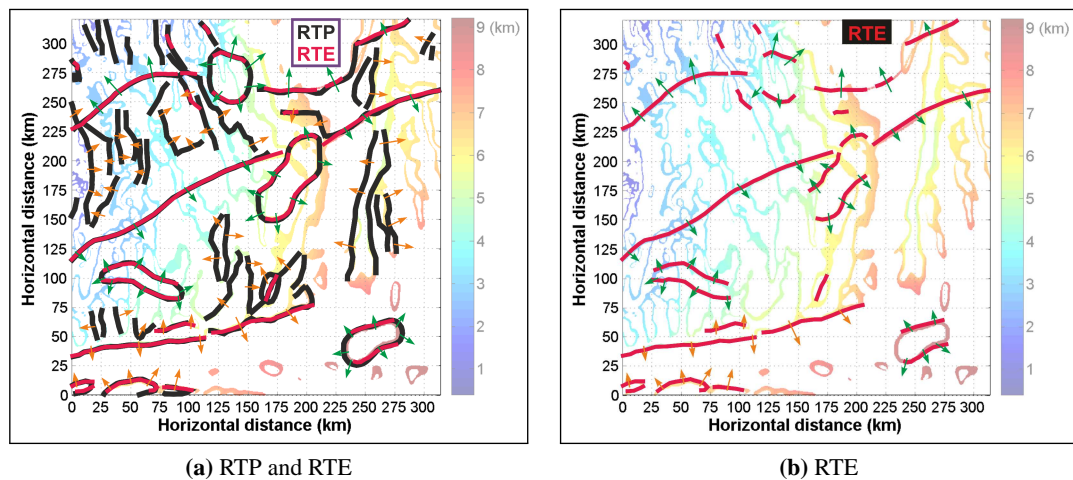


**Figure 5.9:** Structure maps derived from CBM (RTP and/or RTE) grids, overlaid on an image of location and depths at or close to actual CBM source edges (Figure 4.9a). Depth scales apply to locations only. While edges with strike in all directions (Shown in black) were mapped with certainty from the RTP grid, only E-W, NW-SE and NE-SW striking edges (Shown in red) could be mapped with any certainty from the CBM (RTE) grid. Arrows point across edges, from high to lower susceptibility bodies. Green or orange-coloured arrows indicate edges with large or small susceptibility contrasts, respectively. Underlying map image show that several subtle edges were not mapped from the RTP grid (Figure 5.9a). Even more of these edges were not mapped from the RTE grid (Figure 5.9b).

higher to lower  $k$  bodies). While green-coloured arrows represent structures with large  $\delta k$ , orange-coloured arrows represent structures with small  $\delta k$ .

Structures on the RTP grid (Black-coloured in figure 5.9a) were easily mapped by comparing the co-presented location estimates shown in figure 5.8a.<sup>8</sup> On the other hand, the red-coloured (RTE) structures in figure 5.9a were obtained from corresponding RTP and RTE location estimates from the ASA,  $HGM_{(\Delta T)}$ , LW,  $HGM_{(\theta)}$  and "Tilt-Depth" methods (Figure 5.7). These equivalent locations are shown for the various methods in appendix D (Figures D.3 to D.7).

Comparisons between the underlying map image and the RTP structure map in figure 5.9a show that several fault scarp (FS) edges could not be mapped from the CBM (RTP) grid. This is mainly because the subtle anomalies from these sources were masked (swamped) by the larger amplitude anomalies on the grid. Even more of these FS edges could not be mapped from the CBM (RTE) grid (Figure 5.9b), due to the combined effect of local, anisotropy-induced anomaly interference and subtle anomaly masking.

Practically every significant anomaly-generating structure could be mapped from the CBM (RTP) grid, irrespective of their strike and composition (Figure 5.9a). However, only E-W, NW-SE and NE-SW striking structures could be mapped with certainty from the CBM (RTE) grid (Figure 5.9a). Linear and curved edges with N-S strikes cannot be mapped from RTE grids. Also, NNW-SSE, NNE-SSW and North $\pm 20^\circ$  striking structures are difficult to map from RTE grids,

<sup>8</sup>Location estimates from maxima-based methods like ASA,  $HGM_{(\Delta T)}$ , LW and  $HGM_{(\theta)}$  were first decluttered to ease structural mapping, by selectively removing class 1 maxima from these estimates. See appendix D (Figure D.2), for example.

with certainty, especially where anomalies interfere. Although these RTE observations applied to sources of all compositions, spatial relations between anomalies and comparisons between locations estimated from various methods may provide a basis on which other less certain structures may be inferred from RTE grids (Section 5.3.2).

## 5.4 Depths estimated from all source locations using ASA and LW methods.

Depths of CBM (RTP and RTE) grids sources have been estimated using the ASA and LW methods. ASA and LW estimates were obtained by applying equations (2.5.7) and (2.5.8d) to ASA and LW grids, respectively. ASA estimates are shown in figure 5.10, while LW estimates are shown in figure 5.11. ASA estimates were slightly easier than LW estimates. Since LW estimates are derived from the inverse of peak LW amplitudes (Equation 2.5.8d), amplitudes close to zero (*singularities* of Fairhead et al., 2004) result in larger than desired depth estimates. Hence, maxima locations corresponding to singularities and/or spurious peaks due to false (secondary) maxima had to be removed (masked out) from LW grids (Figures 5.3a and 5.3b) before deriving LW depth estimates. This required the specification of a cut-off LW value. By trial and error, I found this value ( $m3$ ) using an algorithm comprising the minimum mean value and the standard deviation on each LW grid (Equation 5.4.1).

$$m1 = \min(\text{mean}(gr, 1)) + 1.5 \times \min(\text{std}(gr, 0, 1)) \quad (5.4.1a)$$

$$m2 = \min(\text{mean}(gr, 2)) + 1.5 \times \min(\text{std}(gr, 0, 2)) \quad (5.4.1b)$$

$$m3 = \text{mean}(m1 + m2) \quad (5.4.1c)$$

where:  $gr$  represents the grid of LW peaks;  $\min(\text{mean}(gr, 1))$  and  $\min(\text{mean}(gr, 2))$  refer to the minimum (min) average (mean) value along the  $x$  (1<sup>st</sup>) and  $y$  (2<sup>nd</sup>) grid dimensions, respectively;  $\min(\text{std}(gr, 0, 1))$  and  $\min(\text{std}(gr, 0, 2))$  refer to the minimum standard deviation (std) along the  $x$  (1<sup>st</sup>) and  $y$  (2<sup>nd</sup>) grid dimensions, respectively; and  $m3$  refers to the cut-off LW peak value used to mask singularities and spurious peaks in  $gr$ .

Two temporary grids in which LW estimates below  $m3$  were treated as singularities and/or spurious LW peaks and were, thus, masked out were generated from the LW of RTP and RTE grids. Only LW (RTP or RTE) estimates at locations that correspond with unmasked values on each temporary grid were retained. The resulting masked/windowed CBM (RTP and RTE) grids are presented in appendix D (Figure D.8). LW depth estimates (Figure 5.11) were obtained from maxima of these windowed LW (RTP and RTE) grids.<sup>9</sup>

Maximum LW estimates (Figure 5.11) were slightly less than that of actual BM basement depths

<sup>9</sup>Locations of LW maxima used for depth estimates (Figure 5.11) were, thus, fewer those shown in figure 5.7d.

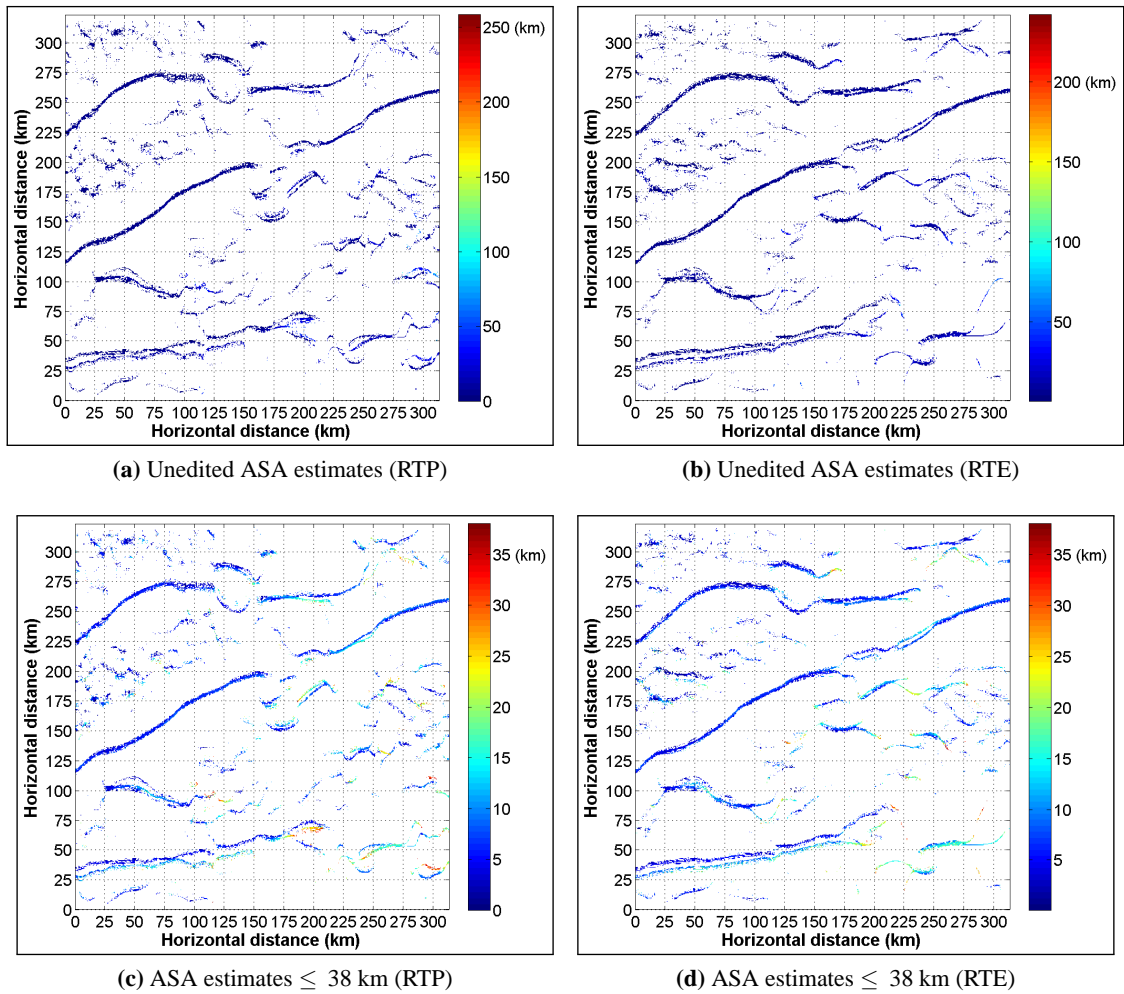


**Figure 5.10:** Unedited and edited ASA estimates from CBM (RTP and RTE) grid sources. Estimated depths are for source edges shown in figure 4.8b. Maximum of unedited ASA estimates were up to 250 km (Figures 5.10a and 5.10b), more than  $20 \times$  the maximum of actual BM basement depths (Figure 4.9b). Estimates were edited using maximum of  $\theta = \pm 27$  estimate, 38 km (Figures 4.14c and 4.14d).

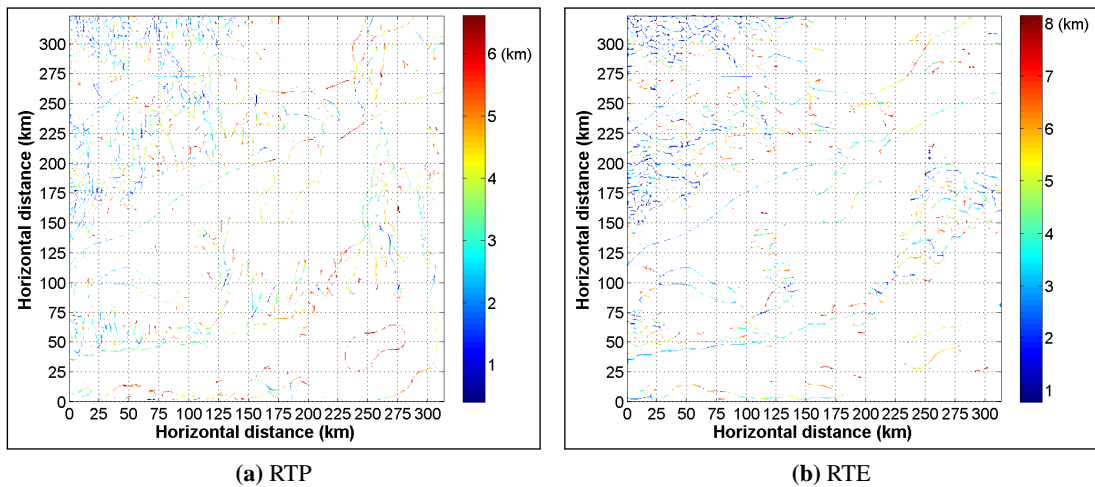


**Figure 5.11:** LW estimates from CBM (RTP and RTE) grid sources. Estimated depths are for source edges shown in figure 4.8b. LW estimates may be deeper for some shallow sources (Compare estimates for sources in NW of CBM grid and actual depths on basement depth grid in figure 4.2a). Maximum LW estimates were within the range of actual depths of BM sources (Figure 4.9b).

(Figure 4.2a), while maximum ASA estimates (Figures 5.10a and 5.10b) were more than  $20 \times$  that of the actual basement depths. However, colour-bars in figures 5.10a and 5.10b suggest ASA estimates to be mostly  $\leq 50$  km. For easy comparison with “Tilt-Depth” method estimates, ASA estimates exceeding the maximum of  $\theta = \pm 27$  estimate, 38 km (Figures 4.14c and 4.14d) were removed (Figures 5.10c and 5.10d). This is well justified, since the 2D mean (average mean) of ASA estimates from CBM (RTP and RTE) grids were 32.09 and 37.03 km, respectively.

Mean average LW estimates of CBM (RTP and RTE) grids were 5.92 and 7.13 km, respectively (Figure 5.11). LW estimates for some shallow sources (NW of grid) were deeper than shown on actual basement depth (NW of figure 4.2a). For  $\theta = \pm 27$  estimates from CBM (RTP and RTE) grids, see appendix C (Figure C.8). The distribution of these estimates will be examined below.

#### 5.4.1 Distributions of ASA and LW estimates compared with actual basement depths.

In this section, I compare composite histograms of ASA or LW estimates with that of actual depths of edges of all BM sources (Figure 4.9b). Where necessary, histograms were colour-coded to reflect source-types in figure 4.8b, at a constant class size of 200 m. The shapes and spreads of these histograms, as well as related statistics:<sup>10</sup> mean (*Av.*), standard deviation (*S.D.*), and coefficient of variation (*CoV*); were used to compare them. Comparisons between distributions did not take locations of estimates into account. Distributions of ASA, LW and  $\theta = \pm 27$  depths estimated from CBM (RTP and RTE) grids are presented as histograms, for comparison, in figure 5.12. Histograms of ASA estimates (Figure 5.12a) were obtained from the ASA estimate grids (Figures 5.10a and 5.10b). These histograms were significantly skewed to the right, with infrequent outliers dominating the  $\geq 50$  km range. Since estimates are to be compared with  $\theta = \pm 27$ -based “Tilt-Depth” estimates, outliers and estimates exceeding the maximum of  $\theta = \pm 27$  estimate, 38 km (Figures 5.12d, 4.14c and 4.14d) were removed from ASA estimates (Figures 5.10a and 5.10b). Figures 5.10c and 5.10d presented grids of edited ASA estimates, but their histograms are presented in figure 5.12c.

The average ASA depth was 11 km for the RTP grid and 9.7 km for the RTE grid. These averages exceed the maximum actual depth of CBM sources (Figure 4.9a). Equivalent statistics for these grids using the LW method were 3.8 and 4.4 km, while they were 5 and 11.2 km for the  $-27 \leq \theta \leq 27$  method. While averages for LW estimates from RTP and RTE grids, and  $-27 \leq \theta \leq 27$  estimates from RTP grid were well within the range of actual depth of CBM sources (Figure 4.9a),  $-27 \leq \theta \leq 27$  estimates from RTE grid exceed the maximum actual source depth. With standard deviation (*S.D.*) of 1.4 km (RTP) and 1.8 km (RTE), LW estimates were less dispersed than ASA estimates, which had *S.D.* of 11.4 km (RTP) and 8.5 km (RTE). These statistics and the associated *CoV* are shown on the histograms in figure 5.12. A summary comparing the number of estimates obtained by each method from these RTP and RTE grids (Figure 5.12) are presented in table 5.2.

<sup>10</sup>Introduced in section 4.4.

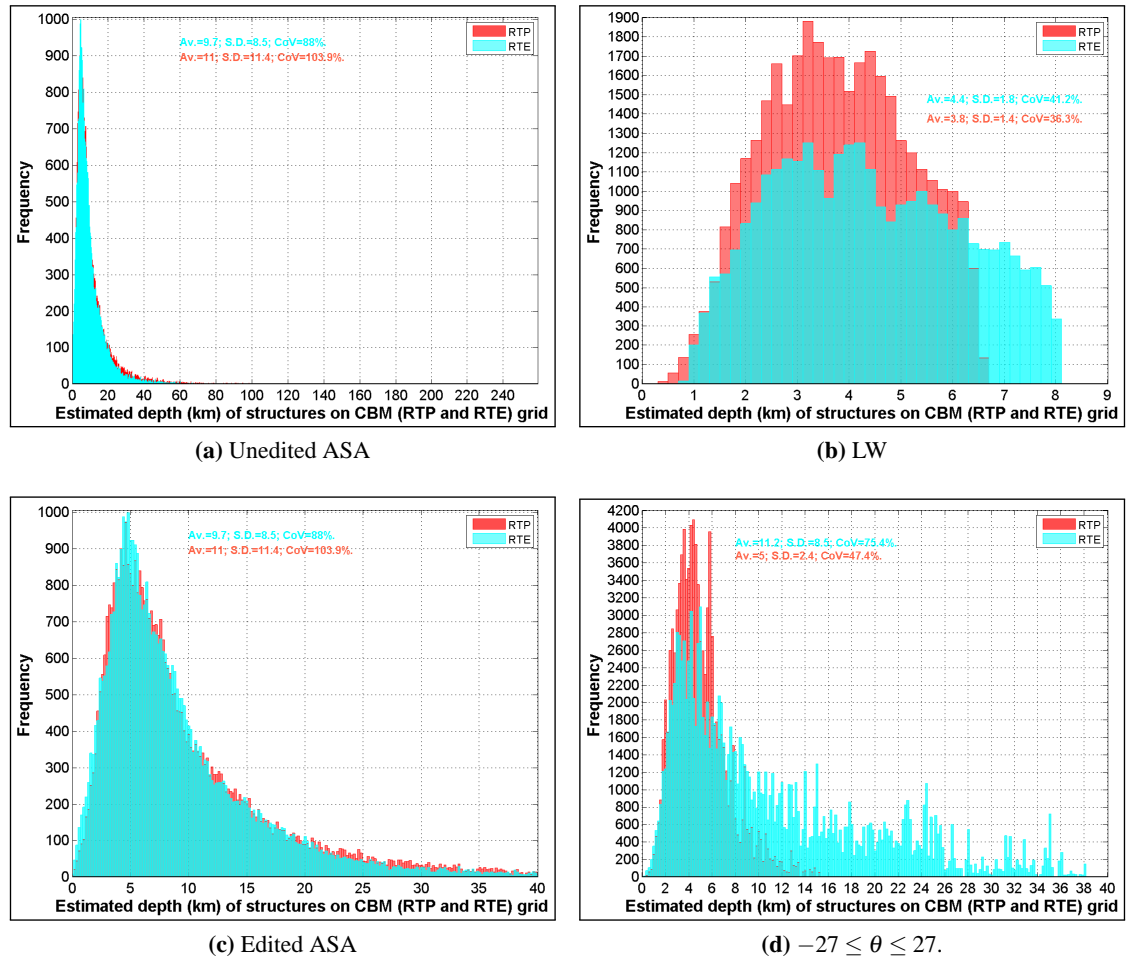


**Figure 5.12:** Histograms for ASA, LW and  $-27 \leq \theta \leq 27$  estimates of source depths from RTP and RTE grids. Histograms of unedited ASA estimates (Figures 5.12a) were mainly skewed to the right, with infrequent outliers dominating the 50-250 km range. These ASA outliers were removed using the maximum of  $-27 \leq \theta \leq 27$  depth estimates (38 km). The distribution on the edited ASA grids (Figures 5.10c and 5.10c) are shown in figure 5.12c. Histograms of LW estimates (Figure 5.12b) were simpler, without any outliers. They show the range of LW estimates from CBM (RTE) grid to be wider than equivalents from the CBM (RTP) grid. Figures 5.13 and 5.14 present detailed, source-type based histograms derived from figures 5.12c and 5.12b.

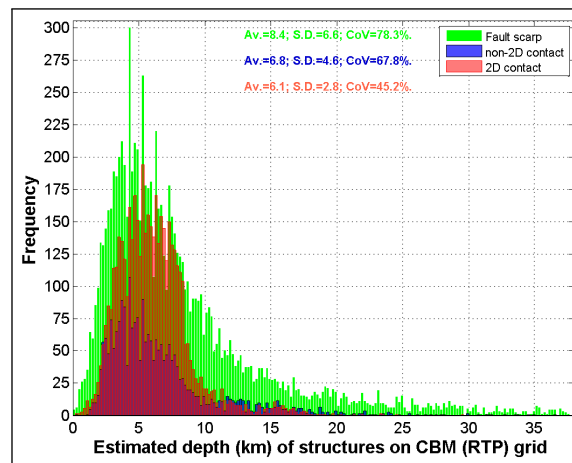
**Table 5.2:** Summary of ASA, LW and  $\theta = \pm 27$  estimates.

Method	Number of estimates for:			Ratio (%) <sup>⊗</sup>	
	RTP	RTE	Total	RTP	RTE
ASA (unedited)	43254	43952	87206	49.6	50.4
ASA (edited)	42553	42624	85177	49.96	50.04
LW	30463	35257	65720	46.35	53.65
$\theta = \pm 27$	134541	92310	226851	59.31	40.69

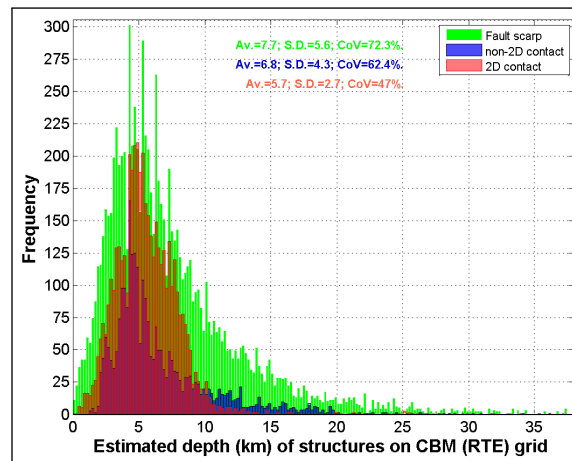
\* Estimates included all source-types (2D and non-2D contacts, and FS).

⊗ Ratio is relative to total number of estimates in figure 5.12.

More LW estimates were obtained from the RTE (54%) than from RTP (46%) grid, while an equal number (50%) of ASA estimates was obtained from RTP and RTE grids (Table 5.2). More  $\theta = \pm 27$  estimates were obtained from RTP (59%) than from RTE (41%) grid. More detailed, source-type based histograms, which highlight the distributions of edited ASA estimates and those of LW estimates were also produced (Figures 5.13 and 5.14). The distribution of ASA and LW estimates are summarised in table 5.3. The table shows that about 30, 15 and 55% of ASA estimates were from 2D contacts, non-2D contacts and FS, respectively, while  $\approx 15, 15$  and 70% of LW estimates were from these respective sources.



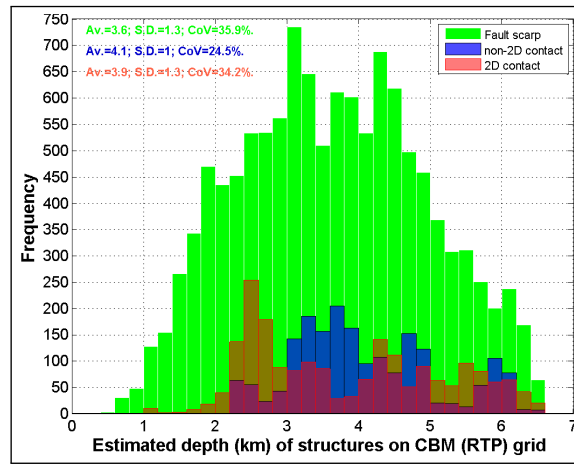
(a) Edited ASA (RTP)



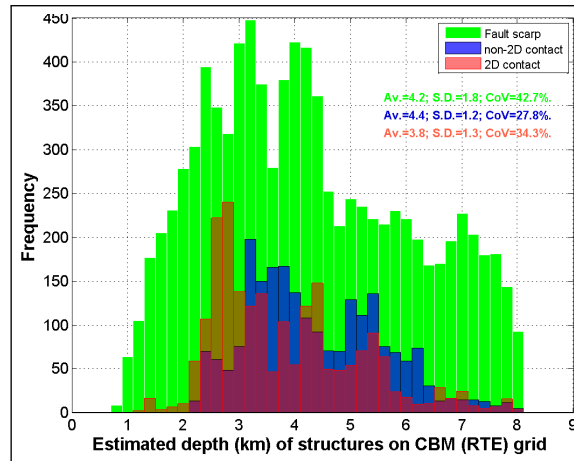
(b) Edited ASA (RTE)

**Figure 5.13:** Histograms for edited ASA estimates of depths of source edges on CBM (RTP and RTE) grids. Figures 5.13a and 5.13b represent the distribution of estimates shown in figures 5.10c and 5.10d, respectively. Histograms are mainly skewed to the right, but with most estimates occurring within the range of actual depth of BM source edge distributions (Figure 4.9b). Distributions for fault scarps (FS) were the most skewed, while the least skewed were those for 2D contacts.

Histograms of ASA estimates (Figures 5.13a and 5.13b) were skewed to the right, with most estimates occurring within the range of actual depths of BM source edges (Figure 4.9b). Distributions for fault scarps (FS) were the most skewed, while the least skewed were those for 2D contacts.



(a) LW (RTP).



(b) LW (RTE).

**Figure 5.14:** Histograms for LW estimates of depths of source edges on CBM (RTP and RTE) grids. Figures 5.14a and 5.14b represent the distribution of estimates shown in figures 5.11a and 5.11b, respectively. Histograms indicate multi-modal distribution of LW estimates, with all estimates occurring within the range of actual depth of BM source edge distributions (Figure 4.9b). Histograms were slightly skewed to the right.

**Table 5.3:** Distributions of ASA and LW estimates, at source edges.

Method	Number of estimates for: <sup>a</sup>			Total	Percentage of estimates (%) <sup>b</sup>		
	2D	Non-2D	FS		2D	Non-2D	FS
ASA (RTP), edited	4725	2418	8887	16030	29.48	15.08	55.44
ASA (RTE), edited	4683	2712	9177	16572	28.26	16.37	55.38
LW (RTP)	2022	1909	11765	15696	12.88	12.16	74.96
LW (RTE)	2095	2213	9122	13430	15.6	16.48	67.92

<sup>a</sup> 2D and FS represent 2D contacts and fault scarps, respectively.

<sup>b</sup> i.e., ratio of the number of estimates per source-type to the total number of estimates from each grid.

However, there were more estimates  $\geq 10$  km for 2D contacts and FS on the RTP than RTE distributions. Since source depths were the same for all CBM grids, these differences were attributed to anisotropy-induced interference between anomalies sourced from FS and contacts on the CBM (RTE) grid (Figure 4.5b). Further evidence is provided by the fact that more ASA estimates were obtained for non-2D contacts on the RTE than RTP distributions (Table 5.3). Otherwise, these ASA (RTP and RTE) estimates (Figures 5.13a and 5.13b) were statistically similar. This similarity is captured by the *CoV* statistics of ASA estimates. *CoV* for RTP estimates were 45.2, 67.8 and 78.3 for 2D contacts, non-2D contacts and FS, respectively. Equivalent for RTP estimates were 47, 62.4 and 72.3%. These and related statistics are shown in figures 5.13a and 5.13b.

Figure 5.14 presents detailed, source-type based histograms derived from figure 5.12b. Histograms of LW estimates (Figures 5.14a and 5.14b) were mainly uniform, although those for 2D and non-2D contacts were multi-modal. Histograms (Figure 5.14) show the range of LW estimates from RTE grid to be wider than equivalents from RTP grid. The maximum estimate from the RTP grid was 6.6 km, while it was 8.1 km for the RTE grid. These were less than the maximum actual depth of CBM source edges (Figure 4.9a). Similar number of estimates were obtained from the RTP and RTE grids.  $\approx 15$ , 15 and 70% of estimates were from 2D contacts, non-2D contacts and FS (Table 5.3). Estimates from 2D and non-2D contacts were statistically similar. Estimates from the RTP grid had *Av.* of 3.9 and 4.1, and *CoV* of 34.2 and 24.5%, respectively. Equivalent from the RTE grid had *Av.* of 3.8 and 4.4, and *CoV* of 34.3 and 27.8%, respectively. *CoV* of 35.9 and 42.7% for estimates of FS from the RTP and RTE grids, respectively, indicates that RTE estimates were slightly more dispersed than RTP estimates. These and related statistics are shown in figures 5.14a and 5.14b. Next, I evaluate ASA and LW estimates with specific reference to source locations.

#### 5.4.2 ASA and LW estimates from all source locations on RTP or RTE grid.

This section examined the errors in ASA and LW estimates in relation to the actual BM depths (Figure 4.9) at equivalent locations on the estimated and actual depth grids. These analyses included every estimated location from the RTP or RTE grid, without consideration for whether or not the estimated locations were accurate.<sup>11</sup> Errors in ASA and LW estimates were compared with those from  $-27 \leq \theta \leq 27$  estimates from the CBM grids (Figures 4.19c and 4.19d). Errors in ASA and LW estimates only at accurate source locations (Figure 5.9) will be the subject of section 5.5.

I begin by comparing ASA and LW estimates obtained from CBM (RTP or RTE) grids with actual source depths at equivalent locations, using composite cross-plots and their related statistics. Constituent cross-plot of these composite cross-plots were obtained separately, and have been colour-coded to reflect the various CBM grid source-types (Figure 4.8b), so that red, blue and green-coloured cross-plots were obtained from 2D contacts, non-2D contacts, and FS, respectively. For example, cross-plots between actual depths and ASA depth estimates of these CBM

<sup>11</sup>This is to simulate what obtains in practice.

sources or errors in estimates are presented in figure 5.15.

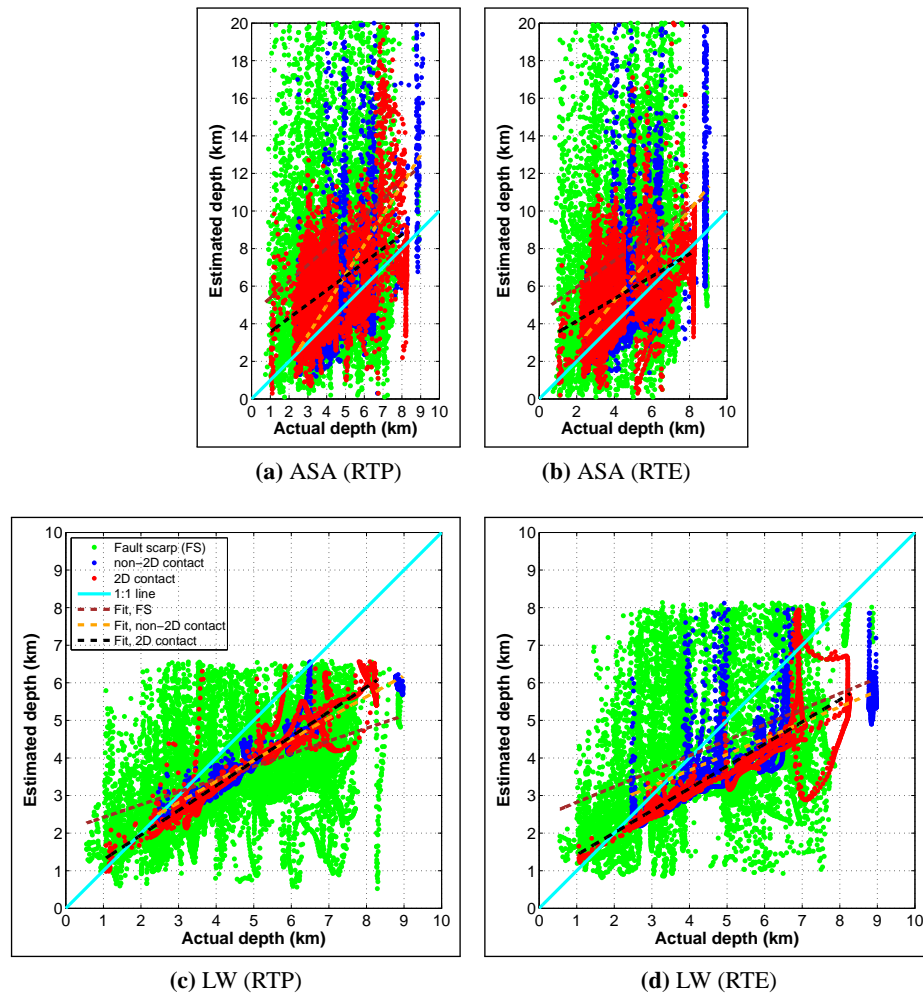


**Figure 5.15:** Comparisons between actual depth and depths estimated from RTP and RTE grids, using ASA and LW methods. Estimates were truncated at 20 km for clarity of figures. The solid cyan-coloured line marks where the 1:1 (100%) correlation between the actual and estimated depths should plot. The legend in figure 5.15c applies to all figures here. Dashed black, gold and brown-coloured lines show linear fits, respectively, to data for 2D contacts (in red), non-2D contacts (in blue), and FS (in green). Note the wider spreads in RTE compared with RTP plots, also in FS data compared with those for 2D and non-2D contacts. For clarity figures were produced to a maximum of 1:2 aspect ratio, while equations describing least-squares functions to each cross-plot, as well as related statistical parameters are presented in table 5.4.

I used three types of composite cross-plots in this section: (1) cross-plots between actual and estimated depths of sources; (2) cross-plots between actual depths of sources and percentage errors in estimate; and (3) cross-plots between depths estimated from the CBM (RTP) grid and its RTE equivalent. Where involved, the actual depths of source(s) were plotted on the abscissae while estimated depths or percentage errors for these sources at equivalent locations were plotted on the ordinates of the cross-plots. Cross-plots which compared RTP with RTE estimates had RTP estimates on the abscissae and RTE estimates on the ordinate. Where cross-plots involved estimated depths, they were limited to 20 km, to keep the figures at a readable 1:2 aspect ratio.

**Table 5.4:** Comparing equations and statistics of least-squares functions to cross-plots shown in figure 5.15.

Sources	Figure 5.15a (RTP)	Figure 5.15b (RTE)
2D	$y = 0.7x + 3; SE = 2.7; r^2 = 22.5\%$	$y = 0.6x + 3; SE = 2.6; r^2 = 16.2\%$
Non-2D	$y = 1.6x - 1; SE = 4.4; r^2 = 26.4\%$	$y = 1.2x; SE = 3.9; r^2 = 23.7\%$
FS	$y = 0.9x + 4; SE = 6.4; r^2 = 5.1\%$	$y = 0.7x + 5; SE = 5.4; r^2 = 4.8\%$
Sources	Figure 5.15c (RTP)	Figure 5.15d (RTE)
2D	$y = 0.7x + 0.6; SE = 0.9; r^2 = 89.7\%$	$y = 0.6x + 0.8; SE = 0.9; r^2 = 76\%$
Non-2D	$y = 0.6x + 1.1; SE = 0.5; r^2 = 91.2\%$	$y = 0.4x + 2; SE = 0.9; r^2 = 45.3\%$
FS	$y = 0.3x + 2.1; SE = 1.3; r^2 = 23.6\%$	$y = 0.4x + 2.4; SE = 1.7; r^2 = 17.9\%$

Cross-plots of ASA or LW depth estimates versus actual depths of all three sources (Figure 5.15) did not have a 1:1 relationship, hence data-points were not on/close to the 1:1 cyan-coloured solid line. Cross-plots exhibited various degrees of spread (variability), with cross-plots for FS depths showing the most variability. Such variabilities, previously observed in cross-plots from “Tilt-Depth” method estimates, are attributable to the fact that FS sources do not meet the strict 2D assumption implied by these methods. Since the weak anomalies due to FS-type sources attenuate rapidly and significantly with source depth, especially with the interference characteristic of RTE grids, I paid no further attention to cross-plots of FS estimates.

To highlight and extract any relationships between the paired dataset in each cross-plot for quantitative comparisons, the best-fitting least-squares function for the paired dataset were computed. Relationships between actual and estimated FS depths were best described by linear least-square lines, with zero intercepts. The coefficients of determination,  $r^2$  (Equation (4.5.1)) and standard errors,  $SE$  (Equation (4.6.1)), quantities which, respectively, express the "goodness-of-fit" and spread of data around least-squares regression lines (Chapra, 2012), will be used to compare the linear least-square lines.<sup>12</sup> These comparisons/correlations were between corresponding grid locations of actual source depths (Figure 4.9a) and ASA or LW estimates. Table 5.5 presents a summary of *corresponding estimates (%)*, i.e., the ratio between the number of corresponding locations of estimated and actual depth locations per source-type, as a measure of the relative effectiveness of ASA and LW methods.

Corresponding estimates (%) for ASA and LW estimates from RTP and RTE grids were similar (Table 5.5). These locations may not, and need not, be equivalent to both CBM (RTP and RTE) grids. Equivalent RTP and RTE locations are examined in section 5.5. For 2D contacts, ASA estimates corresponded with  $\approx 67\%$  (4725) of actual depth locations, while only  $\approx 30\%$  (2095) of LW estimates corresponded with these actual locations (Table 5.5). The table shows that about 25 and 20% of locations of ASA and LW estimates, respectively, corresponded with locations of actual depths of non-2D contacts. Only about 11% location correspondence was attained by ASA and LW estimates for FS depth locations. These equivalence between the correspondence of locations of RTP and RTE depth estimates and actual depth locations appear to confirm the inclination-independence of the ASA and LW methods. Equation of the linear regression line applicable to the cross-plot of each source-type in figure 5.15, as well as the  $SE$  and  $r^2$  value

<sup>12</sup>As in section 5.3.1, statistical significance ( $p$ )=0.05, i.e., confidence interval of 95%.

associated with the fit are presented in table 5.4. These  $r^2$  values will be used to compare ASA and LW estimates below.

**Table 5.5:** Correspondence between grid locations of estimated and actual depths of CBM sources, and correlation between the depth values.

Method	Corresponding estimates, %:*			CoD, $r^2$ (%)**		
	2D	Non-2D	FS	2D	Non-2D	FS
ASA (RTP), edited	67.51	24.64	10.43	22.5	26.4	5.1
ASA (RTE), edited	66.91	27.64	10.77	16.2	23.7	4.8
LW (RTP)	28.89	19.45	13.81	89.7	91.2	23.6
LW (RTE)	29.93	22.55	10.71	76	45.3	17.9

\* This expresses the ratio between the number of corresponding estimated and actual depth locations per source-type shown in figure 4.8b. There were 6999, 9813 and 85197 actual depth locations for 2D contacts, non-2D contacts, and FS, respectively (Figure 4.9a).

\*\*  $r^2$  values reproduced from table 5.4 to ease comparison.

### (A) Errors in ASA estimates.

Linear regression lines to ASA depth estimates from CBM (RTP and RTE) grids (Figures 5.15a and 5.15b) show that 2D contact were the least scattered, with standard error ( $SE$ ) of 2.7 (RTP) and 2.6 (RTE). These and other regression information are presented in table 5.4.  $SE$  for non-2D contacts were 4.4 (RTP) and 3.9 (RTE) indicating intermediate variability, when compared with the widely variable  $SE$  of 6.4 (RTP) and 5.4 (RTE) for FS. Also, regression equations show that mean depths of 2D contacts on RTP and RTE grids were generally underestimated, by about 30 and 40%, respectively. FS were similarly underestimated by about 10 and 30%, respectively. ASA estimates for non-2D contacts were overestimated, by about 60 and 20% on RTP and RTE grids, respectively. However, with  $r^2 \approx 5\%$  estimates for FS need no further consideration. With  $r^2 \geq 20\%$ , cross-plots of percentage errors in ASA depth estimates for 2D and non-2D contacts (Figure 5.16) will now be discussed.<sup>13</sup> The best-fitting quadratic least-squares functions will be used to compare these percentage error versus actual depth cross-plots. Equations describing these quadratic least-squares functions, as well as the related standard errors ( $SE$ ) are presented in table 5.6.

The large dispersion expressed by the  $SE > 180$  for quadratic regression fits to ASA estimates of FS from RTP and RTE grids reflect the extent to which the assumption of 2D contact was violated by these sources. Hence, errors in FS estimates are not included in the discussion below. Although errors could be positive, zero or negative, errors in depths estimated for 2D and non-2D contacts will be discussed mainly in terms of the quadratic regression fits to cross-plots of error in ASA estimates for these sources, i.e., the dashed lines in figures 5.16a and 5.16b. These error estimate fits show that average errors were mainly positive, indicating that source depths were mainly overestimated by the method. Errors ranged from 10 to 150% and 25 to 70% for 2D and non-2D contacts on the RTP grid. For these sources, error in depths estimated from the RTE grid ranged from -5 to 100% and 25 to 45%, respectively, for 2D and non-2D contacts (Figure 5.16b). The error range (margin) were higher for 2D contacts (140% for RTP and 105% for RTE estimates) than for non-2D contacts (45% for RTP and 20% for RTE estimates). These error margins far exceed

<sup>13</sup>Depth errors frequently exceeded 200%. Such are not shown in figure 5.16.

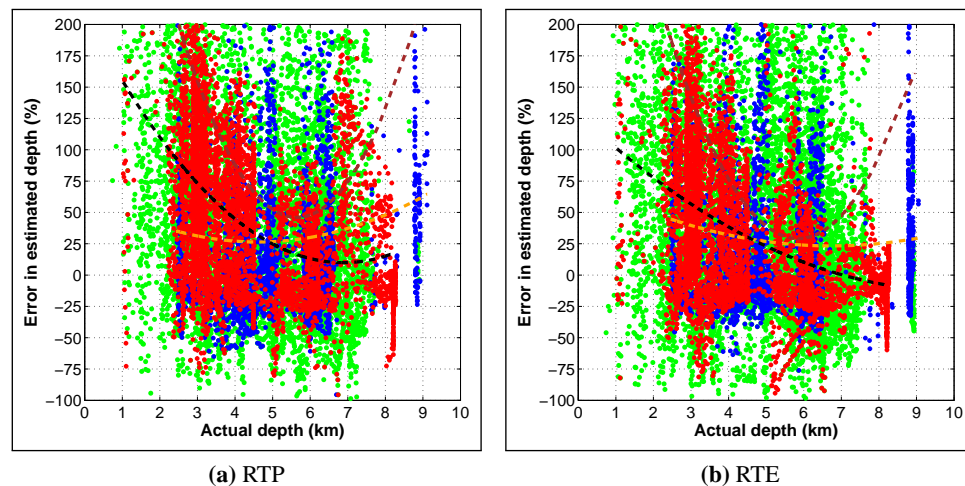


**Figure 5.16:** Comparisons between errors in depths estimated from RTP and RTE grids, using ASA method. Estimates were truncated at 200% for clarity of figures. Dashed black, gold and brown-coloured curves show quadratic fits, respectively, to data for 2D contacts (in red), non-2D contacts (in blue), and FS (in green). See figure 5.15c for the legend to these figures. Note the wider spreads in FS data compared with those for 2D and non-2D contacts. Equations of quadratic least-squares functions on each cross-plot, and the related *SE* statistic are presented in table 5.6.

the  $\pm 20\%$  cited in publications for ASA estimates from RTP data (Reeves, 2005). However, the average (RTE and RTP)  $SE \approx 57$  and  $SE \approx 77$  obtained from the quadratic regressions to estimates of 2D and non-2D contacts, respectively, show that ASA estimates from 2D contacts were less dispersed than those from non-2D contacts on RTP and RTE grids. Thus, the wider error margins observed in estimates from 2D contacts could not be attributed to dispersion in their estimated depths.

**Table 5.6:** Equations and statistics of least-squares functions to cross-plots shown in figure 5.16.

Sources	Figure 5.16a (RTP)	Figure 5.16b (RTE)
2D	$y = 4.2x^2 - 57.8x + 209$ ; $SE = 59.5$	$y = 1.4x^2 - 28x + 128.2$ ; $SE = 54.9$
Non-2D	$y = 1.9x^2 - 17.3x + 66.2$ ; $SE = 79.2$	$y = 1.2x^2 - 15.8x + 76.4$ ; $SE = 74.1$
FS	$y = 15.6x^2 - 175.7x + 541.9$ ; $SE = 184.4$	$y = 13.9x^2 - 162.3x + 503.9$ ; $SE = 181.9$

Regression fits suggest the existence of basement depth control on error margins for estimates of both 2D and non-2D contacts from RTP and RTE grids. For 2D contacts, error only ranged from 10 to 25% (RTP grid, with only 15% margin) or -10 to 25% (RTE grid, with 35% margin) at actual depths exceeding  $\approx 50\%$  of maximum actual basement depth. Hence, the generally wide error margins associated with 2D contacts at depths  $\leq 50\%$  of maximum actual basement depth can be attributed to interference between anomalies from FS and 2D contacts. This control appears to be confirmed by the denser cross-cutting relationship between FS and 2D contacts in the Western half of the CBM grid (Figure 4.8b) at shallow ( $\leq 50\%$  of maximum) actual basement depth (Figure 4.9a).

### (B) Errors in LW estimates.

Next, I discuss cross-plots of LW depth estimates versus actual depths of all three CBM (RTP

and RTE) sources (Figures 5.15c and 5.15d, respectively). Although LW estimates, for all sources from both the RTP and RTE grids, were limited to  $< 7$  km and just over 8 km (Figures 5.15c and 5.15d), respectively, data-points did not cluster onto the 1:1 cyan-coloured solid line. Therefore, LW estimates did not have a 1:1 relationship with actual source depths.

Various degrees of dispersion were exhibited on these cross-plots. The  $SE$ ,  $r^2$  and equations of linear regression fits to LW estimates from the CBM grids (Figures 5.15c and 5.15d) were used to compare dispersions in LW estimates from these RTP and RTE grids. Cross-plots for FS depths were the most variable, with standard error ( $SE > 1$ ) and  $r^2$  of 24% (RTP) and 18% (RTE). For reasons previously stated for ASA estimates, no further attention will be paid to cross-plots of FS estimates. LW estimates of non-2D contacts were the least dispersed, with  $SE$  of 0.5 (RTP) and 0.9 (RTE), and  $r^2$  of 91% (RTP) and 45% (RTE). However, LW estimates from 2D contacts exhibited constant dispersion ( $SE = 0.9$ ) for RTP and RTE grids, and  $r^2$  of  $\approx 90\%$  (RTP) and  $\approx 80\%$  (RTE). These consistencies indicate the LW method to be more effective than ASA methods in estimating depths of 2D and non-2D contacts. Regression equations show that mean LW depths of 2D and non-2D contacts were generally underestimated, respectively, by about 30 and 40% (RTP grid), and 40 and 60% (RTE grid).

Errors in LW estimates are presented in figure 5.17. Quadratic regression fits to cross-plots of these depth errors will now be used to compare LW estimates obtained from CBM (RTP and RTE) grids. Quadratic fits to errors in LW depth estimates of 2D and non-2D contacts (Figures 5.17a and 5.17b) show that average errors were mainly negative, indicating that depths were mainly underestimated by the method. Errors ranged from 0 to -25% and 5 to -30% for 2D and non-2D contacts on the RTP grid. Equivalent for 2D and non-2D contacts from the RTE grid ranged from -5 to -30% and 10 to 38%. The error range (margin) were very close: 25% for 2D contacts at RTP

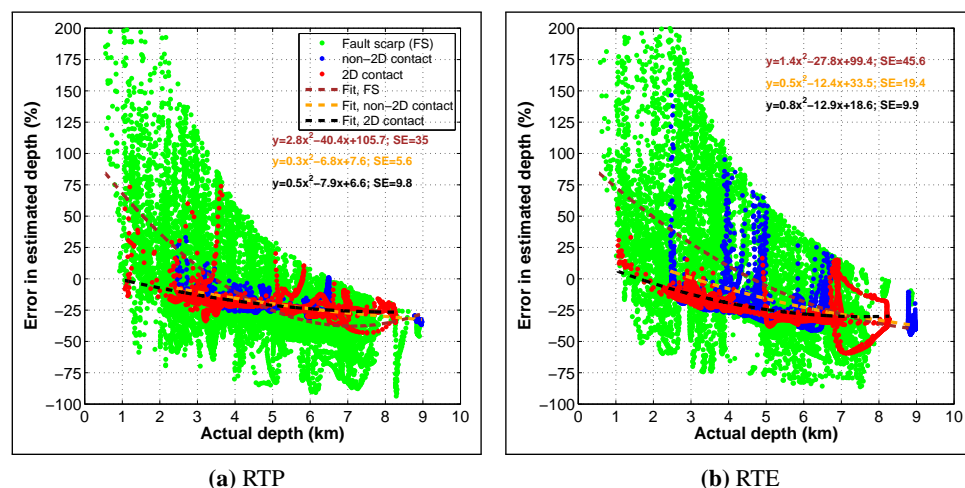


**Figure 5.17:** Comparisons between errors in depths estimated from RTP and RTE grids, using LW method. Estimates were truncated at 200% for clarity of figures. Dashed black, gold and brown-coloured curves show quadratic fits, respectively, to data for 2D contacts (in red), non-2D contacts (in blue), and FS (in green). Note the wider spreads in FS data compared with those for 2D and non-2D contacts. Equations of least-squares fits to each cross-plot and their  $SE$  statistics are shown, with coefficients rounded-off for clarity of figures.

and RTE, respectively; and 35 and 40% for non-2D contacts at RTP and RTE. These error margins show the LW method to be a more effective depth estimator for contact-like sources than the ASA method. The tapering of LW estimates from FS with increasing depth (Figure 5.17) appear to suggest that the LW method may be better able to estimate relatively deeper FS than equivalents at shallower depths.

**(C) Summary of depths estimated for 2D and non-2D contacts, using the  $\theta = \pm 27$ -based “Tilt-Depth”, ASA and LW methods.**

Here, I compare ASA, LW and  $-27 \leq \theta \leq 27$  estimated depths for 2D and non-2D contacts, from CBM (RTP or RTE) grid. Cross-plots of ASA and LW errors (%) were presented in figures 5.16 and 5.17. Similar plots for  $-27 \leq \theta \leq 27$  estimates were presented in figures 4.19c and 4.19d. Average error ranges obtained from these methods are summarised in table 5.7. LW estimates were the most accurate and consistent, and provided minimum depths for these sources.  $\theta = \pm 27$  estimates were also accurate and consistent, providing minimum to intermediate depths for these sources. ASA estimates were the most inconsistent, with large error margins. Hence, depths estimated from this method will be treated as maximum source depths.

**Table 5.7:** Summary of average depth error for ASA, LW and  $-27 \leq \theta \leq 27$  estimates for magnetic (2D and non-2D) contacts on RTP or RTE grid. The magnitude of maximum difference in range of error are shown in brackets. Data for ASA and LW estimates were extracted, respectively, from figures 5.16 and 5.17. Data for  $-27 \leq \theta \leq 27$  estimates were previously presented in table 4.19.

CBM grid/ source types	Error (%) for depths estimated using:		
	ASA	LW	$-27 \leq \theta \leq 27$
<b>(1) RTP</b>			
(i) 2D contacts	10 to 150 (140)	-25 to 0 (25)	-25 to -8 (17)
(ii) non-2D contacts	25 to 70 (45)	-30 to -5 (25)	-35 to -5 (30)
<b>(2) RTE</b>			
(i) 2D contacts	-5 to 100 (105)	-30 to 5 (35)	-35 to 0 (35)
(ii) non-2D contacts	25 to 45 (20)	-38 to 10 (48)	-38 to -8 (30)

## 5.5 Depths estimated from equivalent RTP and RTE locations using the ASA, LW and $\theta = \pm 27$ -based “Tilt-Depth” methods.

This section deals with depths estimated only at equivalent source locations on both the CBM (RTP and RTE) grids, using ASA, LW and  $-27 \leq \theta \leq 27$ -based “Tilt-Depth” methods.<sup>14</sup> Analyses in this section were aimed at determining the degree of error that may be associated with structures estimated from RTE grids with certainty. Thus, only depths estimated for the locations from which structures could be mapped with certainty from the RTE grid (Figure 5.9) will be considered in the evaluations discussed below.

<sup>14</sup>Since locations estimated from RTP grids are usually accurate, these estimates were only for accurate RTE source locations (Figure 5.9a).

Composite cross-plots and related statistics were obtained for depths estimated at equivalent source locations on the CBM (RTP and RTE) grids, using the ASA, LW and “Tilt-Depth” methods.<sup>15</sup> Each cross-plot in these composite cross-plots was obtained separately, and has been colour-coded to reflect the various CBM grid source-types (Figure 4.8b): red, blue and green-coloured cross-plots represent estimates from 2D contacts, non-2D contacts, and FS, respectively. Cross-plots between the actual and estimated depths or associated errors for these CBM sources, obtained using the ASA, LW or  $\theta = \pm 27$ -based “Tilt-Depth” methods are presented in figure 5.18.

Three types of composite cross-plots were used in this section: (1) between actual and estimated depths of sources; (2) between actual depths of sources and percentage errors in estimate; and (3) between depths estimated from the CBM (RTP) grid and its RTE equivalent. Other attributes of these plots remain as introduced in section 5.4.2. Where cross-plots involved estimated depths they were limited to 20 km to keep the figures at a readable 1:2 aspect ratio.

Cross-plots between ASA, LW and “Tilt-Depth” estimated depths and actual depths of all three sources did not have a 1:1 relationship (Figure 5.18), since data-points were not on/close to the 1:1 cyan-coloured solid lines. Various degrees of data spread (dispersion) were exhibited, with cross-plots for FS depths showing the most variability. The large dispersion in FS estimates have already been attributed to the fact that FS sources do not meet the strict 2D assumption implied by either the ASA, LW or “Tilt-Depth” methods. Consequently, no further attention was paid to cross-plots of FS estimates.

The best-fitting least-squares function for the paired dataset presented in each cross-plot was obtained, to highlight relationships. Least-square lines obtained from RTP and RTE grids were compared for their “goodness-of-fit” and spread of data around these lines using statistics like coefficients of determination,  $r^2$  (Equation (4.5.1)) and standard errors,  $SE$  (Equation (4.6.1)).<sup>16</sup> Relationships between actual and estimated FS depths were best described by linear least-square lines (Figure 5.18). Equations describing these linear least-squares functions and related statistical parameters are presented in table 5.8.

Linear regression lines to depths estimated using ASA, LW and “Tilt-Depth” method from CBM (RTP and RTE) grids show estimates from 2D contacts to be the least scattered (Figure 5.18 and table 5.8). Regressions to cross-plots of LW and “Tilt-Depth” estimates of 2D and non-2D contacts exhibited standard errors ( $SE$ ) that were  $< 1$ , irrespective of whether estimates were derived from the RTP or RTE grid (Compare figure 5.18c with 5.18d, and figure 5.18e with 5.18f).  $SE$  for all ASA estimates (RTP or RTE) were  $> 1$  (a similarity shared with FS plots) indicating very wide data dispersions around least-squares lines (Figures 5.18a and 5.18b). The ASA method appears to be the least amenable to the error limits sought in this study.

Cross-plots of the errors associated with depths estimated using ASA, LW or “Tilt-Depth” meth-

---

<sup>15</sup>Hereafter, “Tilt-Depth” method refers to implementations using the  $-27 \leq \theta \leq 27$  range.

<sup>16</sup>Statistical significance ( $p$ )=0.05, i.e., confidence interval of 95%.

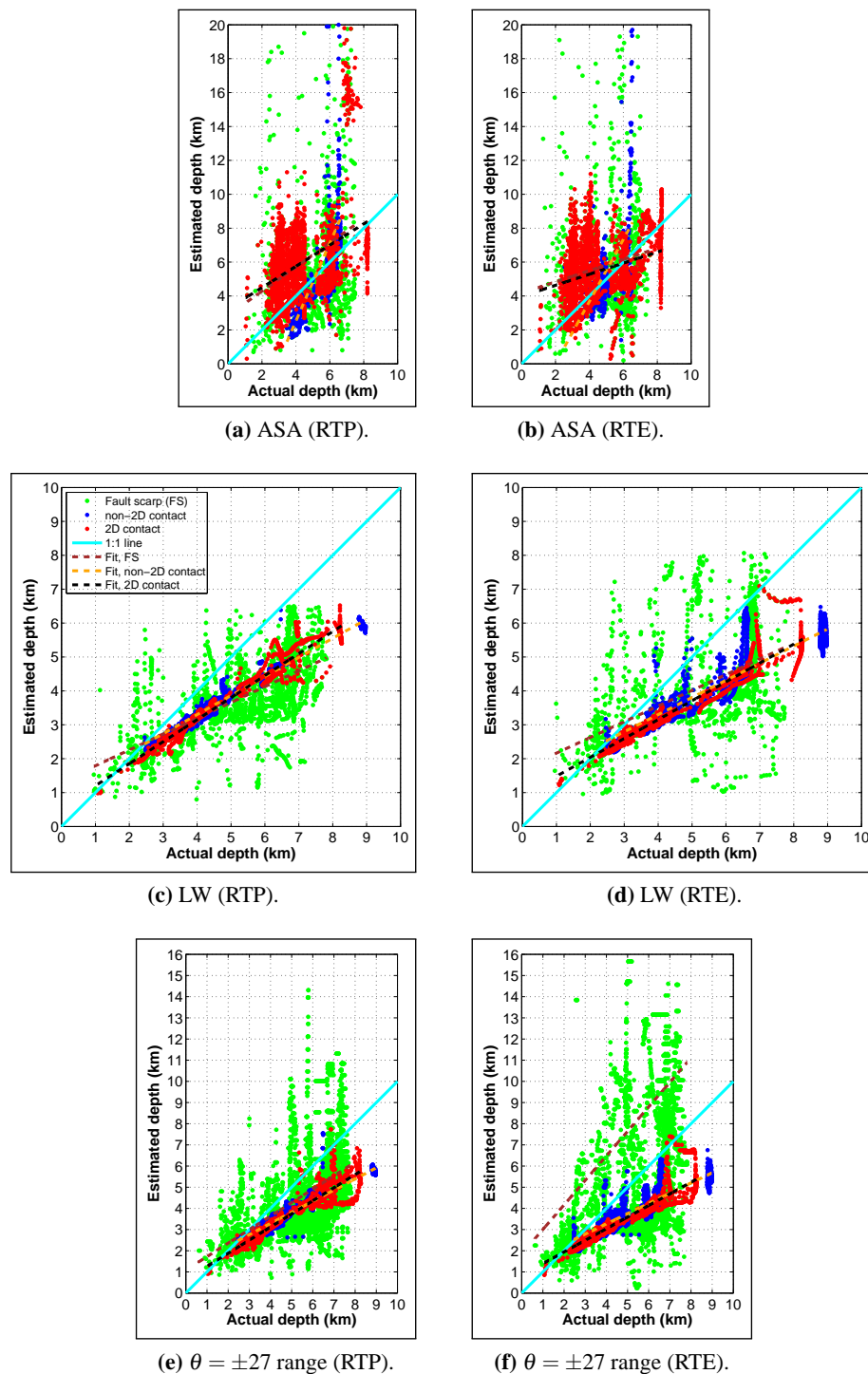


**Figure 5.18:** Depths estimated at equivalent locations on the CBM (RTP and RTE) grids, using the ASA, LW and  $\theta = \pm 27$ -based “Tilt-Depth” methods. Where necessary, estimates were truncated at 20 km for clarity of figures. Legend to figure 5.18c applies to all figures here. Dashed black, gold and brown-coloured lines show linear fits, respectively, to data for 2D contacts (in red), non-2D contacts (in blue), and FS (in green). The solid cyan-coloured line marks where the 1:1 (100%) correlation between the actual and estimated depths should plot. Table 5.8 presents equations of least-squares functions to these cross-plots, as well as related statistical parameters ( $SE$  and  $r^2$ ). FS estimates were more widely spread (larger  $SE$ ) than those for 2D and non-2D contacts.  $SE$  increased from its lowest for LW estimates to its highest for ASA estimates. Hence, estimates from LW and  $\theta = \pm 27$ -based “Tilt-Depth” methods were more reliable than their ASA equivalents. Figures were produced to a maximum of 1:2 aspect ratio.

**Table 5.8:** Equations and statistics of least-squares functions to cross-plots shown in figure 5.18.

Sources	Figure 5.18a (RTP)	Figure 5.18b (RTE)
2D	$y = 0.6x + 3; SE = 2.6; r^2 = 16.6\%$	$y = 0.3x + 4; SE = 1.8; r^2 = 10.6\%$
Non-2D	$y = 2.3x - 7; SE = 3.1; r^2 = 43.3\%$	$y = 1.8x - 4; SE = 3; r^2 = 30.3\%$
FS	$y = 0.7x + 3; SE = 4.5; r^2 = 5.6\%$	$y = 0.3x + 4; SE = 3.5; r^2 = 2\%$
Sources	Figure 5.18c (RTP)	Figure 5.18d (RTE)
2D	$y = 0.6x + 0.6; SE = 0.8; r^2 = 96.7\%$	$y = 0.6x + 0.9; SE = 0.7; r^2 = 93.1\%$
Non-2D	$y = 0.6x + 1.1; SE = 0.4; r^2 = 97.1\%$	$y = 0.5x + 1.3; SE = 0.6; r^2 = 80.8\%$
FS	$y = 0.5x + 1.3; SE = 1.2; r^2 = 43.6\%$	$y = 0.5x + 1.7; SE = 1.5; r^2 = 27.9\%$
Sources	Figure 5.18e (RTP)	Figure 5.18f (RTE)
2D	$y = 0.6x + 0.6; SE = 0.8; r^2 = 92.2\%$	$y = 0.5x + 0.8; SE = 0.7; r^2 = 88\%$
Non-2D	$y = 0.5x + 1.2; SE = 0.4; r^2 = 94\%$	$y = 0.5x + 1.3; SE = 0.6; r^2 = 76.5\%$
FS	$y = 0.6x + 1.1; SE = 2.2; r^2 = 23.4\%$	$y = 1.2x + 1.8; SE = 7.8; r^2 = 5.1\%$

ods (Figure 5.18) are presented in figure 5.19. Relationships between actual depths and errors associated with their estimates were best described by quadratic least-square functions. Equations describing these quadratic least-squares functions, as well as their standard errors (*SE*) are presented in table 5.9. A summary of the range of depth errors obtained from these regression lines to ASA, LW and “Tilt-Depth” estimates is presented in table 5.10.

Dispersions were slightly higher in cross-plots of LW and “Tilt-Depth” estimates from RTE than RTP grid (Compare figure 5.19c with 5.19d and figure 5.19e with 5.19f). LW estimates of 2D and non-2D contacts exhibited the least dispersion in its errors, with *SE* ranging between 3-4 for RTP estimates (Figure 5.19c), and 4-10 for RTE estimates (Figure 5.19d). Regression lines to these estimates showed error in LW estimates to range from -10 to -30 and -5 to -30 for 2D and non-2D contacts (RTP), respectively. RTE equivalents for these sources range from 5 to -30 and -10 to -40, respectively.

$\theta = \pm 27$ -based “Tilt-Depth” estimates of 2D and non-2D contacts exhibited dispersions in its errors (slightly higher than those from LW estimates), with *SE* ranging between 5-6 for RTP estimates (Figure 5.19e), and 6-10 for RTE estimates (Figure 5.19f). Regression lines to “Tilt-Depth” estimates showed error to range from -10 to -30 and -5 to -30 for 2D and non-2D contacts (RTP), respectively. RTE equivalents for these sources range from 0 to -35 and -12 to -42, respectively.

Since it was difficult to convincingly determine any narrow error limit (range) from the cross-plots of ASA estimates from RTP and RTE grids, henceforth, no further considerations is paid to the method.

Thus far, semi-automatic methods have been examined using the simple and/or complex “Bishop” model (SBM and/or CBM) grids. Evaluations were based on the exactly known locations and depths of SBM and/or CBM sources. In appendix E, I compare interpretations from RTP and RTE of a real, field-derived  $\Delta T$  grid from Southern Tanzania, for further observations that can facilitate interpretation of  $\Delta T$  (RTE) datasets.

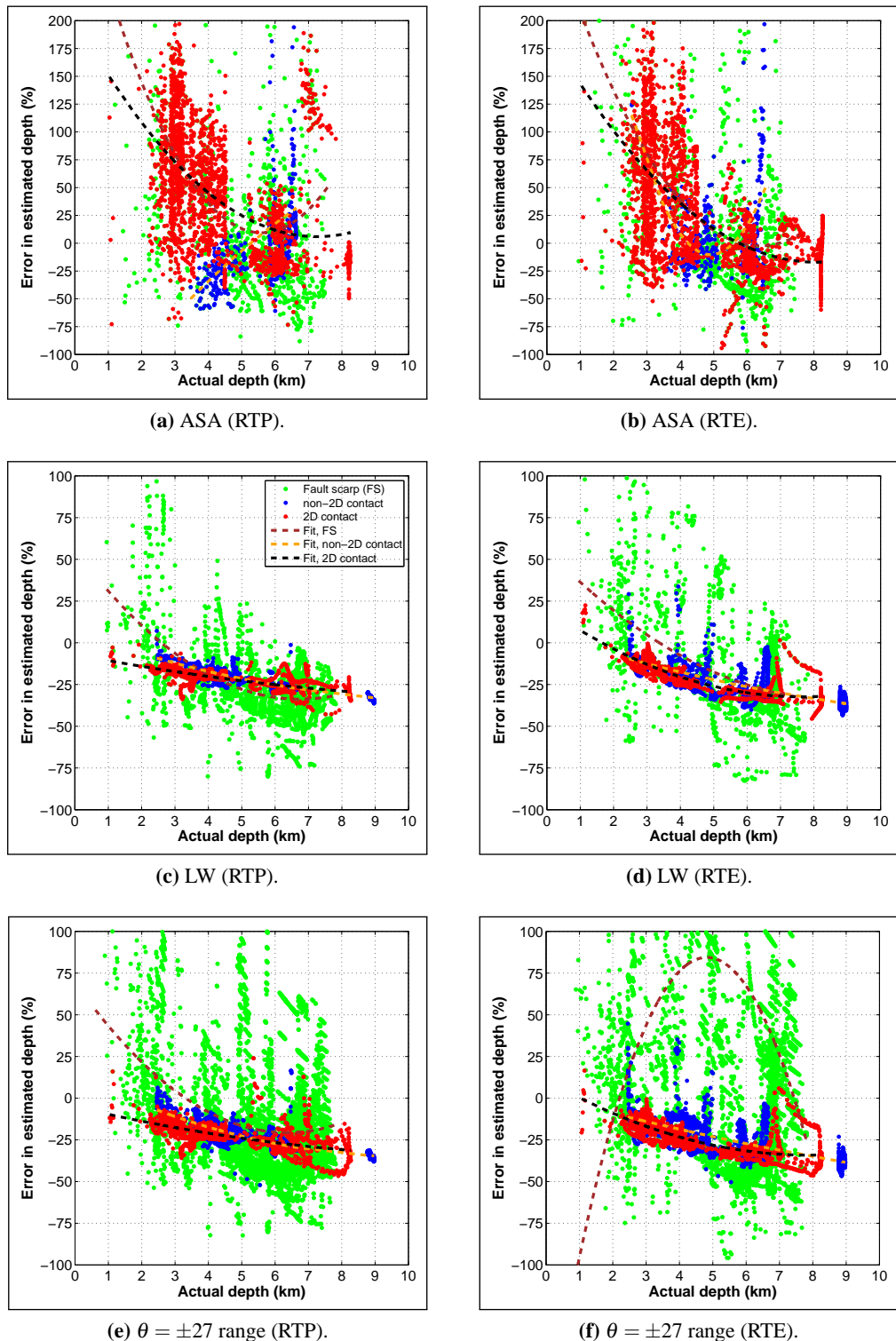


**Figure 5.19:** Error in depths estimated at equivalent locations on the CBM (RTP and RTE) grids, using the ASA, LW and  $\theta = \pm 27$ -based “Tilt-Depth” methods. The legend to figure 5.19c applies to all other figures here. Equations of least-squares functions to these cross-plots, as well as related standard errors ( $SE$ ) are presented in table 5.9. FS estimates were more widely spread (larger  $SE$ ) than those for 2D and non-2D contacts.  $SE$  increased from its lowest for LW estimates to its highest for ASA estimates. Hence, estimates from LW and  $\theta = \pm 27$ -based “Tilt-Depth” methods were more reliable than their ASA equivalents.

**Table 5.9:** Equations and statistics of least-squares functions to cross-plots shown in figure 5.19.

Sources	Figure 5.19a (RTP)	Figure 5.19b (RTE)
2D	$y = 3.7x^2 - 53.8x + 201.3$ ; $SE = 48.9$	$y = 3.2x^2 - 51.7x + 191.7$ ; $SE = 43.5$
Non-2D	$y = -1.5x^2 + 40.7x + 173.2$ ; $SE = 43.4$	$y = 22.4x^2 - 220x + 529.8$ ; $SE = 40$
FS	$y = 10.5x^2 - 117.2x + 337.2$ ; $SE = 97$	$y = 7.3x^2 - 92.7x + 293.5$ ; $SE = 91.1$
Sources	Figure 5.19c (RTP)	Figure 5.19d (RTE)
2D	$y = 0.1x^2 - 3.8x - 7$ ; $SE = 3.7$	$y = 0.9x^2 - 13.8x + 20.3$ ; $SE = 4.7$
Non-2D	$y = 0.3x^2 - 7.1x + 6.3$ ; $SE = 3.3$	$y = 0.2x^2 - 6.5x + 5.1$ ; $SE = 8.5$
FS	$y = 2x^2 - 26.5x + 55.6$ ; $SE = 20.3$	$y = 1.2x^2 - 20.4x + 55.5$ ; $SE = 28.8$
Sources	Figure 5.19e (RTP)	Figure 5.19f (RTE)
2D	$y = 0.2x^2 - 4.7x - 5.2$ ; $SE = 5.5$	$y = 0.7x^2 - 11.5x + 11.1$ ; $SE = 5.9$
Non-2D	$y = 0.5x^2 - 9.8x + 14$ ; $SE = 4.6$	$y = 0.1x^2 - 5.4x + 1.4$ ; $SE = 9.4$
FS	$y = 2.2x^2 - 28.3x + 69.5$ ; $SE = 33.5$	$y = -12.3x^2 - 118.8x + 201.8$ ; $SE = 133.3$

**Table 5.10:** Summary of average error in depths estimated at corresponding 2D and non-2D contacts locations on CBM (RTP and RTE) grids, using the ASA, LW and  $\theta = \pm 27^\circ$ -based ‘‘Tilt-Depth’’ methods. The magnitude of maximum difference in range of error are shown in brackets.

CBM grid/ source types	Error (%) for depths estimated using:		
	ASA <sup>a</sup>	LW <sup>b</sup>	$-27 \leq \theta \leq 27^\circ$ <sup>c</sup>
<b>(1) RTP</b>			
(i) 2D contacts	5 to 150 (145)	-30 to -10 (20)	-30 to -10 (20)
(ii) non-2D contacts	-50 to 30 (85)	-30 to -5 (25)	-30 to -5 (25)
<b>(2) RTE</b>			
(i) 2D contacts	-20 to 140 (160)	-30 to 5 (35)	-35 to 0 (35)
(ii) non-2D contacts	-10 to 120 (130)	-40 to -10 (30)	-42 to -12 (30)

<sup>a</sup> Extracted from figures 5.19a and 5.19b.

<sup>b</sup> Extracted from figure 5.19c and 5.19d.

<sup>c</sup> Extracted from figure 5.19e and 5.19f.

## 5.6 Summary of edge location and depth estimation from RTE grids

### (A) Location estimation

ASA peaks are slightly broader in cross-section than  $HGM_{(\Delta T)}$ , LW and  $HGM_{(\theta)}$  peaks. Hence, ASA anomalies from sufficiently close sources may readily coalesce to form dominant peaks or interfere destructively, compared with these other methods. Consequently, the ASA method imaged relatively well isolated CBM (RTP and RTE) grid sources better. Because of its dependence on both susceptibility contrast ( $\delta k$ ) and vertical derivative, only shallow subtle FS were imaged by the ASA method. However, non-North-South striking 2D contacts (i.e, with strike outside the  $N \pm 20^\circ$  range), as well as the Northern and Southern non-2D contact-like edges of 3D sources were well imaged by the ASA method.  $HGM_{(\Delta T)}$  peaks are narrower than ASA peaks, persisting as separate peaks for most adjacent anomalies. Hence, the  $HGM_{(\Delta T)}$  method performed better than the ASA method at imaging subtle FS, clearly outlining all non-North-South striking 2D contacts, intersections between sources, as well as all the non-2D contact-like edges of 3D sources. Like the ASA method, the  $HGM_{(\Delta T)}$  method also depends on  $\delta k$ . Hence, where sources with significant  $\delta k$  occur, they were preferentially imaged at the expense of the subtle FS.

The indirect dependence of Tilt angles ( $\theta$ ) and local wavenumber on  $\delta k$  means that the ‘‘Tilt-

Depth”, LW or  $HGM_{(\theta)}$  methods were able to equally image edges of both subtle and dominant sources. While maxima locations represent source edges for LW and  $HGM_{(\theta)}$  methods, equivalent locations are marked by the  $\theta = 0$  contour for the “Tilt-Depth” method. The LW and  $HGM_{(\theta)}$  methods depend on second-order derivatives. Hence, they are sensitive to noise and interference effects. Also, sufficiently close LW or  $HGM_{(\theta)}$  maxima interfere to generate secondary maxima. The complex nature of the CBM grid and the complex anomaly interference that resulted from RTE-induced azimuthal anisotropy also led to complex  $\theta$ , LW or  $HGM_{(\theta)}$  estimates, which correlated poorly with their RTP equivalents. However, these comparisons, and those from the less complex Tanzania grids (Appendix E, figure E.4), show that  $\theta$  estimates were very reliable, and easier to interpret, for relatively well isolated 2D structures. Only  $HGM_{(\Delta T)}$ ,  $HGM_{(\theta)}$ , ASA and LW estimates that are coincident or closest to  $\theta$  and/or SVD estimates should be treated as certain and retained. An integrated approach to edge location estimation from RTE of  $\Delta T$  grids should commence with ASA and  $HGM_{(\Delta T)}$ , then SVD and  $\theta$ , and finally LW and  $HGM_{(\theta)}$ .

### **(B) Depth estimation**

FS depths estimated from the RTP or RTE grid, using the ASA, LW and  $\theta = \pm 27^\circ$ -based “Tilt-Depth” methods, were highly dispersed and erroneous, compared with estimates for 2D and non-2D contacts. ASA estimates of the depths of 2D and non-2D contacts from the CBM (RTP or RTE) grid were unreliable. Similar estimates of contact depths from the RTE grid, using LW and  $\theta = \pm 27^\circ$ -based “Tilt-Depth” methods, were as good as those obtained from the RTP grid. Although errors in estimates of 2D and non-2D contact depths clustered tightly around and along regression lines for these contacts, these clusters and their trend lines were not aligned with or around the 1-to-1 line (which marks equivalence between actual and estimated source depths). LW and  $\theta = \pm 27^\circ$ -based “Tilt-Depth” methods underestimated depths of 2D contacts by up to 30% from RTP and RTE grids, and underestimated non-2D contacts by up to 40% from the RTE grid.

## Chapter 6

# Interpretation of northeastern (NE) Nigeria aeromagnetic dataset.

---

### 6.1 The study area (NE Nigeria).

#### 6.1.1 Location

The study area is located within longitudes 8° E and 18° E and latitudes 8° N and 16° N, in the NE part of Nigeria (Figure 6.1).<sup>1</sup>Nigeria is generally a hot country, with an average temperature of 27° C (Iloeje, 1981). Temperature ranges vary significantly with location and between the two seasons; the rainy and the dry season. The main controlling factors of temperature in Nigeria are the amount of rainfall and elevation (Udo, 1970). The amount of precipitation generally decreases as the elevation increases from the Southern parts of the country northwards. Consequently, the vegetation cover grades from dense equatorial rainforests in the South, through Savannah grasslands in the middle belt, to the very sandy and sparse grass patches of the Sahel-type savannah in the NorthEast of Nigeria (Iloeje, 1981; Udo, 1970). Kogbe (1983) reports grasslands, bare-rock surfaces and sparse woodlands from the northern highlands. Arid conditions of NE Nigeria (the study area) are attributable to the persistence of the dry season, which can be 7 or more months long, every year.

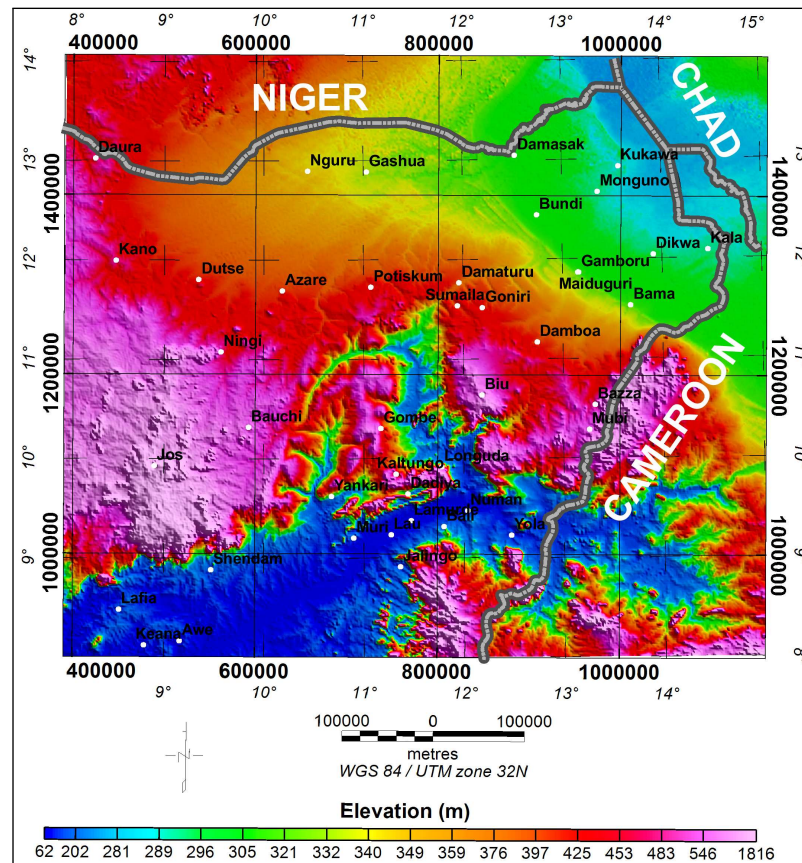
The study area consists of most of the highest, and therefore the coldest, locations above mean sea level (msl) in Nigeria. These locations include: the > 1 km high Mambilla/Adamawa Plateau (Taraba State) in the Mambilla/Adamawa Highlands in the Eastern part of the study area; the 1.28 km high Jos Plateau (Plateau State) in the Central Highlands to the West of the study area; and, the 0.7 km high Biu Plateau in Borno State. According to Iloeje (1981) these locations are typically characterised by warm to cold temperate and montane-type climates, with temperatures always below 25°C. Figure 6.1b, which has been extracted from the 30 m × 30 m SRTM-derived digital elevation dataset, presents the elevation and main topographic features of NE Nigeria. The

---

<sup>1</sup>For clarity of details, magnified versions of figure 6.1b and most NE Nigeria-wide figures shown in this chapter, are also presented in appendix H.



(a) Political map shows study area.



(b) Elevation above msl (m).

**Figure 6.1:** Map showing: (a) the location and extent (shaded) of the study area in Nigeria (Commonwealth, 2011). Inset is the location of Nigeria on the globe; and (b) the topography of NE Nigeria. Figure 6.1b was extracted from the 1 arc-second ( $\approx 30$  m) SRTM elevation dataset (Farr et al., 2007). Maps also show main cities/towns and river system of the area. A magnified version of figure 6.1b is shown in appendix H (Figure H.1).

SRTM datasets are presented at an absolute height and absolute geolocation error, respectively, of  $\approx 6\%$  and  $\approx 12\%$  (Farr et al., 2007). NE Nigeria in the context of this research includes both the SouthWestern Chad basin and the Upper Benue Trough, the geology and main tectonic elements of which are presented in section 6.1.2.

For ease of comparison between maps, maps covering similar areas are presented using similar geographic (Equatorial Mercator/Clarke 1880 spheroid) and/or UTM (WGS 84/UTM Zone 32N) graticules.

### 6.1.2 Geology

Benkhelil (1989) described the Benue Trough as a major NE-SW intracontinental Cretaceous basin which is filled with folded Cretaceous sediments and scarce volcanic rocks, is about 1000 km long and about 50 to 100 km wide, and runs from the Niger delta to the Chad basin. Guiraud (1990) reconstructed the Early Cretaceous tectonic history of the Upper Benue Trough, subdividing this part of the Benue Trough into three (3) sub-basins on the basis of the general strike of structures of regional extent. The sub-basins and their orientations are as follows (Figure 6.2): (i) the Gongola and Kerri-Kerri sub-basins, which make up the Northern branch and trend  $N10^\circ E$ ; (ii) the Yola sub-basin or eastern branch, which trends W-E; and (iii) the Bashar-Muri sub-basin, which is the southern branch and trends  $N50^\circ E$ . These elements of NE Nigeria are presented in figure 6.2, which shows both the areal extent, as well as the outcrop geology of the study area. Note that sedimentary rocks in these basins directly overlie crystalline basement rocks of Precambrian age, as is the case throughout Africa (Key, 1992). Locations of outcropping sedimentary rocks/sediments and basement/sediment contacts have been extracted for use in comparing the structural and depth maps that will be obtained from this geophysical study.

Murat (1972) subdivided Southern Benue Trough sedimentary-fill using eustatic sea level fluctuations. Subsequently, stratigraphic studies of other Nigerian depocentres have mainly adopted this approach. The chronological successions and lateral equivalence of sedimentary units in the study area are presented in figure 6.3. The relative ages of sediments were determined using their faunal contents (biostratigraphic methods). Carter et al. (1963), Petters & Ekweozor (1982), Benkhelil et al. (1989), Kogbe (1989), Guiraud (1990) and Okosun (1992) provide detailed descriptions of NE Nigeria sedimentary succession.

The outcrop geology of NE Nigeria (Figure 6.2) also include Precambrian and Palaeozoic crystalline, as well as Late Mesozoic and Cenozoic volcanic rocks. McCurry (1989) recognised four types of Palaeozoic and Precambrian rocks in Northern Nigeria. They are: (I) the *basement complex*, which includes all pre-Proterozoic rocks like para and orthogneisses, basic and calcareous schists, granites, marbles, quartzites, as well as Birrimian age metasediments. Several cycles of regional tectonothermal activities have altered most basement complex rocks to migmatites and gneissose equivalents, containing reworked fabrics; (II) Younger metasediments are low meta-

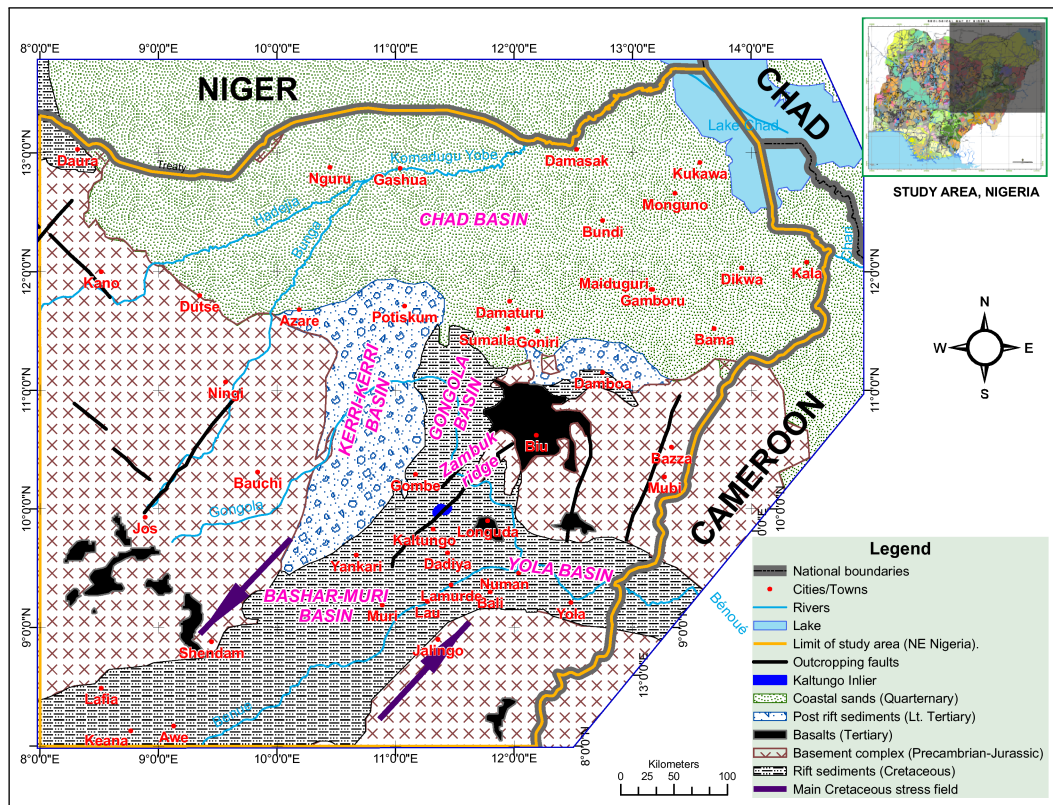


**Figure 6.2:** Simplified geological map of NE Nigeria, showing the major tectonic magnetic distinct rock units (Modified from Benkheilil et al., 1989, NGSA, 2006 and Frere, 2010). Superimposed on this map is the main Cretaceous stress field, purple arrows (Fairhead & Binks, 1991). Note outcropping NE-SW, NW-SE, and NNE-SSW trending faults. Inset is geological map of Nigeria, showing study area (shaded). A magnified version of this figure is shown in appendix H (Figure H.2).

AGE		UPPER BENUE TROUGH			SE CHAD (BORNU) BASIN	DEPOSITIONAL ENVIRONMENT	
		YOLA SUB-BASIN	GONGOLA SUB-BASIN				
CENOZOIC	QUATERNARY	Pleistocene	ND	Kerri Kerri Formation	Chad Formation	Lacustrine (Continental)	
	TERTIARY	Pliocene	ND		ND	Continental (Lacustrine or deltaic)	
		Miocene	ND		ND	Volcanic/Continental	
		Oligocene	Volcanics (Basalts)		ND	Continental (Lacustrine or deltaic)	
		Eocene	ND		ND		
		Palaeocene	ND		ND		
MESOZOIC	CRETACEOUS	Mastrichtian	ND	Gombe Sandstones	Gombe Sandstones	Estuarine-deltaic (Transitional)	
		Campanian	ND	Gombe Sst/Fika Shales	Fika Shales	Deep marine	
		Santonian	=====	=====	=====	Non-deposition/Erosion	
		Coniacian	Lamja Numaiha Sekuliye Jessu Dukul	Pindiga Gongila	Fika Shales	Fika Shales	Deep marine
		Turonian	Yoide	Yoide	Gongila Formation	Gongila Formation	Estuarine (Transitional)
		Cenomanian	Yoide	Yoide			
		Aptian-Albian	Bima Sandstones	Bima Sandstones	Bima Sandstones	Bima Sandstones	Continental
		Pre-Aptian	BASEMENT COMPLEX				Non-deposition/Erosion

**Figure 6.3:** Lithostratigraphic chart for NE Nigeria (Adapted from Avbovbo et al., 1986; Kogbe, 1989; Matheis, 1989; Olugbemiro et al., 1997). ND represents periods of non-deposition.

morphogenetic psammitic and pelitic sediments. Also, conglomerates and interbedded lavas may occur; (III) Older Granite Series include rocks emplaced during the Pan African tectonothermal event and mainly include basic and intermediate mafic/felsic rocks like gabbro, diorite, and massive quartz or hydrothermal vein deposits. The main alteration process affecting this rock series is granitisation of basic and ultrabasic mineral phases; and (IV) Jurassic Basalts and other volcanics emplaced during the late and final stages of the Pan African tectonothermal event. Similar crystalline rocks have been reported from the SouthWestern parts of Nigeria (Rahaman, 1989). Ekwueme (1990) also reported Precambrian rocks of similar compositions from SouthEastern Nigeria. These rocks have been encountered in wells at various depths in most parts of Nigeria (Avbovbo, 1980).

Woakes et al. (1987) subdivided these basement rocks into three groups, based on their metamorphic history. These are: (I) Medium-to-high grade, polymetamorphic, migmatite-gneiss-quartzite complex of Pan-African ( $\approx 600$  Ma) to Eburnean (2200-1680 Ma) age (Caen-Vachette & Umeji, 1988); (II) N-S trending low grade, metavolcanic units in schist belts of upper Proterozoic supracrustal rocks which are folded into rocks of the migmatite-gneiss-quartzite complex; and (III) Pan-African aged Older Granite rock suite constituting migmatite-gneiss quartzite complex and rocks of the schist belts. The Pan-African orogeny is mainly associated with medium-grade metamorphism but also mega-shear zones and granitic batholiths, characterized by a high temperature gradient. Kampunzu et al. (1993) report similar alkaline assemblages from the East African rift.

### 6.1.3 Tectonic framework.

Burke (1977) inferred a collisional tectonic (subduction) origin for the Benue Trough, based on the occurrence of andesitic and related intrusives in its SouthEastern parts. However, these andesitic rocks were not found when Olade (1978) re-examined rock samples from the Ogbagu-1 and Ikono-1 oil exploration wells of Burke (1977). Also, after examining petrogenetic assemblages from Cretaceous-Recent volcanism in the Benue Trough, including older Abakiliki flood basalts, Olade (1978) showed that the basalts were potash-depleted and, therefore, of oceanic crust composition. Hence, the composition of Cretaceous-Recent volcanic basalts in Nigeria is further strong evidence of the rift (extensional tectonic) origin of the Benue Trough. Avbovbo et al. (1986) provides other evidences for the rift origin of the Benue Trough, observed from seismic sections acquired from NE Nigeria. These evidences include: (i) the zig-zag pattern of faults on these seismic sections; and (ii) the fact that folds observed on deep seismic reflectors generally die out with reducing depths and along the direction of sedimentary pinch-out. The dominant force responsible for creating sediment accommodation during the formation of the intracontinental sag Chad basin was the combined weight of sediments and the water responsible for their deposition (Burke, 1976).

The Benue Trough is a mega-Shear zone, which lies entirely between the continental extensions of the Romanche and Chain Charcot fractures (Ajakaiye et al., 1986; Fairhead & Okereke, 1990; Fairhead & Binks, 1992). The Trough is marked by a 400 km-wide positive axial gravity

anomaly (Fairhead & Okereke, 1990), which thins to about 70 km in the Upper Benue Trough (Adighije, 1979). Girdler (1983) associated these broad axial positive anomalies with the presence of a thinned crust. Thinned crusts are thought to develop when dense upper mantle material gain access to and is emplaced at shallow depths in the crust. The broad axial positive gravity anomalies are geophysical expressions of these denser materials. After comparing the seismicity map of Africa for the 1964 to 1975 period with the gravity-deduced lithospheric thinning map of Africa, Girdler (1983) observed that thinned crusts were not associated with some seismically-active rifts, concluding that crustal fracturing and faulting may precede the development of lithospheric thinning. While the thickness of the crust in the area South of the Yola basin (Figure 6.2) has been estimated to be about 34 km (Stuart et al., 1985), these authors also showed that the crust beneath the Yola basin is thinned by  $\approx 12$  km. Thus, the preferred tectonic origin of the axial positive gravity anomaly of the Benue Trough is that of a failed rift or an aulacogen (Fairhead & Okereke, 1990; Guiraud et al., 1992). However, Karner et al. (2005) has reported the occurrence of a rift, which is associated instead with axial negative free air and Bouguer gravity anomalies, which could not be explained by either crustal intrusions (locally elevated Moho) or magmatic underplating. They attributed this negative correlation between the sediments and the gravity data as a consequence of differences in the flexural strength of the lithosphere during rifting and during sedimentation.

Nigeria is entirely located within the Pan African orogenic (mobile) tectonic belt, and has experienced episodes of widespread crustal rejuvenation since the occurrence of this tectonothermal event some  $550 \pm 100$  Ma (Woakes et al., 1987; Wright, 1985). Hence, NE Nigeria is underlain by reactivated and heterogeneous crystalline Precambrian crust with Cretaceous to Quaternary age sediments infilling the Trough and associated basins. The Upper Benue Trough is part of the more extensive West African rift System (WAS), which in turn, is an arm of the West and Central African Rift System (WCARS). The WCARS is a chain of genetically and physically-related intra-continental rifts (Fairhead & Green, 1989; Fairhead & Okereke, 1990; Guiraud et al., 1992 and Fairhead et al., 2012) that straddles Africa from Nigeria through Cameroon to the Kenyan rifts (Fairhead & Binks, 1991). The associated rift basins are a result of lithospheric shear and extension tectonics of McKenzie (1978) type, resulting from the passive response of the African plate to the opening of the South Atlantic rifts and the stresses generated by the northward propagation of the rift (Fairhead & Okereke, 1990). Phases of compressional tectonics related to the collision of the African and Eurasian plates and the onset of major readjustments in the relative motion of the African plate are recorded in sediments within the Trough (Maurin et al., 1986; Benkheilil, 1989). The isostatic response has been the passive upwelling of buoyant mantle material, concomitant ductile deformation of the lower crust mainly in the form of necking or thinning, and brittle deformation of upper crustal crystalline basement. This has resulted in overall subsidence and high angle block-bounding planar normal faults (Genik, 1992; Mandl, 2000). Such faults are known to control the distribution, architecture and basin-fill history of sedimentary depocenters. The tectonic setting of the area is consistent with the McKenzie (1978) rift basin model (Fairhead & Okereke, 1990). The Benue Trough runs parallel to the Cameroon line, which is a tectonic fault stretching from Sao Tome and Principe to Nigeria (Fitton, 1980 and Okereke, 1988).

Crustal extension and subsidence temporarily ceased in the Campanian (75 Ma ago) leading to the propagation of the Equatorial Atlantic Shear Zones into the study area. Maurin et al. (1986) discussed the presence of sinistral movements along NNE shear faults in the Benue Trough using the “en echelon” disposition of some fold axes in the Middle Benue. These sinistral shear movements (marked in figure 6.2 using grey-coloured arrows) and folding are thought to have resulted from the changes in stress patterns which accompanied the propagation of the Equatorial Atlantic Shear Zones into the study area as a result of the differential opening of the Central and South Atlantic Oceans (Fairhead, 1988b; Fairhead & Okereke, 1987, 1990). This has led to the inversion of basin-fill (Avbovbo et al., 1986; Benkhelil, 1987).

Odeyemi (1981) and Ekwueme (1990) suggest that the Nigerian basement complex suffered its most extensive reworking and remobilisation during the Pan-African tectonothermal event ( $550\pm 100$  Ma), when the preferred direction of plate motion and fractures was NorthEast-SouthWest (NE-SW). The presence of NorthWest-SouthEast (NW-SE) trends in relicts or older Nigerian basement complex rocks have also been interpreted to represent previous reworking and remobilisation induced by the Kibaran tectonothermal event ( $1100\pm 200$  Ma). Grant (1985) show that extensive granitisation, such as characterised the extensive remobilisation of the Nigerian basement, depletes the magnetite content of extrusive calc-alkaline (Fe-Ti oxides and silica-rich) metamorphic rock assemblages. By the same process, magnetite may be concentrated in intrusive equivalents of these calc-alkaline rocks, which are of acidic-to-intermediate composition (Grant, 1985). Since bulk rock magnetism depends on the magnetite content of rocks (Section 2.2.3), it is valid to assume that the distribution of magnetic anomalies in NE Nigeria reflects the composition of the underlying magnetic basement.

## 6.2 NE Nigeria TMI anomaly ( $\Delta T$ ) dataset and its quality.

### 6.2.1 The dataset.

The TMI anomaly ( $\Delta T$ ) grid used for this study (Figure 6.4) was obtained from reducing two aeromagnetic total magnetic field intensity (TMI) datasets released for this research (Appendix F) by: (1) GETECH Group Plc., UK.<sup>2</sup>; and (2) Dr. Sally Baritt of the ITC, Enschede, The Netherlands. While GETECH supplied a *TMI anomaly ( $\Delta T$ ) grid*, Dr. Baritt’s complimentary dataset for the northern-most part of NE Nigeria were TMI (T) data supplied in their *raw (un-reduced) state, as a spreadsheet of observations*. The first challenge was to reduce Dr. Baritt’s data to the same specification as the GETECH dataset (Appendix F), and then to merge the two datasets. Further details on these two datasets and the procedure adopted to address these challenges, are presented in appendix F.

---

<sup>2</sup>GETECH Group Plc., UK is shortened to GETECH in future references, for brevity

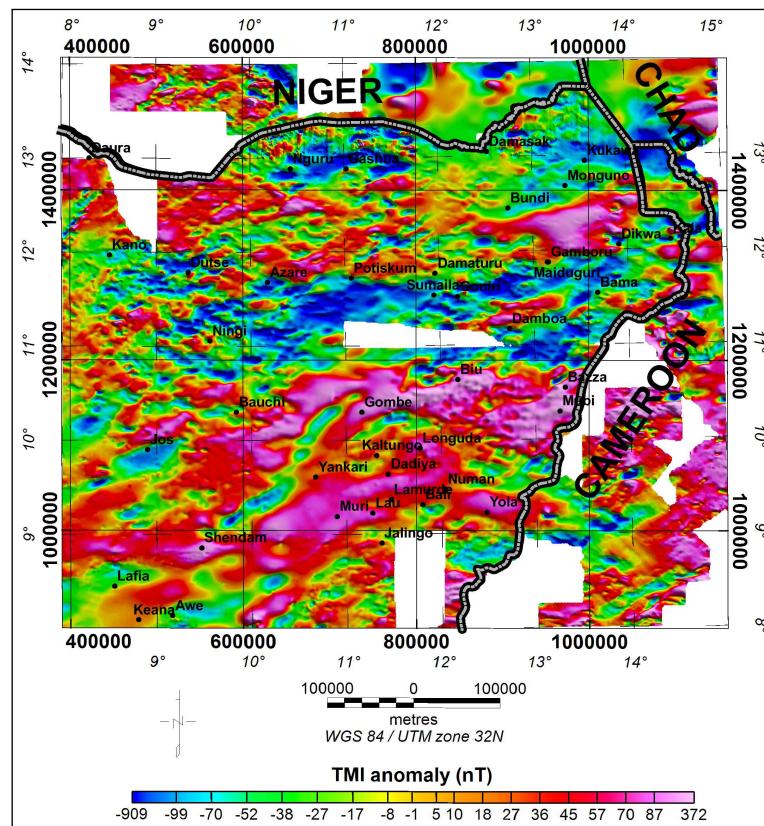


**Figure 6.4:** The NE Nigeria TMI anomaly ( $\Delta T$ ) dataset, obtained from merging GETECH and Dr. Barritt's grids (Appendix F). Thick and wavy black line is the Nigerian border in the study area. A magnified version of this figure is shown in appendix H (Figure H.3).

The NE Nigeria aeromagnetic dataset (Figure 6.4) was compiled as part of the African Magnetic Mapping Project (AMMP), which lasted from January 1989 to mid 1992 (Barritt et al., 1993; Fairhead et al., 1997). The AMMP was conducted by a consortium of institutions, including the Institute of Geophysics and Tectonics (IGT), University of Leeds, and the ITC, Enschede, The Netherlands (Barritt et al., 1993). The  $1 \times 1^\circ$  (1:250000 scale) TMI anomaly map sheets<sup>3</sup> show that the flightline directions during surveys were generally NorthNorthWest-SouthSouthEast (NNW-SSE) and North-South (N-S). The maps also show that the AMMP aeromagnetic data for Nigeria were collected during the 1975 to 1976 period by three companies; Polservice Geopol<sup>TM</sup>, Fairey Surveys Limited<sup>TM</sup> and Hunting Geology and Geophysics Limited<sup>TM</sup>.

About 50% of these NE Nigeria TMI datasets were obtained at nominal flying heights (mtc, i.e. mean terrain clearance) of 500 ft ( $\approx 150$  m), while the remaining 50% were acquired at 2500 ft ( $\approx 760$  m). While the flightline spacing was kept constant at 2 km, the tieline spacings varied in relation to the flying height: 10 km when flying height is 2500 ft; 20 km when the flying height is 500 ft. Furthermore, the maps show that, when the flying height is 2500 ft, the flightlines were oriented  $0/180^\circ$  (N-S) and the tielines were oriented  $90/270^\circ$  (East-West, W-E). On the other hand, when the flying height is 500 ft, the flightlines were oriented  $150/330^\circ$  (NorthNorthWest-SouthSouthEast, NNW-SSE) and the tielines were oriented  $60/240^\circ$  (NorthNorthEast-SouthSouthWest,

<sup>3</sup>The map sheets were provided by Professor C. S. Okereke, Department of Geology, University of Calabar, Calabar, NIGERIA.

NNE-SSW). The direction of the flightlines were perpendicular to the direction of strike of the major geological features in the area. The tielines were oriented perpendicular to the flightlines. These survey design specifications are typical for geological basin reconnaissance during petroleum exploration (ULIS, 1993).

Although considerable improvements have been achieved in the area of spatial data processing, Fairhead et al. (1997) indicated that processing artefacts, e.g., long wavelength distortions due to lack of adequate regional controls may be present in some AMMP sub-grids. Efforts to minimise these artefacts are reported to include (Barritt et al., 1993): (I) Filtering off of TMI wavelengths hundreds of kilometres (100-800 km) in width, to remove long wavelengths introduced by data processing procedures, like merging and gridding (Fairhead et al., 1997). The Lowes-Mauersberger spectrum plot obtained for MAGSAT (Magnetic Field Satellite 1979-1980) dataset (Figure 2.1), was used to initially remove the core and crustal fields from the AMMP grid ULIS (1993); and (II) The filtered wavelengths in (I) were then replaced with crustal MAGSAT TMI data which had been stably downward-continued to 1 km above the Earth's surface. Other processing problems led to a not so smooth merge along the common edges of some AMMP constituent grids (Fairhead et al., 1997). This problem may have resulted from errors introduced during the manual digitisation of the TMI maps. Other sources of this error may be inadequate levelling or positioning of TMI observations at varying flight heights. Some of these problems were observed in the NE Nigeria dataset (Figure 6.4).

The geology of NE Nigeria consists mainly of Albian-Pleistocene sedimentary rocks, as well as Precambrian crystalline basement complex and Cretaceous volcanic rocks (Section 6.1.2). While such sedimentary rocks are generally considered to be non-magnetic, the more Fe- and Mg-rich crystalline rocks are considered magnetic (Grant & West, 1965; Reford, 1964; Bath, 1968; Nettleton, 1971). Therefore, the boundaries between these rock-types represent interfaces/across which significant magnetic susceptibility contrasts ( $\delta k$ ), hence, magnetic anomalies exist (Blakely, 1996). Such  $\delta k$  interfaces may also occur within sedimentary rocks, generating weak magnetic anomalies (e.g., <10 nT (Nabighian et al., 2005; Pilkington et al., 2006) and <50 nT (Pozza et al., 2004)). Fortunately, these weak magnetic anomalies are not detectable at flight heights exceeding 300 m (Pilkington et al., 2006). Since the  $\Delta T$  dataset for this study was acquired at an average mean terrain clearance exceeding 450 m,  $\Delta T$  are considered to derive only from the magnetic crystalline basement and volcanic rocks underlying the area.

Recently, a higher resolution  $\Delta T$  dataset was acquired (2003 to 2010) by Fugro Airborne Surveys for the Federal Government of Nigeria (Chandler, 2010), at 500 m line spacing and 80 m mtc. At different stages of this research we made efforts (Appendix G), including a personal visit to both the Nigerian Ministry of Mines and Solid Minerals Development, now Nigerian Ministry of Mines and Steel Development and the Geological Survey of Nigeria to secure some of this dataset. Oil companies, like Chevron, Total and Shell, with significant interest in the study area were also approached (e.g., figure G.2) to help extend the study beyond NE Nigeria, but without success. Consequently, the  $\Delta T$  dataset in figure 6.4 is the basis of all interpretations of NE Nigeria

basement structure and composition in this chapter.

### 6.2.2 Dataset quality.

No information on pre-survey quality control and calibration was available for the NE Nigeria  $\Delta T$  dataset. While flightlines had constant spacing of 2 km, tielines were either 10 or 20 km apart. The original NE Nigeria  $\Delta T$  dataset was thus, a coarse mosaic of cell sizes of 2 km  $\times$  10 km and 2 km  $\times$  20 km, and did not contain  $\Delta T$  data for intervening NE Nigeria locations. Hence, the dataset was interpolated by GETECH at  $\approx \frac{1}{4}$  of the sampling interval onto a 1 km  $\times$  1 km grid, to provide data for unsampled locations (ULIS, 1993). Consequently, approximately 80% of the available  $\Delta T$  data grid for NE Nigeria has been interpolated (Section 6.2.1). Reid (1980) showed the dependence of the quality of all post-acquisition data processing on survey design specifications. The two quantities which control the fidelity of discrete frequency-domain and time-domain datasets are, respectively, the Nyquist frequency,  $f_N$  (Sheriff, 2002) and Nyquist wavenumber,  $r_N$  (Reid, 1980). Equation (6.2.1) relates  $r_N$ ,  $\lambda_N$  and  $\Delta x$ . The 1 km sampling interval imposes a Nyquist frequency,  $f_N$  (Equation (6.2.1a)) of 0.5 cycles/ km and Nyquist wavenumber,  $r_N$  (Equation (6.2.1b)) of  $\pi$  cycle/ km on the  $\Delta T$  dataset from NE Nigeria. Therefore, anomalies on the NE Nigeria dataset are at much higher frequencies than the  $f_N$  of the original dataset.

$r_N$  and  $\lambda_N$  specify the limits of wavenumbers and wavelengths that can be accurately represented within a discrete dataset. Wavelengths ( $\lambda$ ) below  $\lambda_N$  are *aliased*, i.e., *rolled into wavelengths*  $> \lambda_N$ . To avoid aliasing, therefore, the power of the radial average spectrum of the data must be negligible for all  $\lambda < \lambda_N$  (Reid, 1980). All wavenumber components of the NE Nigeria dataset below  $r_N = \pi$  cycle/ km would have been irrecoverably lost to aliasing due to the filtering effects of re-sampling, gridding and contouring processes.

$$f_N = \frac{f_s}{2} \quad (6.2.1a)$$

$$r_N = \frac{2\pi}{\lambda_N} \equiv \frac{\pi}{\Delta x} \quad (6.2.1b)$$

where  $f_s = \frac{1}{\Delta x}$  is sampling frequency,  $\Delta x$  is sampling interval, and  $\lambda_N = 2\Delta x$  is Nyquist wavelength.

The constant sampling interval of 1 km along both flightlines and tielines ( $\Delta x \equiv \Delta y$ ) means that the minimum  $\Delta T$  wavelength resolvable on the NE Nigeria dataset is 2 km (Equation 6.2.1). This limit poses no problem because the regional features of interest to this study should usually have wavelengths in excess of 50 km (Ajakaiye et al., 1986).

Reeves & Wu (1989) show that potential field data are adequately sampled once the sampling interval ( $\Delta x$ ) is less than one-half ( $\frac{1}{2}$ ) of the source-sensor separation, i.e., the mean height of the magnetometer above the magnetic source (the magnetic basement in NE Nigeria). The  $\frac{1}{2}$  to  $\frac{1}{5}$  of the flightline spacing chosen for gridding the Nigerian AMMP dataset meet this criterion. The

resulting high fidelity dataset was not expected to pose any aliasing problems. If present, however, aliasing effects could be identified on airborne magnetic maps and their derivatives as stripes, which are parallel to the flightlines (Pedersen et al., 1990), and minimised by frequency-domain-based filtering.

Smith & O’Connell (2005) and O’Connell & Owers (2008) show that both the bi-cubic (Akima) and MINC gridding techniques can spatially alias anomalies when the major axes (trend) of the anomaly is oblique (acute) to the flightline direction, resulting in “boudinage patterns” on the new grids. These “boudinage patterns” of Smith & O’Connell (2005) were not observed in the NE Nigerian aeromagnetic dataset (Figure 6.4). However, interpolation involves mathematical prediction of anomalies for unsampled locations, and can lead to inaccuracies. Similarly, navigation problems may result in incoherences between flightlines. Any inaccuracies due to these sources will be treated as noise. Although noise content in the NE Nigeria  $\Delta T$  data have been suppressed (smoothed) by the application of a low-pass upward-continuation (to 1 km) filter (Nabighian, 1972; Pedersen et al., 1990; Reid, 1980), any remaining noise may be amplified to unacceptable limits when computing spatial derivatives from the  $\Delta T$  data, especially vertical derivatives when calculated in the Fourier domain (Fairhead, 2007; Li, 2003; McMullan & McLellan, 1997). Hence, processes requiring such computations require special attention.

Using the expected value of the power spectrum profile derived from a reduced-to-pole (RTP) ensemble of magnetised blocks (Spector & Grant, 1970), Reid (1980) defined the amount (%) of the  $\Delta T$  power aliased ( $F_T$ ), a measure of frequency loss, as the ratio between two quantities;  $\bar{h}$  (the mean terrain clearance, i.e., mean height of the magnetometer above the magnetic basement) and  $\Delta w$  (Equation (6.2.2)):

$$F_T = \exp \left\{ \frac{-2\pi\bar{h}}{\Delta w} \right\} \quad (6.2.2)$$

where  $\Delta w$  refers to the least between flightline spacing and the sampling interval.

Equation (6.2.2) holds only when  $r\Delta h \leq 0.5$ , where  $r$  is the wavenumber,  $h$  is the distance between the magnetometer and the top of the magnetic basement and  $\Delta h = h_{max} - h_{min}$  (amplitude of  $h$  variations). The optimum ratio for  $\frac{\Delta w}{\bar{h}}$  is 2:1 for  $\Delta T$  surveys, 1:1 for vertical gradients of  $\Delta T$  surveys or 1:0.5 for forward-modelling of isolated  $\Delta T$  (Reid, 1980). Thus, to keep aliased power below 5% when interpolating/gridding aeromagnetic survey data, the maximum flightline spacing must not exceed twice the mean height of the magnetometer above the magnetic source. Lower sampling rates along flightlines than specified for the flightline spacing will further ensure high fidelity of acquired data (Reid, 1980).

Outcropping basement complex rocks dominate more than 45% of the study area while basement complex rocks are readily encountered at shallow depths (< 1 km) in boreholes (Avbovbo, 1980). These are indications of the generally high ( $\geq 1$ )  $\frac{\Delta w}{\bar{h}}$  ratios, i.e., low  $F_T$  (Equation (6.2.2)) of the NE Nigeria dataset. These quantities seem to reflect the fact that the Nigeria data were acquired

along flightlines, which were generally perpendicular to the dominant geological strike, ensuring that short wavelength power constitutes a small fraction of the dataset (Reid, 1980).

### 6.2.3 Reduced-to-equator (RTE) of dataset.

This section describes the further processing required to transform the merged  $\Delta T$  dataset (Figure 6.4) to one that could be used for interpretation. A primary processing step was to transform the dataset presented in figure 6.4 to its RTE equivalent (Section 2.3.2), since NE Nigeria straddles the geomagnetic equator (Appendix A). Grids of inclination and declination across the area were required (Figures 6.5a and 6.5b, respectively), to transform the dataset to its RTE equivalent. The inclination of the geomagnetic field vector ranged from about  $-7$  to  $7^\circ$  (Figure 6.5a), while the declination of the vector ranged from about  $-5.5$  to  $-2.5^\circ$  (Figure 6.5b). Actual ground measurements of these elements of the geomagnetic field in parts of the study area agree well with the DGRF (1945-1985) global field model (Ofoegbu, 1986, 1988).

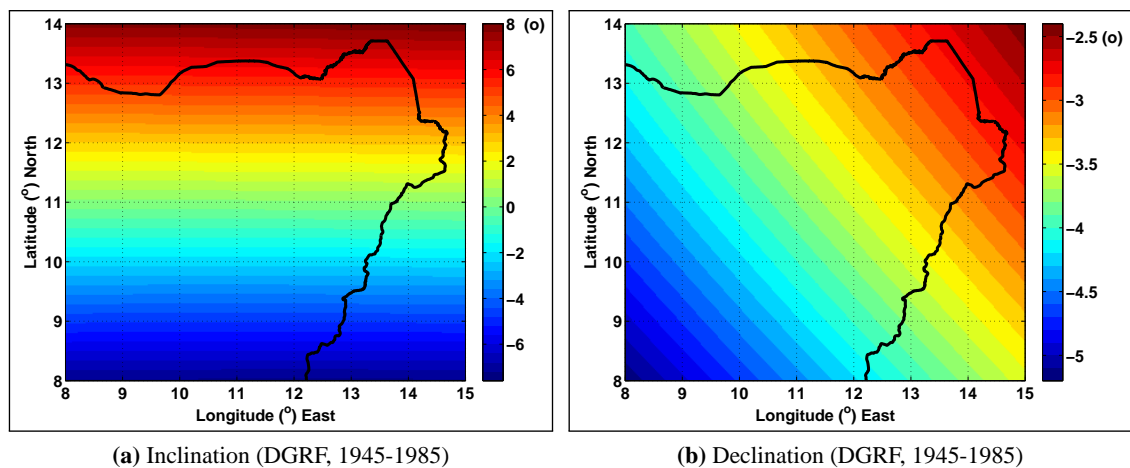


**Figure 6.5:** Inclination and declination of the regional DGRF (1945-1985), NE Nigeria, during mean aeromagnetic data acquisition date of 1<sup>st</sup> January, 1975. The Nigerian boundary around NE Nigeria is shown in black.

Because the dataset (Figure 6.4) covered more than  $10^\circ$  in range of geomagnetic latitudes, its RTE transformation was cumbersome and not at all straight-forward. The steps involved were similar to those of Arkani-Hamed (1988); Swain (2000), including the following:

(1) First, the range of inclinations on the inclination grid for NE Nigeria (Figure 6.5a) was divided into ten (10) equal parts (bands). Each division was allowed to overlap adjacent divisions by  $0.5^\circ$ , giving a total overlap between divisions of  $1^\circ$ . Then the grid of declination (Figure 6.5b) was also divided into ten (10) equal bands, each corresponding to the overlapping inclination band;

(2) The mean inclination and declination from corresponding pairs of inclination and declination bands were used to transform the entire NE Nigeria  $\Delta T$  dataset to its RTE equivalent, resulting

in 10 different RTE versions of the dataset. However, each RTE version was only accurate over the area defined by the band (sub-grid) used for the transformation. Subsequently, based on the dimensions of the inclination and declination bands, ten (10) accurately RTE-transformed bands of  $\Delta T$  datasets were extracted from these 10 different RTE versions of the dataset;

(3) Finally, the 10 accurately-transformed bands of RTE-transformed TMI data grid were merged to produce the RTE equivalent (Figure 6.6) of the NE Nigeria  $\Delta T$  dataset (Figure 6.4). Comparisons between the ranges of power and the shapes of power spectra of NE dataset in figures 6.4 and 6.6 (Figure F.3, appendix F) show that the RTE-transformed dataset display significant improvements in signal power, as power is more focussed along the better defined linear segments of the RTE power spectrum. However, although the RTE process considerably simplifies anomalies, the process introduces azimuth-dependent complexities in anomaly amplitudes and shapes, resulting in their displacement relative to locations of their sources (Section 2.3.3).

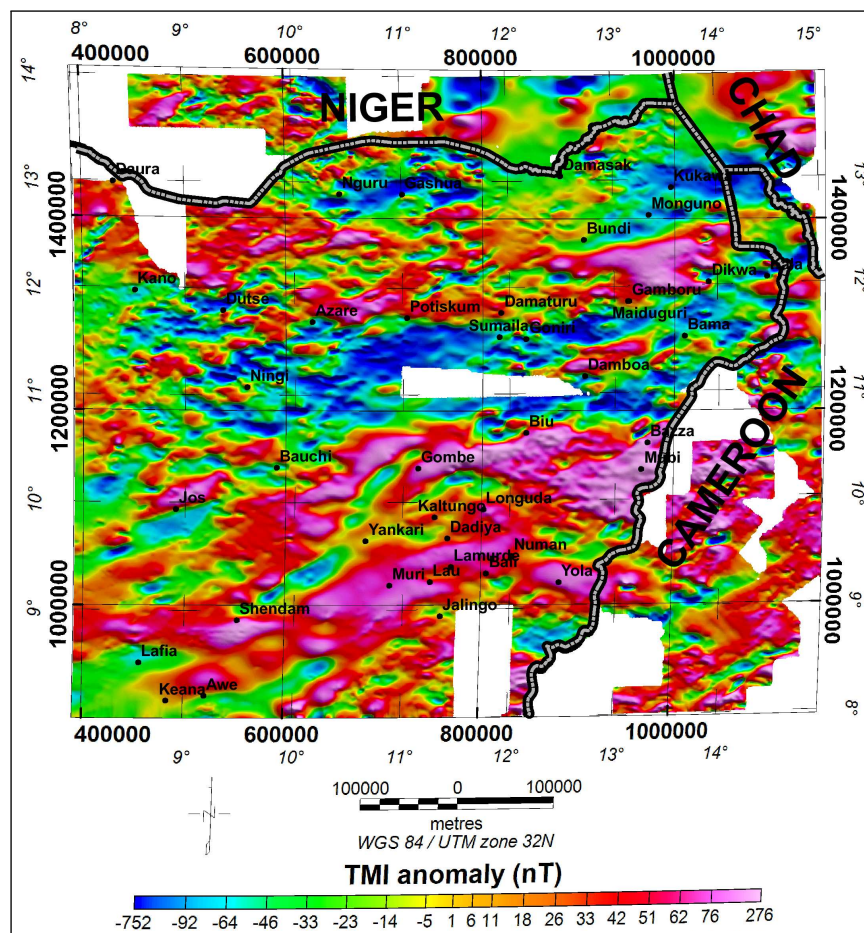


**Figure 6.6:** RTE of NE Nigeria  $\Delta T$  grid (Figure 6.4). The Nigerian border with Niger, Chad and Cameroon is shown. Major cities/towns are shown in white for easy reference. A more annotated, magnified version of this figure is shown in appendix H (Figure H.4).

Although  $\Delta T$  can be traced across the RTE grid (Figure 6.6), linear striations that correlate roughly with the 150/330° flightline direction, tend to mask some anomalies. These micro-levelling prob-

lems are, to a lesser degree, obvious on the original  $\Delta T$  grid (Figure 6.4), but have been enhanced by the RTE process. So, further processing ensued with micro-levelling of the data. The RTE grid (Figure 6.6) was micro-levelled using bidirectional gridding in Oasis montaj<sup>TM</sup>. The grid was then filtered to rid it of wavelengths shorter than 3.5 km, using a 3<sup>rd</sup>-order Butterworth filter with 3.5 km cut-off wavelength. Figure 6.7 presents maps of the resulting short wavelength (Figure 6.7a) and long wavelength (Figure 6.7b) components of the levelled RTE of  $\Delta T$  grid (Figure 6.6). It is these derived grids that will be used to map basement structures, their relationships and depths across NE Nigeria.

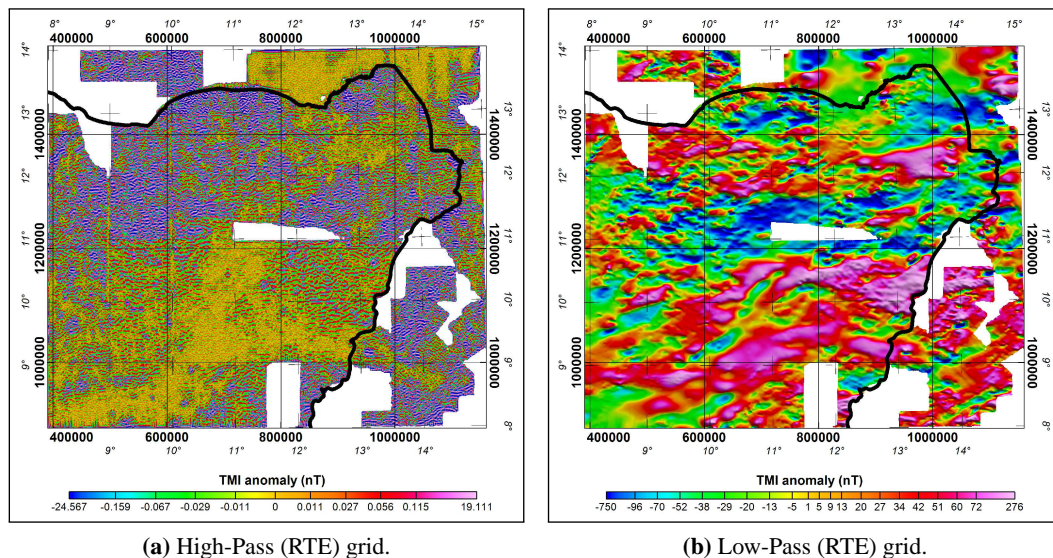


**Figure 6.7:** 3<sup>rd</sup>-order Butterworth-filtered versions of the RTE of NE Nigeria  $\Delta T$  grid. The filter cut-off wavelength ( $\lambda_c$ ) used was 3.5 km, the sampling interval of the Nigerian dataset. While grid shown in figure 6.7a represents all wavelengths less than  $\lambda_c$ , grid shown in figure 6.7b represents all wavelengths exceeding  $\lambda_c$ . Black wavy line in (a) and (b) represent the Nigerian boundary around the study area. Magnified versions of these figures are presented in appendix H (Figure H.5).

### 6.3 Qualitative structural interpretation

I begin by describing observations drawn from both the grid of  $\Delta T$  wavelengths  $< 3.5$  km (Figures 6.7a) and that of  $\Delta T$  wavelengths  $> 3.5$  km (Figure 6.7b). While only brief attention is paid to figure 6.7a, a lot more focus is on the grid of longer wavelength RTE  $\Delta T$  (Figure 6.7b), from which various spatial amplitude derivatives and Tilt angles have been computed for use both in further qualitative and quantitative interpretations (Section 6.4). In general, the interpretation strategy I have adopted for this study is based on the procedure recommended by Gunn et al. (1997) and Li (2003) for interpreting aeromagnetic data from regions with limited geologic control.

This interpretation involved both the outcrop geology (Figure 6.2) and the tectonic framework of the study area (Sections 6.1.2 and 6.1.3), which were based mainly on Benkhelil (1989), Fairhead & Green

(1989) and Fairhead & Okereke (1990). Qualitative observations made while examining model  $\Delta T$  profiles (Chapter 3), “Bishop” model grids (Chapters 4 and 5) and the Ruhuhu sub-grid from Southern Tanzania (Appendix E) were also integrated into this interpretation.

### 6.3.1 Amplitudes, shapes and wavelengths of anomalies ( $\Delta T$ ) from NE Nigeria.

I begin by repeating pertinent conclusions drawn from comparisons between RTP and RTE equivalents of  $\Delta T$  datasets in chapters 3 to 5: (I) *Positive amplitudes were directly located above rocks with higher magnetisation and/or shallow depths on RTP of  $\Delta T$  datasets. This relationship was reversed on RTE of  $\Delta T$  datasets.* Throughout this discussion, therefore, **NE Nigeria  $\Delta T$  will be described by their actual amplitudes on the  $\Delta T$  (RTE) grid/map (Figure 6.6). That way, positive RTE  $\Delta T$  will represent negative RTP  $\Delta T$ , and vice versa.**<sup>4</sup> Consequently, locations of basement rocks with higher magnetisations and/or shallow depth should positively correlate with negative anomalies on the NE Nigeria (RTE) dataset (Figure 6.6), with positive anomalies indicating locations underlain by lower magnetisation and/or deep sources; (II) The reverse-polarised RTE  $\Delta T$  were almost half their RTP equivalents in amplitude; (III) RTE amplitudes varied with the azimuth of its source (two-dimensional magnetic edges or faults). Consequently,  $\Delta T$  magnitudes were highest for W-E striking edges, intermediate for NW-SE and NE-SW striking edges, minimum for NNW-SSE and NNE-SSW striking faults, and zero for N-S trending faults; (IV) The shape of  $\Delta T$  from NNW-SSE and NNE-SSW striking faults depended on their degree of isolation and linearity, i.e., en-echelon or dissected faults develop dipole-like anomalies; and (V) All W-E striking dipolar anomalies were preferentially extended further West and East of their sources. Unisolated dipolar anomalies from adjacent sources usually interfered to produce anomalies that were altogether unrelated, both in magnitude and extent, to their causative bodies.

As expected, North-South (N-S) trending  $\Delta T$  were not observed on the NE Nigeria (RTE) grid (Figure 6.6). Also, while a swarm of NE-SW trending  $\Delta T$  occur, only a handful of NW-SE, NNW-SSE and NNE-SSW striking  $\Delta T$  are observable on this grid. This observation is important, because faults with these attitudes have been reported from the combined outcrop (Guiraud, 1990), geophysical data and Side-looking airborne radar, SLAR (Benkhelil, 1987, 1989) studies of parts of the study area. Comparisons between RTE and RTP of the Ruhuhu grid (Appendix E, Figures E.3 to E.5) showed that RTE grids sourced from locations at which N-S and near N-S ( $N \pm 20^\circ$ ) trending sources abound do not image N-S striking sources, but can be dominated by prominent W-E, NW-SE and/or NE-SW trending anomalies, which result from interference between adjacent discrete dipolar anomalies that develop along the discontinuous (en-echelon) edges of these sources (Figure 2.8).

The N-S, NNW-SSE and NNE-SSW trending structures reported from NE Nigeria may very well have originated from the transmission of regional crustal stresses through pliable sediments, in di-

<sup>4</sup>The NE Nigeria  $\Delta T$  (RTE) grid (Figure 6.6) will be hereafter referred to as NE Nigeria (RTE) grid or RTE grid.

rections which may be unrelated to those etched in the underlying magnetic basement, and responsible for the observed  $\Delta T$ . The widespread Santonian (80 Ma) compressional event which reactivated pre-existing dextral Pan African shear zones in the study area (Maurin et al., 1986; Benkhelil et al., 1989), was capable of such un-correlated deformation in the overlying sediments. In that case, N-S, NNW-SSE and NNE-SSW striking structures (Benkhelil, 1987, 1989; Guiraud, 1990) will be limited to the outcropping sediments, and will have no equivalent trends in the basement beneath NE Nigeria, as imaged by  $\Delta T$  (RTE) grid. To constrain my efforts at relating  $\Delta T$  shapes and trends on the RTE grid (Figure 6.6) to structures reported from NE Nigeria, I will use an equivalent grid of Bouguer gravity (BA) anomalies, provided by Getech Plc., UK (Figure 6.8). This grid was compiled from profiles of various vintages, and presented on a  $5' \times 5'$  regular grid in Equatorial Mercator Projection ULIS (1988). BA grids present bulk rock density variations of both the crust and upper mantle.

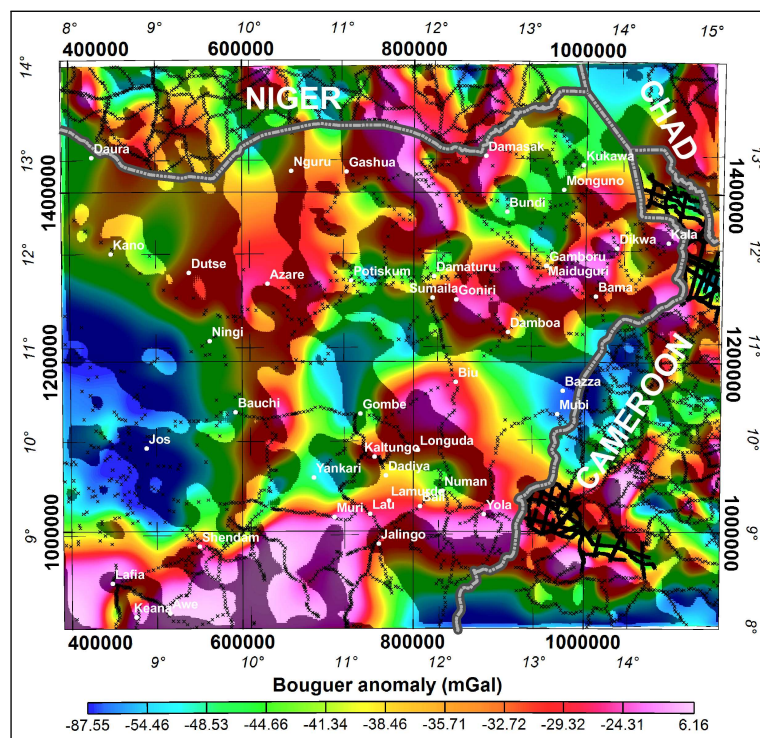


**Figure 6.8:** Bouguer gravity anomaly (BA) grid of NE Nigeria. Locations of gravity stations from which the grid was obtained is superimposed to indicate the limited constraint that can be derived from this sparse dataset within NE Nigeria. The data provides better constraint outside the study area. White labels refer to neighbouring countries and selected towns/cities in Nigeria. A magnified version of this figure, with more annotations, is shown in appendix H (Figure H.6).

The gravity station distribution is sparse within the study area compared with neighbouring countries (Figure 6.8). Therefore, the BA grid is biased in favour of locations with dense stations. However, the grid is slightly better constrained in the NorthEastern (Maiduguri-Monguno-Dikwa area), NorthCentral (Potiskum-Damaturu), SouthCentral and SouthEast (Gombe-Kaltungo-Jalingo-Yola area), as well as Western and SouthWestern (Jos-Shendam area) parts of the study area (Figure 6.8). It is mainly at such locations that this grid will be used to constrain inferred structures.

Negative BA of long wavelengths dominate the African continental crust compared with its surrounding oceanic crust (R. Hartley, 1996). Some of these long wavelength BA were observed (in blue) in the Western (Jos area), Eastern (Mubi-Bazza area) and SouthEastern parts of NE Nigeria (Figures 6.8 and H.6 in appendix H). However, several shorter wavelength anomalies with positive or negative amplitude are superimposed on the large negative long wavelength BA. These short wavelength positive BA occur where the crust is thin (mantle is elevated, i.e., shallow), while negative BA occur where the crust is relatively thick (mantle is deeper). Where these short wavelength anomalies are linear, their trends have been traced and labelled (in grey) in figure H.6 (Appendix H). The figure shows that BA with N-S and near-N-S ( $N\pm 20^\circ$ ) strikes occur in the Northern and Southern parts of NE Nigeria (labelled A-A'), while W-E and near-W-E striking BA (labelled D-D') seem to be limited to the SouthWestern and SouthEastern parts of NE Nigeria. NW-SE and NE-SW trending BA (B-B' and C-C') also occur. However, the BA grid is dominated by NW-SE trends. Isolated three-dimensional (3D) anomalies also occur, e.g., in the Kaltungo-Biu area. The variously-oriented linear BA trends confirm the presence of N-S and near-N-S crustal trends as indicated by Benkhelil (1989) and Guiraud (1990).

Other observations from the NE Nigeria (RTE) grid (Figure 6.6) include (See figure H.4 in appendix H for more annotations): (1)  $\Delta T$  trend mostly NE-SW; (2)  $\Delta T$  are generally blocky, with jagged East-West (E-W) directed edges. These may have resulted from discontinuities in the structure responsible for the observed anomaly; (3) A broad, W-E trending negative RTE  $\Delta T$  (denoted by white A in figure H.4) dominates the area bound on its Northern end by the following locations; Kano, North of Dutse, North of Azare, Daura, Goniri, Maiduguri, and Gamboru. The Southern limits of this anomaly runs from just North of Bauchi, Biu to about 70 km North of Mubi. The excellent correlation between the central part of this anomaly and parts of the negative BA establishes it as originating from underlying basement sources; (4) The broad negative anomaly in (3) is dissected on its West by two prominent, but discontinuous NE-SW trending positive RTE anomalies (one is SW of Azare, and the other is NW of Bauchi and appears to extend to, and beyond, the Jos area) and on its East by two other anomalies of similar characteristics (Bama town is located between these anomalies). These two sets of anomalies are sub-parallel to each other (Black lines in figure H.4), and seem to have originated within the positive (RTE) anomaly-dominated belt below. The extensive discretisation of the Western and Eastern parts of the broad negative RTE anomaly in (3) is consistent with the degree of interference that would be induced by the presence of the N-S and near-N-S striking basement sources (Figure H.6, appendix H), although invisible on the RTE grid (Figure 6.6), especially when intersected by the dominant NE-SW striking sources in (4); (5) Above and parallel to this belt is a belt dominated by more NE-SW trending anomalies, shown to continue from the Southern parts of the study area by the 5 and 8 km upward-continued equivalents of the Nigerian (RTE) grid (Appendix F, Figure F.4); (6) The Western and Eastern limits of the Benue Trough appears to be marked by two prominent NE-SW trending, positive RTE anomalies (Grey lines in figure H.4, appendix H). These anomalies, respectively, extend from about 75 km NE of Lafia to Damaturu, and from about 50 km East of Wukari through the North of Jalingo and Numan towards Mubi; and (7) That the Benue Trough

(area sandwiched) between these anomalies is not homogeneous is indicated by a sub-parallel NE-SW trending, but negative RTE anomaly. Together, these linear anomalies appear to be offset by several NW-SE and E-W trending anomalies between Keana and Gombe (Black dashed lines in figure H.4). The offsets are more obvious on the negative anomaly than their adjoining positive (RTE) anomalies. Similar trends were mapped from some positive BA (Figure H.6) at these locations, where they generally correlate with negative RTE anomalies (Figures 6.7b and their upward-continued equivalents shown in figure F.4), e.g., axial positive BA in the Benue Trough correspond to the negative anomalies described in (3) and (4) above. The same correlation is observed around Gashua, Dutse and Bauchi. However, significant departures from such correlations were observed in the Jos, Biu and Mubi areas (Marked by black letters B, C and D in figure H.4, appendix H). These non-correlations are discussed further below.

A circular, negative  $\Delta T$ , with isolated positive  $\Delta T$  lobes to its North and South seem to mark the source of the dormant Biu Plateau (Figure 6.6 and black letter C in figure H.4, appendix H). This volcanic conduit is located some 35 km due West of Biu, with a maximum radius of  $\approx 25$  km. Similar conduits appear to occur some 60 km NNE of Kaltungo (about 50 km NNW of Longuda). Two major linear anomalies; one trending NE-SW and the other trending NW-SE, tend to intersect close to the centres of these volcanic conduits (Figures 6.6 and H.4), where a large (150 km wide) positive three-dimensional (3D) BA also occurs (Figure 6.8). Therefore, the intersecting NE-SW and NW-SE  $\Delta T$  may identify locations beneath which denser upwelling upper mantle materials may have flown, i.e., thinned crust.

High amplitude, positive (RTE)  $\Delta T$  (equivalent to negative RTP  $\Delta T$ ) are observed over the Jos plateau area, as well as the area up to 170 km NW of Mubi (Black letters B and D in figure H.4, appendix H, respectively), suggesting that the magnetic basement is deeper at these locations than in the surrounding areas. In other words,  $\Delta T$  suggest the presence of a basement depression (basin). But, geological observations from these areas show that plateaus consisting of volcanic rocks outcrop in these areas (Ajakaiye et al., 1986; Caen-Vachette & Umeji, 1988). Therefore the positive (RTE)  $\Delta T$  observed at these two locations may have resulted from the depletion of magnetite and related phase changes (Grant, 1985) during granulite facies metamorphism-induced migmatization of pre-existing basement (McCurry, 1989). That these observations derive from deep-seated sources is confirmed by their correlation with long wavelength negative BA labelled E and F in figure H.6 (Appendix H), as well as their persistence on the 5 and 8 km upward-continued NE Nigeria (RTE) grid (Figure F.4).

Anomalies on the high-pass (HP) filtered grid (Figure 6.7a) will be described mainly in terms of perceived rates of change of anomaly wavelengths and/or continuity ( $F_{amp}$ ) across the grid. Variations in  $F_{amp}$  across the grid correlates well with major outcrop features in NE Nigeria, since high  $F_{amp}$  corresponds to outcropping or shallow crystalline basement (short wavelength  $\Delta T$ ) and low  $F_{amp}$  corresponds to sediment-covered (deeper) crystalline basement (longer wavelength  $\Delta T$ ), respectively (Compare figures 6.7a and 6.2). High  $F_{amp}$  (labelled A in black in appendix H, figure H.5a) dominates much of the study area, especially, the Northern 50% (from latitude  $10^{\circ} 50''$

N). High  $F_{amp}$  (shallow) basement underlie two major parts of NE Nigeria: (i) North and NW parts, e.g., Gashua, Kano, Sumaila, Ningi and Azare area; and (ii) NNE of Biu, i.e., South of Maiduguri down to Bazza.<sup>5</sup>

Low  $F_{amp}$  (labelled B in black in appendix H, figure H.5a) were associated with a relatively smaller area North of Maiduguri in the Chad basin, the Upper Benue Trough (Gongola and Kerri-Kerri basins) and the Middle Benue Trough (Bashar-Muri and Yola basins). These parts of NE Nigeria characterised by low  $F_{amp}$  correlate well with known crustal depressions, where the basement is generally expected to be deep. Hence, low  $F_{amp}$  appears to indicate the spatial limits and orientations of *basinal or basin-like* structures, i.e., *sedimentary depocenters*. An example occurs in the area just North of Maiduguri, suggesting the presence of a narrow, but deep basement surrounded by broad, relatively shallow basement beneath the Nigerian sector of the Chad basin.

Intermediate  $F_{amp}$  (labelled C in black in appendix H, figure H.5a) were associated with the volcanic conduits and Palaeogene (Tertiary) emplacement of basaltic intrusions and the associated amphibolite-granulite facies metamorphism (Wright, 1985). The area covered by intermediate  $F_{amp}$  include the following (Figure H.2): (i) the area  $\approx$  100 km North of Jos; (ii) the area North, up to 100 km East, and NE of Lafia through Potiskum, to the South and SouthWest of Damaturu; (iii) the area South of Yola, South of Jalingo and East of Wukari; (iii) the area South of Damboa, North and NorthWest of Biu, and Mubi; and (iv) South of Kala, North of Dikwa and Monguno, Kukawa and Damasak to the North, and the area NE and NW of Damaturu. The correlation of this intermediate  $F_{amp}$  locations with isolated short wavelength, negative-to-positive three-dimensional BA (Figure H.6), as well as with Tertiary alkaline to peralkaline (Biu-Mubi area) and Jurassic alkaline to tholeiitic (Jos) and alkaline-calc alkaline (Benue Trough) metamorphic/igneous assemblages of Wright (1989), is evidence of the extent of migmatisation and granitisation of the basement complex (McCurry, 1989) during the opening of the Benue Trough and associated intracontinental basins in NE Nigeria (Benkhelil et al., 1989). Trends reported here conform with those of Benkhelil (1989).

A few generally near-N-S trends were also apparent from the high-pass (HP) filtered grid (Figure 6.7a), at boundaries between high and intermediate  $F_{amp}$ . These are traced by the grey lines in figure H.5a (Appendix H). Inferences based on  $F_{amp}$  variations require further refinements, e.g., integration with enhanced versions of the RTE dataset.

The inferences and conclusions I have reached above, as well as subsequent, interpretations can be erroneous, if the unknown details relating to the acquisition and initial processing of the NE Nigeria dataset (Section 6.2.1, and figure 6.4) were to have resulted in a significantly biased dataset. If that were the case, important anomalies on the dataset may have been masked, introducing significant errors to my interpretations for NE Nigeria.

<sup>5</sup>See appendix H, figure H.2 for basin and other locations cited in this section.

### 6.3.2 Location and trends of basement-involved faults, and other structures in NE Nigeria.

Locations of 2D and non-2D structural edges from RTE of the complex “Bishop” model grid were only effectively mapped by integrating estimates from the “Tilt-Depth” ( $\theta$ ), the Second vertical derivatives (SVD), Analytic signal amplitude (ASA), Local wavenumber (LW), Horizontal gradient magnitude (HGM) of  $\theta$  ( $HGM_{(\theta)}$ ) and HGM of  $\Delta T$  ( $HGM_{(\Delta T)}$ ) methods (Chapters 5 and 6, and appendix E).

Results obtained from comparing locations of structural edges estimated using these functions from RTE and RTP equivalents of “Bishop” model grids (Sections 5.3.2, 5.3.3 and 5.6) and a Southern Tanzania subgrid (Appendix E) show that:

(I) NW-SE, NE-SW, ENE-WSW, WNW-ESE and W-E striking structures on both RTP and RTE grids correlated strongly and positively;

(II) NNW-SSE and NNE-SSW ( $N \pm 20^\circ$ ) trending structures showed no correlations at all;

(III) The relative spatial density or frequency and closeness of NNW-SSE and NNE-SSW trending structures relative to NW-SE, NE-SW, ENE-WSW, WNW-ESE and W-E striking structures on any grid was critical to the degree of destructive interference observed on a  $\Delta T$  grid. The further W-E extension of W-E trending anomalies and dipolar anomalies from NNW-SSE and NNE-SSW trending structures was the main source of the destructive interference (anomaly cancellation) and  $\Delta T$  losses on RTE grids;

(IV) Because of the indirect dependence of Tilt angles ( $\theta$ ) and local wavenumber on  $\delta k$  the “Tilt-Depth”, LW and  $HGM_{(\theta)}$  methods were able to equally image edges of both subtle and dominant sources. While LW and  $HGM_{(\theta)}$  maxima represent locations of source edges,  $\theta = 0$  contour marked equivalent locations for the “Tilt-Depth” method. However, adjacent LW or  $HGM_{(\theta)}$  maxima may interfere to generate secondary maxima, requiring constraint based on estimates from ASA,  $HGM_{(\Delta T)}$ , SVD and  $\theta$  of the same  $\Delta T$  dataset;

(V) While  $\theta$  estimates for relatively well isolated 2D structures were very reliable and easier to interpret, only  $HGM_{(\Delta T)}$ ,  $HGM_{(\theta)}$ , ASA and LW estimates that are coincident or closest to  $\theta$  and/or SVD estimates should be treated as certain;

(VI) The presence of near-N-S ( $N \pm 20^\circ$ ) striking edges on RTE grids were indicated by isolated linear frequency changes across SVD of these grids. These edges can be mapped from isolated linear stacks of short wavelength, E-W trending zero contours of the SVD, and maxima of the  $HGM_{(\Delta T)}$ , ASA, LW and  $HGM_{(\theta)}$ . Every maxima location trace (scores 1 to 4 of [Blakely & Simpson, 1986](#)) from the  $HGM_{(\Delta T)}$ , ASA, LW and  $HGM_{(\theta)}$  methods is required to effectively map locations of near-N-S edges, by inference, from RTE grids; and

(VII) An integrated approach to edge location estimation from RTE of  $\Delta T$  grids should commence with ASA and  $HGM_{(\Delta T)}$ , then SVD and  $\theta$ , and finally LW and  $HGM_{(\theta)}$ .

The NE Nigeria (RTE) grid was transformed to its spatial vertical and horizontal derivatives, from which 'special functions' (Phillips, 2000) or enhanced (Finn & Morgan, 2002; Gunn et al., 1997) grids were derived. Enhancements applied to NE Nigeria (RTE) grid (Figure 6.6) included the second vertical derivatives (SVD), horizontal gradient magnitude ( $HGM_{(\Delta T)}$ ), analytic signal amplitude (ASA), local wavenumber (LW), Tilt angles ( $\theta$ ), and horizontal gradient magnitude of  $\theta$  ( $HGM_{(\theta)}$ ).<sup>6</sup> The potential advantages to interpretation that transforming the NE Nigeria (RTE) grid to its  $\theta$  and  $HGM_{(\theta)}$  equivalents were outlined in section 2.6.1.

Here, enhanced versions of NE Nigeria (RTE) grid (Figure 6.6) will be used to map the horizontal locations, trends/continuity of, and relationships between anomalous magnetic structures in the NE Nigeria basement, with attempts made to correlate major structures observed on the enhanced with the outcrop geology of Maurin et al. (1986), Benkhelil (1989); Benkhelil et al. (1989) and Guiraud (1990) and long wavelength Bouguer gravity anomaly map (Figure 6.8). However, since near-N-S ( $N\pm 20^\circ$ ) striking edges generate spurious  $\Delta T$  that can make it difficult to correctly image non-N-S striking edges, extreme caution will be exercised when correlating observations.

Figures 6.9a, 6.9b, 6.10a and 6.10b, respectively, present the SVD, the additive inverse of  $\theta$ , ASA and  $HGM_{(\Delta T)}$  equivalents of the NE Nigeria (RTE) grid.<sup>7</sup> The LW and  $HGM_{(\theta)}$  equivalents of these grids are shown in figures 6.11a and 6.11b, respectively.  $HGM_{(\Delta T)}$ , ASA, LW and  $HGM_{(\theta)}$  are absolute values (non-directional), hence, are not affected by polarity changes (Sections 5.2 and 5.3).

I begin by examining the grids in figures 6.9a, 6.9b, 6.10a and 6.10b for similarities between structural trends already indicated on the grids in figures H.4, H.6 and H.5a, with special interest in confirming the presence or absence of near-N-S striking basement structures. The ASA grid (Figure 6.10a) is dominated by the characteristic pearly or dipole-like anomalies, some of which align to form 'strings of pearls' (Figure 2.8), especially, in the area North of latitude  $10^\circ 50'$  N (Appendix H, figure H.8a). Such anomalous strings occur above discontinuous (en echelon), near-N-S striking magnetic sources and their edges in RTE datasets (Section 2.4.2). Similar near-N-S striking anomalies occur at similar locations, and are shown along with other trends as dashed-black lines, on the  $HGM_{(\Delta T)}$  map (Appendix H, figure H.8b), as well as on the SVD (Appendix H, figure H.7a). Examples of near-N-S striking anomalies occur in the Dikwa, Bama and Bazza area (NE part of the study area), and in the Gashua area (Northern parts of the study area). On these grids, other linear features of the magnetic basement appear to be limited to the Gombe area and the area South of latitude  $10^\circ 50'$  N, where mainly well-defined NE-SW and NW-SE striking magnetic edges occur, as well as the area just South of Bundi and Monguno (in the Chad basin),

<sup>6</sup>The  $HGM_{(\theta)}$  is also recently introduced special function (Verduzco et al., 2004).

<sup>7</sup>Additive inverse of  $\theta$  translates  $\theta$  of RTE amplitudes to their correct polarities. This correction addresses polarity changes observed between  $\theta$  of RTP and RTE grids (Section 4.3.2). Throughout this chapter, references to  $\theta$  will imply its additive inverse.

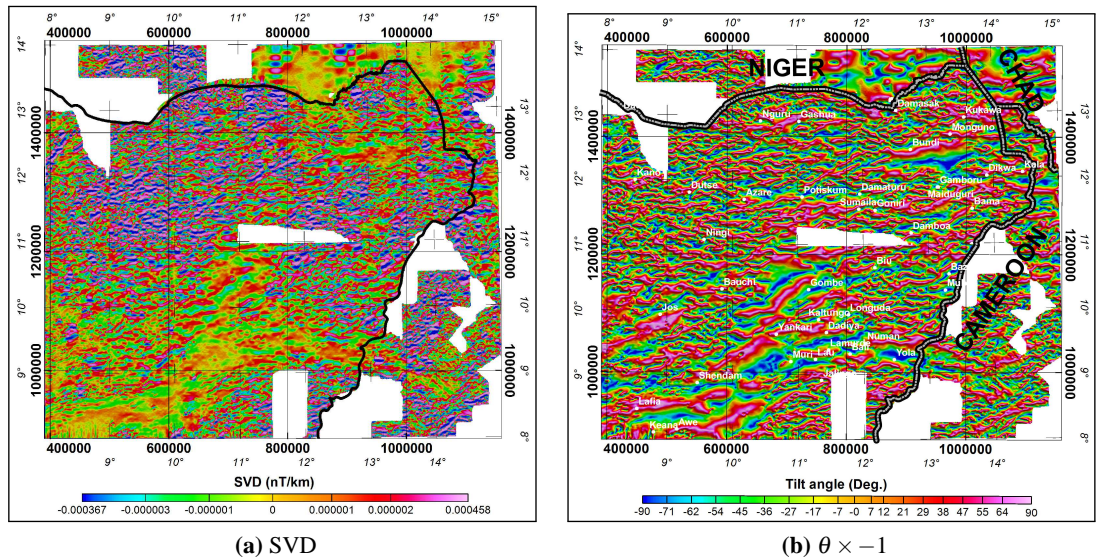


**Figure 6.9:** SVD and  $\theta$  maps of NE Nigeria. These maps were derived from the Low-Pass filtered  $\Delta T$  grid (Figure 6.7b). Locations of structural edges are estimated using SVD=0 or  $\theta = 0$  contours. Magnified versions of these figures are presented in appendix H (Figure H.7).

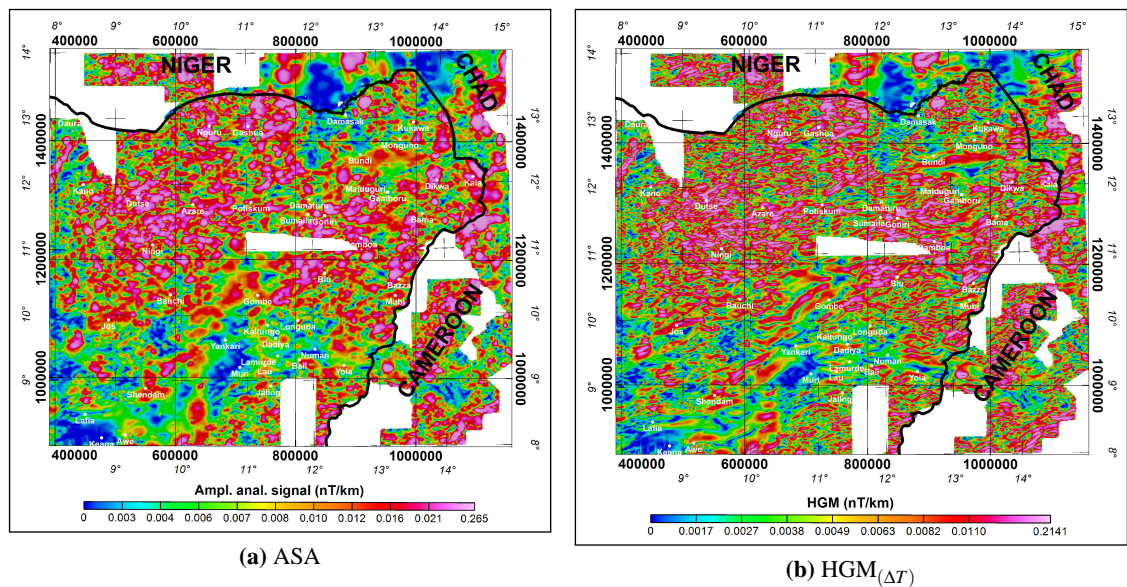


**Figure 6.10:** ASA and  $HGM_{(\Delta T)}$  maps of NE Nigeria. Maps were derived from the Low-Pass filtered  $\Delta T$  grid (Figure 6.7b). Local maxima of ASA or  $HGM_{(\Delta T)}$  estimate locations of structural edges. Magnified versions of these figures are presented in appendix H (Figure H.8).

where a prominent W-E trending anomaly occurs. It was nearly impossible to independently map isolated anomalies (structures) from the LW and  $HGM_{(\theta)}$  maps (Figure 6.11), as well as the SVD map (Figure 6.9a). These maps were integrated mainly to map lateral extents, since locations dominated by sedimentary rocks in figure H.2, i.e., deep basements (depocenters) were generally characterised either by greenish-yellow coloured SVD anomalies (Appendix H, figure H.7a), light-green to greenish blue LW anomalies (Appendix H, figure H.9a), or greenish-blue to deep blue  $HGM_{(\Delta T)}$  anomalies (Appendix H, figure H.8b) and  $HGM_{(\theta)}$  anomalies (Appendix H, figure H.9b).

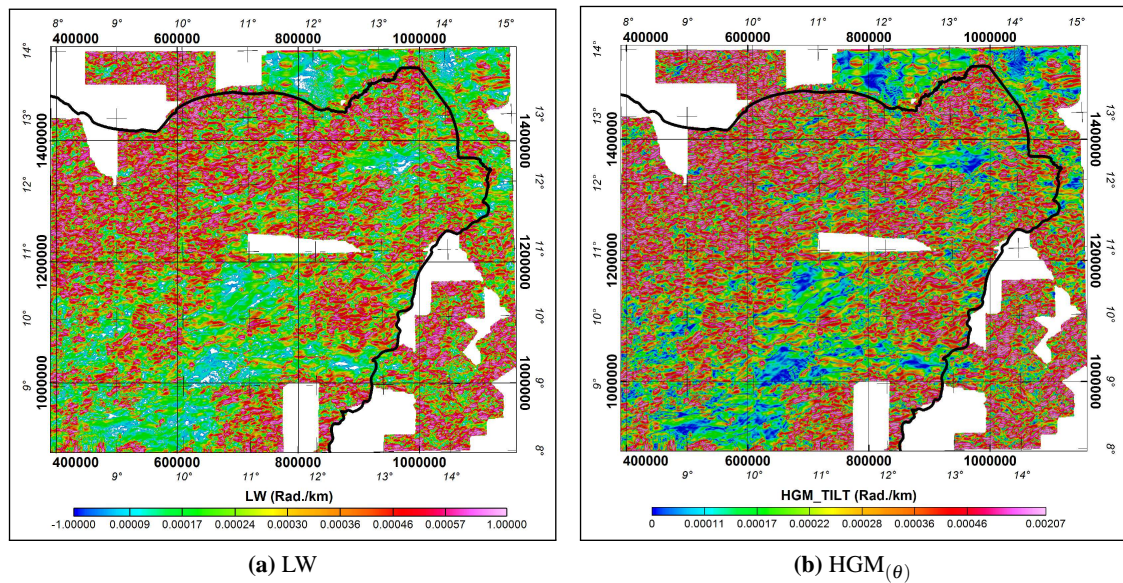


**Figure 6.11:** LW and  $HGM_{(\theta)}$  maps of NE Nigeria. Maps were derived from the Low-Pass filtered  $\Delta T$  grid (Figure 6.7b). Local maxima of LW or  $HGM_{(\theta)}$  estimate locations of structural edges. Note that values that tend very close to 0 have been masked from the LW grid (Figure 6.11a). Magnified versions of these figures are presented in appendix H (Figure H.9).

More than all other functions, more plausible anomalous structures with strike directions other than  $N\pm 20^\circ$  were imaged on the  $\theta$  map (Figure 6.9b), e.g., in the Jos area. Integrating interpretations from  $\theta$  and SVD maps allowed the mapping of intricate tectonic structures of the NE Nigeria basement. Especially obvious from these functions was the relationship between transpressional and transtensional structures in the Gombe, Kaltungo, Numan and Biu area. This may reflect the independence of  $\theta$  derivatives from  $\delta k$ . Locations of magnetic structural edges (contacts) have been extracted from all grids shown in figures 6.9, 6.10 and 6.11, using methods described in sections 4.5 and 5.3. These locations are presented in appendix F (Figures F.5, F.6 and F.7), but have been integrated to infer the fault locations presented in figure 6.12, with trends on the  $\theta$  location estimates map (Figures F.5) as the main basis. To ease comparisons, locations where sediments and/or basement-sediment contact outcrop in NE Nigeria (Figure 6.2) have been superimposed on inferences presented in figure 6.12.

The difference between the character of my interpretation of the Tanzania dataset (Figure E.5) and that of figure 6.12 or H.10 is that the former only considered edge locations for sources on the Ruhuhu grid (Tanzania), while the latter have superimposed edge location estimates on inferences of basement configuration between edge locations for sources in NE Nigeria. The inclusion of inferences of basement configuration from entire special function grids of NE Nigeria defines the principal difference in character between interpretations for NE Nigeria and those for the Ruhuhu area of Tanzania (Figure E.5).

Fault (source edge) orientations across NE Nigeria (Figure 6.12) display four distinct sub-parallel sets: (I) three NE-SW striking sets; (II) at least four NW-SE trending sets; (III) three nearly N-S trending sets; and (IV) one W-E striking set. NW-SE trending faults cross-cut NE-SW trending

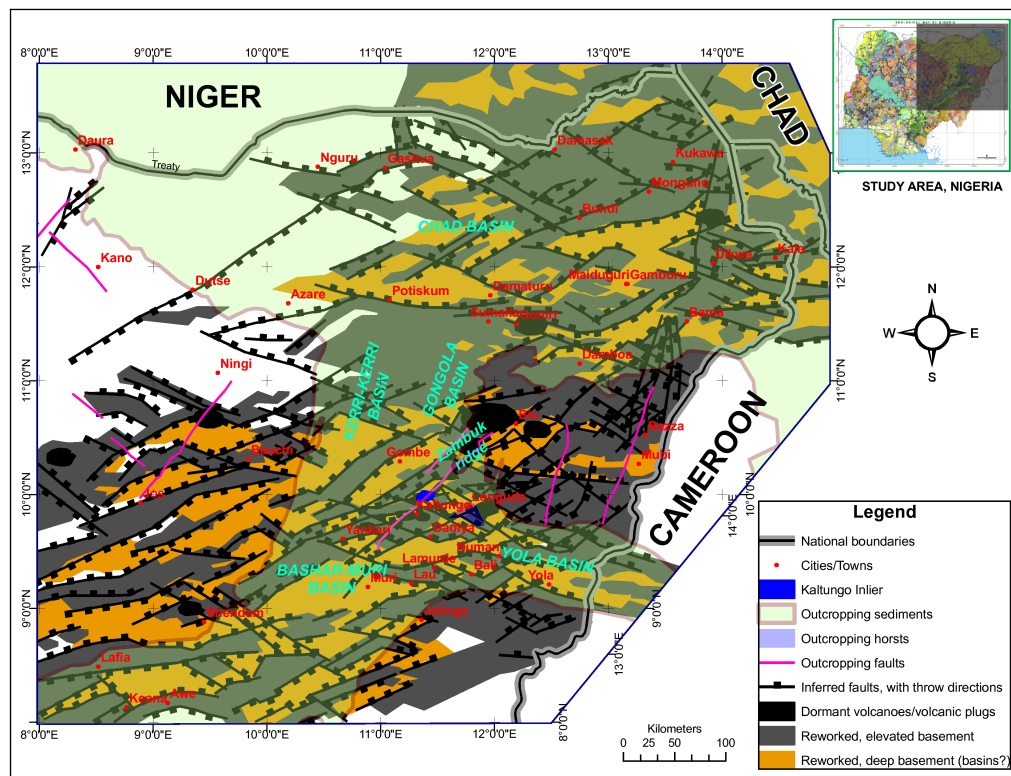


**Figure 6.12:** Gross magnetic basement structure map of NE Nigeria, showing the major tectonic units in the basement. Elevated basement is loosely used to represent possible basement horsts (where they occur within deep basement) or plutonic, granite-like emplacements (where they occur within the “homogeneous basement”). Locations of outcropping sediments and/or basement-sediment contact in NE Nigeria extracted from figure 6.2 is superimposed to ease comparisons. A magnified version of figure 6.12 is shown in appendix H (Figure H.10).

faults in the Maiduguri, Mubi, Kaltungo, Jalingo and Shendam areas of NE Nigeria. Sets of NE-SW striking faults occur across the Jos-Bauchi axis, Shendam-Yankari axis, South of Jalingo, Gombe area, as well as the area North of Potiskum, Damaturu and Maiduguri. Sets of NW-SE striking faults occur: in the Gashua-Maiduguri-Bama axis; about 40 km NW of Bazza, extending NW through Potiskum to the Dutse areas; in the Kaltungo-Yola axis; and in the area 150 km NE of Lafia. Sets of N-S striking faults occur: North of Bazza; and Gashua. The only set of W-E striking faults occur in the Awe-Lafia area.

Since  $\theta > 0$  on RTP and  $\text{RTE} \times -1$  datasets only occur over footwalls or the upthrown sides of vertical faults (Figure 3.1), masking all locations where  $\theta < 0$  on the NE Nigeria  $\theta$  grid (Appendix F, figure F.8), leaves locations where probably elevated basements (possibly basement horsts or plutons) occur (Figure 6.12). These  $\theta$  anomalies were constrained using SVD, ASA and  $\text{HGM}_{(\theta)}$  anomalies (Figures 6.9a, 6.10a and 6.10b). Along with both the NE Nigeria (RTE) and gravity datasets (Figures 6.6 and 6.8, respectively), these anomalies were also used to map probable locations of dormant volcanoes (or volcanic plugs) in the area (Figure 6.12). The possible distribution of “basin-like” structures (i.e., locations of long wavelength anomalies) in figure 6.12 was mapped by integrating observations on rates of change and/or continuity of  $\Delta T$ , as well as SVD,  $\text{HGM}_{(\Delta T)}$ , ASA, LW and  $\text{HGM}_{(\theta)}$  anomaly wavelengths.

The  $HGM_{(\Delta T)}$  grid remarkably resolved linear structures that correlate well with those on the additive inverse of  $\theta$  grid. These grids show several NE-SW trending linear anomalies, which are offset by a few NW-SE striking features. A major NE-SW feature resolved on these grids corresponds to the axial positive Bouguer anomaly of the Benue Trough. This extensive basement horst, identified using the direction of increasing  $\theta$  (Figure F.8), up to 50 km in width, extends from about 30 km NW of Makurdi to the Kaltungo area (distance of  $\approx 350$  km) where it appears to have aided the emplacement of the Kaltungo Inlier (Benkhelil, 1989). This axial basement horst is intersected by NW-SE trending linear edges in the Shendam area, the Muri area, and the area South of Kaltungo. In the Muri area, the horst bifurcates into two arms for about 50 km, where it is bisected by the NW-SE trending Northern boundary fault of the Yola basin. One  $\approx 25$  km thick NNE-SSW arm runs under the Gongola basin, around the Western boundary of the Kaltungo Inlier and terminates in the vicinity of the root of the Biu volcano (at about 35 km NW of Biu). The second  $\approx 15$  km thick NE-SW arm, appears to thicken in the vicinity of its intersection with the NW-SE trending Northern boundary fault of the Yola basin, bifurcating into two NE-SW trending horst structures. The Western arm of these 10-15 km wide NE-SW horsts runs through the middle of the Kaltungo Inlier, while the other arm circumvents the Eastern side of the Kaltungo Inlier. These two then meet up and terminate at the root of the Biu volcano. Other structures identified in the magnetic basement of NE Nigeria include: (I) a 30-50 km wide, NE-SW trending horst in the area SW of Jos. The propagation direction of the horst structure coincides with the linear NE-SW striking outcrops of basalts in the area (Figure 6.2); (II) the NE-SW trending linear anomalies which mark the limits of the Benue Trough. The location and orientation of these basement horsts and other linear structures clearly indicate the impact of the Gulf of Guinea transform faults in NE Nigeria (Ajakaiye et al., 1986; Benkhelil & Robineau, 1983). The linear NE-SW propagation direction and continuity of SVD,  $HGM_{(\Delta T)}$  and positive  $\theta$  anomalies, as well as their correlation with axial positive gravity anomalies in the Lower Benue Trough (Benkhelil, 1989; Benkhelil et al., 1989; Fairhead & Okereke, 1987, 1990) are further proofs of the tectonic origin of the Benue Trough.

The Jos, Kaltungo, Longuda and Mubi areas, well documented for their outcropping tholeiitic (alkaline) basalts and undifferentiated crystalline basement fabrics (Benkhelil, 1989; Benkhelil et al., 1989; Wright, 1985), were also mapped as basin-like (Figure 6.12). Hence, the following questions arise: (1) Why are these areas identified as basinal features? (2) Could it be that magnetisations in rocks of these areas are low, even though they are mainly igneous?

Tholeiitic (sodic and potassic) basalts are believed to be fractional crystallization products of silica-rich primary basaltic magma (Benkhelil, 1989), which are deficient in Fe and Ti (Grant, 1985). These basalts, common to orogenic belts like the Pan African belt in Nigeria, typically have lower Fe:Ti ratios and are, therefore, weakly magnetic (Grant, 1985). However, basalts which crystallize at low oxidation states are highly magnetic (Grant, 1985), e.g., Olivine basalts are characteristically strongly magnetic, and can be several orders of magnitude more magnetic than calc-alkaline (tholeiitic) basalts (Gunlågsson et al., 2006). If these rocks were not calc-alkaline in composition and of Tertiary age, the observed decreased magnetisation could be explained in

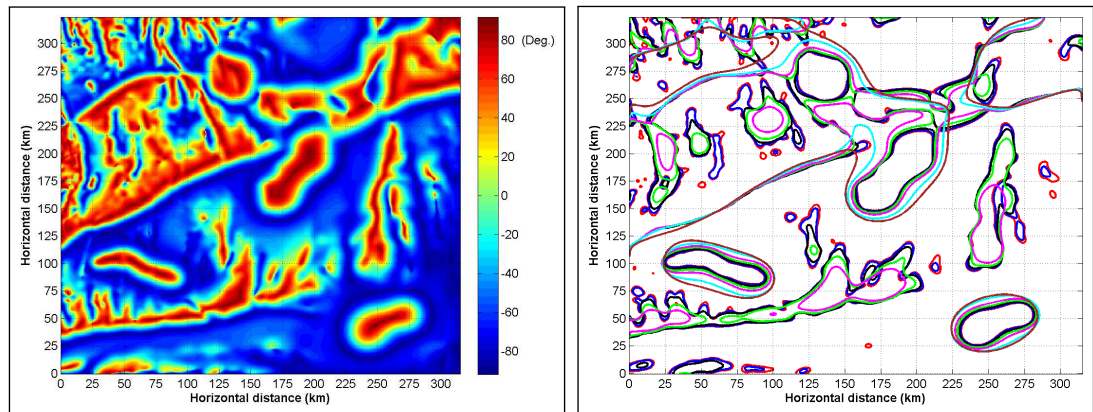
terms of: (1) the presence of remanent magnetisation (Section 2.2.3) or, (2) self-demagnetisation effects (Clark & Emerson, 1999; Telford et al., 1990). Self demagnetization occurs when the direction of the net resultant (effective) magnetisation of anomalous magnetic bodies is different from that of the inducing magnetisation vector (Clark & Emerson, 1999). It is at its maximum in magnetic materials with large susceptibilities ( $k > 0.1$  S.I. Units, Telford et al., 1990). For such materials, the direction of net magnetisation is normal to their sides (faces), and thus, the geometry of the anomalous magnetic body (Krahenbuhl & Li, 2007). In conclusion, the inclusion of the Jos, Kaltungo and Mubi areas in the basinal areas of NE Nigeria (Figure 6.12) is a consequence of its basement originating from silica-rich magmas. Incidentally, intermediate rates of change in anomaly wavelengths on NE Nigeria grids, e.g., the SVD grid (Figure 6.9b) correlate remarkably well with the Mubi, Kaltungo and Jos magnetite-deficient basements. Other areas underlain by similar basement were thus inferred to include the Gombe, Bauchi, Yola, Jalingo, the dissected axial basement horsts of the Benue Trough, as well as, a belt (up to 40 km wide) located about 30 km North of Monguno and Gubio in the NNE corner of the study area.

### 6.3.3 Attitude of basement faults in NE Nigeria.

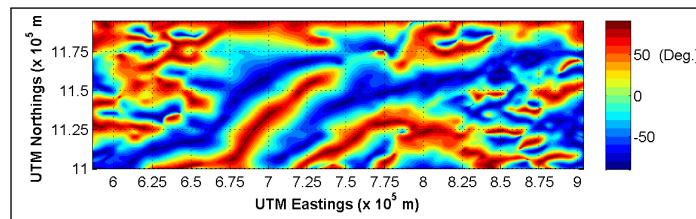
A major consequence of the inverse-squared relationship between  $\Delta T$  and depth or distance from the anomaly source (Equation (2.5.1)) is that  $\Delta T$  amplitudes decay rapidly with increasing distance away from sources. Consequently, when  $\Delta T$  datasets from vertical magnetic edges are upward-continued,  $\theta=0$  contour lines for such datasets diverge outwards, away from the edges. Lahti & Karinen (2010) showed that  $\theta=0$  contour lines diverged symmetrically away from vertical edges, but asymmetrically away from dipping magnetic edges, as continuation heights increased. They proposed this continuation-induced spreading as a means for identifying dipping two-dimensional structures. This technique was tested using two  $\Delta T$  datasets: (I) the CBM (RTP) grid (Figure 4.5a); and (II) an extract from the NE Nigeria (RTE) dataset (Figure 6.7b), covering the area between the North of Kaltungo and South of Biu.  $\theta$ -transformed versions of the un-continued  $\Delta T$  dataset are shown, respectively, in figures 6.13a and 6.13c.

Subsequently, the  $\Delta T$  datasets were upward-continued,  $\theta$ -transformed and the  $\theta=0$  contour lines from the resulting grids were co-plotted for comparison. While the CBM (RTP) dataset was upward-continued to 1, 3, 6, 10, 20 and 30 km, the extract from NE Nigeria (RTE) grid was upward-continued to 2, 4, 8, 10, 20 and 30 km. The zero contours obtained from the  $\theta$ -transformed versions of these upward-continued  $\Delta T$  datasets are shown, respectively, in figures 6.13b and 6.13d.

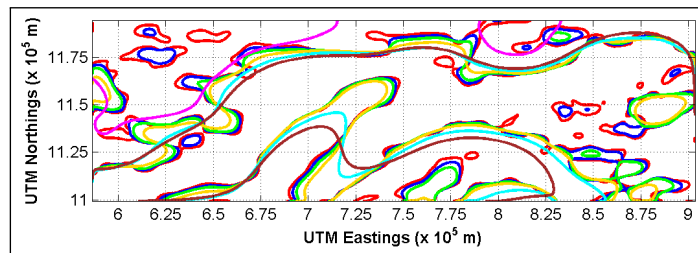
The basement beneath the CBM grid, like that beneath NE Nigeria, is of heterogeneous magnetic composition. However, unlike the CBM grid which is dissected only by vertical structural edges or magnetic susceptibility contrasts (Section 4.2.2), attitudes (dips) of structural edges in the Nigerian basement are unknown. By examining attitudes of  $\theta = 0$  contours at well isolated, vertical 2D and non-2D edges inferred from the CBM grid, a technique was developed for inferring the attitudes



(a)  $\theta$  of "complex Bishop model", CBM (RTP) grid. (b)  $\theta=0$  contours for upward-continued CBM grids.



(c)  $\theta$  of extract from NE Nigeria (RTE) grid.



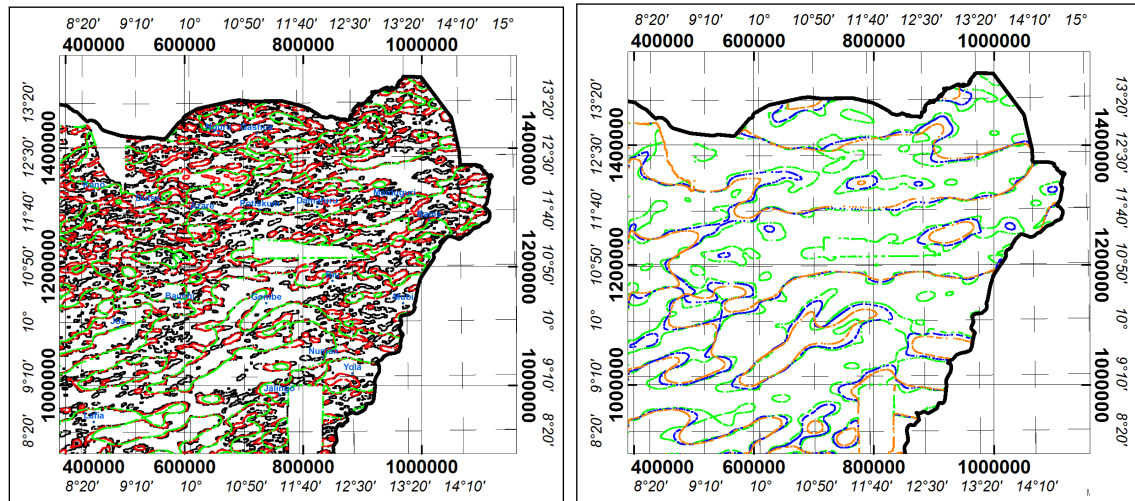
(d)  $\theta=0$  contours for upward-continued extract from NE Nigeria grid.

**Figure 6.13:** A comparison between  $\theta = 0$  contour lines for upward-continued versions of the CBM (RTP) grid and an extract from NE Nigeria RTE grid: (a)  $\theta$  grid for CBM (RTP); (b)  $\theta = 0$  contours for CBM (RTP) is in red, but in blue, black, green, magenta, cyan and brown, when upward-continued, respectively, to 1, 3, 6, 10, 20 and 30 km; (c)  $\theta$  grid for an extract from the Kaltungo area of the NE Nigeria (RTE); (d)  $\theta = 0$  contours for  $\theta$  grid in (c) is in red, but blue, green, gold, magenta, cyan and brown, when upward-continued, respectively, to 2, 4, 8, 10, 20 and 30 km.

of prominent faults mapped from the NE Nigeria dataset.

Results from  $\theta$ -transformed upward-continued CBM (RTP) grids show that contrary to [Lahti & Karinen \(2010\)](#)'s observations,  $\theta=0$  contour lines stack on each other where  $\Delta T$  from vertical contacts suffer minimum interference (Figure 6.13b), e.g., the two-dimensional (2D) contact running through grid nodes (100,175) and (275,250), as well as nodes (50,40) and (175,70). The asymmetric divergence of  $\theta=0$  contour lines observed in figure 6.13b were, mainly, consequences of  $\Delta T$  interference due to critical anomaly source width-to-depth requirements (e.g., [Zhang, 2001](#) and [Flanagan & Bain, 2012b](#)). Even then,  $\theta=0$  contour lines for the first four continuations stack nicely on the edges of these sources. Observations from  $\theta=0$  contour lines from  $\theta$ -transformed NE Nigeria (RTE) grid extract (Figure 6.13d) appear to be similar to those made in figure 6.13b. Based on these observations, and in order to assess the attitudes (relative to the vertical plane) of the faults iden-

tified in NE Nigeria (Figure 6.12), the RTE grid was upward-continued to 5, 8, 20 and 30 km. These upward-continued NE Nigeria  $\Delta T$  grids were transformed to their  $\theta$ -equivalents.  $\theta=0$  contours obtained from these  $\theta$  grids are presented, for clarity, in two separate figures (Figures 6.14a and 6.14b). Examples of  $\theta$  grids obtained from these upward-continued NE Nigeria (RTE) grid are presented (Appendix F, Figures F.9a and F.9b). The dominantly overlapping  $\theta = 0$  contour lines (Figure 6.14) indicate great depths of origin for long wavelength components of NE Nigeria  $\Delta T$  dataset.



(a)  $\theta=0$  contours: 1, 5 and 8 km upward-continued.

(b)  $\theta=0$  contours: 8, 20 and 30 km upward-continued.

**Figure 6.14:** Maps showing the spread of  $\theta = 0$  contours of NE Nigeria (RTE) dataset (Black contour in (a) away from structural edges/faults. Figure 6.14a also shows  $\theta = 0$  contour for the 5 km (Red) and 8 km (Green) upward-continued grids equivalents.  $\theta = 0$  contours for the 8 km (Green), 20 km (Blue) and 30 km (Gold) upward-continued equivalents are shown in figure 6.14b. Magnified versions of these figures are presented in appendix H (Figure H.11).

Based on the overlap or otherwise of  $\theta=0$  contour lines in figure 6.14, fault segments or entire faults shown in figure 6.12 have been sub-divided into vertical and/or dipping faults. Also, the axes of three-dimensional (3D) or near-3D structures have been identified from closures of  $\theta=0$  contour lines. These structural classifications are presented in figure 6.15, and will be used to propose a synopsis of the tectonic history of NE Nigeria in chapter 7.

## 6.4 Depth estimates from semi-automatic inversion methods.

Depths of edges of magnetic structures in NE Nigeria were estimated using the "Tilt-Depth" and local wavenumber (LW) methods, whilst assuming that major structures in the area can be approximated by vertical, 2D magnetic contacts. These methods were chosen based on observations in chapters 4 and 5. Also estimating depths using "Tilt-Depth" and LW methods was straight-forward, since the methods do not require using a moving window.

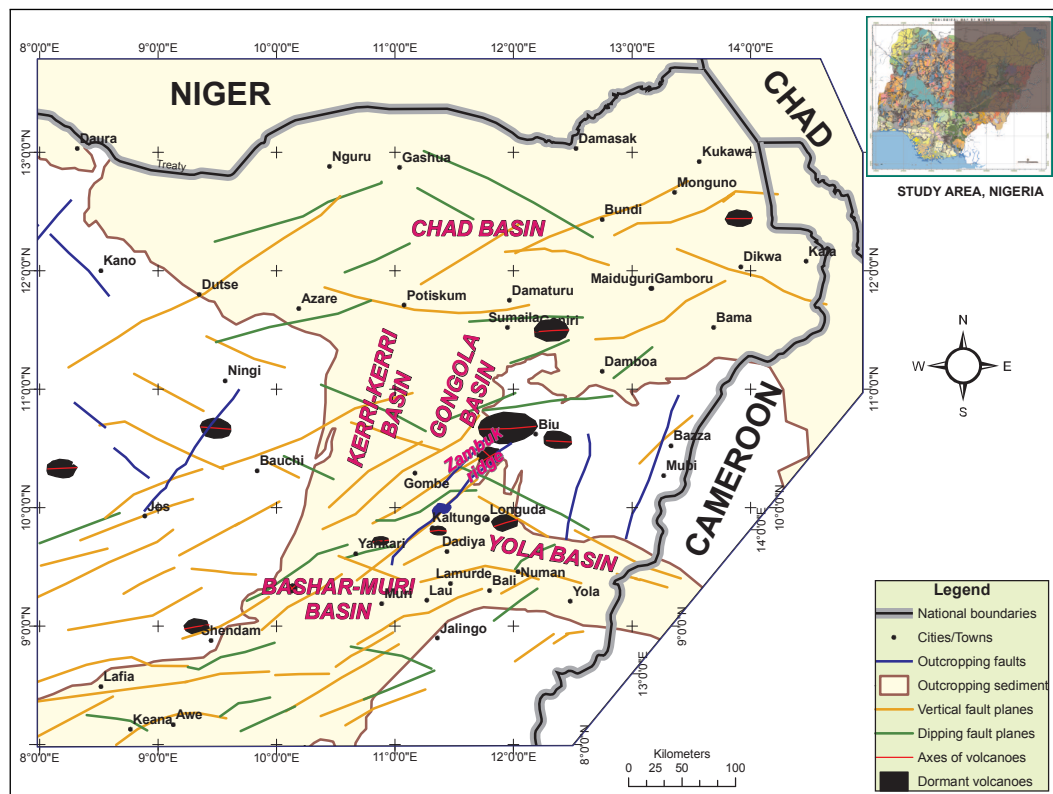


**Figure 6.15:** Attitude of prominent faults and volcanic features in NE Nigeria basement, inferred using  $\theta = 0$  contours of variously upward-continued NE Nigeria (RTE) grids. Attitudes were inferred from the overlap or relative separation between  $\theta$  ( $\theta=0$ ) contours in figure 6.14. Faults and volcanic features were originally presented in figure 6.12. Geological basins in these vicinities are labelled, in line with figure 6.2, to provide context. Locations of outcropping sediments and/or basement-sediment contact in NE Nigeria extracted from figure 6.2 is superimposed to ease comparisons. A magnified version of figure 6.15 is shown in appendix H (Figure H.12).

The "Tilt-Depth" method was implemented in two modes, using the  $\theta \leq \pm 45$  and  $\theta \leq \pm 27$  ranges. The input grid used for depth estimation was the 3.5 km Low-Pass 3<sup>rd</sup>-order Butterworth filtered NE Nigeria (RTE) grid (Figure 6.7b). Estimates from each method were corrected for the 1 km upward-continuation of the dataset (Appendix F), and are presented in figures 6.16 and 6.17, respectively.

Representative profiles across these depth estimate grids (Figures 6.16, H.14a, and H.14b) are shown in figure 6.18. These, along with other profiles (Appendix F; Figures F.10, F.11 and F.12), whose paths are shown in figures 6.16, H.14a, and H.14b, were chosen such that, wherever possible, they were located within the  $\theta = \pm 27$  and  $\pm 45$  distance on the "Tilt-Depth" method estimates grid (Figure 6.17), as well as transect the Chad basin, Gongola/Kerri-Kerri basins, Yola basin and the SW corner of the study area, on all depth estimates grids. In general, profiles of estimates from the LW and  $\theta \leq \pm 27$  range-based "Tilt-Depth" methods display remarkably good correlation. The LW method provided the deepest and most erratic estimates, while the  $\theta = \pm 27$ -based "Tilt-Depth" method provided smoother, intermediate estimates. Several attempts at using running averages to smooth and minimise rapid serrations of LW profiles prior to plotting the profiles, resulted in poorly correlating and less satisfactory LW depth profiles.

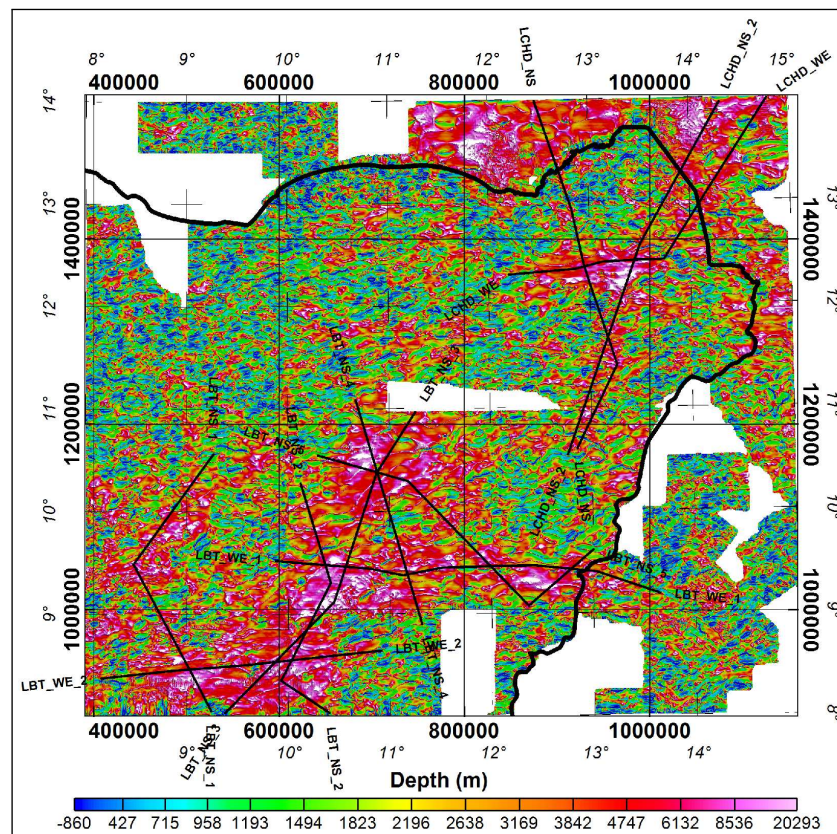
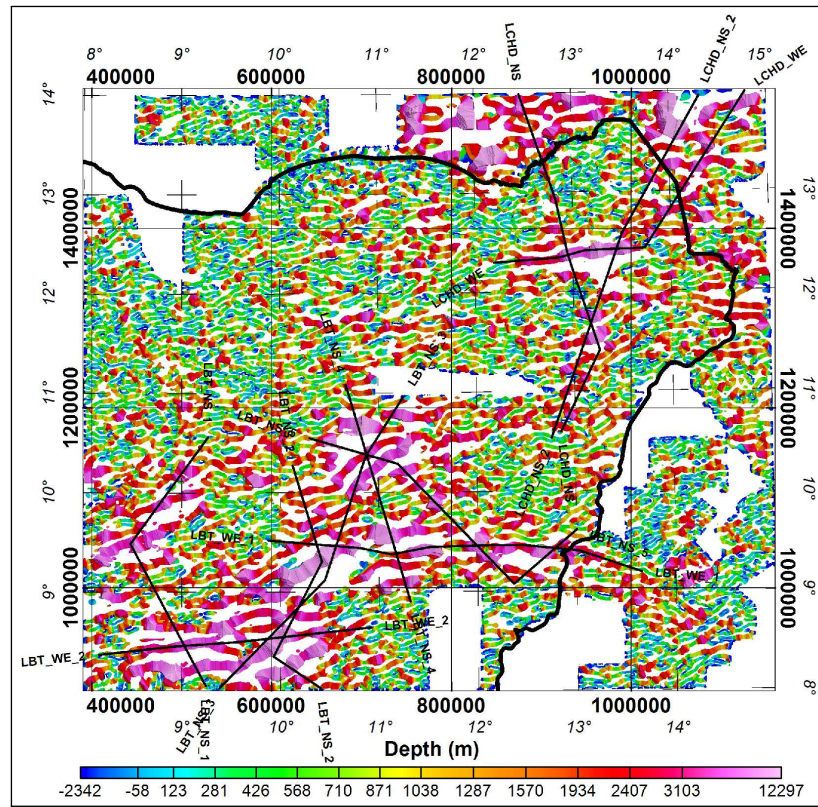


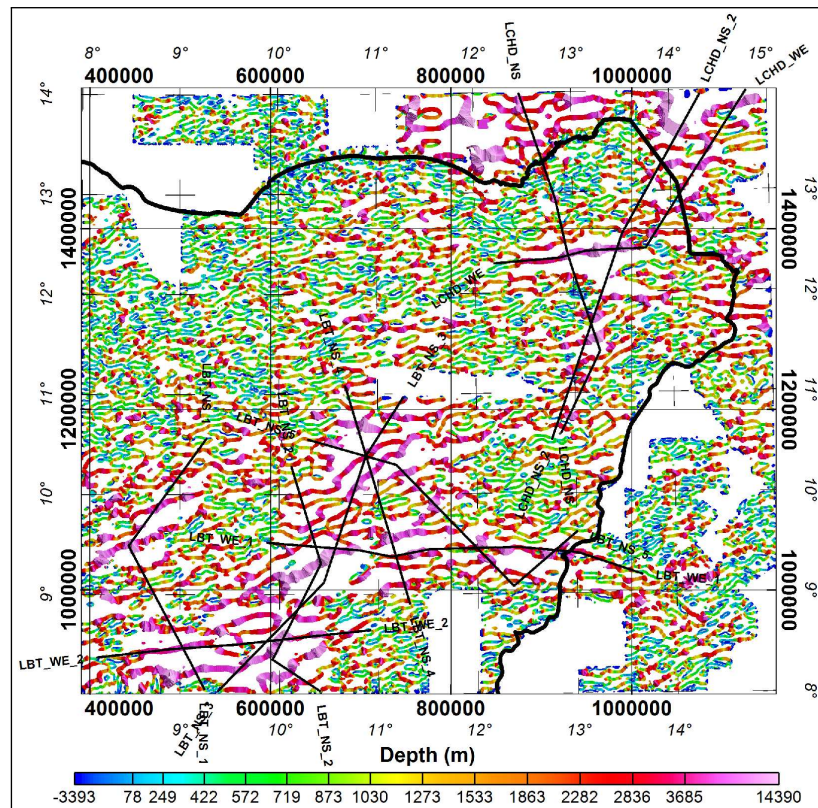
**Figure 6.16:** Local wavenumber (LW) method depth estimates. Superimposed are selected profiles, which are also shown in figure 6.17 and compared in figures 6.18, F.10, F.11 and F.12. A magnified version of figure 6.16 is presented in appendix H (Figure H.13).

Next, I use averages of the depths estimated from the three methods (Figures 6.16 and 6.17), constrained by the qualitative structure map in figure 6.12, as well as configurations indicated along the various profiles above (Figures 6.18 and appendices F.10, F.11 and F.12), to generate a depth-structure map (Figure 6.19), for sediment-covered parts of NE Nigeria only. Mean depths to magnetic basement across the area are also shown as variously-coloured contour lines, at 2 km intervals in the figure. Since sediments are generally non-magnetic, basement depths in figure 6.19 are equivalent to sediment thickness (Thompson, 1982; Reeves, 2005; Reynisson et al., 2009). However, because depths were inferred from contact/edge locations and do not account for fault throws, depths on figure 6.19 represent minimum sediment thickness. These minimum estimates require  $\approx 40\%$  of their values to be added to the isopach contour value to correct them for errors in their estimation.

These figures show that basement horsts, with depths ranging from about 1 km in the Maiduguri area to about 2.5 km, dominate the NE Nigeria basement. Various-orientated, discrete rhomboid depocenters, with maximum sediment thickness exceeding 10 km and widths ranging from 25 to 50 km, appear to occur in the basement beneath the Chad basin, Gongola/Kerri-Kerri basins, Yola basin, Muri-Bashar and the SW corner of the study area. Except for the Yola basin, these depocenters are completely isolated, at depth, from adjacent depressions outside the study area. These “Tilt-Depth” and LW methods estimates agree very well with trends of recent basement



(a)  $\theta = \pm 45$  range.



(b)  $\theta = \pm 27$  range.

**Figure 6.17:** “Tilt-Depth” method depth estimates, from  $\theta = \pm 45$  and  $\theta = \pm 27$  ranges. Superimposed are selected profiles from which variations in basement depths from “Tilt-Depth” and LW methods are subsequently compared in figures 6.18, F.10, F.11 and F.12. Magnified versions of figures H.14a and H.14b are presented in appendix H (Figure H.14).

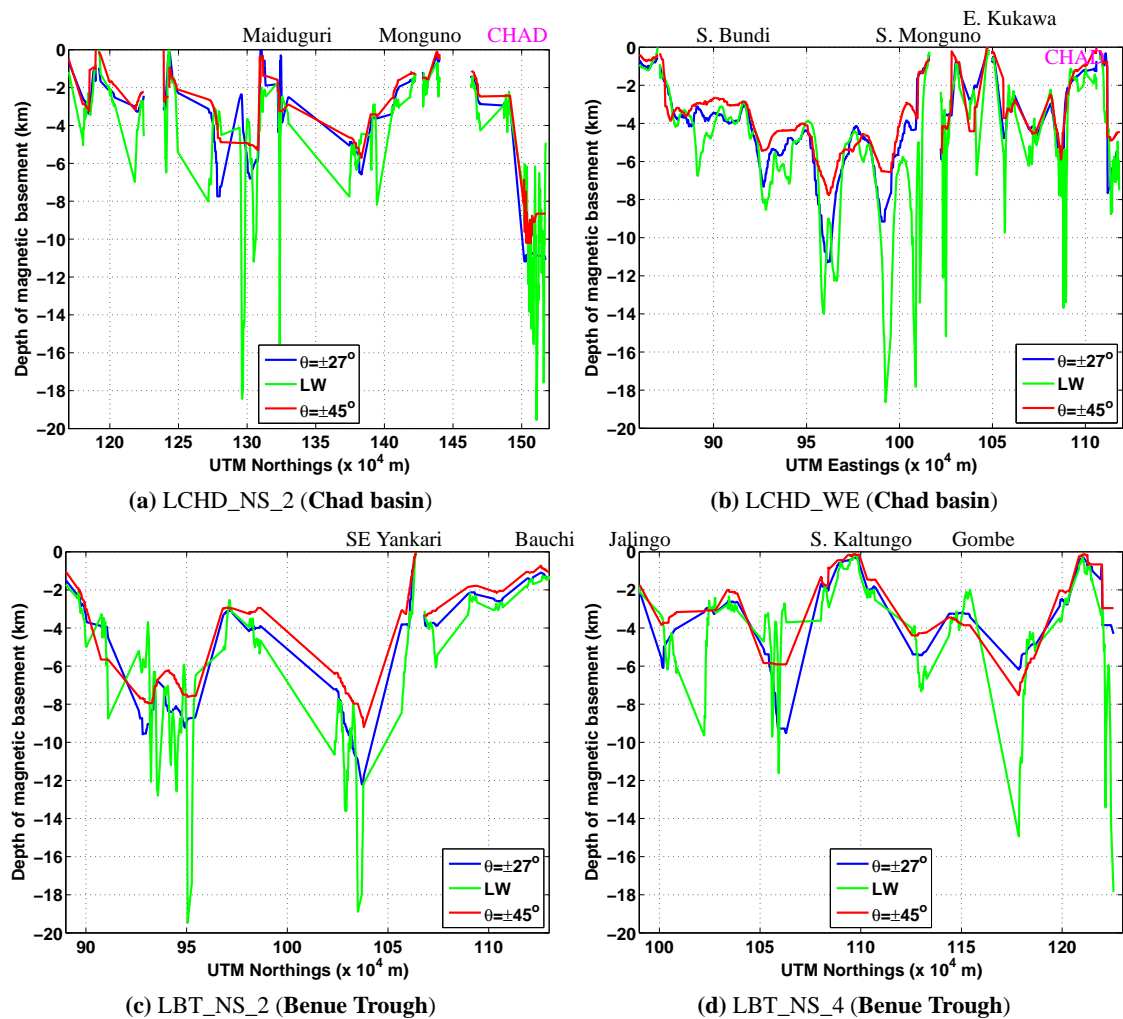


**Figure 6.18:** North-South (NS) and East-West (WE) profiles showing the variations in depths estimated using local wavenumber (LW) and  $\theta = \pm 45$  and  $\theta = \pm 27$ -based “Tilt-Depth” methods from SouthWestern Chad basin, NE Nigeria. “Tilt-Depth” method profiles were extracted from figure 6.17, while LW method profiles were extracted from figure 6.16. Note the relative stability of “Tilt-Depth” method estimates. The locations and identities of these profiles were shown in figures 6.17 and 6.16. Cities/towns (Figure 6.15) close to profile locations are shown in black, while fuchsia-coloured labels indicate profile parts outside NE Nigeria.

depth estimates from high-resolution aeromagnetic data (Chandler, 2010, p.18 and Reford, 2010), as well as with estimates from Avbovbo (1980), who showed (from well data) that basement rocks were encountered at generally shallow depths (below 2 km) throughout the study area, but that narrow structural indentations in the basement also occur within which sediment thicknesses were in excess of 2 km.

The Kanadi and Albarka wells, with total depths of 3,048 and 3,470 m, respectively (Olugbemiro et al., 1997), and the Kemar - 1, Murshe - 1, Tuma - 1 and Ziyé - 1 wells with total depths of 1.8, 2.8, 2.7 and 2.9 km, respectively (Obaje et al., 2004) encountered only fluvio-deltaic sedimentary successions. These wells show that depths to basement in this area well exceeds 2 km in the Chad basin (NE parts of the study area). But the poor constraint on the locations of these wells in the cited publications (Olugbemiro et al., 1997; Obaje et al., 2004) means that it was difficult to conclusively compare these well depths with “Tilt-Depth” and LW estimates at those locations. However, in this

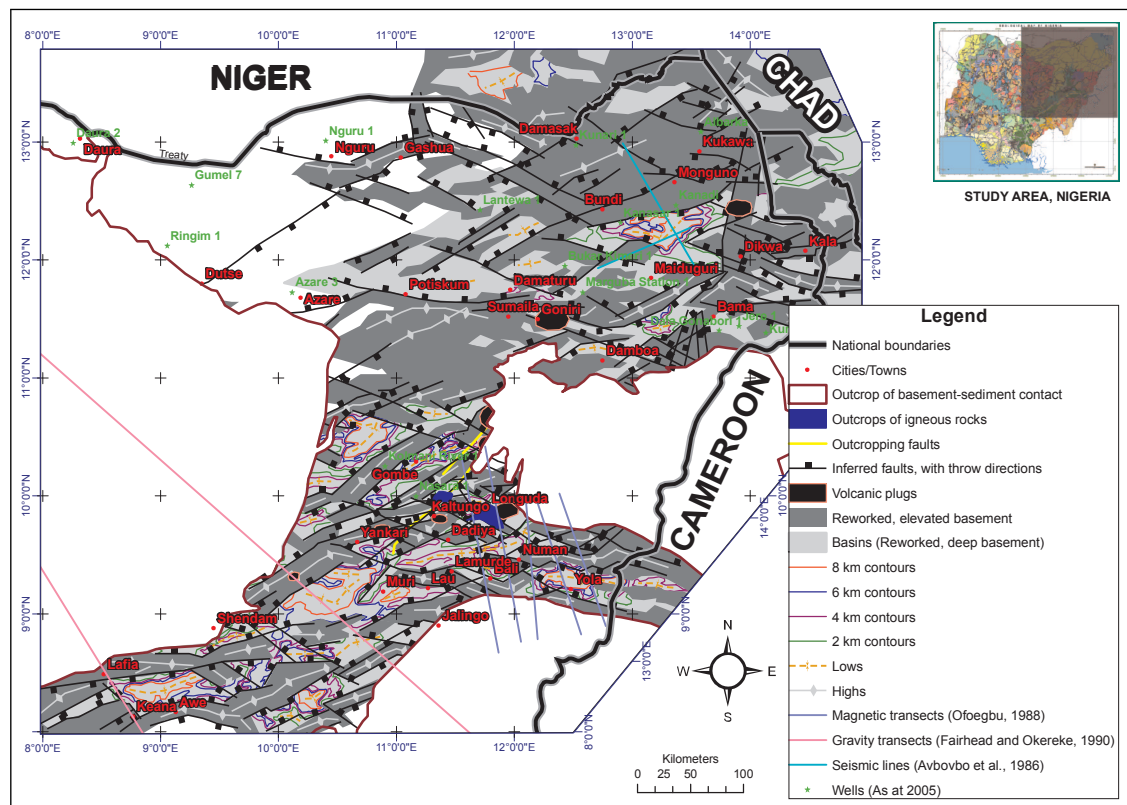


**Figure 6.19:** Depth-structure map of sedimentary basin area of NE Nigeria showing the major depositional centers and horst structures. Faults, horsts and basins were extracted from figure 6.12. To be corrected, estimates require  $\approx 40\%$  of their values to be added to the isopach contour values shown. The location of profiles, as well as approximate locations of some exploratory wells presented in previous studies of parts of the study area are also shown. Well locations were extracted from Avbovbo (1980), Olugbemiro et al. (1997), and Obaje et al. (2004). Information presented are limited to the basin area enclosed by the basement-sediment contact in figure 6.2. A magnified version of this figure is shown in appendix H (Figure H.15).

area of the Chad basin, “Tilt-Depth” and LW estimates (Figure 6.19) were also in good agreement with the deep depocenter (deep basement) implied by the inference of locally thick sedimentary fill ( $>10$  km) from 2D seismic sections (Avbovbo et al., 1986).

In the Kerri-Kerri/Gongola basin area (Upper Benue Trough), the 3 km deep Kolmani River - 1 well (Obaje et al., 2004; Epuh et al., 2012, Figure 12), as well as the Kuzari - 1 and Nasara - 1 wells, which were drilled to depths of about 1.7 km (Obaje et al., 2004), encountered only sedimentary rocks. These wells, as well as inferences from 3D seismic data (Epuh et al., 2012) also agree well with the “Tilt-Depth” and LW estimates presented in figure 6.19.

Profiles indicate that the Kaltungo Inlier and the basaltic plateau of the Longuda area (Figure 6.2) are surface expressions of a 20 to 50 km wide basement horst which extends from the surface down to depths of about 5 to 6 km. The Kaltungo-Dadiya axis appears to be dominated by shallow basement horsts that are about 25 km in width, at their tops (Figures 6.18d and F.11c). These separate the Kerri-Kerri/Gongola basins from the Bashar-Muri basin (Figure 6.2). The area South of Kaltungo is underlain by shallow basement rocks, which appear even shallower in the Jalingo area.

## 6.5 Distribution of magnetic susceptibilities in NE Nigeria.

Apparent magnetic susceptibilities were obtained for NE Nigeria, using the “Tilt-Depth”-analytic signal amplitude method (Section 2.5.5). The method required a grid containing maxima of the analytic signal amplitude, ASA grid (Figure 6.10a), as well as a grid containing estimates of depth at these contact locations. Depths estimated using the “Tilt-Depth” method were used (Figure H.14b). The resulting apparent magnetic susceptibility contrasts ( $\delta k$ ) grid is presented in figure 6.20. Susceptibility values obtained could neither be directly related to the general range of

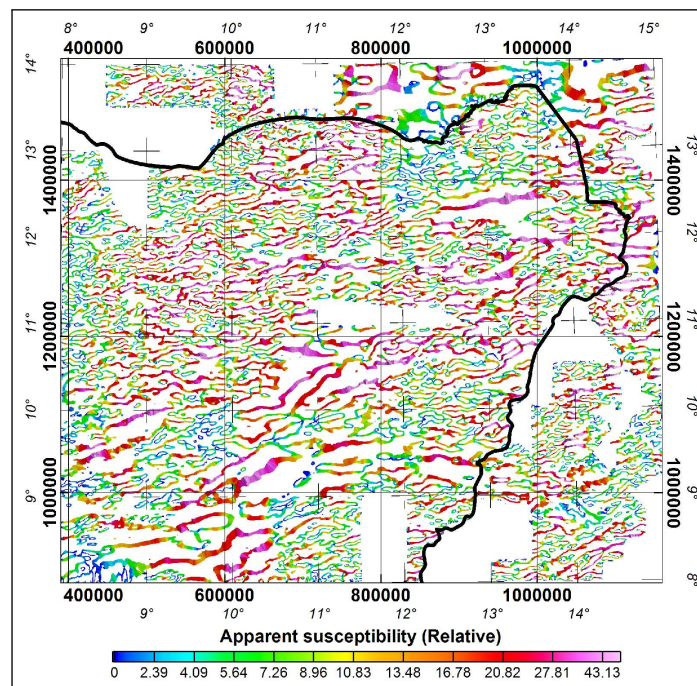


**Figure 6.20:** Relative magnetic susceptibility contrasts estimated for NE Nigeria using “Tilt-Depth”-analytic signal amplitude method (Equation (2.5.9c)). These estimates were derived from the Low-Pass NE Nigeria (RTE) grid (Figure 6.7b). An interpretation of these  $\delta k$  estimates is presented in figure 6.21.

rock susceptibilities (Dobrin & Savit, 1988; Telford et al., 1990) nor to the sparse susceptibility estimates available for parts of the Benue Trough. Estimated magnetic susceptibility estimates from parts of the Benue Trough include those by: (i) Ajakaiye (1981) who indicated that they range from 0.009 to 0.0097 SI Units for rocks in the Benue Trough, with an average of 0.012 SI Units for granite and granitoid basement rocks; and, (ii) Abubakar et al. (2010); Shemang et al. (2001) using 0.012 SI Units for the basement rocks in the Gongola basin area obtained magnetic susceptibilities of, respectively, 0.0476 SI Units and from 0.302 to 0.364 SI Units, for basic and ultrabasic intrusive rocks of NE Nigeria. Shemang et al. (2001)’s estimates are more than one order of magnitude higher than those of Abubakar et al. (2010). In order to avoid discrepancies such as these, susceptibility contrasts ( $\delta k$ ) estimated for NE Nigeria using the “Tilt-Depth”-analytic signal amplitude method (Figure 6.20) were interpreted qualitatively, since the data must be related in some way to the magnitude of the susceptibility that is responsible for the analytic signal amplitude (ASA) peaks at these locations (Nabighian, 1972; MacLeod et al., 1993).

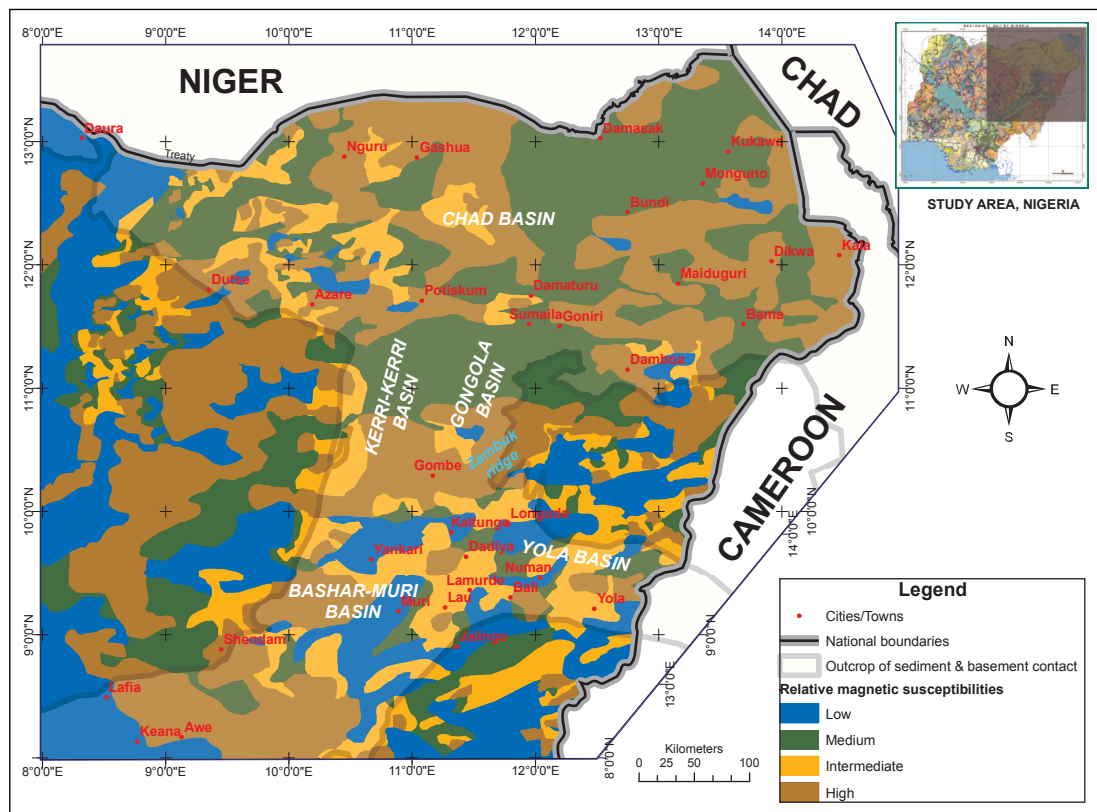


**Figure 6.21:** Relative magnetic susceptibility distribution map for NE Nigeria basement. This map is based on the susceptibility estimates shown in figure 6.20. Geological basins in these vicinities are labelled, in line with figure 6.2, to provide context. Locations of outcropping sediments and/or basement-sediment contact in NE Nigeria extracted from figure 6.2 is superimposed to ease comparisons.

A qualitative interpretation map derived from figure 6.20 is presented in figure 6.21, which expresses the relative composition (magnetic susceptibility distribution) of basement beneath NE Nigeria as a function of specific range of susceptibilities (Figure 6.20). The map characterises the magnetic susceptibility of NE Nigeria basement rocks as: (1) **Low**, when  $k < 5$  (Coloured blue in figure 6.21); (2) **Medium**, when  $k$  is from 5 to 9 (Coloured green in figure 6.21); (3) **Intermediate**, when  $k$  is from 9 to 13 (Coloured gold in figure 6.21); and, (4) **High**, when  $k > 13$  (Coloured brown in figure 6.21). Figure 6.21 indicates that basement rocks with the highest magnetic susceptibilities (Brown-coloured) are associated with NE-SW trending structures along the Benue rift, the area around Maiduguri in SW Chad basin, as well as, the Jos, Azare, and Gashua areas.

## Chapter 7

### Discussion and conclusions

---

#### 7.1 Discussion

##### 7.1.1 General observations from comparing RTE and RTP of profile and gridded model $\Delta T$ datasets

The “Tilt-Depth” method requires  $\Delta T$  datasets to be transformed to their RTP or RTE equivalents before the method is applied. “Tilt-Depth” method of locations and depths of two-dimensional (2D) contacts of various effective inclinations of magnetisation ( $\phi$ ), depths ( $z_{mod}$ ), strikes ( $A$ ) and dips ( $d$ ) were obtained from RTP and RTE equivalents of  $\Delta T$  datasets, which were generated along profiles across these contacts (Chapter 3).<sup>1</sup> Comparisons between these estimates show errors in “Tilt-Depth” method estimates to be invariant to changes in source depths, but sensitive to changes in the inclination of effective magnetisation ( $\phi$ ) and dips ( $d$ ) of sources. At error limits of  $\pm 20\%$ , the method effectively imaged locations and determined depths of 2D contacts when dip ranges from  $75$  to  $105^\circ$ ,  $\beta = 180 \pm 25^\circ$  and Koenigsberger ratio ( $Q$ )  $\leq 1$ .<sup>2</sup>

Analyses of the relationship between  $Q$ ,  $\alpha$ ,  $\beta$  and  $\phi$  (Section 3.3.4) show that the simplification of remanence-laden anomalies afforded by collinear magnetisations ( $\beta = 180 \pm 25^\circ$ ) results from effective magnetisation direction ( $\phi$ ) being kept at  $\leq 10^\circ$  from  $\alpha$  (Figures 3.10c, 3.10d and 3.11). These figures also show that deviations between  $\alpha$  (RTP or RTE) and  $\phi$  are  $\leq 10^\circ$  for all directions of remanent magnetisation ( $\beta$ ), when  $Q < 0.2$  (Figure 3.11). Consequently, the effects of  $\beta$  on RTP or RTE of datasets for which *a priori* information suggests  $Q < 0.2$  can be treated as negligible, though not collinear. McEnroe et al. (2009) and Thébault et al. (2010) suggest that  $Q \leq 0.5$  in the continents.

Errors in “Tilt-Depth” method location estimates were insensitive to changes in the strike of these well isolated idealized vertical contacts at RTP or RTE. This was expected for RTP estimates, since unlike RTE anomalies, RTP anomalies are not affected by shape changes (anisotropy). But,

---

<sup>1</sup>RTP or RTE implies that induced magnetisation direction ( $\alpha$ ) is either vertical or horizontal, respectively.

<sup>2</sup>The  $\beta = 180 \pm 25^\circ$  range expresses collinearity between induced and remanent magnetisations (Bath, 1968).

RTE  $\Delta T$  amplitudes were at their highest for East-West striking contacts. Along with their total horizontal derivatives, these amplitudes decreased systematically and monotonically as contact strike changed from East-West to zero for North-South striking contacts.

The complex “Bishop” model (CBM) dataset meets these  $\phi$ ,  $Q$  and  $d$  specifications, hence can be correctly transformed to its RTP or RTE equivalent. However, because sources of the CBM dataset vary, and often cross-cut each other, the dataset contains interfering anomalies whose locations and depths are known. Locations of the edges of these sources were also estimated from RTP and RTE equivalents of the CBM dataset, using the “Tilt-Depth” ( $\theta$ ) method. These estimates were compared with equivalents obtained from five additional methods: the Second vertical derivatives (SVD), Analytic signal amplitude (ASA), Local wavenumber (LW), as well as the Horizontal gradient magnitude (HGM) of  $\theta$  ( $\text{HGM}_{(\theta)}$ ) and HGM of  $\Delta T$  ( $\text{HGM}_{(\Delta T)}$ ) methods (Chapters 4 and 5), to complement the “Tilt-Depth” method. The following observations resulted from these comparisons:

(1) Positive amplitudes of RTP anomalies and their derived functions are directly located above sources with higher susceptibilities and/or shallow depths, while negative anomalies are located above sources with lower susceptibilities and/or deep depths. This relationship is reversed for RTE anomalies. Hence, additive inverses of  $\theta$  and SVD of RTE anomalies were required to bring these anomalies in phase with their RTP equivalents, for comparison.

(2) Sources (structural edges) of all strikes or azimuthal orientation, including North-South (N-S), are imaged/preserved on RTP datasets. However, N-S edges are not imaged on RTE datasets. This is because RTE anomaly amplitude and shape vary with the strike of their source, i.e., *anisotropy*. Consequently, RTE amplitudes are highest (at half their RTP equivalents) for E-W striking edges, intermediate for NW-SE and NE-SW striking edges, minimum for  $N\pm 20^\circ$  (NNW-SSE and NNE-SSW) striking edges, and zero for N-S trending edges. Consequently, N-S striking edges cannot be imaged from RTE datasets.

(3) NNW-SSE and NNE-SSW striking edges may also not be preserved on RTE grids, unless they are well isolated and with extensive linear segments. This is because dipole-like anomalies with E-W trends develop where linear edges are dissected (Figure 2.8). When in close proximity to other anomalies these dipolar anomalies interfere to displace the resulting anomaly trends from those of their sources. The frequency and relative proximity of NNW-SSE and NNE-SSW trending sources relative to other sources is critical to the degree of interference, as well as the preservation, of anomalies observed on RTE datasets.

(4)  $\theta$  serves as an automatic-gain-control (AGC) filter by equally enhancing subtle and dominant anomalies. Thus,  $\theta$  reflects changes in the depths, rather than the amplitudes, of anomalous edges across grids. However,  $\theta$  was more sensitive to anomaly interference from adjacent anomalies. Consequently, locations estimated from the  $\theta = 0$  contour require constraints from SVD locations, in particular.

(5) Depths of 2D and non-2D edges mapped from RTP and RTE grids were obtained using the “Tilt-Depth”, LW and ASA methods. The error in estimates obtained from equivalent locations on both RTP and RTE datasets were also compared. These comparisons show both the “Tilt-Depth” and LW methods to underestimate the actual depth of sources on the datasets, while the ASA method severely underestimated and overestimated depths from these datasets. “Tilt-Depth” and LW estimates were, thus, easier to utilise and interpret.

(6) Errors in depths estimated for 2D contacts were: (i) 25% (RTP) and 35% (RTE) for  $|\theta| \leq 27$ -based "Tilt-Depth" method; (ii) 35% (RTP) and 40% (RTE) for  $|\theta| \leq 45$ -based "Tilt-Depth" method; and (iii) 25% (RTP) and 30% (RTE) for LW method.

(7) Errors in depths estimated for the Northern and Southern non-2D edges of 3D sources were: (i) 35% (RTP) and 45% (RTE) for  $|\theta| \leq 27$ -based "Tilt-Depth" method; (ii) 40% (RTP and RTE) for  $|\theta| \leq 45$ -based "Tilt-Depth" method; and (iii) 30% (RTP) and 40% (RTE) for LW method.

Maximum depth errors were generally higher for non-2D than they were for 2D contacts. They were also higher for RTE than they were for RTP grids. This error information was presented in tables 4.6 and 5.7.

Since these methods are based on the assumption of 2D basement sources (contacts with constant strike, infinite thickness and width), and geological sources rarely satisfy these assumptions, departures from these assumptions and local interference effects are routinely invoked to explain these errors (Vacquier et al., 1951, Reeves, 2005). However, Flanagan & Bain (2012a) show that significant errors ( $\approx 30\%$ ) in depths estimated from profile datasets can also result when the assumption that basement has infinite thickness is invalid. For example, up to  $\approx 8\%$  error may be introduced to "Tilt-Depth" method estimates when the thickness-to-depth ratio of the magnetic source,  $\frac{Th}{Z}$  is 9 or 10 (Flanagan & Bain, 2012a). Consequently, the  $\frac{Th}{Z}$  ratio for NE Nigeria will be explored when discussing the Nigerian dataset in order to apply adequate corrections to depths estimated for the area.

### 7.1.2 Mapping NE Nigeria basement

The observations above (Section 7.1.1) were applied to the NE Nigeria RTE grid (Figure 6.6). Fortunately,  $\theta$  and SVD of the NE Nigeria RTE grid (Figure 6.9b) show the study area to be dominated by relatively well-defined, and relatively well-isolated, series of related NE-SW, NW-SE and E-W linear structures, which I interpret to be faults. By integrating locations estimated from the  $\theta$ , LW, ASA, SVD,  $HGM_{(\theta)}$  and  $HGM_{(\Delta T)}$  methods, more subtle and intricate structural imprints in the NE Nigeria basement are obvious. The basement is dominated by en-echelon arrangements of basement horsts and depressions, which are generally bound by faults that exceed 200 km in length (Figure 6.12). Basement horsts in figure 6.12 represent locations where lithospheric extension have emplaced hotter upwelling upper mantle material at shallower depths beneath thinned, lower

density NE Nigeria continental crust. From observations of the Main Ethiopian Rift, [Biggs et al. \(2009\)](#) showed that such segmented magmatic intrusions characterise mature rifts. These horsts, along with the dormant volcanic features, were mainly imaged using the  $\theta$  grid (Figure 6.9b), by exploiting the fact that positive  $\theta$  values only occur above higher susceptibility sources.

Four distinct trends were observed in the mainly sub-parallel fault sets (Figure 6.12). These include: (1) three dominant fault sets with NE-SW strikes; (2) four fault sets with NW-SE strikes; (3) three nearly N-S striking fault sets; and (4) two E-W striking fault sets. Such variations in the orientation of structural features reflect variations in orientations of dominant tectonic (tensile and/or compressive) stresses across the area. NE-SW striking faults occur in the Jos-Bauchi axis, Shendam-Yankari axis, South of Jalingo, Gombe area, and North of Potiskum, Damaturu and Maiduguri; NW-SE striking faults occur in the Gashua-Maiduguri-Bama axis, NW of Bazza through Potiskum to Dutse areas, Kaltungo-Yola axis and NE of Lafia; N-S striking faults occur North of Bazza and Gashua; while E-W striking faults occur in the Awe-Lafia and Yola areas. These trends are in good agreement with [Benkhelil \(1982\)](#), [Maurin et al. \(1986\)](#) and [Benkhelil \(1989\)](#) (Figure 6.2). The dominant NE-SW faults appear to have steep, near-vertical dips (Figure 6.15). Lower than average relative magnetic susceptibilities characterise much of the Western and Southern halves of the study area (Figure 6.21), suggesting that relatively homogeneous upper crustal assemblages dominate these locations. However, higher than average susceptibilities characterise locations that were directly associated with the propagating Benue rift.

Grids of depths estimated for the area using the LW and “Tilt-Depth” methods have been used to further constrain locations of apparently deep basement (Figure 6.12). Averages of these estimates are presented in figure 6.19.<sup>3</sup> Since sediments are mainly non-magnetic, and depths were determined only at contact/edge locations, basement depths presented in figure 6.19 are equivalent to minimum sediment thickness, and do not account for fault throws ([Thompson, 1982](#); [Reeves, 2005](#); [Reynisson et al., 2009](#)). Sediment thickness commonly exceeded 8 km in the discrete depositional centres that are scattered across the otherwise shallow (0 to 2 km deep) NE Nigeria basement.

The only *a priori* crustal thickness information available for the study area, with which to examine the validity of the infinite basement thickness assumed during depth estimation ([Flanagan & Bain, 2012a](#)), are from gravity and seismic profile studies by [Fairhead & Okereke \(1988\)](#) and [Stuart et al. \(1985\)](#), respectively.<sup>4</sup> Crustal thicknesses determined from gravity profiles across the Benue Trough and Yola basin were  $\approx 24$  and 19 km, respectively ([Fairhead & Okereke, 1988](#)) and 23 km for the Cameroon extension of the Yola basin ([Stuart et al., 1985](#)). The Conrad and Mohorovicic discontinuities in the adjoining uplifted cratonic margins were estimated to be at depths of 12.5-14.5 and 34 km, respectively ([Stuart et al., 1985](#)).<sup>5</sup> With a minimum crustal thickness ( $Th$ ) of  $\approx 20$  km over

<sup>3</sup>The “Tilt-Depth” method was implemented in two modes, using  $\theta = \pm 45$  and  $\theta = \pm 27$  ranges.

<sup>4</sup>The locations of gravity profiles of [Fairhead & Okereke \(1990\)](#) are shown in figure 6.19.

<sup>5</sup>The Conrad discontinuity represents the seismic boundary between the upper and lower crust, while Mohorovicic discontinuity represents the boundary between the crust and mantle.

the basins,  $\approx 35$  km (normal crust) flanking the rift and average estimated depth ( $Z$ ) of about 2 km (Figures 6.16 and 6.17),  $\frac{Th}{Z}$  (Flanagan & Bain, 2012a) ranges from 10 to 17. Therefore, there is no need to correct depths estimated for NE Nigeria for additional errors due to finite thickness of basement.

Since the methods underestimate depth by about 30% (Tables 4.6 and 5.7) the 2 km interval isopach contours shown in figure 6.19 require 30% of its current value to be added to correct for the error in its underestimation. Consequently, sediment thicknesses exceed 11 km in the discrete depositional centres that are scattered across the otherwise shallow (<3 km deep) NE Nigeria basement. These depths agree well with the total depths of wells completed in the basement, whose locations are also shown in figure 6.19.

The depocenters are mainly rhomb-shaped basins, typical of stress regimes characterised by localised compressions within an overall tensile regime (Storti et al., 2001). Faults, basement horsts and depocenters are generally orientated ENE-WSW in Chad basin, NE-SW in Gongola/Kerri-Kerri and Bashar-Muri basins, and NW-SE to E-W in Yola basin (Figure 6.19). In general, basement horsts trend mainly NE-SW, are generally sandwiched between faults, thicker in the Southern parts of the study area, and continuous for long distances, often in excess of 150 km, unless where they are displaced by NW-SE striking faults. These 25 to 50 km thick structures are located on the positive gravity anomaly reported to occupy the axis of the Benue trough (Fairhead & Okereke, 1990), and are shown on the  $\theta$  grid (Figure 6.9b) to persist beneath and around the Kaltungo Inlier and Longuda plateau, to the volcanic base of the Biu Plateau. These structures are, therefore, related both in their origin, and mineralogical compositions, which are well reported in outcrop studies of rocks of the area.

### 7.1.3 Propositions and synopsis of tectonic evolution

According to Ziegler & Cloetingh (2004, Figure 1), the main mechanism of plate motion and thinning and/or rifting of the lithosphere is the combined influence of frictional forces on the base of the lithosphere due to asthenospheric convection, deviatoric tensional stresses within thinned lithosphere as a consequence of an elevated Mohorovicic discontinuity, and far-field stresses transmitted from plate boundaries. These stresses repeatedly exploit lineaments in the basement (sites of structural weakness) by rejuvenating them during tectonic events, even at lower than normal stress levels (Daly et al., 1989; Kusznir & Ziegler, 1992; Ziegler & Cloetingh, 2004). Far-field lithospheric stresses are often invoked to explain the origins of deformation everywhere in the Benue Trough (Ajakaiye et al., 1986; Benkhelil, 1989; Fairhead & Okereke, 1990), using the extensional rift basin model of McKenzie (1978). This model accounts only for the instantaneous lithospheric response to extensional stresses and ignores contributions from the other two lithospheric influences, which correspond to post- and syn-rift adjustments to crustal thinning (Kusznir et al., 1995).

The mainly N040 to 065° and N115 to 135° trends on the structure maps (Figures 6.12 and 6.19) are consistent with the various directions of maximum principal stress ( $\sigma_1$ ) measured in Cretaceous rocks in the area (Benkhelil, 1989, Figure 10).  $\sigma_1$  was directed NNE-SSW during the Middle Cretaceous, NW-SE to NNW-SSE during the Late Cretaceous, and N-S to NNE-SSW during the Tertiary (Benkhelil, 1989, Figure 10). These variations must reflect local variations in tectonic controls of events in NE Nigeria.

By carefully examining basement trends in figure 6.12, a new sequence of events, which includes observations that indicate local contributions from post- and syn-rift influences is presented for the tectonic evolution of the study area (Figure 7.1). This sequence also incorporates the following general principles on rift propagation: (1) The preferred direction of rift propagation is always perpendicular to the direction of the least compressive stress in the lithosphere (Vink, 1982), hence dependent on the state of deviatoric (differential) stress in the lithosphere. Therefore, direction of propagation of continental rifts must change to reflect local changes in the regional stress field (Vink, 1982); (2) New fault systems may be induced in competent basement (Ziegler & Cloetingh, 2004); (3) Propagating rifts induce different amounts of extension in different parts of a progressing rift. Hence, rifts in continental masses are diachronous (Vink, 1982, Keranen & Klempner, 2008); and (4) Propagating rifts may proceed in one or more directions, contemporaneously, with or without components of extension (Martin, 1984).

Locations and orientations of two estimated faults and the basement horst sandwiched between them correlate perfectly with the two major outcropping faults that link the Kaltungo Inlier to both the Zambuk Ridge and the Biu Plateau (Figures 6.12 and 6.19). These correlations, as well as the persistence and spatial relationships of NE Nigeria basement structures, provide the basis for inferring directions of tectonic stress propagation, barricade or breaching across the area (Figure 7.1).

The study area is dominated by high angle (near-vertical to vertical) faults (Figure 6.15), which were determined from the co-plotting of  $\theta = 0$  contours of progressively upward-continued equivalents of the RTE dataset (Figure 6.14). Optimally aligned high angle faults are easier to reactivate (King et al., 1994) by strike-slip than dip-slip transfer faults (Daly et al., 1989; Ziegler & Cloetingh, 2004), particularly, where strike slip dominates compression (Fossen, 2010; Lowell, 1995). Consequently, the main mechanism of propagation of the Benue rift in NE Nigeria is strike-slip movements, which preferably exploited transfer faults along pre-existing shear zones of structural weakness composed of mylonites, cataclasites and fault breccia, e.g., the  $\approx 150$  km long Kaltungo lineament, along which the Kaltungo Inlier lies (Maurin et al., 1986; Guiraud et al., 1989). Well over 60 km of sinistral strike-slip movement has taken place along such Benue Trough shear zones (Fairhead & Okereke, 1990). Associated with these displacements were crustal extensions of  $\approx 65$  and 55 km in the Gongola and Yola basins, respectively (Fairhead & Okereke, 1987), and  $\approx 95$  km extension accompanied by  $\approx 14$  km thinned crust over a 300 km distance in the Benue Trough (Fairhead & Okereke, 1990).<sup>6</sup>

---

<sup>6</sup>Locations cited are indicated in figure 7.1.

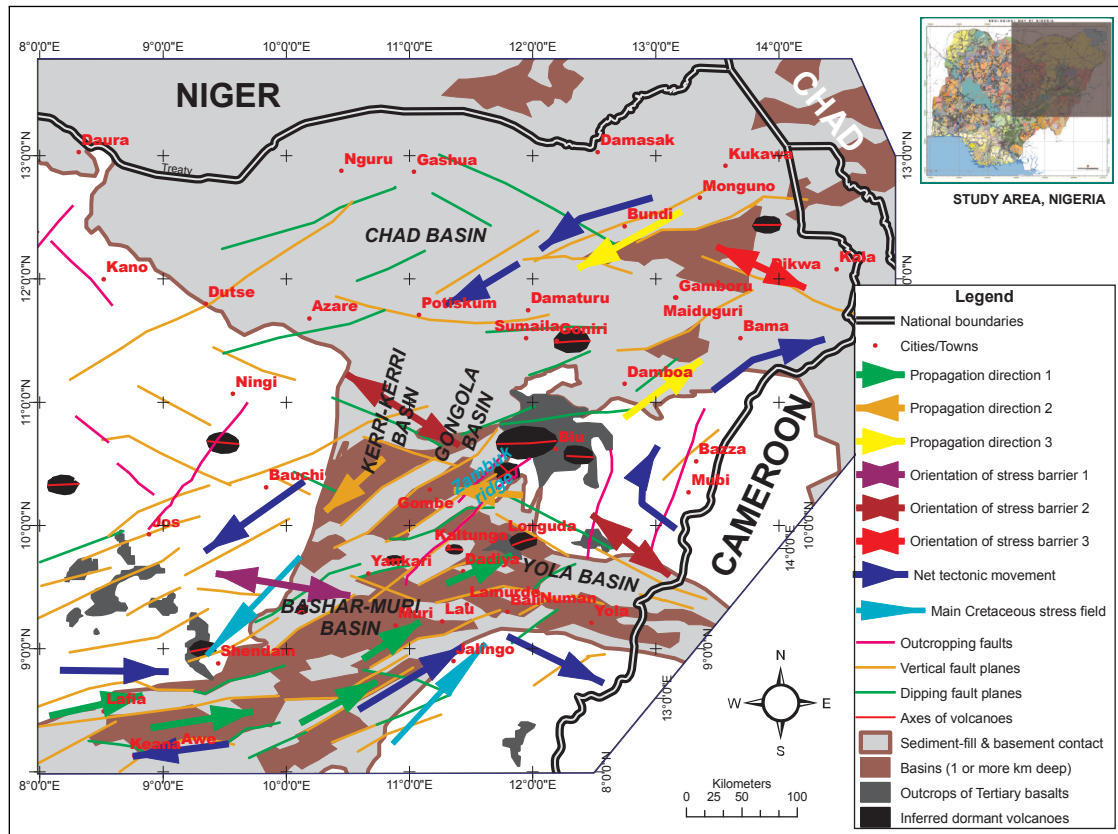


**Figure 7.1:** Inferred directions of propagation of the Benue rift, Mesozoic tectonism, and sedimentary features of NE Nigeria. Tectonic map reflects the combined orientations of basement faults inferred from figures 6.12 and 6.15. Coloured arrows are used to indicate the direction of propagation of the Benue rift (Single-headed green, chocolate or yellow arrows), orientations of stress barriers, i.e., main axes of strain (Arrows with double-heads pointing in opposing directions), and the net/resultant direction of shear strain (Grey single-headed arrows). Inferred basins with sedimentary-fill > 1 km (Deep-brown shading), dormant volcanoes (Black) and the orientation of their major axes (red-coloured lines), as well as outcropping sediment fill (Light-grey shading), sediment-basement contact (Brown lines), faults (Black lines) and volcanic rocks (Dark Gray) are also shown.

The rhomboid geometry of the basement depressions (basins) and horst structures (Figure 6.19) are typical expressions of pull-apart basins, indicative of compressional stress regimes at play under generally tensile stress regimes (Aydin & Nur, 1982; Bonini et al., 1997; Gurbuz, 2010). However, while the amounts of crustal thinning reported from parts of the study area ( $\approx 14$  km; Fairhead & Okereke, 1990) may be consistent with the dominantly pure shear strain regimes required by the McKenzie (1978) model, the amount of extension is not. For instance, 3 to 9 times more crustal extension occurred in the Benue Trough than in the East African Rift (Fairhead & Green, 1989).

Combined with the dispositions and compositions of outcropping basement horsts (the Kaltungo Inlier and Zambuk Ridge and Tertiary volcanics) in the Kaltungo, Zambuk, Longuda and Biu areas (Figure 6.2), their inferred equivalents, as well as the density of faults mapped in the area (Figure 6.12), these structures seem to reflect origins in transient, mixed (transitions from extensional to compressional) stress regimes. Such regimes seem to be more characteristic of the flexural cantilever model (Wernicke & Burchfiel, 1982) than the McKenzie (1978) model. Ramsey & Chester (2004) show that hybrid deformation fabrics (with transitional confining pressures) are to be ex-

pected in such terrains.<sup>7</sup> Therefore, transpressional and transtensional deformation in the area may have been more widespread in the basement than is generally thought, and responsible for the complex and often chaotic deformation recorded by Benkhelil (1982), Maurin et al. (1986) and Benkhelil (1989).<sup>8</sup> Hence, the propositions below apply the model of Wernicke & Burchfiel (1982) to structures presented in figures 6.12 and 6.19:

(1) The Benue Rift propagated into the study area from its SouthWestern end (Gulf of Guinea) along NE-directed vertical and dipping lineaments/faults (Figure 7.1). These trends suddenly changed to E-W in the Lafia, Keana, Awe and up to Shendam area. This indicates that significant rejuvenation of mainly E-W lineaments and deflection of the propagating rift occurred in the area. The arcuate trend of horst structures in this area, as well as the initiation of the first rhomboid basin between these horsts, suggests emplacements by compressional regimes, and the occurrence of flow barriers (Daly et al., 1989) in the area. Local compressions in this part of the rift could have resulted from collision between the otherwise free, NorthEasterly propagating rift and the Precambrian-Jurassic wall rocks of the Jos Plateau (Figures 6.2). This sudden restraint may have induced vortex flow and rapid volume changes in the melted crustal/mantle materials associated with the rifting process, resulting in significantly boosted differential stresses.

Basement expressions of this turbulence include temporary reactivations of near-E-W trending lineaments/faults, and the near-E-W deflection of the main axis of rift propagation, and associated horst structures. The generally E-W orientation of structures in this area coincides with those inferred for far-field extensional stresses in the area South of the study area, i.e., Middle and Lower Benue Trough (Fairhead & Green, 1989; Fairhead & Okereke, 1990), perhaps indicating that maximum extension in the Benue Trough occurred in this area, since strain is easily concentrated along lineaments (Ziegler & Cloetingh, 2004).<sup>9</sup>

Location of prominent basement horsts correlate well with those of the long wavelength axial positive gravity anomalies of Fairhead & Okereke (1990), at generally shallow depths (<2 km), except at locations of transcurrent faults (Figure 6.19). Hence, these prominent horsts are interpreted to represent emplacements of deep/lower crustal materials at shallow depths.

(2) Since rifting progressed into the continent along a NorthEasterly direction (Fairhead & Okereke, 1990), and stresses related to rift propagation dissipated in this direction, the thickness and strength of the unstretched crust, as well as resistance to rifting must also have increased in a NorthEasterly direction.

(3) Coincident movements along continental extensions of the Romanche and Chain Charcot

---

<sup>7</sup>This is because extensional and shear deformation fabrics represent end members of a continuous transition from tensile to compressive stress regimes, while hybrid fractures are produced during mixed (transitions from extensional to compressional) stress regimes (Ramsey & Chester, 2004).

<sup>8</sup>Wernicke & Burchfiel (1982)'s model adequately incorporates McKenzie (1978)'s model with post- and syn-rift adjustments to crustal thinning (Kusznir et al., 1995).

<sup>9</sup>Relatively small strains are associated with extension features, hence, the principal axes of stress and strain are often coincident (Fossen, 2010).

fracture zone (Ajakaiye et al., 1986; Fairhead & Okereke, 1990; Fairhead & Binks, 1992) seem to have combined with transpressional stresses in the Lafia, Keana and Awe area, to reactivate NE-SW trending lineaments and faults in the outcropping basement complex North and NE of the area (Figure 6.12). This set of faults dominates the Shendam-Jos axis and extends through the Bashar-Muri and Kerri-Kerri/Gongola basins, respectively, into the Zambuk Ridge and Chad basin, and serve as major conduits by which strike-slip stresses were transmitted in NE Nigeria basement.

(4) NorthWesterly extensions between these transform fault-controlled, NE-SW striking, high angle faults allowed crustal/sub-crustal melts to be emplaced at shallower depths (basement horsts), reactivating the NW-SE trending faults that cross-cut NE-SW equivalents throughout the study area. Ebinger et al. (2010) observed that strain in the locality of similarly segmented rifts were frequently accommodated through axial dike intrusions resulting in the redistribution of builtup stresses and continued propagation of the rift.

The dispositions of these NW-SE faults relative to basins, the generally thinner NW-SE horsts, and the good correlation between NE-SW faults and horsts with the Pan African (600±50 Ma) age inlier of Older granite in the Kaltungo area (Figure 6.2), along the main axis of the Benue Rift and its sinistral displacement by a post-Pan African mega fault (Maurin et al., 1986), suggest this trend to be the main path by which significant transpression-related strains were dissipated into extensional features in the basement.

(5) The configuration of near-vertical and vertical faults suggests that five major centres of stress may have seen to the thorough reactivation of NE Nigeria (Figure 7.1). They include: **Centre 1** consisting of the Lafia, Awe, Keana and area South of Shendam, which is dominated by E-W trending structures; **Centre 2** consisting of the area North and East of Shendam, North and NW of Jalingo, and up to Biu. Mainly sub-parallel NE-SW structures dominate this area. Significant terminations of major NW-SE striking faults and horsts against these NE-SW striking structures occur in the areas between Yankari and Biu as well as the area to its East; **Centre 3** or Yola basin area, where E-W faults dominate shorter NW-SE and NE-SW trends; **Centre 4** consisting of the area North of Biu and between Damboa, Goniri, Sumaila, Potiskum, Azare and Ningi. This area appears to be dominated by a massive E-W oriented basement whose finer structural details were transparent to the methods used.<sup>10</sup> Hence, an alternative interpretation could be that this apparently homogeneous structure resulted from interference between adjoining E-W trending RTE anomalies from N-S and/or near-N-S trending basement structures (Sections 2.4.2 and 4.3); **Centre 5** consisting of the narrow area due North of Mubi, through Bama and Dikwa to East of Monguno, where near-N-S structures cross-cut NE-SW and NW-SE structures; and **Centre 6** consisting of the area North of Potiskum, Damaturu and Maiduguri. Here, NE-SW structures are offset by near E-W and WNW-ESE structures.

(6) Faults, horsts and volcanic features of the basement are strain localisation structures (e.g., Fossen,

<sup>10</sup>Note that data were missing for parts of this area (Figure 6.4).

2010). Hence, significant strains are induced in basement rocks in and around these six centres as the rifting process is either allowed to proceed, interrupted or deflected along reactivated lineaments in the crust. The near-vertical to vertical faults shown in figure 7.1 seem to serve as conduits, barriers or baffles to rift propagation-related stress transmission: (i) *conduits* allow steady-state transmission of stress; (ii) *barriers* barricade or deflect stress transmission; or (iii) *baffles* temporarily barricade transmission and subsequently fail as ambient stress exceeds bearing capacities of barriers.

(7) Apart from the stress barricading event in the Lafia area, barriers and/or baffles should be mainly located where NW-SE trends intersect or terminate against NE-SW trends, i.e, locations at which trends oblique to previous propagation trends are reactivated. Such intersections or terminations occur mainly in Centres 2, 3, 5 and 6. Some of these barriers are associated with inferred volcanic plugs and correlate well with the Kaltungo Inlier, as well as outcrops of Tertiary basalts in the Biu and Longuda areas (Figures 7.1 and 6.12).

(8) Under the generally compressive stress regime, the sudden stress relief and crustal reorganisation that should characterise barriers and baffles may easily induce rapid volume changes and turbulent flows, with components of vortex flow in the melted crustal/mantle materials.<sup>11</sup> This should result in high angle (quasi)-thrust faulting of significantly boosted differential stresses in the crust.<sup>12</sup> Stresses so amplified can be readily translated to transpressional regimes (Turner & Williams, 2004), further increasing the incidence of strike-slip faulting, while shortening and inverting sedimentary-fills of previously extensional depocenters or basins (Lowell, 1995; Turner & Williams, 2004). This may explain the rhomboid shape of basins (Figure 6.19) and high incidence of vertical faults in sedimentary rock outcrops reported throughout the Upper Benue Trough (Maurin et al., 1986; Benkhelil, 1989) and Chad basin (Avbovbo et al., 1986).

(10) Vortex flows at these barriers/baffles may have induced large differential stresses ( $\geq 100$  MPa) at shallow depths (about 2 km) in the crust (Behr & Platt, 2011, Figure 1), leading to quasi-thrusting along high angle faults. This would have temporarily elevated the Moho, melted lower crust assemblages and created the alkali-rich magma chambers from which the Tertiary basalts derive. The presence of such deeply-rooted mafic-to-ultramafic rocks at very shallow depths was invoked by Abubakar et al. (2010) to explain the large magnetic susceptibility values required to interpret  $2\frac{1}{2}D$  forward models of  $\Delta T$  data from this area. According to USGS/VHP (2011), the range of temperatures at which basalts are erupted is 1100 to 1250°C, which are typical ranges of temperatures in the Earth's mantle. Injections of similar magma into propagating Afar rift segments by contemporaneous depletion of adjacent magma chambers have been observed (Wright et al., 2006; Ebinger et al., 2010). Models of syn-rift migrations of magma (Corti et al., 2004) allow for the presence of large differential stresses at shallow depths in the crust.

---

<sup>11</sup>Vortex flow is used to describe spinning motion about an imaginary axis within a fluid.

<sup>12</sup>Behr & Platt (2011, Figure 1) show that the magnitude of differential stresses induced in the lower crust of extensional terranes during normal, strike-slip or thrust faulting may exceed 100 MPa at depths of  $\approx 10$ , 6 or 2 km, respectively.

The disposition of faults and horsts in Centre 2 and the different compositions of the the Kaltungo Inlier, Zambuk Ridge and Biu Plateau show that the Kaltungo Lineament, other sub-parallel faults as well as horsts were exploited, at different geologic times, to emplace these volcanic rocks. Consequently, these locations may be preferred targets in exploration campaigns for commercial deposits of geothermally-emplaced and/or supergene enrichments of metallic sulphides and oxides. Such mineralisations occur SouthEast of the study area (Woakes et al., 1987).

(11) It seems that the Yola Arm of the Benue Trough (Yola basin) developed after NW-SE trends, which generally terminate against NE-SW trends in Centre 2, were reactivated to relieve the strain localised in the Kaltungo area by baffles located in the Yankari and SW Biu areas (Figure 7.1). This proposed origin of the Yola basin is well supported by the correspondence between inferred directions of stress barriers 1 and 2 (Figure 7.1) and the trend of the Yola Arm. For instance, analyses of remotely-sensed lineaments show the dominant trend to be WNW-ESE in the Lamurde area (Koopmans, 1986), where Aptian sediments outcrop in the  $\approx 100$  km long and 15 km wide Lamurde Anticline. This location correlates well with the WNW-ESE striking high angle faults that must have temporarily barricaded the NorthEasterly propagation of the rift, leading to significant basement uplift in the Lamurde area and reactivation of extensive E-W and short near-N-S trends, ultimately forming the Yola Arm.

Another evidence for this proposed origin is provided by a linear alignment of inferred volcanoes in the Kaltungo and Longuda areas, which suggests  $\approx 25^\circ$  clockwise rotation away from the Kaltungo Lineament, along a clearly deflected fault in the Dadiya area. Unlike the existing interpretation which was inconsistent with an overall NorthEasterly sinistral strike-slip movement across the Upper Benue Trough (Benkhelil, 1982), the current interpretation is consistent with this sense of transcurrent movement throughout the study area (Single-headed, deep-blue arrows in figure 7.1).

(12) Basement horsts and their bounding faults converge in the vicinity of Kaltungo, Zambuk Ridge and Biu, where a major NW-SE stress baffle separates the study area into two major tectonic domains: (1) Upper Benue Trough; and (2) Gongola/Kerri-Kerri/Chad basin. The disposition of structures in the area (Figures 6.12 and 6.15) and the directions of tectonic stress propagation or barrier inferred from them (Figure 7.1) suggest larger intensity and more chaotic deformation in the area South of an imaginary line defined by Azare, Potiskum, Sumaila, Goniri, and Bama (The Upper Benue Trough domain) than North of this line (The Chad basin domain).

(13) Net displacements in the Upper Benue Trough, along with resistance by the massive, rigid basement in Centre 4 may have served to deflect and transmit crustal extension and sinistral shear displacements, mainly, through NE-SW trends in the Gongola/Kerri-Kerri basins to a network of NE-SW and NW-SE trends in the Biu, Goniri and Damboa areas. The generally NorthEasterly propagating stresses were then deflected by means of near-N-S trends to reactivate NE-SW and NW-SE trends in the Chad basin, circumventing the rigid basement in Centre 4.

(14) NE-SW trends in Northern Cameroon and Central Chad Republics, are more optimally located for reactivation by the, possibly amplified, NorthEasterly propagating stresses, than equivalent trends in SW Chad basin (Nigeria). Hence, more rift-related deformation attended reactivated lineaments in these areas, ultimately dissipating strain to the East Niger Basin, Niger Republic (Fairhead & Green, 1989; Fairhead & Okereke, 1990), than to the SW Chad basin. Thus, lineaments in the SW Chad basin area were largely shielded from the extensive Early Cretaceous reactivation. This explains the ENE-WSW trend of the SW Chad basin, whose stratigraphy is well documented (Petters & Ekweozor, 1982, Avbovbo et al., 1986, Alalade & Tyson, 2010).

(15) The Yola and SW Chad basins appear to have developed as strain relief features. This is a view which is contrary to the generally accepted claim of the existence of a failed arm of a rift beneath the Gongola basin (e.g., Shemang et al., 2001).

#### 7.1.4 Significance to petroleum exploration

This study shows that discrete depocenters (Figure 6.19), with sediment thickness exceeding 10 km, occur throughout NE Nigeria (Section 7.1.2). After correcting for its underestimation by about 40% (Tables 4.6 and 5.7), sediment thickness generally exceeds 11 km in the discrete depositional centres that are scattered across the otherwise shallow (<3 km deep) NE Nigeria basement. These depths agree well with the total depths of wells completed in the basement, whose locations are also shown in figure 6.19, as estimates from seismic sections (Avbovbo et al., 1986). However, if rift propagation along these depocenters were along pure shear-controlled strike slip faults, inferences drawn from 2D seismic datasets like those of Avbovbo et al. (1986) may not be enough for evaluating the petroleum play and prospect in these depocenters, since pure shear strike slip faults do not involve vertical displacements (Daly et al., 1989; Fossen, 2010).

Exploratory wells in NE Nigeria appear to be located above basement horsts, at total depths that are consistent with the isopach contours (Figure 6.19).<sup>13</sup> Hence, these wells could not present the complete sedimentary succession of the depocenters, a key requirement for successful hydrocarbon exploration. However, source rock evaluations using drill cuttings from wells suggest the existence of significant potentials for hydrocarbon generation at intermediate depths in the Chad basin (Petters & Ekweozor, 1982; Olugbemi et al., 1997; Alalade & Tyson, 2010) and Gongola/Kerri-Kerri basin (Obaje et al., 2004). Adequate structural styles required for migration and entrapment of hydrocarbons exist (Avbovbo et al., 1986; Genik, 1992; Lawal et al., 2005). However, the occurrence of basin inversion in the Chad basin (Avbovbo et al., 1986), and the fact that hydrocarbon finds continue to elude prospectors, are indicative of a more complex petroleum play in the study area. Therefore, the key to successfully exploring these basins lie in optimally positioning wells to exploit the axis of depocenters (Avbovbo et al., 1986).

---

<sup>13</sup>Well locations were extracted from Avbovbo (1980), Avbovbo et al. (1986), Olugbemi et al. (1997), Obaje et al. (2004) and Lawal et al. (2005).

This study shows that the SW Chad (Bornu) basin is underlain by a single, generally NE-SW trending,  $\approx 100 \text{ km} \times 50 \text{ km}$  graben (Figure 6.19) with sediment fill exceeding 10 km along its trough (Section 7.1.2). Figure 6.19, along with profiles across the basin (e.g., figure 6.18b) show it to be completely isolated from the adjoining Central Lake Chad, Termit, and N'gel Edji basins of Chad, Cameroon and Niger Republics. Isolation of the basin is ensured by the intersection of a nearly N-S striking basement horst on which is centred a dormant volcano on its East, and a generally NorthEasterly massif of reworked basement horsts that lies everywhere North of the basin.

Although depocenters are genetically related, based on strain intensities perceived from relations between structural elements in figure 6.12 and the inferred tectonic propagation stress directions (Figure 7.1), these depressions (basins) belong to two distinct sub-tectonic domains: (1) the Upper Benue Trough (Gongola/Kerri-Kerri/Bashar-Muri basins); and (2) the Chad basin domains. Since intensity varies across these domains, the structural style and deformation fabric characterising them should also vary. So also should the exploration strategy adopted for each domain.

### 7.1.5 Significance to seismic hazard preparedness

Significant seismic hazards characterise the study area. The density of the structural elements etched into the NE Nigeria basement (Figure 6.12) reflects the amount of reworking induced by far-field tensional stresses associated with rifting and crustal readjustments in the Benue Trough. These stresses were transmitted along major faults that originated in the Gulf of Guinea (Ajakaiye et al., 1986; Fairhead & Okereke, 1990). Ajakaiye et al. (1987), Langer et al. (1987) and Amponsah (2004) indicate that seismicity across regional faults in parts of West Africa are interconnected. Ajakaiye et al. (1987) implied such a relationship between the 28<sup>th</sup> of July, 1984 Accra, Ghana earthquake and coincident seismic events in and Ijebu-Ode, Nigeria. Consequently, future propagations of crustal rupture due to buoyant mantle materials beneath NE Nigeria are bound to rapidly access and re-activate these generally weak and incompetent zones in the basement, especially reverse faults with significant dips to relieve focussed strain. Such sudden changes in static stresses trigger earthquakes (King et al., 1994), as dynamic stresses associated with such reactivations in extensional regimes are more easily exploited than in purely compressional regimes (Hill, 2008). Further stresses induced by the resulting geodynamic reorganisation may also trigger volcanic activity (Walter et al., 2009).

Unfortunately, like faults in the Wenchuan area of Sichuan Province, China which were generally considered aseismic until an  $\approx 7.9$  magnitude earthquake struck the area on 12<sup>th</sup> May 2008 (Purcaru, 2008; BBC News, 2012; USGS, 2012), faults in the study area are also treated as aseismic. However, figures 6.12 and 6.19 show that extensive basement horsts and their bounding faults converge in the vicinity of Yankari, Kaltungo, Longuda and Biu. Such convergence of faults and basement structures have been associated with the highest fault slip-rates recorded for the Wenchuan earthquake (Shen et al., 2009). Shen et al. (2009) also stress the significant rates at

which the resulting strain may be transmitted through adjoining fault segments.

Seismological and Global Positioning System (GPS) studies of the Wenchuan earthquake, combined with Interferometric Synthetic Aperture Radar (InSAR) measurements show that a maximum vertical slip of  $\approx 6$  m accompanied by  $\approx 5$  m lateral slip in a dextral sense was associated with a rupture  $\approx 320$  km long (Shen et al., 2009). The Wenchuan earthquake claimed over 70,000 lives, injured well over 400,000 people, displaced over 5 million people (UNICEF, 2009; BBC News, 2012).

## 7.2 Conclusions

### 7.2.1 Locating structural edges from RTE grids

The “Tilt-Depth” method requires  $\Delta T$  datasets to be transformed to their RTP or RTE equivalents prior to application of the method. I have compared estimates of locations of anomalous edges from RTP and RTE equivalent datasets, and find that the degree of correlation between edges from equivalent anomalies depend on the geometry and orientation of sources. Poor correlations are mainly caused by RTE-induced shape (amplitude and phase) changes or anisotropy. Comparisons show that NW-SE, NE-SW, ENE-WSW, WNW-ESE and E-W striking two-dimensional (2D) structures correlate strongly and positively, and can be identified with certainty from RTE datasets. NNW-SSE and NNE-SSW anomalies show positive correlations where sources are well isolated, and poor-to no correlation where they are not and anomalies interfere. Such edges are difficult to identify with any certainty from RTE grids.<sup>14</sup>

E-W striking dipolar RTE anomalies occur where NNW-SSE and NNE-SSW striking 2D edges are dissected. Where these anomalies are not sufficiently isolated on RTE grids, they usually interfere to produce anomalies that are altogether unrelated, both in magnitude, extent and trend, to their sources.

RTE anomalies from non-2D Western and Eastern edges of E-W oriented three-dimensional (3D) sources, are preferentially extended further to the West and East of these sources. These extensions potentially increase the risks of further interference with adjacent anomalies. Also, these non-2D edges have a generally N-S trend, making these edges difficult to identify on RTE datasets.

Tests using profile datasets show that error in “Tilt-Depth” method estimates were invariant to changes in source depths, but sensitive to changes in the effective inclination of magnetisation ( $\phi$ ) and dips of sources. At error limits of 0-20%, the method effectively estimates locations and depths of 2D contacts when dip is within the  $75 \leq d^\circ \leq 105$  range, inclination of remanent magnetisation relative to induced magnetisation is within the  $155 \leq \beta^\circ \leq 205$  range (magnetisations

---

<sup>14</sup>See glossary (Section 0.1) for full meanings of acronyms.

are collinear), and Koenigsberger ratio ( $Q$ ) of remanent to induced magnetisation amplitudes  $\leq 1$ . Relationships between  $Q$ ,  $\alpha$ ,  $\beta$  and  $\phi$  suggests that the simplification of remanence-laden anomalies due to magnetisations being collinear results from deviations of  $\phi$  from  $\alpha$  of  $\leq 12^\circ$  when  $Q \leq 1$ .<sup>15</sup> Similar deviations occur between  $\phi$  from  $\alpha$ , for all  $\beta$  values, when  $Q \leq 0.2$ . Hence, remanent magnetisation is negligible for RTP or RTE datasets when *a priori* information suggests  $Q \leq 0.2$ .

Analyses of the relationship between  $Q$ ,  $\alpha$ ,  $\beta$  and  $\phi$  show that the simplification of remanence-laden anomalies afforded by collinear magnetisations ( $155 \leq \beta^\circ \leq 205$ ) results from effective magnetisation direction ( $\phi$ ) being kept at  $\leq 10^\circ$  from  $\alpha$  (Figures 3.10c, 3.10d and 3.11). These figures also show that deviations between  $\alpha$  (RTP or RTE) and  $\phi$  are  $\leq 10^\circ$  for all directions of remanent magnetisation ( $\beta$ ), when  $Q < 0.2$  (Figure 3.11). Consequently, the effects of  $\beta$  on RTP or RTE of datasets for which *a priori* information suggests  $Q < 0.2$  can also be considered negligible, though not collinear.

The complex “Bishop” model (CBM) dataset met these  $\phi$ ,  $Q$  and dip specifications, hence was easily transformed to its RTP or RTE equivalent. Sources of the CBM dataset, whose locations and depths are known, vary in shape and orientation, and sometimes cross-cut each other. Consequently, anomalies from adjacent and/or cross-cutting CBM sources interfered, complicating the spatial relationship between locations of anomalies relative to their sources, especially on the RTE dataset. The combined effects of source geometries, source orientations and anomaly interference on “Tilt-Depth” method estimates of locations of CBM source edge were examined using RTP and RTE equivalents of the CBM dataset. These “Tilt-Depth” method estimates were then compared with equivalents obtained using second vertical derivative (SVD), analytic signal amplitude (ASA), local wavenumber (LW), as well as the horizontal gradient magnitude (HGM) of  $\theta$  ( $HGM_{(\theta)}$ ) and HGM of  $\Delta T$  ( $HGM_{(\Delta T)}$ ) methods.

Positive amplitudes of RTP anomalies and these derived functions are directly located above sources with higher susceptibilities and/or shallow depths, while negative anomalies are located above sources with lower susceptibilities and/or deep depths. This relationship is reversed for RTE anomalies. Hence, additive inverses of  $\theta$  and SVD of RTE anomalies were required to bring these anomalies in phase with their RTP equivalents, for comparison.

$\theta$  presented an elegant automatic-gain-control (AGC) filter for imaging anomalies of all amplitudes and wavelengths on RTP grids. However, interference due to the presence of NNW-SSE and NNE-SSW on RTE grids affects  $\theta$  anomalies more, as comparisons with grids of other phase-based methods (LW and  $HGM_{(\theta)}$ ) show. Hence, interpreting RTE datasets require a suite of methods to image NNW-SSE, NNE-SSW and N-S striking sources.

The presence of N-S and/or near-N-S trending 2D edges can be inferred from RTE grids, using linear stacks of short wavelength E-W striking maxima of  $HGM_{(\Delta T)}$ , ASA, LW and  $HGM_{(\theta)}$  of

---

<sup>15</sup>The 155 to 205° range expresses collinearity between induced and remanent magnetisations (Bath, 1968).

RTE grids. Only location grids containing all maxima traces (i.e., including [Blakely & Simpson \(1986\)](#) scores 1 to 4) should be used for this purpose, since the short wavelength trends that identify these edges are otherwise removed.

Correspondences between the zero contours of SVD and  $\theta$  of RTE grids indicate estimates at their correct orientations and locations, irrespective of source geometry. The Northern and Southern edges of 3D sources are well imaged by additional correspondences between  $HGM_{(\Delta T)}$ , ASA, LW and  $HGM_{(\theta)}$ .

The  $HGM_{(\Delta T)}$ , ASA, LW and  $HGM_{(\theta)}$  methods are sensitive to noise and generate secondary or false maxima from interference anomalies. Therefore, only locations at which estimates from all these methods are coincident with, parallel or closest to  $\theta$  and/or SVD estimates are to be retained as certain, for inclusion in the final RTE interpretation.

Barring interference from adjacent anomalies, locations of NW-SE, NE-SW, ENE-WSW, WNW-ESE and E-W striking anomalous edges can be determined from any RTE grid, at the level of confidence of an equivalent RTP grid, as long as these trends dominate the RTE grid (both in frequency and density) relative to NNW-SSE and NNE-SSW trending edges. Only the Northern and Southern non-2D edges of 3D sources can be determined with certainty from RTE grids.

### 7.2.2 Depths of structural edges from RTE grids

The "Tilt-Depth" method is sensitive to contributions from non-magnetic basement topography to the  $\Delta T$  dataset. Hence, the method requires datasets to be upward-continued prior to its deployment. Comparisons between actual source depths and their estimates from RTP or RTE of such datasets show "Tilt-Depth" method estimates from  $-27 \leq \theta \leq 27$  range to be more accurate than those from the  $-45 \leq \theta \leq 45$  range. Depths estimated for vertical 2D and non-2D contacts from RTP or RTE dataset using the  $-27 \leq \theta \leq 27$  range-based "Tilt-Depth" method were compared with estimates from the local wavenumber (LW) and analytic signal (ASA) methods, at equivalent locations on the actual and estimated depth grids. The error in these estimates show (Table 5.7) that:

- (1) the "Tilt-Depth" and LW methods underestimate the actual depth of sources on gridded datasets. The ASA method provides both severely underestimated and overestimated depths from these datasets. "Tilt-Depth" and LW estimates were, thus, easier to utilise and interpret;
- (2) "Tilt-Depth" and LW methods underestimate 2D edges from RTP grid by up to 25% of their actual depths. These sources are underestimated by up to 35% of their actual depths from RTE grids;
- (3) actual depths of the Northern and Southern non-2D edges of 3D sources on RTP grids are

underestimated by up to 30 and 35%, respectively, by the LW and "Tilt-Depth" methods;

- (4) only the "Tilt-Depth" method consistently underestimates 2D and non-2D contacts from RTE grids. by up to 40%; and
- (5) the LW method overestimates and underestimates 2D and non-2D contacts from RTE grids. Error in these estimates ranged from -30 to 5% and from -40 to 10%, respectively.

However, when LW and "Tilt-Depth" estimates were limited to equivalent locations on the RTP and RTE grids, these methods underestimated depths of 2D contacts by up to 30% from RTP and RTE grids, but underestimated non-2D contacts by up to 40% from the RTE grid (Table 5.10).

### 7.2.3 Structural features of the basement

The structural map of NE Nigeria obtained from this study (Figure 6.12) show that the basement is dissected by mainly NE-SW trending faults, against which NW-SE faults mainly terminate. These are mainly high angle (near-vertical) faults, which are basement expressions of crustal lineaments that have been reactivated several times during episodes of tectonic activity. The relationship between these inferred faults and other structures in the basement, along with outcrop information, have been used to establish their control on tectonic strain dissipation and origins of basin deformation style, the geometry of extensional features like basement horsts, and locations of volcanic relicts.

"Tilt-Depth" and Local wavenumber method depth estimates show that discrete depocenters occur in all parts of the study area (Figure 6.19). These were mainly half grabens. In particular, the depocenter in SW Chad basin appeared to be completely isolated, and without communication with the adjoining basins in Cameroon, Chad and Niger Republics. Once corrected for the  $\approx$  40% underestimation, "Tilt-Depth" and Local wavenumber methods depth ranged from 0 to about 11 km, and agree well with depths obtained from boreholes across the study area (Section 6.4, and Figure 6.19), and from seismic data interpretation in the Chad basin. The basement is at generally shallow depths ( $<0.5$  km), and frequently occurs at depths  $<2.5$  km (as shallow horsts) within depocenters or basins (Figure 6.19).

## Bibliography

- Abubakar, Y. I., Umegu, M. N., & Ojo, S. B., 2010. Evolution of Gongola basin, Upper Benue Trough, NorthEastern Nigeria, *Asian Journal of Earth Sciences*, **3**(2), 62–72.
- Adighije, C., 1979. Gravity field of Benue Trough, Nigeria, *Nature Journals*, **282**, 199–201.
- Affleck, J., 1957. Discussion of V. Baranov's paper, "A new method of interpretation of aeromagnetic maps, Pseudogravimetric anomalies", *Geophysics*, **22**(2), 382–383.
- Airo, M.-L. & Wennerström, M., 2010. Application of regional aeromagnetic data in targeting detailed fracture zones, *Journal of Applied Geophysics*, **71**(2-3), 62–70.
- Ajakaiye, D. E., 1981. Geophysical investigation of the Benue trough - A review, *Earth Evolutionary Science*, **1**, 126–136.
- Ajakaiye, D. E., Hall, D. H., Millar, T. W., Verheijen, P. J. T., Awad, M. B., & Ojo, S. B., 1986. Aeromagnetic anomalies and tectonic trends in and around the Benue Trough, Nigeria, *Nature*, **319**, 582–584.
- Ajakaiye, D. E., Daniyan, M. A., Ojo, S. B., & Onuoha, K. M., 1987. The July 28, 1984 SouthWestern Nigeria earthquake and its implications for the understanding of the tectonic structure of Nigeria, *Journal of Geodynamics*, **7**(3-4), 205–214.
- Alalade, B. & Tyson, R. V., 2010. Hydrocarbon potential of the late Cretaceous Gongola and Fika Formations, Bornu (Chad) basin, NE Nigeria, *Journal of Petroleum Geology*, **33**(4), 339–354.
- Amponsah, P. E., 2004. Seismic activity in Ghana: Past, present and future, *Annals of Geophysics*, **47**(2/3), 96–111.
- Arkani-Hamed, J., 1988. Differential reduction-to-the-pole of regional magnetic anomalies, *Geophysics*, **53**, 1592–1600.
- Arkani-Hamed, J., 2007. Differential reduction to the pole: Revisited, *Geophysics*, **72**, L13–L20.
- Avbovbo, A. A., 1980. Basement geology in the sedimentary basins of Nigeria, *Geology*, **8**(7), 323–327.
- Avbovbo, A. A., Ayoola, E. O., & Osahon, G. A., 1986. Depositional and structural styles in Chad Basin of Northeastern Nigeria, *The American Association of Petroleum Geologists*, **70**(12), 1787–1789.
- Aydin, A. & Nur, A., 1982. Evolution of pull-apart basin and their scale independence, *Tectonics*, **1**(1), 91–105.
- Baranov, V., 1957. A new method of interpretation of aeromagnetic maps, pseudogravimetric anomalies, *Geophysics*, **22**(2), 359–383.
- Baranov, V. & Naudy, H., 1964. Numerical calculation of the formula of reduction to the magnetic pole, *Geophysics*, **29**(1), 67–79.
- Barracough, D. R., 1987. International Geomagnetic Reference Field: The Fourth Generation, *Physics of the Earth and Planetary Interiors*, **48**, 279–292.
- Barritt, S. A., Fairhead, J. D., & Misener, D. J., 1993. The African Magnetic Mapping Project,

- ITC Journal*, **2**, 122–131.
- Bath, G. D., 1968. Aeromagnetic anomalies related to remanent magnetism in volcanic rock, Nevada Test Site, *Geological Society of America Memoir*, **110**, 135–146.
- BBC News, 2012. China earthquake, [http://news.bbc.co.uk/1/hi/in\\_depth/asia\\_pacific/2008/china\\_quake/default.stm](http://news.bbc.co.uk/1/hi/in_depth/asia_pacific/2008/china_quake/default.stm), Page accessed on Wednesday, 7/11/2012, and last updated at 14:24 GMT, Thursday, 16/02/2012.
- Beard, L. P., 2000. Detection and identification of North-South trending magnetic structures near the magnetic equator, *Geophysical Prospecting*, **48**, 745–761.
- Behr, W. M. & Platt, J. P., 2011. A naturally constrained stress profile through the middle crust in an extensional terrane, *Earth and Planetary Science Letters*, **303**, 181–192.
- Belley, F., Ferré, E. C., Martín-Hernández, F., Jackson, M. J., Dyar, M. D., & Catlos, E. J., 2009. The magnetic properties of natural and synthetic  $(Fe_x, Mg_{1-x})_2SiO_4$  olivines, *Earth and Planetary Science Letters*, **284**, 516–526.
- Benkhelil, J., 1982. Benue Trough and Benue Chain, *Geological Magazine*, **119**(2), 155–168.
- Benkhelil, J., 1987. Cretaceous deformation, magmatism, and metamorphism in the Lower Benue Trough, Nigeria, *Geological Journal*, **22**(Thematic Issue), 467–193.
- Benkhelil, J., 1989. The origin and evolution of the Cretaceous Benue Trough (Nigeria), *Journal of African Earth Sciences*, **8**(2/3/4), 251–282.
- Benkhelil, J. & Robineau, B., 1983. Le fosse de la Benoue est-il un rift?, *Bulletin des Centre de Recherches Exploration-Production Elf-Aquitane*, **7**(1), 315–321.
- Benkhelil, M., Guiraud, J. F., & Saugy, L., 1989. The Bornu-Benue Trough, the Niger Delta and its Offshore: Tectono-sedimentary reconstruction during the Cretaceous and Tertiary from geophysical data and geology, in *Geology of Nigeria*, edited by C. A. Kogbe, chap. 15, pp. 277–309, Rock View (Nigeria) Limited, 2nd edn.
- BGS, 2000. Groundwater Quality: Tanzania, <http://www.bgs.ac.uk/downloads>, Accessed online on 12/09/2010.
- BGS, 2011. Magnetic poles, <http://www.geomag.bgs.ac.uk/education/poles.html>.
- Biggs, J., Amelung, F., Gourmelen, N., Dixon, T. H., & Kim, S.-W., 2009. InSAR observations of 2007 Tanzania rifting episode reveal mixed fault and dyke extension in an immature continental rift, *Geophysical Journal International*, **179**, 549–558.
- Blakely, R. J., 1996. *Potential theory in gravity and magnetic applications*, Cambridge University Press, Cambridge, UK.
- Blakely, R. J. & Simpson, R. W., 1986. Short Note: Approximating edges of source bodies from magnetic or gravity anomalies, *Geophysics*, **51**(7), 1494–1498.
- Blakely, R. J., Brocher, T. M., & Wells, R. E., 2005. Subduction-zone magnetic anomalies and implications for hydrated forearc mantle, *Geology*, **33**, 445–448.
- Bonini, M., Souriot, T., Boccaletti, M., & Brun, J., 1997. Successive orthogonal and oblique extension episodes in a rift zone: Laboratory experiments with application to the Ethiopian Rift, *Tectonics*, **16**(2), 347–362.
- BP, 2012. BP Statistical Review of World Energy, [www.bp.com/statisticalreview](http://www.bp.com/statisticalreview), Retrieved October 25, 2012.

- Briggs, I. C., 1974. Machine contouring using minimum curvature, *Geophysics*, **39**, 39–48.
- Brodie, R. C., 2002. Airborne and ground magnetics, in *Geophysical and remote sensing methods for regolith exploration.*, edited by E. Papps, vol. 144, pp. 33–45, CRCLEME.
- Burke, K., 1976. The Chad Basin: An active intra-continental basin, *Tectonophysics*, **36**, 197–206.
- Burke, K., 1977. Aulacogens and continental breakup, *Ann. Rev. Earth Planet. Sci.*, **5**, 371–396.
- Butler, D. K., 2003. Implications of magnetic backgrounds for unexploded ordnance detection, *Journal of Applied Geophysics*, **54**, 111–125.
- Caen-Vachette, M. & Umeji, A. C., 1988. Geology and geochronology of the Okene area: Evidence for an Eburnean orogenic cycle in South-Central Nigeria, *Journal of African Earth Sciences (and the Middle East)*, **7**(1), 121–126.
- Cain, J. C., Wang, Z. G., Schmitz, D. R., & Meyer, J., 1989. The geomagnetic spectrum for 1980 and core crustal separation., *Geophysical Journal International*, **97**, 443–447.
- Campbell, W. H., 2003. *Introduction to geomagnetic fields*, Cambridge University Press, UK.
- Carter, J. D., Barber, W., Talt, E. A., & Jones, J. P., 1963. The geology of parts of Adamawa, Bauchi and Bomu provinces in Northeastern Nigeria, *Bulletin Geological Survey of Nigeria*, **30**, 1–109.
- Chandler, G., 2010. Putting Nigeria on the map, *Earth Explorer*, **1**, 16–19, Published by Geosoft Inc., Canada.
- Chapra, S. C., 2012. *Applied Numerical Methods with MATLAB for Engineers and Scientists*, McGraw-Hill, New York, 3rd edn., ISBN: 978-0-07-340110-2.
- Clark, D. A. & Emerson, D. W., 1999. Self-demagnetization, *Preview*, **79**, 22–25, Australian Society of Exploration Geophysicists.
- Commonwealth, 2011. Commonwealth country profiles: Nigeria., <http://www.thecommonwealth.org/YearbookHomeInternal/138917/>.
- Cook, K. L., 1950. Quantitative interpretation of vertical magnetic anomalies over veins., *Geophysics*, **15**(4), 667–686.
- Cooper, G. R. J. & Cowan, D. R., 2006. Enhancing potential field data using filters based on the local phase, *Computers and Geosciences*, **32**, 1585–1591.
- Cordell, L. & Grauch, V. J. S., 1982. Mapping magnetic basement zones from aeromagnetic data in the San Juan Basin, New Mexico, *SEG Expanded Abstracts, Gravity and Magnetic Maps* **2**, 246–247.
- Cordell, L. & Grauch, V. J. S., 1985. Mapping basement magnetization zones from aeromagnetic data in the San Juan basin, New Mexico., in *The Utility of Regional Gravity and Magnetic Anomaly Maps*, edited by W. J. Hinze, pp. 181–197, Society of Exploration Geophysicists, Society of Exploration Geophysicists, Tulsa, Oklahoma, USA.
- Corti, G., Bonini, M., Sokoutis, D., Innocenti, F., Manetti, P., Cloetingh, S., & Mulugeta, G., 2004. Continental rift architecture and patterns of magma migration: A dynamic analysis based on centrifuge models, *Tectonics*, **23**, TC2012.
- Cratchley, C. R., P.Louis, & Ajakaiye, D. E., 1984. Geophysical and geological evidence for the Benue-Chad Basin Cretaceous rift valley system and its tectonic implications, *Journal of*

- African Earth Sciences*, **2**(2), 141–150.
- Daly, M. C., Chorowicz, J., & Fairhead, J. D., 1989. Rift basin evolution in Africa: The influence of reactivated steep basement shear zones, in *Inversion Tectonics*, edited by M. A. Cooper & G. D. Williams, vol. 44 of **Special Publications**, pp. 309–334, Geological Society, London.
- Dobrin, M. B. & Savit, C. H., 1988. *Introduction to geophysical prospecting*, McGraw-Hill Inc., USA., 4th edn.
- Ebinger, C., Ayele, A., Keir, D., Rowland, J., Yirgu, G., Wright, T., Belachew, M., & Hamling, I., 2010. Length and Timescales of Rift Faulting and Magma Intrusion: The Afar Rifting Cycle from 2005 to Present, *Annual Review of Earth and Planetary Science*, **38**, 439–466.
- Ekwueme, B. N., 1990. Rb-Sr ages and petrologic features of Precambrian rocks from the Oban massif, SouthEastern Nigeria, *Precambrian Research*, **47**(3-4), 271–286, Geochemistry and Mineralization of Proterozoic Mobile Belts Series.
- Epuh, E. E., Olorode, D. O., & Nwilo, P. C., 2012. Analysis of Gongola Basin depositional sequence using seismic stratigraphy, *Global Journal of Pure and Applied Science and Technology*, **2**, 9–21.
- Everitt, B. S., 2006. *The Cambridge Dictionary of Statistics*, Cambridge University Press, 2nd edn.
- Fairhead, J., 1988. Late mesozoic rifting in africa, in *Triassic-Jurassic Rifting*, edited by W. Manspeizer, vol. 22 of **Developments in Geotectonics**, pp. 821–831, Elsevier, Amsterdam.
- Fairhead, J. D., 1988. Mesozoic plate tectonic reconstructions of the central South Atlantic Ocean: The role of the West and Central African rift system, *Tectonophysics*, **155**, 181–191.
- Fairhead, J. D., 2007. Gravity and magnetics in today's oil and mineral industry (Extensively updated in 2006), Course notes, GETECH c/o School of Earth Sciences, University of Leeds, Leeds LS2 9JT, UK.
- Fairhead, J. D. & Binks, R. M., 1991. Differential opening of the Central and South Atlantic Oceans and the opening of the West African rift system, *Tectonophysics*, **187**, 191–203.
- Fairhead, J. D. & Binks, R. M., 1992. A plate tectonic setting for Mesozoic rifts of West and Central Africa, *Tectonophysics*, **213**, 141–151.
- Fairhead, J. D. & Green, C. M., 1989. Controls on rifting in Africa and the regional tectonic model for the Nigeria and East Niger rift basins, *Journal of African Earth Sciences*, **8**(2/3/4), 231–249.
- Fairhead, J. D. & Okereke, C. S., 1987. A regional gravity study of the West African rift system in Nigeria and Cameroon and its tectonic interpretation, *Tectonophysics*, **143**, 141–159.
- Fairhead, J. D. & Okereke, C. S., 1988. Depths to major density contrasts beneath the West African riftsystem in Nigeria and Cameroon based on spectral analyses of gravity data, *Journal of African Earth Sciences*, **7**(5/6), 769–777.
- Fairhead, J. D. & Okereke, C. S., 1990. Crustal thinning and extension beneath the Benue Trough based on gravity studies, *Journal of African Earth Sciences (and the Middle East)*, **11**(3-4), 329–335.
- Fairhead, J. D. & Williams, S. E., 2006. Evaluating normalized magnetic derivatives for structural mapping, *SEG Expanded Abstracts*, **25**(1), 845–849.

- Fairhead, J. D., Misener, D. J., Green, C. M., Bainbridge, G., & Reford, S. W., 1997. Large scale compilation of magnetic, gravity, radiometric and electromagnetic data: The new exploration strategy for the 90s, in *Proceedings of Exploration '97: Fourth Decennial International Conference on Mineral Exploration*, edited by A. G. Gubbins, pp. 805–816, GEO/FX, Paper 103.
- Fairhead, J. D., Williams, S. E., & Flanagan, G., 2004. Testing magnetic local wavenumber depth estimation methods using a complex 3D test model, *SEG Expanded Abstracts*, **23**(1), 742–745.
- Fairhead, J. D., Salem, A., Williams, S., & Samson, E., 2008. Magnetic interpretation made easy: The Tilt-Depth-Dip- $\delta K$  method, *SEG Expanded Abstracts*, **27**, 779–783.
- Fairhead, J. D., Salem, A., Cascone, L., Hammill, M., Masterton, S., & Samson, E., 2011. New developments of the magnetic Tilt-Depth method to improve structural mapping of sedimentary basins, *Geophysical Prospecting*, **59**(6), 1072–1086.
- Fairhead, J. D., Stanislav, M., Green, C. M., Masterton, S., & Yousif, M. E., 2012. Regional plate tectonic controls on the evolution of the West and Central African Rift System, with a focus on the Muglad Rift Basin, Sudan, *Sudanese Association of Petroleum Geoscientists (SAPEG) Journal*, pp. 14–29.
- Farr, T. G., Rosen, P. A., Caro, E., Crippen, R., Duren, R., Hensley, S., Kobrick, M., Paller, M., Rodriguez, E., Roth, L., Seal, D., Schaffer, S., Shimada, J., Umland, J., Werner, M., Oskin, M., Burbank, D., & Alsdorf, D., 2007. The shuttle radar topography mission, *Reviews of Geophysics*, **45**, RG2004 (1–33).
- Finlay, C. C., Maus, S., Beggan, C. D., Bondar, T. N., Chambodut, A., Chernova, T. A., Chulliat, A., Golovkov, V. P., Hamilton, B., Hamoudi, M., Holme, R., Hulot, G., Kuang, W., Langlais, B., Lesur, V., Lowes, F. J., Luhr, H., Macmillan, S., Manda, M., McLean, S., Manoj, C., Menvielle, M., Michaelis, I., Olsen, N., Rauberg, J., Rother, M., Sabaka, T. J., Tangborn, A., Toffner-Clausen, L., Thebault, E., Thomson, A. W. P., Wardinski, I., Wei, Z., & Zvereva, T. I., 2010. International Geomagnetic Reference Field: The Eleventh Generation, *Geophysical Journal International*, **183**(3), 1216–1230.
- Finn, C. A. & Morgan, L. A., 2002. High-resolution aeromagnetic mapping of volcanic terrain, Yellowstone National Park, *Journal of Volcanology and Geothermal Research*, **115**, 207–231.
- Fitton, J. G., 1980. The Benue trough and Cameroon Line - A migrating rift system in West Africa, *Earth and Planetary Science Letters*, **51**(1), 132–138.
- Flanagan, G. & Bain, J. E., 2012. Depth Extent - An Overlooked Parameter in Magnetic Depth Estimation, *EAGE Expanded Abstracts*.
- Flanagan, G. & Bain, J. E., 2012. Depth Extent - A Practical Example in Magnetic Depth Estimation, *EAGE Expanded Abstracts*.
- Fossen, H., 2010. *Structural Geology*, Cambridge University Press.
- Frere, M., 2010. Airborne geophysical coverage of the Federal Republic of Nigeria: Phase 1 Interpretation, Tech. rep., Fugro Airborne Surveys.
- Friis-Christensen, E., Lühr, H., Hulot, G., Haagsmans, R., & Purucker, M., 2009. Geomagnetic research from space, *Eos Trans. AGU*, **90**(25), 213–214.
- Garland, G. D., 1971. *Introduction to geophysics. Mantle, core and crust.*, W. B. Saunders Co.

- Genik, G. J., 1992. Regional framework, structural and petroleum aspects of rift basins in Niger, Chad and the Central African Republic (C.A.R.), *Tectonophysics*, **213**, 169–185.
- Gerovska, D. & Araúzo-Bravo, M. J., 2006. Calculation of magnitude magnetic transforms with high centricity and low dependence on the magnetization vector direction, *Geophysics*, **71**(5), I21–I30.
- Gerovska, D. & Stavrev, P., 2006. Magnetic data analysis at low latitudes using magnitude transforms, *Geophysical Prospecting*, **54**, 89–98.
- GETECH, 2007. Tanzania aeromagnetic data, Confidential Report G0725, GETECH Plc., UK.
- Girdler, R. W., 1983. Processes of planetary rifting as seen in the rifting and breakup of Africa, *Tectonophysics*, **94**, 241–252.
- Grant, F. S., 1985. Aeromagnetism, geology and ore environments, I. Magnetite in igneous, sedimentary and metamorphic rocks: An overview., *Geoexploration*, **23**, 303–333.
- Grant, F. S. & West, G. F., 1965. *Interpretation theory in applied geophysics*, McGraw-Hill Book Company, USA.
- Grauch, V. J. S. & Hudson, M. R., 2007. Guides to understanding the aeromagnetic expression of faults in sedimentary basins: Lessons learned from the central Rio Grande rift, New Mexico, *Geosphere*, **3**, 596–623.
- Grauch, V. J. S., Hudson, M. R., & A.Minor, S., 2001. Aeromagnetic expression of faults that offset basin fill, Albuquerque basin, New Mexico, *Geophysics*, **66**, 707–720.
- Grauch, V. J. S., Bauer, P. W., & Kelson, K., 2004. Preliminary interpretation of high-resolution aeromagnetic data collected near Taos, New Mexico, in *New Mexico Geological Society Guidebook*, vol. 55th Field Conference of **Geology of the Taos Region**, pp. 244–256.
- Gubbins, D., 2010. Terrestrial Magnetism: Historical Perspectives and Future Prospects, *Space Science Reviews*, **155**, 9–27, 10.1007/s11214-010-9675-6.
- Guiraud, M., 1990. Tectono-sedimentary framework of the early Cretaceous Continental Bima Formation (Upper Benue Trough, NE Nigeria), *Journal of African Earth Sciences*, **10**(1/2), 341–353.
- Guiraud, M., Ajakaiye, D. E., & Ugodulunwa, F. X. O., 1989. Characterisation of Late Cretaceous NE-SW sinistral wrench faults in the Upper Benue Trough (Nigeria) using Microtectonic and Aeromagnetic Data, *Journal of African Earth Sciences*, **9**(1), 9–21.
- Guiraud, R., Binks, R. M., Fairhead, J. D., & Wilson, M., 1992. Chronology and geodynamic setting of Cretaceous-Cenozoic rifting in West and Central Africa, *Tectonophysics*, **213**, 227–234.
- Gunn, P. J., Maidment, D., & Milligan, P. R., 1997. Interpreting aeromagnetic data in areas of limited outcrop, *AGSO Journal of Australian Geology and Geophysics*, **17**(2), 175–185.
- Gunnlaugsson, H., Helgason, O., Kristjansson, L., Nørnberg, P., Rasmussen, H., Steinþorsson, S., & Weyer, G., 2006. Magnetic properties of olivine basalt: Application to Mars, *Physics of the Earth and Planetary Interiors*, **154**, 276–289.
- Gurbuz, A., 2010. Geometric characteristics of pull-apart basin, *Lithosphere*, **2**(3), 199–206.
- Hall, D. H., 1959. Direction of polarization determined from magnetic anomalies, *Journal of Geophysical Research*, **64**(11), 1945–1959.

- Haney, M., Johnston, C., Y., L., & Nabighian, M., 2003. Envelopes of 2D and 3D magnetic data and their relationship to the analytical signal: Preliminary results, *SEG Expanded Abstracts*, **22**, 592–595, 73rd Annual International Meeting, Society of Exploration Geophysics.
- Hansen, R. O. & Pawlowski, R. S., 1989. Reduction to the pole at low latitudes by Wiener filtering, *Geophysics*, **54**(12), 1607–1613.
- Hill, D. P., 2008. Dynamic stresses, coulomb failure, and remote triggering, *Bulletin of the Seismological Society of America*, **98**, 66–92.
- Hogg, R. V. & Craig, A. T., 1995. *Introduction to Mathematical Statistics*, Macmillan, New York, 5th edn.
- Hood, P. J. & Teskey, D. J., 1989. Aeromagnetic gradiometer program of the Geological Survey of Canada, *Geophysics*, **54**(8), 1012–1022.
- Hudson, M. R., Grauch, V. J. S., & Minor, S. A., 2008. Rock magnetic characterization of faulted sediments with associated magnetic anomalies in the Albuquerque Basin, Rio Grande rift, NewMexico, *Geological Society of America Bulletin*, **120**(5-6), 641–658.
- Hulot, G., Olsen, N., Thibault, E., & Hemant, K., 2009. Crustal concealing of small-scale core-field secular variation, *Geophysical Journal International*, **177**, 361–366.
- Hulot, G., Balogh, A., Christensen, U. R., Constable, C. G., Manda, M., & Olsen, N., 2010. The Earth's Magnetic Field in the Space Age: An Introduction to Terrestrial Magnetism, in *Terrestrial Magnetism*, edited by G. Hulot, A. Balogh, U. R. Christensen, C. Constable, M. Manda, & N. Olsen, vol. 155 of **Space Sciences Series of ISSI**, pp. 1–7, Springer, The Netherlands, 1st edn.
- IAGA Working Group V-8, 1996. International Geomagnetic Reference Field, 1995 revision, *Physics of the Earth and Planetary Interiors*, **97**, 23–26, IAGA (International Association of Geomagnetism and Aeronomy) Division V, Working Group 81.
- IEA, 2011. World Energy Outlook 2011, <http://www.worldenergyoutlook.org/>, Retrieved October 24, 2011.
- Iloje, N. P., 1981. *A New Geography of Nigeria*, Longman Nigeria, Ikeja, Nigeria, Nigerian edn., ISBN: 058260396X.
- Ingersoll, R. V., 1988. Tectonics of sedimentary basins, *Geological Society of America Bulletin*, **100**(11), 1704–1719.
- Jia, Z. & Meng, L., 2009. Magnetic gradients produced by a 2D homogeneous polygonal source, *Geophysics*, **74**(1), L1–L6.
- Kampunzu, A. B., Caron, J. H., & Lubala, R. T., 1993. The East African rift, magma genesis and astheno-lithospheric dynamism, *Episodes*, **9**, 211–216.
- Karner, G. D., Studinger, M., & Bell, R. E., 2005. Gravity anomalies of sedimentary basins and their mechanical implications: Application to the Ross Sea basins, West Antarctica, *Earth and Planetary Science Letters*, **235**, 577–596.
- Kaufman, A. A., Hansen, R. O., & Kleinberg, R. L. K., 2009. *Principles of the magnetic methods in geophysics*, Elsevier, Oxford, UK.
- Keating, P. & Zerbo, L., 1996. An improved technique for reduction to the pole at low latitudes, *Geophysics*, **61**(1), 131–137.

- Keranen, K. & Klemperer, S. L., 2008. Discontinuous and diachronous evolution of the Main Ethiopian Rift: Implications for development of continental rifts, *Earth and Planetary Science Letters*, **265**, 96–111.
- Key, R. M., 1992. An introduction to the crystalline basement of Africa, in *Hydrogeology of Crystalline Basement Aquifers in Africa*, edited by E. P. Wright & W. G. Burgess, no. 66 in Geological Society Special Publication, pp. 29–57, The Geological Society of London.
- King, G. C. P., Stein, R. S., & Lin, J., 1994. Static stress changes and the triggering of earthquakes, *Bulletin of the Seismological Society of America*, **84**(3), 935–953.
- Kogbe, C. A., 1983. Geological interpretation of Landsat imageries across Central Nigeria, *Journal of African Earth Sciences*, **1**(3/4), 213–220.
- Kogbe, C. A., 1989. Paleogeographic history of Nigeria from Albian times., in *Geology of Nigeria*, edited by C. A. Kogbe, chap. 14, pp. 257–275, Rock View (Nigeria) Limited, 2nd edn.
- Koopmans, B. N., 1986. A comparative study of lineament analysis from different remote sensing imagery over areas in the Benue Valley and Jos Plateau Nigeria, *International Journal of Remote Sensing*, **7**(12), 1763–1771.
- Krahenbuhl, R. A. & Li, Y., 2007. Influence of self-demagnetization effect on data interpretation in strongly magnetic environments, *SEG Expanded Abstracts*, **26**, 713–717, SEG/San Antonio Annual Meeting.
- Kusznir, N. J. & Ziegler, P. A., 1992. The mechanics of continental extension and sedimentary basin formation: A simple-shear/pure-shear flexural cantilever model, *Tectonophysics*, **215**, 117–131.
- Kusznir, N. J., Roberts, A. M., & Morley, C. K., 1995. Forward and reverse modelling of rift basin formation, *Geological Society, London, Special Publications*, **80**(1), 33–56.
- Lahti, I. & Karinen, T., 2010. Tilt derivative multiscale edges of magnetic data, *The Leading Edge*, **29**, 24–29.
- Langer, C. J., Bonilla, M. G., & Bollinger, G. A., 1987. Aftershocks and surface faulting associated with the intraplate Guinea, West Africa, earthquake of 22 December, 1983, *Bulletin of the Seismological Society of America*, **77**(5), 1579–1601.
- Lanza, R. & Meloni, A., 2006. *The Earth's Magnetism: An introduction for Geologists*, Springer-Verlag Berlin Heidelberg.
- Lawal, K. M., Umego, M. N., & Ojo, S. B., 2005. New insight into the geology of the chad basin, *Nigerian Journal of Physics*, **Vol. 17S**, 165–170.
- Leeder, M. R. & Gawthorpe, R. L., 1987. Sedimentary models for extensional tilt-block/half-graben basins, in *Geological Society of London, Special Publications*, pp. 139–152, Geological Society London, UK.
- Lelievre, P. G. & Oldenburg, D. W., 2009. A 3D total magnetization inversion applicable when significant, complicated remanence is present, *Geophysics*, **74**(3), L21–L30.
- Lelievre, P. G., Oldenburg, D. W., & Phillips, N., 2006. 3d magnetic inversion for total magnetization in areas with complicated remanence, *SEG Expanded Abstracts*, pp. 953–957, SEG Annual Meeting in New Orleans.
- Leu, L.-K., 1981. Use of reduction-to-the-equator process for magnetic data interpretation, *SEG*

- Expanded Abstracts*, Proceedings of the 51st Annual International Meeting of the SEG, Los Angeles, California.
- Li, X., 2003. On the use of different methods for estimating magnetic depth, *The Leading Edge*, **November**, 1090–1099.
- Li, X., 2008. Magnetic reduction-to-pole at low latitudes: Observations and considerations, *The Leading Edge*, **August**, 260–270.
- Li, Y. & Oldenburg, D. W., 2001. Stable reduction to the pole at the magnetic equator, *Geophysics*, **66**(2), 571–578.
- Li, Y., Shearer, S., Haney, M., & Dannemiller, N., 2004. Comprehensive approaches to the inversion of magnetic data with strong remanent magnetization, *SEG Expanded Abstracts*, pp. 1191–1194, 74th Annual International Meeting.
- Li, Y., Yang, Y., & Liu, T., 2010. Derivative-based techniques for geological contact mapping from gravity data, *Earth Sciences*, **21**(3), 358–364.
- Lin-ping, H. & Zhi-ning, G., 1998. Discussion on 3-D analytic signal by Walter R. Roest, Jacob Verhoef, and Mark Pilkington, *Geophysics*, **63**, 667–670.
- Lowell, J. D., 1995. Mechanics of basin inversion from worldwide examples, in *Basin Inversion*, edited by J. G. Buchanan & P. G. Buchanan, vol. 88, pp. 39–57, Geological Society Special Publication.
- Lowes, F. J., 1974. Spatial power spectrum of the main geomagnetic field and extrapolation to the core, *Geophysical Journal of the Royal Astronomical Society*, **36**, 717–730.
- Luo, Y. & Xue, D.-J., 2009. Stable reduction to the pole at low magnetic latitude by probability tomography, <http://www.agu.org/wps/ChineseJGeo/52/04/ly.pdf>.
- Luo, Y., Xue, D.-J., & M., W., 2010. Reduction to the pole at the geomagnetic equator, <http://www.agu.org/wps/ChineseJGeo/53/06/ly.pdf>.
- Lyatsky, H., 2004. The meaning of anomaly, *CSEG Recorder*, **29**(6), 50–51.
- MacLeod, I. N., Jones, K., & Dai, T. F., 1993. 3-D analytic signal in the interpretation of total magnetic field data at low magnetic latitudes, *Exploration Geophysics*, **24**, 679–688.
- Macmillan, S., 2007. IGRF, International Geomagnetic Reference Field, in *Encyclopedia of geomagnetism and paleomagnetism*, edited by D. Gubbins & E. Herrero-Bervera, Encyclopedia of earth sciences series, chap. Part 9, pp. 411–412, Springer, Dordrecht, The Netherlands.
- Mandl, G., 2000. *Faulting in Brittle Rocks. An Introduction to the Mechanics of Tectonic Faults.*, Springer-Verlag, Berlin, Heidelberg.
- Martin, A. K., 1984. Propagating rifts: Crustal extension during continental rifting, *Tectonics*, **3**(6), 611–617.
- Matheis, G., 1989. Short review of the geology of the Chad basin in Nigeria, in *Geology of Nigeria*, edited by C. A. Kogbe, chap. 19, pp. 341–346, Rock View (Nigeria) Limited, 2nd edn.
- Maurin, J., Benkhelil, J., & Robineau, B., 1986. Fault rocks of the kaltungo lineament (Nigeria) and their relationships with the benue trough, *Journal of the Geological Society of London*, **143**, 587–599.
- Maus, S., 2010. An ellipsoidal harmonic representation of earth's lithospheric magnetic field to

- degree and order 720, *Geochem. Geophys. Geosyst.*, **Q06015**(11).
- Maus, S. & Haak, V., 2002. Is the long wavelength crustal magnetic field dominated by induced or by remanent magnetisation?, *Journ. Ind. Geophysical Union*, **6**(1), 1–5.
- Maus, S., Sazonova, T., Hemant, K., Fairhead, J. D., & Ravat, D., 2007. National geophysical data center candidate for the world digital magnetic anomaly map, *Geochemistry Geophysics Geosystems*, **8**(6), Q06017.
- Maus, S., Yin, F., Luhr, H., Manoj, C., Rother, M., Rauberg, J., Michaelis, I., Stolle, C., & Muller, R. D., 2008. Resolution of direction of oceanic magnetic lineations by the sixth-generation lithospheric magnetic field model from CHAMP satellite magnetic measurements, *Geochemistry Geophysics Geosystems*, **9**, Q07021(1–10).
- Maus, S., Barckhausen, U., Berkenbosch, H., Bournas, N., Brozena, J., Childers, V., Dostaler, F., Fairhead, J. D., Finn, C., von Frese, R. R. B., Gaina, C., Golynsky, S., Kucks, R., Luhr, H., Milligan, P., Mogren, S., Muller, R. D., Olesen, O., Pilkington, M., Saltus, R., Schreckenberger, B., Thébault, E., & Tontini, F. C., 2009. EMAG2: A 2-arc min resolution Earth Magnetic Anomaly Grid compiled from satellite, airborne, and marine magnetic measurements, *Geochemistry Geophysics Geosystems*, **10**, Q08005 (1–12).
- Maus, S., Alken, P., & Nair, M., 2010. Geomagnetic and electric field models, <http://www.geomag.us/models/>, Last modified: Sunday, 26-Sep-2010 15:26:02 MDT.
- Maus, S., Macmillan, S., McLean, S., Hamilton, B., Thomson, A., Nair, M., & Rollins, C., 2010. The US/UK World Magnetic Model for 2010-2015, Tech. Rep. NESDIS/NGDC., NOAA.
- McCurry, P., 1989. A general review of the geology of the Precambrian to Lower Palaeozoic rocks of Northern Nigeria, in *Geology of Nigeria*, edited by C. A. Kogbe, chap. 1, pp. 13–37, Rock View (Nigeria) Limited, 2nd edn.
- McEnroe, S. A., Fabian, K., Robinson, P., Gaina, C., & Brown, L. L., 2009. Crustal magnetism, lamellar magnetism and rocks that remember, *Elements*, **5**, 241–246.
- McKenzie, D., 1978. Some remarks on the development of sedimentary basins, *Earth and Planetary Science Letters*, **40**, 25–32.
- McLean, S., Macmillan, S., Maus, S., Lesur, V., Thomson, A., & Dater, D., 2004. The US/UK World Magnetic Model for 2005-2010, Tech. Rep. NESDIS/NGDC-1., National Oceanic and Atmospheric Administration (NOAA), USA.
- McMullan, S. R. & McLellan, W. H., 1997. Measured is better, in *Proceedings of Exploration '97: Fourth Decennial International Conference on Mineral Exploration*, edited by A. G. Gubbins, pp. 805–816, GEO/FX, Paper 103.
- Merrill, R. T., McElhinny, M. W., & McFadden, P. L., 1996. *The magnetic field of the Earth, paleomagnetism, the core, and the deep mantle.*, Academic Press, London.
- Miller, H. G. & Singh, V., 1994. Potential field tilt a new concept for location of potential field sources, *Journal of Applied Geophysics*, **32**, 213–217.
- Minty, B. R. S., 1991. Simple micro-levelling for aeromagnetic data, *Exploration Geophysics*, **22**, 591–592.
- Moskowitz, B. M., 1991. *Hitchhiker's Guide to Magnetism*, Institute for Rock Magnetism, Environmental Magnetism Workshop held 5-8 June 1991 at the Institute for Rock Magnetism.

- Murat, R. C., 1972. Stratigraphy and paleogeography of the Cretaceous and lower Tertiary in southern Nigeria, in *African geology*, edited by T. F. J. Dessauvage & A. J. Whiteman, pp. 251–266, Ibadan University Press, Ibadan, Nigeria.
- Nabighian, M. N., 1972. The analytic signal of two-dimensional magnetic bodies with polygonal cross-section: Its properties and use for automated anomaly interpretation, *Geophysics*, **37**(3), 507–517.
- Nabighian, M. N., Grauch, V. J. S., Hansen, R. O., LaFehr, T. R., Y. Li, J. W. P., Phillips, J. D., & Ruder, M. E., 2005. The historical development of the magnetic method in exploration, *Geophysics*, **70**(6), 33ND–61ND.
- Nettleton, L. L., 1971. *Elementary gravity and magnetics for geologists and seismologists*, Monograph Series No. 1, Society of Exploration Geophysics, Tulsa USA.
- NGDC, 2010. Estimated values of magnetic field properties, <http://ngdc.noaa.gov/geomag/magfield.shtml>, 16th May, 2010.
- NGSA, 2006. Geological map of Nigeria, Tech. rep., Nigerian Geological Survey Agency (NGSA).
- Obaje, N. G., Wehner, H., Abubakar, M. B., & Isah, M. T., 2004. Nasara-1 well, Gongola Basin (Upper Benue Trough, Nigeria): Source-rock evaluation, *Journal of Petroleum Geology*, **27**(2), 191–206.
- O’Connell, M. D. & Owers, M., 2008. A line spacing compression method and an improved minimum curvature operator for grid interpolation of airborne magnetic surveys, *Exploration Geophysics*, **34**(3), 148–154.
- Odeyemi, I., 1981. A review of the orogenic events in the Precambrian basement of Nigeria, West Africa, *Geologische Rundschau*, **70**, 897–909, 10.1007/BF01820170.
- Ofoegbu, C. O., 1985. Interpretation of an aeromagnetic profile across the Benue Trough of Nigeria, *Journal of African Earth Sciences*, **3**(3), 293–296.
- Ofoegbu, C. O., 1986. Preliminary results from a pseudogravity study of the Benue Trough, Nigeria, *Journal of African Earth Sciences*, **5**(2), 187–192.
- Ofoegbu, C. O., 1988. An aeromagnetic study of part of the Upper Benue Trough, Nigeria, *Journal of African Earth Sciences*, **7**(1), 77–90.
- Okereke, C. S., 1988. Contrasting modes of rifting: The Benue Trough and Cameroon Volcanic Line, West Africa, *Tectonics*, **7**(4), 775–784.
- Okosun, E. A., 1992. Cretaceous ostracod biostratigraphy from Chad Basin in Nigeria, *Journal of African Earth Sciences*, **14**(3), 327–339.
- Olade, M. A., 1978. Early Cretaceous basalt volcanism and initial continental rifting in Benue Trough, Nigeria, *Nature*, **273**, 458–459.
- Olsen, N., Hulot, G., & Sabaka, T. J., 2010. Measuring the Earth’s Magnetic Field from Space: Concepts of Past, Present and Future Missions, in *Terrestrial Magnetism*, edited by G. Hulot, A. Balogh, U. R. Christensen, C. Constable, M. Manda, & N. Olsen, vol. 155 of **Space Sciences Series of ISSI**, pp. 65–93, Springer, The Netherlands, 1st edn.
- Olugbemiro, R. O., Ligouis, B., & Abaa, S. I., 1997. The Cretaceous series in the Chad Basin, NE Nigeria: Source rock potential and Thermal maturity, *Journal of Petroleum Geology*, **20**(1),

51–68.

- Parasnis, D. S., 1997. *Principles of applied geophysics*, Chapman and Hall, London, UK.
- Paterson, N. R. & Reeves, C. V., 1985. Applications of gravity and magnetic surveys: The state-of-the-art in 1985, *Geophysics*, **50**(12), 2558–2594.
- Pedersen, L. B., Rasmussen, T. M., & Dyrelius, D., 1990. Construction of component maps from aeromagnetic total field anomaly maps, *Geophysical Prospecting*, **38**, 795–804.
- Peters, L. J., 1949. The direct approach to magnetic interpretation and its practical application, *Geophysics*, **14**, 290–320.
- Petters, S. W. & Ekweozor, C. M., 1982. Petroleum geology of Benue Trough and Southeastern Chad Basin, Nigeria, *AAPG Bulletin*, **66**(8), 1141–1149.
- Phillips, J. D., 1997. Potential-Field Geophysical Software for the PC, Version 2.2, <http://pubs.usgs.gov/of/1997/0725/report.pdf>.
- Phillips, J. D., 2000. Locating magnetic contacts: A comparison of the horizontal gradient, analytic signal, and local wavenumber methods, in *70th Annual International Meeting, Society of Exploration Geophysics Expanded Abstracts*, vol. 19, pp. 402–405.
- Phillips, J. D., Hansen, R. O., & Blakely, R. J., 2007. The use of curvature in potential-field interpretation, *Exploration Geophysics*, **38**, 111–119.
- Pilkington, M., 2007. Locating geologic contacts with magnitude transforms of magnetic data, *Applied Geophysics*, **63**, 80–89.
- Pilkington, M. & Keating, P., 2004. Contact mapping from gridded magnetic data - a comparison of techniques, *Exploration Geophysics*, **35**, 306–311.
- Pilkington, M., Snyder, D. B., & Hemant, K., 2006. Weakly magnetic crust in the Canadian Cordillera, *Earth and Planetary Science Letters*, **248**, 476–485.
- Pozza, M. R., Boyce, J. I., & Morris, W. A., 2004. Lake-based magnetic mapping of contaminated sediment distribution, Hamilton Harbour, Lake Ontario, Canada, *Journal of Applied Geophysics*, **57**, 23–41.
- Press, W. H., Teukolsky, S. A., Vetterling, W. T., & Flannery, B. P., 1992. *Numerical Recipes in C: The Art of Scientific Computing*, Cambridge University Press, 2nd edn., ISBN 0521431085.
- Purcaru, G., 2008. The Great Sichuan Earthquake of May 12, 2008 (Mw7.9) - An Unpredictable Earthquake, [http://www.agu.org/meetings/fm08/fm08-sessions/fm08\\_S31B.html](http://www.agu.org/meetings/fm08/fm08-sessions/fm08_S31B.html), Eos Trans. AGU, 89 (53), Fall Meet. Supplement, Abstract S31B-1919.
- Purucker, M. E. & Clark, D. A., 2011. Mapping and Interpretation of the Lithospheric Magnetic Field, in *Geomagnetic Observations and Models*, edited by H. B. M. M. & K. M., vol. 5 of **IAGA Special Sopron Book Series**, chap. 13, pp. 311–337, Springer, Netherlands, ISBN: 978-90-481-9858-0.
- R. Hartley, A. B. Watts, J. D. F., 1996. Isostasy of Africa, *Earth and Planetary Science Letters*, **137**, 1–18.
- Rahaman, M. A., 1989. Review of the basement geology of South-Western Nigeria, in *Geology of Nigeria*, edited by C. A. Kogbe, chap. 14, pp. 39–56, Rock View (Nigeria) Limited, 2nd edn.
- Ramsey, J. M. & Chester, F. M., 2004. Hybrid fracture and the transition from extension fracture to shear fracture, *Nature*, **428**, 63–66.

- Ravat, D., Hildenbrand, T. G., & Roest, . W., 2003. New way of processing near-surface magnetic data: The utility of the Comprehensive Model of the Magnetic Field, *The Leading Edge*, **August**, 784–785.
- Reeves, C., 2005. *Aeromagnetic Surveys: Principles, Practice & Interpretation*, Geosoft Inc., Canada.
- Reeves, C. V. & Wu, C., 1989. Adequate sampling in magnetic profiling, the resolution of closely-spaced magnetic sources and their importance to image-enhancement techniques for magnetic anomaly maps, Tech. rep., European Association of Exploration Geophysicists, Presentation at the 51st Meeting and Technical Exhibition (29 May-2 June, 1989), West Berlin.
- Reford, M. S., 1964. Magnetic anomalies over thin sheets, *Geophysics*, **29**(4), 532–536.
- Reford, M. S. & Sumner, J. S., 1964. Aeromagnetism, *Geophysics*, **29**(4), 482–5116.
- Reford, S., 2010. Processing and interpretation of airborne geophysical data: Phase II, [http://www.mmsd.gov.ng/Downloads/Reford\\_Process\\_Interp.pdf](http://www.mmsd.gov.ng/Downloads/Reford_Process_Interp.pdf).
- Reid, A. B., 1980. Aeromagnetic survey design, *Geophysics*, **45**, 973–976.
- Reid, A. B., FitzGerald, D., & Flanagan, G., 2005. Hybrid Euler magnetic basement depth estimation: Bishop 3D tests., *SEG Expanded Abstracts*, SEG International Exposition and 75th Annual Meeting, Houston, USA.
- Reynisson, R. F., Fanavoll, S., Waag, G., & Ebbing, J., 2008. Feasibility study of electromagnetic, gravimetric and aeromagnetic methods in sub-basaltic settings., *EAGE Expanded Abstracts*, 70th EAGE meeting, Rome, Italy.
- Reynisson, R. F., Ebbing, J., & Skilbrei, J. R., 2009. The use of potential field data in revealing the basement structure in sub-basaltic settings: An example from the More margin, offshore Norway, *Geophysical Prospecting*, **57**, 753–771.
- Reynolds, J. M., 1997. *An introduction to applied and environmental geophysics*, John-Wiley & Sons, UK.
- Roberts, P. H. & Glatzmaier, G. A., 2000. Geodynamo theory and simulations, *Reviews of Modern Physics*, **72**(4), 1081–1123.
- Rosendahl, B. R., 1987. Architecture of continental rifts with special reference to East Africa, *Annual Review of Earth and Planetary Science*, **15**, 445–503.
- Sabaka, T. J., Olsen, N., & Purucker, M. E., 2004. Extending comprehensive models of the Earth's magnetic field with Orsted and CHAMP data, *Geophysical Journal International*, **159**, 521–547.
- Salem, A., Williams, S., Fairhead, J. D., Ravat, D., & Smith, R., 2007. Tilt-Depth method: A simple depth estimation method using first-order magnetic derivatives, *The Leading Edge*, **26**(12), 1502–1505.
- Salem, A., Williams, S., Fairhead, J. D., Smith, R., & Ravat, D., 2008. Interpretation of magnetic data using tilt-angle derivatives, *Geophysics*, **73**(1), L1–L10.
- Schlüter, T., 2006. *Geological atlas of Africa: With notes on stratigraphy, tectonics, economic geology, geohazards and geosites of each country*, Springer, 2nd edn., with contributions by Martin H. Trauth.
- Shemang, E. M., Ajayi, C. O., & Jacoby, W. R., 2001. A magmatic failed rift beneath the

- Gongola arm of the upper Benue trough, Nigeria?, *Journal of Geodynamics*, **32**, 355–371.
- Shen, Z.-K., Sun, J., Zhang, P., Wan, Y., Wang, M., Bürgmann, R., Zeng, Y., Gan, W., Liao, H., & Wang, Q., 2009. Slip maxima at fault junctions and rupturing of barriers during the 2008 Wenchuan earthquake, *Nature Geoscience*, **2**, 718–724.
- Sheriff, R. E., 2002. *Encyclopaedic dictionary of applied geophysics*, Geophysical Reference Series No. 13, Society of Exploration Geophysicists, Tulsa, USA, 4th edn.
- Silva, J. B. C., 1986. Reduction to the pole as an inverse problem and its application to low-latitude anomalies, *Geophysics*, **51**, 369–382.
- Smellie, D. W., 1956. Elementary approximations in aeromagnetic interpretation, *Geophysics*, **21**, 1021–1040.
- Smith, R. A., 1959. Some depth formulae for local magnetic and gravity anomalies, *Geophysical Prospecting*, **7**, 55–63.
- Smith, R. S. & O'Connell, M. D., 2005. Interpolation and gridding of aliased geophysical data using constrained anisotropic diffusion to enhance trends, *Geophysics*, **70**(5), V121–V127.
- Smith, R. S., Thurston, J. B., Dai, T. F., & MacLeod, I. N., 1998. iSPI<sup>TM</sup> - the improved source parameter imaging method, *Geophysical Prospecting*, **46**, 141–151.
- Smith, S. W., 2003. *The Scientist and Engineer's Guide to Digital Signal Processing*, Newnes, USA.
- Spector, A. & Grant, F., 1970. Statistical models for interpreting aeromagnetic data, *Geophysics*, **35**(2), 293–302.
- Stanley, J. M., 1977. Simplified magnetic interpretation of the geologic contact and thin dike., *Geophysics*, **42**(6), 1236–1240.
- Storti, F., Rossetti, F., & Salvini, F., 2001. Structural architecture and displacement accommodation mechanisms at the termination of the Priestley Fault, Northern Victoria Land, Antarctica, *Tectonophysics*, **341**, 5–12.
- Stuart, G. W., Fairhead, J. D., Dorbath, L., & Dorbath, K. C., 1985. A seismic refraction study of the crustal structure associated with the Adamawa Plateau and Garoua Rift, Cameroon, West Africa, *Geophysical Journal of the Royal Astronomical Society*, **81**(1), 1–12.
- Swain, C. J., 1976. A FORTRAN program for interpolating irregularly spaced data using the difference equations for minimum curvature, *Computers and Geosciences*, **1**, 231–240.
- Swain, C. J., 2000. Reduction-to-the-pole of regional magnetic data with variable field direction, and its stabilisation at low inclinations, *Exploration Geophysics*, **31**, 078–083.
- Telford, W. M., Geldart, L. P., & Sheriff, R. E., 1990. *Applied geophysics*, Cambridge University Press, Cambridge, UK, 2nd edn.
- Thébault, E., Purucker, M., Whaler, K. A., Langlais, B., & Sabaka, T. J., 2010. The Magnetic Field of the Earth's Lithosphere, in *Terrestrial Magnetism*, edited by G. Hulot, A. Balogh, U. R. Christensen, C. Constable, M. Manda, & N. Olsen, vol. 155 of **Space Sciences Series of ISSI**, pp. 95–127, Springer, The Netherlands, 1st edn.
- Thompson, D. T., 1982. EULDPH, A new technique for making computer-assisted depth estimates from magnetic data, *Geophysics*, **47**(1), 31–37.
- Thurston, J. B. & Smith, R. S., 1997. Automatic conversion of magnetic data to depth, dip, and

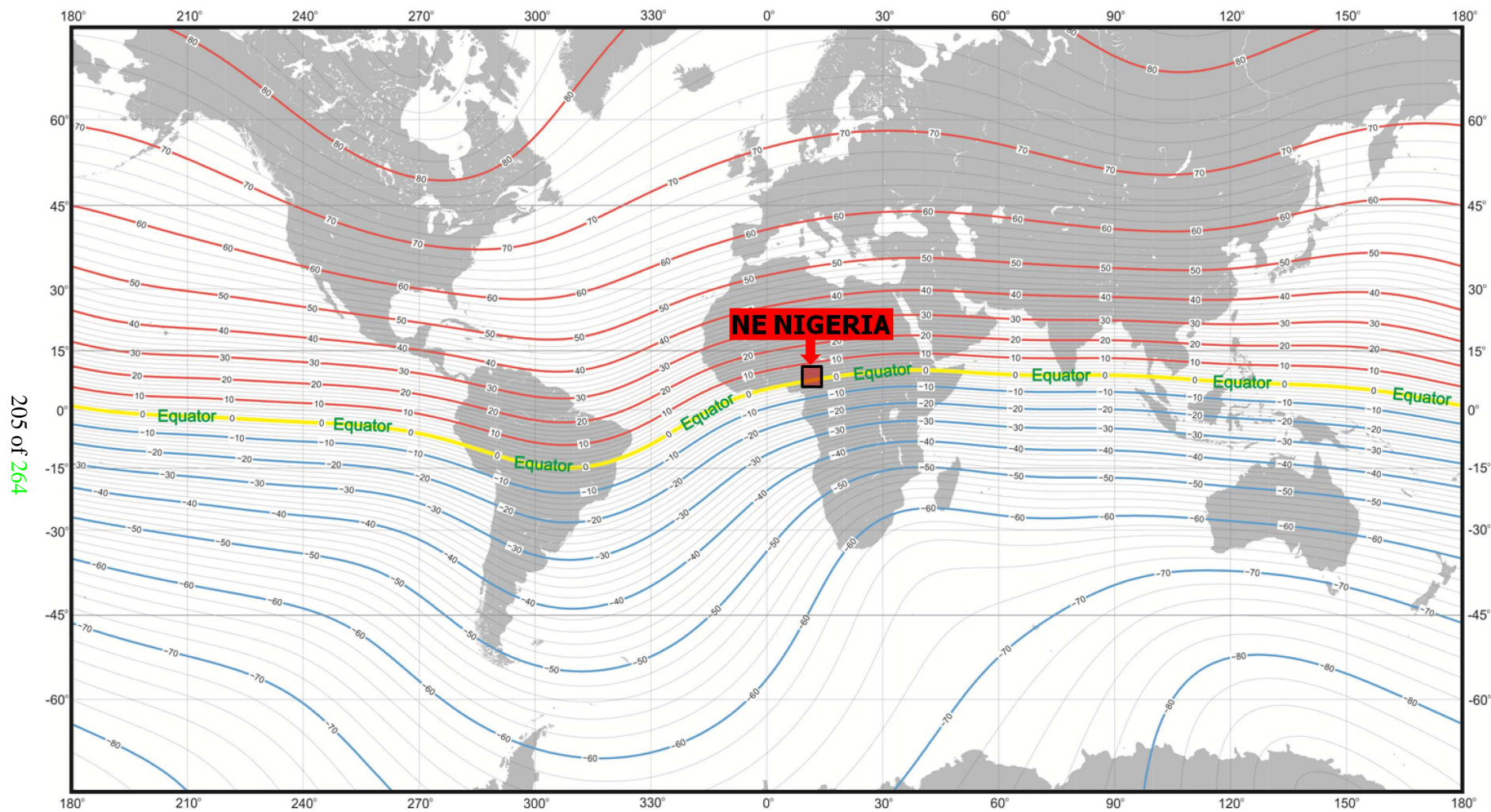
- susceptibility contrast using the SPI<sup>TM</sup> method, *Geophysics*, **60**(3), 807–813.
- Thurston, J. B., Smith, R. S., & Guillon, J. C., 2002. A multimodel method for depth estimation from magnetic data, *Geophysics*, **67**, 555–561.
- TPDC, 2010. Current oil and gas exploration activities, Tanzania, Tech. rep., Tanzania Petroleum Development Corporation (TPDC).
- Turner, J. P. & Williams, G. A., 2004. Sedimentary basin inversion and intra-plate shortening, *Earth-Science Reviews*, **65**, 277–304.
- Twiss, R. J. & Moores, E. M., 1992. *Structural Geology*, W. H. Freeman and Company, New York, 2nd edn.
- Udo, R. K., 1970. *Geographical Regions of Nigeria.*, Heinemann Educational Books, London, Nairobi.
- ULIS, 1988. The African Gravity Project (AGP), Tech. rep., University of Leeds Industrial Services (ULIS).
- ULIS, 1993. African Magnetic Mapping Project, Tech. rep., University of Leeds Industrial Services (ULIS).
- UNICEF, 2009. Sichuan earthquake: One Year Report, Tech. rep., United Nations International Children's Emergency Fund (UNICEF).
- USGS, 2012. Magnitude 7.9 - Eastern Sichuan, China, <http://earthquake.usgs.gov/earthquakes/eqinthenews/2008/us2008ryan/us2008ryan.php>, Page last modified: October 28, 2012 05:05:12 UTC; accessed Wednesday, 7/11/2012.
- USGS/VHP, 2011. Glossary of Volcano and Related Terminology: Basalts, [http://vulcan.wr.usgs.gov/Glossary/volcano\\_terminology.html](http://vulcan.wr.usgs.gov/Glossary/volcano_terminology.html), Last updated: 08/14/06, by Lyn Topinka; Accessed 19/02/2011.
- Vacquier, V., Steenland, N. C., Henderson, R. G., & Zietz, I., 1951. *Interpretation of aeromagnetic maps*, no. 47 in Memoir, Geological Society of America.
- Verduzco, B., Fairhead, J. D., Green, C. M., & MacKenzie, C., 2004. New insights into magnetic derivatives for structural mapping, *The Leading Edge*, **23**, 116–119.
- Vink, G., 1982. Continental rifting and the implications for plate tectonic reconstructions, *Journal of Geophysical Research*, **87**(B13), 10,677–10,688.
- Walter, T. R., Wang, R., Acocella, V., Neri, M., Grosser, H., & Zschau, J., 2009. Simultaneous magma and gas eruptions at three volcanoes in Southern Italy: An earthquake trigger?, *Geology*, **37**(3), 251–254.
- Webring, M., 1981. MINC: A gridding program based on minimum curvature, Open File Report 81-1224, U.S. Geological Survey.
- Wernicke, B. & Burchfiel, B. C., 1982. Modes of extensional tectonics, *Journal of Structural Geology*, **4**(2), 105–115.
- Whitehead, N., 2010. *Montaj Grav/Mag Interpretation: Processing, Analysis and Visualilization System for 3D Inversion of Potential Field Data for Oasis montaj v7.1 - Tutorial and User Guide*, Geosoft Incorporated, Release date: 2/8/2010.
- Wickerham, W. E., 1954. The gulf airborne magnetic gradiometer, *Geophysics*, **19**(1), 116–123.
- Williams, S., 2004. *Extended Euler deconvolution and interpretation of potential field data from*

- Bohai Bay, China*, Ph.D. thesis, Department of Earth Sciences, School of Earth and Environment, University of Leeds, Leeds, U.K.
- Williams, S., Fairhead, J. D., & Flanagan, G., 2002. Realistic models of basement topography for depth to magnetic basement testing, *SEG Expanded Abstracts*, **21**, 814–817.
- Williams, S. E., Fairhead, J. D., & Flanagan, G., 2005. Comparison of grid Euler deconvolution with and without 2D constraints using a realistic 3D magnetic basement model, *Geophysics*, **70**(3), L13–L21.
- Wilson, B. C., Helmstaedt, H., & Dixon, J. M., 1992. Deformation and Intrusion in Deeply Buried Rocks: Creep, High-Angle Ductile and Brittle Shear, and Congruent Shear Arrays., in *Basement tectonics 7: Proceedings of the Seventh International Conference on Basement Tectonics.*, edited by R. Mason, vol. 1, pp. 83–92, Kluwer Academic, Dordrecht; Boston, MA.
- Wilson, C. R., Tsoflias, G., Bartelmann, M., & Phillips, J., 1997. A high precision aeromagnetic survey near the glen hummel field in texas; identification of cultural and sedimentary anomaly sources, *The Leading Edge*, **16**(1), 37–42.
- Winch, D. E., Ivers, D. J., Turner, J. P. R., & Stening, R. J., 2005. Geomagnetism and Schmidt quasi-normalization, *Geophysical Journal International*, **160**, 487–504.
- Woakes, M., Rahaman, M. A., & Ajibade, A. C., 1987. Some metallogenic features of the Nigerian Basement, *Journal of African Earth Sciences*, **6**(5), 655–664.
- Wright, J. B., 1985. *Geology and mineral resources of West Africa*, George Allen and Unwin, London, With contributions from D. A. Hastings, W. B. Jones and H. R. Williams.
- Wright, J. B., 1989. Volcanic rocks in Nigeria, in *Geology of Nigeria*, edited by C. A. Kogbe, chap. 1, pp. 13–37, Rock View (Nigeria) Limited, 2nd edn.
- Wright, T. J., Ebinger, C., Biggs, J., Ayele, A., Yirgu, G., Keir, D., & Stork, A., 2006. Magma-maintained rift segmentation at continental rupture in the 2005 Afar dyking episode, *Nature*, **442**, 291–294, 20 July 2006.
- Zhang, J., 2001. An analysis of the accuracy of magnetic source-body geometry determined from the 3D analytic signal, *Geophysics*, **66**, 579–581.
- Ziegler, P. A. & Cloetingh, S., 2004. Dynamic processes controlling evolution of rifted basins, *Earth-Science Reviews*, **64**, 1–50.
- Zoback, M. D., 2007. *Reservoir Geomechanics*, Cambridge University Press.

## **Appendix A**

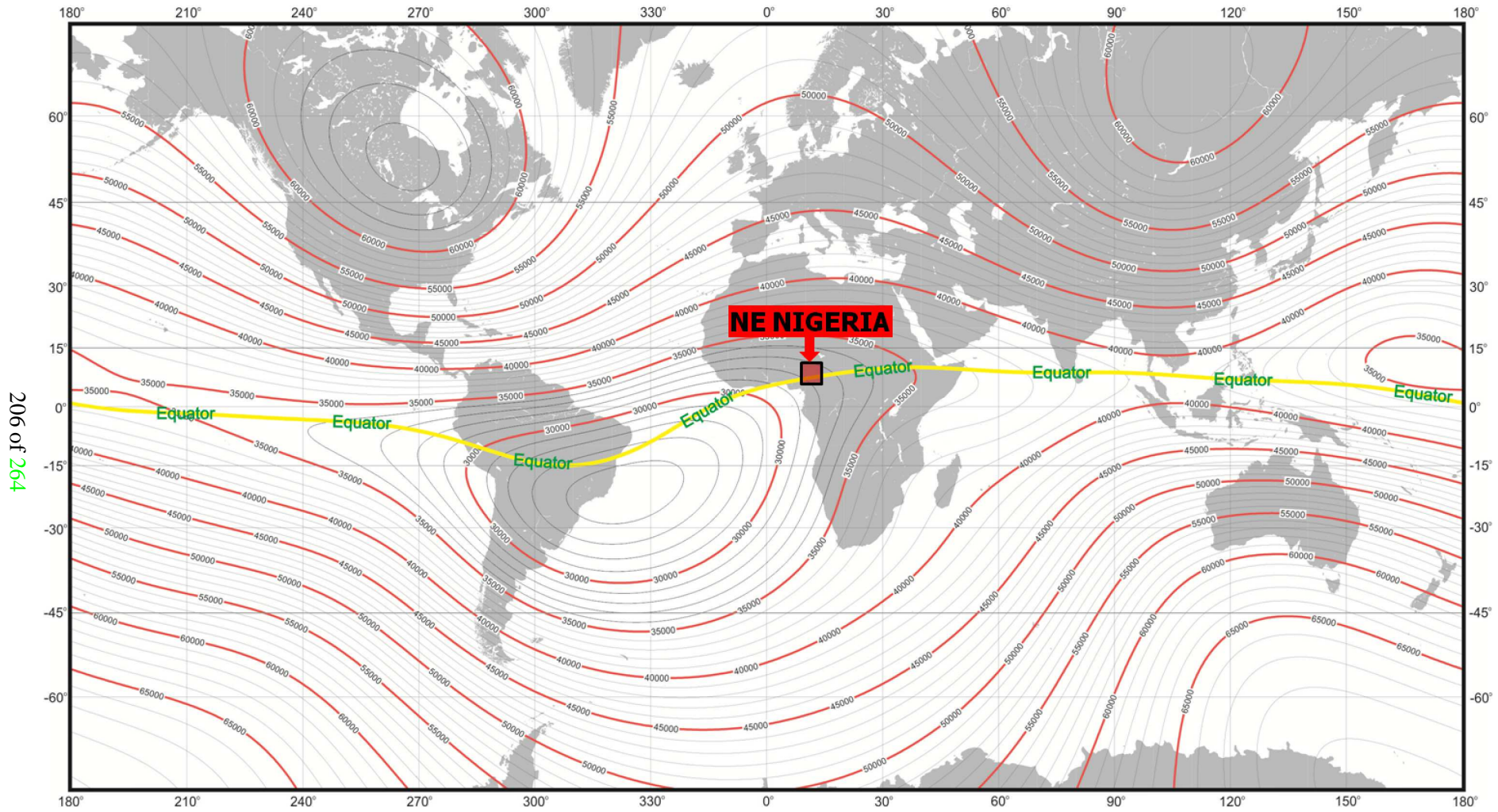
**Attitude and amplitudes of the main or dipolar geomagnetic field.**

---



205 of 264

**Figure A.1:** Global map of the inclination of the main geomagnetic field, i.e., 11<sup>th</sup> generation IGRF for 1900-2015 (Finlay et al., 2010), showing the location of NorthEastern Nigeria (Red-shaded black rectangle) relative to the geomagnetic equator (Yellow line). Observe that the geomagnetic equator runs through the study area.

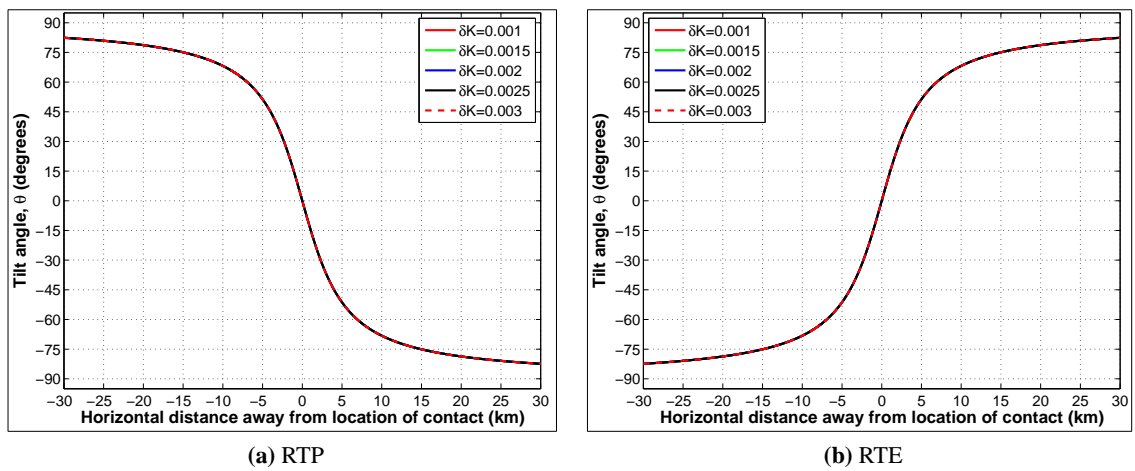


206 of 264

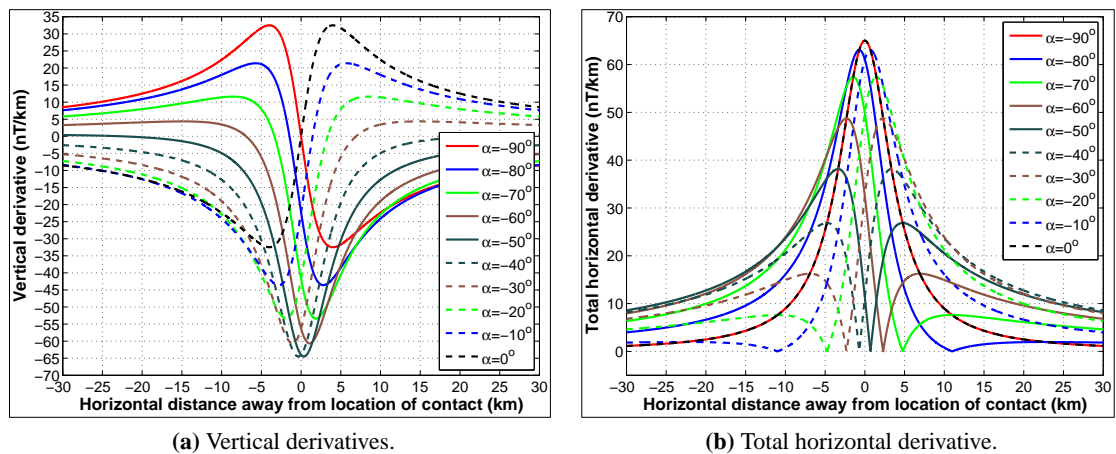
**Figure A.2:** Global map of the magnitude of the main geomagnetic field, i.e., 11<sup>th</sup> generation IGRF for 1900-2015 (Finlay et al., 2010). Map also shows the location of NorthEastern Nigeria (Red-shaded black rectangle) and the geomagnetic equator (Yellow line). Note the relatively smaller TMI amplitudes in NE Nigeria.

## Appendix B

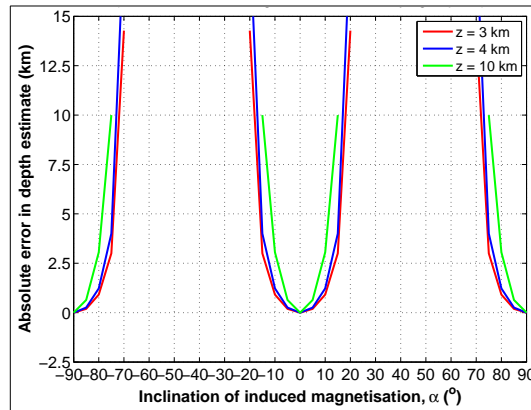
“Tilt-Depth” method estimates from two-dimensional (2D) magnetic contacts.



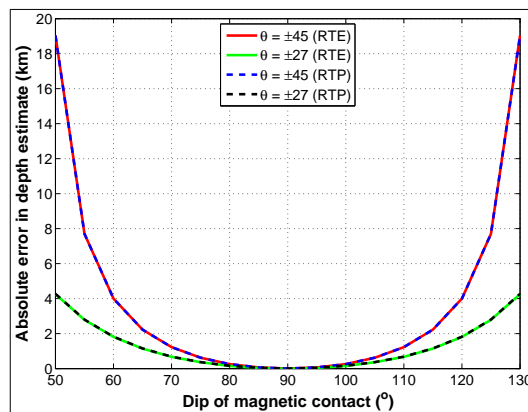
**Figure B.1:** Testing computer codes using the independence of  $\theta$  from vertical, E-W magnetic 2D contacts at RTP on susceptibility contrasts ( $\delta k$ ).



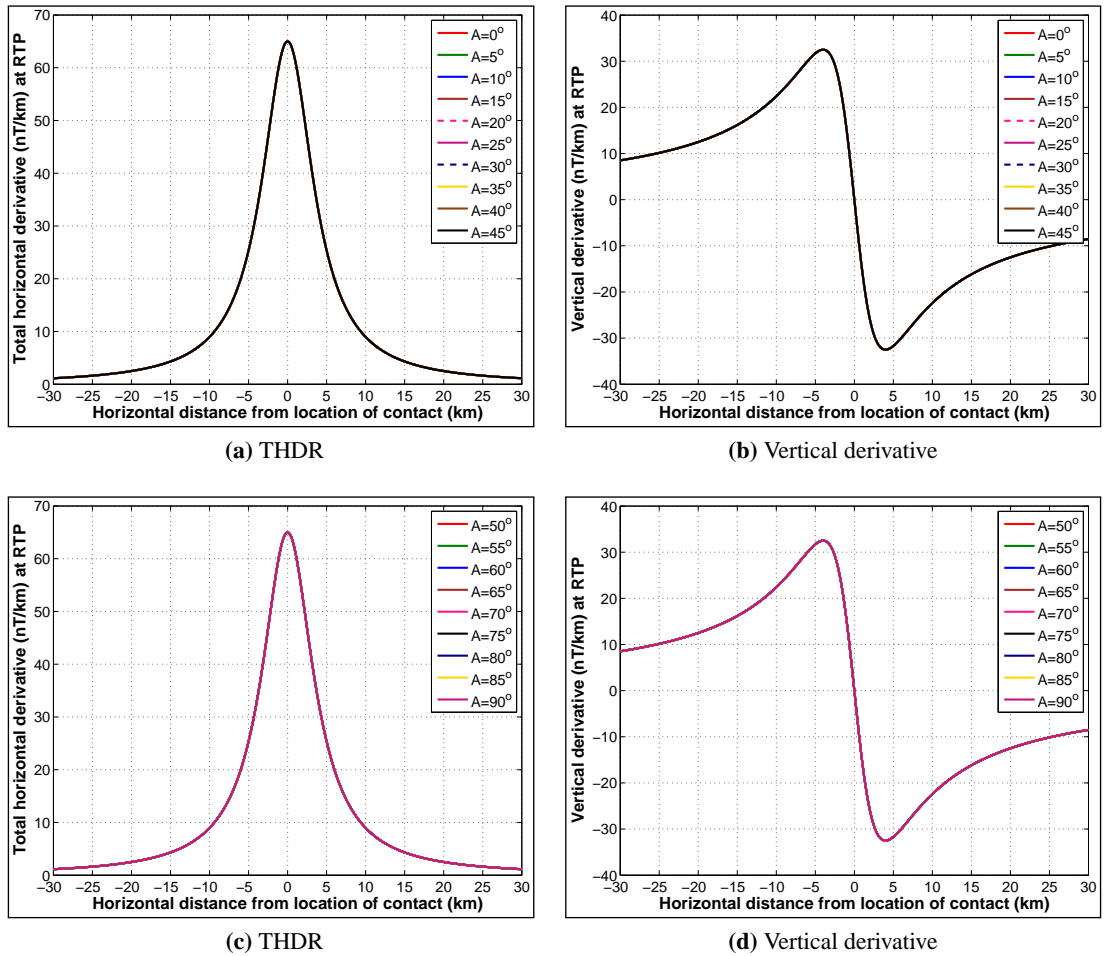
**Figure B.2:** Effects of inclination of induced magnetisation ( $\alpha$ ) on the shape and amplitude of derivatives of  $\Delta T$  from vertical, E-W, 2D contacts in the Southern geomagnetic hemisphere.  $\alpha$  ranged from  $0$  to  $-90^\circ$ : (a) Vertical derivatives; and (b) Total horizontal derivative.



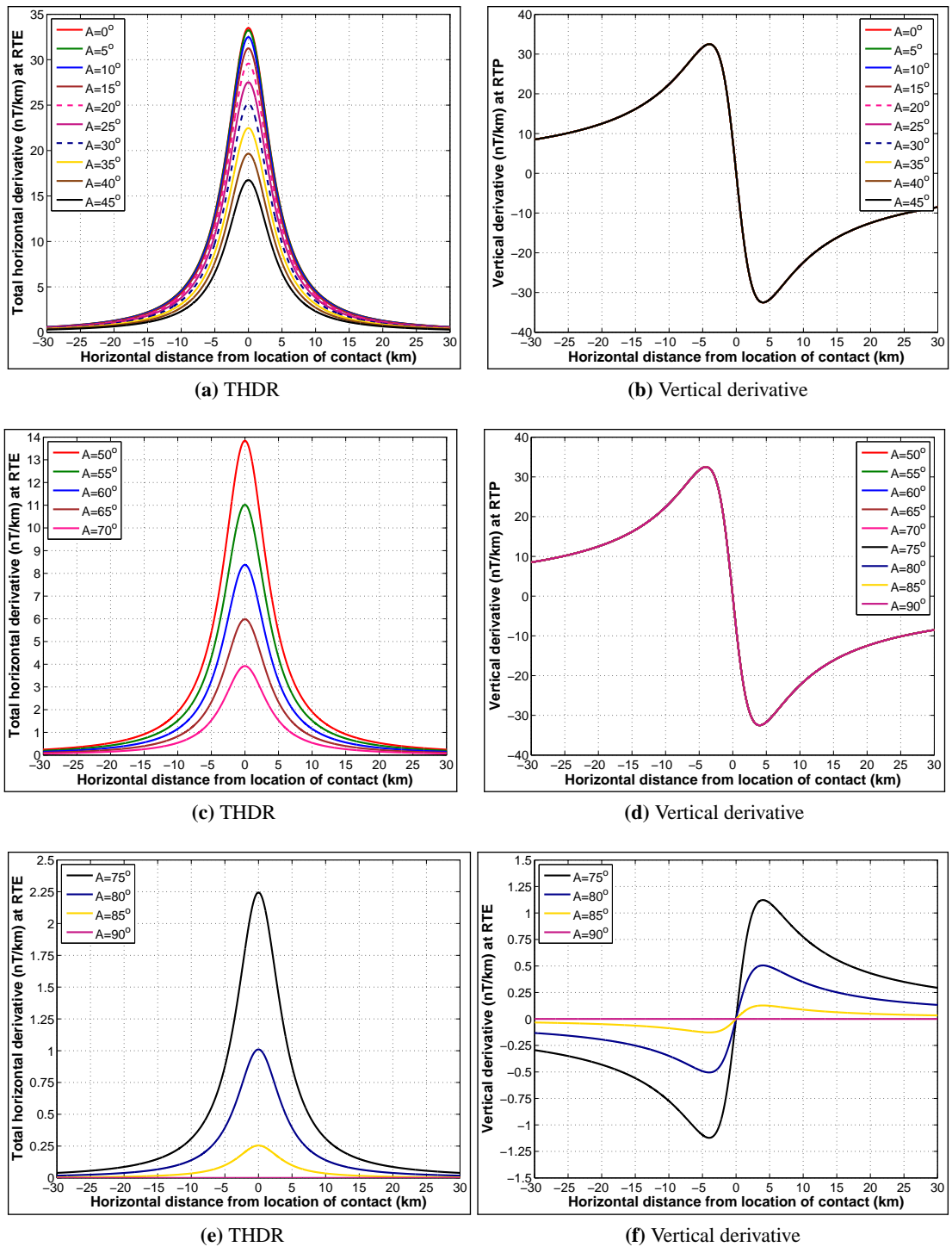
**Figure B.3:** Absolute error in depth estimates from "Tilt-Depth" method for vertical, East-West striking, 2D magnetic contacts: Effects of induced magnetisation and depth of the contact.



**Figure B.4:** Absolute error in depths of dipping East-West striking, 2D contacts at RTP or RTE, estimated using the  $\theta = \pm 27$  or  $45$  range. Depth estimates and percentage errors are presented in figure 3.15. Only error ranging from 0 to 100% are shown in figure 3.15b.



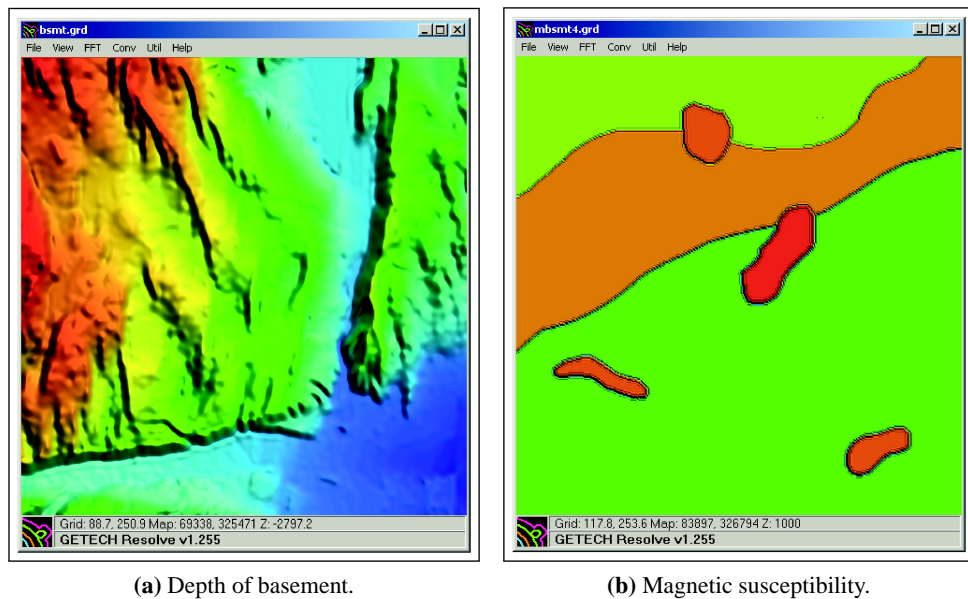
**Figure B.5:** Effects of the strike azimuth of vertical, 2D contacts on first-order Cartesian derivatives (total horizontal derivatives, THDR and vertical derivatives) of their  $\Delta T$  (RTP). THDR is  $\frac{\partial \Delta T}{\partial H}$ , while vertical derivative is  $\frac{\partial \Delta T}{\partial z}$ . Note that amplitudes and shapes of derivatives are the same, irrespective of the strike of 2D contact.



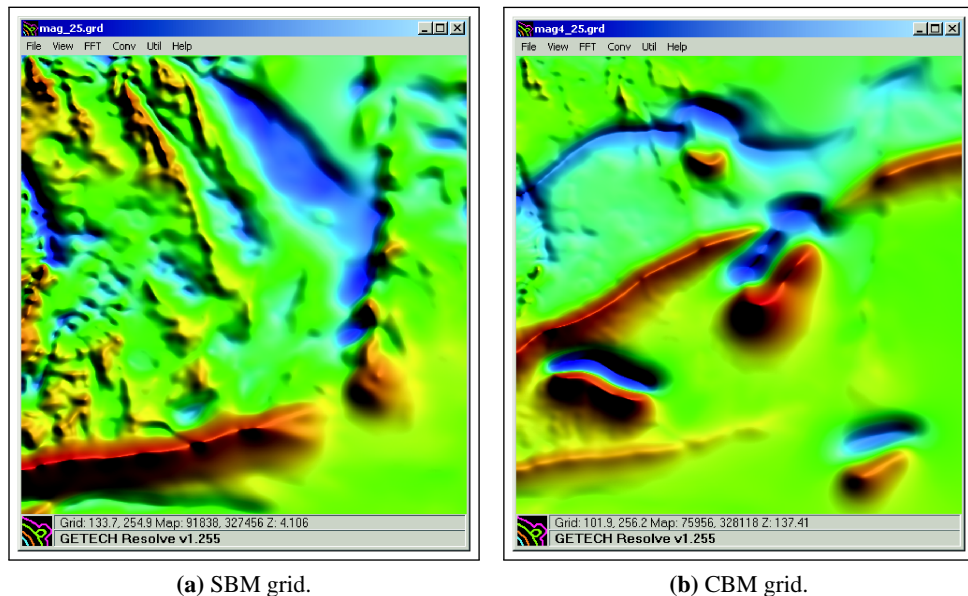
**Figure B.6:** Effects of the strike azimuth of vertical, 2D contacts on first-order Cartesian derivatives (total horizontal derivatives, THDR and vertical derivatives) of their  $\Delta T$  (RTE). THDR is  $\frac{\partial \Delta T}{\partial z}$ , while vertical derivative is  $\frac{\partial \Delta T}{\partial H}$ . Amplitudes and shapes of derivatives vary systematically from a maximum when contact strikes East-West ( $A = 0^\circ$ ) to 0 when the contact strikes North-South ( $A = 90^\circ$ ), unlike when contacts were at RTP (Figure B.5).

## Appendix C

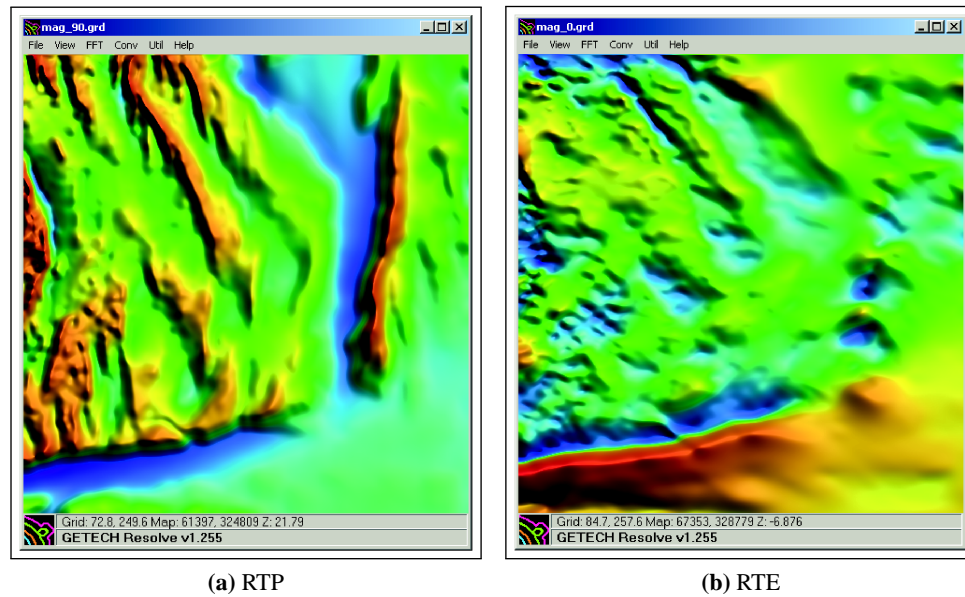
### “Tilt-Depth” method applied to “Bishop” model $\Delta T$ grids.



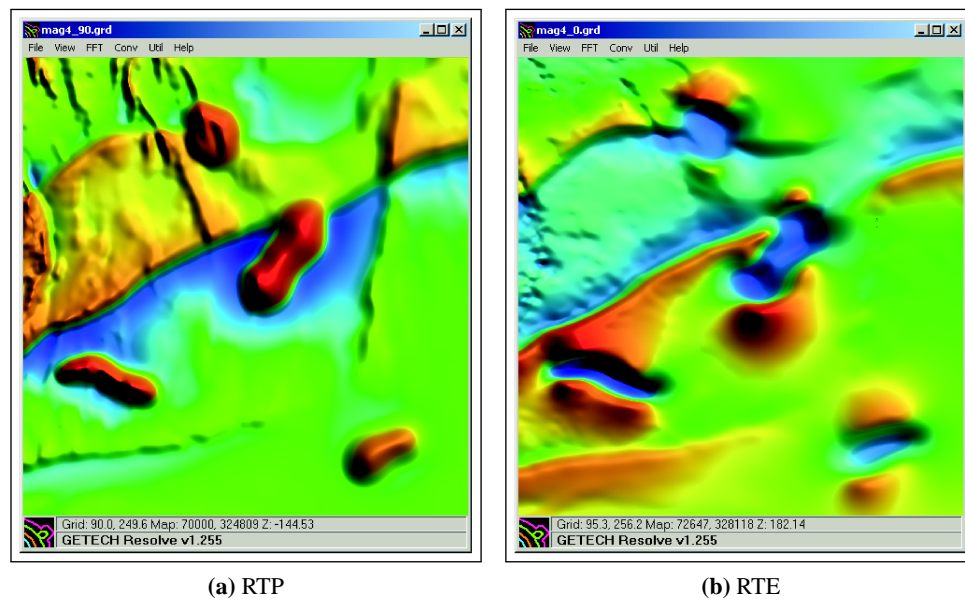
**Figure C.1:** Enhanced (GETgrid<sup>TM</sup>) visualization of the input grids for “Bishop” models: (a) Same grid as in figure 4.2a; (b) Same grid as in figure 4.2b.



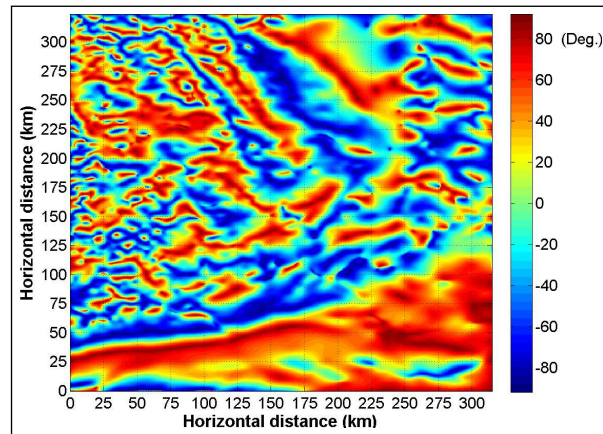
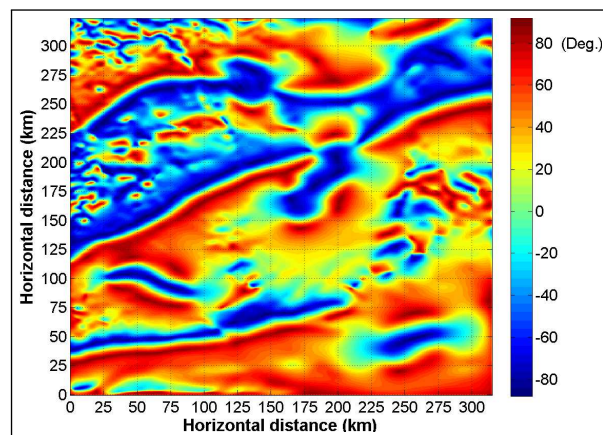
**Figure C.2:** Enhanced (GETgrid<sup>TM</sup>) visualization of the “Bishop” model  $\Delta T$  grids for inclination of induced magnetisation of 25°: (a) SBM grid, same as in figure 4.3a; and (b) CBM grid, same as in figure 4.3b.



**Figure C.3:** Enhanced (GETgrid<sup>TM</sup>) visualization of the simple “Bishop”  $\Delta T$  model (SBM) grids: (a) Same as in figure 4.4a; and (b) Same as in figure 4.4b.



**Figure C.4:** Enhanced (GETgrid<sup>TM</sup>) visualization of the complex “Bishop” model (CBM) grids: (a) Same as in figure 4.5a; and (b) Same as in figure 4.5b.

(a)  $\theta$  of SBM grid (RTE).(b)  $\theta$  of CBM grid (RTE).

**Figure C.5:**  $\theta$  equivalents of RTE-transformed simple and complex “Bishop” model (SBM and CBM) grids (Figures 4.3a and 4.3b). Note that negative  $\theta$  anomalies on figures C.5a and C.5b correspond, respectively, to positive  $\theta$  anomalies on figures 4.6a and 4.7a. Hence, the additive inverse ( $\times -1$ ) of  $\theta$  grids (Figures 4.6b and 4.7b) were computed, respectively, from figures C.5a and C.5b, for comparison with their equivalent  $\theta$  of RTP grids (Figures 4.6a and 4.7a).

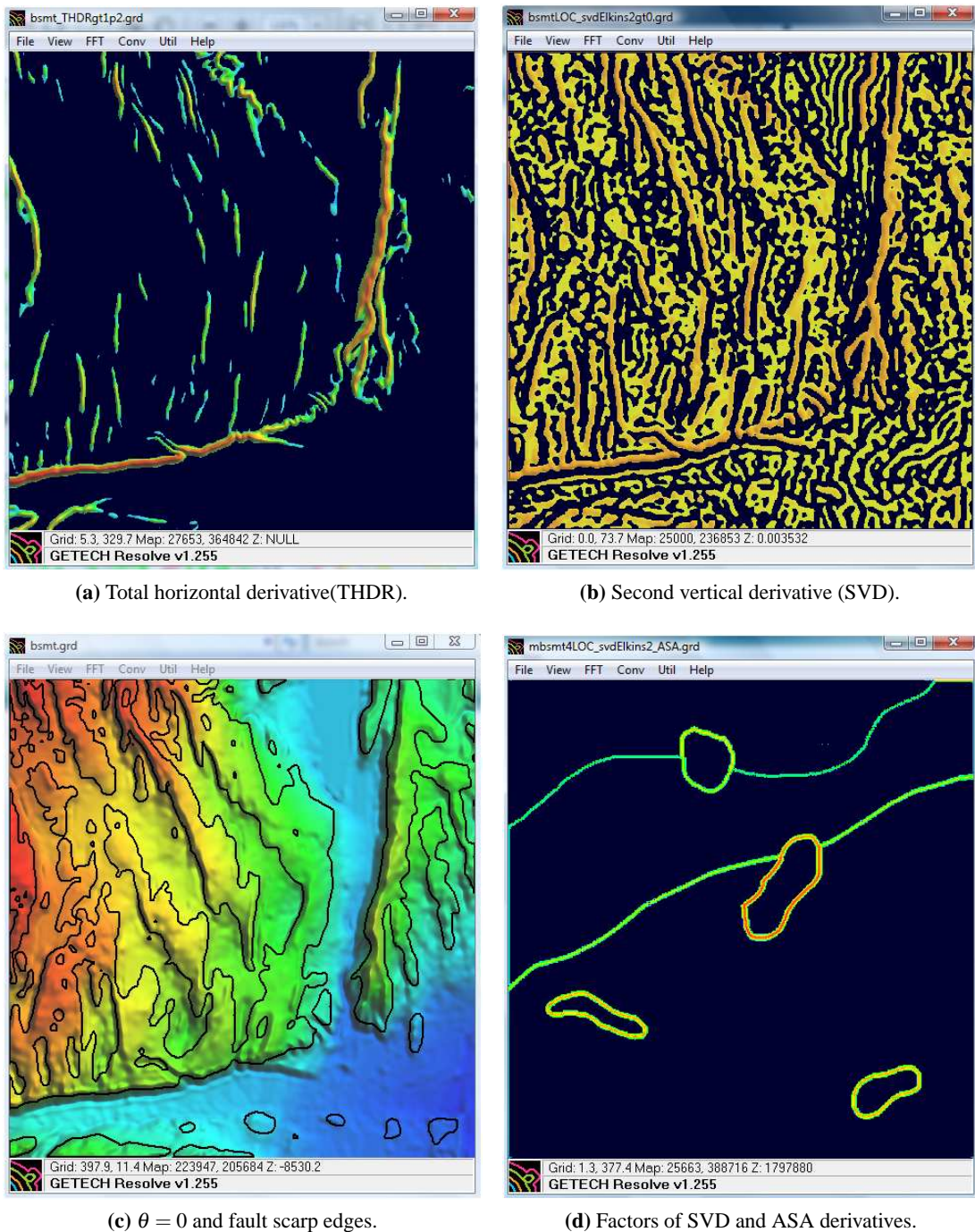


**Figure C.6:** Examples showing how locations of edges on the input basement grids in figures 4.2a and 4.2b were extracted. The THDR grid (Figure C.6a) could not outline the inflection points (edges), so SVD was applied to the grid. The SVD grid (Figure C.6b) enhanced more features than are relevant to the study. The  $\theta = 0$  contours of the SBM (RTP) grid (Figure 4.4a) did a better job of tracing the location of edges of the basement fault scarps as shown (Figure C.6c). The best trace of edge locations on the variable basement grid (Figure 4.2b) was obtained after applying SVD and analytic signal amplitude (ASA). To further enhance the locations for extraction, the resulting grid was multiplied by a certain factor, as reflected by the large Z value shown (Figure C.6d).

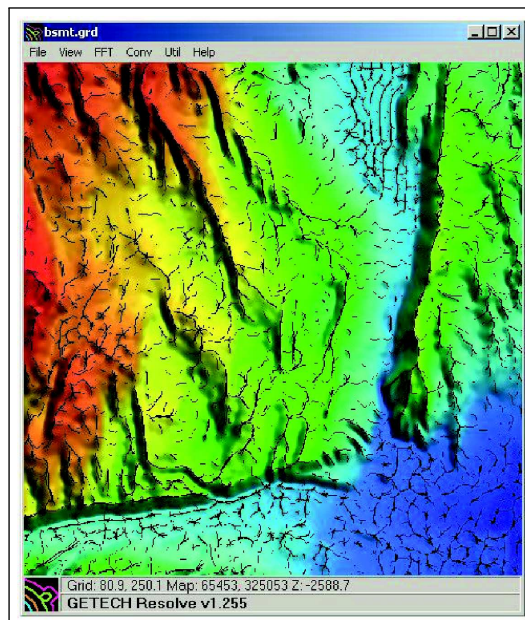
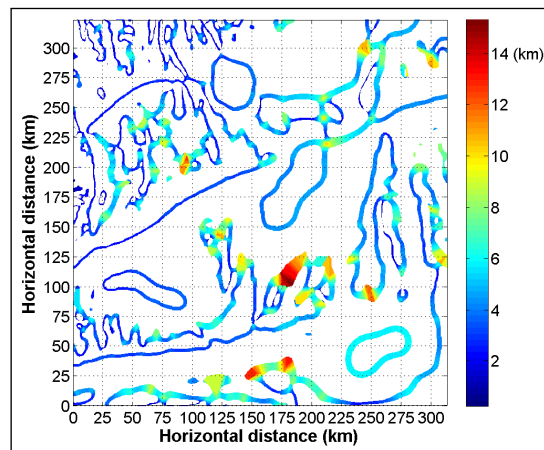
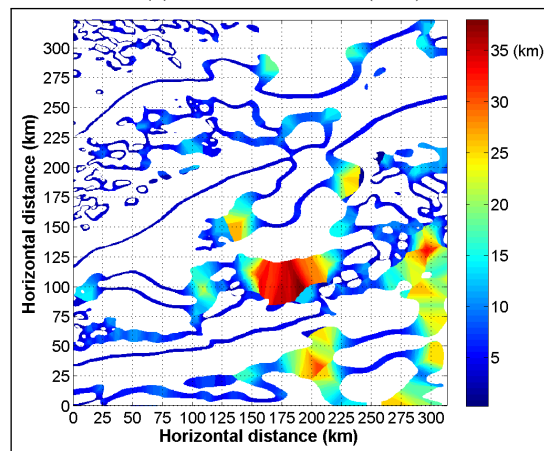


**Figure C.7:** An attempt to extract the actual locations of structural edges on the model “Bishop” basement grid, using analytic signal amplitude. Figure also shows traces of edges using maxima or peaks) of fault scarps (Black-coloured traces obtained from method of [Blakely & Simpson \(1986\)](#), introduced in section [2.5.2](#).



(a)  $\theta = \pm 27$  estimates (RTP)



(b)  $\theta = \pm 27$  estimates (RTE)

**Figure C.8:**  $\theta = \pm 27$  estimates from CBM (RTP and RTE) grid sources. Maximum estimates from CBM (RTP and RTE) grid were generally deeper than the range of actual depths of BM sources (Figure 4.9b).

## Appendix D

### Estimates from “Bishop” model TMI anomaly ( $\Delta T$ ) grids using other methods.

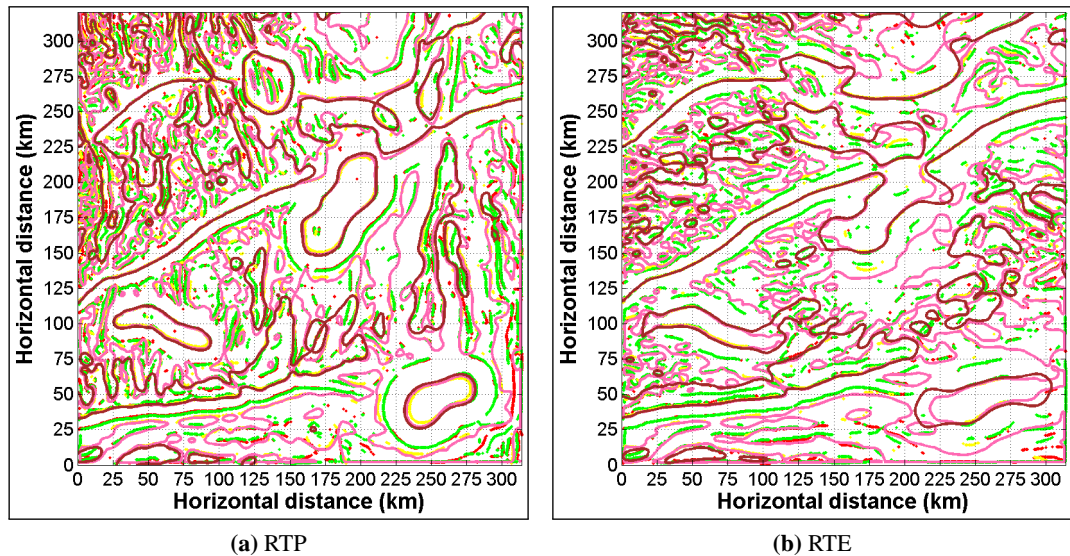


**Figure D.1:** Comparisons between estimates of edge locations on CBM (RTP or RTE) TMI anomaly grids. Estimated location plots are colour-coded for easy identification of the method used:  $HGM_{(\Delta T)}$  (Yellow); SVD (Pink); LW (Red);  $\theta$  (Brown, dashed line); and  $HGM_{(\theta)}$  (Green). Because of the wider spread of ASA estimates, they were not included here. In this figure, estimates from LW were plotted first, followed by  $HGM_{(\theta)}$ ,  $HGM_{(\Delta T)}$  and SVD estimates. Figure 5.8 is equivalent to this figure, but includes ASA estimates. Note that figures here are cleaner, and the ASA can be re-introduced later to constrain interpretations.

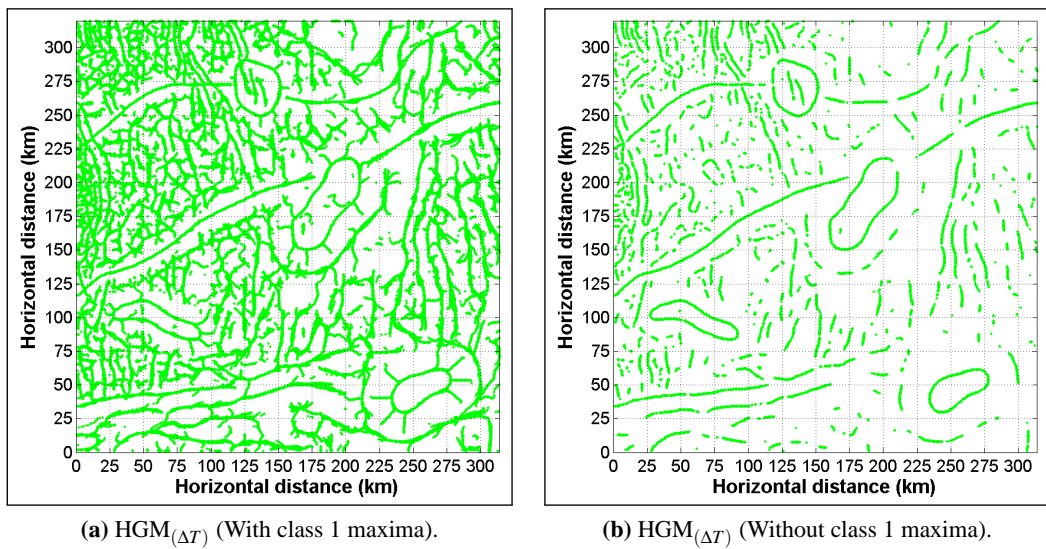


**Figure D.2:** Demonstrating the additional clarity gained by editing estimated locations obtained from CBM (RTP) grid, using  $HGM_{(\Delta T)}$  method. Continuity of  $HGM_{(\Delta T)}$  peaks (edges) reduced as lower class peaks were removed. Location estimates in figure D.2b are more representative of actual CBM sources (Figure 4.8b) and easier to interpret than those in figure D.2a.

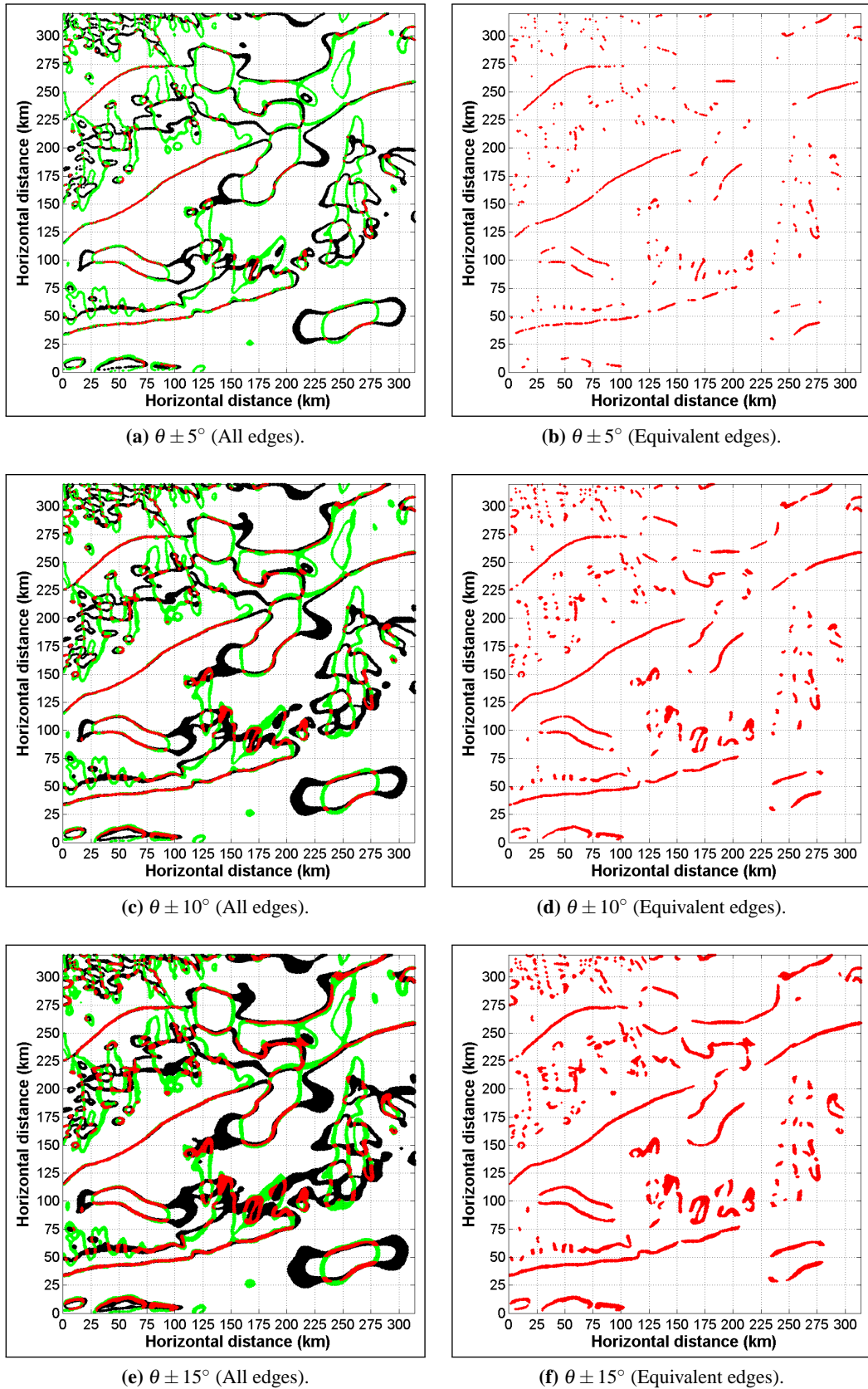


**Figure D.3:** Equivalent locations obtained from  $\theta$  of CBM (RTP and RTE) grids (In red), compared with  $\theta$  of CBM (RTP and RTE) grid locations (In green and black, respectively). Continuity and complexity of equivalent edges increased as the  $\theta^\circ$  range used increased. Using  $|\theta| > 15^\circ$  range offered no further advantage, in this example.

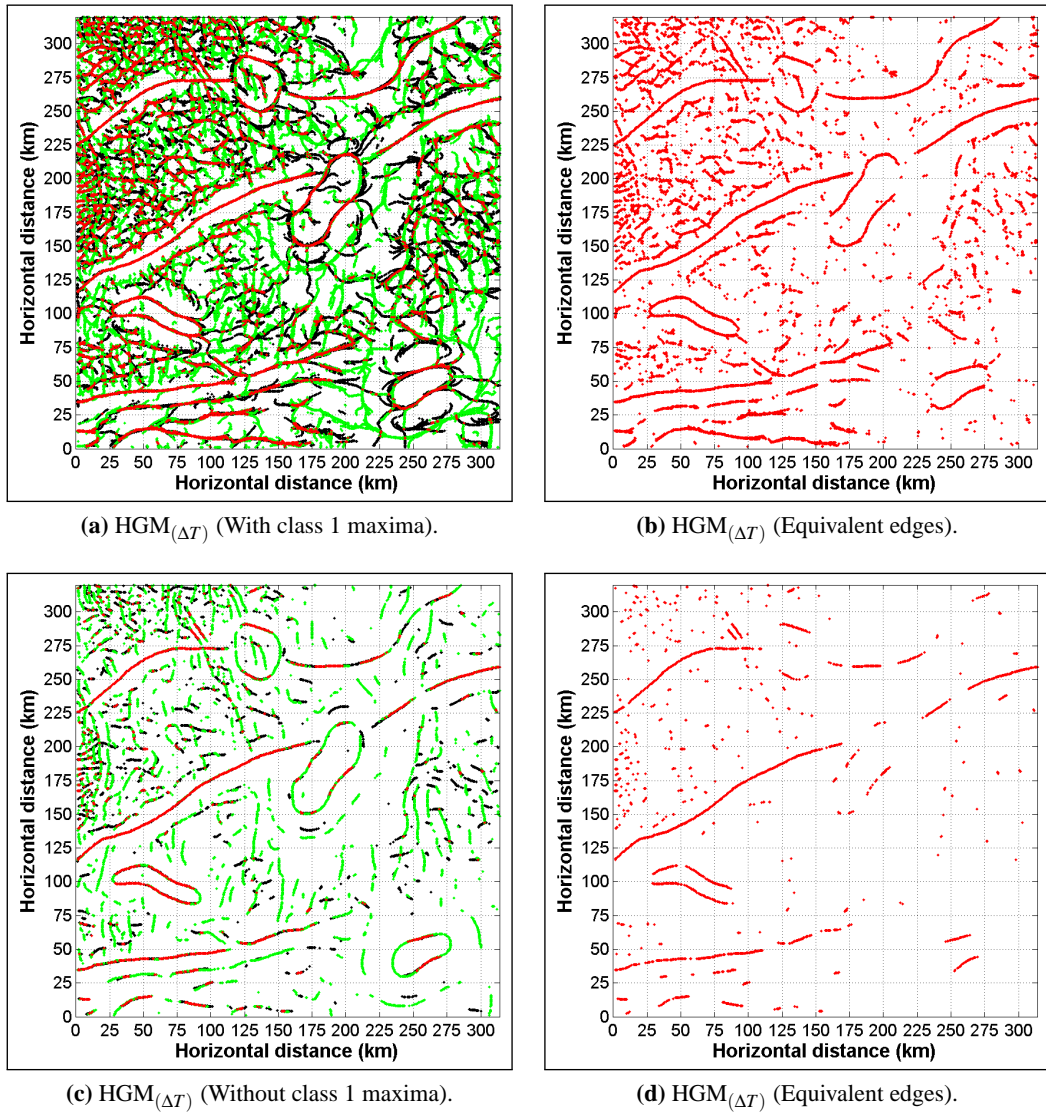


**Figure D.4:** Equivalent locations obtained from  $HGM_{(\Delta T)}$  of CBM (RTP and RTE) grids (In red), compared with  $HGM_{(\Delta T)}$  of CBM (RTP and RTE) grid locations (In green and black, respectively).

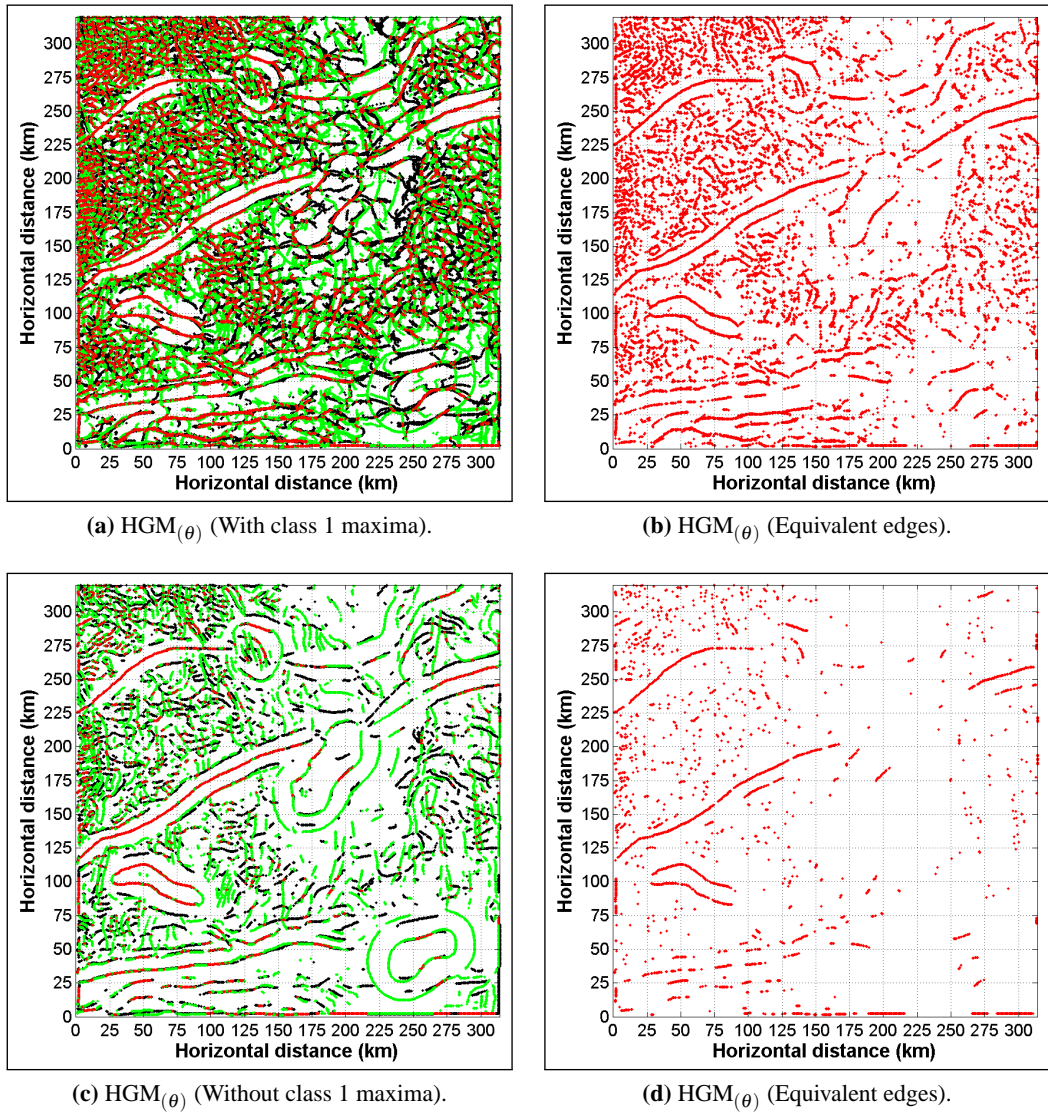


**Figure D.5:** Equivalent locations obtained from  $HGM_{(\theta)}$  of CBM (RTP and RTE) grids (In red), compared with  $HGM_{(\theta)}$  of CBM (RTP and RTE) grid locations (In green and black, respectively).

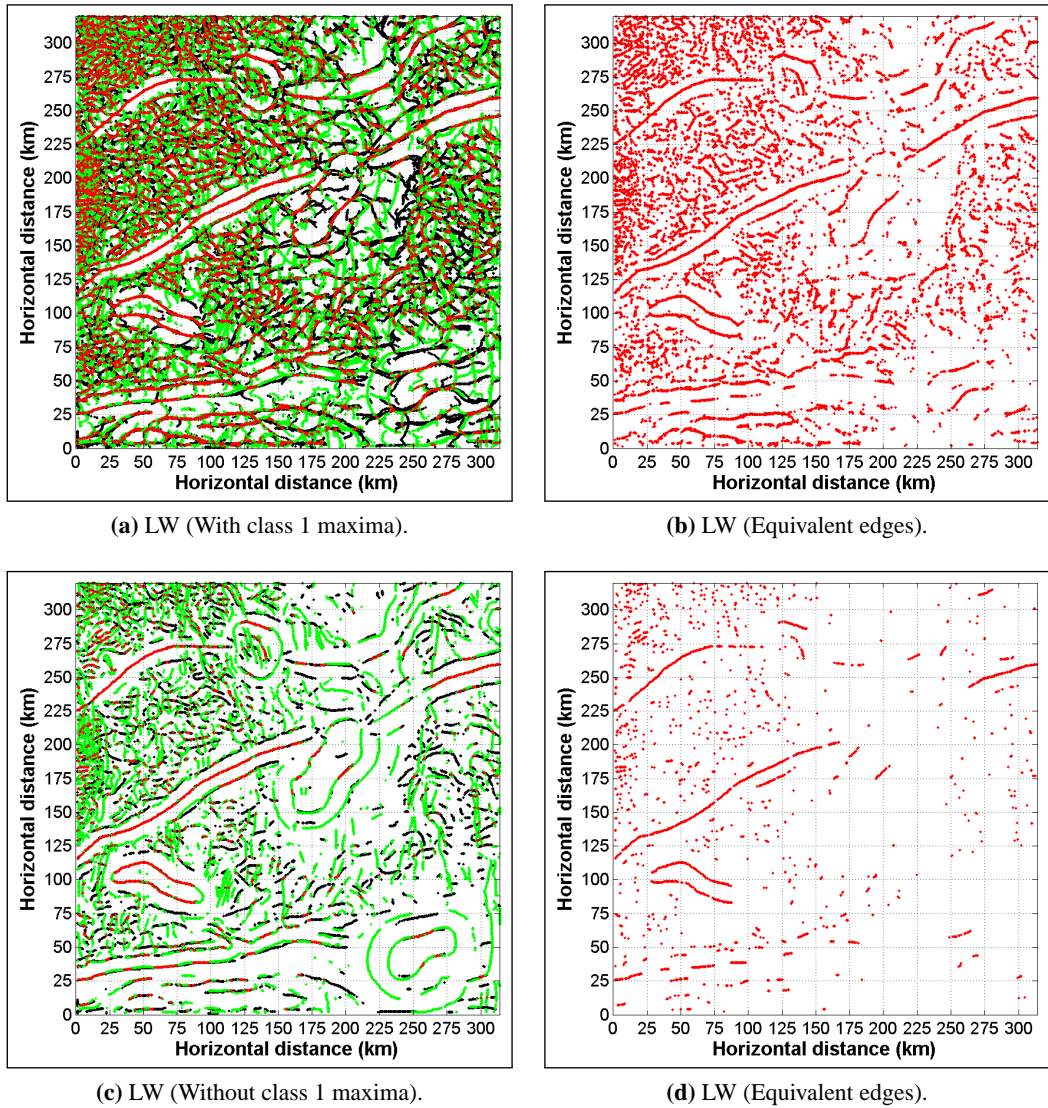


**Figure D.6:** Equivalent locations obtained from LW of CBM (RTP and RTE) grids (In red), compared with LW of CBM (RTP and RTE) grid locations (In green and black, respectively).

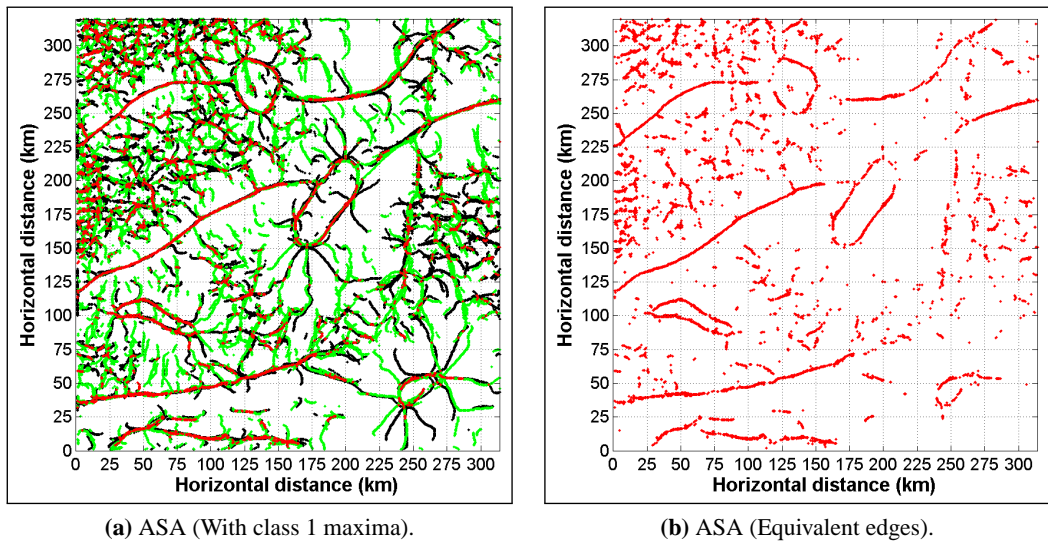


**Figure D.7:** Equivalent locations obtained from ASA of CBM (RTP and RTE) grids (In red), compared with ASA of CBM (RTP and RTE) grid locations (In green and black, respectively).

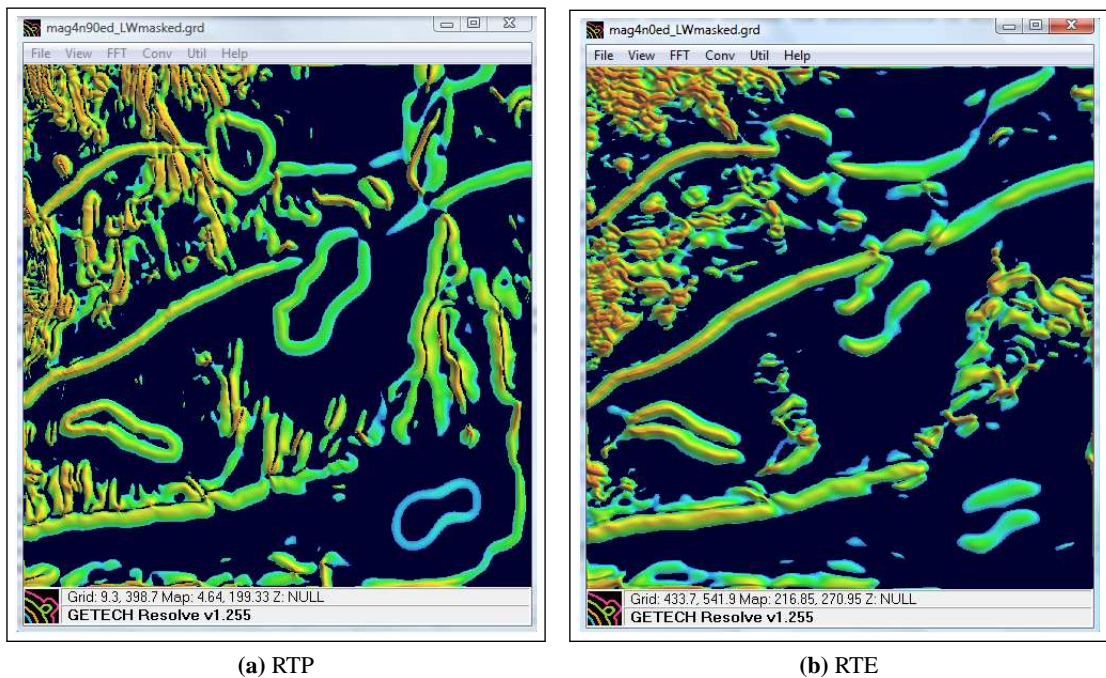


**Figure D.8:** Windowed versions of the LW of CBM (RTP and RTE) grids (Figures 5.3a and 5.3b). Grids were windowed using cut-off LW value determined using equation 5.4.1. LW depths in figure 5.11 were estimated from maxima extracted from these grids.

## Appendix E

### Comparisons between interpretations from RTP and RTE of a Southern Tanzania TMI anomaly ( $\Delta T$ ) grid.

#### E.1 Introduction

Geological complexities presented in field-derived (real)  $\Delta T$  datasets can be more challenging than those offered by the “Bishop model” grids considered in chapters 4 and 5. Complexities may result from cross-cutting relationships between magnetic structures (e.g., heterogeneous basement terrain, dykes, other intrusives, etc.) with more varied susceptibility contrasts and/or strike. Field derived  $\Delta T$  datasets also contain systematic and random measurement errors. Hence, semi-automatic methods evaluated in chapters 4 and 5 will now be further examined in terms of their effectiveness in locating magnetic sources, using a real  $\Delta T$  dataset. Since the main focus of this section is to evaluate the effect of RTE-induced azimuthal anisotropy on source location estimates from such  $\Delta T$  grids, the real dataset used here must be transformable to both RTP and RTE. Consequently,  $\Delta T$  dataset from Southern Tanzania, where the average inclination and declination of the geomagnetic field ( $-43^\circ$  and  $-4^\circ$ , respectively) allowed for valid RTP and RTE transformations, was preferred.

#### E.1.1 Regional tectonic framework and geological setting of Southern Tanzania

The geology and tectonic framework of Southern Tanzania presented here rely extensively on extracts from BGS (2000), Schlüter (2006) and TPDC (2010). A modified geological map of the area, derived from these sources is presented in figure E.1.

The tectonic fabric of the Tanzanian basement complex consist both of geological structures (Figure E.1) preserved from four major tectonic events including the Permo-Triassic breakup of Gondwanaland, as well as the post-Cretaceous and the on-going, regional crustal extension which characterises the East African continental margin (TPDC, 2010). The major regional tectonic elements include a NNW-SSE rift, a E-W graben, a NNE-SSW aulacogen and the right-lateral wrench fault, which is directly related to the drift of Madagascar from Eastern Africa during Late Jurassic-Middle Cretaceous times (TPDC, 2010).

Early phases of rifting of the crust during extension produced interior (sag) basins and passive margin (rift) basins along the Indian Ocean coasts of Tanzania. The rift basins include the Mandawa basin (NE of the Masasi Spur) and Ruvuma basin (SE of the Masasi Spur). The Selous basin is located south of the NNE-SSW trending aulacogen. The E-W trending Rufiji trough cross-cuts the aulacogen and coastal rifts. Most of these and related features give rise to the Southern Tanza-

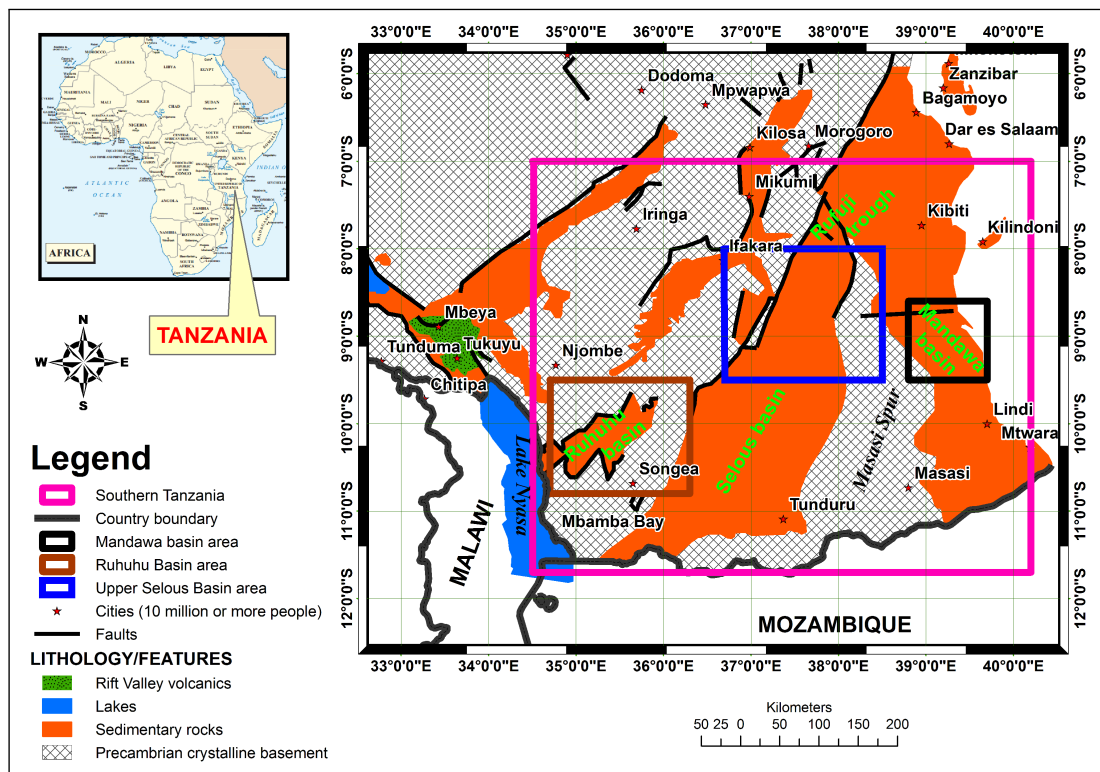


**Figure E.1:** Geological map of Southern Tanzania showing non-magnetic sedimentary and possibly dominantly magnetic basement rocks (Modified from BGS (2000), Schlüter (2006) and TPDC (2010)). The pink rectangle shows the limit of the available  $\Delta T$  data from this area (Section E.2). Brown, Black and Blue-coloured rectangles show areas where basement structures of interest to this study might be located, in the Mandawa, Ruhuhu, and Upper Selous basin areas. Inset political map of Tanzania shows the location of Southern Tanzania.

nia  $\Delta T$  grid (Figure E.2).

### E.1.2 Southern Tanzania $\Delta T$ dataset

The dataset was originally acquired by GeoSurvey International, from 1977 to 1979, at 1 km flight-line spacing, with 10 km tieline spacing, and 120 m flying height (AGL) using a Geometrics<sup>TM</sup> G-803 proton precession magnetometer. A processed  $\Delta T$  data grid was provided by GETECH Plc., UK for this study as a 250 m upward-continued and 250 m linked grid in Lambert Conformal Conic projection (Spheroid: Clark 1880). This dataset was not part of the African Magnetic Mapping Project (AMMP). Prior to its release for this study the data had been levelled and IGRF-reduced (GETECH, 2007). In order to minimise interference from higher frequency anomalies, the dataset was further upward-continued by 250 m, so that the total continuation height of this dataset (Figure E.2) is 500 m. The attitude of the geomagnetic field in Southern Tanzania (average inclination and declination of  $-43^\circ$  and  $-4^\circ$ , respectively) allows for the easy transformation of the  $\Delta T$  dataset (Figure E.2) to both its RTP and RTE equivalents.

## E.2 Methodology and processing adopted

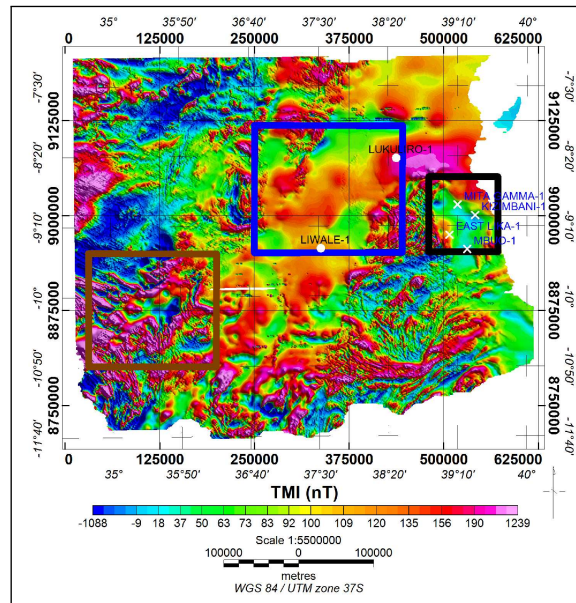


**Figure E.2:** Southern Tanzania  $\Delta T$  grid. Grid was upward-continued to 500 m. Brown, Black and Blue-coloured rectangles represent the areas shown in figure E.1. A subgrid of the  $\Delta T$  grid shown here will be extracted from each of these enclosed areas. These subgrids will be enhanced and the one with the most complicated structural relations will be retained for further evaluation. White X and solid white circle symbols represent wells abandoned within basement and sediments, respectively.

**E.2.1 Extracting subgrids from Southern Tanzania TMI anomaly ( $\Delta T$ ) grid.** The approximately 522 km  $\times$  612 km coverage of Southern Tanzania  $\Delta T$  grid (Figure E.2) meant that the grid was too large for use for detailed evaluation of locations estimated using various methods. Hence, three smaller grids (*subgrids*) were extracted, respectively, from the Mandawa, Ruhuhu, and Upper Selous basin areas, based on complexity of basement anticipated from the geological map (Figure E.1). These subgrids are shown in figures E.3a, E.3b and E.3c and are, respectively, Mandawa, Ruhuhu or Selous subgrid, to reflect their location over parts of the Mandawa basin, Ruhuhu basin or Northern Selous basin area.<sup>1</sup>

### E.2.2 RTP and RTE of $\Delta T$ subgrids from Southern Tanzania.

A measure of simplification is attained when anomalies are transformed to their RTP or RTE equivalents (Section 2.3). This remains true when the direction of remanent magnetisation is  $\leq 30^\circ$  relative to the direction of induced magnetisation (Section 3.3.4). Hence, anomalies on the Mandawa, Ruhuhu and Selous subgrids (Figures E.3a, E.3b and E.3c) must be transformed to their respective RTP and RTE equivalents, to simplify anomalies prior to the application of semi-automatic methods of source edge location and depth estimation.

The Definitive Geomagnetic Reference Field (DGRF) elements, required to transform each subgrid to its RTP and RTE equivalents, are presented on table E.1. These elements were used to transform each subgrid (Figures E.3a, E.3b and E.3c) to its RTP and RTE equivalents. RTP and RTE equivalents of the Mandawa, Ruhuhu and Selous  $\Delta T$  subgrids are also presented in figure E.3).

<sup>1</sup>Selous will henceforth refer to Northern or Upper Selous.

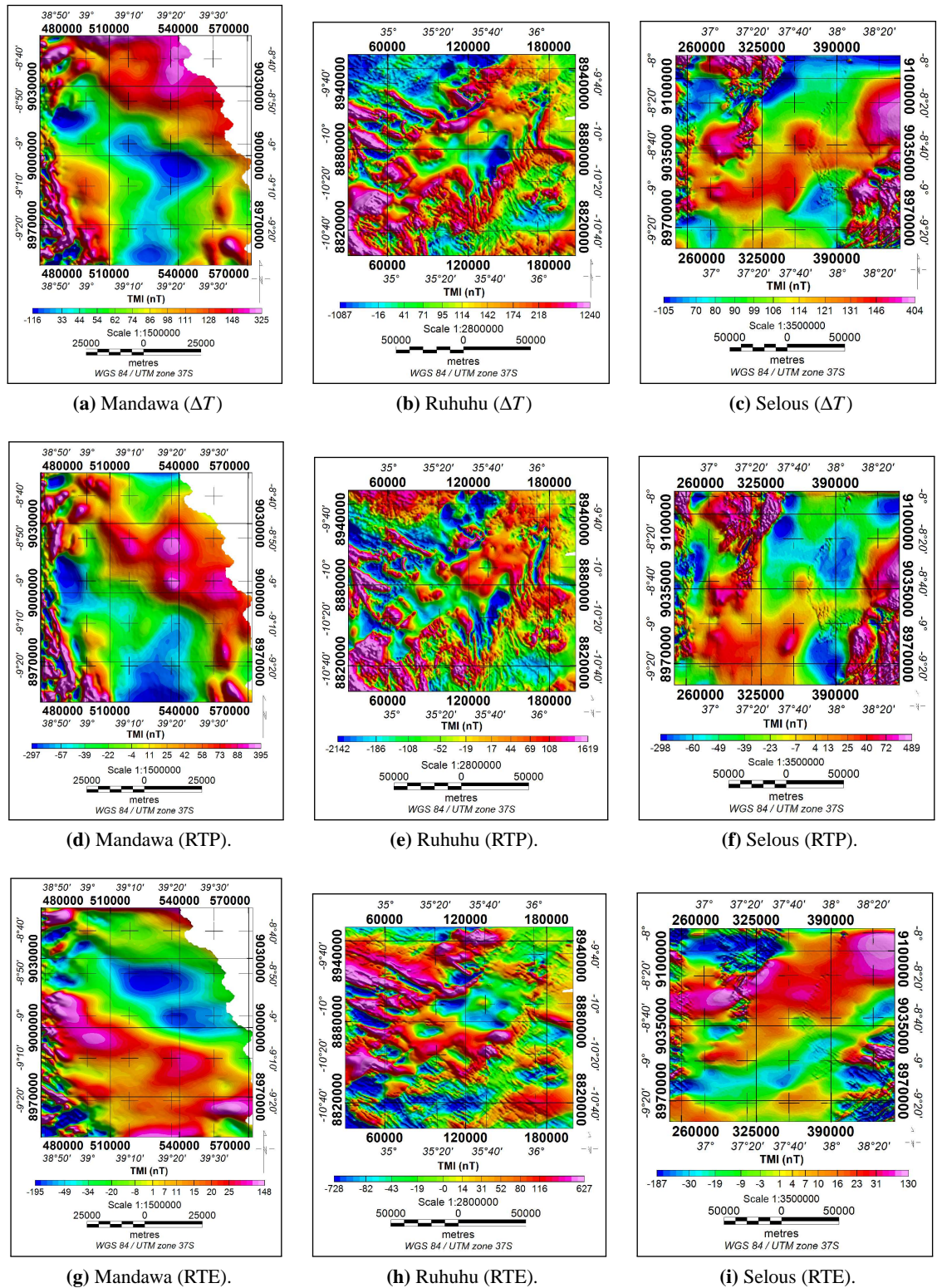


**Figure E.3:**  $\Delta T$  and their RTP or RTE equivalents: (a) Mandawa basin area, where  $\Delta T$  (RTP) (Figure E.3d) appear to be simple and isolated, with major NW-SE and minor NNW-SSE and NNE-SSW trends; (b) Ruhuhu basin area, where  $\Delta T$  (RTP) of various shapes and orientations, including near-North-South (near-N-S), occur (Figure E.3e); (c) Selous basin area, where major NW-SE, NNW-SSE, NNE-SSW and minor N-S trending  $\Delta T$  (RTP), that are simple and isolated, occur (Figure E.3f); (d), (e) and (f) are, respectively, RTE equivalents of grids in figures E.3d, E.3e and E.3f. While sources striking in all directions are imaged on the RTP grids, North-South (N-S) sources are not imaged on RTE grids. Whether sources with  $N \pm 20^\circ$  strikes are imaged or not depends on their degree of isolation. NW-SE, NNW-SSE and NNE-SSW trending sources are imaged on RTE grids.

**Table E.1:** Geomagnetic field elements for  $\Delta T$  subgrids extracted from Southern Tanzania grid (Figures E.3a, E.3b and E.3c).

subgrid	TMI (nT)	Incl. (°)	Decl. (°)
Mandawa	33672	-42.22	-3.67
Ruhuhu	33461	-45.2	-4.05
Selous	33655	-42.5	-3.45

### E.3 Comparisons between location estimates from RTP and RTE of $\Delta T$ grid

Previous work (Sections 4.3.2 and 4.4, and chapter 5) shows that, in the absence of anomaly interference, Tilt angles ( $\theta$ ) of RTP data give clear indications of the horizontal location of the edges of anomalous magnetic structures. This  $\theta$  property was exploited to compare RTP versions of the three subgrids in terms of  $\theta$  anomaly complexity: character, size, degree of isolation and relationships.<sup>2</sup>

The Ruhuhu  $\Delta T$  subgrid (Figure E.3b) was preferred for evaluating RTP and RTE location estimates, since  $\theta$  anomalies on this subgrid were more complex. Therefore, SVD,  $HGM_{(\Delta T)}$ , ASA,  $\theta$ , LW and  $HGM_{(\theta)}$  equivalents of the RTP and RTE of the Ruhuhu grids (Figures E.3e and E.3h) were obtained. Estimates of edge locations on the Ruhuhu (RTP and RTE) subgrids have been extracted from the SVD,  $HGM_{(\Delta T)}$ , ASA,  $\theta$ , LW and  $HGM_{(\theta)}$  grids. These extracted locations are presented in figure E.4 (RTP in red, and RTE in blue).

Comparisons between the structural map obtained from the RTE and RTP of Ruhuhu grid (Figure E.5) show that all, including the abundant  $N\pm 20^\circ$  trending edges in the Eastern and Southern parts of Ruhuhu grid, were well imaged on the RTP map (Figure E.5a). On the contrary, the abundant  $N\pm 20^\circ$  trending edges were not imaged at all on the RTE map (Figures E.5b). The map also shows that mainly NE-SW, NW-SE and E-W edges are more likely to be imaged in their correct locations on RTE grids. However, locations where near-N-S ( $N\pm 20^\circ$ ) trending edges occurred on the RTP grid are dominated by prominent E-W trending anomalies on the RTE grid (Figure E.4), generated from interference between close discrete dipolar anomalies which develop along discontinuous (en-echelon) 2D edges (Figure 2.8).

<sup>2</sup>This decision assumed that edges of magnetic sources in the area are vertical, and with 2D contact-like cross-section (Section 2.4.1).

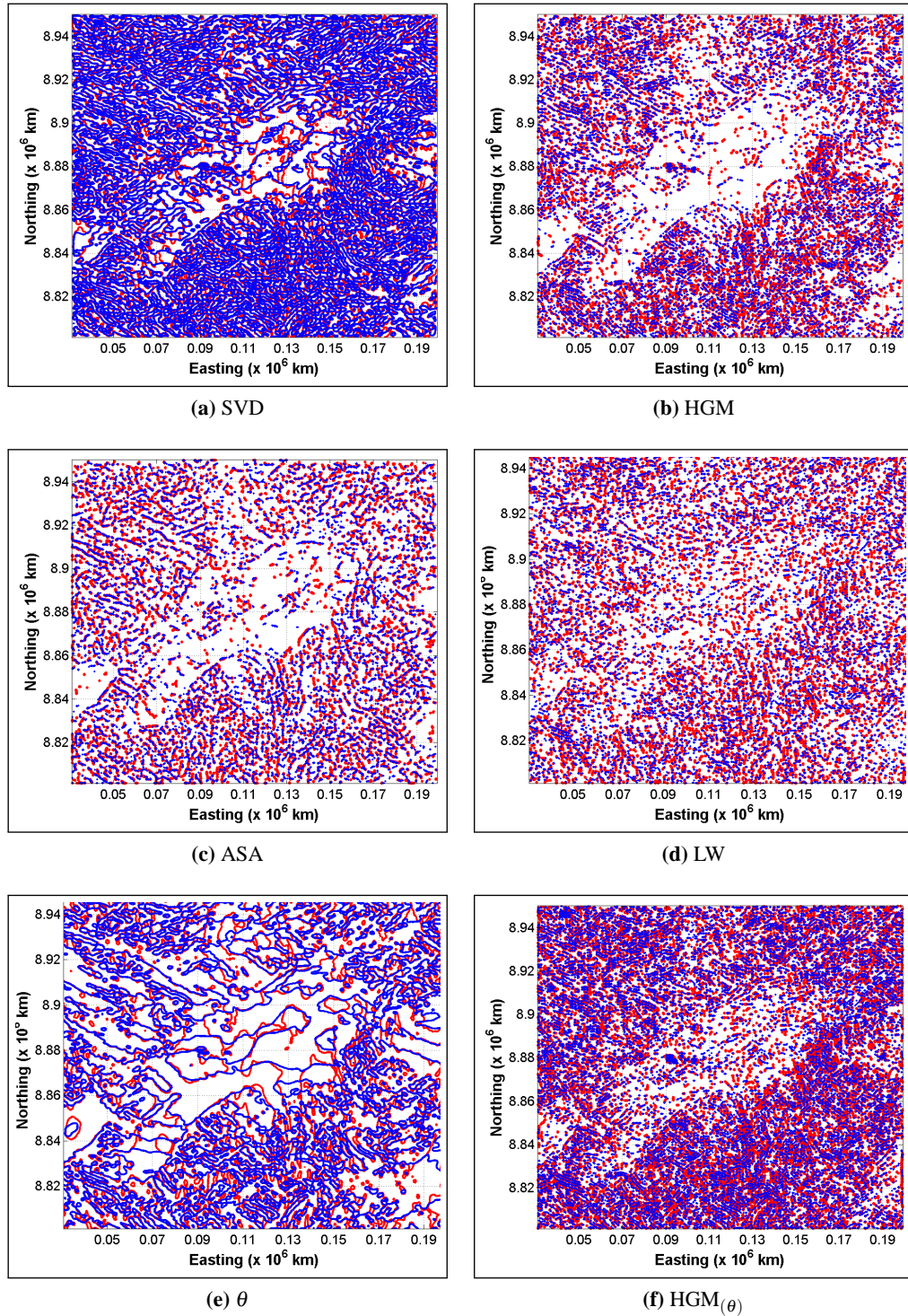


**Figure E.4:** Comparisons between locations of sources estimated from the RTP or RTE versions of the **Ruhuhu subgrid** (Figures E.3e and E.3h). Locations estimated from the RTP subgrid are in red, while those from the RTE subgrid are in blue.

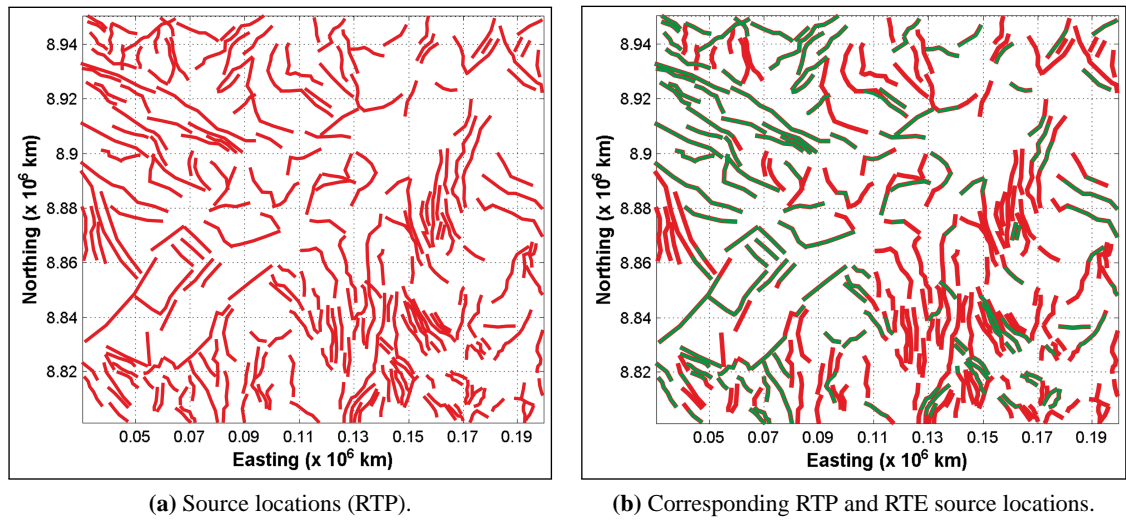


**Figure E.5:** Integrated structural interpretations of locations extracted from RTP and/or RTE of **Ruhuhu** subgrid (Figure E.4). Locations that are equivalent to both RTE and RTP grids are traced in green.

## Appendix F

### NE Nigeria dataset.

#### Introducing the available NE Nigeria TMI (T) dataset.

The TMI anomaly grid used for this study (Figure 6.4) was obtained from reducing Dr. Sally Barritt's dataset (Figure F.1b), and then merging them with the GETECH Group Plc., UK dataset (Figure F.1a).<sup>1</sup> The procedure adopted is described below:

(i) **Reduction of TMI data from Dr. Sally Barritt (Figure F.1b).**

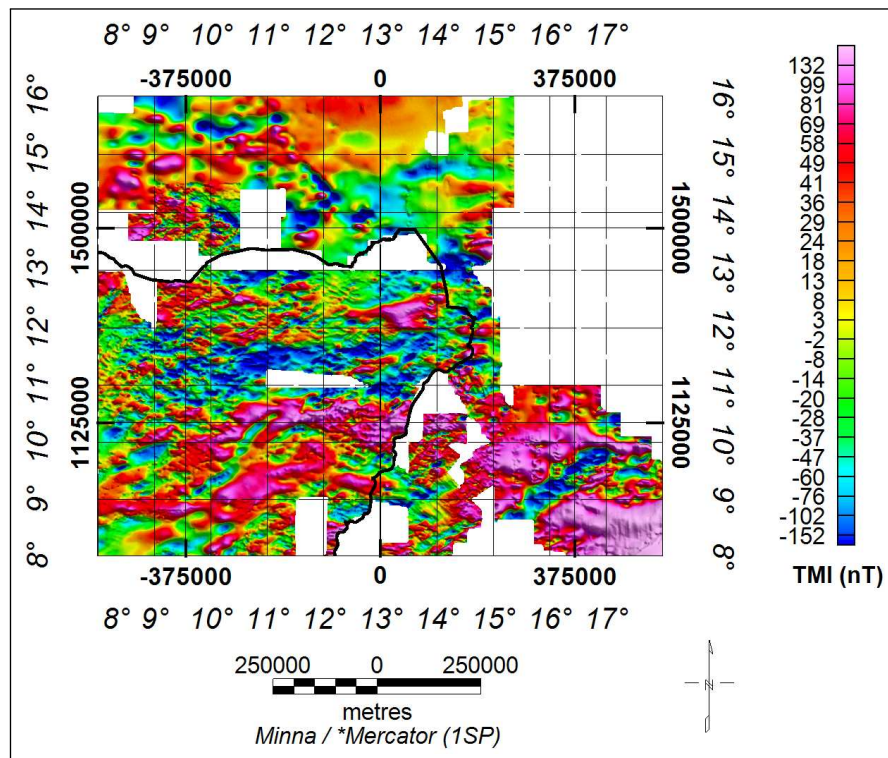
- (a) First, I restored the background TMI value (25000 nT) indicated on the original TMI map sheets<sup>2</sup>, to the dataset.
- (b) Ravat et al. (2003) recommended the Definitive Geomagnetic Reference field (DGRF) for removing the Earth's core sourced magnetic field contributions from magnetic surveys conducted over relatively short time spans, or within the same geomagnetic epoch. Hence, a sub-grid (Figure F.2) of the 1945-1985 DGRF (Barraclough, 1987), which describes the Earth's main (dipolar) magnetic field ( $T_{core}$  Equation (2.2.3)) for the survey period (*circa* 1<sup>st</sup> January, 1974) was subtracted from Dr. Sally Barritt's dataset.<sup>3</sup>
- (c) The dataset was also corrected for  $T_{external}$  contributions using the mean value of the diurnal variation for the duration of the survey.
- (d) The resulting  $\Delta T$  values were gridded, using the minimum curvature (MINC) method (Briggs, 1974; Swain, 1976; Webring, 1981), at 400 m intervals ( $\frac{1}{5}$  of the 2 km flight-lines spacing), at the barometric survey height (mean terrain clearance or mtc + topoagp) specified in the TMI data spreadsheet from Dr. Barritt. The MINC method uses a 5 x 5 rhombic biharmonic operator and is better suited to surveys in which the flightline spacings are either constant or close to constant (Briggs, 1974; Webring, 1981; O'Connell & Owers, 2008). Recently, however, Smith & O'Connell (2005) and O'Connell & Owers (2008) showed that both the MINC and bi-cubic (Akima) gridding methods can, by their nature, spatially alias anomalies when the major axes (trend) of the anomaly is oblique (acute) to the flightline direction.

---

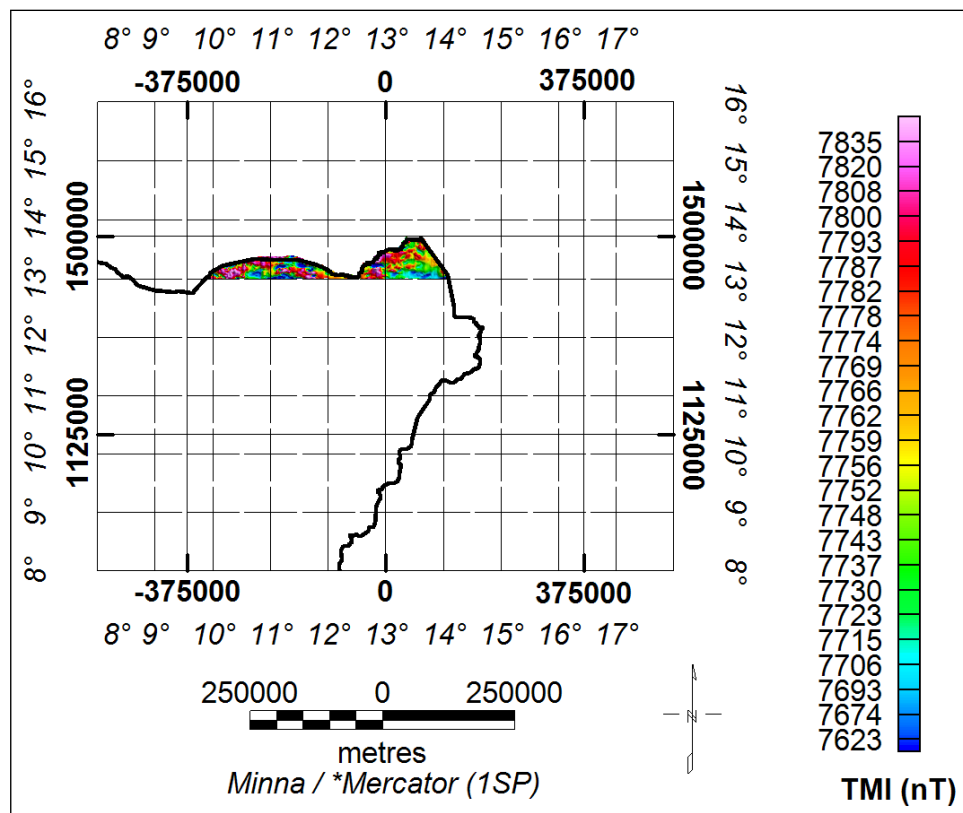
<sup>1</sup>GETECH Group Plc., UK is shortened to GETECH in future references.

<sup>2</sup>Provided by Professor C. S. Okereke, Department of Geology, University of Calabar, Calabar, NIGERIA.

<sup>3</sup>The DGRF in figure F.2 was generated using Oasis montaj<sup>TM</sup>, a Geosoft Inc., Canada's commercial software.



(a) GETECH's TMI anomaly ( $\Delta T$ ) dataset.



(b) Dr. Sally Baritt's TMI (T) dataset.

**Figure F.1:** Available TMI datasets from NE Nigeria. Un-reduced complimentary dataset in figure F.1b has been gridded to show location relative to GETECH data in figure F.1a. Note the difference in data range between figures F.1a and F.1b. Thick black line represents the Nigeria border.

- (e) Using these barometric heights, I upward-continued the gridded  $\Delta T$  grid to 1 km mtc.
  - (f) I then projected this  $\Delta T$  grid into the equatorial Mercator (EM) coordinate system using the Clarke 1880 spheroid, as specified for data in figure F.1a.
  - (g) Finally, I re-gridded the  $\Delta T$  data at 1 km  $\times$  1 km grid intervals, using the MINC method.
- (ii) **Merging the GETECH and Dr. Barritt's  $\Delta T$  datasets.** The  $\Delta T$  grid obtained from Dr. Barritt's TMI dataset did not match the GETECH grid in figure F.1a at their common boundary. Besides levelling problems, there was a 10-15 seconds gap between the grids. The procedure adopted to address these additional problems is briefly described below;
- (a) I began by micro-levelling (Minty, 1991) the  $\Delta T$  grid derived from Dr. Barritt's spreadsheet.
  - (b) I then imported this micro-levelled and the GETECH grids into the same basemap.
  - (c) Using the arithmetic mean from each grid, and several profiles across the edges of both  $\Delta T$  grids, I was able to derive a 'regional' correction grid.
  - (d) I then separately DC-shifted both  $\Delta T$  data datasets using the calculated 'regional' correction grid.
  - (e) By interpolating between the grids, a piece of grid which smoothly linked the edges of both grids was obtained.
  - (f) The DC-shifted grids and the smooth, linking grid were then merged together using a Geosoft (Oasis montaj<sup>TM</sup>) GX<sup>4</sup> called "gridstch".
  - (g) Finally, seven (7) passes of the weighted 3 $\times$ 3 moving-average Hanning low pass (LP) filter was applied to the merged  $\Delta T$  grid for 'light cosmetic' (Fairhead, 2007, p.135) smoothening. This final grid, shown in figure 6.4, is the input dataset for all interpretations of NE Nigeria basement structure and composition in chapter 6. Even at large magnifications, the "boudinage patterns" of Smith & O'Connell (2005) were not observed in the NE Nigerian dataset.

**The GETECH  $\Delta T$  dataset for Nigeria and its environs** (Figure F.1a) is reported to have resulted from the following processes (Barritt et al., 1993; ULIS, 1993):

- (i) TMI data were extracted from each map sheets by on-screen digitisation. The computer-aided method deployed allowed the user to choose one of four digitisation modes, namely; a gridded mode, a grid-contour intercept mode, a flightline-contour mode, and a random point

---

<sup>4</sup>'GX' is an acronym for "Geosoft eXecutable".

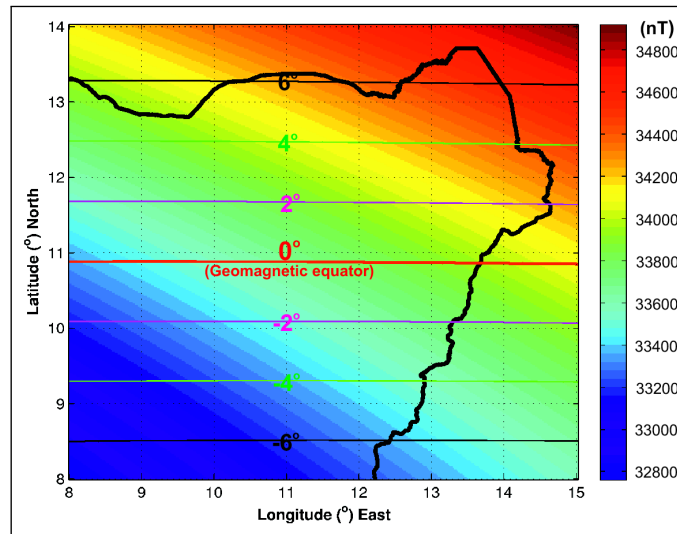


**Figure F.2:** Spatial relationship between inclination (Horizontal lines) and TMI amplitude of the regional DGRF (Barracough, 1987) in NE Nigeria, for 1<sup>st</sup> January, 1974. The Nigerian boundary is shown in black. Extracted contours of  $\alpha$  (The lines) show the: geomagnetic equator ( $\alpha = 0^\circ$  in red);  $\alpha = 2^\circ$  and  $-2^\circ$  (in pink);  $\alpha = 4^\circ$  and  $-4^\circ$  (in green); and  $\alpha = 6^\circ$  and  $-6^\circ$  (in black).

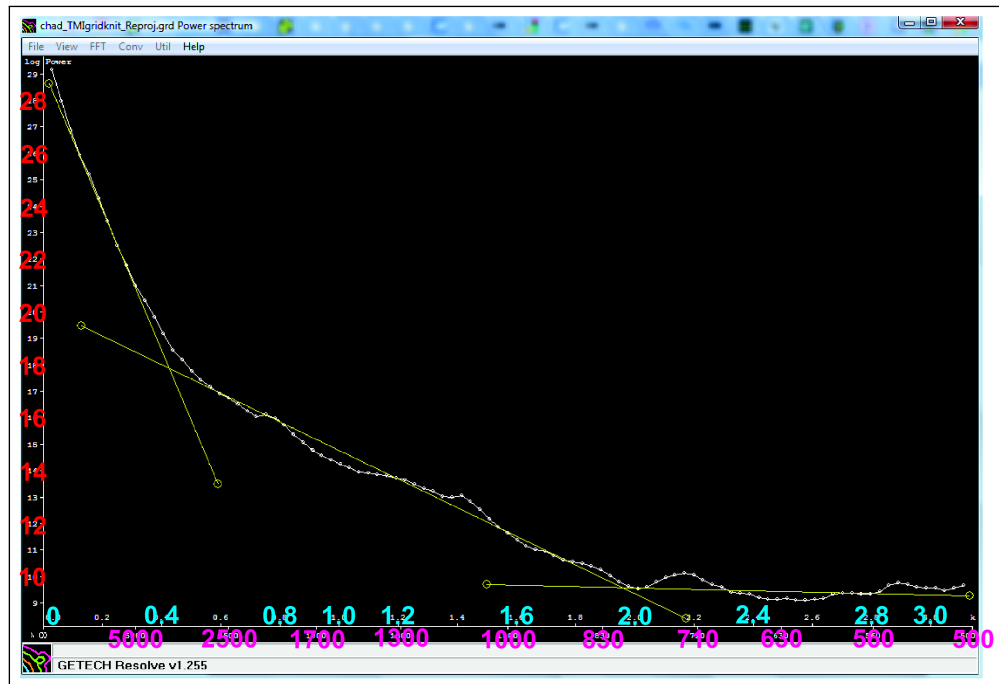
mode.

- (ii) By adding the background TMI values to the digitised TMI values from the map sheets, the actual recorded field magnetometer values were recreated.
- (iii) For each map, these digitised data values was gridded at between  $\frac{1}{2}$  to  $\frac{1}{5}$  of the flight line spacing, at the survey height specified on each map sheet. Based on the aeromagnetic survey characteristics and the orientation of major structures in the area covered by each map sheet, the minimum curvature (MINC) gridding method (Briggs, 1974; Swain, 1976; Webring, 1981) was preferred.
- (iv) Where data appeared to be oversampled along the flightline, a low-pass (LP) linear or non-linear dealiasing filter was applied to the gridded TMI data along the flightline direction.
- (v) Each TMI map's equivalent grid was then upward-continued to 1 km mean terrain clearance (mtc).
- (vi) Adjacent 1 km upward-continued TMI grids were then merged to produce a large AMMP  $\Delta T$  grid.
- (vii) The Definitive Geomagnetic Reference Field (DGRF) coefficients for the period, 1945 to 1985 (Barracough, 1987) was used to compute and remove the main (regional) field up to harmonic degree 8.
- (viii) The resulting AMMP grid was reprojected using the Equatorial Mercator (EM) coordinate system and the Clarke 1880 spheroid. This grid was then preserved as 1 km  $\times$  1 km grid

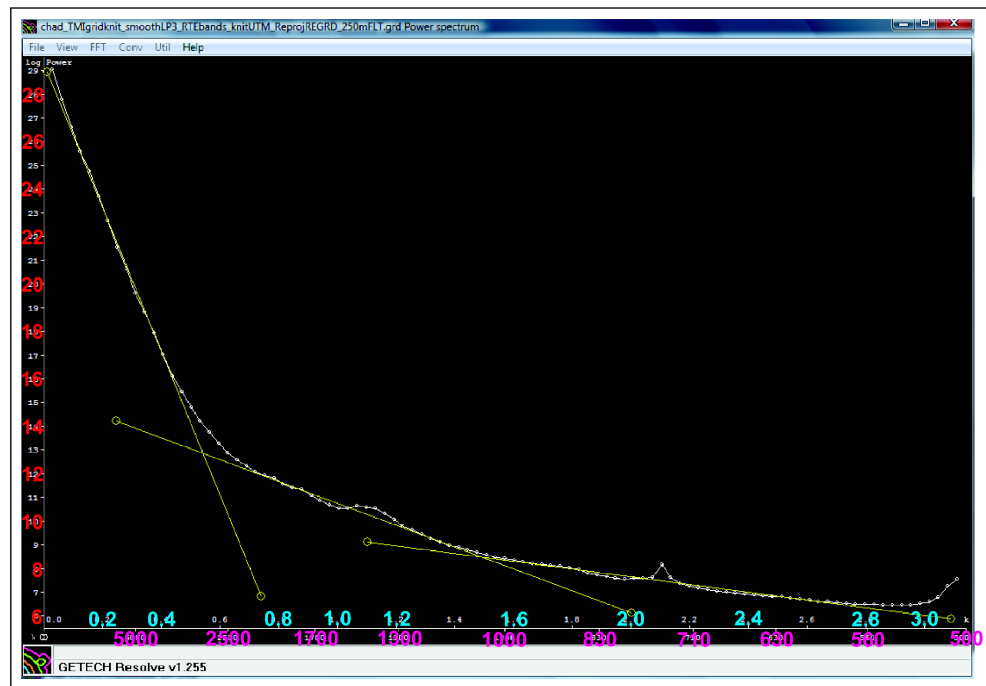
draped on topography.

(ix) The GETECH  $\Delta T$  grid (Figure F.1a) is an extract from the AMMP grid.

The DGRF (Figure F.2) shows that amplitudes of the inducing dipolar field in NE Nigeria ranged from about 32,800 to 35,800 nT, from SouthWest to NorthEast, while inclination of the inducing field ( $\alpha$ ) ranged from about  $-8^\circ$  to  $8^\circ$  (from South to North). The low inclinations of the geomagnetic field in this area (Figure F.2) means that the data require RTE transformation, with inevitable RTE-induced problems (Section 2.3.3).

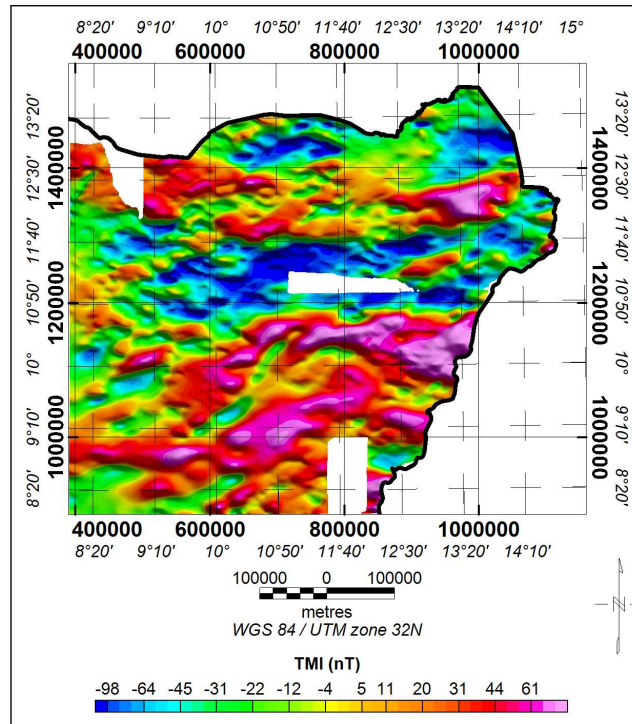


(a)  $\Delta T$  grid (Figure 6.4).

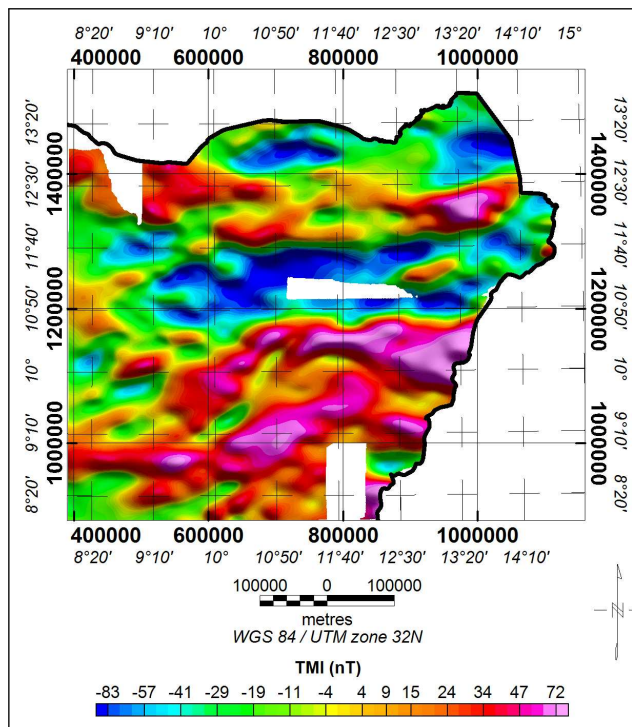


(b)  $\Delta T$  (RTE) grid (Figure 6.6).

**Figure F.3:** Power spectra for NE Nigeria: (a)  $\Delta T$  grid; and (b) its RTE equivalent. Figures have been edited to add more legible labels at selected axis tick-marks. Three (3) lines reflecting the slope of different segments of the spectra are shown, for comparison. Note the relatively focussed spectral power in all three segments on the RTE spectrum (b).

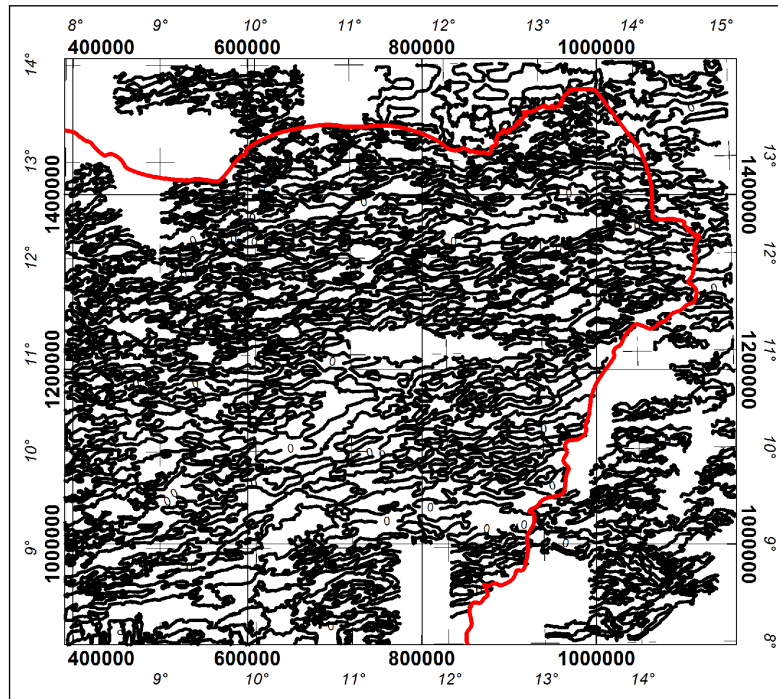


(a) 5 km upward-continued (Cut-off  $\lambda = 5$  km).

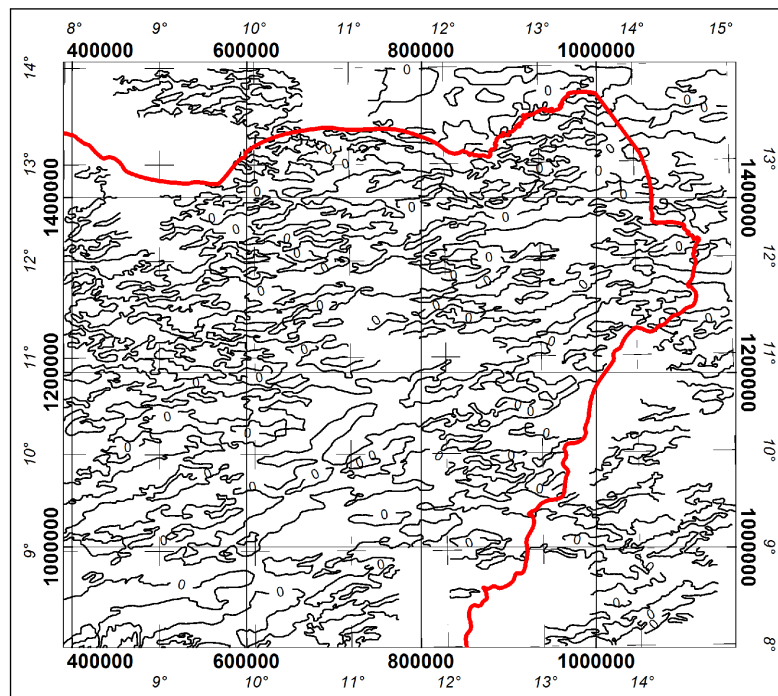


(b) 8 km upward-continued (Cut-off  $\lambda = 30$  km).

**Figure F.4:** Low-pass (LP)-filtered TMI (RTE) anomaly data from NE Nigeria upward-continued to: (a) 5 km and (b) 8 km, derived from figure 6.6. The low-pass (LP)-filter cut-off wavelength ( $\lambda$ ) for each upward-continued  $\Delta T$  (RTE) data was chosen from its radially averaged power spectrum.

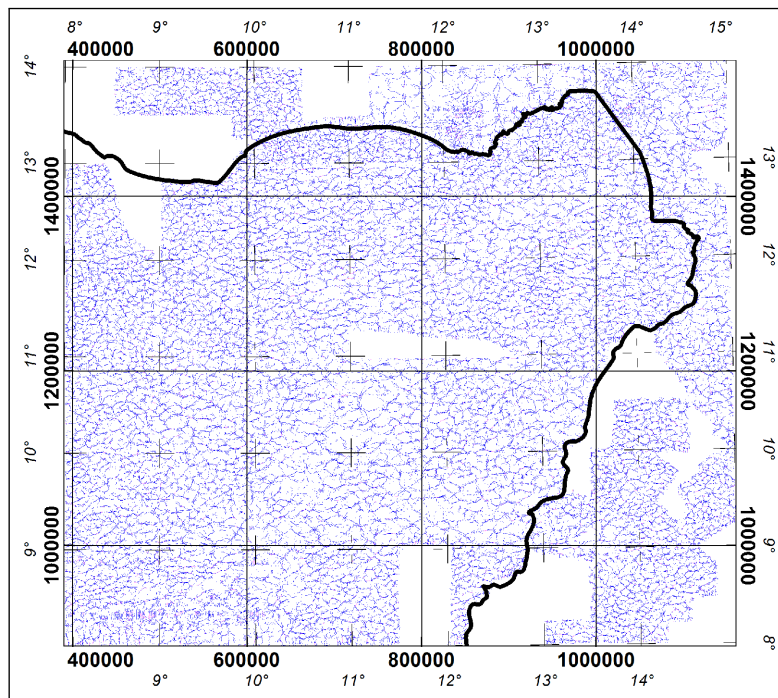


(a) SVD

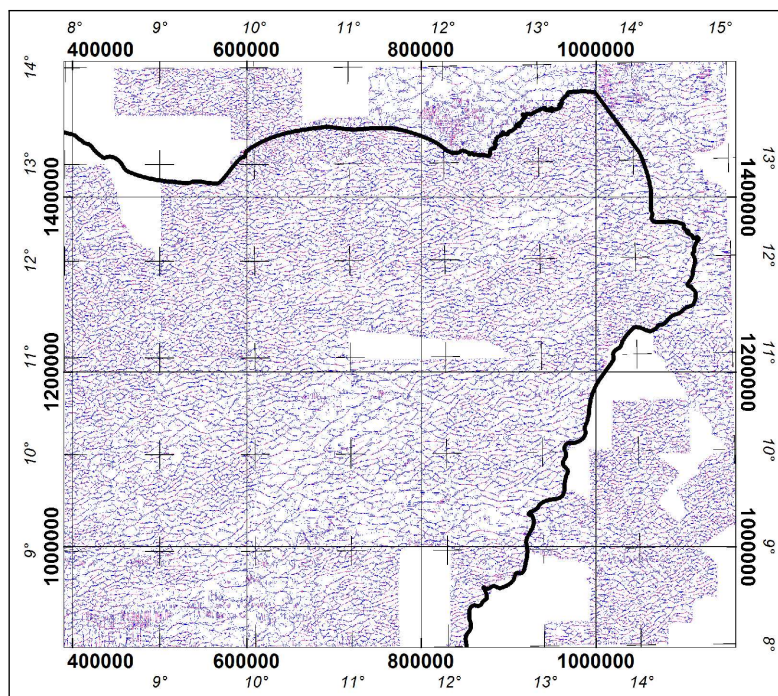


(b)  $\theta$

**Figure F.5:** Locations estimated from SVD and  $\theta$  maps of NE Nigeria, shown in figure 6.9. Locations are estimated using SVD=0 or  $\theta = 0$  contours.

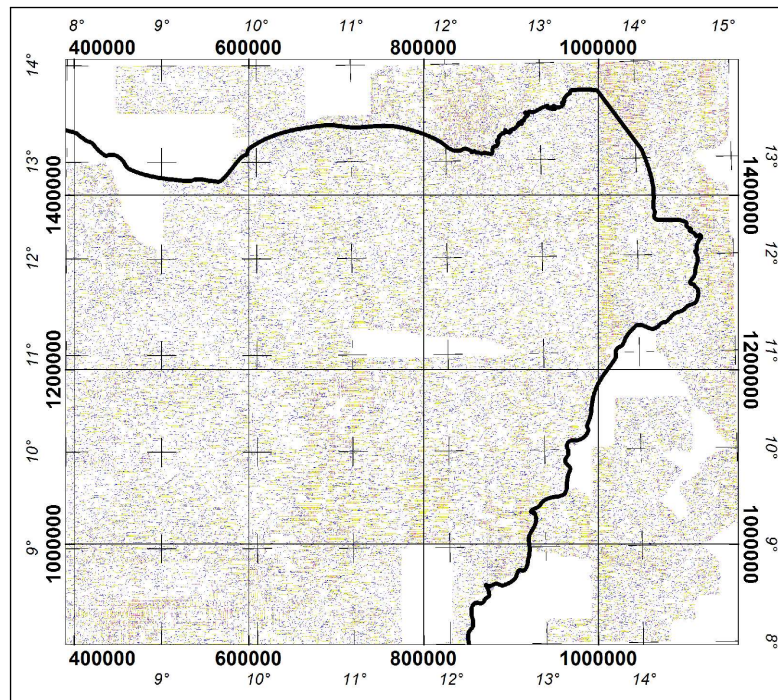


(a) ASA

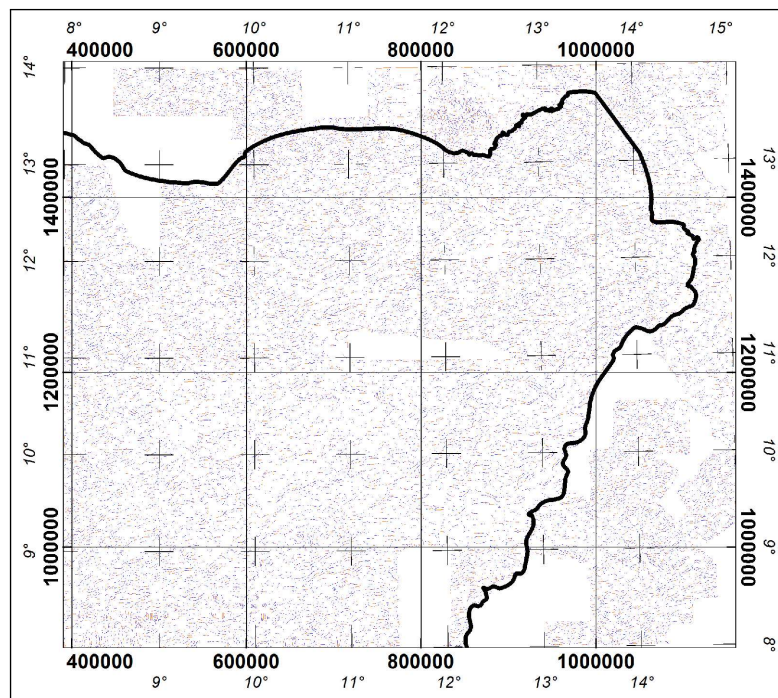


(b)  $HGM_{(\Delta T)}$

**Figure F.6:** Locations estimated from ASA and  $HGM_{(\Delta T)}$  maps of NE Nigeria, shown in figure 6.10). Locations represent local maxima of ASA or  $HGM_{(\Delta T)}$ .



(a) LW



(b)  $HGM_{(\theta)}$

**Figure F.7:** Locations estimated from LW and  $HGM_{(\theta)}$  maps of NE Nigeria, shown in figure 6.11). Locations represent local maxima of LW or  $HGM_{(\theta)}$ .

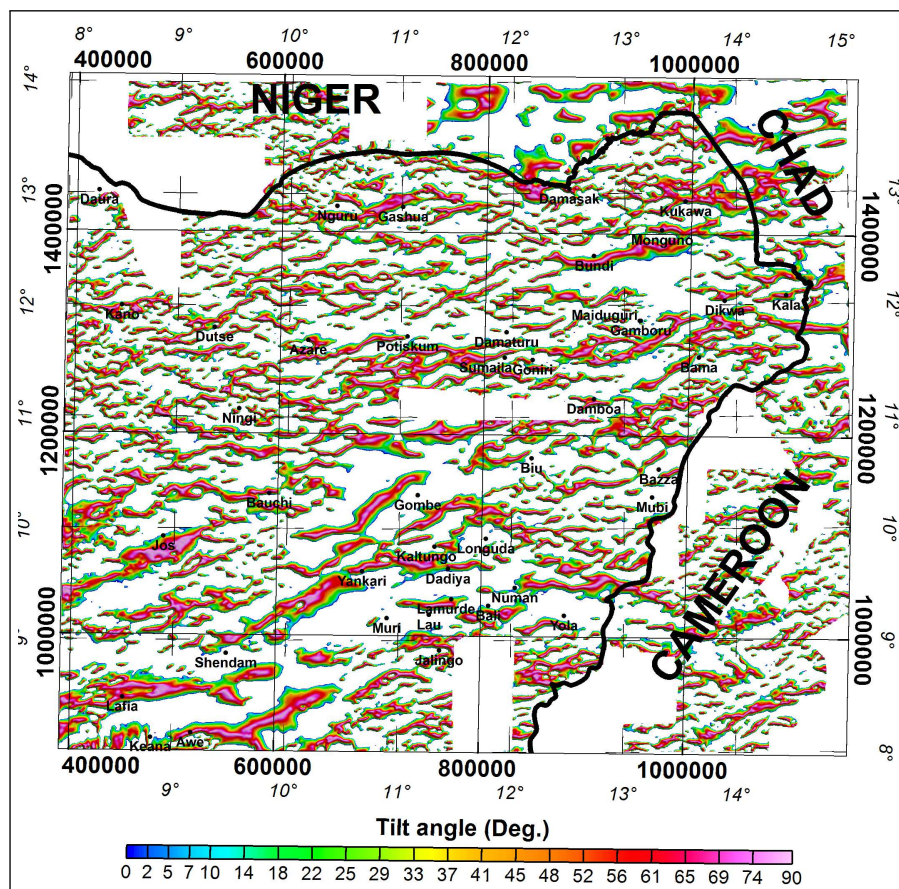
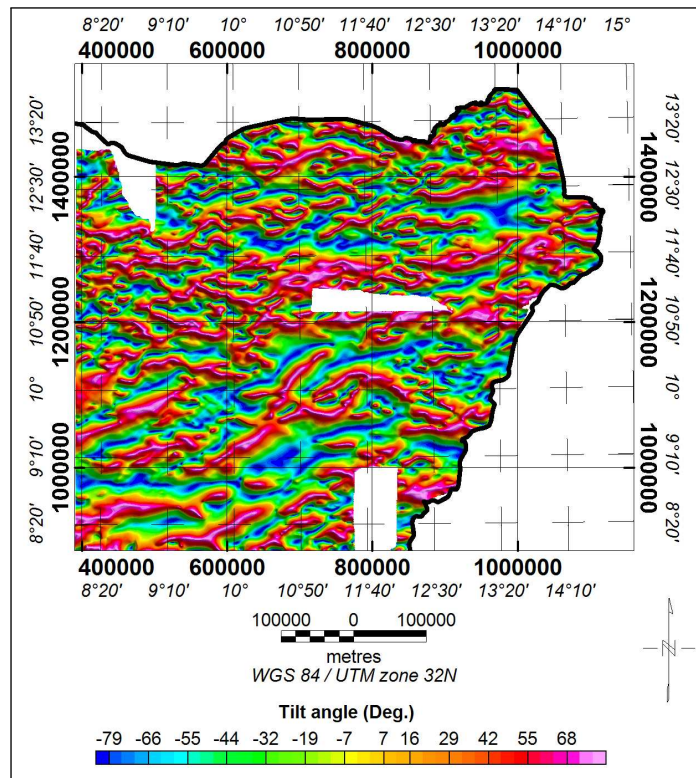
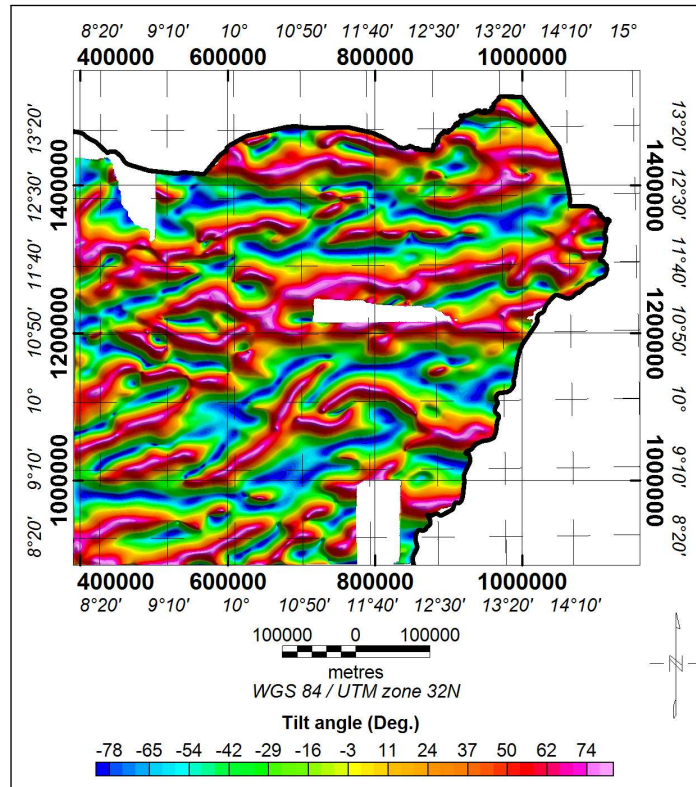


**Figure F.8:** Additive inverse ( $\times -1$ ) of  $\theta \geq 0$  map of NE Nigeria. Map was obtained from grid in figure 6.9b, by masking grid locations where  $\theta < 0$ , leaving only locations where possibly elevated basement (horsts or plutons) may occur.



(a) 5 km upward-continued.



(b) 8 km upward-continued.

**Figure F.9:** Additive inverse ( $\times -1$ ) of  $\theta$ -transformed 5 km (a) and 8 km (b) upward-continued NE Nigeria  $\Delta T$  (RTE) grid, derived from figure F.4.

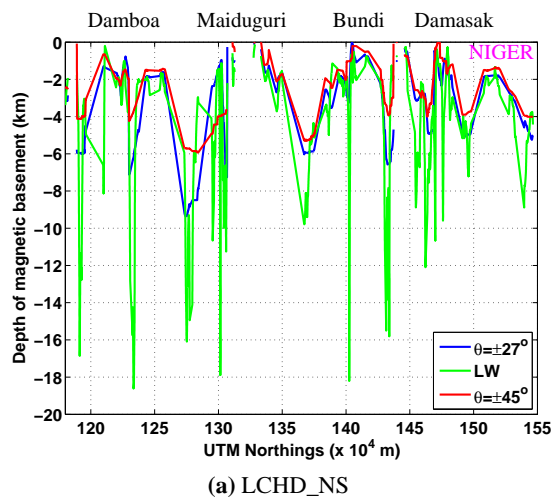


**Figure F.10:** North-South (NS) and East-West (WE) profiles showing the variations in depths estimated using local wavenumber (LW) and  $\theta = \pm 45$  and  $\theta = \pm 27$ -based “Tilt-Depth” methods from SouthWestern Chad basin, NE Nigeria. “Tilt-Depth” method profiles were extracted from figure 6.17, while LW method profiles were extracted from figure 6.16. Note the relative stability of “Tilt-Depth” method estimates. The locations and identities of these profiles were shown in figures 6.17 and 6.16. Cities/towns (Figure 6.15) close to profile locations are shown in black, while fuchsia-coloured labels indicate profile parts outside NE Nigeria.

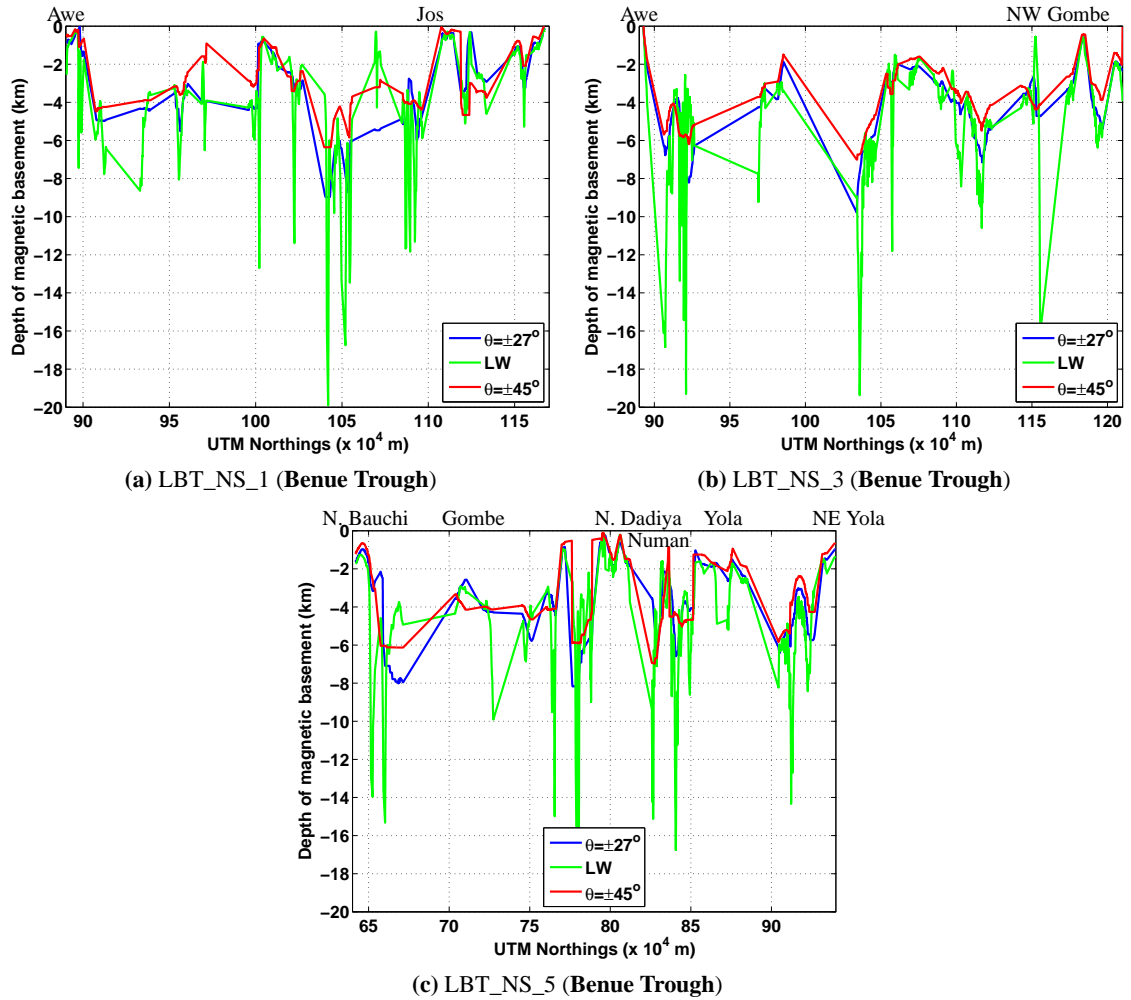


**Figure F.11:** North-South (NS) profiles showing variations in depths estimated using LW and  $\theta = \pm 45$  and  $\theta = \pm 27$ -based “Tilt-Depth” methods from Upper Benue Trough, NE Nigeria. “Tilt-Depth” method profiles were extracted from figure 6.17, while LW method profiles were extracted from figure 6.16. Note the relative stability of “Tilt-Depth” method estimates. The locations and identities of these profiles were shown in figures 6.17 and 6.16. Cities/towns (Figure 6.15) close to profile locations are shown in black.

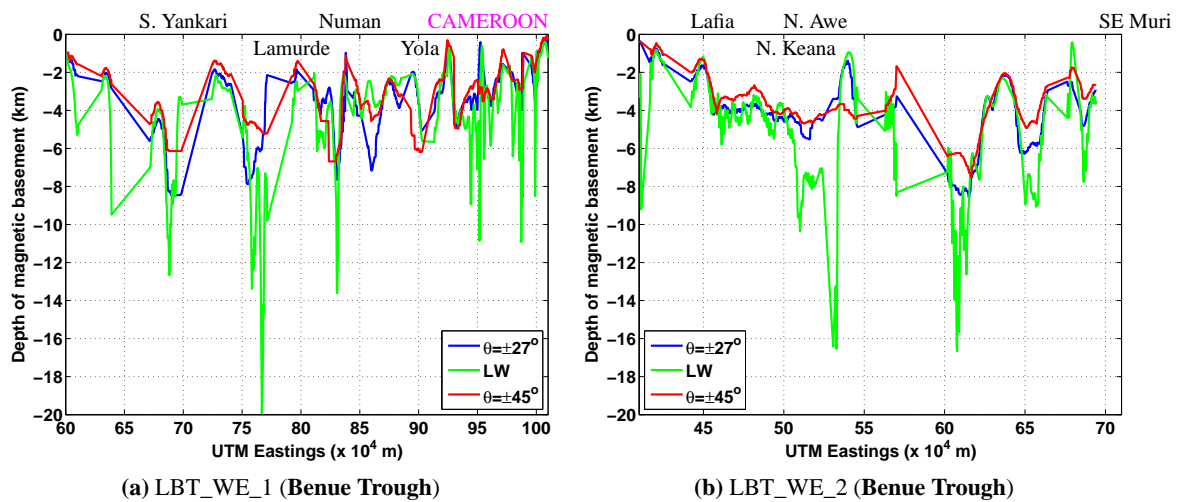


**Figure F.12:** East-West (E-W) profiles showing variations in depths estimated using LW and  $\theta = \pm 45$  and  $\theta = \pm 27$ -based “Tilt-Depth” methods from Upper Benue Trough, NE Nigeria. “Tilt-Depth” method profiles were extracted from figure 6.17, while LW method profiles were extracted from figure 6.16. Note the relative stability of “Tilt-Depth” method estimates. The locations and identities of these profiles were shown in figures 6.17 and 6.16. Cities/towns (Figure 6.15) close to profile locations are shown in black, while fuchsia-coloured labels indicate profile parts outside NE Nigeria.

## Appendix G

### Correspondences requesting more NE Nigeria datasets for constraint.

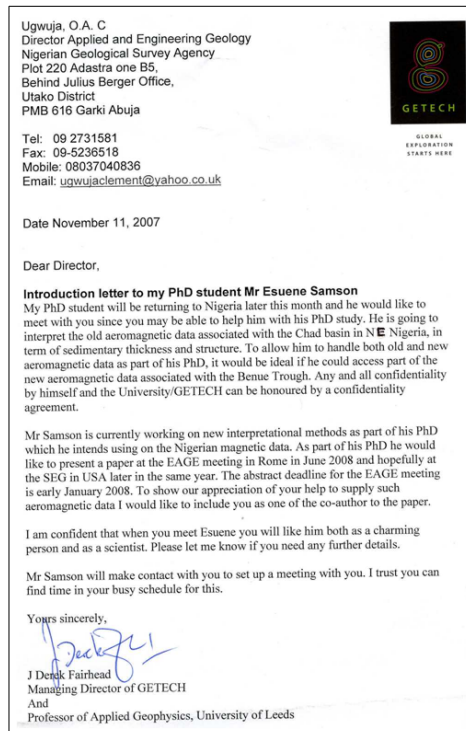


**Figure G.1:** Letter to a Nigerian government official requesting his assistance with the new aeromagnetic dataset from Nigeria (Chandler, 2010).

Prof JD Fairhead  
School of Earth and Environment  
University of Leeds  
LEEDS  
LS2 9JT  
Email [jdf@getech.com](mailto:jdf@getech.com)

C/o Jerry Heusel,  
Chevron

Date 3 Nov 2006

Dear Jerry,  
Letter to interested Oil companies

Mr Esuene Samson PhD study  
Provisional Title " A geophysical study of the Middle Benue and Chad Basins of Nigeria to determine their geological structure and evolution"

As supervisor to Mr Samson I wish to support his request for geophysical and geological data in addition to the gravity and magnetic data that GETECH can provide (Figure 1) for his PhD study. The study will not be restricted to just the Nigerian segments of the rift basins but will include parts of Cameroon, Chad and Niger for completeness. There are no plans for additional data acquisition but to maximise the use of available data.

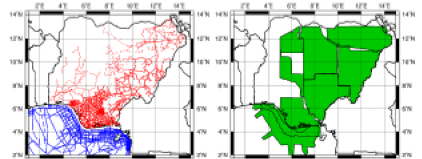


**Figure 1: Gravity and aeromagnetic coverage of Nigeria compiled by GETECH**

The data sets being sort includes:

**Gravity Data:** Some years ago several Oil companies carried out detailed gravity surveys of the Middle Benue. The companies included to my knowledge Chevron and Total but the third company I cannot remember. These data are important to include in the study due to their spatial coverage and the availability of new high resolution aeromagnetic data over the same area (see below).

**Aeromagnetic Data:** In addition to the aeromagnetic data shown above new higher resolution aeromagnetic data have been collected by Fugro for The Ministry of Solid Minerals Development (see Figure 2). Access to Block C is of interest here. It may be

(a) Page 1



**Figure 2: High resolution aeromagnetic coverage completed with Block C highlighted**

that access to this new data, promised for 2007, will be more easily obtained by oil companies working in Nigeria than by a Nigerian PhD student studying in the UK. I believe oil companies will be basically invested in such data and will want to access it as soon as it is available.

**Seismic and Well Data:** Limited seismic and well data does exist for the Middle Benue and Chad basin of Nigeria but accessing it may be difficult. Oil companies may already hold such data and it may be easily to access through you than the Ministry.

**Plan of Oil Company involvement**

Subject to one or more oil companies contributing data to the PhD study on an open access or confidentiality basis, the companies will be kept informed on the progress of the study by the student presenting a progress and final report. Such presentation can be to the group or individually, subject to shared travel/subsistence funds being provided by the companies involved.

Finally I consider this integrated geophysical study is worth while for the PhD student to be involved in, since it will involve developing and refining depth estimation methods to map basement as well as trying to understand a multi phase evolution process of rifting. I will be his supervisor and colleagues within GETECH also have experience and knowledge of the region to ensure more than adequate supervision of the study. The University, the student and I (University/GETECH) are able to enter into any necessary data confidentiality conditions required.

I trust you are able to support such a study and look forward to hearing from you.

Yours Sincerely,  
*(due to being on the road in Asia /Australia, I cannot sign this letter)*

J Derek Fairhead  
Prof of Applied Geophysics  
University of Leeds  
(CEO of GETECH Group plc)  
Attachments: Letter and documents relating to the Student

(b) Page 2

**Figure G.2:** Letter to a Chevron Inc, USA official requesting his assistance with additional geological and geophysical dataset from NE Nigeria and neighbouring regions. Similar letters were also sent to Total and Shell.

## Appendix H

Magnified, and/or more annotated, versions of some NE Nigeria-wide figures presented in chapter 6.

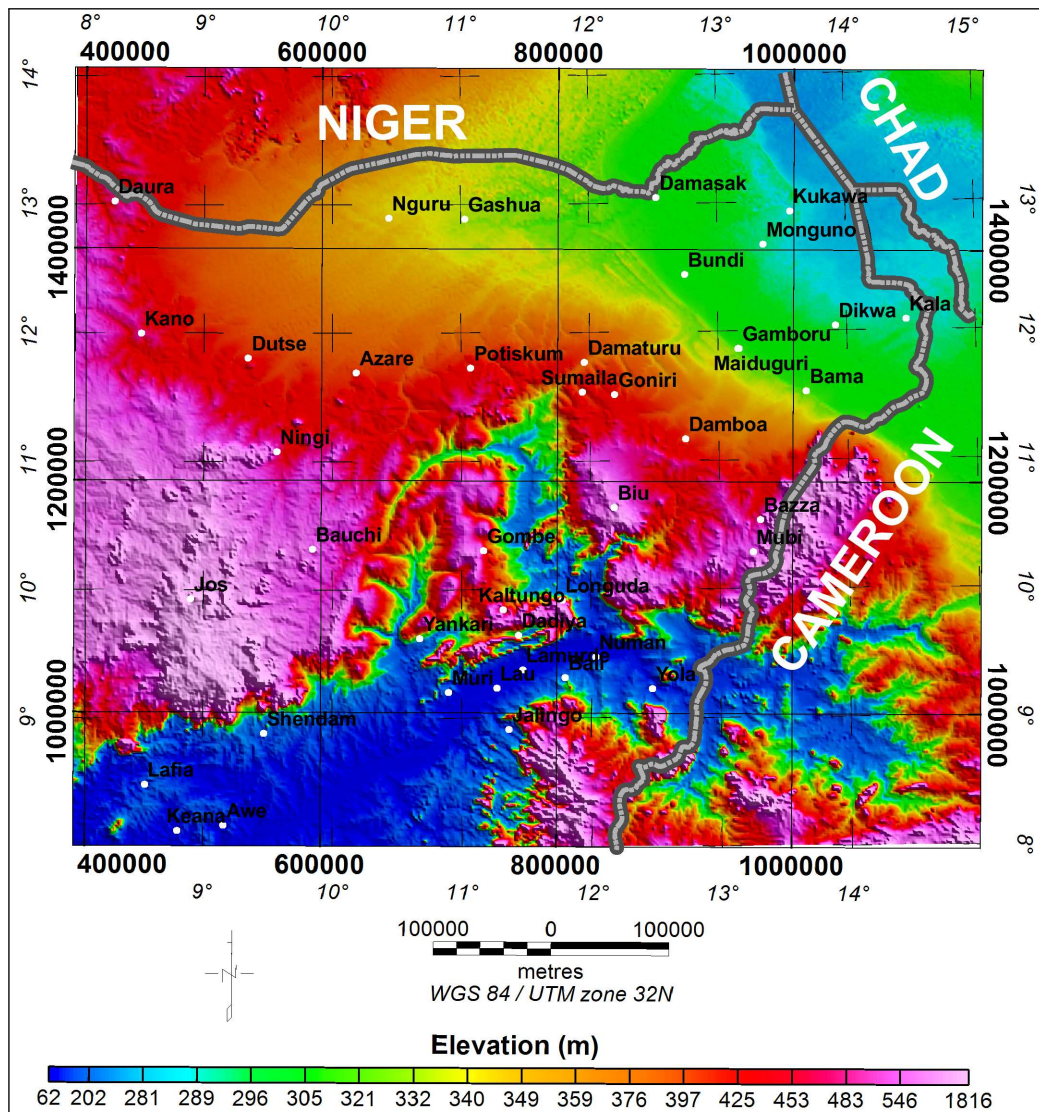


Figure H.1: Topography of NorthEastern Nigeria (Figure 6.1b).

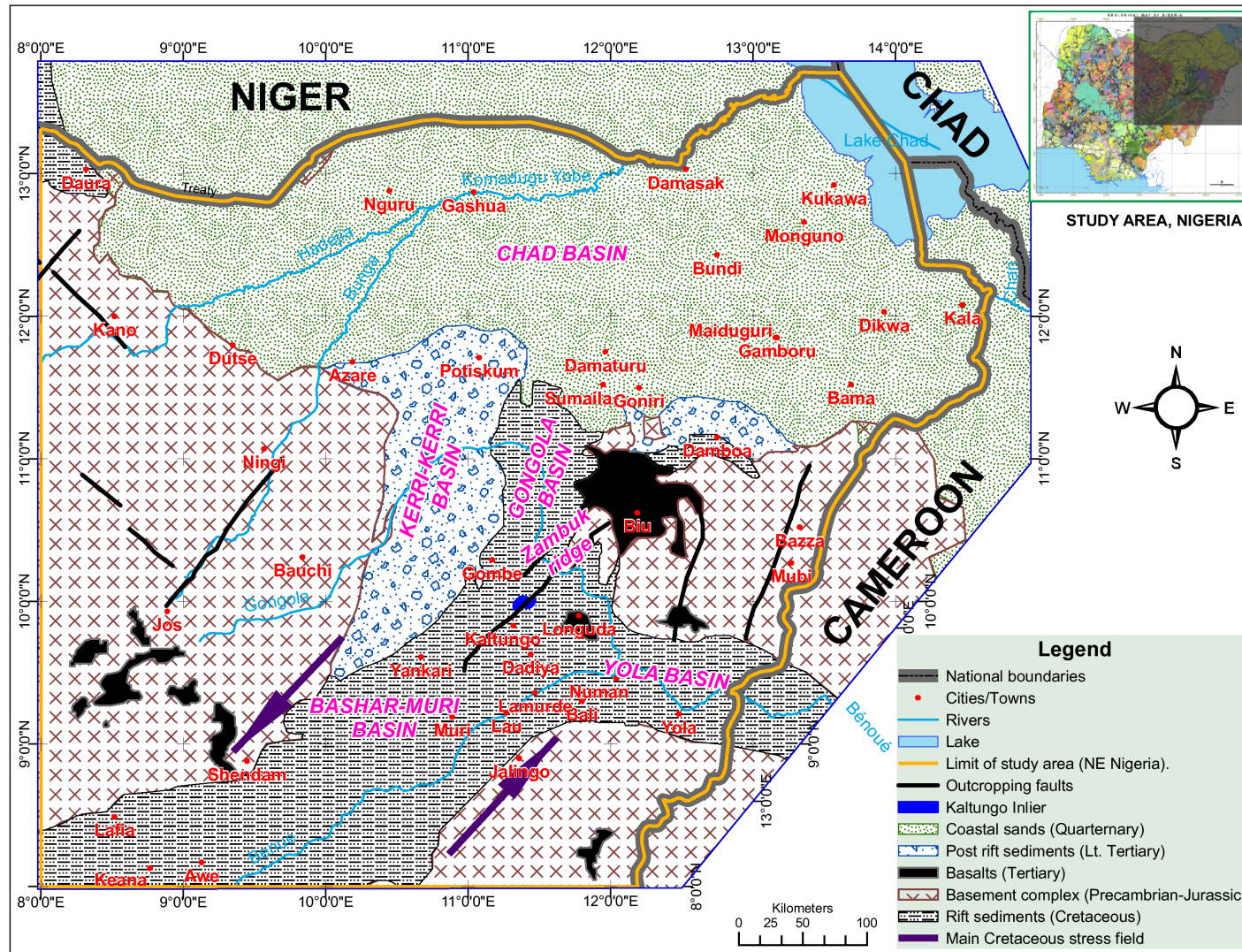


Figure H.2: Simplified geological map of NorthEastern Nigeria (Figure 6.2).

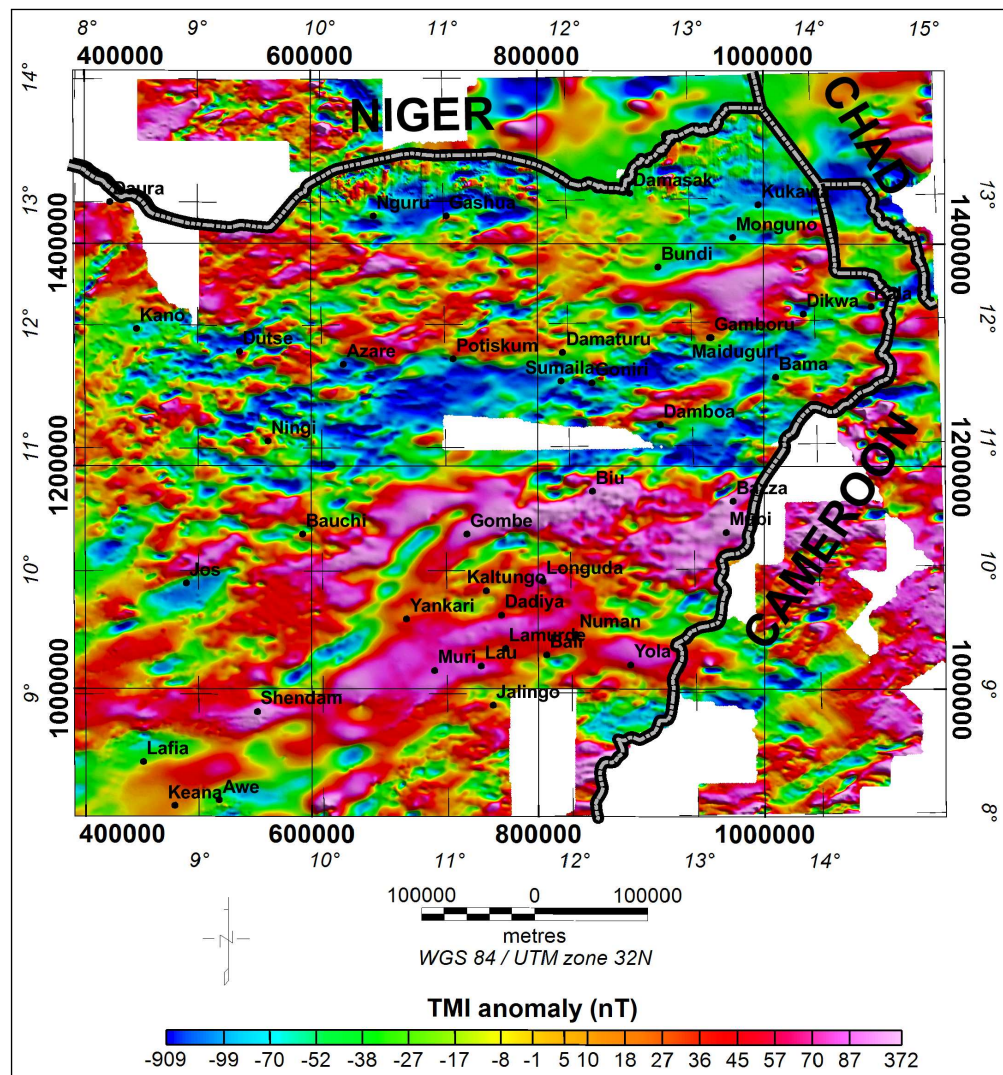


Figure H.3: NE Nigeria  $\Delta T$  dataset (Figure 6.4).

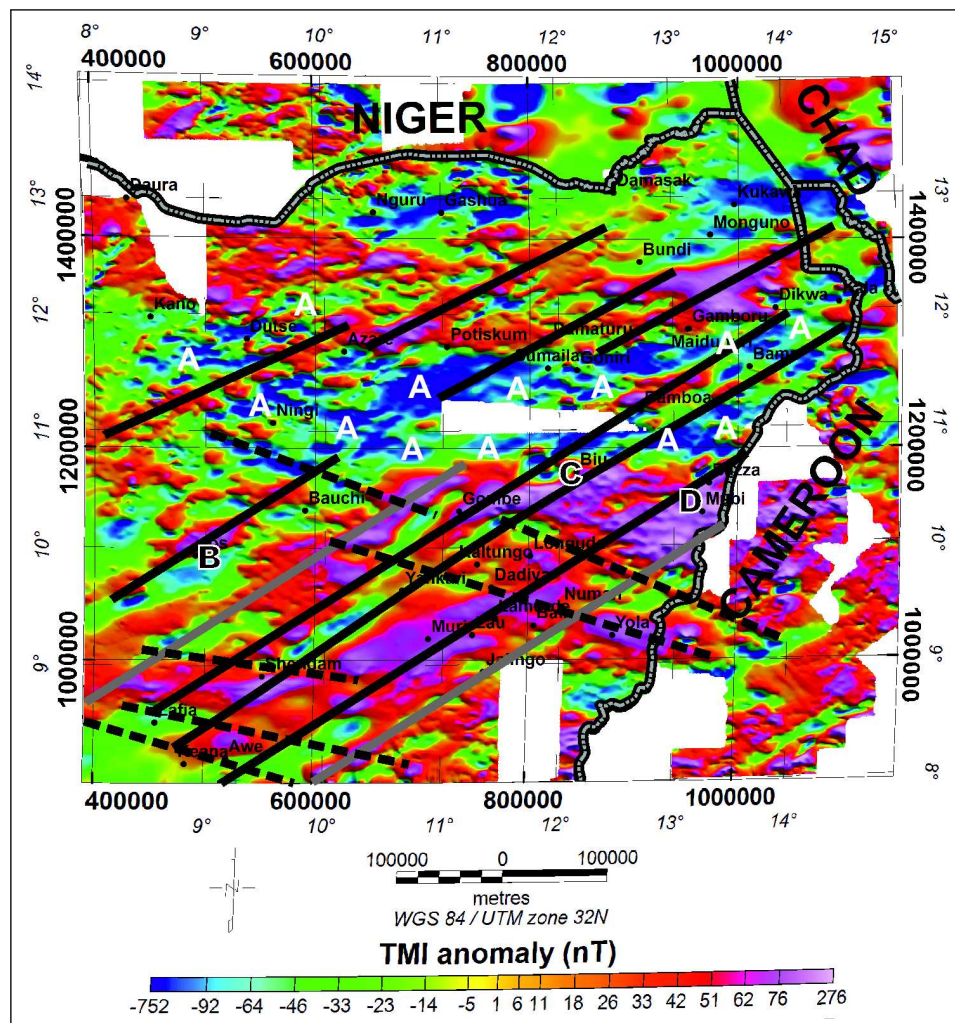
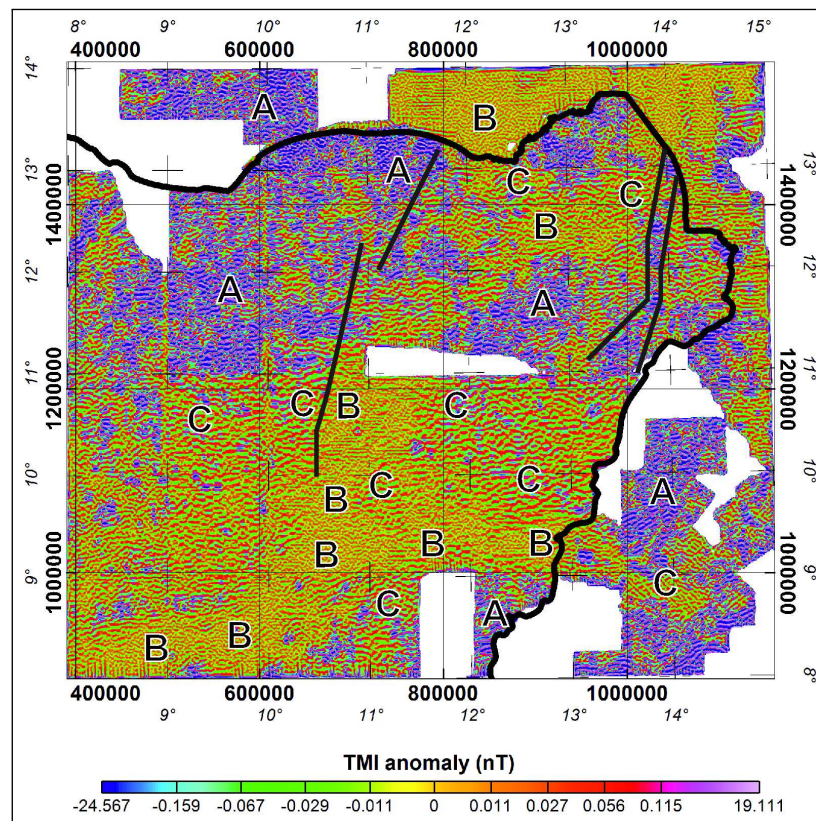
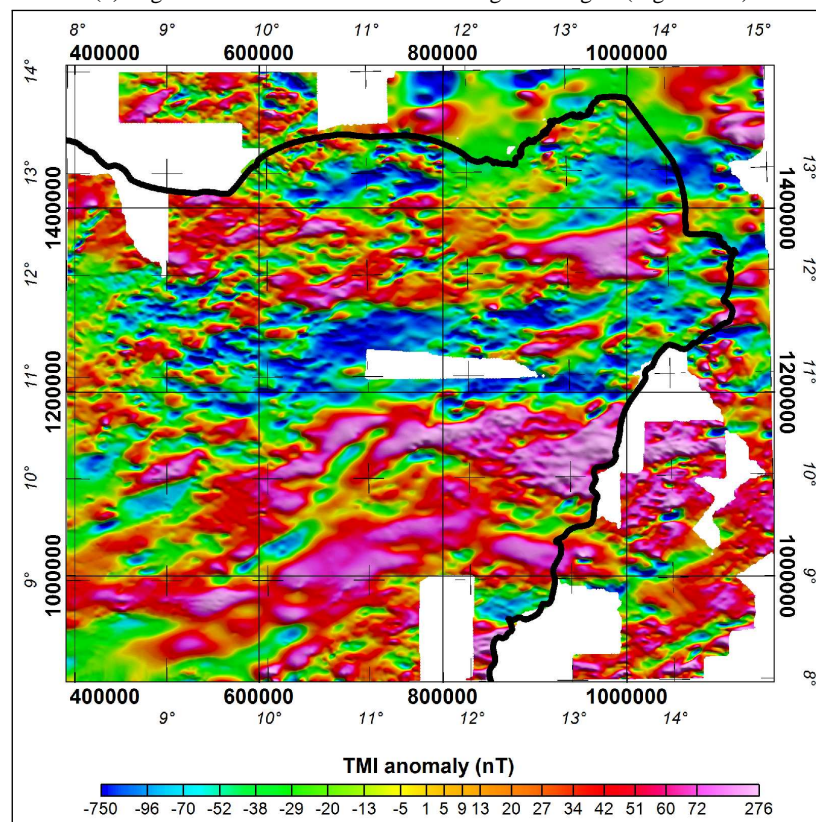


Figure H.4: RTE of NE Nigeria  $\Delta T$  grid (Figure 6.6).



(a) High-Pass Butterworth-filtered NE Nigeria  $\Delta T$  grid (Figure 6.7a).



(b) Low-Pass Butterworth-filtered NE Nigeria  $\Delta T$  grid (Figure 6.7b).

**Figure H.5:** 3<sup>rd</sup>-order Butterworth-filtered versions of NE Nigeria (RTE) grid shown in figure 6.7. Black lines trace near-N-S striking SVD anomaly trends, while the letters A, B and C represent subdivisions of the basement into shallow, deep or intermediate, respectively, on the basis of  $F_{amp}$  (See section 6.3.1).

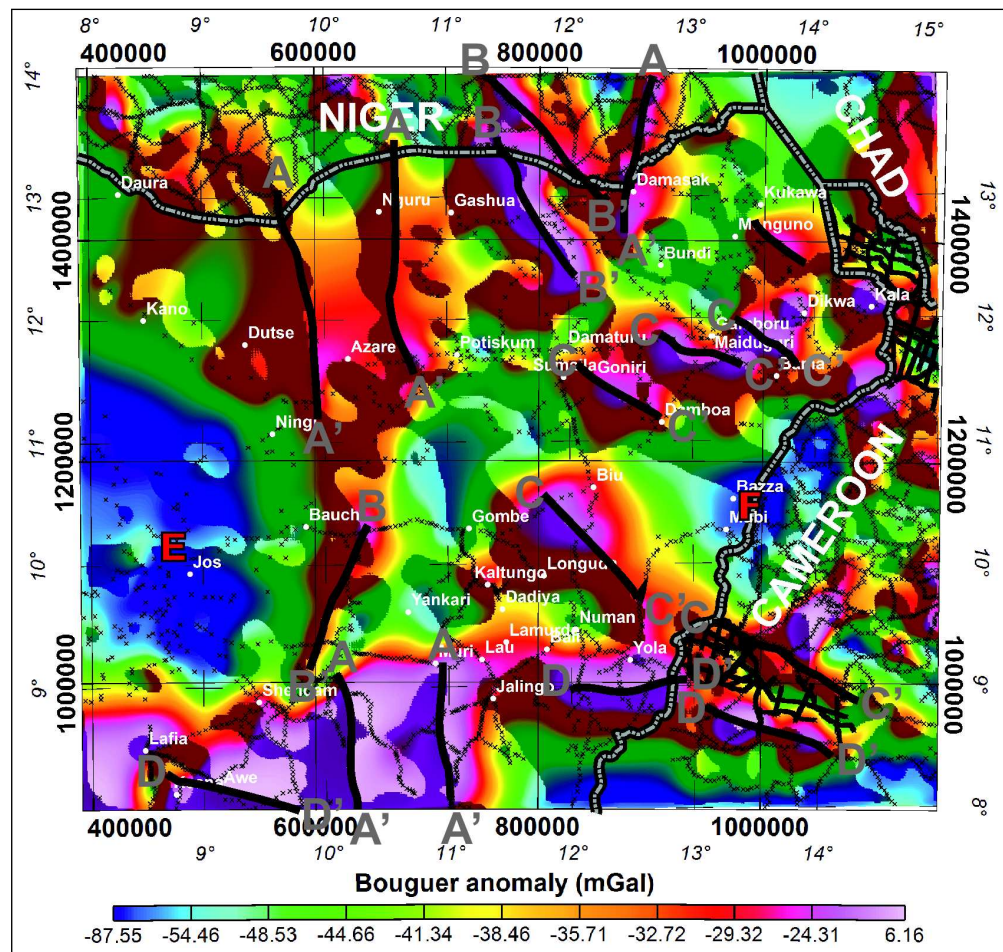
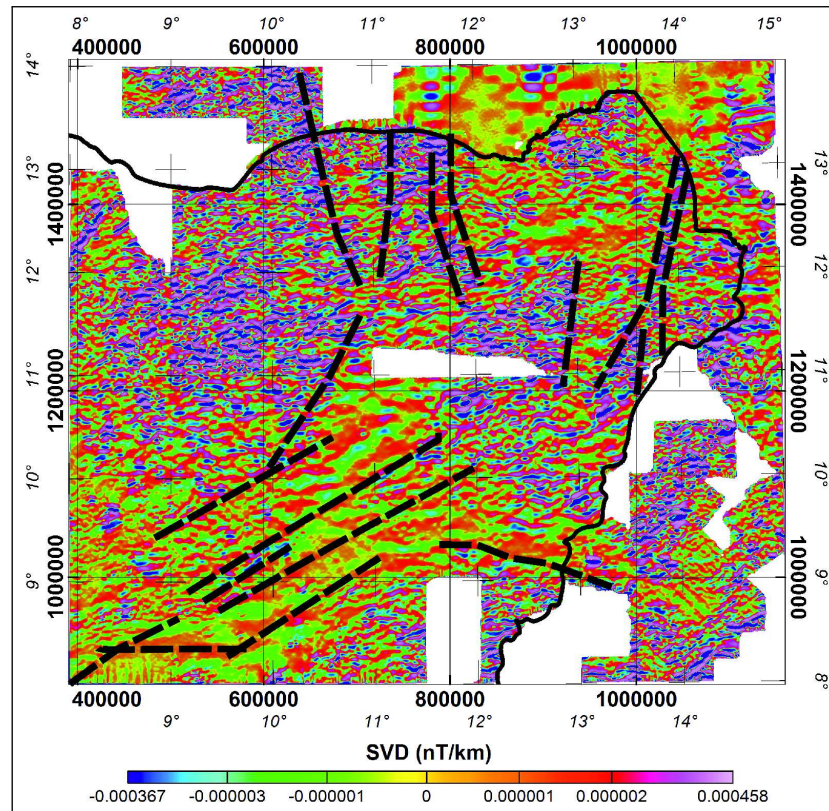
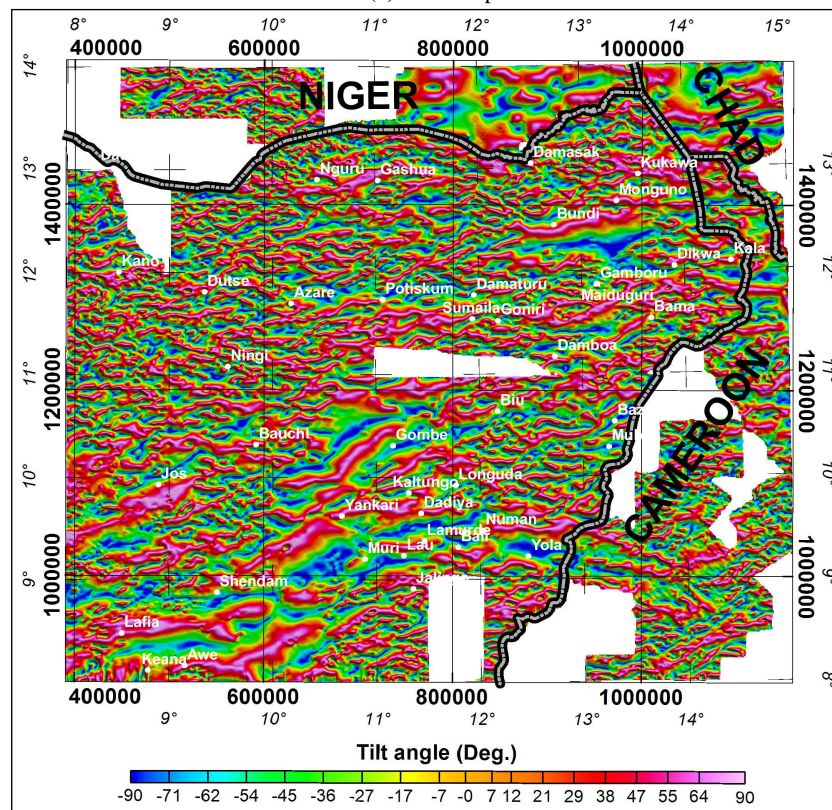


**Figure H.6:** Bouguer gravity anomaly (BA) grid shown in figure 6.8. Trends of linear short wavelength BA of positive or negative amplitude are shown (in black) and labelled (in grey). Note that isolated three-dimensional (3D) anomalies (labelled E and F, in red) also occur.

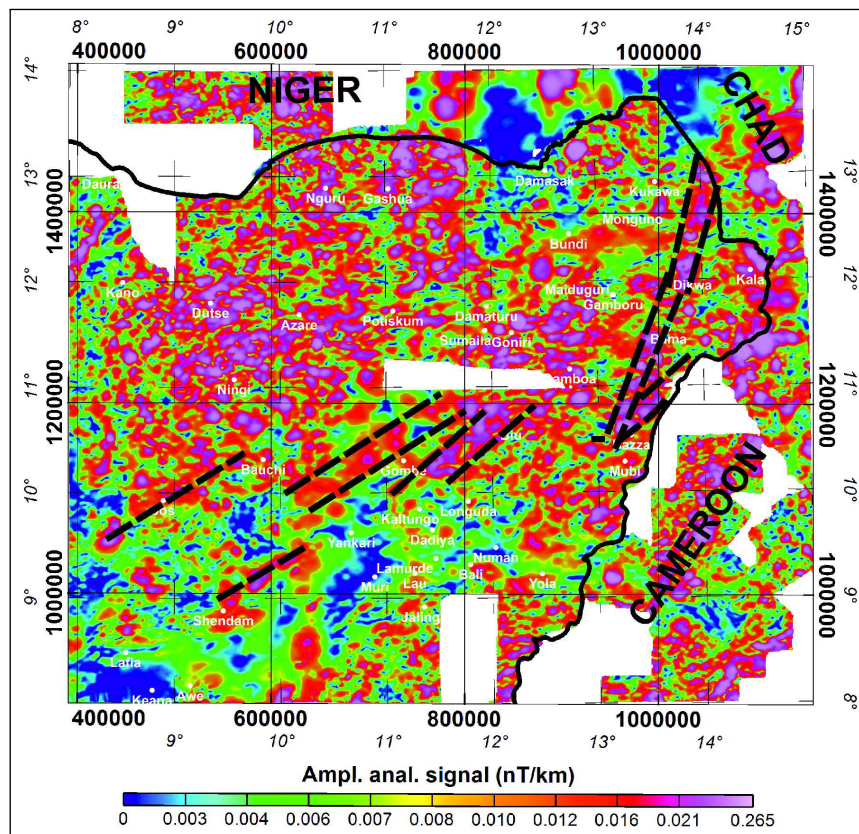


(a) SVD map

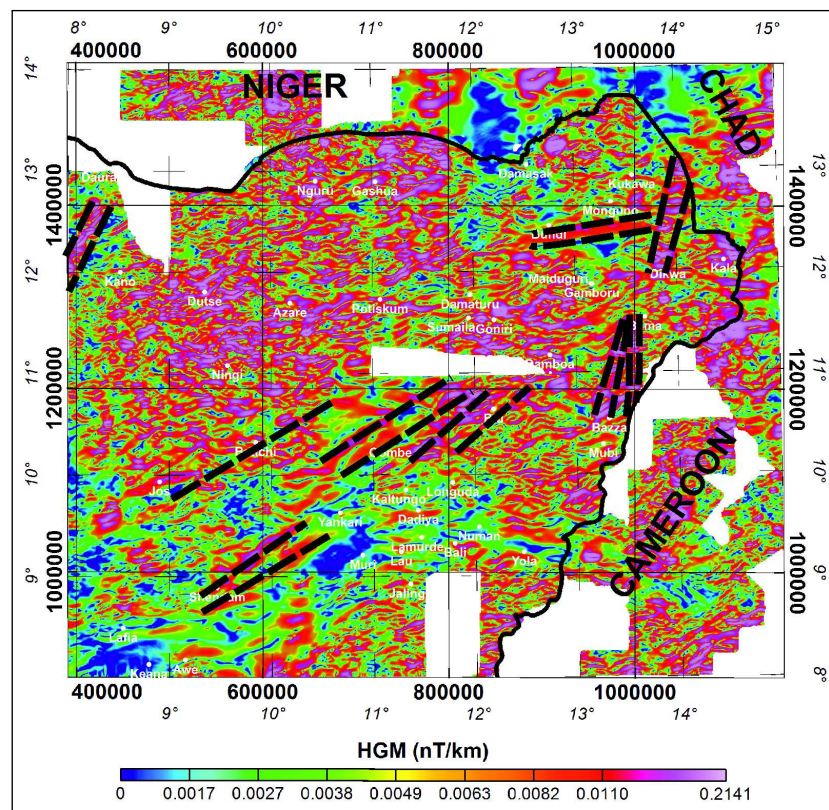


(b)  $\theta$  map

Figure H.7: SVD and  $\theta$  maps shown in figure 6.9. Black dashed lines trace anomaly trends.

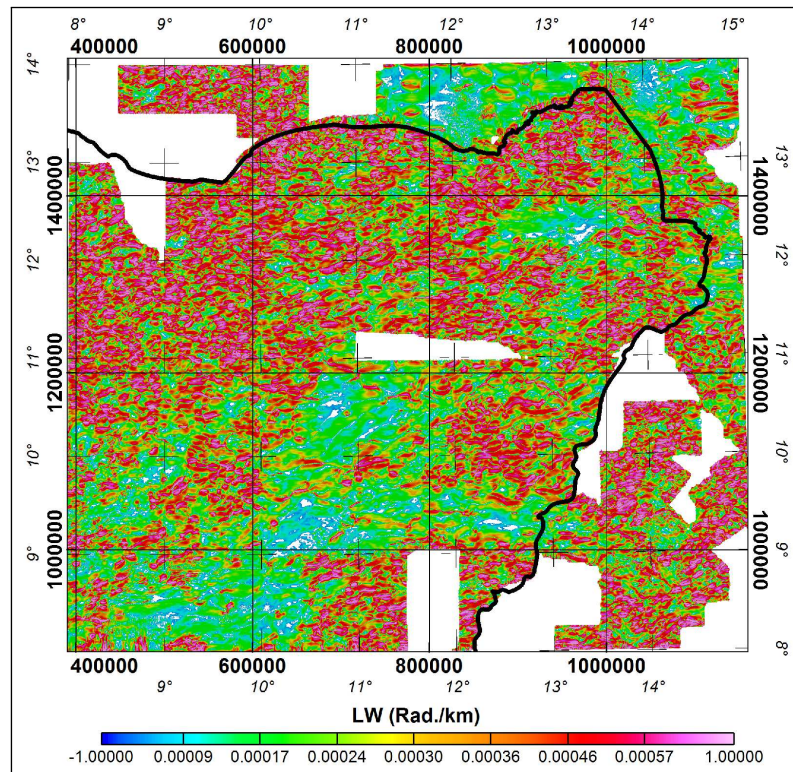


(a) ASA map

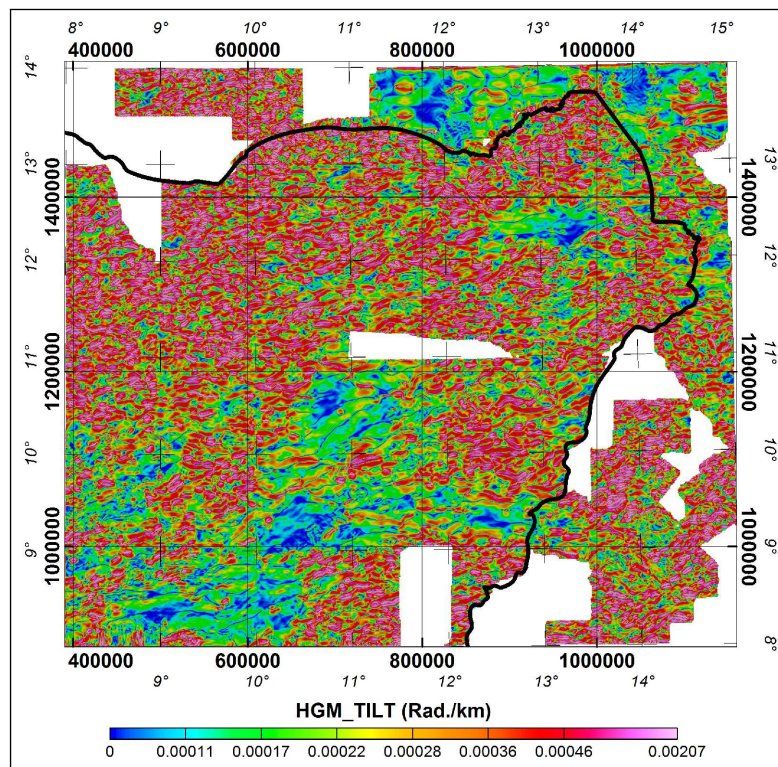


(b)  $HGM_{(\Delta T)}$  map

**Figure H.8:** ASA and  $HGM_{(\Delta T)}$  maps shown in figure 6.10. Black dashed lines on maps trace ASA and  $HGM_{(\Delta T)}$  anomaly trends.



(a) LW map



(b) HGM<sub>(θ)</sub> map

Figure H.9: LW and HGM<sub>(θ)</sub> maps shown in figure 6.11.

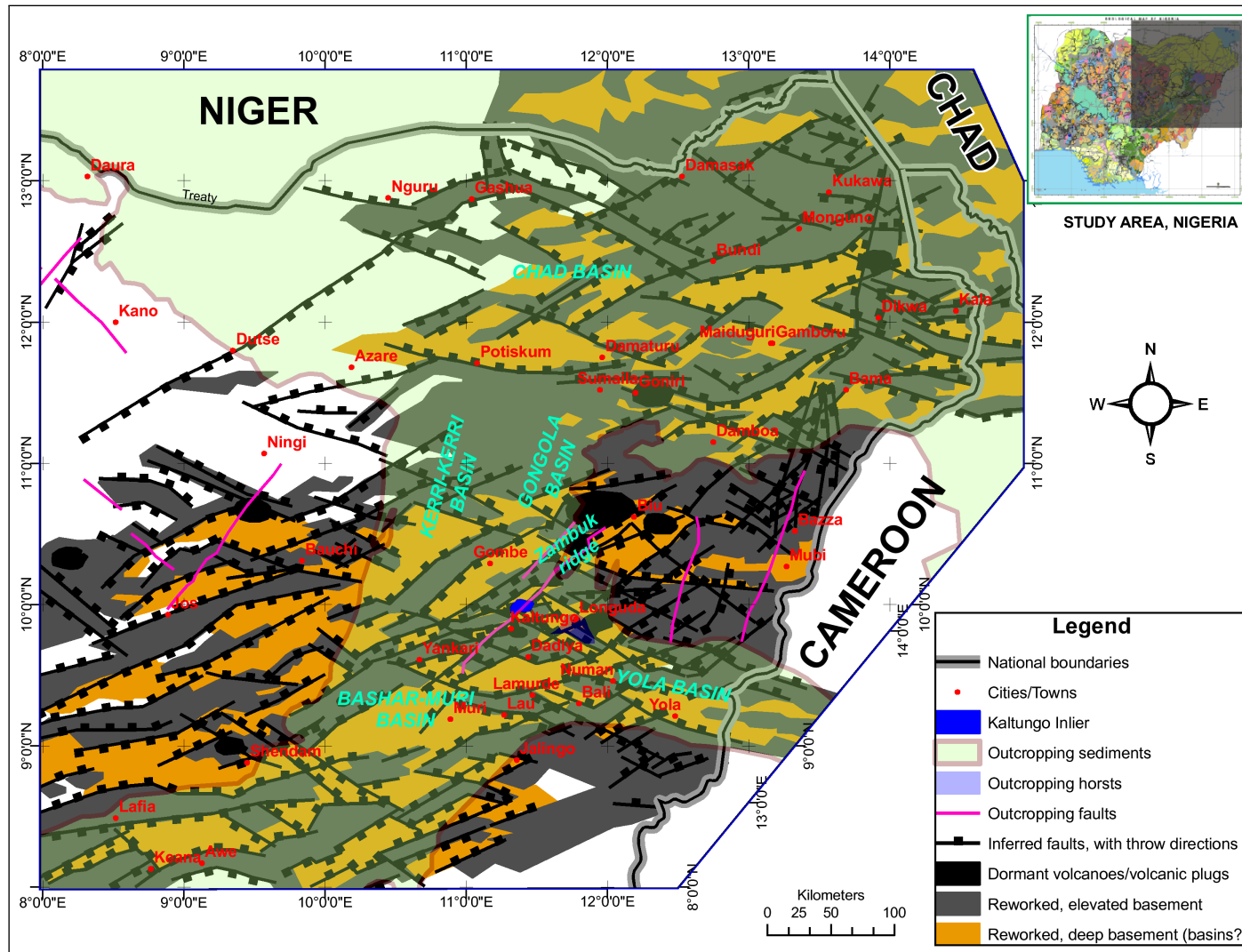
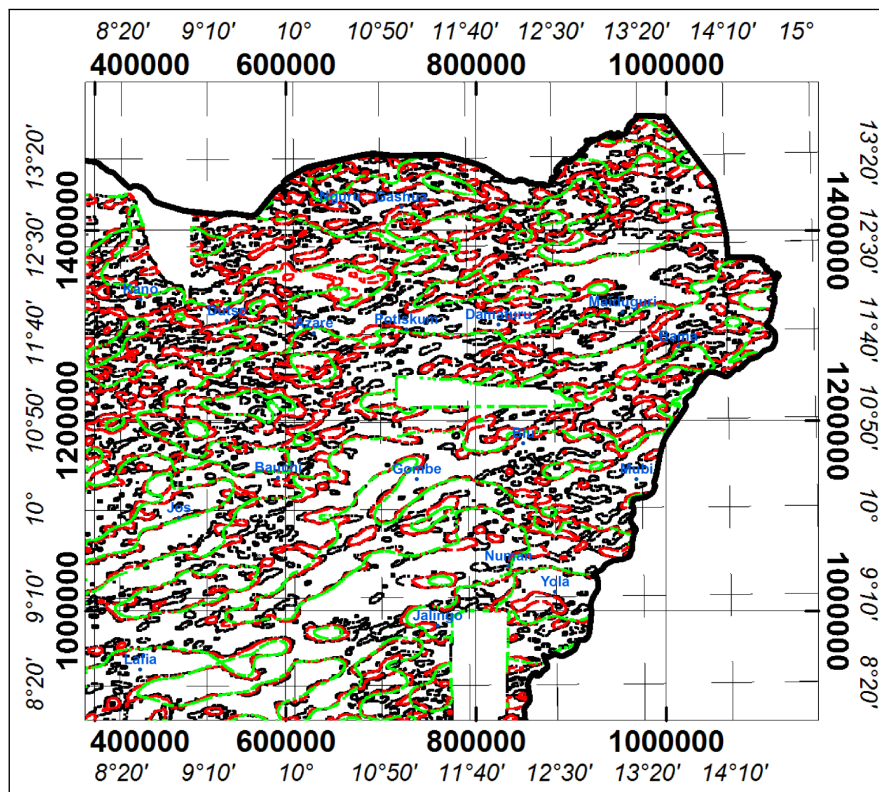
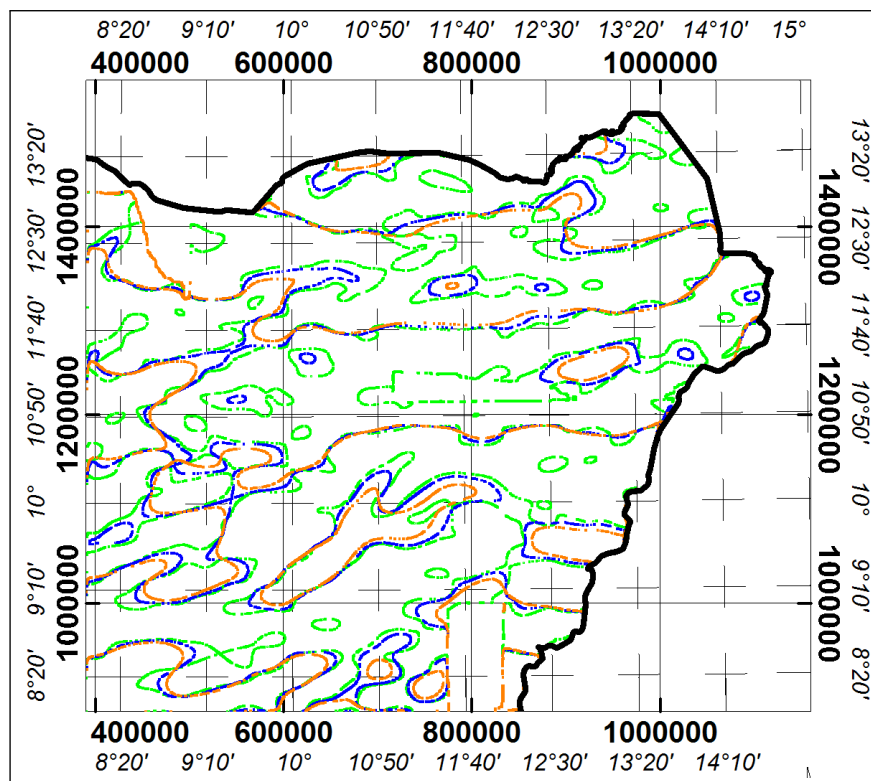


Figure H.10: Gross magnetic basement structure map of NE Nigeria (Figure 6.12).



(a)  $\theta=0^\circ$  contours: 1, 5 and 8 km upward-continued (Figure 6.14a).



(b)  $\theta=0^\circ$  contours: 8, 20 and 30 km upward-continued (Figure 6.14b).

**Figure H.11:** Maps showing the spread of  $\theta = 0$  contours of variously upward-continued NE Nigeria (RTE) dataset shown in figure 6.14.

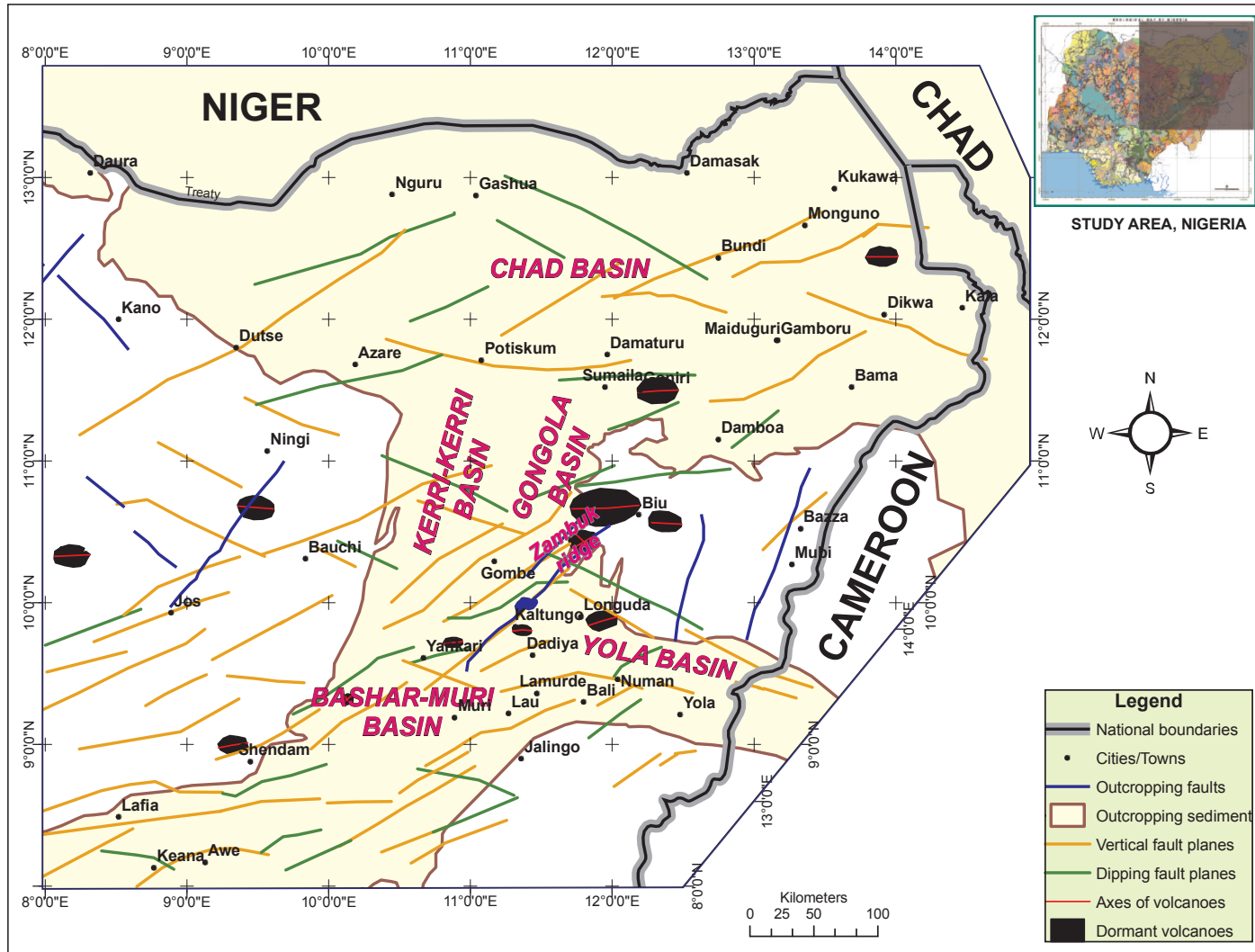


Figure H.12: Attitude of prominent faults and volcanic features in NE Nigeria basement (Figure 6.15).

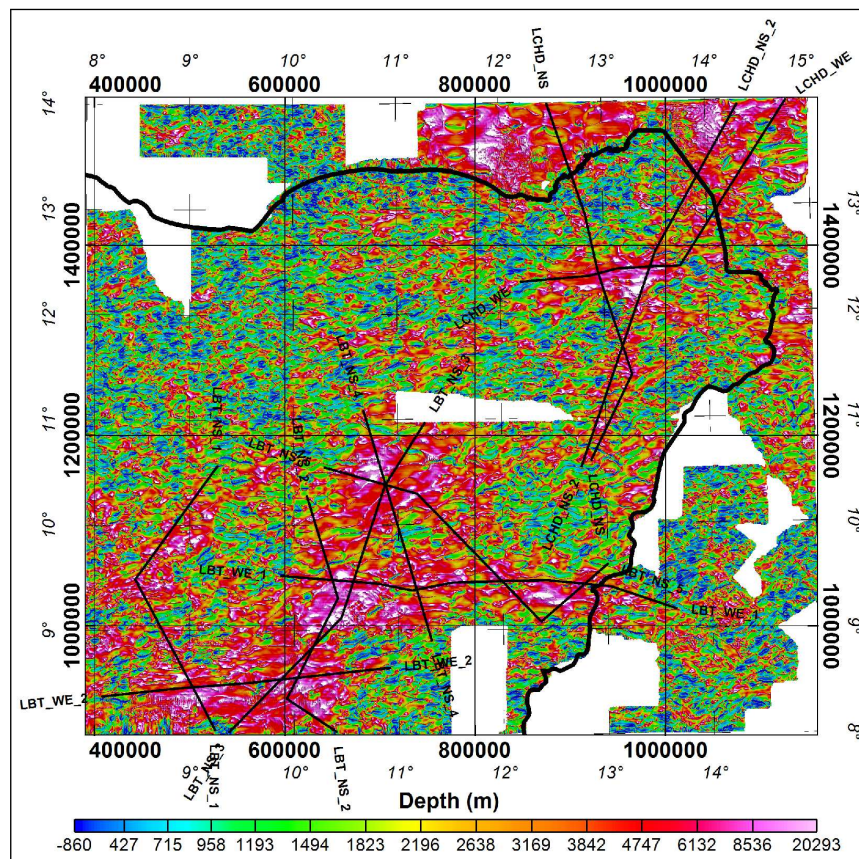
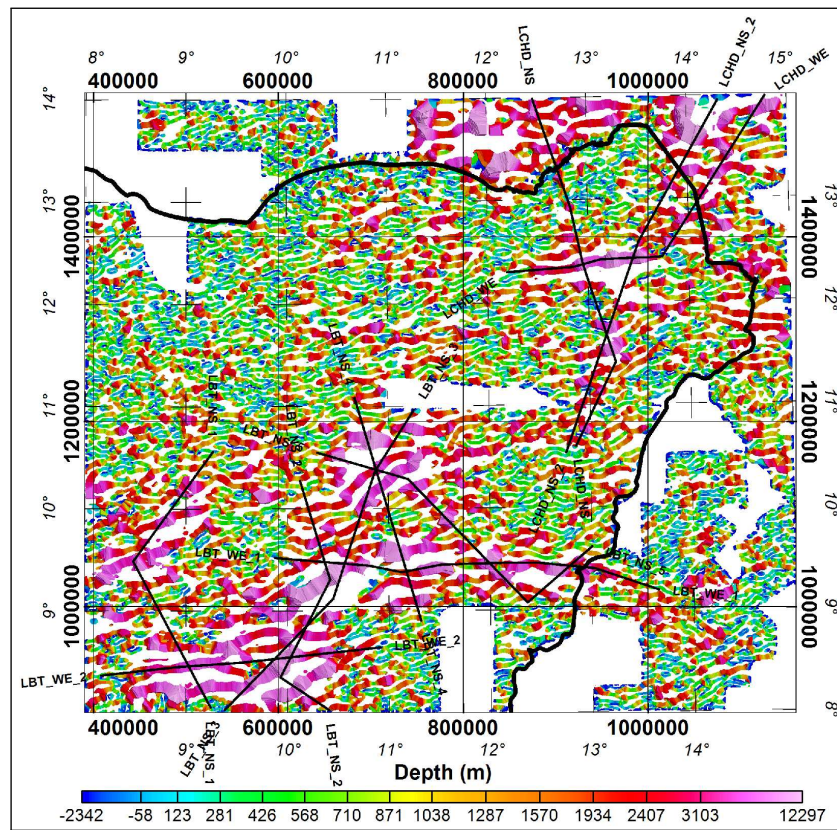
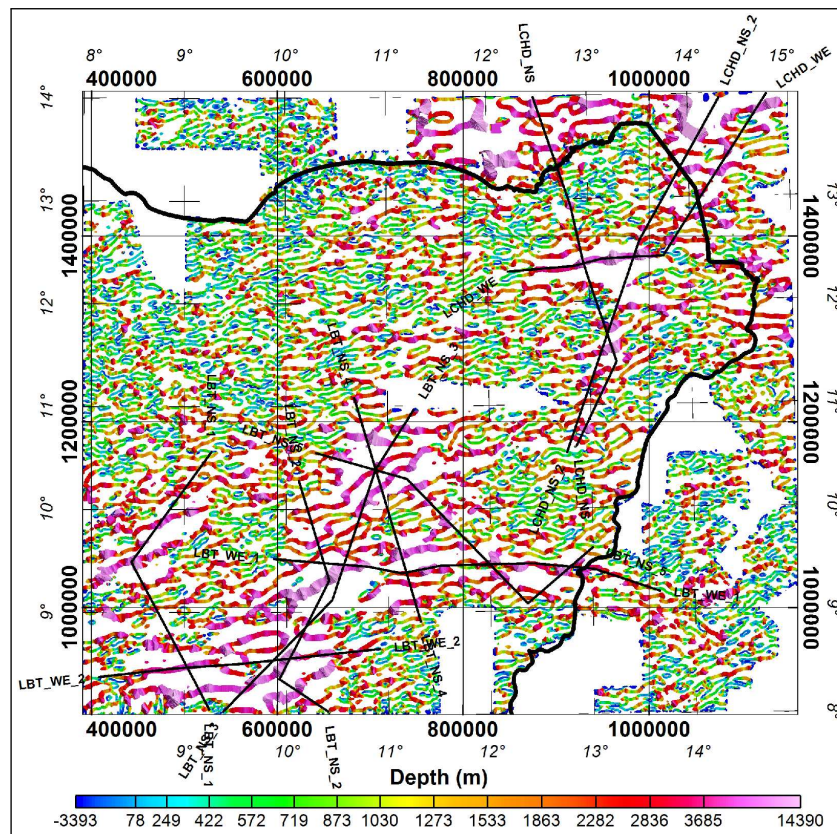


Figure H.13: Local wavenumber (LW) method depth estimates shown in figure 6.16.



(a)  $\theta = \pm 45$  range.



(b)  $\theta = \pm 27$  range.

Figure H.14: “Tilt-Depth” method depth estimates previously shown in figure 6.17.

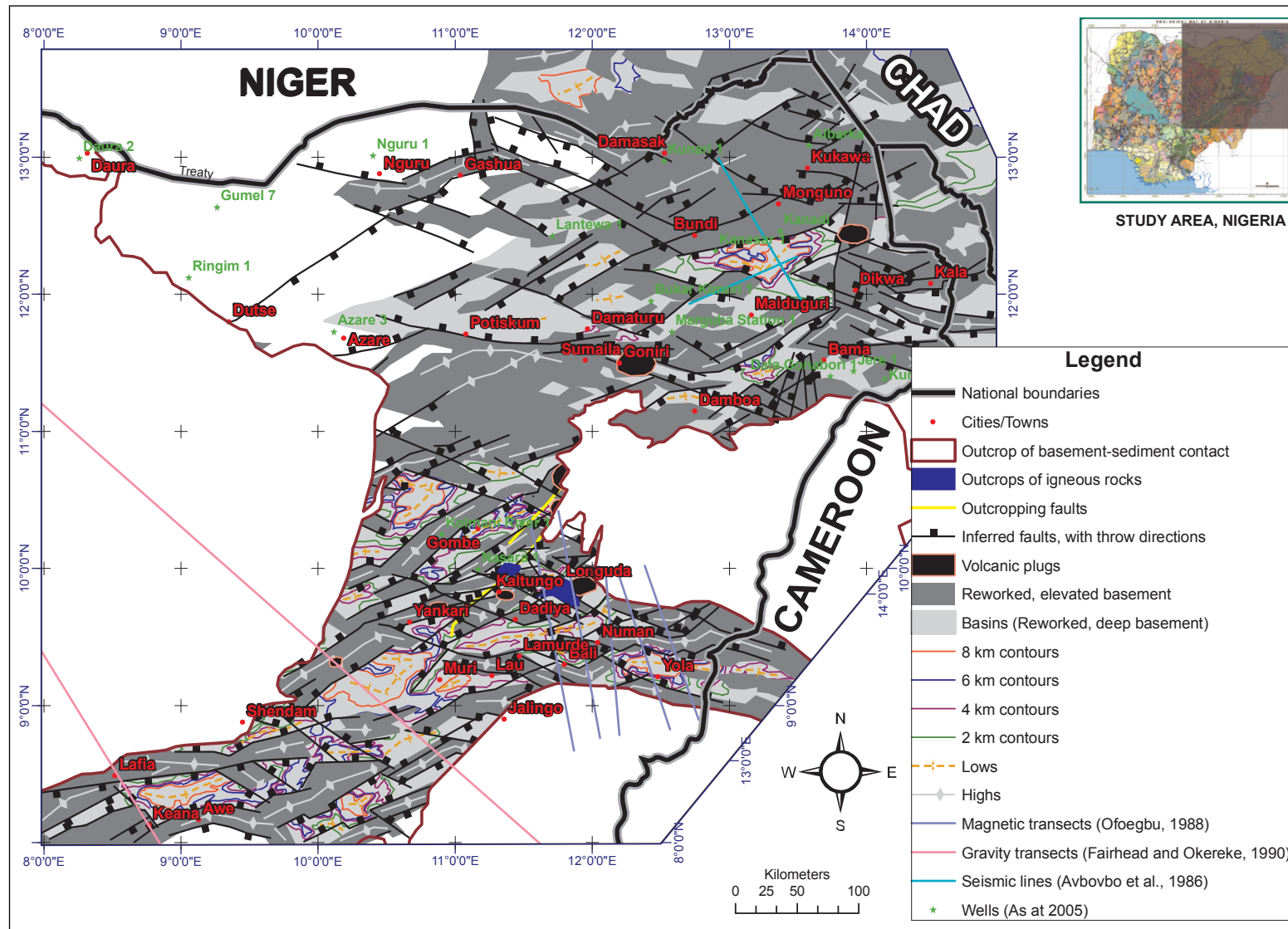
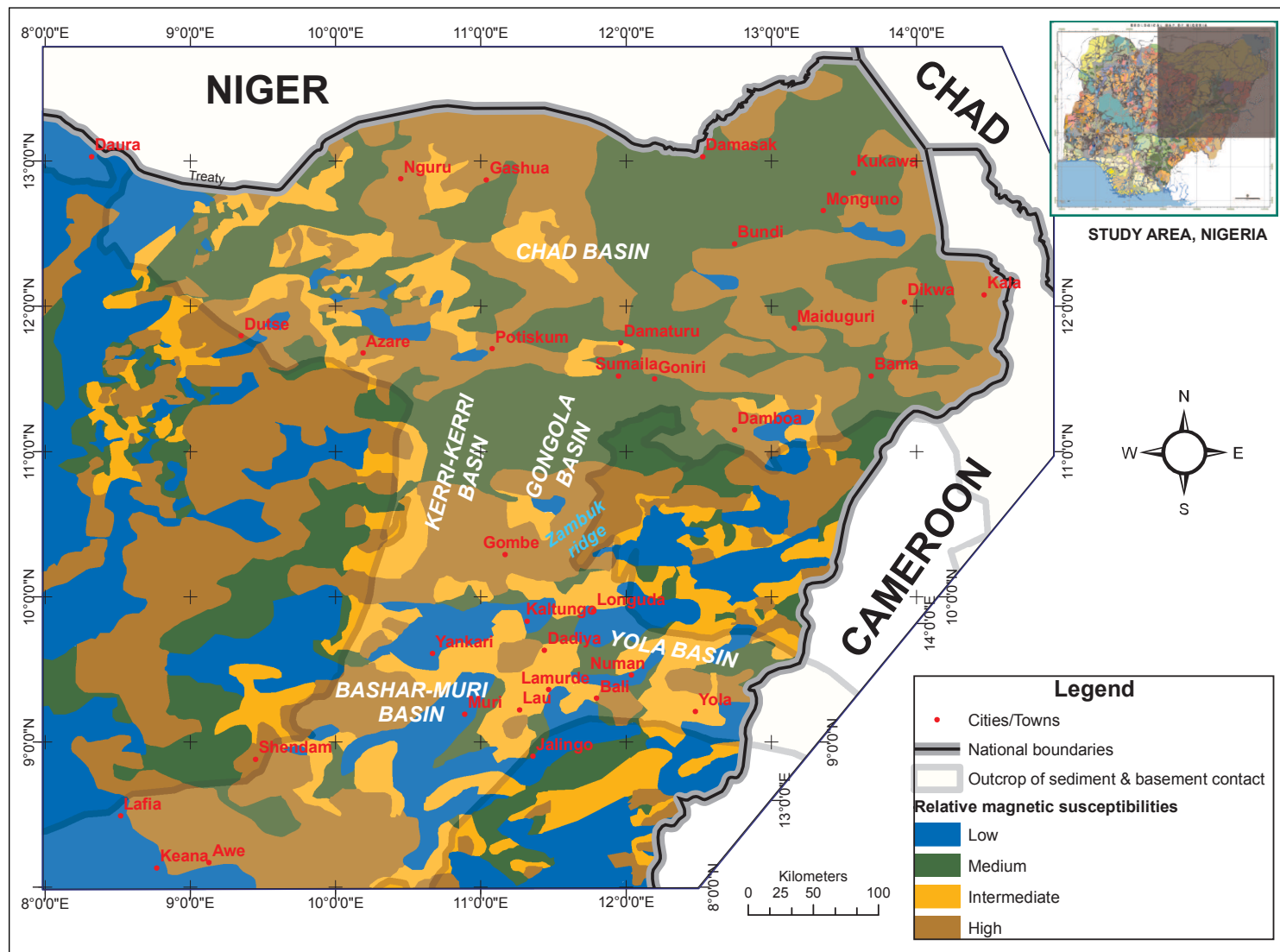
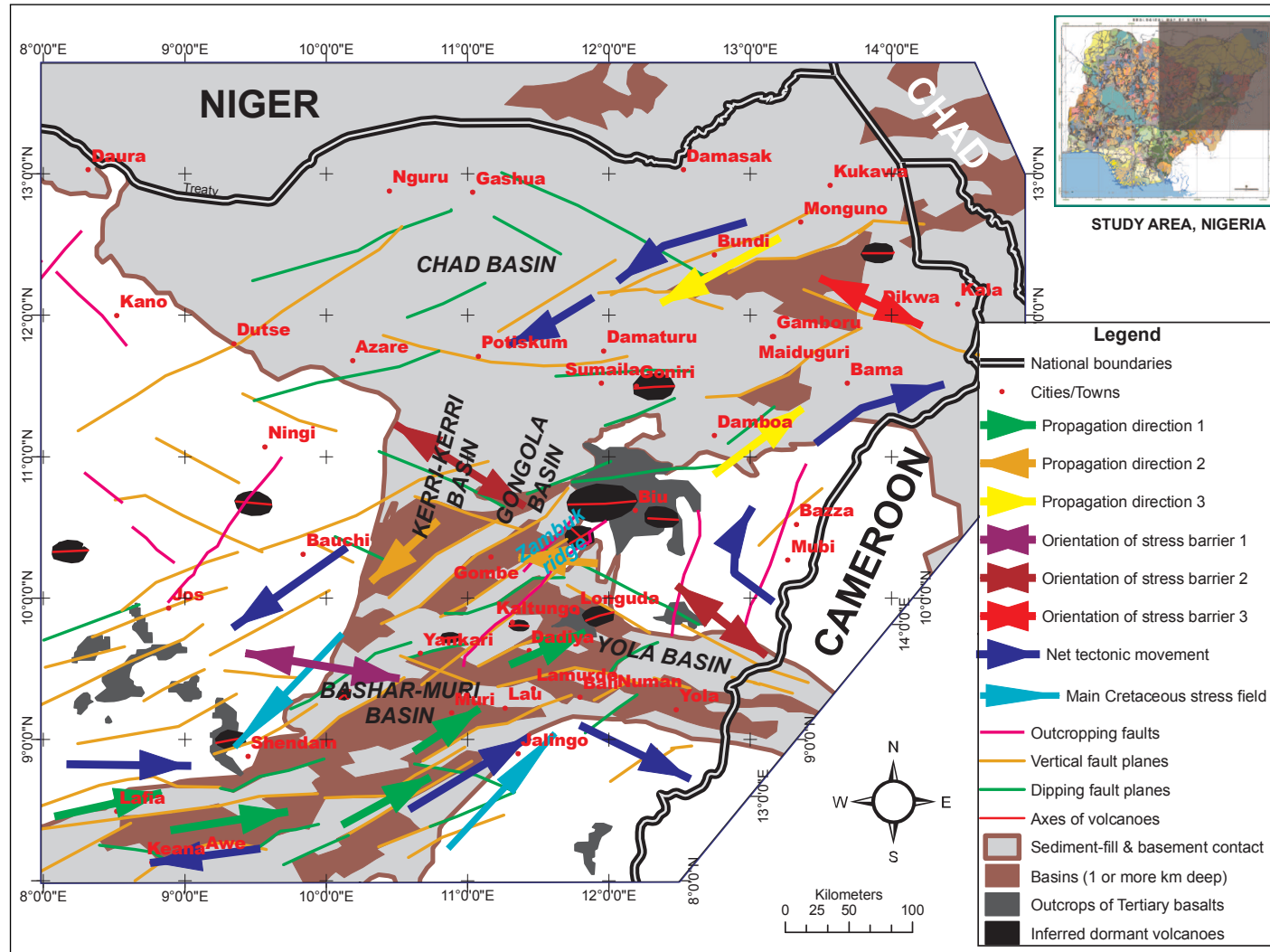


Figure H.15: Depth-structure map of sedimentary basin area of NE Nigeria showing the major depositional centers and horst structures (Figure 6.19).



**Figure H.16:** Relative magnetic susceptibility distribution map of NE Nigeria basement shown in figure 6.21.



**Figure H.17:** Inferred directions of propagation of the Benue rift and Mesozoic tectonism in study area (Figure 7.1).